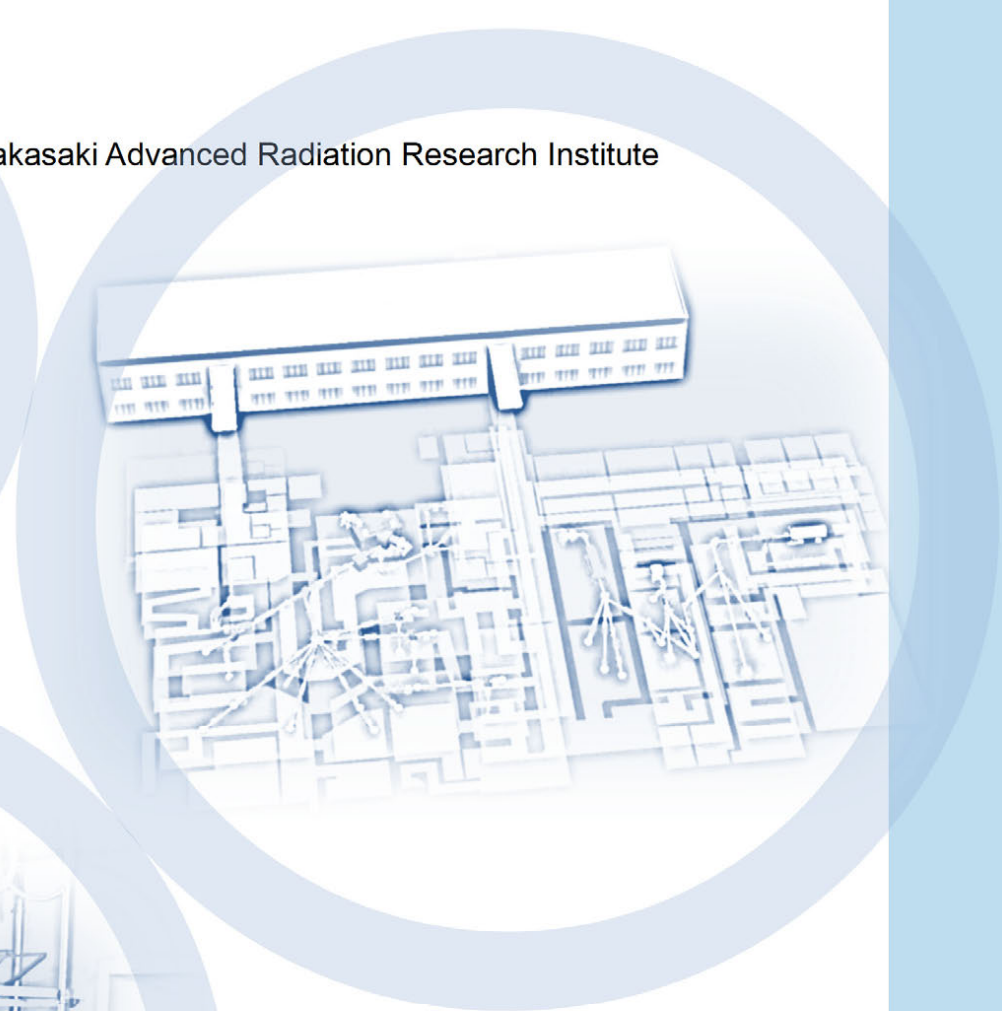
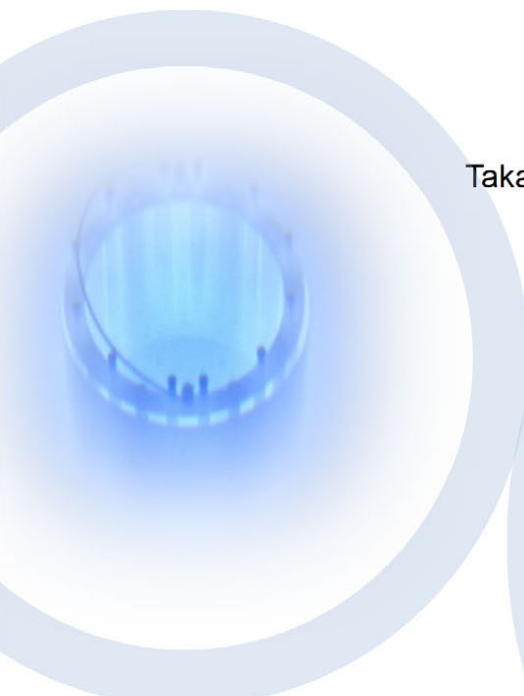


QST Takasaki Annual Report 2017

Takasaki Advanced Radiation Research Institute



National Institutes for Quantum and
Radiological Science and Technology

Preface



Hisayoshi Itoh

Director General
Takasaki Advanced Radiation Research Institute
Quantum Beam Science Research Directorate
National Institutes for Quantum and Radiological Science and
Technology

National Institutes for Quantum and Radiological Science and Technology (QST) was established in April of 2016 by integrating the National Institute of Radiological Sciences (NIRS) and some institutes promoting quantum beam science research and nuclear fusion research in the Japan Atomic Energy Agency (JAEA). The QST has three R&D directorates, *i.e.*, Quantum Beam Science Research Directorate (QuBS), Radiological Science Research and Development Directorate, and Fusion Energy Research and Development Directorate. In the QuBS, in which two research institutes of Takasaki Advanced Radiation Research Institute (TARRI) and Kansai Photon Science Institute (KPSI) are involved, we are intensively performing fundamental and applied research in a wide range of fields like materials science, life science, and quantum beam technology, using advanced beam facilities. Every institute has two research sites, *i.e.*, Takasaki and Tokai sites of TARRI, and Kizu and Harima sites of KPSI. Typical beam facilities we used are Takasaki Ion Accelerators for Advanced Radiation Application (TIARA) at the Takasaki site, Japan Proton Accelerator Research Complex (J-PARC) at the Tokai site, Japan-Kansai Advanced Relativistic Engineering Laser System (J-KAREN) at Kizu site, and highly sophisticated beamlines of Super Photon Ring-8 GeV (SPring-8) at Harima site.

In the TARRI, we have 17 Research Projects making quantum beam science R&Ds with TIARA, 2 MeV electron accelerator, ^{60}Co gamma-ray irradiation facilities, etc., for contributing to the progress of science and technology as well as the promotion of industry. Especially for strongly promoting alliance with industries, the Advanced Functional Polymer Materials Group has been launched under QST innovation hub program to develop next generation graft-polymer materials with combined use of quantum beam processing and analysis techniques as well as materials informatics. We are also performing R&D of advanced ion beam technology at the Beam Engineering Section of the Department of Advanced Radiation Technology. In addition, our beam facilities are opened to industry, academia, and governmental research institutes, and the beam time is allocated for users based on the evaluation of their R&D programs.

This Annual Report covers the research activities at the TARRI primarily for the fiscal year 2017 (FY 2017). This report consists of two parts, Part I and Part II. In Part I, the recent activities of all Research Projects of TARRI are described and Part II presents the recent R&D results obtained by using quantum beam facilities of the TARRI. This part is composed of 113 research papers in the fields of

materials science, life science, and advanced quantum beam technology, and 8 status reports on operation/ maintenance of the quantum beam facilities. It should be noted as a typical topic in the field of materials science, a large degree of spin polarization has been successfully generated in the conduction electrons of single layer graphene (SLG) in the SLG/yttrium iron garnet (YIG, $\text{Y}_3\text{Fe}_5\text{O}_{12}$) heterostructure without breaking the Dirac-cone states. The obtained results reveal the usefulness of graphene/magnetic insulator heterostructures for the spin current manipulation in graphene-based spintronic devices. In the life science field, the imaging technique for therapeutic ion beams has been developed by measuring low-energy secondary electron bremsstrahlung. The beam trajectories in the phantom have been clearly imaged with a pinhole camera. As for the advanced quantum beam technology, a scheme of carrier-envelope-phase (CEP)-stable pulse generation from a free-electron laser oscillator has been proposed by the continuous injection of CEP-stable seed pulses using an external laser. The scheme will open a door of attosecond X-ray pulses and ultrafast laser science. For details of all R&Ds performed at the TARRI, please refer to the main text of this Annual Report.

Concerning the status of quantum beam facilities, three electrostatic accelerators of TIARA were operated steadily and safely as well as MeV-electron and ^{60}Co gamma-ray irradiation facilities. The main coils of the AVF cyclotron, in which a serious layer short was found in December 2016, have been temporarily repaired to bypass 4 of 10 layers of the coils. The maximum energy of the cyclotron was reduced to 60 %, as a result. We are preparing to replace the coils in FY 2018.

Finally, we extend gratitude to both our domestic and foreign colleagues for their cooperation, support, and encouragement for our quantum beam science R&Ds as well as technological advance in the facilities of TARRI.

Facilities

Charged particle beams and RI facilities

Takasaki Ion Accelerators for Advanced Radiation Application (TIARA) consisting of four ion accelerators, an electron accelerator, and gamma irradiation facilities are available to researchers in QST and other organizations for R&D activities on new functional and environmentally friendly materials, biotechnology, radiation effects of materials, and quantum beam analysis. We are developing microbeams, single ion hits and uniform wide-area irradiation technique at the cyclotron. In addition, technical developments of three dimensional in-air PIXE analysis and production/acceleration of cluster ion beam such as C₆₀ fullerene at the electrostatic accelerators are in progress.

Takasaki Ion Accelerators for Advanced Radiation Application: TIARA



TIARA facility



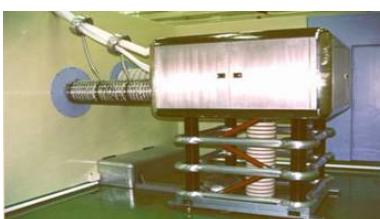
Cyclotron



Tandem accelerator



Single-ended accelerator

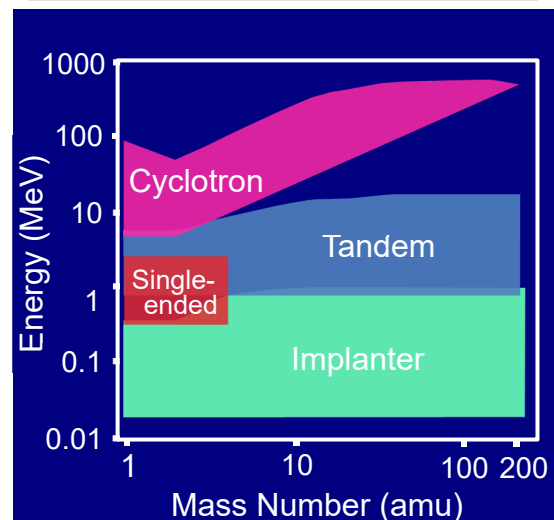


Ion implanter

Typical available ions

Accelerator	Ion	Energy (MeV)
AVF Cyclotron (K=110MeV)	H	10~ 90
	He	20~ 107
	C	75~ 320
	Ne	75~ 350
	Ar	150~ 520
	Fe	200~ 400
	Kr	210~ 520
	Xe	324~ 560
	Os	490
Tandem Accelerator (3 MV)	H	0.8~ 6.0
	C	0.8~ 18.0
	Ni	0.8~ 18.0
	Au	0.8~ 18.0
	C ₆₀	0.8~ 6.0
Single-ended Accelerator (3 MV)	H	0.4~ 3.0
	D	0.4~ 3.0
	He	0.4~ 3.0
	e ⁻	0.4~ 3.0
Ion Implanter (400 kV)	H	0.02~ 0.38
	Ar	0.02~ 0.38
	Bi	0.02~ 0.37
	C ₆₀	0.02~ 0.36

Energy-element range covered by the four accelerators



Cobalt-60 gamma-ray and electron beam irradiation facilities



Gamma-ray irradiation facility building



Gamma-ray irradiation room



Electron accelerator
(0.5~2.0 MeV 0.1~30 mA)



Electron irradiation room with conveyor system

Specification

Apr.2018

Name of facility	Cobalt-60 activity(PBq)	Number of rooms	Principal utilization
Co No.1 bld.	9.5	3	Radiation-resistance test Radiation effects on polymers
Co No.2 bld.	8.2	3	R & D on functional organic materials, dosimetry
Food Irrad.	2.8	2	Radiation effects on biological substance and semiconductors

Dose-rate range

Unit : kGy/h

Name of room	10 ⁻⁴	10 ⁻³	10 ⁻²	10 ⁻¹	10 ⁰	10 ¹	10 ²	10 ³	10 ⁴	10 ⁵
Co No.2					—					
Co No.7				—						
Food No.1		—								
EB accel.								—		

Contents

Part I

1. Materials Science	1
P1-1 Functional Polymer Research Project	2
Leader : Yasunari Maekawa	
P1-2 Advanced Catalyst Research Project	3
Leader : Tetsuya Yamaki	
P1-3 Positron Nano-Science Research Project	4
Leader : Atsuo Kawasuso	
P1-4 Two-dimensional Material Spintronics Research Project	5
Leader : Seiji Sakai	
P1-5 Semiconductor Radiation Effects Research Project	6
Leader : Takeshi Ohshima	
P1-6 Biocompatible Materials Research Project	7
Leader : Mitsumasa Taguchi	
P1-7 Environmental Polymer Research Project	8
Leader : Noriaki Seko	
P1-8 Element Separation and Analysis Research Project	9
Leader : Hironori Ohba	
P1-9 Advanced Functional Polymer Materials Research Group	10
Leader : Yasunari Maekawa	
2. Life Science	11
P2-1 Ion Beam Mutagenesis Research Project	12
Leader : Yutaka Oono	
P2-2 Microbeam Radiation Biology Research Project	13
Leader : Tomoo Funayama	
P2-3 Medical Radioisotope Application Research Project	14
Leader : Noriko S. Ishioka	
P2-4 Generation of Radioisotopes with Accelerator Neutrons Research Project	15
Leader : Kazuyuki Hashimoto	
P2-5 Radiotracer Imaging Research Project	16
Leader : Naoki Kawachi	
P2-6 Radiation and Biomolecular Science Research Project	17
Leader : Akinari Yokoya	
P2-7 Biomolecular Function Research Project	18
Leader : Motoyasu Adachi	
P2-8 Biomolecular Structure and Dynamics Research Project	19
Leader : Taro Tamada	
3. Advanced Quantum-Beam Technology	21
P3-1 Laser Compton Scattering Gamma-ray Research Project	22
Leader : Ryoichi Hajima	
P3-2 Beam Engineering Section	24
Section Manager : Yasuyuki Ishii	

Part II

1. Materials Science	25
1-01 Single Event Effect Evaluation Results of Cu-based Atom Switch ROM and FPGA	28
1-02 Recovery of Radiation Degradation in InGaP Solar Cells by Light Soaking	29
1-03 Effects of Cosmic Radiation on Time-measuring Analog–digital Mixed ASICs	30
1-04 Radiation Response of Silicon Carbide Junction Field Effect Transistors	31
1-05 Evaluation of Radiation Hardness on Carbon Nanotube Field Effect Transistor	32
1-06 Radiation Damage Tests of Semi-Conductors	33
1-07 Research of the Radiation Tolerance in Space Environment of General Electronic Devices	34
1-08 Preparation of Nano-Structure Controlled Ion-Exchange Membranes by Ion Beams for Application to Seawater Concentration	35
1-09 Preparation of Titanium Dioxide Nanocones Using Ion Track-etched Membranes as Template	36
1-10 Electron Beam Induced Formation of Pt Particles on Ceria Films	37
1-11 Microscopic Observations of Nanostructure in Oxide Ceramics Irradiated with Swift Heavy Ions at Grazing Incidence	38
1-12 Utilization of Ion Implantation for Synthesis of Nitrogen-doped Carbon Material with Catalytic Activity (3)	39
1-13 Control of Pore Shapes in Track-etched Membranes by Using Depth Distribution of LET	40
1-14 DFT Study of the Pt Nanoparticles on the Ar-ion Irradiated Glassy Carbon Substrate	41
1-15 Prediction of Scintillation Light Yield by Heavy Ions Based on Sub-micron Radiation Transport Calculation and Förster Effect	42
1-16 Study on Planar Perfect Blackbody from Etched Ion Tracks	43
1-17 Preparation of Nitrogen-doped Carbon-based Catalysts by Electron-Beam Irradiation During High Temperature Pyrolysis	44
1-18 Electron-Beam Irradiated Electrode of a Redox Flow Battery for Low Internal Resistances	45
1-19 Overvoltage Reduction of Membrane Bunsen Reaction by Using Radiation-grafted Cation Exchange Membranes	46
1-20 Proton Selectivity and Permeability of Cross-linked Radiation-grafted Cation-Exchange Membranes for Efficient HI Concentration	47
1-21 Characterization of (111)-oriented $Ti_{1-x}Al_xN$ Thin Films on Monocrystalline AlN by Reactive CVD	48

1-22	Ion Irradiation-Induced Novel Crystal Lattice Plane Spacing Change in Silicon Carbide Nanotubes	49
1-23	Fabrication and Evaluation of Nanoparticles Bi-Ti-O Ferroelectric Materials by Ion Irradiation	50
1-24	Development of Hydrogen Permselective Membranes by Radiation-Induced Graft Polymerization into Ion-Beam Irradiated Poly Vinylidene Chloride Films	51
1-25	Development of Radiation-grafted Cation and Anion Exchange Membranes for Reverse Electrodialysis Process	52
1-26	The Relationship Between Membrane Properties and Hierarchical Structure of Radiation Grafted Anion Conducting Polymer Electrolyte Membranes	53
1-27	Effect of γ -Ray Irradiation on Friction Property of Poly(vinyl alcohol) Cast-drying on Freeze-thawed Hybrid Gel	54
1-28	Changes in Mechanical Properties of Polyethylene by Gamma-ray Irradiation in Water ...	55
1-29	Synthesis of Fibrous Grafted Adsorbent Having Sulfur-based Functional Group	56
1-30	Development of Boron Removal Technique Combined Grafted Powder Adsorbent with Spring Type Filter	57
1-31	Amidoxime and Ammonium Fabric Adsorbents Prepared by Radiation Grafting for Chromium Removal	58
1-32	Surface Crosslinking of Silicone Rubber by Electron Beam Irradiation	59
1-33	Study on Hydrogen Generation from Cement Solidified Products Loading Low-level Radioactive Liquid Wastes at Tokai Reprocessing Plant	60
1-34	Effects of Displacement Damage, Helium and Hydrogen on Electrical Properties of Silicon Carbide	61
1-35	Effects of Self-Ion Irradiation on Rhenium Distribution and Microstructure in Tungsten-Rhenium Alloy	62
1-36	Hydrogen Gas Measurements of Phosphate Cement Irradiated During Heat Treatment ...	63
1-37	Effect of Damage Depth Profile on Hydrogen Isotopes Dynamics in W	64
1-38	Experimental Results of Swelling Behavior of FMS Steels Under ADS Irradiation Conditions	65
1-39	Irradiation Tests of Radiation Hard Components and Materials for ITER Blanket Remote Handling System	66
1-40	Development of Radiation Resistant Monitoring System in Light Water Reactor	67
1-41	Development of the Predicting Method for the Long Term Corrosion Under Irradiation	68
1-42	Synergetic Effect of He, H and Displacement Damages on the Void Swelling Behavior of F82H	69
1-43	Change in Hardness of FeCuMn Alloy by Energetic Ion Irradiation	70

1-44	Study on Synthesis of Pd Catalyst from Eluent After Separation Process for High-level Liquid Waste Based on Radiation-induced Reaction	71
1-45	Characterization of Adsorbent for U and Pu Recovery from Degraded PUREX Solvent	72
1-46	Gamma ray Irradiation Durability of CMPO Adsorbent for MA(III) Recovery	73
1-47	Synthetic Reference Sample by Electron Irradiation for IR Measurement of Carbon Concentration in Silicon Crystal	74
2.	Life Science	75
2-01	Validation of Ion Species and Beam Size Availability in Collimating Ion Microbeam System of TIARA	78
2-02	Reduction of Clonogenicity and Inhibition of 5-bromo-2'-deoxyuridine Incorporation in Glioblastoma Cells After Gamma-ray and Carbon-ion Irradiation	79
2-03	Bystander Cellular Effects Induced in Normal Human Fibroblasts by 190 MeV $^{12}\text{C}^{6+}$ and 220 MeV $^{20}\text{Ne}^{8+}$ Ions	80
2-04	LET and Ion Species Dependence of Oxidative Damage in DNA Sheet Generated Along Ion Beam Track	81
2-05	Cell Cycle Arrest and Reentry in <i>Bombyx</i> Embryo at Cleavage Stage After Heavy Ion Irradiation	82
2-06	Carbon-ion Microbeam Revealed Abscopal Activation of Microglia After Lesions by Irradiation in Medaka Embryonic Brain	83
2-07	Development of Wettable Ultra-thin Microfluidic Chip for Immobilization of <i>C. elegans</i> During Microbeam Irradiation	84
2-08	Effects of Carbon Ion Irradiation on Swimming in the Nematode <i>C. elegans</i>	85
2-09	Apparent Distance Between Lesions in DNA Irradiated with $^4\text{He}^{2+}$ Beam in a Cell-Mimetic Aqueous Solution	86
2-10	Genome Wide Analysis of Rice Mutants Isolated from Ion-Beam-Mutagenized Population	87
2-11	Mutation Frequency in Flavonoid Genes Under Different Flavonoid Phenotypic Conditions	88
2-12	Mutagenesis of the Oil-producing Algae by Ion Beam Irradiation	89
2-13	Screening of Root Nodule Bacteria for Salinity Tolerance Using Ion Beams Irradiation	90
2-14	Ion Beam Breeding of Rice for the Mutation Breeding Project of the Forum for Nuclear Cooperation in Asia (FNCA)	91
2-15	The Moss <i>Physcomitrella patens</i> Is Hyperresistant to DNA Double-strand Breaks Induced by Ionizing Radiation	92
2-16	Evaluation of Particle Fluence of Cluster and Monomer Ion Beams Using a Solid-state Track Detector	93

2-17	Induction of Chromosomal Aberrations in <i>Albuca virens</i> ($2n=6$, Hyacinthaceae) via Ion Beam Irradiation	94
2-18	Improvement of Cut Flower Weight of Autumn-flowering Spray Chrysanthemum 'Kyura Syusa'	95
2-19	Development of New Strains with Sporeless Mutation in Mushrooms Using Ion Beam Irradiation	96
2-20	Breeding of Non-Urea Producing Gunma KAZE Yeasts Which Are Suitable for Export	97
2-21	Effect of Ion-Beam Irradiation on the Sensitivity of Oleaginous Yeast <i>Lipomyces starkeyi</i> Against Fatty Acid Synthesis-Inhibitor Cerulenin	98
2-22	Mutation Breeding of <i>Tweedia caerulea</i> 'Pure Blue' by Ion Beam Irradiation	99
2-23	Genome Analysis of the Radioresistant Bacterium <i>Deinococcus aerius</i> TR0125	100
2-24	Effect of Ion Beams and Gamma Rays Irradiation on Mutation Induction in <i>Bacillus subtilis</i> Spores	101
2-25	Study of the Lethal Effect Caused by the Various LET Particle Ion Beam in Budding Yeast <i>S. cerevisiae</i>	102
2-26	Microflora Analysis of Black Pepper Using MALDI-TOF Mass Spectrometry and Decontamination by Gamma-ray Irradiation	103
2-27	Breeding of New Potted Flower Varieties Using Ion Beam	104
2-28	Creation of Mutant Cultivars by Ion Beam Irradiation to Diploid and Tetraploid <i>Tweedia caerulea</i>	105
2-29	Analysis of Response Deficient Mutants of <i>Streptomyces coelicolor</i> to Contact-dependent Stimuli	106
2-30	Knockout and Plasmid Complementation of the <i>pprA</i> Gene in the Radioresistant Bacterium <i>Deinococcus radiodurans</i>	107
2-31	Effects of Growth Stages on Cadmium Accumulation in Shoot of Oilseed Rape Plants	108
2-32	A Simulation Study on Imaging of Carbon-Ion Beams Using a Pinhole Camera Measuring Secondary Electron Bremsstrahlung	109
2-33	Development of a Cost-Effective Compton Camera for Targeted Alpha-Particle Radiotherapy	110
2-34	Comparison of Iron Localization in <i>Lotus japonicus</i> Root Using Micro-PIXE	111
2-35	Analysis of Trace Elements in Acute Myelogenous Leukemia Cell Line Using In-Air Micro-PIXE	112
2-36	Elemental Analysis of the Lungs in Patients with Idiopathic Pulmonary Fibrosis	113
2-37	Long-term Fluorine Penetration from Fluoride-containing Luting Materials to Dentin	114
2-38	Boron Analysis and Imaging of U251 Cells by Using Micro-Particle Induced X/Gamma Ray Emission	115

2-39	Search Trace Elements in Brain Microvascular Endothelial Cells (BMECs) and Effects of Nicotine on Trace Element in BMECs	116
2-40	Kinetics of Encapsulated Hyaluronic Acid-Protamine Particle After Intravenous Injection	117
2-41	Astatinated Antibody Fragment for Reducing Renal Radioactivity Levels	118
3.	Advanced Quantum-Beam Technology	119
3-01	Fabrication of Mach-Zehnder Waveguide Embedded in Biocompatible Thin Film by Proton Beam Writing	121
3-02	Refractive Index Change and Thermo-Optic Effect in Polydimethylsiloxane Nanocomposites with Oxide Nanoparticles Induced by Proton Beam Writing	122
3-03	Quantification of Damage to a Biomolecular Sample in Transmission SIMS Using MeV C ₆₀ Primary Ions	123
3-04	Lithium Distribution Analysis in All-solid-state Lithium Battery Using Maxicrobeam PIXE and PIGE Techniques	124
3-05	Vacancy-induced Magnetism in GaN Film Probed by Spin-polarized Positron Beam	125
3-06	Dopant Dependence on Vacancy Defects in Ion-Beam Synthesized β -FeSi ₂ Films	126
3-07	Properties of Scintillation Emission Signal from Nd:YAG/Cr:YAG Composite by Gamma Ray Irradiation	127
3-08	Status Report on Technical Developments of the TIARA AVF Cyclotron	128
3-09	Dynamic Behavior of Elements with Low Atomic Numbers in Lithium Oxide Ceramics Under Irradiation	129
3-10	Analysis of Linear Energy Transfer Effects on the Scintillation Properties of Ce:Gd ₃ Al ₂ Ga ₃ O ₁₂ (GAGG)	130
3-11	Measurements of Relative Angular Distribution of the n-p Elastic Scattering Reaction for 45-MeV Neutrons	131
3-12	Photo-stimulated Luminescence of G2000 and Recovery by Annealing	132
3-13	Technical Development of Continuous Uniform Ion Irradiation for Production of Track-etched Membranes	133
3-14	Flux Enhancement of Carbon Ion Beams Guided by Cylindrical Glass Channel	134
3-15	The Number Distribution of Emitted Negative Secondary Ions for Sub MeV C ₆₀ Impacts ..	135
3-16	Shape Elongation of Embedded Metal Nanoparticles Induced by C ₆₀ Cluster Ion Irradiation	136
3-17	Observation of Magnetic Depth Profiles for C Cluster Ion Irradiated FeRh Thin Films with Depth-resolved X-ray Magnetic Circular Dichroism	137
3-18	Porous Structure on Ge Surface Formed by C ₆₀ Ion Beam Irradiation	138

3-19	Ion Energy Dependence of Optical Absorption Spectra for Silica Glass Implanted with Ag Ions	139
3-20	Micro-PIXE Analysis Study of Ferrite Products Synthesized from Simulated Radioactive Liquid Waste Containing Chemical Hazardous Elements	140
3-21	Ion Beam Induced Luminescence of Eu^{3+} extracted by HDEHP	141
3-22	Dating of the Yamada Fault Distributed on Tango Peninsula Using Radiation Defect Radical Centers	142
3-23	Preliminary Test of a Penning Ionization Gauge Ion Source with Electromagnets for a Compact Ion Microbeam System	143
3-24	Reduction of Beam Diameter by Optimization of an Extraction Condition in a Compact Ion Microbeam System	144
3-25	Status Report on Technical Developments at Electrostatic Accelerators	145
4.	Status of Quantum-Beam Facilities	147
4-01	Utilization Status at TIARA Facility	148
4-02	Operation of the AVF Cyclotron	149
4-03	Operation of Electrostatics Accelerators in TIARA	150
4-04	Operation of the Electron Accelerator and the Gamma-ray Irradiation Facilities	151
4-05	Utilization Status of the Electron Accelerator and the Gamma-ray Irradiation Facilities	152
4-06	Radiation Monitoring in TIARA	153
4-07	Radioactive Waste Management in TIARA	154
4-08	Facility Use Program in Takasaki Advanced Radiation Research Institute (TARRI)	155
Appendices	157
Appendix 1	Publication list	158
Appendix 2	Type of Research Collaboration and Facilities Used for Research	179
Appendix 3	Examples of Typical Abbreviation Name for Organizations in National Institutes for Quantum and Radiological Science and Technology, and Japan Atomic Energy Agency	181

Part I

Part I

1. Materials Science

P1-1	Functional Polymer Research Project	2
	Leader : Yasunari Maekawa	
P1-2	Advanced Catalyst Research Project	3
	Leader : Tetsuya Yamaki	
P1-3	Positron Nano-Science Research Project	4
	Leader : Atsuo Kawasuso	
P1-4	Two-dimensional Material Spintronics Research Project	5
	Leader : Seiji Sakai	
P1-5	Semiconductor Radiation Effects Research Project	6
	Leader : Takeshi Ohshima	
P1-6	Biocompatible Materials Research Project	7
	Leader : Mitsumasa Taguchi	
P1-7	Environmental Polymer Research Project	8
	Leader : Noriaki Seko	
P1-8	Element Separation and Analysis Research Project	9
	Leader : Hironori Ohba	
P1-9	Advanced Functional Polymer Materials Research Group	10
	Leader : Yasunari Maekawa	

P1-1 Functional Polymer Research Project

Leader : Yasunari Maekawa



Project "Functional Polymer Research" has been developing the functional polymer materials for high performance fuel cells and hydrogen collection systems by using quantum beams such as electron beams, γ -rays and ion beams. We have synthesized the proton- and anion-conducting electrolyte membranes (PEM and AEM) and the hydrogen permselective membranes. We report herein two recent developments: poly (ether ether keton) (PEEK)-based PEMs and poly (ethylene-co-tetrafluoroethylene) (ETFE)-based AEMs for hydrogen- and alkaline hydrated hydrazine-fuel cells applied in automobiles {1-24~26 in Part II}.

Preparation of PEEK-based PEMs by using a combination of radiation induced graft polymerization and atom transfer radical polymerization [1]

Atom transfer radical polymerization (ATRP) is expected as a promising technique for the formation of effective ion channels in PEMs. In this study, we succeeded in the preparation of PEMs based on PEEK that possesses highest mechanical and thermal properties among engineering plastics by combining radiation induced graft polymerization (RIGP) and ATRP.

Poly (chloromethyl styrene) (CMS) as macroinitiator for ATRP was introduced by RIGP in the PEEK film at 40 °C. The ATRP of styrene (St) and ethyl p-styrenesulfonate (ETSS) has proceeded from the grafted CMS at 50 °C without any concurrent thermal polymerization. At CuBr concentration of 0.05 M in acetonitrile, the grafting degrees (GDs) of St and ETSS increased linearly and reached 112% and 381% after 18 h and 24 h, respectively, as shown in Fig. 1. ATRP speed gradually decreased at the CuBr concentration higher than 0.04 M. This would be due to the reduction of reactivity or the diffusion of monomer. The PEM prepared by hydrolysis of ETSS-grafted PEEK-CMS film with an ion exchange capacity (IEC) of 2.70 mmol g⁻¹ exhibited proton conductivity of 0.180 S cm⁻¹ and water uptake of 161%. These are similar conductivity and higher water uptake than a conventional PEEK-PEM prepared by RIGP (IEC=2.74 mmol g⁻¹) [2].

Development of the 4-vinylimidazolium/St-co-grafted AEMs [3]

In the previous study, we reported the relationship between the morphology and properties of imidazolium-based AEMs with GD of 91%. In the present study, the imidazolium-based AEMs with different GDs were analysed by the small angle X-ray scattering (SAXS) to reveal the effect of ionic structure on conducting properties.

AEMs with GDs of 30%, 48%, 91%, and 108% were prepared by RIGP of 2-methyl-1-vinylimidazole and St into ETFE films and followed by N-alkylation with methyl iodide. As the results of SAXS, the mean distance between two ionic clusters in AEMs was approximately 1.0 nm at 80% RH, which is GD-independent. The number of water molecules per cation of AEMs was in the range of 3.9 to 5.3. These values were quite smaller than those of PEMs. Namely, as the GD increases, the volume of the graft polymers (hydrophilic regions) in AEM increases without any influence on the ionic structure in the conducting regions of AEMs. At RH < 80%, therefore, the dissociated ion-pairs are distributed isolatedly in the hydrophilic

domains (ion-channels). As shown in Fig. 2, the disconnected ion channels cause to the decrease in the ion conductivity at RH < 80%, resulted in low power generation efficiency of AEM-type fuel cell.

References

- [1] T. Hamada *et al.*, *Macromol. Chem. Phys.* **218**, 1700346 (2017).
- [2] T. Hamada *et al.*, *J. Mater. Chem. A*, **3**, 20983 (2015).
- [3] K. Yoshimura *et al.*, *Soft Matter*, **13**, 8463 (2017).

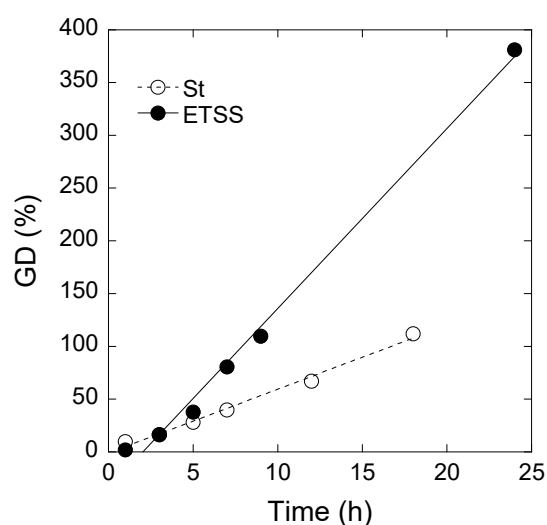


Fig. 1. The grafting degree (GD) as a function of polymerization time for ATRP of St and ETSS into PEEK-CMS films using CuBr catalyst.

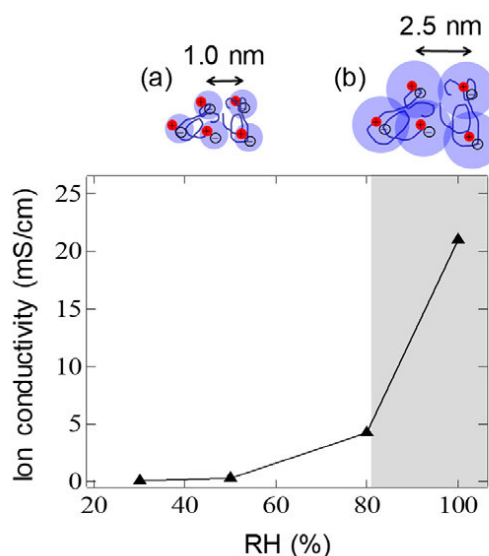
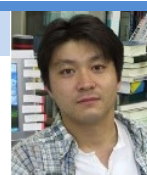


Fig. 2. RH dependence of ion conductivity of AEM with GD of 91% at room temperature and schematic illustration of ionic cluster at (a) RH < 80% and in water.

P1-2 Advanced Catalyst Research Project

Leader : Tetsuya Yamaki



Our main target is to develop catalytic materials for next-generation energy devices for future hydrogen society by effective use of ion and electron beams. The advantage of our overarching research strategy is that these quantum beams can lead to high-energy defect creation, active-site formation via non-equilibrium chemical reactions, and micro-to-nano fabrication, which have a great potential to facilitate the development of novel functional materials through innovative interdisciplinary methodologies. This report deals with applications of the charged-particle beams to R&D for component materials in proton exchange membrane fuel cells {1-08~20 in Part II}.

Non- and low-platinum electrocatalysts prepared by irradiation with keV-ion and electron beams [1, 2] {1-10, 12, 17~20}

Non- or low-platinum (Pt) oxygen reduction reaction (ORR) electrocatalysts are needed to lower the device cost. Our advanced methods using low-energy keV ions as well as electron beams were pursued for the preparation of carbon-based non-Pt catalysts and highly-active Pt nanoparticles (NPs).

Recently, Pt NPs supported on the glassy carbon (GC) substrate pre-irradiated with Ar ions have been found to exhibit the high ORR activity due to their tuned electronic structures [1]. This finding motivated us to investigate how the activity is affected by the ion-induced defects in a metal oxide, which is a well-known promoter in the Pt electrocatalysts. Especially, cerium dioxide (CeO_2) is known to produce oxygen vacancies easily due to the knock-on and electronic effects of ion beams. Thus, we prepared the CeO_2 films with controlled orientations for the subsequent Pt-NP deposition.

The radiofrequency magnetron sputtering was done with a sintered CeO_2 target in an Ar- O_2 gas mixture. The CeO_2 films were grown with a thickness of 17 nm on c- and r-plane sapphire substrates at a temperature of 150 °C. The post-annealing treatment was performed in air at various temperatures between 400 and 1000 °C.

X-ray diffraction (XRD) patterns indicated mixed (001) and (111) crystal phases at 150 °C on both substrates. Figure 1 shows the ratio of (002)/(111) peak-area intensities for the CeO_2 films on the different substrates as a function of post-annealing temperature. The post-annealing above 800 °C seemed to enhance dramatically the growth of (001)-oriented CeO_2 films; highly oriented CeO_2 (001) films were formed on c- and r-plane sapphire substrates at 1000 °C. The deposition of the Pt NPs on the obtained CeO_2 films is now in progress.

New nano-sized materials prepared by swift-heavy-ion technology and their applicability [3-5] {1-08, 09, 11, 13~16}

An MeV-GeV heavy-ion beam gives one-dimensional polymer nanostructures through its high energy deposition within a limited cylindrical area along the path, *i.e.*, an ion track. Crosslinking reactions occur in the ion track, yielding a nanowire by subsequent development to remove the non-crosslinked parts (referred to as a single-particle nanofabrication technique), while degradation reactions occur to afford a straight nanopore after

preferential dissolution of the ion track (referred to as a track etching technique). We have recently developed a variety of new nanomaterials [3-5] such as ion-conductive membranes and catalyst supports.

Nanostructure-controlled cation- and anion-exchange membranes (CEMs and AEMs) were prepared by a so-called ion-track grafting technique for applications to seawater concentration process. A 25- μm -thick poly(ethylene-co-tetrafluoroethylene) (ETFE) film was irradiated with 560 MeV ^{129}Xe at a fluence of 1.0×10^9 ions/ cm^2 . The irradiated ETFE films were immersed in grafting solutions and then afforded to chemical modifications of the grafted chains. Figure 2 shows the membrane resistance of the nanostructure-controlled CEMs as a function of the water content, comparing the results for a commercially-available CEM, Neosepta® CMX (ASTOM Co., Ltd.). The membrane resistance decreased dramatically at higher water contents; it reached $0.18 \Omega \text{ cm}^2$ at the minimum, corresponding to one tenth of that of CMX. We are also interested in transport numbers toward potential application to electro dialysis desalination processes and fuel cells.

References

- [1] T. Kimata *et al.*, Surf. Coat. Tech. **306**, 123 (2016).
- [2] S. Yamamoto *et al.*, J. Cryst. Growth, **468**, 262 (2017).
- [3] M. Higa *et al.*, Bull. Soc. Sea Water Sci. Jpn. **71**, 37 (2017).
- [4] T. Yamaki *et al.*, Bull. Soc. Sea Water Sci. Jpn. **72**, 62 (2018).
- [5] A. Horio *et al.*, Radiat. Phys. Chem. **142**, 100 (2018).

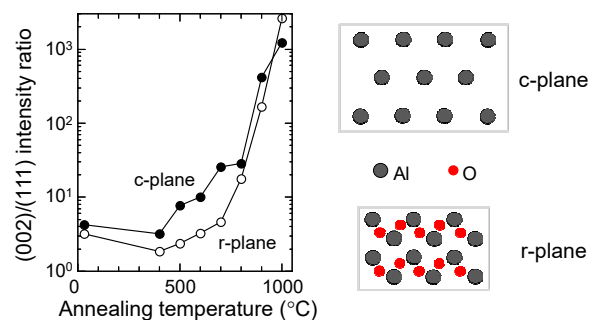


Fig. 1. Intensity ratios of CeO_2 (002) and (111) in the XRD patterns of CeO_2 films on c- and r-plane sapphire substrates at various post-annealing temperatures.

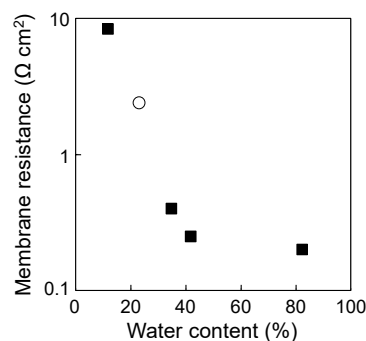


Fig. 2. Membrane resistance vs. water content. An open circle shows the result for Neosepta® CMX.

P1-3 Positron Nano-Science Research Project

Leader : Atsuo Kawasuso



The aim of the project “Positron Nano-Science” is to develop new and potential positron beam technologies for the advanced solid state physics. So far, we have been developing (i) the spin-polarized surface positronium spectroscopy that is substantially useful for detecting spin-polarization of electrons at the first surface layer, (ii) the spin-polarized positron annihilation spectroscopy in strong magnetic field for detecting vacancy-induced magnetism and (iii) the low-energy positron diffraction for the structural analysis of heavy metal surfaces. In this report, we pick up the achievements of theme (i) in the last fiscal year (2017).

Spin polarization in graphene and h-BN probed by spin-polarized surface positronium spectroscopy [1]

Graphene is thought to be a promising spin transportation medium because of its high carrier mobility and long spin relaxation time. There are two major spin injection methods into graphene. One is the direct bonding of graphene to ferromagnets. The other is the tunneling injection from a ferromagnet through an insulative barrier layer. h-BN may be a good barrier layer material due to its wide band gap (~6 eV) and good lattice matching with graphene. In the former, it is, of course, important to inspect if graphene can be spin-polarized by ferromagnets. In the latter, it is important to confirm if the barrier layer can maintain its unpolarized and insulative states under the contact with ferromagnets.

The upper panel of Fig. 1 shows the spin polarizations of graphene on ferromagnetic Co(0001) and Ni(111), and paramagnetic Ru(0001). After heat treatment, finite spin polarization appears in graphene on Co and Ni, while no spin polarization exists in graphene on Ru. These manifest that graphene is spin-polarized by ferromagnets and the magnetic proximity effect surely exists. From the lower panel of Fig. 1, h-BN is also spin-polarized by Co and Ni and in addition very similarly to graphene. This is against to the initial anticipation for h-BN.

Through theoretical considerations based on first principles calculation, the above results were naturally explained as follows. When graphene and h-BN are placed in contact with the same ferromagnet (*i.e.*, Co or Ni), the electronic states are strongly and similarly modulated with losing their original characters because of hybridization between graphene or h-BN and the ferromagnet. That is, graphene is spin-polarized by ferromagnets, but, instead, the Dirac dispersion is lost. Undesirably, h-BN is also spin-polarized with the disappearance of the band gap. If these are serious problems when realizing graphene-based devices, some means needs to be considered.

Positronium formation mechanism at Si surfaces [2]

In order to establish the surface positronium spectroscopy, it is important to reveal the formation mechanism of positronium in detail. So far, three positronium formation channels are known to exist: The negative work function mechanism, the surface positron-mediated process and the scattering-neutralization process.

Recently, as a new positronium formation process, the exciton-like mechanism is proposed to occur at Si

surfaces. That is, before positronium is emitted into vacuum, an excitonic electron-positron pair is formed at surface. However, to confirm this hypothesis, it seems that more detailed experiments and theoretical considerations are needed. Thus, we investigated the positronium formation at Si(111) and Si(001) surfaces by changing the doping level systematically over the range 300-1000 K.

Consequently, the temperature dependence of positronium fraction varied with the doping condition, and there were practically no differences between the two surface orientations. In heavily doped n-type Si ($n \geq 10^{18} \text{ cm}^{-3}$), the positronium fraction (I_{Ps}) increased above 700 K and reached more than 95% at 1000 K. In undoped and lightly doped Si ($n, p \lesssim 10^{15} \text{ cm}^{-3}$), I_{Ps} decreased from 300 K to 500 K and increased above 700 K. In heavily doped p-type Si ($p \geq 10^{18} \text{ cm}^{-3}$), I_{Ps} increased in two steps: one at 500-600 K and one above 700 K. Overall, the positronium fraction increased with the amount of n-type doping. These phenomena were found to be dominated by two kinds of positronium with energies of 0.6-1.5 eV and 0.1-0.2 eV, that were attributed to the work function mechanism and the surface-positron-mediated process, respectively, with contributions from conduction electrons. The positron work function was estimated to be positive. This agrees with first principles calculation. The positive positron work function implies that the formation of excitonic electron-positron bound states begins in the bulk subsurface region and transits to the final positronium state in the vacuum.

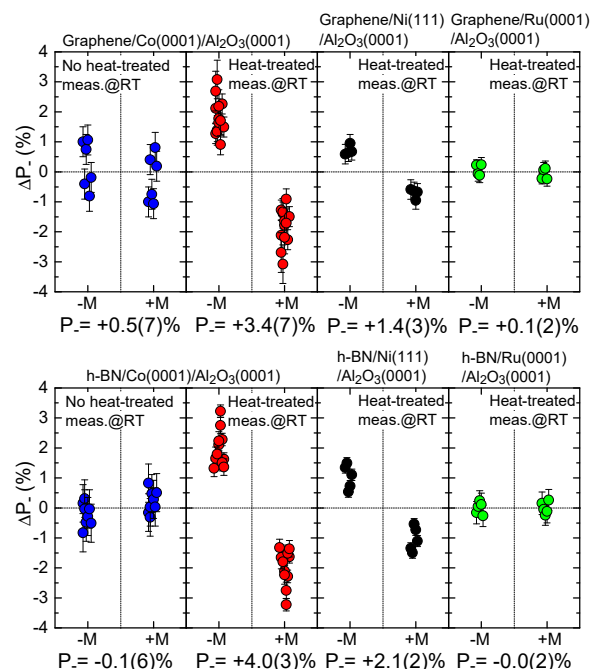


Fig. 1. Spin polarizations obtained for graphene (upper panel) and h-BN (lower panel) on ferromagnet Co(0001) and Ni(111), and paramagnetic Ru(0001).

References

- [1] A. Miyashita *et al.*, Phys. Rev. B, **97**, 195405 (2018).
- [2] A. Kawasuso *et al.*, Phys. Rev. B, **97**, 245303 (2018).

P1-4 Two-dimensional Material Spintronics Research Project

Leader : Seiji Sakai



Our project was newly-established in 2017 aiming at developing novel quantum electronics and spintronics techniques for future information technology by taking advantages of the low dimensionality and quantum electronic properties of two-dimensional materials and related heterostructures. The advanced quantum beam techniques of QST and of our research groups (Two-dimensional Material Spintronics Project and QST Advanced Laboratory for Quantum Materials Science) could allow us to explore and design the local atomic and electronic structures in low-dimensional materials, heterostructures and even at their interfaces above the technological limits in nanomaterials science so far.

Dirac-cone spin polarization of graphene induced by magnetic proximity effect of magnetic insulator [1]

Graphene has been attracted special attention as one of the most useful materials in nanospintronics due to the outstanding spin transport properties resulting from the Dirac-cone derived from the p_z orbitals in the two-dimensional carbon honeycomb lattice of graphene. Recently, the use of the proximity effect in graphene/magnetic insulator heterostructures has been theoretically proposed as an alternative to compensate for the weakness of the spin-orbit interaction and gap-less nature of graphene in developing spin transistors. By employing spin-polarized metastable He atom deexcitation spectroscopy (SPMDS), we successfully demonstrated that indeed a large degree of spin polarization can be generated in the conduction electrons of single layer graphene (SLG) in the SLG/yttrium iron garnet (YIG, $Y_3Fe_5O_{12}$) heterostructure without breaking the Dirac-cone states (Fig. 1) [1]. Our study revealed the usefulness of graphene/magnetic insulator heterostructures for the spin current manipulation in graphene-based spintronic devices.

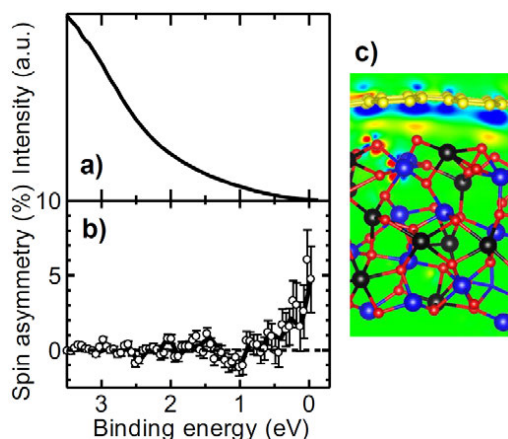


Fig. 1. SPMDS spectra of the SLG/YIG heterostructure representing (a) the electronic states of SLG and (b) their spin polarization and (c) the theoretically simulated model which reproduces the SPMDS results. In (a) the energy region of 0 eV (the Fermi level) \sim 2 eV, where the signal intensity changes linearly, corresponds to the Dirac-cone of with a linear band dispersion. In (b) the large positive spin asymmetry seen below the Fermi level (0 \sim 1 eV) shows the large spin polarization of conduction electrons in the Dirac cone. The positive sign of the spin asymmetry indicates the negative sign of the electron spin

polarization in principle. In (c) the yellow, red, blue and black spheres show C, O, Fe and Y atoms, respectively. The reddish and bluish colors represent the positive and negative spin polarization of the electronic states at the SLG/YIG interface, respectively. It is clearly seen in (c) that the C p_z orbitals, which dominate the Dirac-cone, is negatively spin-polarized.

Interface-induced perpendicular magnetic anisotropy in cobalt/hexagonal boron nitride heterostructures [3]

The recent findings of the graphene-induced perpendicular magnetic anisotropy (PMA) have opened up novel applications of the magnetic metal/graphene heterostructures in developing high-density magnetic memory devices [2]. In this year, it was further revealed by in situ synchrotron X-ray magnetic circular dichroism (XMCD) spectroscopy that hexagonal boron nitride (h-BN) with a honeycomb lattice composed of B and N in a similar manner to graphene also brings about significant PMA in ferromagnetic Co nanoparticles in the heterostructure of Co nanoparticles and h-BN (Fig. 2) [3]. The remarkably-high thermal and chemical stabilities of h-BN even superior to graphene as well as its insulating property can make h-BN a promising substrate and insulating material for magnetic memory devices.

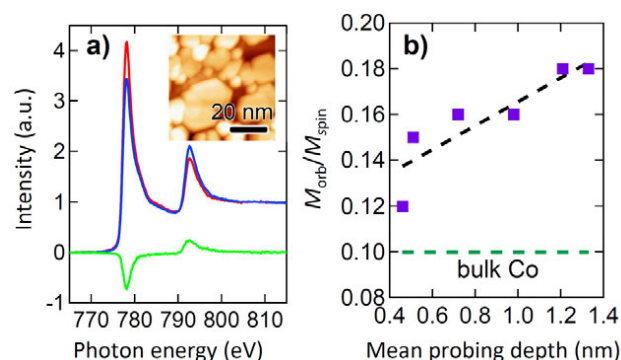


Fig. 2. XMCD spectroscopy results for the Co nanoparticle/h-BN heterostructure fabricated on a Pt(111) surface. (a) Co $L_{2,3}$ -edges X-ray absorption spectra measured in remanence after applying magnetic fields parallel (red curve) and antiparallel (blue curve) to the photon helicity of the circularly-polarized X-ray beam, which was perpendicularly incident on the sample surface, and the XMCD spectrum (green curve); the difference between the red and blue curves. The inset shows a scanning tunnelling microscopy image of the Co nanoparticles with a mean diameter of 20 nm and mean height of 1.6 nm. The strong XMCD intensity in the figure shows that the Co nanoparticles are ferromagnetic with PMA. (b) Result of the depth-resolved analysis of the spin and orbital magnetic moment (M_{spin} and M_{orb}) calculated from the XMCD spectrum. The M_{orb}/M_{spin} ratio is plotted as a function of the means probing depth together with the ratio in bulk hcp Co. An enhancement of the orbital magnetic moment at the Co/h-BN interface was deduced as a possible origin of the PMA from the increase of the M_{orb}/M_{spin} ratio with the increase of the probing depth toward the height of the Co nanoparticles.

References

- [1] S. Sakai *et al.*, Adv. Funct. Mater. **28**, 1800462 (2018).
- [2] Y. Matsumoto *et al.*, J. Mater. Chem. C, **1**, 5533 (2013).
- [3] T. Watanabe *et al.*, Appl. Phys. Lett. **112**, 022407 (2018).

P1-5 Semiconductor Radiation Effects Research Project

Leader : Takeshi Ohshima



Recently, technologies based on quantum effects, such as quantum computation, quantum cryptography information and quantum sensing, are hot topics since the quantum technologies can change our life to be more comfortable, safer and more secure. A key element to realize quantum technologies is color centers of which optical and spin properties can be manipulated with high fidelity. We create color centers in wide bandgap semiconductors such as diamond and silicon carbide (SiC) using ion and electron beams, and investigate their optical and spin properties. On the other hand, when semiconductor devices are irradiated with radiations such as ions, electrons and gamma-rays, their characteristics degrades and as a result, the malfunctions occur. We study radiation response of semiconductor devices to understand their radiation degradation/malfunction mechanism, in order to establish radiation resistant technologies for development of long lifetime and highly reliable semiconductor devices that can be used in high radiation environments such as space, nuclear and accelerator facilities {1-01, 02, 04, 23 in Part II}.

Single photon source at the surface of SiC pn diodes [1, 2]

SiC is regarded as a promising host material for single photon sources (SPSs) which act as quantum bits and/or quantum sensors. In previous studies [3, 4], we reported that a new SPS was created in SiC by oxidation although its atomic structure has not yet been identified. For realizing quantum applications, it is important to develop fabrication process of SPSs into electronic devices. In this study, we report the SPS in SiC pn diodes.

In-plane p⁺nn⁺ diodes were fabricated on n-type epitaxial 4H-SiC layer grown on an n-type 4H-SiC substrate. N⁺ and p⁺ regions for p⁺nn⁺ diodes were formed using phosphorus and aluminum ion implantation, respectively, at 1073 K and subsequent annealing at 2073 K for 30 min. The field oxide was formed by pyrogenic oxidation at 1373 K. Figure 1 shows a confocal photoluminescence (PL) map obtained from the n-type epitaxial-layer of an in-plane SiC p⁺nn⁺ diode. The PL measurement was carried out at RT using an excitation laser at 532 nm. Bright luminescent spots are observed in Fig. 1. As a result of photocount-time-correlation-function measurement, anti-bunching behavior was obtained for the luminescent spot. This result indicates that the luminescent spot acts as an SPS at RT. Thus, it is revealed that SPS can be introduced in SiC p⁺nn⁺ diodes during device fabrication.

Thermal stability of radiation-induced deep level defects in SiC [5, 6]

Electrical properties of semiconductor devices are degraded by deep levels created by irradiation. Therefore, it is important to understand radiation induced deep levels and their annealing properties. In this study, we investigate thermal stability of deep levels in SiC.

n-type 4H-SiC epitaxial layers were irradiated with He (2 MeV) ions at 5×10^9 /cm². The deep levels were analyzed by deep level transient spectroscopy (DLTS) measurements in temperature ranges from 100 up to 700 K. Two electron traps Z₁/Z₂ and EH₆/EH₇ assigned to

the two different charge state transitions of the carbon vacancy, V_C, respectively have been observed in the as-grown epitaxial layer although their concentrations were very low (Black dotted line in Fig. 2). By the irradiation, new deep levels, ET₂ and EH₃ are introduced in addition to increase in Z₁/Z₂ and EH₆/EH₇ (Red line in Fig. 2). However, the second DLTS measurement reveals the almost complete removal of ET₂ and the partial removal of EH₃, while the concentration of Z₁/Z₂ have further increases, due to the relatively low temperature annealing up to 700 K, accomplished during the first temperature scan (Blue dash-dot line in Fig. 2). The obtained result suggests that ET₂ and EH₃ are also V_C-related deep levels, and they change to Z₁/Z₂ by annealing at 700 K.

References

- [1] H. Tsunemi *et al.*, Mater. Sci. Forum, **924**, 204 (2018).
- [2] T. Ohshima *et al.*, J. Phys. D: Appl. Phys. **51**, 333002 (2018).
- [3] A. Lohrmann *et al.*, Nat. Commun. **6**, 7783 (2015).
- [4] A. Lohrmann *et al.*, Appl. Phys. Lett. **108**, 021107 (2016).
- [5] I. Capan *et al.*, Mater. Sci. Forum, **924**, 225 (2018).
- [6] I. Capan *et al.*, J. Appl. Phys. **123**, 161597 (2018).

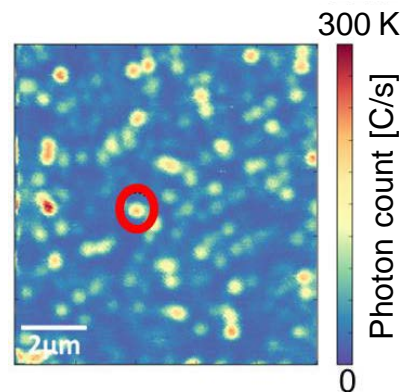


Fig. 1. A confocal PL map obtained from an n-region of an in-plane SiC pi(n)-n diode at RT. Excitation laser: 532 nm, 1 mW. Long-pass filter: 647 nm.

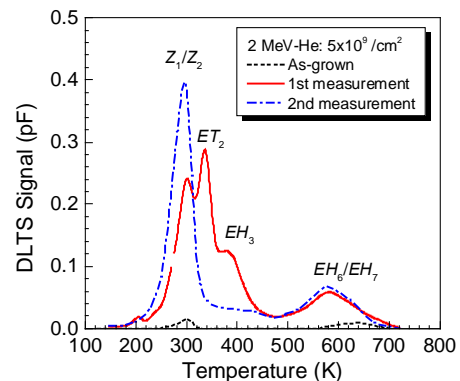


Fig. 2. DLTS spectra for as-grown (Black dot line), 2 MeV-He (5×10^9 /cm²) irradiated n-type 4H-SiC epitaxial layer. Red solid and blue dash-dot lines depict spectra for as-irradiated (1st DLTS measurement) and it observed after 1st DLTS measurement (2nd DLTS measurement), respectively.

P1-6 Biocompatible Materials Research Project

Leader : Mitsumasa Taguchi



Project “Biocompatible Materials Research” has been developing the functional biocompatible materials based on the radiation-induced crosslinking technique. The obtained materials can be utilized for the bio-devices in diagnostic, treatment and regenerative medicine {1-27 in Part II}.

Microfabrication of biocompatible hydrogels by proton beam writing [1]

Recently, biocompatible organic devices are widely developed in cell technology and biomedical engineering fields. The cell behaviours, such as attachment, growth, gene expression and differentiation, are strongly affected by the stiffness, hydrophilicity, microstructure and electronic charge of the substrate materials. Since hydrogel has the similar stiffness and hydrophilicity of tissues in the mammalian body, it is expected to be applied as a biological scaffold material. Radiation crosslinking is extensively used as a strong tool to produce functional materials without any toxic crosslinking reagents. Proton beam writing (PBW) technique has a capability to fabricate next-generation 3D microdevices.

Hydroxypropyl cellulose (HPC) and sodium carboxymethyl cellulose (CMC) were dissolved in ultrapure water. A 30% HPC aqueous solution and a 50% CMC aqueous solution were prepared in paste-like states, and irradiated with 3.0 MeV focused proton microbeam under atmospheric pressure conditions. On account of the 1-mm air gap for easy installation of the sample, the beam spot size on the sample surface was estimated at approximately 12 μm in FWHM. The penetration depths of the protons in the HPC and CMC aqueous solutions were approximately 98 and 88 μm , respectively. The HPC and CMC aqueous solutions were also irradiated with 2.0 MeV electron beam as a reference.

After careful washing with water after the irradiation, insoluble hydrogels were obtained from both the proton and electron beam irradiated samples. The gel fractions of the HPC and CMC hydrogels by the irradiation were estimated as the weight ratio of the dried crosslinked hydrogel to that of polymer before irradiation. The gel fractions increased with an increase in dose, and were similar to those by the electron beam irradiation, as shown in Fig. 1. The swelling of the hydrogels in distilled water was estimated by dividing the weight of the swollen hydrogel by that of dried hydrogel. The swelling of the hydrogels produced by the proton beam were also the same as that by the electron beam. Proton and electron beams are low LET (Linear Energy Transfer) radiation, and the hydrogels are formed by reactions of hydroxyl radical from water molecule by the indirect-effect. So proton and electron beams produce the hydrogel having the same gel fraction and swelling. Other physical properties, such as stiffness, tensile strength and elongation, of microfabricated hydrogels by the proton beam could not be measured because of small sample size. Those properties could be estimated from the electron beam experiment based on the formation mechanism of the hydrogel.

HPC and CMC microstructured hydrogels with line-and-space, hole and character-based patterns on polyethylene

terephthalate film, were successfully obtained using the PBW technique (Fig. 2). Line-and-space patterned hydrogel was used for the evaluation of two dimensional resolution of PBW. The produced tetragonal hydrogel was about 20 μm (minimum 10 μm and maximum 50 μm) larger than the irradiation plan because of the scattering of the proton beam by the beam extraction window foil and air, and the swelling of the hydrogel. The stiffness of the hydrogel was easily controlled by changing the dose.

HeLa cells were cultured on the obtained HPC and CMC hydrogels at 37 $^{\circ}\text{C}$. The structure of HeLa cell is flat and spread-out on a hard Petri dish, but a sphere on the soft CMC hydrogel, similar to its natural structure. No cells, however, adhered and grew on the HPC hydrogel. The difference must be due to chemical properties of the base polymers. Cell adhesion on the HPC hydrogel, which is a non-ionic polymer, is obviously less than that of anionic CMC hydrogel, indicating that the electric charge of the polymer should be a significant factor for HeLa cell adhesion. Microfabrication of HPC and CMC by the use of PBW is expected to produce new biocompatible functional hydrogels for use in microfluidic devices and as cell scaffolding materials in bio-/medical-applications.

Reference

[1] N. Nagasawa *et al.*, Nucl. Instrum. Meth. Phys. Res. B, **409**, 102 (2017).

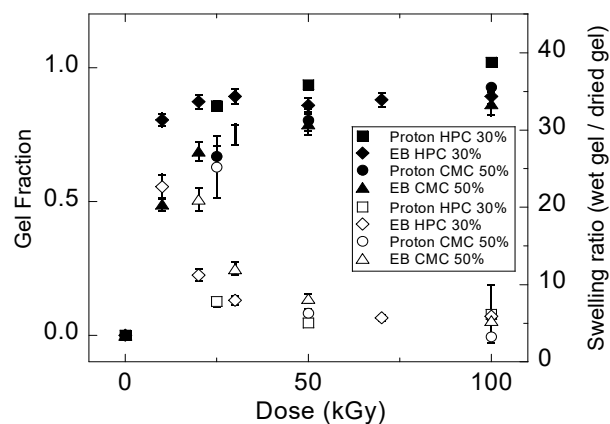


Fig. 1. Gel fraction (left axis, solid symbol) and swelling (right axis, open symbol) of HPC and CMC hydrogels produced by 3.0 MeV proton beam or 2.0 MeV electron beam irradiation.

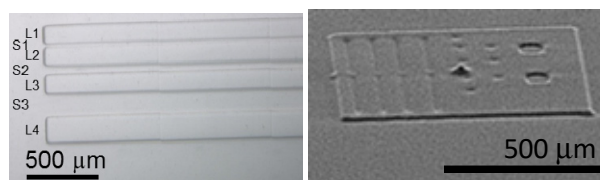


Fig. 2. Swollen microfabricated HPC hydrogel produced by focused proton microbeam. Left: lines (L) and spaces (S) are L1: 139 μm , S1: 21 μm , L2: 136 μm , S2: 48 μm , L3: 133 μm , S3: 156 μm and L4: 187 μm , respectively. Planned sizes are L1: 100 μm , S1: 50 μm , L2: 100 μm , S2: 100 μm , L3: 100 μm , S3: 200 μm and L4: 150 μm . Right: 3D image of microfabricated hydrogel.

P1-7 Environmental Polymer Research Project

Leader : Noriaki Seko



Project “Environmental Polymer Research” has been developing the functional polymer fabrics for metal adsorbents by radiation induced graft polymerization technique using such as electron beams and γ -rays. The developed adsorbents can be expected for applications in removing and recovering trace metal ions from water. To development high performance adsorbents, we started this research from both basic and applied science {1-29~32 in Part II}.

Basic research study in radiation-induced grafting [1]

To suppress homopolymerization in the monomer solution and to precisely control the grafting process as much as possible, we tried to introduce reversible addition fragmentation chain transfer (RAFT) polymerization into the simultaneous irradiation grafting system.

For this purpose, a RAFT agent, 2-cyano-2-propyl benzodithioate (CPB), was added to the simultaneous irradiation grafting systems, where the ethylene-tetrafluoroethylene copolymer (ETFE) film was completely immersed in the chloromethylstyrene (CMS) monomer solution for γ -ray irradiation under nitrogen gas environment at room temperature. The grafted ETFE films were treated in xylene at 120 °C for more than 44 h. The extracted graft chains from the grafted materials and the homopolymer in the monomer solution were analyzed using GPC and NMR instruments.

The NMR results indicated that only the grafted poly(CMS) were detached from the grafted ETFE films and dissolved in the xylene solvent during the immersion. The degree of grafting and homopolymerization increased with increasing irradiation dose, and decreased with increasing the concentration of RAFT agent.

The molecular weight (Mn) and polydispersion index (PDI) of the poly(CMS) graft chains and homopolymerized in the solution were shown in Table 1. The poly(CMS) graft chains showed a narrow Mn range of 7700 - 9400 and a PDI quite higher than 1.0, indicating that the conventional radical polymerization still plays an important role in the interior of the ETFE films. On the contrary, the Mn of the homopolymer in the solution increased with increase in irradiation dose, and the PDI was very close to 1.0, showed a typical RAFT polymerization in the monomer solution.

Furthermore, although the graft polymerization and homopolymerization were performed in the same reactor, the Mn of the graft chains was quite higher than that of homopolymer in the solution. The former was more than three times higher than the latter. Therefore, the polymerizations in the monomer solution and in the ETFE films were different from each other. By addition of RAFT agent, the grafting and homopolymerization were considerably suppressed, and the RAFT polymerization in the ETFE films and in monomer solution occurred more dominantly. The molecular weight of the graft chains polymerized in the films was several times higher than the homopolymer formed in the solution.

Applied research study in removing chromium from wastewater [2]

Chromium are widely used in industrial processes, and the wastewater from these industries contains both Cr(III) and Cr(VI) ions. The Cr(VI) is much more toxic than Cr(III). In this work, we modified an existing nonwoven fabric by radiation grafting. For this purpose, an amidoxime fabric adsorbent was synthesized by co-grafting of acrylonitrile (AN) and methacrylic acid (MAA) and subsequent amidoximation with hydroxylamine, while an ammonium fabric adsorbent was synthesized by grafting of chloromethylstyrene (CMS) and subsequent quaternization with trimethylamine. The amidoxime adsorbent and the ammonium adsorbent with high density of functional group of 4.5 and 3.5 mmol/g, respectively, were used in the adsorption tests for the chromium removal study in the batch and column modes.

At pH 5.0, both the Cr(III) and Cr(VI) could be removed by ammonium adsorbents, and the Cr(III) could be also removed by the amidoxime adsorbents to a large extent in the batch mode. Therefore, the ammonium adsorbent was used for the column test. However, although the Cr(III) concentration (0.1 ppm) in the inflow solution was very low, the Cr(III) was soon detected in the outflow solution. The Cr(III) adsorption capacity of the adsorbents was only about 0.12 mg/g. On the contrary, when the Cr(VI) solution was fed, the Cr(VI) ions could be removed up to a large outflow volume more than 600 mL, showing a high Cr(VI) adsorption capacity of about 130.65 mg/g. The high Cr(VI) adsorption capacity of the ammonium adsorbents was due to the well anion exchange between the Cr(VI) anions and the adsorbents. To remove the Cr(III) from water, similar test was performed using the amidoxime adsorbents. In this case, it was found that the amidoxime fabric adsorbent was well removed the Cr(III) up to a high amount volume of 120 mL, showing a reasonable Cr(III) adsorption capacity of 31.68 mg/g.

References

- [1] J. Chen, N. Seko, *Polymers*, **9**, 307 (2017).
- [2] N. Hayashi, J. Chen, N. Seko, *Polymers*, **10**, 744 (2018).

Table 1

Molecular weight (Mn) and polydispersity index (PDI) of the grafted poly(CMS) chains and the homopolymer.

Dose (kGy)	In ETFE films		In solution	
	Mn	PDI	Mn	PDI
16	9400	2.1	760	1.1
30	8600	1.8	1200	1.1
50	7700	1.6	1400	1.2
66	7800	1.7	1600	1.3
88	7700	1.5	2200	1.3

Dose rate: 1.0 kGy/h, mole ratio of RAFT agent to CMS monomer: 1/72.

P1-8 Element Separation and Analysis Research Project

Leader : Hironori Ohba



Quantum beams are versatile sources for materials processing and analysis. Our project explores synthesis of novel nanomaterials by ion or electron irradiation, and basic process of the laser-matter interaction to separate elements from radioactive waste or analyze elements under harsh environments. For materials synthesis, newly structured multi-walled carbon nanotubes inside silicon carbide nanotubes have been found. For element analysis, we study influences of the laser medium in radiation environment for the application of microchip laser-induced breakdown spectroscopy (LIBS). The recent results of our project are introduced as follows {1-22, 3-07 in Part II}.

Ion irradiation-induced novel crystal lattice plane spacing change in silicon carbide nanotubes [1] {1-22}

SiC offers exciting opportunities in electronic devices and in structural materials at high temperature. In this study, the effect of ion irradiation on crystal lattice plane spacing change in SiC nanotube was investigated by using in-situ transmission electron microscopy (TEM) observation technique.

Figure 1 shows the effect of ion fluence on the crystal lattice plane spacing in SiC nanotube by ion irradiation at room temperature and 700 °C, evaluated from selected area electron diffraction patterns of in-situ TEM. From this result, the lattice plane spacing of crystals in the nanotube increases in increasing ion fluence at room temperature, while that at 700 °C decreases monotonically up to the irradiation damage of 24.1 dpa. Many defects induced by ion irradiation may remain in SiC, and their amount increases with increasing irradiation damage at room temperature, eventually converting the crystals to amorphous SiC. This could explain the increasing lattice plane spacing in the SiC nanotube irradiated at room temperature. At irradiation damage higher than 1.1×10^{20} ions/m², we could not evaluate the lattice plane spacing due to complete amorphization of SiC crystals. The lattice plane spacing slightly decreases from 0.254 to 0.252 nm, which is very consistent with the {111} lattice plane spacing of bulk 3C-SiC [1]. These results support that the lattice plane spacing in the as-synthesized SiC nanotube may be slightly larger due to these inherent defects [1].

Properties of scintillation emission signal from Nd:YAG/Cr:YAG composite by gamma ray irradiation {3-07}

Decommissioning of TEPCO Fukushima Daiichi nuclear power plant needs information on post-accident environment inside nuclear reactor core. A remote sensing technique that is available in a narrow space is crucial for the inspection of the damaged reactor. So, a fiber-optic probe LIBS is considered one of the promising methods [2]. However, radiation effects to optical properties and laser operation needs to be investigated considering their influences in the radiation environment. This time as an influence to the properties by high dose irradiation environment, we measured scintillation emission from a monolithic Nd:YAG/Cr:YAG composite ceramics, where Nd:YAG is a gain medium and Cr:YAG is a saturable absorber used in a microchip laser [3].

The emission spectra from the YAG composite during the gamma-ray irradiation for the dose rate from 0.19 to 10 kGy/h is shown in Fig. 2. In these scintillation spectra, specific peaks corresponding to fluorescence from excited neodymium ions were observed. The intensity of the spectra increased with the increase of the dose rate. The scintillation signal intensity for the YAG composite was proportional to the radiation dose rate as shown in inset of Fig. 2, and stable with elapsed time. The features make the YAG composite not only the laser medium but also suitable to radiation dose monitor applicable to severe radiation environments.

References

- [1] T. Taguchi *et al.*, *Acta Materialia*, **154**, 90-99 (2018).
- [2] M. Saeki *et al.*, *J. Nucl. Sci. Tech.* **51**, 930-38 (2014).
- [3] H. Sakai *et al.*, *Opt. Express*, **16**, 19891-99 (2008).

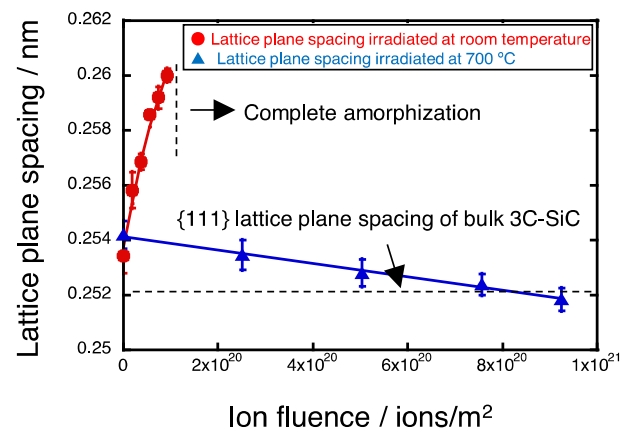


Fig. 1. Effect of ion fluence on the crystal lattice plane spacing in SiC nanotube by ion irradiation at room temperature and 700 °C.

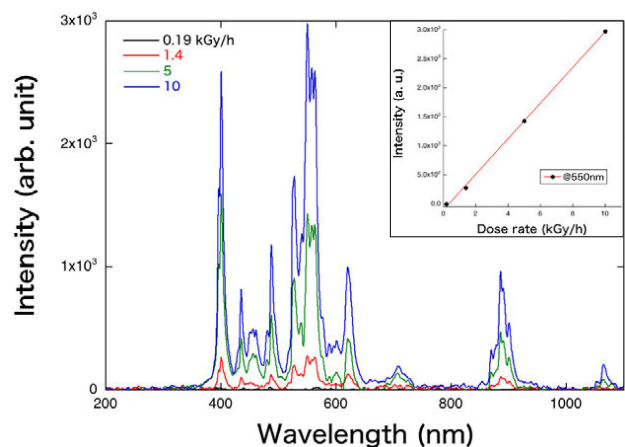


Fig. 2. Emission spectra from Nd:YAG/Cr:YAG microchip composite induced by gamma-ray irradiation for the dose rate from 0.19 to 10 kGy/h. The inset denotes the relationship between emission intensity and dose rate at wavelength of 550 nm.

P1-9 Advanced Functional Polymer Materials Research Group

Leader : Yasunari Maekawa



The research of “Advanced Functional Polymer Materials Group” has been focused on efficient development technique for advanced functional polymer materials, which are widely used in advanced devices and construction materials. The technique includes materials informatics such as machine learning and neural network in addition to the established radiation techniques regarding to the radiation-induced graft polymerization and the X-ray/neutron structural analysis. This group has been conducting mainly the R&D for “Advanced functional polymer materials alliance” under QST innovation hub program in collaboration with participant companies.

Research plan for “Advanced functional polymer materials alliance”

As the first year of the alliance program, we had set the following research subjects and goals.

[1] **Reactivity prediction:** Preparation of functional polymer samples by radiation-induced graft polymerization to accumulate property data by experiment and quantum calculation to establish database for reactivity (polymerizability) prediction.

[2] **Structural data accumulation:** Analysis of hierarchical structures of polymer materials using quantum beam facilities such as small angle X-ray/neutron scattering (SAXS/SANS). The structural data should be enhanced as well as visualized and digitalized by multi-scale simulation methods such as molecular dynamics and quantum calculations.

[3] **Function prediction:** The function of polymer materials is evaluated using statistical analysis such as least-square method, multivariate analysis, and machine learning (neural network etc.) from property and structural data. The materials informatics system will be established based on the relationship between function and these data, so-called “inverse problem analysis”.

[4] **Database preparation:** To setup database for materials informatics of polymers. The data extraction methods are improved using soft-ware or web-services of data-extraction from scientific articles and web-sites.

Target polymer functional materials are set to polymer electrolyte membranes with proton and anion-conducting types (PEM and AEM) for fuel cells and metal ions absorbent fabrics for rare metal recovery system.

Determination of key parameters for the durability of AEMs

For AEM, which is one of the target functional materials, we tried to find essential parameters governing alkaline and oxidative durability of AEMs, which is one of the most important functions. This is because the stabilities at high temperature in highly basic and oxidative conditions under the operation environment are required to AEMs for platinum-free alkaline fuels cells.

For alkaline stability of the graft-type poly(ethylene-co-tetrafluoroethylene) (ETFE)-based AEMs, we had figured out that AEMs having a copoly(1-vinyl-2-methylimidazolium hydroxide-co-styrene) (MVIm/St) grafts showed high alkaline durability among the other anion-conducting grafts (Fig. 1). When AEMs with the MVIm/St graft compositions of 6/4, 4/6, and 2/8 were prepared by using radiation-

induced graft polymerization with ETFE films, in which the ion exchange capacities were almost same with 1 mmol/g, the degradation rate of anionic groups in the AEMs increased with the increases of the amount of St. Accordingly, the composition of grafts is very effective to the improvement of alkaline durability.

Recently, we succeeded in the improvement of oxidation-stabilities of the AEMs by introducing the crosslinking structure in graft polymer chains. ETFE films irradiated with γ -rays were immersed into argon-purged monomer solution consisting of MVIm, St, and divinylbenzene (DVB) for 2 ~ 5 h at 60 °C, and then *N*-alkylated. Grafting degrees of the prepared MVIm/St/DVB-grafted AEMs were a maximum of 97%. The prepared AEMs with ion exchange capacities of 0.9 to 1.9 mmol/g exhibited water uptakes of 15 ~ 49%, and ionic conductivities of 6 ~ 197 mS/cm at 60 °C. The rate of decrease in their ion conductivities was relatively slower than that of the non-crosslinked AEM. Figure 2 shows the oxidative stability of AEMs in 3% H₂O₂ aq. with 2 ppm FeSO₄ at 80 °C. Relative weight loss gradually increased with increase in the ion conductivity of the AEMs. The relative weight loss of the MVIm/St/DVB-grafted AEMs decreased up to about 1/4 in comparison with the non-crosslinked AEM with similar ion conductivity.

From the above approaches, tentatively, we conclude that the structures of anion conducting groups, the monomer ratio of copolymer grafts, and crosslinker are the essential parameter for the important function, “durability” of AEMs in the material informatics.

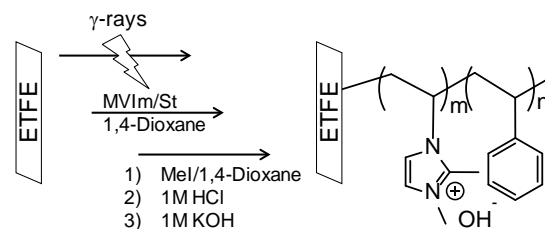


Fig. 1. Preparation procedure of the MVIm/St-grafted AEMs.

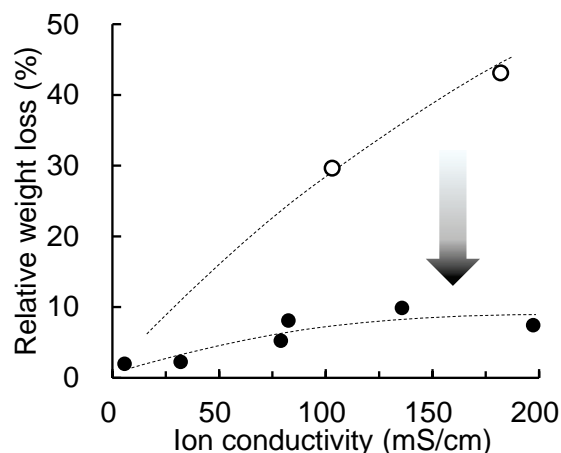


Fig. 2. Oxidation stabilities of the MVIm/St/DVB-grafted AEMs, (●) and the MVIm/St-grafted AEMs, (○).

Part I

2. Life Science

P2-1	Ion Beam Mutagenesis Research Project	12
	Leader : Yutaka Oono	
P2-2	Microbeam Radiation Biology Research Project	13
	Leader : Tomoo Funayama	
P2-3	Medical Radioisotope Application Research Project	14
	Leader : Noriko S. Ishioka	
P2-4	Generation of Radioisotopes with Accelerator Neutrons Research Project	15
	Leader : Kazuyuki Hashimoto	
P2-5	Radiotracer Imaging Research Project	16
	Leader : Naoki Kawachi	
P2-6	Radiation and Biomolecular Science Research Project	17
	Leader : Akinari Yokoya	
P2-7	Biomolecular Function Research Project	18
	Leader : Motoyasu Adachi	
P2-8	Biomolecular Structure and Dynamics Research Project	19
	Leader : Taro Tamada	

P2-1 Ion Beam Mutagenesis Research Project



Leader : Yutaka Oono

The long-term objective of our project is to develop applications of quantum beam technology in applied biological fields such as sustainable agriculture and environmental conservation. Ion beams are recognized as useful mutagens for plant and microbe breeding because they are thought to cause mutations by distinct mechanism from chemical mutagens or gamma rays. To develop more efficient ion-beam mutagenesis techniques, we have tried to understand the characteristics of the ion-beam-induced mutations by using specific gene markers or genome wide sequencing {2-10, 11, 16, and 25 in Part II}. In addition, under collaborations with academic or industrial research organizations, many valuable mutants in plants, algae, fungi, and bacteria have been successfully generated by ion-beam irradiation {2-12~14, 18~22, 24, 27~29}. Revealing molecular biology basis of radio resistant organisms is another major business of our project {2-15, 23, and 30}.

Seeds or seedlings? Which should be irradiated for effective mutagenesis? [1]

The first step of ion-beam breeding toward to creating new plant varieties is mutagenesis, irradiating plant tissues with ion beams. Dry seeds, seedlings, or excised tissues are usually used as initial materials for ion-beam irradiation. Although, in many cases, several types of the plant tissues can be irradiated technically, choosing which type of plant tissues to be irradiated is dependent on living style of the plant and ease in handlings before and after irradiation. It has been concerned that choice of tissue type may affect proportion of induced mutations. However, little is known about effect of tissue type used for irradiation on induced mutations.

To evaluate the effect of tissue type on frequency and types of mutations, Hase et al. irradiated *Arabidopsis* dry seeds and seedlings by carbon ion beams with doses corresponding to 50% and 75% of the shoulder of the survival curve [125 Gy and 175 Gy for dry seeds (shoulder dose; 241 Gy), and 30 Gy and 20 Gy for seedlings (shoulder dose; 41 Gy), respectively]. M2 (next generation of mutagenized population) seeds were harvested from the M1 plants grown from both the irradiated seeds and seedlings. Then, DNA extracted from randomly chosen individual M2 plants were subjected to a whole genome sequencing to investigate characteristics of the induced mutations. As a result, the total mutation frequency in the plants from dry seeds irradiation was 1.4-1.9 times higher than that from seedling irradiation (Fig. 1). This difference mainly depended on the frequency of InDels (insertions and the deletions) in DNA, which was 3 times higher in dry seed irradiation than seedling irradiation. The results clearly suggested that the physiological status of the plant tissue used for irradiation affects the frequency and types of mutations. Because InDels disrupt gene function with high possibility if they arise within DNA region encoding a gene, the result also suggested that using dry seeds as irradiating materials is more preferable to obtain loss of function mutations.

Metabolic changes caused by ion-beam irradiation revealed a carbon flow relevant to a toxic compound in plant cells [2]

Our research has mostly focused on genetic effects of ion beams in plants and microbes. However, as well as other ionizing radiation, ion-beam irradiation directly affects plant growth, development, and also biochemistry in a plant cell. Miyagi et al. evaluated the effects of ion-beam irradiation on oxalate and other primary metabolites in leaves of *Rumex obtusifolius*. *R. obtusifolius* is a weed that contains high amounts of vitamin C and amino acids but also contains high amounts of soluble oxalate, a toxic metabolite, in its leaves. The work was conducted as a part of an effort to create a *R. obtusifolius* variety with low-oxalate contents and to establish it as an edible plant. The results showed that oxalate content in *R. obtusifolius* leaves grown from carbon-ion-beam-irradiated seeds was increased compared with that from un-irradiated seeds. Metabolome analysis of ion-beam effects using Capillary Electrophoresis-Mass Spectrometry (CE-MS) revealed that contents of citrate and ascorbate showed strong positive correlations with the contents of oxalate, whereas negative correlations were observed between the contents of oxalate and amino acids. This observation indicates that ion-beam irradiation caused an increase and a decrease in the carbon flows from glycolysis and to amino acids, respectively, and that oxalate content correlates with extent of the carbon flow from the TCA cycle to the isocitrate pathway. Therefore, manipulation of the carbon flow to the isocitrate pathway would be effective to regulate the oxalate level in plants.

References

- [1] Y. Hase *et al.*, *Sci. Rep.* **8**, 1394 (2018).
- [2] A. Miyagi *et al.*, *Plant Physiol. Biochem.* **122**, 40 (2018).

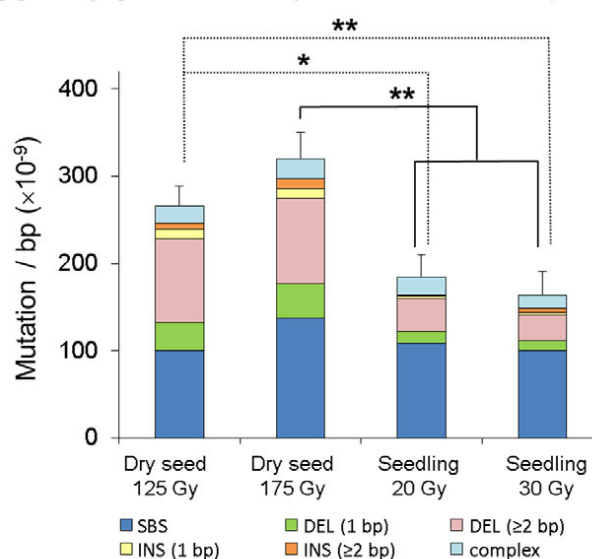


Fig. 1. Frequency and types of mutations induced by carbon-ion irradiation. Error bars represent standard errors for total mutation frequency. Asterisks indicate significant difference in total mutation frequency (t-test, $p < 0.05$ * and $p < 0.01$ **).

P2-2 Microbeam Radiation Biology Research Project

Leader : Tomoo Funayama



Microbeam enables irradiation of a specific region of biological target under a microscope view. This unique irradiation method enables us to induce radiation damage on only targeted region of biological specimen. The aim of Project "Microbeam Radiation Biology" is to develop a technology to irradiate biological samples locally using microbeam system of TIARA, and is to promote biological analysis using it. To achieve the goal, we carried out a research to improve the performance of our ion microbeam system {2-01, 2-07 in part II} and conduct biological study {2-02~06 in part II}.

Microbeam research using model animals [1-2]

Research using our microbeam are not limited to the radiation effect analysis on cultured cells. In FY2017, we reported microbeam irradiation research using nematode *C. elegans* [1] and medaka fish [2].

From the beginning of the biological utilization of our microbeam, we have analyzed the function of the irradiated region of individual with heavy-ion micro-radiosurgery (Fig. 1). Heavy-ion micro-radiosurgery is a method that irradiates excess dose of heavy-ion beam to local parts of organisms and suppresses gene expression at the target region. Using this method, we conducted research of fate map analysis of silkworm embryo [3], mechanism analysis of knob formation of silkworm instar [4] and root hydrotropism of plant root [5]. Micro-laser ablation is known as a similar method for inactivating the function of specific parts of individual organisms. However, it destructs cells and tissue structure completely by heat. In contrast, heavy-ion micro-radiosurgery maintains the tissue structure, and suppress only gene expression. Therefore, micro-radiosurgery has advantages compared with laser ablation in elucidating the mechanism of biological phenomena in which cells cooperate together.

Using this approach, we recently tried to analyze a mechanism of motility suppression of nematode *C. elegans* that are exposed to high-dose radiation. This small animal is known as a good model for neurobiology, and when the worms are exposed to high dose radiation, its whole body movement declines. We thought that by targeting and irradiating specific areas of *C. elegans* with microbeams, we can explore areas involved in this phenomena. In past experiments of microbeam irradiation, which analyze apoptosis induction on worm gonad [6], we performed anesthetic treatment to the worms in order to immobilize and target them. However, when anesthesia treatment is performed, it is difficult to measure motility immediately after irradiation. Therefore, we established a method to hold nematodes in polydimethylsiloxane microfluidic chip without anesthesia. The immobilized worms were irradiated on its head, which include central nervous system (CNS), intestine, and tail with a carbon ion microbeam of 20 μm in diameter with a dose of 500 Gy. However, we could not observe significant decrease of whole body motility in any three regions irradiated. From this result, it is suggested that nematode body bends are realized by cooperative control of whole body rather than centrally controlled by CNS [1].

The research using medaka fish was carried out to analyze the local irradiation effect on medaka brain.

Microglia is the resident immune cells in vertebrate brain and known to be involved in neuroinflammation in damaged brain. To analyze local radiation effect of vertebrate brain, we irradiated only right robe of optic tectum of medaka embryo with carbon ion microbeam of 250 μm in diameter, and thereafter, observed the activation of microglial cells. Immediately after irradiation, we observed apoptosis induction and activation of microglia in only irradiated region. However, at 72 hours after irradiation, we found that the activated microglia distributed over to the whole optic tectum. This result indicated that local irradiation to the optic tectum of medaka embryo induces neuroinflammation in abscopal region [2].

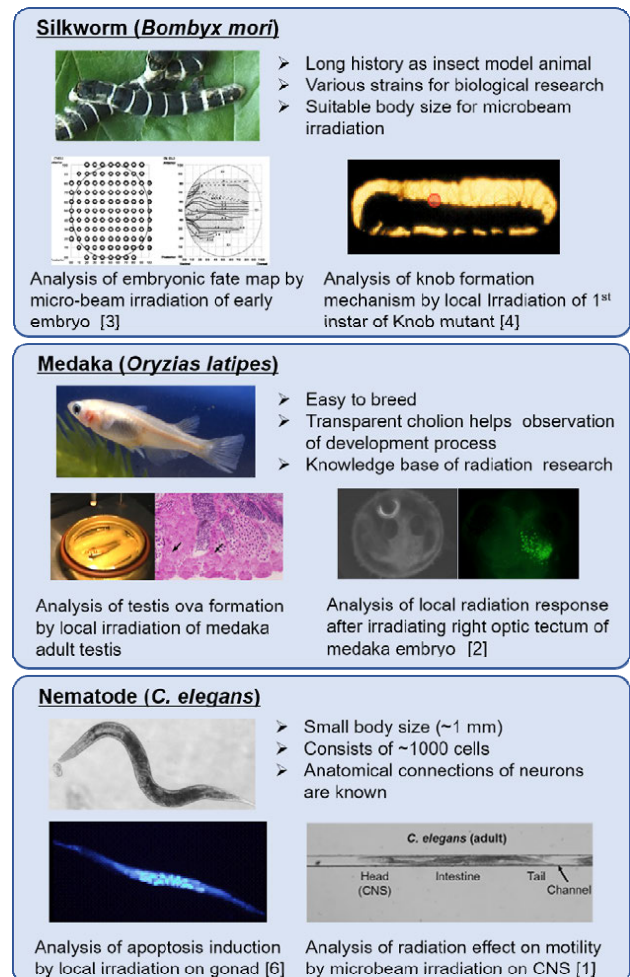


Fig. 1. Research of model animals using TIARA microbeam.

References

- [1] M. Suzuki *et al.*, J. Radiat. Res. **58**, 881 (2017).
- [2] T. Yasuda *et al.*, Int. J. Mol. Sci. **18**, 1428 (2017).
- [3] K. Kiguchi *et al.*, Nucl. Instrum. Meth. Phys. Res. B. **210**, 312 (2003).
- [4] K. Fukamoto *et al.*, J. Radiat. Res. **48**, 247 (2007).
- [5] Y. Miyazawa *et al.*, J. Radiat. Res. **49**, 373 (2008).
- [6] T. Sugimoto *et al.*, Int. J. Radiat. Biol. **82**, 31 (2006).

P2-3 Medical Radioisotope Application Research Project

Leader : Noriko S. Ishioka



The research objective of our project is to develop the radiopharmaceuticals labelled with useful radioisotopes for cancer diagnosis and therapy. Our project focuses on research of the radioisotope drug delivery system (RI-DDS) using bioactive compounds such as antibodies and peptides in order to make the most of the ability of radioisotopes. We also search for novel molecular targets that enable effective diagnosis or therapy with radiopharmaceuticals {2-40 in Part II}.

Antitumor effects of radionuclide treatment using α -emitting ^{211}At -astato-benzylguanidine in a PC12 pheochromocytoma model [1]

Patients with malignant pheochromocytoma have limited treatment options. ^{131}I -iodo-benzylguanidine (^{131}I -MIBG) is a false analog of norepinephrine and is taken into the pheochromocytoma cell via norepinephrine transporter. Therefore, targeted radionuclide therapy (TRT) using ^{131}I -MIBG can improve survival in patients with malignant pheochromocytoma because of the cytotoxic effects of β -radiation. However, even with high doses of ^{131}I -MIBG, survival is still limited and ^{131}I -MIBG is associated with radiation-induced side effects such as bone marrow suppression and lung injury. Therefore, new therapeutic approaches are required to treat malignant pheochromocytoma.

A new generation of TRT involves the use of α -particles. The α -particle has high mean energy deposition and a limited range in tissue, resulting in strong therapeutic effects with minimal side effects. ^{211}At is an α -emitting halogen and has similar characteristics to ^{131}I . Therefore, ^{211}At is suitable for labeling of a benzylguanidine analog, and ^{211}At -MABG will have characteristics similar to those of ^{131}I -MIBG. Furthermore, ^{211}At -MABG should be more effective and have fewer side effects theoretically. However, this possibility has not been evaluated in an animal model of pheochromocytoma. We aimed to evaluate the therapeutic effects of ^{211}At -MABG in a pheochromocytoma model.

Cell survival and DNA double-strand break (DNA-DSB) were evaluated after ^{211}At -MABG treatment using rat pheochromocytoma cell line PC12. We evaluated biodistribution and antitumor effects of ^{211}At -MABG using PC12 tumor-bearing mice. For therapeutic treatment, tumor-bearing mice received intravenous injections of ^{211}At -MABG (0.28, 0.56, 1.11, 1.85, 3.70 and 5.55 MBq; five mice per group). Tumor volumes were evaluated for 8 weeks after ^{211}At -MABG administration. The control group of ten mice received phosphate-buffered saline.

^{211}At -MABG treatment dose-dependently suppressed survival of PC12 cells and increased the proportion of cells with DNA-DSB. The biodistribution study showed higher uptake of ^{211}At -MABG in tumors than that in other organs at all time points. ^{211}At -MABG was rapidly taken up in tumors, and the accumulation remained high at 24 h. The ^{211}At -MABG-treated mice showed significantly lower relative tumor growth during the first 38 days than the control mice (Fig. 1(a) and (b)). The relative tumor volumes on day 21 were $509.2\% \pm 169.1\%$ in the control mice and $9.6\% \pm 5.5\%$ in the mice receiving 0.56 MBq ($p < 0.01$). In addition, the mice treated with 0.28, 0.56 and 1.11 MBq of ^{211}At -MABG

showed only a temporary weight reduction, with recovery in weight by day 10 (Fig. 1(c)). In conclusion, ^{211}At -MABG exhibited a strong tumor volume-reducing effect in a mouse model of pheochromocytoma without severe side effects. Therefore, ^{211}At -MABG might be an effective therapeutic agent for the treatment of malignant pheochromocytoma.

Reference

[1] Y. Ohshima *et al.*, *Eur. J. Nucl. Med. Mol. Imaging*, **45**, 999 (2018).

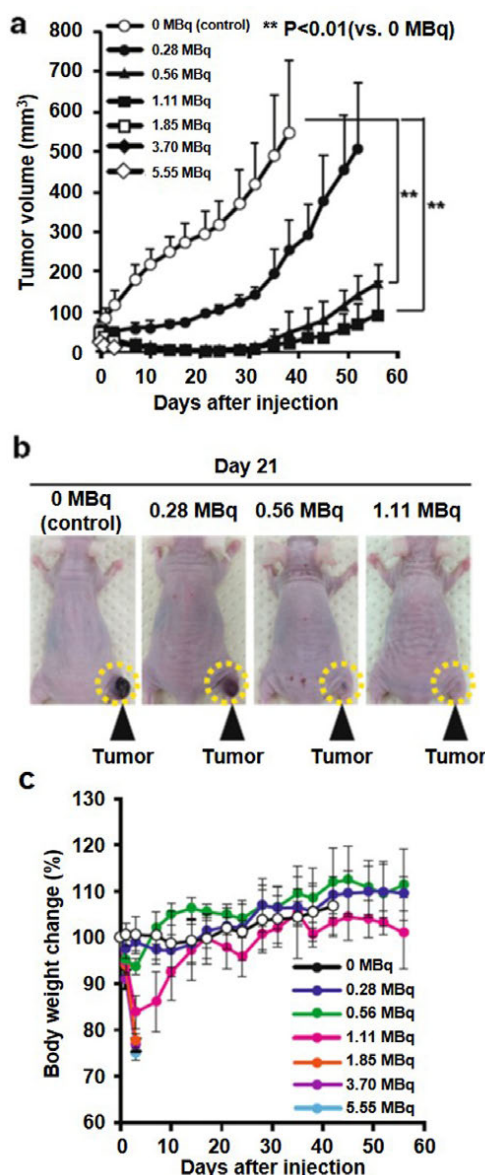


Fig. 1. Effects of ^{211}At -MABG on tumor volume in PC12 tumor-bearing mice. (a) Tumor growth curves after treatment with ^{211}At -MABG ($n=5$). ** $p < 0.01$ vs. 0 MBq (control). (b) Representative images of mice on day 21 after treatment with ^{211}At -MABG and control (0 MBq). Dashed circles indicate tumors. (c) Body weight changes after treatment with ^{211}At -MABG in PC12 tumor-bearing mice shown as means with standard deviations ($n=5$).

P2-4 Generation of Radioisotopes with Accelerator Neutrons Research Project



Leader : Kazuyuki Hashimoto

In our project, we have developed the production of medical radioisotopes (RI) for cancer diagnosis and therapy such as $^{99}\text{Mo}/^{99\text{m}}\text{Tc}$, ^{90}Y , ^{67}Cu , and ^{64}Cu using fast neutrons from a cyclotron accelerator. The neutrons were obtained by irradiating 40-50 MeV deuterons to beryllium or carbon. A separation and purification method of aimed radioisotope from the target materials and radioactive impurities has also been developed. We also investigate the production of medical RI such as ^{211}At and $^{95\text{m}}\text{Tc}$ by the tandem accelerator in Tokai (Japan Atomic Energy Agency). Our final goal is to build a domestic production system of medical radioisotopes using accelerator driven neutrons.

Measurement and estimation of the ^{99}Mo production yield by $^{100}\text{Mo}(n,2n)^{99}\text{Mo}$ [1]

Molybdenum-99, the mother radionuclide of $^{99\text{m}}\text{Tc}$, has been produced by a limited number of research reactors. However, a global shortage of ^{99}Mo was occurred by an unscheduled shutdown of some of the reactors in 2008-2009. Since then, we have developed the alternative production method of ^{99}Mo by accelerator driven neutrons $\{^{100}\text{Mo}(n,2n)^{99}\text{Mo}\}$.

The $(n,2n)^{99}\text{Mo}$ is produced with a minimum level of radioactive waste and without radioisotopes of Tc other than $^{99\text{m}}\text{Tc}$. Using the newly developed thermo-chromatographic apparatus, high separation efficiency of about 90% was obtained through a repeated milking process of $^{99\text{m}}\text{Tc}$ from a molten $^{100}\text{MoO}_3$ sample of 100 g, and 99% of the enriched $^{100}\text{MoO}_3$ sample was recovered [2]. The pharmaceutical quality of $^{99\text{m}}\text{Tc}$ recovered from the $(n,2n)^{99}\text{Mo}$ by our thermo-chromatographic method was satisfied the regulatory requirements for the radiopharmaceuticals of $^{99\text{m}}\text{Tc}$ [3].

The next key stage is to determine optimum conditions for producing the $(n,2n)^{99}\text{Mo}$ from an economical point of view. Therefore, we measured the yield of ^{99}Mo produced by the $^{100}\text{Mo}(n,2n)^{99}\text{Mo}$ reaction using neutrons provided by the $\text{C}(d,n)$ reaction at a deuteron energy of 40 MeV. The ^{99}Mo yield was shown to agree well with a yield estimated using the latest data on neutrons from the $\text{C}(d,n)$ reaction and the evaluated cross section of the $^{100}\text{Mo}(n,2n)^{99}\text{Mo}$ reaction. On the basis of the agreement, it was shown that the calculated ^{99}Mo yield from a 150 g ^{100}MoO sample indicates that about 30% of the demand for ^{99}Mo in Japan can be met with a single accelerator that provides 40 MeV, 2 mA deuteron beams. Furthermore, the elution of $^{99\text{m}}\text{Tc}$ from ^{99}Mo twice per day would meet about 50% of the demand for $^{99\text{m}}\text{Tc}$ in Japan by assuming that $^{99\text{m}}\text{Tc}$ radiopharmaceuticals formed after separating $^{99\text{m}}\text{Tc}$ from ^{99}Mo can be delivered to hospitals from a radiopharmaceutical company within 6 h. The present result encourages us to employ the ^{99}Mo production method by using accelerator neutrons in order to ensure a constant and stable supply of ^{99}Mo for domestic use.

Thin layer chromatography for astatine and iodine in solutions prepared by dry distillation [4]

From the view point of medical use of radionuclides, the ^{211}At is a prospective candidate for utilization in

targeted alpha therapy. The understanding of basic chemical properties of astatine has been required to develop targeted alpha therapy agents for cancers. In this study, astatine and iodine inorganic chemical species in solutions prepared by dry distillation have been determined by the control experiments of thin layer chromatography (TLC).

The ^7Li beams supplied from the Japan Atomic Energy Agency tandem accelerator were used for the production of astatine and iodine radionuclides in the $^7\text{Li}+^{211}\text{At}$ and $^7\text{Li}+^{211}\text{At}$ reactions [5, 6]. No-carrier-added astatine $^{208,209,210,211}\text{At}$ and iodine $^{120,121,123}\text{I}$ were separated and purified from irradiated targets by dry distillation, and recovered in ethanol or water as a solvent. Astatine in the aqueous solution was reacted with an oxidation or a reduction agent. Separation of astatine and iodine ions was conducted by TLC on a silica gel plate with an ethanol/water solution. The distributions of the activities on the TLC plates were measured by imaging plates and visualized by Bioimaging Analyzer System (BAS).

The results of TLC for radioactive astatine and iodine as shown in Fig.1 reveals that astatine is successfully separated and identified as At^- , AtO_3^- , AtO_4^- , while, iodine is I^- . The identification was carried out by comparing R_f values with those of standard iodine species, I^- , IO_3^- and IO_4^- . Besides, dependence of relative amounts of astatine anions on the solutions as shown in Fig. 1b-f strongly supports the three oxidation states of astatine are assigned to At^- (I), AtO_3^- (V) and AtO_4^- (VII).

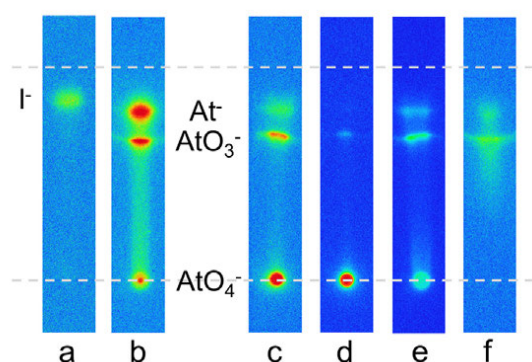


Fig. 1. Results of TLC experiments visualized by BAS: **a** iodine ethanol solution, **b** astatine ethanol solution, **c** astatine aqueous solution, **d** astatine aqueous solution + KIO_4 , **e** astatine aqueous solution + Na_2SO_3 , **f** astatine aqueous solution + hydrazine hydrate.

References

- [1] F. Minato *et al.*, J. Phys. Soc. Jpn. **86**, 114803 (2017).
- [2] M. Kawabata *et al.*, J. Phys. Soc. Jpn. **86**, 053201 (2017).
- [3] Y. Nagai *et al.*, J. Phys. Soc. Jpn. **86**, 053202 (2017).
- [4] I. Nishinaka *et al.*, J. Radioanal. Nucl. Chem. **318**, 897 (2018).
- [5] I. Nishinaka *et al.*, J. Radioanal. Nucl. Chem. **304**, 1077 (2015).
- [6] I. Nishinaka *et al.*, J. Radioanal. Nucl. Chem. **314**, 1947 (2017).

P2-5 Radiotracer Imaging Research Project

Leader : Naoki Kawachi



The aim of our project of “Radiotracer imaging” is to measure, visualize the radiation sources, and characterize the biological processes of organs, using radioisotopes (RI) and imaging apparatus. We will establish systematized techniques for live-imaging using radiotracers, nuclear imaging apparatus, and kinetic analytical methods for understanding the transport function related to agriculture and medicine within living systems (2-31~33 in Part II).

Development of imaging techniques for therapeutic ion beams by measuring low-energy secondary electron bremsstrahlung

Monitoring techniques for therapeutic ion-beams are studied worldwide. Recently, we proposed a beam-imaging technique by measuring low-energy secondary electron bremsstrahlung (SEB) [1] and clinical applicability of this method is under investigation using Monte Carlo simulations and therapeutic ion-beams [2, 3].

We performed a feasibility study by imaging a therapeutic carbon-ion beam and monitoring the range of the beam with a pinhole camera for X-rays by measuring SEB. A beam-irradiation experiment was performed at Gunma University Heavy Ion Medical Center (GHMC). Figure 1 represents a photograph of the experimental setup. A horizontal carbon-ion beam with 290 MeV/u energy was perpendicularly incident onto a water phantom; SEB photons from the beam trajectory in the phantom were measured by a pinhole camera. The developed pinhole camera composed of a tungsten shield containing a pinhole collimator and a detector consisting of scintillator array of cerium-doped gadolinium aluminum gallium garnet (GAGG) optically coupled to silicon photomultiplier-tube, with a pinhole diameter of 0.15 cm, as obtained from Monte Carlo simulations. The field of view of the pinhole camera on the xy-plane corresponded to the area where both $|x|$ and $|y|$ were smaller than 14.65 cm and which was divided into 32×32 pixels. The center of the pinhole was located at $z=98$ cm in front of the water phantom. The number of incident carbon ions was 4.7×10^{11} .

Figure 2(a) represents the reconstructed image of the experimental result. In this image, the beam trajectory was clearly imaged and the length of the trajectories seems to coincide with the expected range, 16.46 cm, calculated using Ziegler's range table. Figure 2(b) shows a projection of Fig. 2(a) on the x-axis.

For the experimental result depicted in Fig. 2(b), we evaluated whether the expected range position coincided with the estimated range position, where the ratio of count to the maximum count coincided with the ratio 0.191; this ratio was deduced from another of our simulation studies. The red dashed line in Fig. 2(b) represents the line connecting the right and left data around the estimated range position. As a result, the estimated range from the dashed line in Fig. 2(b) was 16.02 ± 0.14 cm and was slightly shorter than the expected range, 16.46 cm.

In summary, we showed that the beam trajectories were clearly imaged measuring SEB. In the simulation result, the range positions could be pinpointed by the position where the ratio was 0.191. For the experimental

result, the position which was pinpointed by the ratio of 0.191 slanted 0.44 cm to the negative direction of x-coordinate from the expected range position.

References

- [1] M. Yamaguchi *et al.*, Phys. Med. Biol. **57**, 2848 (2012).
- [2] M. Yamaguchi *et al.*, Nucl. Instrum. Meth. Phys. Res. A, **833**, 199 (2016).
- [3] M. Yamaguchi *et al.*, Rev. Sci. Instrum. **88**, 014301 (2017).

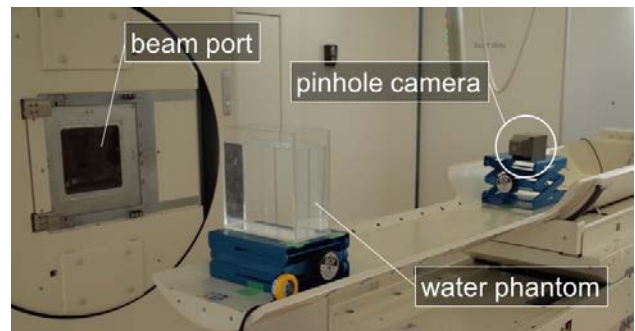


Fig. 1. A photograph of the experimental setup. A pinhole camera and a water phantom were placed on height-adjustable tables on the treatment bed. Carbon beams were irradiated from the beam port.

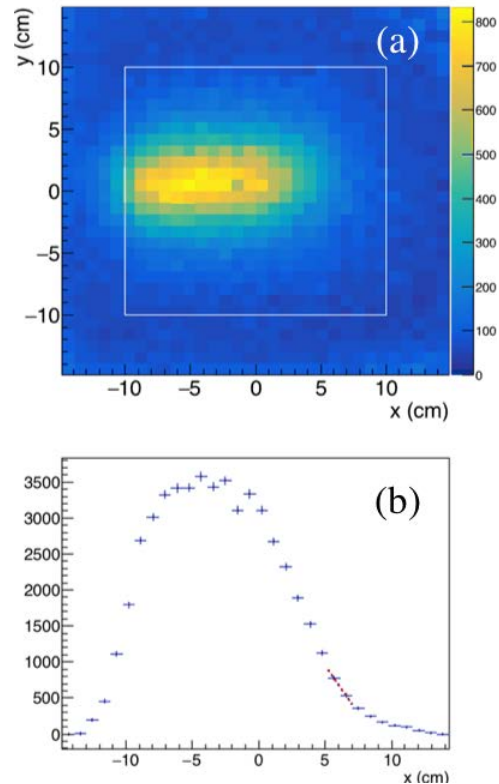


Fig. 2. (a) The reconstructed images for the experiment. White rectangles represent the edges of the phantoms. Stored values of the histograms are the numbers of events having 30 - 60 keV energy detected in the pinhole camera. (b) The projections of the beam profile onto the x-axis.

P2-6 Radiation and Biomolecular Science Research Project

Leader : Akinari Yokoya



The objective of our project is to elucidate the radiation effect of living systems from molecular to cellular level using various advanced radiation sources. Theoretical approaches are also applied for mathematical modeling of molecular and cellular responses to irradiation using computer simulation techniques. It is one of the unique characters of our group that both experimental and theoretical researchers cooperate closely to promote our projects. This allows us to understand the complex radiobiological phenomena from the physical point of view of "Systems Biology".

Studying the effect of phenotypic changes on tumorigenesis using mathematical model

Tumorigenesis is thought to be a multistage process with gradual accumulation of mutations in a number of different genes, however, no prerequisites, particularly for its dynamics, have been found yet. How many and what kind of mutations are required to transform a single normal cell to a cancer cell? This question still has no answer. However, biological pathway that transforms normal cell into cancer cell may not be a single pathway, there are well known three sequential state changes, *i.e.* initiation, promotion and progression (IPP). This is a so-called multistage carcinogenesis model. Therefore, effect of the phenotypic changes by gene mutation on its microenvironment and growth dynamics of cancer cells (tumorigenesis) are studied using a mathematical model made up from the combination of Cellular Potts Model (CPM) and two-stage IP (Initiation-Promotion) model. The CPM is based on a biological hypothesis called differential adhesion hypothesis first proposed by Steinberg. The CPM assigns a spin σ to each lattice site, (i, j) and packed sites which have same spin number defines a cell. Each cell has an associated cell type, τ . At each simulation time steps, total system energy correspond to cell-cell or cell-substrate adhesion energy, elastic bending energy and surface tension energy are minimized by Monte Carlo method and time progresses. Two different cellular properties, *i.e.* elastic property and adhesion property of cell membrane, are introduced to study its effect on the tumorigenesis. Four different types of cells are mathematically constructed and fourteen different combinations of the phenotypic different mutations are incorporated into multistage dynamics of carcinogenesis. Simulation results show that the final state of the system highly depending on the combinations of the mutation phenotypes, two main distinct states, a) exponential growth of cancer cells, b) no tumor or regulation of the ratio of cancer cells to normal cells, are found (Fig. 1).

Molecular kinetics of ion-pair dissociation in water

Understanding of water-mediated molecular events is of crucial importance because various molecular processes in chemistry and biology proceed in water. One of the most typical examples is ion-pair dissociation in water. With this model system, we explore the fundamental mechanism of water-mediated molecular process by using molecular dynamics simulations and

free-energy analysis [1]. Results of the calculations clarifies the relation between two essential solvent features: the water coordination number and water-bridge formation. These two are related in a complex way. Both are necessary to describe ion-pair dissociation. The mechanism constructed with both solvent variables is shown in Fig. 2, which clearly explains the individual roles. The water coordination number is critical for starting ion-pair dissociation. Water-bridge formation is also important because it increases the likelihood of ion-pair dissociation by reducing the dissociation free-energy barrier. Additional Ca-Cl and NH₄-Cl calculations show that these conclusions are unaffected by changes in the ion charge and shape. These results will contribute to future explorations of many other molecular events such as surface water exchange, protein-ligand dissociation, and DNA radiation damage because the same mechanism of water mediation is involved in such events.

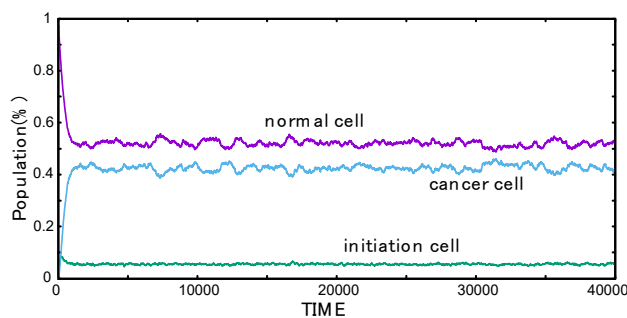


Fig. 1. Plot of the population dynamics of each cell (normal, initiation, cancer). Y-axis shows rate of each cell populations to the total cell population. A kind of regulation of aggregate size is seemed to exist in the system.

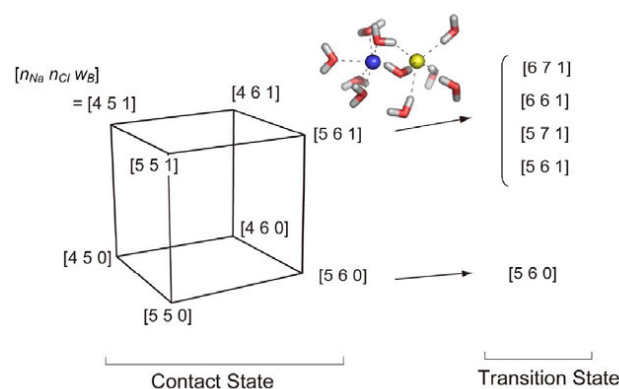


Fig. 2. Mechanism of the water-mediated Na-Cl dissociation. n_{Na} and n_{Cl} are the coordination numbers of Na⁺ and Cl⁻, respectively. w_B denotes the water bridge formation: on ($w_B=1$) and off ($w_B=0$).

Reference

[1] Y. Yonetani, Mol. Phys. **115**, 2987 (2017).

P2-7 Biomolecular Function Research Project

Leader : Motoyasu Adachi



Protein molecules play fundamental roles in biological system and exhibit unique functions on molecular recognitions, chemical reactions and energy transfer. Our research project has been focused on developments of the molecular design based on protein functional analysis using neutron, X-ray diffractions and ultra-short pulse laser. Firstly, we introduce our basic research concept (Fig. 1) and then activities regarding to two protein functional analyses to obtain useful knowledge for molecular engineering and application for industry and human health.

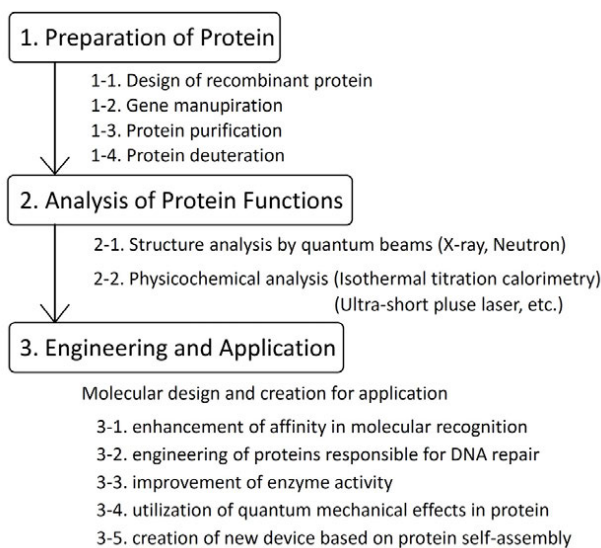


Fig. 1. Research concept of our project.

Neutron structure of the T26H mutant of T4 phage lysozyme provides insight into the catalytic activity of the mutant enzyme and how it differs from that of wild type [1]

T4 phage lysozyme is an inverting glycoside hydrolase that degrades the murein of bacterial cell walls by cleaving the β -1,4-glycosidic bond. This enzyme is one of the traditional enzyme that have been studied by the group of Dr. B. W. Matthews by protein engineering. Previously, they reported that the substitution of the catalytic Thr26 residue to a histidine converts the wild type from an inverting to a retaining enzyme. Here, we have determined the neutron structure of the perdeuterated T26H mutant (Fig. 2(a)). The objective is to clarify the protonation states of Glu11 of an acid/base catalyst and the substituted His26, which are key in the retaining reaction. The 2.09-Å resolution structure shows that the imidazole group of His26 is in its singly protonated form in the active site as shown in Fig. 2(b), suggesting the deprotonated bound substrate as a nucleophile. In contrast, the carboxyl group of Glu11 could be partially protonated and interacts with the unusual neutral state of the guanidine moiety of Arg145, as well as two heavy water molecules. The respective protonation states of Glu11 and His26 are consistent with the bond lengths determined by an unrestrained refinement of the high-resolution X-ray structure of T26H at 1.04-Å resolution.

The detailed structural information, including the coordinates of the deuterium atoms in the active site, provides insight into the distinctively different catalytic activities of the mutant and wild type enzymes (1-4 and 2-1 in Fig. 1).

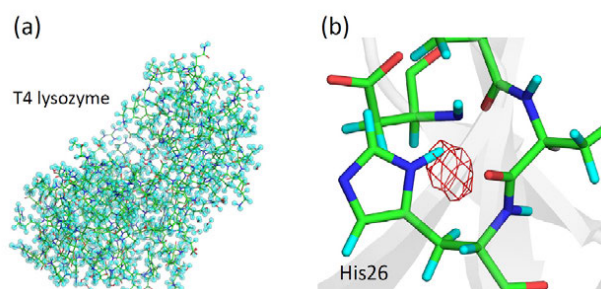


Fig. 2. (a) Structure of perdeuterated T4 lysozyme T26H mutant. (b) Density maps of deuterium atom in His26.

Poly-pentagonal ice-like water networks observed in an activity-improved variant of ice-binding protein [2]

Poly-pentagonal water networks were recently observed in a protein capable of binding to ice crystals. In this study, to examine such water networks and clarify their role in the ice binding, we determined X-ray crystal structures of a 65-residue defective isoform of a Zoarcidae-derived IBP (wild type, WT) and its five single mutants (A20L, A20G, A20T, A20V, and A20I). As a result, poly-pentagonal water networks composed of about 50 semicathrate waters were observed solely on the strongest A20I mutant as shown in Fig. 3. It appears to include a tetrahedral water cluster exhibiting a perfect position match to the first prism plane of a single ice crystal. Inclusion of another symmetrical water cluster in the poly-pentagonal network showed a perfect complementarity to the waters constructing the pyramidal ice plane. These results will provide new insights into the mechanism for the holding property of its poly-pentagonal water network, and lead to the elucidation of the function to bind to the specific ice planes (2-1 and 3-1 in Fig. 1).

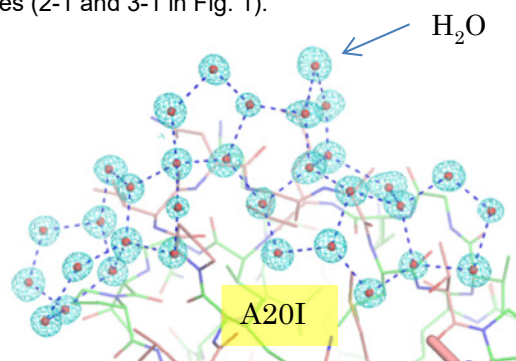


Fig. 3. Electron density maps of water molecules observed on A20I mutant of the ice binding protein.

References

- [1] T. Hiromoto *et al.*, *Protein Sci.* **26**, 1953 (2017).
- [2] S. Mahatabuddin *et al.*, to be published.

P2-8 Biomolecular Structure and Dynamics Research Project

Leader : Taro Tamada



The relationship between protein structure and dynamics is important for ultimate understanding of protein functions. Project "Biomolecular Structure and Dynamics Research" aims to contribute to a wide range of biological and life sciences by performing research and development of molecular imaging method using neutrons, along with other quantum beams like X-rays and computer simulations. In this report, we describe our latest activities for protein structure and dynamics.

Enzyme having improved low-temperature activity and its production method [1]

Cold adaptation of enzymes is a favorable character for their industrial application because it can reduce heating costs to reach the optimal temperature for enzymatic activities. Structural feature of cold-adapted enzymes is regarded as high flexibility. The high structural flexibility, particularly around the active site, is translated into low-activation enthalpy, low-substrate affinity, and high specific activity at low temperatures. On the other hand, the high flexibility can cause structural instability, resulting in lower enzymatic activity. Therefore, the good balance between structural flexibility and stability is crucially important for industrial application of enzymes. We focused the regulation of salt bridges in protein structures, which contribute to structural stabilities.

Endo-1,4- β -mannanase have been used for various bioprocesses such as bleaching of softwood pulps, declining viscosity of feeds and foods, and clarifying beverages. We have already reported that the earthworm *Eisenia fetida* has some cold-adapted enzymes, however, mannanase from *E. fetida* (Ef-Man) showed only weak activity at lower temperatures (~ 30 °C). We determined the crystal structure of Ef-Man at 1.7 Å resolution (Fig. 1(a)) [2]. The overall structure of Ef-Man is similar to those of the glycoside family 5 family proteins, and tertiary structures around the active site are conserved among endo-1,4- β -mannanase families. Ef-Man has 12 salt bridges, and we focused three salt bridges which have pairwise (R213-D251 and R301-D300) and bifurcated (R125-D193) hydrogen bonding interaction between side chains (Fig.1(b)). We designed and produced three Ef-Man mutants, R125K, R213K, and R302K. Enzymatic activities in all mutants improved at lower temperatures, especially the activity of R302K was about three times higher than that of wild type at 20 °C.

Dynamics changes related to allosteric control of protein functions [3]

Complex biological phenomena are performed by coordinated expressions of functions of various proteins. For many systems, precise control of the expressions of the protein functions is done by allosteric mechanism, in which binding of "effector" molecule(s) modifies the activity of the protein. Allosteric control of protein functions is thus an important mechanism that underlies many biological phenomena. Hemoglobin (Hb), an O₂ transporter, is probably the most famous allosteric protein. Binding of O₂ to one of the four O₂-binding sites increases the affinity of other sites. While high resolution X-ray structural models are currently available for both the

deoxy tense (T) and fully-liganded relaxed (R) states of Hb, the molecular mechanism of allosteric control still remains elusive. Recent studies suggest importance of the dynamics of the proteins.

Here we investigated the dynamics of the deoxy and CO forms of human Hb (corresponding to the T and R states, respectively), using quasielastic neutron scattering (QENS) under near physiological conditions, in order to extract the dynamics changes upon ligation. The QENS measurements were carried out using the spectrometer, BL02 (DNA), at the MLF J-PARC. Figure 2 shows the apparent diffusion coefficients (D_{app}) of deoxyHb and COHb, along with the simulated values assuming the rigid crystallographic structure. These results imply that whereas D_{app} of deoxyHb can be described by assuming translational and rotational diffusion of a rigid body, those of COHb need to involve an additional contribution of internal large-scale motions such as subunit motions, as shown in the models in Fig. 2. On the other hand, the local atomic motions were similar. These findings reveal the presence of internal large-scale motions in Hb, and further demonstrate that this internal mobility is governed allosterically by the ligation state of the heme group.

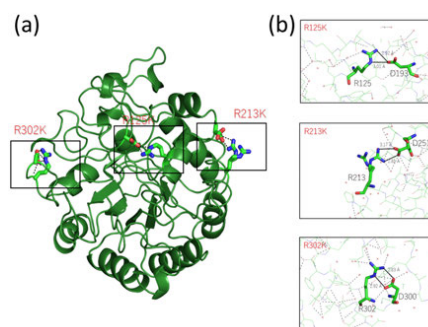


Fig. 1. Crystal structure of Endo-1,4- β -mannanase from *Eisenia fetida*. (a) Overall structure. (b) Pairwise and bifurcated hydrogen bonding interaction in salt bridge.

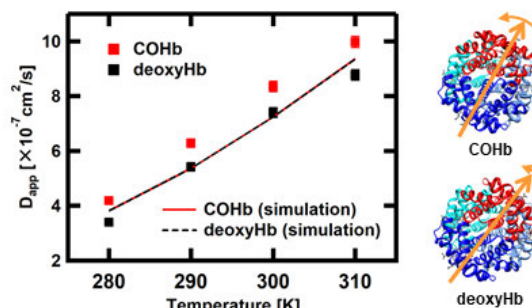


Fig. 2. The apparent diffusion coefficients (D_{app}) of COHb and deoxyHb, along with the simulated values based on the crystal structures. On the right side, the structural models of COHb and deoxyHb are shown with the different subunit motions.

References

- [1] T. Tamada and Y. Hirano, Japanese Patent Application No. 2017-219234 (2017).
- [2] M. Ueda *et al.*, Enzyme Microb. Tech. **117**, 15 (2018).
- [3] S. Fujiwara *et al.*, J. Phys. Chem. B, **121**, 8069 (2017).

Part I

3. Advanced Quantum-Beam Technology

P3-1	Laser Compton Scattering Gamma-ray Research Project	22
	Leader : Ryoichi Hajima	
P3-2	Beam Engineering Section	24
	Section Manager : Yasuyuki Ishii	

P3-1 Laser Compton Scattering Gamma-ray Research Project

Leader : Ryoichi Hajima



The research objective of LCS γ -ray Research Project is developing the technologies of high-brilliance γ -ray generation and exploring its scientific and industrial applications such as nuclear physics, nuclear astrophysics and non-destructive measurement of nuclear material. The γ -ray source is based on laser Compton scattering (LCS), which enables one to generate energy-tunable mono-energetic γ -rays. In the research project, we are developing critical components for electron accelerators to achieve small-emittance and high-average current beams, γ -ray optics and a Monte Carlo simulation code.

Generating carrier-envelope-phase stabilized few-cycle pulses from a free-electron laser oscillator [1]

Stabilization of carrier-envelope phase (CEP) is one of the essential technologies of the modern ultrashort pulse lasers. CEP-stable pulses can be applied to optical comb for ultra-precise spectroscopy, quantum control of chemical reaction and high-harmonic generation (HHG) for attosecond pulse generation. We propose a scheme to generate CEP-stable pulses from a free-electron laser oscillator. The CEP stabilization is realized by the continuous injection of CEP-stable seed pulses from an external laser to the free-electron laser oscillator whose cavity length is perfectly synchronized to the electron bunch repetition. Figure 1 shows a schematic view of the proposed method. Operated at a midinfrared wavelength, the proposed method is able to drive a photon source based on HHG to explore the generation of isolated attosecond pulses at photon energies above 1 keV with a repetition of > 10 MHz. The HHG photon source will open a door to full-scale experiments of attosecond x-ray pulses and push ultrafast laser science to the zeptosecond regime.

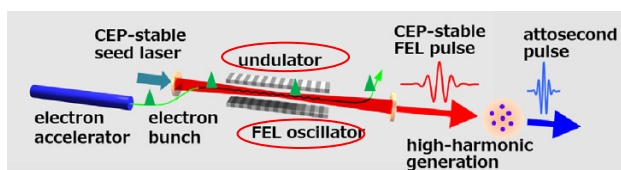


Fig. 1. A schematic view of the proposed scheme to generate CEP-stable FEL pulses by continuous seeding of CEP-stable pulses from an external laser. The FEL pulse can be utilized for high-harmonic generation to obtain attosecond X-ray pulses in the energy range of 1-10 keV.

Gamma-ray vortices from nonlinear inverse Thomson scattering of circularly polarized light [2]

Inverse Thomson scattering (or Laser Compton scattering) is a radiation process that produces high-energy photons both in nature and in the laboratory. By increasing the laser intensity at the collision point, the scattering goes into a nonlinear regime to generate photons containing higher harmonic components. We theoretically show that the higher harmonic γ -ray produced by nonlinear inverse Thomson scattering of circularly polarized light is a γ -ray vortex, which means that it possesses a helical wave front and carries orbital angular momentum as shown in Fig. 2. Our work explains a recent

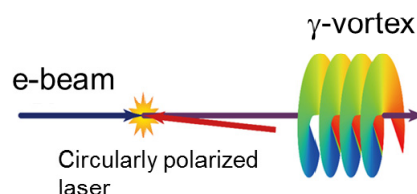


Fig. 2. A schematic view of the γ -ray vortex generation from a nonlinear Thomson scattering of circularly polarized laser with an electron beam.

experimental result regarding nonlinear inverse Thomson scattering that clearly shows an annular intensity distribution as a remarkable feature of a vortex beam. Our work implies that γ -ray vortices should be produced in various situations in astrophysics in which high-energy electrons and intense circularly polarized light fields coexist. Nonlinear inverse Thomson scattering is a promising radiation process for realizing a γ -ray vortex source based on currently available laser and accelerator technologies, which would be an indispensable tool for exploring γ -ray vortex science.

Possible precise measurement of Delbrück scattering using polarized photon beams [3]

The advent of high-flux-polarized γ -ray sources makes possible the nearly isolated precise measurement of the vacuum contribution, Delbrück scattering, to the elastic scattering of these photons off nuclei. Because of the fact that the elastic scattering of the photons is a coherent summation of four processes and that up to now unpolarized sources have been used, the isolated measurement of Delbrück scattering has not been performed. We show that for the appropriate choice of scattering angles, photon polarization, and energies this scattering can be measured nearly independently of other scattering processes. Figure 3 plots calculated differential scattering amplitudes for elastic photon scatterings from Sn, which shows Delbrück scattering can be distinguished from other scattering processes by observing the scattering at $\theta = 70$ degrees. Such precise measurement of the vacuum contributes to scattering and the possibility of the detection of new physics.

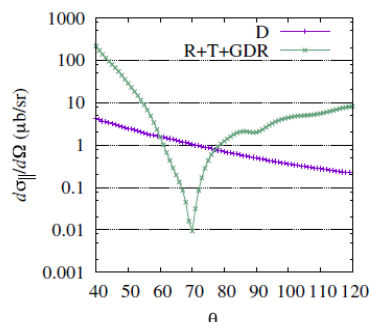


Fig. 3. Calculated differential scattering amplitudes for elastic photon scattering from Sn. Amplitudes of Delbrück (D), Rayleigh (R), Nuclear Thomson (T) and giant dipole resonance (GDR) scatterings are plotted separately.

Including Delbrück scattering in GEANT4 [4]

Elastic scattering of γ -rays is significant interaction among γ -ray interactions with matter. Therefore, the planning of experiments involving measurements of γ -rays using Monte Carlo simulations usually includes elastic scattering. However, current simulation tools do not provide a complete picture of elastic scattering. The majority of these tools assume Rayleigh scattering is the primary contributor to elastic scattering and neglect other elastic scattering processes, such as nuclear Thomson and Delbrück scattering. We develop a tabulation-based method to simulate elastic scattering in one of the most common open-source Monte Carlo simulation toolkits, GEANT4. We collectively include three processes, Rayleigh scattering, nuclear Thomson scattering, and Delbrück scattering. Our simulation more appropriately uses differential cross sections based on the second-order scattering matrix instead of current data, which are based on the form factor approximation. Moreover, the superposition of these processes is carefully taken into account emphasizing the complex nature of the scattering amplitudes. The simulation covers an energy range of $0.01 \text{ MeV} \leq E \leq 3 \text{ MeV}$ and all elements with atomic numbers of $1 \leq Z \leq 99$. Figure 4 shows an example of calculation, the angular distribution of elastically scattered γ -rays at 2.754 MeV by different elements. We also validated our simulation by comparing the differential cross sections measured in earlier experiments with those extracted from the simulations. We find that the simulations are in good agreement with the experimental measurements. Differences between the experiments and the simulations are 21% for uranium, 24% for lead, 3% for tantalum, and 8% for cerium at 2.754 MeV. Coulomb corrections to the Delbrück amplitudes may account for the relatively large differences that appear at higher Z values.

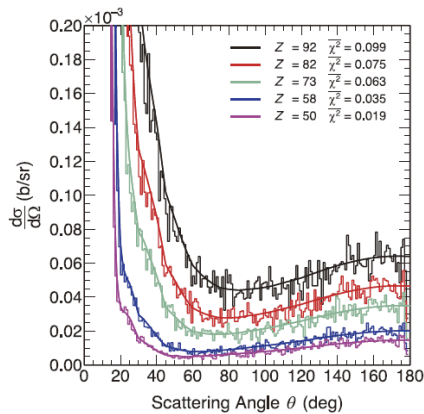


Fig. 4. The angular distribution of elastically scattered γ -rays at 2.754 MeV by different elements (the histograms). The smooth curves are the differential cross sections. The total incident number of photons is 10^9 . Each histogram is normalized to the corresponding differential cross section at 0 deg.

Low-lying dipole strength in ^{52}Cr [5]

The low-lying dipole strength in ^{52}Cr was measured in nuclear resonance fluorescence experiments using a quasimonochromatic, linearly polarized photon beam. The parities of the excited dipole states were determined by the intensity asymmetry of resonantly scattered γ -rays with respect to the polarization plane of the incident photon beam. We observed 62 resonances at excitation energies between 7.5 and 12.1 MeV. The observed M1 and E1 strengths were compared via random-phase-

approximation calculations using the Skyrme interaction. The effects of two-particle-two-hole configuration mixing and tensor force on dipole strength distributions were investigated.

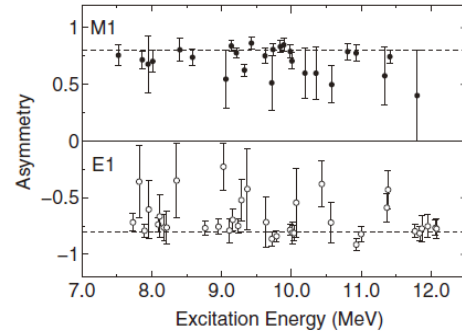


Fig. 5. Azimuthal intensity asymmetry obtained for E1 (open circles) and M1 (filled circles) transitions in ^{52}Cr . The experimental sensitivity q ($= 0.8$) deduced from the numerical calculation is indicated by dashed lines.

Nondestructive inspection system for special nuclear material using inertial electrostatic confinement fusion neutrons and laser Compton scattering γ -rays [6]

A neutron/ γ -ray combined inspection system for hidden special nuclear materials (SNMs) in cargo containers has been developed. This inspection system consists of an active neutron-detection system for fast screening and a laser Compton backscattering γ -ray source in coupling with nuclear resonance fluorescence (NRF) method for precise inspection as shown in Fig. 6. Proof-of-Principle experiments of the neutron and γ -ray systems were carried out at the Reactor Research Institute, Kyoto University and the Kansai Photon Science Institute, QST, respectively. By using numerical simulations based on the data taken from these PoP systems, the system designed by this program can detect 1 kg of highly enriched ^{235}U (HEU) hidden in an empty 20-ft container within several minutes.

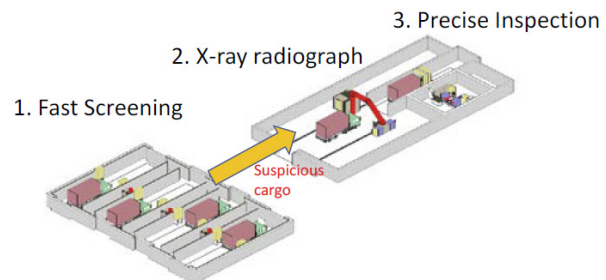


Fig. 6. Schematic drawing of the designed overall inspection system. The number of the lane of the fast screening system will be chosen by the sea port demand.

References

- [1] R. Hajima and R. Nagai, Phys. Rev. Lett. **119**, 204802 (2017).
- [2] Y. Taira *et al.*, Sci. Rep. **7**, 5018(2017).
- [3] J. K. Koga and T. Hayakawa, Phys. Rev. Lett. **118**, 204801 (2017).
- [4] M. Omer and R. Hajima, Nucl. Instrum. Meth. Phys. Res. B, **405**, 43-49 (2017).
- [5] T. Shizuma *et al.* Phys. Rev. C **96**, 044316 (2017).
- [6] H. Ohgaki *et al.*, IEEE Trans Nucl. Sci. **64**, 1635-40 (2017).



The research objectives in our section are development of various accelerator-related-techniques including ion-beam-irradiation-techniques and ion-beam-analyses. Each member has been engaging in individual researches more than one. In recent and remarkable studies, the microscale patterns of colour centres in an Ag-activated phosphate glass were fabricated using a focused MeV proton beam. On the other hand, the beam diameter formed by a compact ion microbeam system was reduced by producing a several-hundred-keV beam under decreasing a divergence angle of an incident beam into an acceleration lens system {1-43, 45~46, 2-34~40, 3-01~04, 08, 11~21, 23~25 in Part II}.

Two-photon excited microscale patterns of colour centre in Ag-activated phosphate glass written by focused proton beam [1]

Microscale patterns were written in an Ag-activated phosphate glass using a focused proton beam with two different energies, 1.7 and 3 MeV, respectively. Two-D and 3D microscale patterns are visualized and reconstructed by combining two-photon confocal microscopy with femtosecond (fs) pulses generated from a mode-locked Ti: sapphire laser operating at 700 nm. The reconstructed images were analytically evaluated by means of lateral=axial dose distributions and radiophotoluminescent (RPL) spectra of the microscale patterns based on proton-induced Ag⁰ and Ag²⁺ centres. In addition, a significant broadening of the Bragg curve of the experiment in comparison with the simulation was discussed.

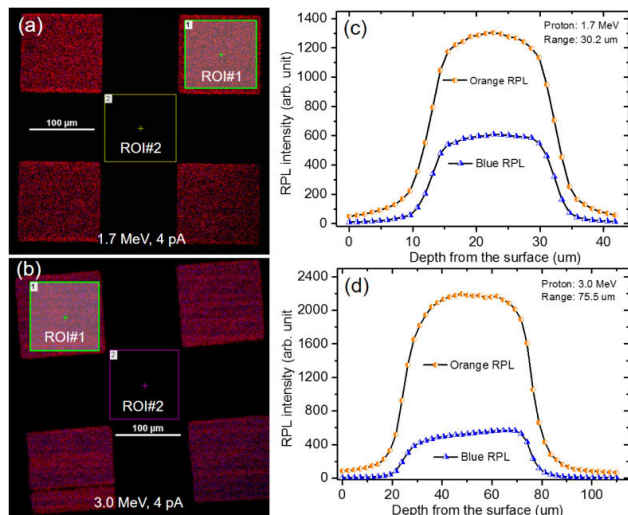


Fig. 1. Two-D images of the square pattern written by multiple-shot proton beam irradiation with energies of (a) 1.7 and (b) 3.0 MeV and setting position of two ROIs. Corresponding dose distribution profiles as a function of depth from the surface for orange and blue RPL at energies of (c) 1.7 and (d) 3.0 MeV.

Figures 1(a) and 1(b) show 2D images of the square patterns with a total of 35 image layers [Fig. 1(a)] and a total of 47 image layers [Fig. 1(b)], which were written by focused proton beams with different energy of 1.7 and 3 MeV, respectively. Two ROIs (ROI#1 and ROI#2) were

set, and then each background (ROI#2) was subtracted from that of the RPL signal (ROI#1). Each figure shows the corresponding RPL intensity profiles along the axial direction for the orange and blue RPL signals as shown in Figs. 1(c) and (d). The estimated distances between the surfaces and the peak intensity of the luminescence profile along the depths, as shown in two graphs of Fig. 1, were in good agreement with the Bragg peak positions for protons of 1.7 and 3 MeV energies, respectively.

Beam diameter reduction by optimization of an extraction condition with a compact ion microbeam system [2]

A compact proton microbeam system with the energy range of several hundred keV has been developed as a prototype of a compact MeV beam system. The beam diameters formed under former conditions were limited to 5.8 μm at 120 keV, though the beam diameter was expected to reduce within 1 μm. The main reason of the large diameter was considered to be the magnitude of the divergence angle of an incident beam into the acceleration lens system. In the present study, the distance between the anode and the extraction electrodes in the ion source of the compact proton microbeam system was arranged shorter to reduce the divergence angle and to generate focused beam within a diameter of 1 μm.

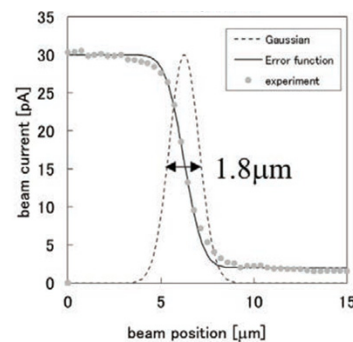


Fig. 2. The relationship between the beam current and the position at the minimum beam diameter.

An experiment to reduce the beam diameter was performed under the condition with the distance at 10 mm. The beam diameter was experimentally evaluated by repeatedly moving a microbeam over a sharp edge using an electrostatic scanner in the distance of 600 μm, in which the beam current was measured by a Faraday cup using a pico-ammeter. The beam current was gradually reduced as shown in Fig. 2. The beam diameters were measured with every fine tuning voltages of the acceleration lenses to obtain the minimum beam diameter. The beam current as a function of beam position is shown in Fig. 2 when the minimum beam diameter was obtained. The minimum beam diameter was estimated to be 1.8 μm by fitting the beam current with the error function.

References

[1] T. Kurobori *et al.*, Jpn. J. Appl. Phys. **57**, 02CC01 (2018).
 [2] T. Ohkubo *et al.*, Phys. Procedia, **90**, 79 (2017).

Part II

Prat II

1. Materials Science

1-01	Single Event Effect Evaluation Results of Cu-based Atom Switch ROM and FPGA	28
	K. Takeuchi, T. Sakamoto, M. Tada, H. Shindo, A. Takeyama and T. Ohshima	
1-02	Recovery of Radiation Degradation in InGaP Solar Cells by Light Soaking	29
	Y. Shibata, T. Sumita, T. Nakamura, A. Ogura, M. Imaizumi, S.-I. Sato and T. Ohshima	
1-03	Effects of Cosmic Radiation on Time-measuring Analog–Digital Mixed ASICs	30
	T. Mizuno, H. Ikeda, A. Ogawa, H. Senshu, K. Umetani and A. Oyane	
1-04	Radiation Response of Silicon Carbide Junction Field Effect Transistors	31
	A. Takeyama, K. Shimizu, T. Makino, Y. Yamazaki, T. Ohshima, S. Kuroki and Y. Tanaka	
1-05	Evaluation of Radiation Hardness on Carbon Nanotube Field Effect Transistor	32
	S. Ishii, T. Hirao and T. Hamano	
1-06	Radiation Damage Tests of Semi-Conductors	33
	C. Ohmori and M. Paoluzzi	
1-07	Research of the Radiation Tolerance in Space Environment of General Electronic Devices	34
	K. Tomita, K. Nakano, K.Ogawa, K. Akashi, T. Maeda, A. Eda, T. Ohshima, S. Onoda and T. Makino	
1-08	Preparation of Nano-Structure Controlled Ion-Exchange Membranes by Ion Beams for Application to Seawater Concentration	35
	T. Yamaki, M. Goto, S. Sawada, H. Koshikawa, A. Kitamura and M. Higa	
1-09	Preparation of Titanium Dioxide Nanocones Using Ion Track-etched Membranes as Template	36
	H. Koshikawa, Y. Sato, S. Yamamoto, M. Sugimoto, S. Sawada and T. Yamaki	
1-10	Electron Beam Induced Formation of Pt Particles on Ceria Films	37
	S. Yamamoto, T. Taguchi, M. Sugimoto, H. Koshikawa and T. Yamaki	
1-11	Microscopic Observations of Nanostructure in Oxide Ceramics Irradiated with Swift Heavy Ions at Grazing Incidence	38
	A. Kitamura, N. Ishikawa, K. Kondo, Y. Okuno, S. Yamamoto, H. Koshikawa and T. Yamaki	
1-12	Utilization of Ion Implantation for Synthesis of Nitrogen-doped Carbon Material with Catalytic Activity (3)	39
	A. Idesaki, S. Yamamoto, M. Sugimoto and T. Yamaki	
1-13	Control of Pore Shapes in Track-etched Membranes by Using Depth Distribution of LET ..	40
	Y. Sato, H. Koshikawa, S. Yamamoto, M. Sugimoto, S. Sawada and T. Yamaki	
1-14	DFT Study of the Pt Nanoparticles on the Ar-ion Irradiated Glassy Carbon Substrate	41
	T. Kimata, K. Kakitani, T. Yamaki, S. Yamamoto, W. Mao, T. Kobayashi and T. Terai	
1-15	Prediction of Scintillation Light Yield by Heavy Ions Based on Sub-micron Radiation Transport Calculation and Förster Effect	42
	T. Ogawa, T. Yamaki and T. Sato	

1-16	Study on Planar Perfect Blackbody from Etched Ion Tracks	43
	K. Amemiya, H. Koshikawa and T. Yamaki	
1-17	Preparation of Nitrogen-doped Carbon-based Catalysts by Electron-Beam Irradiation During High Temperature Pyrolysis	44
	Y. Kanuma, M. Sugimoto, A. Idesaki, S. Yamamoto, H. Koshikawa and T. Yamaki	
1-18	Electron-Beam Irradiated Electrode of a Redox Flow Battery for Low Internal Resistances	45
	H. Ishitobi, S. Yamamoto, K. Oba, H. Koshikawa, T. Yamaki and N. Nakagawa	
1-19	Overvoltage Reduction of Membrane Bunsen Reaction by Using Radiation-grafted Cation Exchange Membranes	46
	T. Kimura, M. Nomura, S. Sawada, T. Yamaki, N. Tanaka and S. Kubo	
1-20	Proton Selectivity and Permeability of Cross-linked Radiation-grafted Cation-Exchange Membranes for Efficient HI Concentration	47
	N. Tanaka, S. Sawada, T. Yamaki and S. Kubo	
1-21	Characterization of (111)-oriented $Ti_{1-x}Al_xN$ Thin Films on Monocrystalline AlN by Reactive CVD	48
	Y. Kasukabe, H. Shimoda, S. Yamamoto and M. Yoshikawa	
1-22	Ion Irradiation-Induced Novel Crystal Lattice Plane Spacing Change in Silicon Carbide Nanotubes	49
	T. Taguchi, S. Yamamoto and H. Ohba	
1-23	Fabrication and Evaluation of Nanoparticles Bi-Ti-O Ferroelectric Materials by Ion Irradiation	50
	H. Abe and Y. Yoneda	
1-24	Development of Hydrogen Permselective Membranes by Radiation-induced Graft Polymerization into Ion-Beam Irradiated Poly Vinylidene Chloride Films	51
	S. Hasegawa, A. Hiroki, S. Sawada and Y. Maekawa	
1-25	Development of Radiation-grafted Cation and Anion Exchange Membranes for Reverse Electrodialysis Process	52
	S. Sawada, M. Yasukawa, M. Higa and Y. Maekawa	
1-26	The Relationship Between Membrane Properties and Hierarchical Structure of Radiation Grafted Anion Conducting Polymer Electrolyte Membranes	53
	K. Yoshimura, Y. Zhao, A. Hiroki, H. Shishitani, S. Yamaguchi and Y. Maekawa	
1-27	Effect of γ -Ray Irradiation on Friction Property of Poly(vinyl alcohol) Cast-drying on Freeze-thawed Hybrid Gel	54
	S. Sasaki, S. Omata, T. Murakami, N. Nagasawa, M. Taguchi and A. Suzuki	
1-28	Changes in Mechanical Properties of Polyethylene by Gamma-ray Irradiation in Water ...	55
	A. Idesaki and M. Taguchi	
1-29	Synthesis of Fibrous Grafted Adsorbent Having Sulfur-based Functional Group	56
	Y. Ueki and N. Seko	
1-30	Development of Boron Removal Technique Combined Grafted Powder Adsorbent with Spring Type Filter	57
	H. Hoshina, N. Kasai, S. Mononobe, K. Kato and N. Seko	
1-31	Amidoxime and Ammonium Fabric Adsorbents Prepared by Radiation Grafting for Chromium Removal	58
	J. Chen, N. Hayashi, Y. Ueki and N. Seko	

1-32	Surface Crosslinking of Silicone Rubber by Electron Beam Irradiation	59
	T. Makabe, M. Oshida, H. Sando, N. Mizote, Y. Ueki and N. Seko	
1-33	Study on Hydrogen Generation from Cement Solidified Products Loading Low-level Radioactive Liquid Wastes at Tokai Reprocessing Plant	60
	F. Sato, R. Matsushima and Y. Ito	
1-34	Effects of Displacement Damage, Helium and Hydrogen on Electrical Properties of Silicon Carbide	61
	T. Nozawa, M. Ando, T. Taguchi and H. Tanigawa	
1-35	Effects of Self-Ion Irradiation on Rhenium Distribution and Microstructure in Tungsten-Rhenium Alloy	62
	T. Miyazawa, T. Hwang, S. Nogami, A. Hasegawa and H. Tanigawa	
1-36	Hydrogen Gas Measurements of Phosphate Cement Irradiated During Heat Treatment ...	63
	K. Irisawa, I. Kudo, T. Taniguchi, M. Namiki, T. Osugi and O. Nakazawa	
1-37	Effect of Damage Depth Profile on Hydrogen Isotope Dynamics in W	64
	Y. Oya, K. Azuma, A. Togari, Q. Zhou, T. Miyazawa and T. Chikada	
1-38	Experimental Results of Swelling Behavior of FMS Steels Under ADS Irradiation Conditions	65
	N. Okubo and N. Ishikawa	
1-39	Irradiation Tests of Radiation Hard Components and Materials for ITER Blanket Remote Handling System	66
	M. Saito, Y. Noguchi, M. Kazawa, K. Nakata and N. Takeda	
1-40	Development of Radiation Resistant Monitoring System in Light Water Reactor	67
	T. Takeuchi, N. Otsuka, H. Nakano, T. Iida, O. Ozawa, T. Shibagaki, H. Komanome and K. Tsuchiya	
1-41	Development of the Predicting Method for the Long Term Corrosion Under Irradiation	68
	T. Sato, Y. Ishijima and F. Ueno	
1-42	Synergetic Effect of He, H and Displacement Damages on the Void Swelling Behavior of F82H	69
	D. Hamaguchi, M. Ando and H. Tanigawa	
1-43	Change in Hardness of FeCuMn Alloy by Energetic Ion Irradiation	70
	A. Iwase, T. Sumie, F. Hori, Y. Saitoh, S. Semboshi and Y. Okamoto	
1-44	Study on Synthesis of Pd Catalyst from Eluent After Separation Process for High-level Liquid Waste Based on Radiation-induced Reaction	71
	T. Ito, S.-Y. Kim and R. Nagaishi	
1-45	Characterization of Adsorbent for U and Pu Recovery from Degraded PUREX Solvent ...	72
	Y. Arai, S. Ohno, S. Watanabe, A. Shibata, K. Nomura, M. Koka and T. Satoh	
1-46	Gamma-ray Irradiation Durability of CMPO Adsorbent for MA(III) Recovery	73
	Y. Miyazaki, S. Watanabe, H. Kofuji, M. Koka and T. Satoh	
1-47	Synthetic Reference Sample by Electron Irradiation for IR Measurement of Carbon Concentration in Silicon Crystal	74
	N. Inoue, S. Okuda and S. Kawamata	

Single Event Effect Evaluation Results of Cu-based Atom Switch ROM and FPGA

K. Takeuchi ^{a)}, T. Sakamoto ^{b)}, M. Tada ^{b)}, H. Shindo ^{a)}, A. Takeyama ^{c)} and T. Ohshima ^{c)}

^{a)} Research and Development Directorate, JAXA,

^{b)} System Platform Research Laboratories, NEC Corp.,

^{c)} Department of Advanced Functional Materials Research, TARRI, QST

Next generation nonvolatile memories (NVM), such as magneto-resistive random access memory (MRAM) resistive RAM (ReRAM) and phase change memory (PCM) are of great interest for replacing conventional NVM. Previous works suggest Ag-based conductive bridge RAM (CBRAM) shows gamma-ray and heavy ion tolerance [1-2] in a certain condition. In this work Cu-based atom switch, which is one of CBRAM was subjected to heavy ion irradiation test.

The radiation tolerance of both Cu-based atom switch ROM and FPGA which are fabricated in 65 nm-node Silicon-On-Thin-Buried-oxide (SOTB) CMOS process, were evaluated by using the TIARA in QST. The chips were irradiated by Xe or Kr ion. Details of irradiation and sample conditions were explained in Table 1 and [3], respectively.

During irradiation, some read-out errors that seem to be caused by CMOS circuit were observed. However, no single event upset (SEU) was observed up to 68.9 MeV/(mg/cm²). The cell state was checked by PC just after irradiation and validated by LSI tester. Moreover, there was a slight change that is negligible in the reading window of ROMs. Figure 1 shows a comparison of shmoo plot between before (left) and after (right) the irradiation. A black arrow indicates the difference between before and after irradiation, which could be negligible.

The estimated upper SEU cross section (σ_{SEU}) of atom switch is calculated as follows,

$$\sigma_{SEU} \leq 1/(fluence \times bit) [cm^2/bit] \quad (1)$$

where *fluence* and *bit* are the total fluence [p/cm²] and total bits embedded in ROM [bit], respectively. In Fig. 2, the estimated SEU cross sections were much smaller than actual cell area (showed in dashed plot), even if the voltage was applied to each cell in irradiations to FPGA. This suggests that atom switches have intrinsic SEU immunity.

Acknowledgments

The present work is a collaboration with System Platform Research Laboratories of NEC Corp. for atom switch evaluation, and collaboration with QST for heavy ion irradiation.

References

- [1] J. R. Jameson *et al.*, IEEE Int. Electron Devices Meet. (2013).
 [2] D. Mahalanabis *et al.*, IEEE Trans. Nucl. Sci. **61**(6), 3557-63 (2014).

[3] K. Takeuchi *et al.*, QST Takasaki Annu. Rep. 2016, **QST-M-8**, 28 (2018).

Table 1
Irradiation conditions.

Ion	¹²⁹ Xe ²⁵⁺	⁸⁴ Kr ¹⁷⁺
Net Energy [MeV]	398	289
LET at Si surface [MeV/(mg/cm ²)]	68.9	40.3
Range in Si [μ m]	35.0	37.3
Total fluence	10 ⁶ - 10 ⁷ [p/cm ²]	

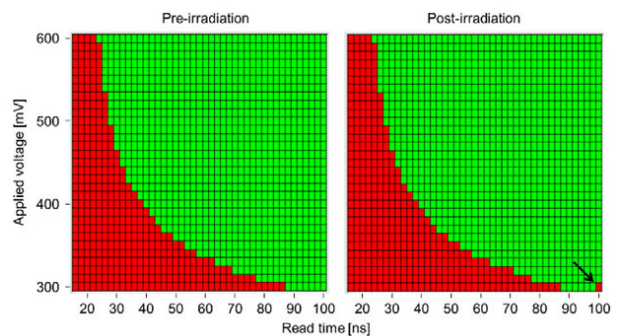


Fig. 1. Shmoo plot of ROM between applied voltage and read time (Green: pass, Red: fail). A black arrow indicates difference between pre-irradiation (left) and post-irradiation (right).

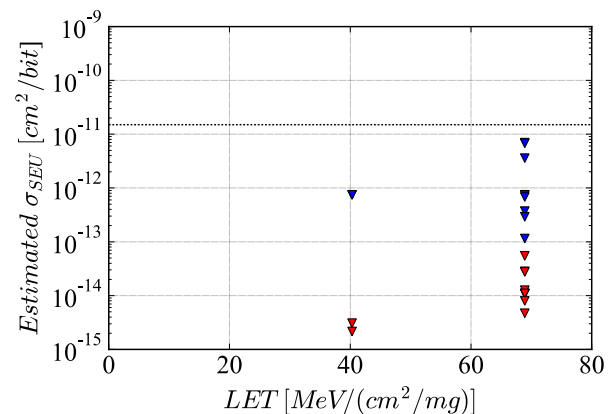


Fig. 2. Actual cell area (dashed line) and estimated SEU cross section (blue down triangle for ROM and red for FPGA, respectively). Down triangle represents each estimated value is expected less than the point in the figure.

1 - 02 Recovery of Radiation Degradation in InGaP Solar Cells by Light Soaking

Y. Shibata ^{a)}, T. Sumita ^{a)}, T. Nakamura ^{a)}, A. Ogura ^{a)}, M. Imaizumi ^{a)}, S.-I. Sato ^{b)} and T. Ohshima ^{b)}

^{a)} Research and Development Directorate, JAXA,

^{b)} Department of Advanced Functional Materials Research, TARRI, QST

Radiation tolerance is one of the important properties for space solar cells. Such a radiation response has been previously investigated for InGaP, GaAs and InGaAs single-junction [1], whose materials also constitute the subcells of the inverted metamorphic triple-junction (IMM3J) solar cells. Recently, we reported on the recovery of radiation degradation in IMM3J solar cells by light soaking and proposed that recovery occurs in the InGaP top cell rather than in the GaAs middle cell or InGaAs bottom cell [2]. In this work, we carried out light soaking experiments on electron irradiated InGaP solar cells to investigate the reason for the recovery of the open-circuit voltage (V_{oc}) after radiation degradation.

The samples studied in this work were two types (Cell A and B) of $\text{In}_{0.48}\text{Ga}_{0.52}\text{P}$ single-junction solar cells with a size of $1\text{ cm} \times 1\text{ cm}$. The sample cells were irradiated 1 MeV electrons with the fluence of 1×10^{15} and $1 \times 10^{16}\text{ cm}^{-2}$. After the irradiations, light soaking was carried out with the duration of up to 50 minutes under Air Mass 0 (AM0, 137 mW/cm^2) simulated solar light. The intensities of the light were 1 sun, and equivalent to 0.28 and 0.52 suns by Neutral Density filters. The terminal of the cells was kept open-circuit during the light soaking. Additionally, current injection under dark was employed to compare the recovery with that observed upon light soaking. The forward injection current was equal to the initial short-circuit current of the cell under AM0.

Figure 1 shows the light-current-voltage (LIV) sweep characteristics that were obtained before and after the irradiation with 1-MeV electrons with a total fluence of $1 \times 10^{16}\text{ cm}^{-2}$ and that after the subsequent 1 sun light soaking. V_{oc} after the light soaking was significantly recovered.

Relation between concentration of radiation-induced defects (N_d) and V_{oc} is expressed by the equation (1):

$$N_d = \Phi_0 n_a \sigma \nu \left[\exp \left(\frac{V_{oc0} - V_{oc\phi}}{C} \right) - 1 \right] \quad (1)$$

where V_{oc0} and $V_{oc\phi}$ are V_{oc} before and after the irradiation, respectively. Assuming that n_a , σ , ν , Φ_0 and C are constant, ratio of the defect concentration before and after the soaking ($N_{dA}/N_{d\phi}$) becomes

$$\frac{N_{dA}}{N_{d\phi}} = \frac{\exp \left(\frac{V_{oc0} - V_{ocA}}{C} \right) - 1}{\exp \left(\frac{V_{oc0} - V_{oc\phi}}{C} \right) - 1} \quad (2)$$

where V_{ocA} is V_{oc} after the soaking, $N_{d\phi}$ and N_{dA} are the defect concentration before and after the light soaking, respectively. Figure 2 plots the ratio between the radiation-induced defect densities before and after light soaking or after current injection for the cells irradiated with 1-MeV

electrons. The fluence was $1 \times 10^{15}\text{ cm}^{-2}$. The number of photo-generated or injected carriers (n) is calculated from the product of the initial I_{sc} and the light soaking duration. The defect density decreases with an increase of either the number of photo-generated or the number of injected carriers. In addition, the trend of the defect density decrease is the same for both light soaking and current injection and is also independent on the light-soaking intensity. In other words, the recovery depends only on the number of photo-generated or injected carriers, if the temperature is constant. Under open-circuit condition, all photo-generated carriers recombine in the cells. In the case of carrier injection, most likely all carriers recombine in the cells as well. The physics behind this phenomenon are rather complex, as explained in the following discussion on possible origins. These results imply that the recombination of carriers contributes to the recovery of V_{oc} after radiation degradation.

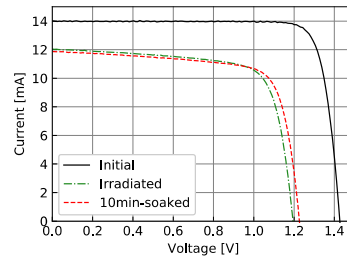


Fig. 1. Changes in current–voltage curves under illumination as a result of 1-MeV electron irradiation and 1 sun light soaking.

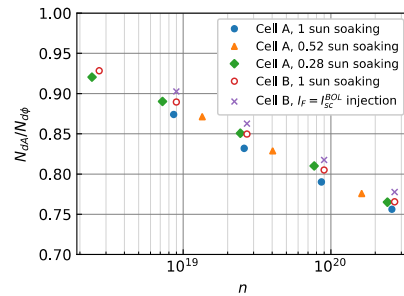


Fig. 2. Ratio between radiation-induced defect densities before and after light soaking or after current injection as a function of the number of photo-generated or injected carriers.

References

- [1] M. Imaizumi *et al.*, Progr. Photovoltaics Res. Appl., **25**, 137-205 (2017).
- [2] Y. Shibata *et al.*, Proc. 11th RASEDA, 65-68 (2015).
- [3] C. Brandt *et al.*, J. Photovoltaics, **3**, 2, 904-08 (2013).

Effects of Cosmic Radiation on Time-measuring Analog-Digital Mixed ASICs

T. Mizuno ^{a)}, H. Ikeda ^{a)}, A. Ogawa ^{b)}, H. Senshu ^{c)}, K. Umetani ^{d)} and A. Oyane ^{d)}

^{a)} Institute of Space and Astronautical Science, Japan Aerospace Exploration Agency,

^{b)} Department of Mechanical Engineering, Graduate School of Engineering, Tokai University,

^{c)} Planetary Exploration Research Center, Chiba Institute of Technology,

^{d)} Faculty of Engineering, Okayama University

Many spacecrafts exploring the moon and planets are equipped with a light detection and ranging (LIDAR) sensor that uses a pulsed laser for altitude measurement, navigational guidance, and mapping as part of scientific observation. Spacecrafts intended to land on the planetary surface are additionally equipped with a laser sensor that can capture a three-dimensional range image, which is necessary for avoiding obstacles at the time of landing.

Within this context, JAXA developed an optical-pulse-detection ASIC (LIDARX) for use as a long-distance LIDAR sensor circuit. LIDARX is intended to shorten the development period of long-distance LIDAR and improve scientific observation performance. Currently, it is a candidate for inclusion on the project, which aims to return samples from a satellite of Mars. In addition, JAXA is developing a 3D distance-image sensor Flash LIDAR through collaborative research with sensor manufacturers. JAXA is designing a range readout circuit (ROIC) on a CMOS process. The basic cell design used for these ASICs is provided by the "Analog-VLSI Open-IP Project" [1]. In the Open-IP Project, detailed parameters are generally disclosed to determine the gate length and the gate width of the transistor.

Since these ranging ASICs are manufactured on a CMOS process, the influence of cosmic ray radiation on the spacecraft must be evaluated. The purpose of this research is to evaluate the single-event effect (SEE) from space radiation in terms of how it affects the ranging ASIC developed by JAXA. The result will determine whether the developed ASIC is suitable for mounting on the spacecraft. In addition, we hope that this result will contribute to future space-device design.

LIDARX is the ASIC being considered for use in the long-distance LIDAR of the Mars satellite sample return project. LIDARX consists of a high-sensitivity charge amplifier that detects charge pulses at the femtocoulomb level and a small-scale digital circuit. It is manufactured in the CMOS 0.35 μm process of the municipal shuttle service.

In this report, we describe the SEE evaluation test of LIDARX using the cocktail M/Q = 5 beams of the AVF cyclotron. The evaluated LIDARX has the same rod tip as the flight item.

LIDARX has 9 normal D-type flip-flops (D-FF) and 108 dual interlocked-cell (DICE) FFs with excellent radiation resistance. The layout area of the D-type FF is 1080 μm^2 , and the DICE FF has area 1720 μm^2 . DICE FFs are important FFs that determine the offset of analog circuits and the gain of amplifiers. The acceleration energy of

cocktail M/Q = 5 beams is 40, 54, 107, 230, and 350 MeV for N, Ne, Ar, Kr, and Xe, respectively. The penetration depth of these heavy ions into silicon is about 30 μm . Since the wiring layer of the LIDARX CMOS 0.35 μm process is about 10 μm thick and the epi layer is less than 10 μm thick, the irradiated ions penetrate to the substrate, even with heavy ion beam described above. Therefore, an effective experiment was possible despite damage to the main coil of the AVF cyclotron at TIARA.

Figure 1 shows the result of a measured single-event upset (SEU) cross section of an FF. The horizontal axis shows the linear energy transfer (LET) against silicon, and the vertical axis shows the SEU cross-sectional area. Relative to a D-FF, the SEU cross-sectional area for a DICE FF is 1/10 or less on the low-energy side and about 1/2 in the saturated region, demonstrating that DICE FFs have high SEU resistance. It is known that the distribution of an SEU cross-section for LET can be approximated by a Weibull curve. By inputting the Weibull curve fitting parameters to CREME 96 [2], the number of SEU occurrences on orbit can be estimated. From the results in Fig. 1, the occurrence of SEU in LIDARX is estimated to be 10^{-6} times/day during interplanetary orbit, and it can be used for the MMX project for 6 years.

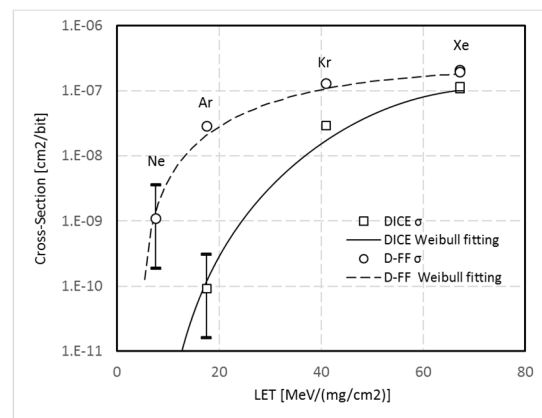


Fig. 1. SEU cross section of LIDARX. The acceleration energies of N, Ne, Ar, Kr, and Xe are 40, 54, 107, 230, and 350 MeV, respectively. Since SEU by Ne irradiation was not observed for a DICE FF, Weibull approximation was calculated assuming one SEU. Error bars indicate 68% confidence intervals for Poisson distribution.

References

- [1] Open-IP Project: <http://research.kek.jp/people/ikeda/>.
 [2] CREME Site: <https://creme.isde.vanderbilt.edu/>.

1 - 04 Radiation Response of Silicon Carbide Junction Field Effect Transistors

A. Takeyama ^{a)}, K. Shimizu ^{b)}, T. Makino ^{a)}, Y. Yamazaki ^{a)}, T. Ohshima ^{a)}, S. Kuroki ^{c)} and Y. Tanaka ^{b)}

^{a)} Department of Advanced Functional Materials Research, TARRI, QST,
^{b)} National Institute of Advanced Industrial Science and Technology,
^{c)} Research Institute for Nano Device and Bio Systems, Hiroshima University

Electronic devices consisted of silicon carbide (SiC) show higher radiation tolerance than conventional silicon devices due to its wide band gap and strong covalent bond. Therefore, SiC metal-oxide-semiconductor field effect transistors (MOSFETs) have been expected as switching devices applied to robots working under high radiation environments [1]. Regardless of intentional studies of SiC MOSFETs, negatively shift of threshold voltage (V_{th}) due to irradiation is still a key issue in terms of practical application. Negative shift of V_{th} is attributed to accumulation of holes (positive charges) generated in the gate dielectric (SiO_2) by gamma-ray irradiation. In contrast, SiC junction field effect transistors (JFETs) substitute p-n junction for the gate dielectric [2] and their radiation response is of interest.

Cross-sectional view of the n-channel depletion mode JFET fabricated used in this study (fabricated by AIST) is illustrated in Fig. 1. Nominal channel length and width were 2.2 and 0.6 μm , respectively. The gate (p^+) was formed by implantation of aluminum ions into an n-type epitaxial layer. Both source and drain (n^+) regions were also formed by phosphorous ion implantation. SiO_2 layer with 1 μm thick were thermally grown to passivate the surfaces. The SiC JFETs were irradiated with gamma-rays up to 2.2 MGy at room temperature in nitrogen atmosphere. After irradiation, electrical properties of the JFET were measured at room temperature. Irradiation and characterization were carried out for two JFETs, named as sample A and B.

Typical drain current (I_D)–gate voltage (V_G) curves of sample A were shown in Fig. 2(a). Drain voltage (V_D) of 3 V was applied to drain electrode. With increasing dose, leakage current increased, nonetheless, it decreased over 300 kGy. The leakage current might conduct along the surface states, since similar dose dependence was not observed for V_{th} and transconductance g_m , which defined as the slope of $I_D - V_G$ curve (data are not shown). At 2.2 MGy, $I_D - V_G$ curve in the current range above 10^{-6} A declined. As g_m is proportional to the product of carrier density and electron mobility, it is suggested that trap states generated in channel region decreased major carrier (electron) density and lowered mobility. Figure 2 (b) is a plot of V_{th} as a function of dose. The value of V_{th} gradually increased due to irradiation irrespective of initial V_{th} . Positive shift of V_{th} indicates effective concentration of electrons in the channel region decreased. While this effect is similar to previously reported for neutron irradiated SiC JFETs [3], we demonstrated in this

study high radiation tolerance of fabricated SiC JFETs against gamma-ray irradiation.

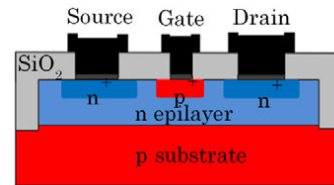


Fig. 1. Cross-sectional view of SiC JFET.

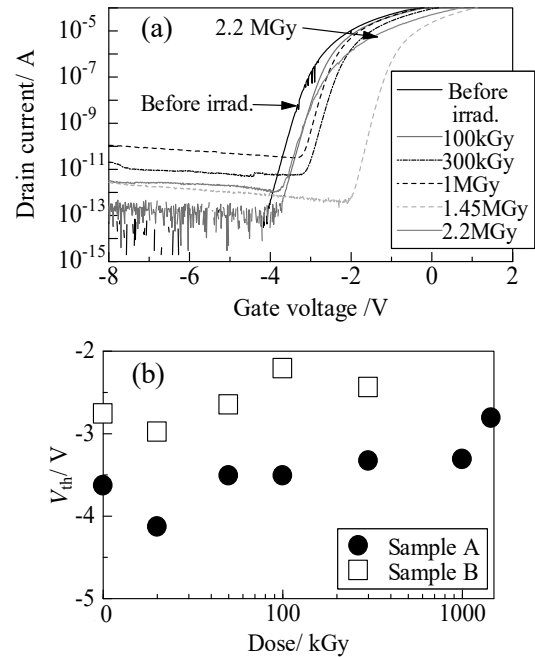


Fig. 2 (a). $I_D - V_G$ curves of SiC JFETs before and after irradiation, (b). V_{th} plotted as a function of absorbed dose.

Acknowledgment

This work was (partially) supported by the research grant from MEXT; “Nuclear Energy S&T and Human Resource Development Project (through concentrating wisdom)”.

References

- [1] T. Ohshima *et al.*, Jpn. J. Appl. Phys. **55**, 01AD01 (2016).
- [2] K. Shimizu *et al.*, Proc. 4th Meet. Adv. Power Semicond., [Nagoya, Japan] (2017/11).
- [3] S. Popelka *et al.*, IEEE. Trans. Nucl. Sci. **61**, 3030 (2014).

1 - 05 Evaluation of Radiation Hardness on Carbon Nanotube Field Effect Transistor

S. Ishii ^{a)}, T. Hirao ^{b)} and T. Hamano ^{b)}

^{a)} Department of Physics, Tokyo Denki University,
^{b)} Department of Accelerator and Medical Physics, NIRS, QST

Carbon nanotube field-effect transistors (CNTFETs) have attracted much attention due to the electrical properties of carbon nanotubes (CNTs), which are superior to those of conventional semiconducting materials such as silicon. Moreover, structural resistance to radiation has been recently reported on CNTs, and thus CNTFET devices are expected to be suitable for radiation environments. Our group investigated the electrical properties of p-type CNTFETs under gamma irradiation in air. CNTFETs showed total dose dependence of the threshold voltage shift, which was attributed to both the charge traps in the gate insulator and the surface of the devices [1].

On the other hand, the conduction type of CNTFET is intrinsically ambipolar. An ambipolar CNTFET is useful for composing a complementary circuit. However, few studies have been reported on the electrical properties of ambipolar CNTFETs because CNTFETs are typically p-type due to oxygen adsorbing on their surfaces when in air. For future application of CNTFET logic circuits in radiation environments, the electrical properties of ambipolar CNTFETs need to be understood.

In this study, we have fabricated ambipolar CNTFETs by passivating the device surface with Al₂O₃ thin film. Gate leakage current (I_G) was evaluated by biasing constant gate voltage (V_{GS}) during gamma irradiation.

Figure 1 shows the schematic of a CNTFET with buried back gate and measurement circuit. Gate electrodes (Ti/Au = 10/150 nm) were patterned on the surface of an SiO₂/p⁺-Si substrate by a lift-off process using photolithography and electron beam evaporation, followed by formation of Al₂O₃ gate insulator (300 nm) by atomic layer deposition (ALD) at 210 °C. The CNT network was made by dispersing an aqueous solution of CNTs using a spin coater. Source and drain electrodes (Ti/Au = 10/200 nm) were then patterned on the CNT network. After electrical isolation of the device by O₂ plasma etching of the CNT network outside of the channel region, the device

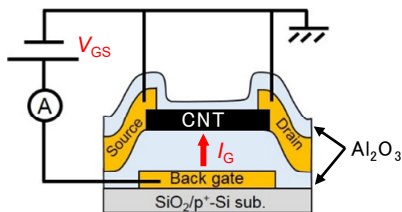


Fig. 1. Schematic of the fabricated carbon nanotube field-effect transistor (CNTFET) and measurement circuit. The channel length and width of the CNTFET were 20 and 100 μm , respectively. The source and drain electrodes were grounded.

surface was passivated with an Al₂O₃ layer (50 nm) by ALD under the same conditions as the formation of the gate insulator.

The CNTFETs were irradiated by gamma rays using the ⁶⁰Co gamma-ray source at Takasaki Advanced Radiation Research Institute with a dose rate of 5.37 kGy/h. Both the source and drain electrodes were connected to ground after confirming the ambipolar properties of CNTFET. Then, I_G was measured by biasing $V_{GS} = +5$ and -5 V before, during, and after gamma irradiation (Fig. 1).

Figure 2 shows the time dependence of I_G . I_G was increased up to about 4.5 nA by gamma irradiation at $V_{GS} = +5$ V and then recovered when the irradiation stopped (Fig. 2(a)). On the other hand, in the case of $V_{GS} = -5$ V, I_G of about 3 nA flowed in the opposite direction to when $V_{GS} = +5$ V (Fig. 2(b)). Electron-hole pairs were generated by the gamma irradiation, and the electrons and holes were driven to the CNT channel and gate electrode, respectively, by V_{GS} . Thus, the gate leakage current generated by gamma irradiation needs to be considered in order to develop complementary circuits using ambipolar CNTFETs.

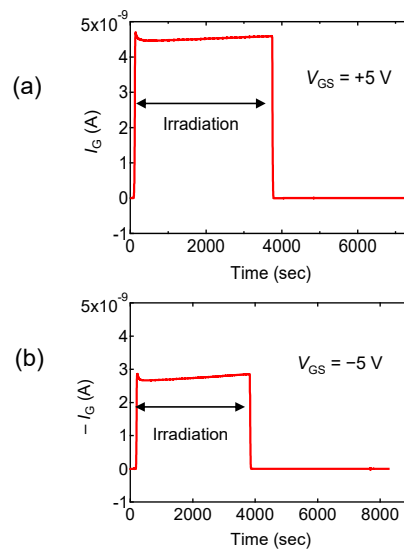


Fig. 2. Time dependence of the gate leakage current, I_G at (a) $V_{GS} = +5$ V and (b) $V_{GS} = -5$ V.

Acknowledgment

The present work is partially supported by the joint usage/research program of the Institute of Materials and Systems for Sustainability (IMaSS), Nagoya University.

Reference

[1] S. Ishii *et al.*, *Physica E*, **86**, 297 (2017).

C. Ohmori^{a)} and M. Paoluzzi^{b)}

^{a)} Accelerator Laboratory, High Energy Accelerator Research Organization (KEK),
^{b)} The European Organization for Nuclear Research (CERN)

In the high intensity proton accelerators, solid state amplifiers using high power Metal-Oxide-Semiconductor Field Effect Transistors, MOSFETs, were not used often because of the radiation effects. In 2012, CERN starts the R&D to use a wideband accelerating cavity system to replace the existing RF accelerating system in the PS booster [1]. And the system includes many high power solid state amplifiers to drive the cavities. By the long-term collaboration efforts, it was found that a compensation scheme to adjust the bias current of MOSFET will extend its life time. Amplifiers were tested with the gamma rays at QST-Takasaki and with the mixed radiation fields in the CHARM, Cern High energy Accelerator Mixed field/facility. Comparing the results from both facilities, it is also possible to evaluate the Single Event Effect, SEE, and neutron effects.

In 2017, we irradiated two sets of 100 W solid state amplifiers with different dose rates at the QST-Takasaki. All amplifiers use VRF151G MOSFET of Microsemi Co. with radiation compensation circuit and RF auto-level control loop to keep 100 W output constant. The devices were protected with thermal switches and fuses to avoid over heat. These amplifiers were located at the positions of the dose rates of 15 Gy/h and 2 Gy/h. Figure 1 shows an amplifier irradiated with the dose rate of 15 Gy/h. The MOSFET has high Drain-Source break-down voltage of 180 V and it will be used for the CERN PS booster RF based on the measurements at the J-PARC MR [2] and other places.



Fig. 1. The setup of irradiation test of solid state amplifier (left) at the QST. Middle and right show the setup to test MOSFETs without RF power.

In total, 2.39 kGy and 319 Gy were irradiated. The dose was measured using Alanine dosimeters, Amino-gray. The gain variation was measured between 0.5 MHz and 5 MHz.

Both amplifiers show an excellent stability of less than 1 dB variation. These amplifiers were shipped to CERN for the test at the irradiation facility, CHARM after replacing MOSFETs. At the CHARM, 5.25×10^{16} protons on target were used. Total Ionizing Dose, TID, of 1.9 kGy, 1-MeV neutron equivalent fluence (cm^{-2}) of 1.09×10^{13} and High Energy Hadron-equivalent fluence (cm^{-2}) of 7.7×10^{12} were irradiated. Gain variations for both tests are shown in Fig. 2. In both cases, the gain variations are less than 1 dB and the compensation scheme worked well [3]. The result suggests the major effect below 2 kGy irradiation on the amplifier using VRF151G is TID.

The radiation results in 2017 show that the solid state amplifier can be used at the PS booster for many years if the MOSFET is properly adjusted according to the TID. The test will be continued at both QST and CHARM.

In parallel, radiation damage test on Access Points [4] and calibration test of OSL dosimeter [5] were performed.

The work is supported by Facility-service system of QST.

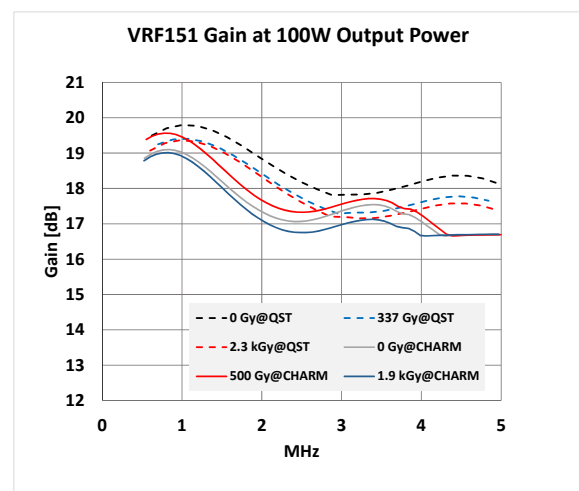


Fig. 2. Gain variations of the amplifiers using MOSFET, VRF151G. Both results at QST-Takasaki and at CHARM are consistent.

References

- [1] CERN Courier: July/August, 12 (2017).
- [2] C. Ohmori *et al.*, Proc. 11th Annu. Meet. Part. Accel. Soc. Jpn., MOOM02, 249-53, [Aomori, Japan], (2014/08).
- [3] C. Ohmori, M. Paoluzzi, CHARM Radiat. Test Rep.
- [4] Y. Kawabata *et al.*, Proc. 14th Annu. Meet. Part. Accel. Soc. Jpn., WEP141, 1282-86, [Sapporo, Japan] (2017/08).
- [5] 橋本 義徳 他, 平成 29 年放射線安全取扱部会年次大会, ポスター発表, [淡路夢舞台国際会議場・淡路市] (2017/10).

Research of the Radiation Tolerance in Space Environment of General Electronic Devices

K. Tomita ^{a)}, K. Nakano ^{a)}, K. Ogawa ^{a)}, K. Akashi ^{a)}, T. Maeda ^{a)}, A. Eda ^{a)},
T. Ohshima ^{b)}, S. Onoda ^{b)} and T. Makino ^{b)}

^{a)} Advanced Engineering Services Co., Ltd. (AES),

^{b)} Department of Advanced Functional Materials Research, TARRI, QST

In small satellite development, commercial off-the-shelf (COTS) devices are needed to use due to some severe restrictions of resource for installed components. For this reason, it is important to keep reliability for using COTS devices in small satellite development. Therefore, in order to ensure reliability for small satellite, our company has evaluated COTS devices mainly for tolerance of single event at Takasaki Advanced Radiation Research Institute (TARRI) from fiscal year 2008.

近年、小型人工衛星の開発が盛んになり、衛星搭載機器の低コスト化、小型化及び高機能化が要求されている。これらの要求を満たすため、民生電子部品の使用が望まれている。しかしながら、一般的に民生電子部品は宇宙環境下での使用を考慮して設計されておらず、耐放射線性は不明である。そこで民生電子部品の宇宙環境における動作状況、劣化状況を放射線試験により確認し、宇宙への適合性を把握する。

放射線の電子部品への影響は、トータルドーズ (TID: Total Ionization Dose) とシングルイベント効果 (SEE: Single Event Effect) の大きく 2 パターンに分けられる。TID は β 線、 γ 線、陽子線により発生する電子部品の性能劣化である。SEE は重粒子の入射により引き起こされる機能障害である。本研究において、民生電子部品の使用を想定している小型人工衛星は、運用期間が 1 年と短いため、TID による影響は少ないと考える。一方、SEE は一度の発生で電子部品そのものや周辺回路を破壊する可能性がある。本研究は、様々な民生電子部品の試験を行い、宇宙環境における耐放射線性の評価を行うことを目的としている。

本研究では量子科学技術研究開発機構施設共用制度を利用し、高崎量子応用研究所 TIARA 第 4 重イオン室の散乱ビーム照射試験装置を用い、AVF サイクロトロンからのカクテルビーム (N, Ne, Ar の 3 線種) で試験した。SEE 発生頻度は、試験により得られた反転断面積、LET (Linear Energy Transfer) 閾値と CREME96 [Cosmic Ray Effects on Micro-Electronics (1996 Revision)] を用いて計算した軌道上放射線分布より算出した。

本研究で民生電子部品の使用を想定している小型人工衛星の軌道条件は、高度 700 km、軌道傾斜角 98 度、衛星構体は 2 mm 厚アルミニウム、運用期間 1 年である。算出した SEE 発生頻度と想定運用期間を比較し、民生電子部品の耐放射線性を評価した。

2017 年度は、民生の過電流検出 IC を試料とした。この IC は、SEL (Single Event Latch-up) や短絡等が発生したときに、大電流が流れることでデバイスや負荷機器が故障することを保護する目的で使用される。

2017 年度に試験を実施した試料、評価項目、試験結果及び想定軌道条件における SEE 発生頻度の算出結果を Table 1 に示す。

本試験では以下を評価項目とした。

- ・ SEL
 - ・ SEFI (FET ゲート駆動出力異常)
 - ・ SEFI (内蔵レギュレータ出力電圧異常)
 - ・ SEFI (IC ステータス出力信号異常)
- (SEFI : Single Event Functional Interrupt)

SEL に関しては、試料の消費電流が SEL 判定閾値 (通常動作時消費電流の 2 倍) 以上に増加した場合に、SEL 発生と判断し、発生回数をカウントした。また、同時に試料の電源リセットにより正常復帰が可能か確認を行った。SEFI に関しては、試料の誤動作を検知した場合に、発生回数をカウントした。

試験の結果、SEL は Ar 照射時に発生したが、電源リセットを行い、正常に復帰することを確認した。また、SEFI としては、FET ゲート駆動出力異常が全線種照射時に発生し、IC ステータス出力信号異常が Ar 照射時に発生した。内蔵レギュレータ出力電圧異常は照射した全線種で発生が確認されなかった。

Table 1 より、過電流検出 IC の SEL、IC ステータス出力信号異常の発生頻度は、想定している 1 年という運用期間に対して小さく、十分な耐放射線性を有することが確認できた。しかし、FET ゲート駆動出力異常に関しては、SEL、IC ステータス出力信号異常と比較して、発生頻度が高く、試料の耐放射線性は低いと考える。本試験での FET ゲート駆動出力異常は、印加するゲート電圧が瞬間的に上昇する事象であった。この事象により、FET が OFF し、負荷機器等への電力供給を停止することがある。よって、使用する際は注意が必要である。

最後に、試料である民生電子部品は、宇宙環境での使用を想定して製造されたものではないため、本試験の結果が部品自身の性能・機能の優劣を示すものではないということを付記しておく。

Table 1. Single event probability.

Specimen	Evaluation Item	LET Threshold (MeV/mg/cm ²)	Cross-sectional area (cm ²)	Single Event Probability (event/year)
Over Current Protection IC	SEL	7.273	1.06 E-06	6.57E-08
	SEFI (Gate Drive Output Error)	0.001	3.90 E-05	2.03E-01
	SEFI (Output Signal Error)	7.273	1.06 E-06	6.57E-08

1 - 08 Preparation of Nano-Structure Controlled Ion-Exchange Membranes by Ion Beams for Application to Seawater Concentration

T. Yamaki^{a)}, M. Goto^{b)}, S. Sawada^{a)}, H. Koshikawa^{a)}, A. Kitamura^{c)} and M. Higa^{d)}

^{a)} Department of Advanced Functional Materials Research, TARRI, QST,

^{b)} Graduate School of Science and Engineering, Yamaguchi University,

^{c)} Fuels and Materials Engineering Division, NSEC, JAEA,

^{d)} Graduate School of Sciences and Technology for Innovation, Yamaguchi University

A seawater concentration process requires ion-exchange electro dialysis membranes with low electrical resistance and high permselectivity. The present study deals with the preparation of nanostructure-controlled cation- and anion-exchange membranes (CEMs and AEMs) by a so-called ion-track grafting technique [1]. This new technique involves irradiation of a polymer substrate with an MeV-GeV heavy-ion beam and the graft polymerization into the resulting latent tracks [2]. If the ion-exchange groups are introduced only into the nanosized cylindrical tracks, the surrounding substrate matrix without any modifications is expected to mechanically prevent any excess swelling, thereby improving the ion transport properties [3].

A 25- μm -thick poly(ethylene-co-tetrafluoroethylene) (ETFE) film was irradiated with 560 MeV ^{129}Xe or 310 MeV ^{84}Kr ion beam. The irradiated ETFE films were immersed in grafting solutions of ethyl *p*-styrenesulfonate (EtSS) and chloromethyl styrene (CMS) and then afforded to hydrolysis and quaternization of the grafted chains for the preparation of CEMs and AEMs, respectively. Not only the EtSS and CMS grafting reactions but also the following hydrolysis and quaternization proceeded quantitatively, resulting in the preparation of the CEMs and AEMs with widely-controlled ion exchange capacities.

Figure 1 shows cross-sectional TEM images of the (a) EtSS- and (b) CMS-grafted ETFE films prepared by irradiation with the Kr ions. This revealed that the straight ruthenium tetroxide (RuO_4)-stained lines with a certain width appeared to be arranged parallel to one another. The black parts would indicate the grafted zone because they were found to contain sulfur (in EtSS) or chlorine (in CMS) in the energy dispersive X-ray mapping analysis. Accordingly, both of the resulting CEM and AEM had a cylindrical electrolyte part with a diameter of approximately 200 nm. In other words, we were able to prepare novel membranes, which possessed nanosized cation- or anion-conductive pathways extending along the ion projectile as was expected.

Figure 2 shows the relationship between a membrane resistance and a transport number for the nanostructure-controlled CEMs. The CEM possessed ion transport properties exceeding those of commercially-available products, that is, a membrane resistance of $< 2.0 \Omega \text{ cm}^2$ and transport number of > 0.98 . An electro dialyzer with a pair of our CEM and a

commercially-available AEM exhibited a higher concentration of chloride in the concentration chamber than a pair of the commercially-available CEM and AEM, where 0.5 mol/L NaCl aqueous solution was used as a seawater model.

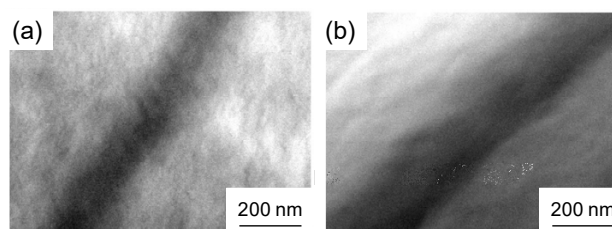


Fig. 1. Cross-sectional TEM images of the (a) EtSS- and (b) CMS-grafted ETFE films.

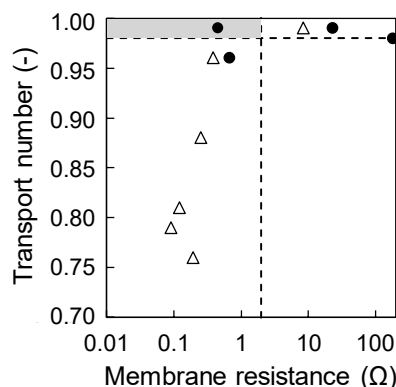


Fig. 2. Relationship between the membrane resistance and transport number of our CEMs prepared at different fluences of (●) 3.0×10^8 and (△) 1.0×10^9 ions/ cm^2 . The broken lines show the performance of the current CEM.

Acknowledgment

This work was partially supported by the Salt Science Research Foundation No. 1521, 1623 and 1717.

References

- [1] M. Higa *et al.*, Bull. Soc. Sea Water Sci. Jpn., **71**, 37 (2017); T. Yamaki *et al.*, *ibid.* **72**, 62 (2018).
- [2] T. Yamaki *et al.*, J. Power Sources **195**, 5848 (2010).
- [3] T. Yamaki *et al.*, Nucl. Instrum. Meth. Phys. Res. B, **435**, 162 (2018).

1 - 09 Preparation of Titanium Dioxide Nanocones Using Ion Track-etched Membranes as Template

H. Koshikawa^{a)}, Y. Sato^{b)}, S. Yamamoto^{a)}, M. Sugimoto^{a)}, S. Sawada^{a)} and T. Yamaki^{a, b)}

^{a)} Department of Advanced Functional Materials Research, TARRI, QST,

^{b)} Graduate School of Science and Technology, Gunma University

Alkaline etching of polymer films irradiated with heavy ions of several hundred MeV leads to the formation of ion track-etched membranes with nanometer-to-micrometer pores in different shapes [1]. The ion-track membranes have been used as templates for generating nanostructures of metals and semiconductors. Particularly, conical pores were prepared by etching the ion tracks from one side and used to obtain metal nanocones [2]. Due to their high surface area, nanocone arrays were expected as catalysts for applications to next-generation electrochemical devices [3]. In this study, we tried to apply this method for the preparation of titanium dioxide nanocones, which involves the formation of non-penetrating conical pores of ion-track membranes, vapor-deposition of an electrode and electrophoresis deposition.

The ion-track membranes composed of a top layer of a 12- μm thick polyimide (PI) and a bottom layer of 50- μm thick polycarbonate (PC) films were stacked on an Al plate and irradiated with 150 MeV ^{40}Ar ions at a fluence of 3.0×10^7 ions/ cm^2 . The bottom PC film, inside which the bombarding ions were stopped, was etched in a 4.0 mol/L sodium hydroxide solution at 60 °C, leading to the formation of non-penetrating conical pores. Figure 1(a) shows the representative scanning electron microscopy (SEM) image of the cross-section of the track-etched membrane. The base diameter of the nanocones was controlled between 380 nm and 1.3 μm by varying the etching time from 20 to 50 min. A very thin platinum layer was then deposited on the pore side of these ion-track membranes, and it was used as a cathode for the electrophoresis. The electrophoretic deposition was conducted at a voltage of 5.0 V in the electrolyte comprising tetraisopropyl orthotitanate, isopropanol, deionized water, and nitric acid [4].

Figure 1(b) presents the SEM image of the titanium dioxide nanocones after dissolving the polymer template in an alkaline aqueous solution. The average base diameter of the nanocones was 1.3 μm , and the height was 3.9 μm . The nanocones surface appeared to be smooth.

Figure 2 shows the X-ray diffraction (XRD) pattern of the titanium dioxide nanocones. There were two peaks at 25.8° and 27.2°, which are ascribed to an anatase (101) and a rutile (110) planes [5], respectively. The crystal structure of the nanocones was a mixture of anatase and rutile-type titanium dioxide. Both peaks were rather broad, indicating the low crystallinity.

In conclusion, the ion-track membranes with non-penetrating conical pores were obtained by heavy ion

radiation. The titanium dioxide nanocones with a base diameter of 1.3 μm and a height of 3.9 μm were prepared within the template by the vapor-deposition of the Pt electrode and electrophoresis deposition.

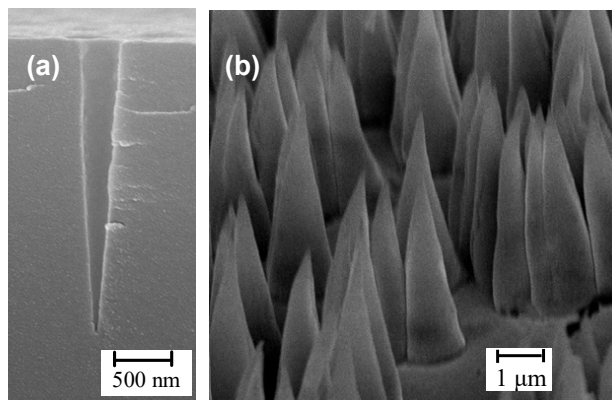


Fig. 1. SEM images of (a) the cross-section of the PC ion-track membrane and (b) the titanium dioxide nanocones.

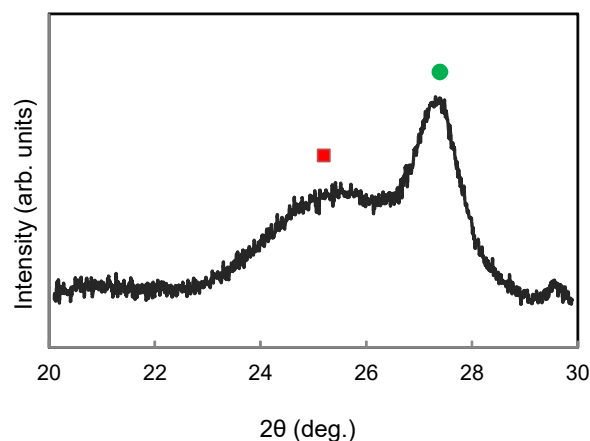


Fig. 2. XRD pattern of titanium dioxide nanocones prepared in the PC ion-track membranes (■: anatase (101); ●: rutile (110)).

Acknowledgment

This work was supported by JSPS KAKENHI Grant Number JP18K11936.

References

- [1] T. Yamaki *et al.*, Nucl. Instrum. Meth. Phys. Res. B, **314**, 77 (2013).
- [2] H. Koshikawa *et al.*, J. Membr. Sci. **327**, 182 (2009).
- [3] J. N. Tiwari *et al.*, J. Power Sources **182**, 129 (2008).
- [4] T. Kurosaki *et al.*, Electrochemistry, **70**, 510 (2002).
- [5] L. Mahoney *et al.*, Molecules, **20**, 21881 (2015).

1 - 10 Electron Beam Induced Formation of Pt Particles on Ceria Films

S. Yamamoto ^{a)}, T. Taguchi ^{b)}, M. Sugimoto ^{a)}, H. Koshikawa ^{a)} and T. Yamaki ^{a)}

^{a)} Department of Advanced Functional Materials Research, TARRI, QST,
^{b)} Tokai Quantum Beam Science Center, TARRI, QST

Cerium oxide (CeO₂) has been used as a promoter in catalysts combined with noble metals such as platinum. In recent years, platinum modified with ceria (Pt-CeO_x) is considered as promising cathode materials for use in polymer membrane electrolyte fuel cells [1]. A key process to make this active is formation of highly dispersed Pt nanoparticles on a ceria surface. Platinum nanoparticles in a solution have been prepared so far by a precipitation method using ionizing radiations such as electron beams and γ -rays [2]. Therefore, there is a strong motivation for us to use this radiation technique for precipitation of the Pt nanoparticles on ceria films, which would be expected to be a model electrocatalyst of Pt-CeO_x.

We deposited the ceria films on mirror-polished glassy carbon (GC) substrates by r.f. magnetron sputtering using a sintered CeO₂ target in an Ar-O₂ gas mixture. The films with thickness of 10 nm were deposited at temperature of 500 °C. The ceria films in an aqueous solution containing 0.1 mmol/L H₂PtCl₆ and 0.5 vol% C₂H₅OH were irradiated with 2 MeV electron beam (~150 kGy at dose rate of 1.5 kGy/s) from a 2 MV electron accelerator. The films with Pt particles were characterized by scanning electron microscope (SEM) and transmission electron microscope (TEM) and Rutherford backscattering spectroscopy (RBS) using a 2.0 MeV ⁴He⁺ beam from a 3 MV single-stage-accelerator.

Figure 1 shows TEM image of Pt nanoparticles on the ceria film. The film was exposed to 50 kGy dose of electron beam in the aqueous solution. TEM sample was prepared by scratching off the film. Formation of spherical Pt nanoparticles with a size of less than 10 nm was observed on the ceria grains.

Figure 2 shows the areal atomic density of Pt and Ce on the GC substrates as a function of electron beam irradiation dose. The areal atomic density of Pt and Ce were measured by RBS using a 2.0 MeV ⁴He⁺ beam. The amount of Pt on ceria increases with increasing the dose. In contrast, the amount of Ce on GC substrates decreases with increasing the dose.

Figure 3 shows SEM top-view images for the (a) un-irradiated ceria film, (b) irradiated with 50 kGy and (c) irradiated with 150 kGy ceria films, respectively. The un-irradiated ceria film was composed of crystalline ceria grains confirmed by XRD measurement. Increasing of precipitated Pt nanoparticles with network like structure was observed on the irradiated films with increasing the dose. The grain size of ceria reduced and the grains partially dropped from GC substrates. The results suggested the dose of electron beam irradiation and the

ceria film thickness were essential parameters to prepare of the model Pt-CeO_x electrocatalysts.

References

- [1] K. Fugane *et al.*, Appl. Mater. Interfaces, **7**, 2698-707 (2015).
- [2] J. Belloni, Catal. Today, **113**, 141-56 (2006).

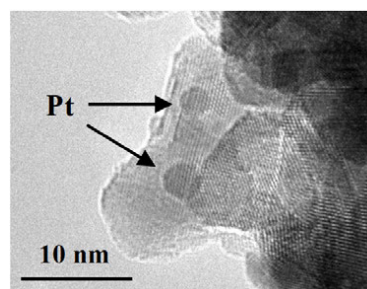


Fig. 1. TEM image of Pt nanoparticles on the ceria film.

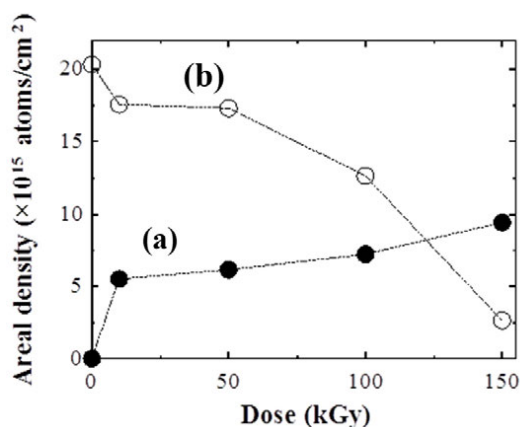


Fig. 2. Areal atomic density of (a) Pt and (b) Ce on GC substrates as a function of electron beam irradiation dose.

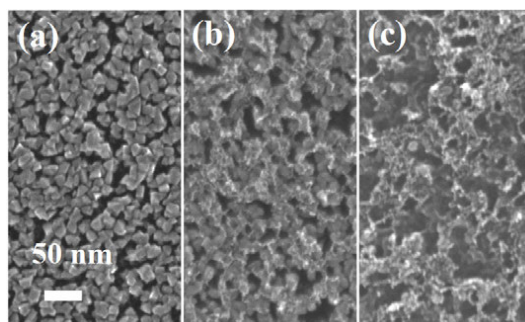


Fig. 3. SEM images of the ceria films on GC substrates. The films were (a) un-irradiated, (b) irradiated with 50 kGy and (c) irradiated with 150 kGy.

1 - 11 Microscopic Observations of Nanostructure in Oxide Ceramics Irradiated with Swift Heavy Ions at Grazing Incidence

A. Kitamura^{a)}, N. Ishikawa^{a)}, K. Kondo^{a)}, Y. Okuno^{a)}, S. Yamamoto^{b)},
H. Koshikawa^{b)} and T. Yamaki^{b)}

^{a)} Fuels and Materials Engineering Division, NSEC, JAEA,

^{b)} Department of Advanced Functional Materials Research, TARRI, QST

The nanostructure formation in oxide ceramics by irradiation with swift heavy ion (SHI) is interesting not only from the technological viewpoint, but also from the viewpoint of the physics of ion-solid interaction. It is well known that nano-sized hillocks are created on the surface of various ceramics by irradiation with SHIs [1]. When SHIs are irradiated at normal incidence, each impact of an SHI results in formation of a single hillock. In contrast, when SHIs are irradiated at grazing incidence, chains of multiple hillocks are formed on the surface of strontium titanate (SrTiO₃) and others [2]. SrTiO₃ is a typical perovskite type oxide (ABO₃) semiconductor. Periodic interactions of an SHI with electrons localized near oxygen atoms has been proposed as a possible scenario for the multiple hillock formation [2]. If localized nature of electrons is changed, morphology of hillocks may change accordingly. The electrical conductivity can be increased by doping a transition metal in the B sublattice. The electrical conductivity of SrTiO₃ increases by more than 8 orders of magnitude by only 0.05wt% doping of niobium (Nb) [3], while the crystal structure hardly changes by the doping. In this study, the effect of the Nb doping in SrTiO₃ on hillock formation was investigated by comparing irradiation-induced nanostructures for SrTiO₃ and Nb-doped SrTiO₃. So far, chains of multiple hillocks have been investigated by using an atomic force microscope (AFM). However, AFM measurement gives resolution errors in a nanometer order due to the curvature of the probe tip [1]. In order to obtain high resolution images of hillocks, we used here a field emission scanning electron microscope (FE-SEM).

Single crystals of SrTiO₃ (100) and 0.05 wt% Nb-doped SrTiO₃ (Nb-SrTiO₃) (100) were selected for the irradiated samples. SrTiO₃ was irradiated with 200 MeV ¹⁹⁷Au ions using a tandem accelerator at Tokai-JAEA. Nb-SrTiO₃ was irradiated with 350 MeV ¹²⁹Xe ions using the LD course of an AVF cyclotron at TIARA. According to the SRIM-2008 code the electronic stopping powers were 28.6 and 26.5 keV/nm for the ¹⁹⁷Au and the ¹²⁹Xe beams, respectively. The samples were irradiated at glancing incidence where the angle between the sample surface and the beam was < 2°. In order to avoid overlapping of individual ion tracks, the fluence was fixed at 2.0×10^{10} ions/cm². The irradiated surface was observed using an FE-SEM. The samples were coated with osmium with a thickness of several nm in order to avoid charge build-up during the observation.

Figure 1(a) shows FE-SEM images of SrTiO₃. Many chains containing some isolated hillocks are formed parallel to the trajectory of the incoming ions. Each chain would be formed by a single traveling ion. The hillocks had a

diameter of around 20 nm, and their size decreased as the ion traveled deeper into the sample. The length of chains was 0.5-1.5 μm depending on the incidence angle [2].

FE-SEM images of the Nb-SrTiO₃ surface are shown in Fig. 1(b). Black lines are observed along to the ion path. These can be interpreted by groove formation at the irradiated surface. Some of the black lines were accompanied with hillocks, but others were not. The width of the lines was about 20 nm, while the length was around 0.5-1.0 μm.

Black lines on the Nb-SrTiO₃ surface originated from continuous modifications along the ion path, whereas hillock chains on SrTiO₃ reflected discontinuous modifications. This morphological change in the SHI-induced nanostructures is attributable to the different electrical conductivities.

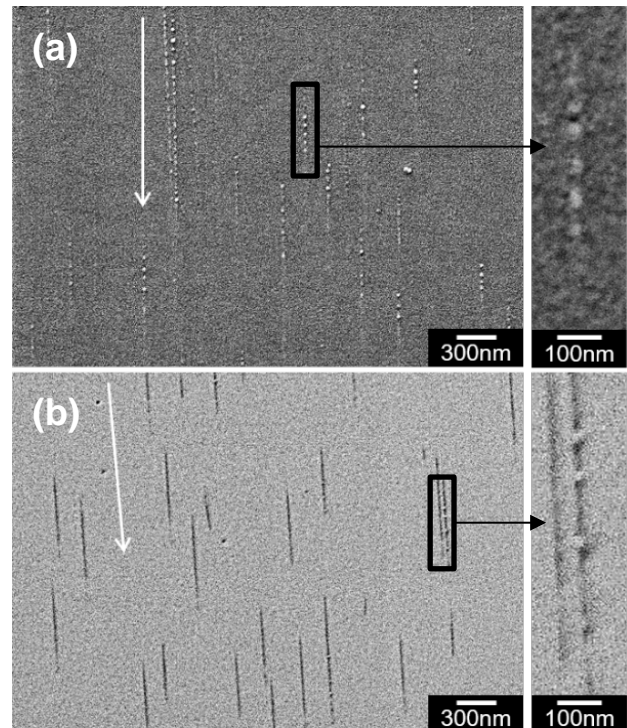


Fig. 1. FE-SEM images of irradiated surfaces of (a) SrTiO₃ and (b) Nb-SrTiO₃. The white arrow indicates the direction of the incoming ions.

References

- [1] N. Ishikawa *et al.*, Nanotechnology **28**, 355701 (2015).
- [2] E. Akcoltekin *et al.*, Nat. Nanotech. **2**, 290-94 (2007).
- [3] J. Karczewski *et al.*, J. Electroceram. **24**, 326 (2010).

A. Idesaki, S. Yamamoto, M. Sugimoto and T. Yamaki

Department of Advanced Functional Materials Research, TARRI, QST

Nitrogen-doped (N-doped) carbon materials which exhibit the catalytic activity for an oxygen reduction reaction (ORR), $O_2 + 4H^+ + 4e^- \rightarrow 2H_2O$, have been considered as platinum-alternative catalyst in the cathode of proton exchange membrane fuel cells. We have studied the fabrication of ORR-active carbon material from a precursor polymer utilizing ion implantation technique. We have reported that nitrogen-ion implantation is effective for synthesis of ORR-active carbon material from a phenolic resin; the obtained carbon material exhibited 0.7 V vs RHE of ORR potential which was 0.2 V higher than that of non-implanted sample [1]. In this work, chemical states of implanted nitrogen in the phenolic resin after implantation and subsequent carbonization was investigated in order to clarify the effect of nitrogen ion-implantation for the improved ORR activity.

Nitrogen-ion (N^+) with 50 keV was implanted into a phenolic resin film with 10 μm -thick on a Si wafer up to a fluence of 1×10^{15} ions/ cm^2 at room temperature in vacuum. After the implantation, the sample was immersed into methanol in order to exfoliate the ion-implanted part of the sample according to a method as shown in Fig. 1. Using this method, ion-rich side of sample can be investigated by X-ray photoelectron spectroscopy (XPS) which gives information about chemical states in a few nm range at surface.

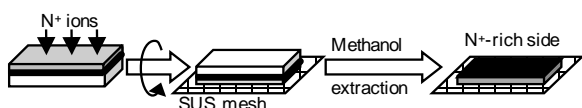


Fig. 1. Scheme of exfoliation of N^+ -implanted part in phenolic resin film.

Figure 2 (a) shows N 1s XPS spectra for the N^+ -implanted phenolic resin. Nitrogen was certainly doped to form N-C bonds of cyanides ($-CN$; 397.5-400.3 eV), azide ($R-N_3$; 397.9-398.7 eV), and N included in organic matrix (398.9-401.0 eV) [2]. Furthermore, it was found that the doped nitrogen was remained after the carbonization at 800 $^{\circ}\text{C}$ to form N-doped graphite structure of pyridinic N (398.5 eV), pyrrolic N (400.5 eV), graphitic N (401.5 eV), and oxidic N (402.5 eV) (Fig. 2 (b)) [3]. A peak of CrN (396.4 - 397.4 eV) in the Fig 2 (b) is caused by contamination from SUS mesh. The spectrum except for CrN component was separated into four peaks at 398.5, 400.5, 401.5, and 401.5 eV and the values of area ratio of 49% (pyridinic N), 40% (pyrrolic N), 6% (graphitic N), and 5% (oxidic N) were obtained. This estimation indicates that N remained after the carbonization is mainly incorporated as pyridinic and pyrrolic N in the graphite structure.

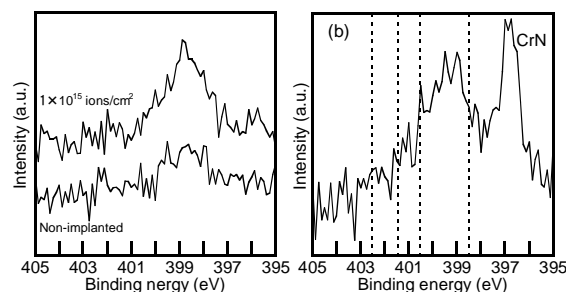


Fig. 2. N 1s XPS spectra of N^+ -implanted phenolic resin: (a) after implantation and (b) after carbonization.

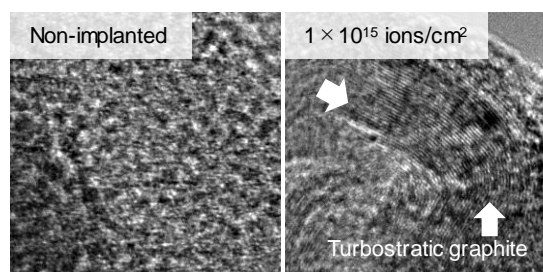


Fig. 3. TEM images of obtained carbon material.

On the other hand, wavy and striped texture due to graphite crystal phase (turbostratic graphite) was observed in TEM image for N^+ -implanted sample although the non-implanted sample exhibited typical amorphous phase (Fig. 3). This suggests that formation of graphite phase in the N^+ -implanted sample was promoted more than that in the non-implanted sample.

It has been reported that incorporation of pyridinic N and formation of turbostratic graphite are necessary to express the ORR activity [4]. In this work, it was found that incorporation of pyridinic N and formation of turbostratic graphite can be realized simultaneously by N^+ -implantation. This is a reason for the improved ORR activity of the carbon material derived from phenolic resin with N^+ -implantation.

Acknowledgment

This work was supported by JSPS KAKENHI Grant Number 15K04736.

References

- [1] A. Idesaki *et al.*, QST Takasaki Annu. Rep. 2016, **QST-M-8**, 47 (2018).
- [2] J. Chastain *et al.*, Handbook of Photoelectron Spectroscopy. ULVAC-PHI, Inc., (1995).
- [3] E. Raymundo-Piñero *et al.*, Carbon, **40**, 597-608 (2002).
- [4] J. Ozaki *et al.*, Electrochimica Acta, **55**, 1864-71 (2010).

1 - 13 Control of Pore Shapes in Track-etched Membranes by Using Depth Distribution of LET

Y. Sato ^{a)}, H. Koshikawa ^{b)}, S. Yamamoto ^{b)}, M. Sugimoto ^{b)}, S. Sawada ^{b)} and T. Yamaki ^{b)}

^{a)} Graduate School of Science and Technology, Gunma University,
^{b)} Department of Advanced Functional Materials Research, TARRI, QST

The passage of high-energy heavy ions in a polymer film leaves damage trails, which are called latent tracks. These can be etched out to form a membrane with micro- and nano-sized pores. The pore shape is known to vary depending on the track-to-radial etch rate ratio (V_T/V_R); in many cases, the V_T ($\mu\text{m}/\text{min}$) largely depended on the linear energy transfer (LET) [1], while the V_R ($\mu\text{m}/\text{min}$) of the large opening stayed constant. This means that the LET would be the most crucial factor for the etching results. Thus, our strategic idea is to control a depth distribution of the LET for making track-etched membranes with different pore shapes.

Generally, when the irradiation was made to provide the uniform LET in depth, the cone-like pores were obtained by track etching from one side only. In contrast, we demonstrated here that an LET gradient enabled us to obtain polyethylene terephthalate (PET) ion-track membranes with bullet- and funnel-like pores.

In order to investigate the etching conditions under which the V_T exhibited significant LET dependence, a 25- μm thick PET film was irradiated with 560 MeV ^{129}Xe or 150 MeV ^{40}Ar ions at a fluence of 3.0×10^7 ions/ cm^2 . These bombarding ions penetrated through the film, and their calculated LET were roughly constant at 12.3 and 3.0 MeV/ μm in the depth direction, respectively. The etching in the conductometric analysis [2] was then performed from both sides of the film using an aqueous NaOH solution at various concentrations and temperatures to estimate the V_T . As a result, the following conditions were found to be the most suitable for our purpose: 6.0 mol/L and 60 °C.

The LET of high-energy heavy ions rapidly decreases just before stopping in a material. According to the results of theoretical calculation, we irradiated a stack of two or three layers including the dummy and PET films with 560 MeV ^{129}Xe ions so that the desired LET gradient can occur from the surface of the sample. Figure 1 shows the experimental configurations for the irradiation of (a) the first 5 μm thick polyimide (PI) layer and the second two 25 μm thick PET films or (b) the first 25 μm thick PI layer and the second 25 μm thick PET film. This figure also presents the calculated depth distribution of the LET in the PET sample. Apparently, the LET decreases from the beam-entry side in (a) and increases from the beam-exit side in (b). The sample was etched for 15 min under the above conditions only from this LET-controlled side.

Figure 2 shows the scanning electron microscopy (SEM) images of the cross-section of the track-etched pores, which were obtained in the case of (a) the decreasing and

(b) increasing LET in the depth direction. The bullet- and funnel-like pores were prepared due to the deceleration and the acceleration of the etching, respectively, *i.e.*, a decrease and an increase in the V_T during the course of etching.

In conclusion, track-etched pore shapes were controlled by varying the V_T in the depth direction. Because of the large LET dependence of V_T , the negative slope of the LET gave the bullet-like pores, while, in contrast, the positive slope gave the funnel-like pores.

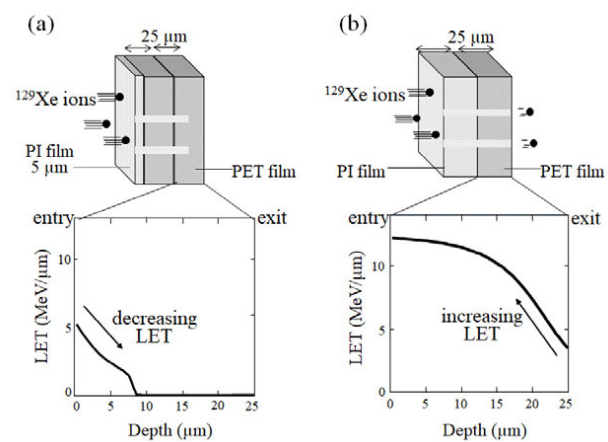


Fig. 1. Experimental configurations for the irradiation. This figure also presents the calculated depth distribution of the LET in the PET sample. The LET was decreased from the beam-entry side in (a) and increased from the beam-exit side in (b).

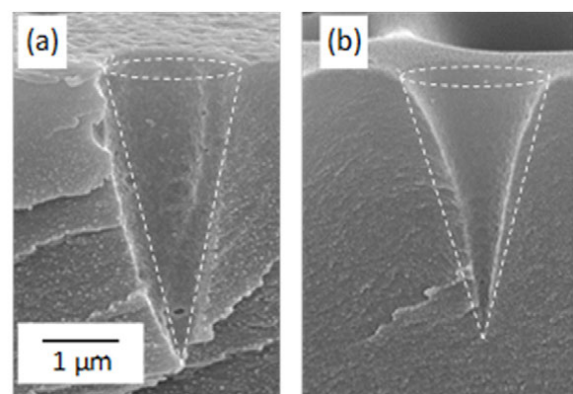


Fig. 2. SEM images of the cross-section of the track-etched pores in (a) a bullet- and (b) funnel-like shapes.

References

- [1] R. Rohani *et al.*, Nucl. Instrum. Meth. Phys. Res. B, **267**, 554 (2012).
- [2] T. Yamaki *et al.*, Bull. Soc. Sea. Water Sci. Jpn., **72**, 62 (2018).

1 - 14 DFT Study of the Pt Nanoparticle on the Ar-ion Irradiated Glassy Carbon Substrate

T. Kimata ^{a, b)}, K. Kakitani ^{c, d)}, T. Yamaki ^{d)}, S. Yamamoto ^{d)}, W. Mao ^{e)},
T. Kobayashi ^{f)} and T. Terai ^{c, e)}

- ^{a)} Department of Materials Science and Engineering, Tokyo Institute of Technology,
^{b)} Ground Systems Research Center, ATLA, Ministry of Defense,
^{c)} Department of Nuclear Engineering and Management, The University of Tokyo,
^{d)} Department of Advanced Functional Materials Research, TARRI, QST,
^{e)} The Institute of Engineering Innovation, The University of Tokyo,
^{f)} RIKEN Center for Advanced Photonics (RAP), RIKEN

Platinum (Pt) nanoparticles with a high oxygen reduction reaction (ORR) activity are pursued as cathode catalysts in polymer electrolyte membrane fuel cells. Recently, Pt nanoparticles on the glassy carbon (GC) substrate irradiated with argon (Ar) ions were found to exhibit a higher ORR activity than those on the non-irradiated one [1, 2]. This suggests that Pt nanoparticles would be electronically influenced by Ar-ion-irradiation-induced lattice defects in the GC substrate. We analyzed the electronic structure of the interface between the Pt nanoparticles and GC substrate by density functional theory (DFT) calculation to explore the mechanism of the activity enhancement [3].

The DFT calculations were performed with Vienna Ab-initio Simulation Package (VASP) using the projector-augmented wave (PAW) method. The generalized-gradient approximation was employed to describe electron exchange-correlation functional, and a plane wave basis set with an energy cutoff of 400 eV was used. The model for the DFT calculations was comprised of three layers of graphene and an icosahedral Pt₁₃ cluster. Each graphitic layer had a 5 × 5 structure, that is, 50 carbon atoms. To simulate the irradiation defects, vacancies with different configurations [a single vacancy only in the upper layer (SV), a double vacancy only in the

upper layer (DV), single vacancies in the upper two layers (2SV), double vacancies in the upper two layers (2DV)] were introduced to the upper two layers.

Figure 1 shows the isosurfaces of the charge difference in the case when the substrate structure was the 2DV. Charge accumulation and depletion mainly occurred in the vicinity of the support-cluster interface; this tendency was clearly observed for all the support structures including the pristine graphite (PG). This suggests that the Pt atoms at the interface were mainly involved in the charge transfer between the Pt₁₃ cluster and the carbon support.

The position of the d-band center, ϵ_d , (average energy of the d-states) relative to the Fermi level was calculated to gain insight into how this charge transfer affects the electronic structure of the interfacial Pt atoms (Table 1). Compared to the case of the PG, when the Pt₁₃ cluster was supported on every defective structure, ϵ_d became lower by 0.14 eV or more. This reduction weakens the binding of O and OH species on the Pt structure and promotes the rate-limiting step of ORR (removal of adsorbed species from the Pt surface). Thus ion-beam irradiation-induced lattice defects result in the enhancement of the ORR activity of Pt nanoparticles.

Acknowledgment

This work was partly performed under the NIMS-RIKEN-JAEA-QST Cooperative Research Program on Quantum Beam Science and Technology.

References

- [1] K. Kakitani *et al.*, Radiation and Industries **141**, 29 (2016) [in Japanese].
[2] T. Kimata *et al.*, ChemRxiv (2017), [Posted on 01.11.2017].
[3] K. Kakitani *et al.*, Surf. Coat. Tech. **355**, 259-63 (2018).

Table 1

Average d-band center values of three Pt atoms in contact with the graphite layers having the various types of defective structures.

substrate	PG	SV	DV	2SV	2DV
ϵ_d (eV)	-2.79	-2.95	-2.94	-3.09	-2.93

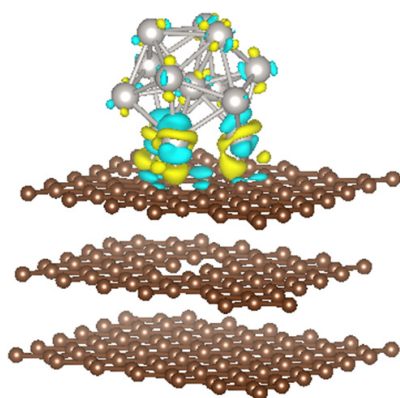


Fig. 1. Isosurfaces of the charge density difference of a Pt₁₃ cluster on the graphite with the 2DV. The density increases in the yellow regions and decreases in the blue regions. The isosurface value is 50 e/nm³.

1 - 15 Prediction of Scintillation Light Yield by Heavy Ions Based on Sub-micron Radiation Transport Calculation and Förster Effect

T. Ogawa ^{a)}, T. Yamaki ^{b)} and T. Sato ^{a)}

^{a)} Environment and Radiation Sciences Division, NSEC, JAEA,

^{b)} Department of Advanced Functional Materials Research, TARRI, QST

Scintillators are the materials which convert the energy of radiation to photons. They are widely used for scientific experiments, medicine, and radiation safety. The light yield of scintillators is in principle proportional to the deposited energy but often suppressed by a quenching effect depending on the incoming radiation energy and species. Previously, strength of quenching and its dependence on incident particle species and energies was estimated by empirical parameterization based on LET [1] but it was pinpointed that the empirical parameterization was inadequate for high-LET particles [2]. This is probably because quenching is dependent on the 3-dimensional configuration of energy deposition but LET is integration of radial energy distribution; therefore information of spatial distribution is lost. Therefore in this study, excitation of fluorescent molecules in scintillators which are exposed to radiation was calculated using the submicron-scale radiation track-structure calculation code. The calculation was done for one of the most typical scintillation materials NE-102A.

Energy deposition in the scintillator crystal by the incident radiation was calculated by a track-structure calculation code RITRACKS [3]. Among energy deposition reactions calculated by RITRACKS, those depositing energies larger than 10 eV were assumed to result in one excited fluorescent molecule. Probability that the excitation energy of one molecule is transferred to another excited molecule by Förster effect was calculated by $1/(1+(r/R_f)^6)$, where r is the distance between the molecules, and R_f is the parameter specific to NE-102A. If the energy was transferred to another excited molecule (assuming that it is at the S_1 state), one of the molecules went to the ground state (S_0 state) and the others went up to the second excited state S_2 and returned to the original excitation state (S_1) after dissipating the received excitation energy as phonons. Finally, the light yield was assumed to be proportional to the number of remaining excited molecules.

The scintillation light yield owing to irradiation by GeV class heavy ions was calculated and compared with experimental literature data [2] in Fig. 1. In all the calculation, scintillator is thin enough to let the incident radiation go through. In case of low-Z particles, energy deposition is spatially dispersed therefore quenching is weak. On the other hand, energy deposition by high-Z is so dense that light emission is suppressed by quenching. Scintillation light yields were estimated by Birks' formula and Chou's formula. As shown in Fig. 1, prediction by Birks'

formula and Chou's formula [4] systematically deviates from the experimental data above 10^3 MeV/(g/cm²). This fact shows that LET is not a good index to estimate the intensity of quenching in the high-LET region. By contrast, the light yields calculated by our model are in good agreement with the literature data even above 10^3 (MeV/(g/cm²)).

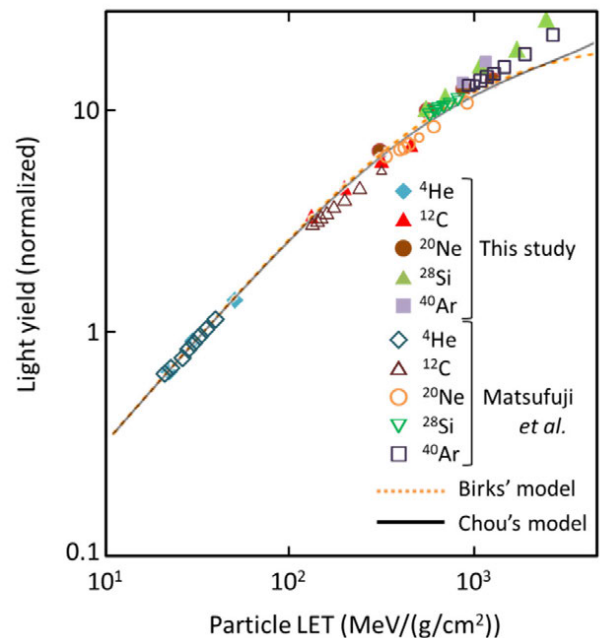


Fig. 1. Comparison of NE-102 scintillator light yield exposed to heavy ion beams. Filled symbols are calculation by the model developed in this study. Open symbols are measurement data taken from [2]. Lines are calculation by LET-based conventional systematics models [1, 4].

References

- [1] J.B. Birks, Proc. Phys. Soc. **A64**, 874 (1951).
- [2] N. Matsufuji *et al.*, Nucl. Instrum. Meth. Phys. Res. A, **437**, 346 (1999).
- [3] I. Plante *et al.*, New J. Phys. **10**, 125020 (2008).
- [4] C. N. Chou, Phys. Rev. **87**, 904 (1952).

K. Amemiya ^{a)}, H. Koshikawa ^{b)} and T. Yamaki ^{b)}^{a)} National Metrology Institute of Japan, AIST,^{b)} Department of Advanced Functional Materials Research, TARRI, QST

Low reflectance black materials have various applications ranging from dark-level suppression to light energy harvesting. Carbon nanotube forests are known as the world blackest materials [1, 2]. Despite the excellent optical performance, they are too fragile to be used widely by general public. Nickel-phosphorous (NiP) black surface, which has high-aspect-ratio conical micropores with oxide black layer, also shows ultra-low reflectance of near 0.1% in the visible and near-infrared range [3, 4]. For longer wavelength, however, the reflectance of NiP black increases owing to its geometry and composition [4], which can be hardly customized for mid-infrared use.

We are developing a novel planar perfect blackbody material from etched ion tracks [5]. Poly allyl diglycol carbonate (CR-39 in trade name) plastic plates were irradiated with energetic heavy ion beams from AVF cyclotron of TIARA; then the samples were etched in an NaOH solution to fabricate randomly arrayed optical micro-cavities (etch pits) on their surface, followed by black layer coating. Some of the prototypes exhibited low reflectance of 0.2-0.4% in UV-VIS, < 2% in NIR respectively [6], while also exhibiting good mechanical durability [7].

For mid-infrared use, the design of the micro-cavity must be optimized. To this end, we employed FDTD (finite differential time domain) code MEEP [8], which can calculate wave-domain optical propagation in materials of three-dimensional geometry. We modelled surface morphology of the micro-cavity array; cone shaped pits filled on CR-39 substrate, having opening radius of 1-5 μm , a pit aspect ratio (h/r , h : depth, r : radius) of 0-5. MEEP requires dielectric functions of actual target materials as Lorentz parameters. For simplicity, we used constant dielectric function, corresponding to constant refractive index of $n \sim 1.5$, as a typical value for dielectric optical materials. Figures 1 and 2 show calculated mid-infrared total reflectance of the micro-cavity array model: cavity aspect-ratio dependence and opening radius dependence, respectively. The results confirm that the cavity aspect ratio should be > 3 , and cavity opening diameter of greater than the wavelength of interest is preferable when targeting $< 0.1\%$ total reflectance.

Ion track etching technique can easily manufacture such high-aspect-ratio micro-cavities of opening well above a few microns at will, by choosing ion species, energy, and exposure density with adequate etching time [7]. Note that the calculation here shows just antireflection characteristics, not including optical absorption, which must be considered to attain an actual planar perfect blackbody in the future work.

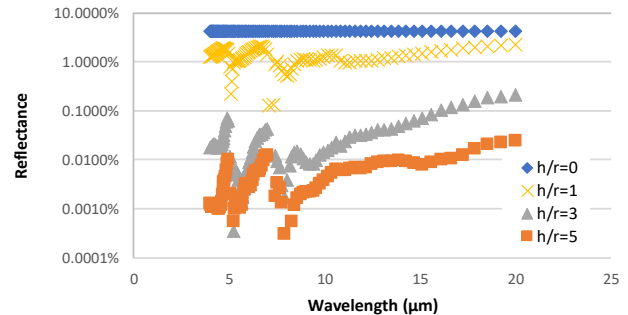


Fig. 1. Calculated total reflectance of the micro-cavity array model: a cavity-aspect-ratio dependence at fixed $r = 5 \mu\text{m}$.

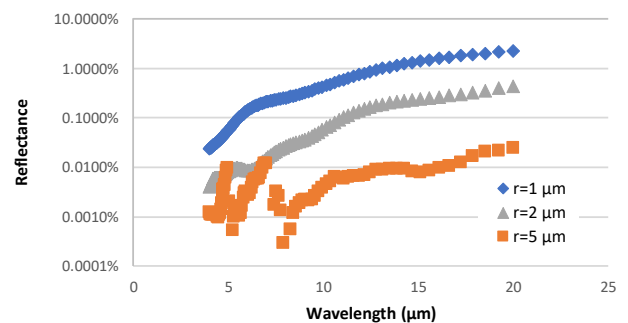


Fig. 2. Calculated total reflectance of the micro-cavity array model: opening-radius dependence at fixed $h/r = 5$.

Acknowledgments

This work has been supported by the Inter-University Program for the Joint Use of JAEA/QST Facilities (proposal no. 16005) from Nuclear Professional School, School of Engineering, The University of Tokyo.

References

- [1] Z. P. Yang *et al.*, Nano Lett. **8**, 446-51 (2008).
- [2] K. Mizuno *et al.*, Proc. Natl. Acad. Sci. U.S.A. **106**, 6044-47 (2009).
- [3] S. Kodama *et al.*, IEEE Trans. Instrum. Meas. **39**, 230-32 (1990).
- [4] K. Amemiya *et al.*, Appl. Opt. **51**, 6917-25 (2012).
- [5] S. Kodaira *et al.*, Radiat. Meas. **46**, 1782-85 (2011).
- [6] K. Amemiya *et al.*, QST Takasaki Annu. Rep. 2016, **QST-M-8**, 40 (2018).
- [7] K. Amemiya *et al.*, Nucl. Instrum. Meth. Phys. Res. B, **356-57**, 154-59 (2015).
- [8] A. F. Oskooi *et al.*, Comput. Phys. Commun. **181**, 687-702 (2010).

1 - 17 Preparation of Nitrogen-doped Carbon-based Catalysts by Electron-Beam Irradiation During High Temperature Pyrolysis

Y. Kanuma^{a)}, M. Sugimoto^{b)}, A. Idesaki^{b)}, S. Yamamoto^{b)},
H. Koshikawa^{b)} and T. Yamaki^{a, b)}

^{a)} Graduate School of Science and Technology, Gunma University,
^{b)} Department of Advanced Functional Materials Research, TARRI, QST

Nitrogen-doped (N-doped) carbon-based catalysts exhibiting an oxygen reduction reaction (ORR) activity are used for polymer electrolyte membrane fuel cells without platinum loading [1]. The ORR activity should be related to N-doped carbon networks. We have been interested in the electron-beam (EB) irradiation methods for doping nitrogen in carbon networks during a thermally non-equilibrated situation. Recently, N-doped carbon was prepared by irradiating the aromatic polymer precursor with EB at 500 °C in an ammonia (NH₃) atmosphere and then heating at 800 °C in nitrogen (N₂) [2]. However, the resulting samples did not have a sufficient amount of nitrogen because nitrogen was readily released in the second carbonization step. In this study, the nitrogen doping was done by the one-step EB irradiation during the pyrolysis at 800 °C in NH₃.

A precursor was a phenolic resin (Gunei Chemical, PSK-2320) or its mixture with 5% cobalt(II) chloride (CoCl₂). This was irradiated with 2 MeV EB at a dose of up to 35 MGy in NH₃ at 800 °C. The samples were characterized by X-ray diffraction (XRD) analysis and X-ray photoelectron spectroscopy (XPS). The electrocatalytic activity was tested by the linear sweep voltammetry (LSV) with a rotating disk electrode (RDE). The catalyst powder was dispersed in a mixture of a Nafion solution, ethanol and water and applied onto the surface of a glassy carbon electrode. The LSV was carried out in a 0.5 M H₂SO₄ solution saturated with N₂ (N₂-LSV) or with O₂ (O₂-LSV). The net ORR voltammograms were obtained by subtracting the N₂-LSV from the O₂-LSV. Finally, the obtained data were compared between EB-irradiated and unirradiated samples.

The XRD patterns of the EB-irradiated and unirradiated samples had a relatively sharp peak due to a turbostratic structure (results not shown). The N 1s XPS spectra were deconvoluted into four peaks corresponding to pyridinic-N (N-1), pyrrolic- or pyridinium-like-N (N-2), quaternary-N (N-3) and pyridinic oxide-N (N-4). Figure 1 shows the distributions of the N species in the carbon-based catalysts. The quantitative analysis indicated that the N/C ratio was higher for the EB-irradiated sample than for the unirradiated one. In particular, the difference in the amount of the pyridinic-N was noted remarkably. This suggests that the EB irradiation enabled us to enhance the nitrogen doping even during the high-temperature pyrolysis. Figure 2 shows the ORR voltammogram of the samples. In this figure, the ordinate represents the current density per

geometric area of the disk electrode, which means the specific catalytic activity. The catalytic activity was higher for the EB-irradiated sample than for the unirradiated one probably because the amount of nitrogen, especially pyridinic N, in the carbon network became high.

In summary, the EB irradiation during the pyrolysis and carbonization at 800 °C was found to enhance nitrogen doping in the carbon-based catalysts and finally improve their ORR activity.

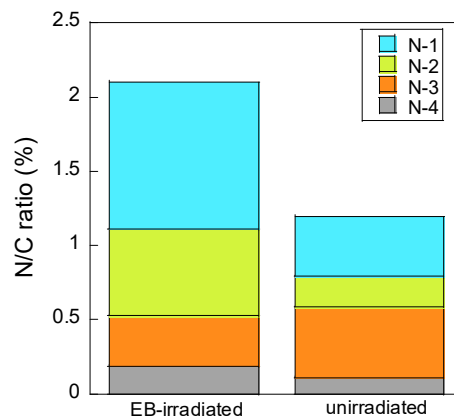


Fig. 1. Distributions of doped N species in the samples.

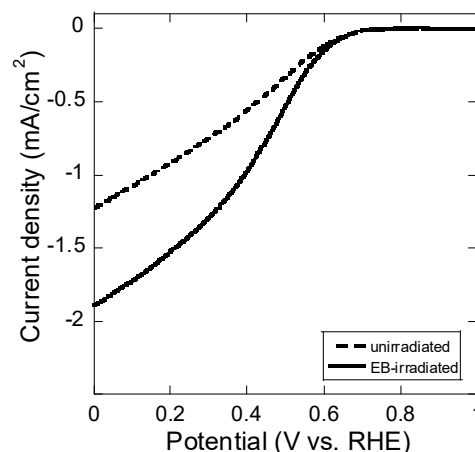


Fig. 2. ORR voltammograms of the samples. Temperature: RT, electrolyte: 0.5 M H₂SO₄, rotation: 1500 rpm.

References

- [1] Y. Nabae *et al.*, *Sci. Rep.*, **6**, 23276 (2016).
- [2] Y. Kanuma *et al.*, *QST Takasaki Annu. Rep.* 2016, **QST-M-8**, 46 (2018).

1 - 18 Electron-Beam Irradiated Electrode of a Redox Flow Battery for Low Internal Resistances

H. Ishitobi^{a)}, S. Yamamoto^{b)}, K. Oba^{b, c)}, H. Koshikawa^{b)}, T. Yamaki^{b)} and N. Nakagawa^{a)}

^{a)} Division of Environmental Engineering Science, Gunma University,
^{b)} Department of Advanced Functional Materials Research, TARRI, QST,
^{c)} Graduate School of Science and Technology, Gunma University

A vanadium redox flow battery (VRFB) has attracted much attention due to its ability to store renewable energy [1]. Its promising characteristic is to be able to design battery capacity and power flexibly, to measure accurately the state of charge during operation, etc. In contrast, improvement of current density by reducing the reaction resistance and ohmic resistance is still required for commercialization. Air oxidation treatments are often performed to add active sites (*i.e.*, surface oxygen groups) on the carbon (graphite) electrode. To enhance redox activity, electron beam irradiation could be a key to make defects in the electrode. The defects could be sources for surface oxygen groups produced by air oxidation. Also, the surface area enlarged by the activation effect of the air oxidation can reduce ohmic resistance. In this work, we carried out two-step treatment, *i.e.*, electron beam irradiation and air oxidation. The current-voltage characteristic of the electrodes with/without irradiation was measured.

The electrode materials (MFK carbon papers, Mitsubishi Chemical Corp.) were irradiated with an electron beam (2.0 MeV, 4.62×10^{13} e cm⁻²) and oxidized under air at 500 °C for 3 h. Oxidized carbon papers without irradiation were used as a reference. Three layers of carbon papers were compressed to around 3/4 of their initial thickness and put to both negative and positive sides as electrodes. We used a custom-built single cell made of acrylic resin and interdigitated flow field [2]. The current-voltage measurement was carried out at a scan rate of 2 mVs⁻¹ without recharge during the operation. An electrolyte flow rate per geometric area was 6.2 mL cm⁻² min⁻¹. All experiments were performed at room temperature.

Figure 1 shows Raman spectra of the samples. The I_D/I_G ratio, which corresponds a degree of graphitization, increased after electron beam irradiation and air oxidation. This result suggests that the defects in the carbon material were effectively introduced by these treatments.

Figure 2(a) shows current-voltage curves of VRFB. At 1.1 V, the irradiated electrode showed 7% higher current density compared to the non-irradiated electrode. This result indicates that the internal resistances were reduced by the electron beam irradiation. The ohmic resistance of the irradiated electrode was 8% lower than that of the non-irradiated electrode (Fig. 2 (b)). The lower ohmic resistance could be explained by relatively large surface area of the electrode due to enhanced oxidation with the electron beam irradiation and the heat treatment in air. The IR-corrected voltage, which shows a voltage drop

without ohmic loss, is shown in Fig. 2(b). The irradiated electrode had lower corrected voltage drop than the non-irradiated electrode. This result suggests that the reaction resistance was reduced by the addition of active sites.

In summary, we tried to reduce the internal resistances of VRFB by the electron beam irradiation and the air oxidation. The irradiated electrode showed 7% higher current density compared to the non-irradiated electrode.

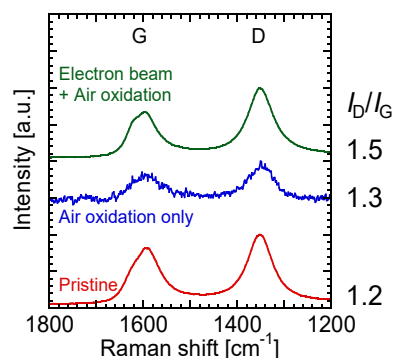


Fig. 1. Raman spectra of the samples.

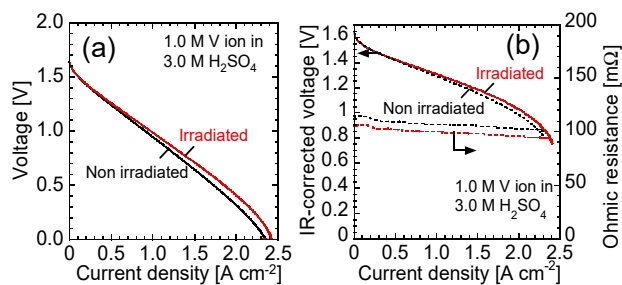


Fig. 2. Current-voltage curves of VRFB. (a) Raw data and (b) IR-corrected data and ohmic resistance.

Acknowledgments

We greatly thank Prof. Shoji Tsushima (Osaka Univ.) for his fruitful advice, and financial supports from The Iwatani Naoji Foundation's Research Grant and JSPS KAKENHI.

References

- [1] E. Sum and M. Skyllas-Kazacos, J. Power Sources **15**, 179 (1985).
- [2] S. Tsushima *et al.*, Abst. ECS Meet., No.1664, [San Francisco, USA] (2013/10).

1 - 19 Overvoltage Reduction of Membrane Bunsen Reaction by Using Radiation-grafted Cation Exchange Membranes

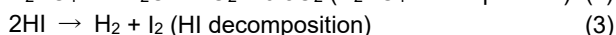
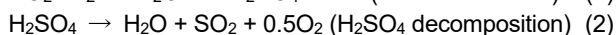
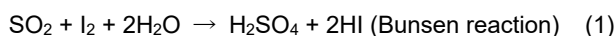
T. Kimura ^{a)}, M. Nomura ^{a)}, S. Sawada ^{b)}, T. Yamaki ^{b)}, N. Tanaka ^{c)} and S. Kubo ^{c)}

^{a)} Department of Applied Chemistry, Shibaura Institute of Technology,

^{b)} Department of Advanced Functional Materials Research, TARRI, QST,

^{c)} Hydrogen Application Research and Development Unit, NHRC, JAEA

Hydrogen is an attractive energy carrier, as it generates electricity without CO₂ emission by fuel cells. One of the promising large-scale hydrogen production techniques is thermochemical water splitting Iodine-Sulfur (IS) process [1] that is composed of the following three reactions:



The Bunsen reaction is performed *via* electrolysis using a cation exchange membrane (CEM) [2]. We succeeded in performing the membrane Bunsen reaction by using a commercially-available Nafion membrane [2, 3]. However, the applied voltage was so high that the electrolytic cell could not be suited for practical use. In this study, therefore, we used radiation-grafted CEMs for the membrane Bunsen reaction to reduce the cell voltage.

The CEMs were prepared by γ -ray irradiation (10 kGy) of poly(ethylene-*co*-tetrafluoroethylene) (ETFE) films, grafting of styrene and divinylbenzene (DVB) for 1 to 24 h, and sulfonation of the grafted styrene units. The ion exchange capacity (IEC) of the obtained CEM was evaluated by a neutralization titration method using an aqueous NaOH solution. The proton conductivity was measured by a two-probe AC impedance technique.

The membrane Bunsen reaction tests were carried out at 20 °C. An aqueous solution of H₂SO₄ (3.2 mol/kg) and SO₂ (1.2 mol/kg) was used as an anolyte, while an aqueous solution of HI (2.5 mol/kg) and I₂ (2.5 mol/kg) was used as a catholyte. Galvanostatic electrolysis was performed for 3 h at the current density of 200 mA/cm². Electrolytes were sampled at every 1 h interval from both the cathode and anode sides. The concentration of contained H₂SO₄ and HI was measured by the titration with NaOH and Na₂S₂O₃.

The three radiation-grafted CEMs with different IECs of 0.90, 1.6, and 2.4 mmol/g were used for the Bunsen reaction tests. The H₂SO₄ and HI concentration increased proportionally with time, indicating that no side reactions occurred. The final concentrations of H₂SO₄ and HI were ca. 3.6 and 3.3 mol/kg, respectively, in all the tests.

Figure 1 shows the cell voltage as a function of the current density. The cell voltage increased with increasing the current density. The overvoltage was defined as the difference between the cell voltages at 0 and 200 mA/cm². Table 1 shows the summary of the overvoltages for the different CEMs. The overvoltage decreased with an increase in the IEC of our grafted CEMs; at 2.4 mmol/g,

the minimum overvoltage was 0.40 V, which was lower than that of Nafion (0.65 V). The main reason for this result can be explained by considering higher proton conductivity (0.15 S/cm) compared with that for the Nafion (0.083 S/cm).

In conclusion, the overvoltage of the membrane Bunsen reaction was reduced by using a radiation-grafted CEM with a high IEC. This achievement would make us to expect the practically-feasible reaction system for the efficient IS process.

Acknowledgement

This work was partially supported by Council for Science, Technology and Innovation (CSTI), Cross-ministerial Strategic Innovation Promotion Program (SIP), “energy carrier” (Funding agency: JST).

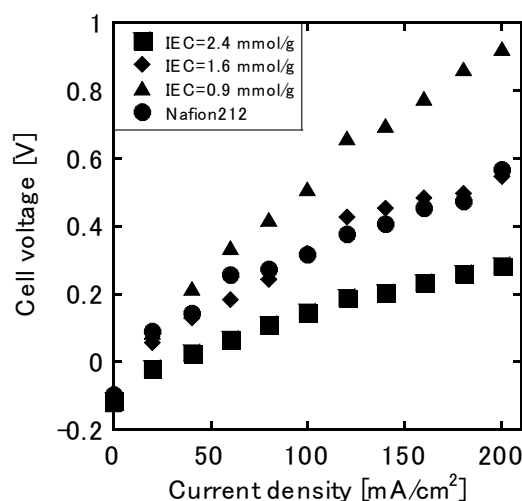


Fig. 1. Relationship between the current density and cell voltage for the membrane Bunsen reaction.

Table 1. Overvoltage in the membrane Bunsen reaction.

Membrane type	IEC (mmol/g)	Overvoltage(V)
Grafted CEMs	0.90	1.1
	1.6	0.65
	2.4	0.40
Nafion 212	0.90	0.65

References

- [1] S. Kasahara *et al.*, J. Chem. Eng. Jpn., **36**, 887-99 (2003).
- [2] M. Nomura *et al.*, AIChE J., **50**, 1991-98 (2004).
- [3] M. Nomura *et al.*, QST Takasaki Anu. Rep. 2015, **QST-M-2**, 45 (2017).

Proton Selectivity and Permeability of Cross-linked Radiation-grafted Cation-Exchange Membranes for Efficient HI Concentration

N. Tanaka^{a)}, S. Sawada^{b)}, T. Yamaki^{b)} and S. Kubo^{a)}

^{a)} Department of Hydrogen and Heat Application Research and Development, HTGRC, JAEA,

^{b)} Department of Advanced Functional Materials Research, TARRI, QST

Thermochemical water-splitting Iodine-Sulfur (IS) process [1] is known to be a promising method for hydrogen production. In the IS process, a new cation-exchange membrane prepared by the radiation-induced graft polymerization has been applied to the electroelectrodialysis (EED) in order to enrich hydrogen iodide (HI) in an HI-I₂-H₂O mixture (HIx solution) [2, 3]. The membrane performance should be improved for the efficient HI concentration. For this purpose, important factors are the proton (H⁺) selectivity and permeability; they can be represented by indexes such as a transport number of H⁺ (t_+) and a cell voltage (E) [2], respectively. In our previous study [4], cross-linked grafted chains were found to have the effect of increasing the t_+ value, that is, improving the H⁺ selectivity, while, in contrast, how the crosslinking affects E has been still unknown. Considering the importance of optimizing the membrane performance, we investigated here both of the t_+ and E indexes of the cation-exchange membrane with different ion exchange capacities (IECs).

The membranes were prepared by pre-irradiation of the ETFE film with γ -rays, the graft polymerization of styrene (St) with 5 vol% divinylbenzene (DVB) or without DVB, and sulfonation. The resulting crosslinked and non-crosslinked membranes are referred to as ETFE-St/DVB and ETFE-St, and their IEC ranged 1.3-3.2 mmol/g and 1.1-2.0 mmol/g, respectively. The t_+ and E values were measured using a filter-press type EED cell [2], to which a direct current of 200 mA/cm² was supplied for 4 hours at 313 K. The feeding HIx solution contained HI = 10 mol/kg and I₂ = 10 mol/kg.

Figure 1 shows the variation of t_+ as a function of IEC. The values were higher for ETFE-St/DVB than for ETFE-St at a given IEC, indicating that ETFE-St/DVB would have higher H⁺ selectivity. They showed the declining trend with an increase in the IEC and seemed to merge to the same value. The advantage of DVB for H⁺ selectivity could reduce at a higher IEC.

Figure 2 shows the variation of E as a function of IEC. The E value was higher for ETFE-St/DVB than for ETFE-St. This result indicates that the introduction of the cross-linked chains would reduce the H⁺ permeability. The E value decreased with an increase in the IEC, suggesting that the higher IECs could mitigate the negative effect of the DVB crosslinking. In the IEC range investigated for ETFE-St/DVB, the E decreased by 70% approximately while the t_+ decreased by 20%. The more drastic decrease in E leads to the conclusion that the higher IECs would be preferred for the HI concentration.

In conclusion, the H⁺ selectivity and permeability had the trade-off relationship in ETFE-St/DVB, but the IEC was one of the key parameters and could be optimized for the HI-concentration performance.

References

- [1] S. Kubo *et al.*, Nucl. Eng. Des. **233**, 355 (2004).
- [2] N. Tanaka *et al.*, J. Membr. Sci. **411-12**, 99 (2012).
- [3] T. Yamaki *et al.*, Polymer **45**, 6569 (2004).
- [4] N. Tanaka *et al.*, J. Membr. Sci. **456**, 31 (2014).

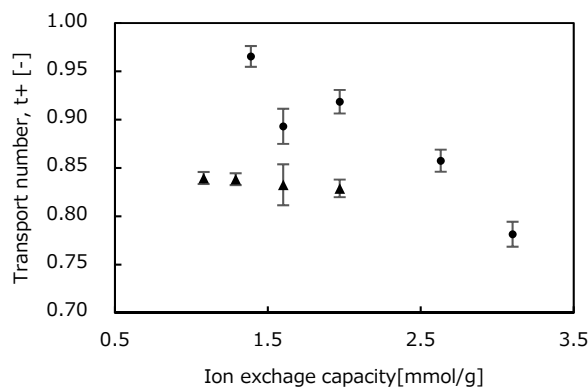


Fig. 1. IEC dependence of t_+ of ETFE-St/DVB (●) and ETFE-St (▲).

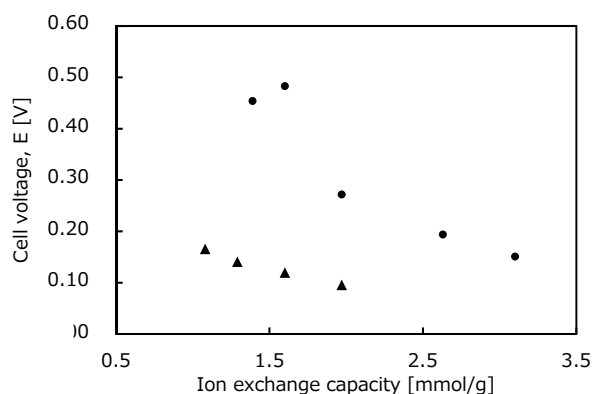


Fig. 2. IEC dependence of E of ETFE-St/DVB (●) and ETFE-St (▲).

1 - 21 Characterization of (111)-oriented $Ti_{1-x}Al_xN$ Thin Films on Monocrystalline AlN by Reactive CVD

Y. Kasukabe ^{a), b)}, H. Shimoda ^{b)}, S. Yamamoto ^{c)} and M. Yoshikawa ^{c)}

^{a)} Global Learning Center, Tohoku University, ^{b)} Department of Metallurgy, Tohoku University, ^{c)} Department of Advanced Functional Materials Research, TARRI, QST

Films of $Ti_{1-x}Al_xN$ have been known as the material which exhibits superior mechanical and thermal properties, and those are widely used as coatings for industrial applications such as cutting tools. Irrespective of those attracting performance, little is studied on the growth mechanism as well as the chemical process. In this work, $Ti_{1-x}Al_xN$ thin films have been prepared by reactive Chemical Vapor Deposition (CVD) and analyzed by Field Emission Gun Scanning Electron Microscopy (FEG-SEM), Transmitting Electron Microscope (TEM) [1], and X-ray Diffraction (XRD).

Recently, it has been reported that $Ti_{1-x}Al_xN$ films have been grown by use of the titanium tetrachloride, $TiCl_4$, and c-plane (0001) monocrystalline hexagonal aluminium nitride, AlN, precursors [2]. The AlN has been prepared at 1500 °C with the gas mixture of NH_3 and $AlCl_3$ on c-plane (0001) monocrystalline hexagonal sapphire. During the $Ti_{1-x}Al_xN$ growth, hydrogen gas is supplied in order to promote the reactivity. The growth has been performed at various temperatures between 800 °C and 1200 °C on the 100-nm-thick monocrystalline AlN on sapphire.

Figure 1 shows the surface morphologies of $Ti_{1-x}Al_xN$ layers deposited at (a) 800 °C, (b) 900 °C, (c) 1000 °C and (d) 1200 °C on monocrystalline AlN substrates. At temperatures lower than 1000 °C, surface morphologies appear to be smooth. As the temperature is raised, the grain size appears to become larger, but there is almost no substantial change between 800 °C and 1000 °C (Fig. 1(a)-(c)). However, the surface morphology deposited at 1200 °C (Fig. 1 (d)) is quite different from the others. The grains are much smaller than those fabricated at less

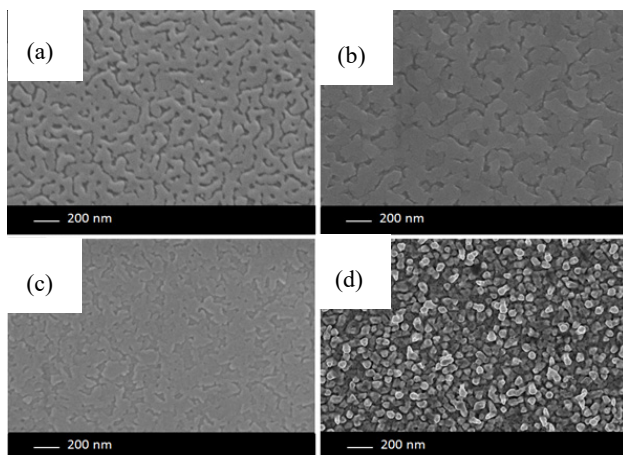


Fig. 1. Surface morphologies of the layers fabricated on monocrystalline AlN at (a) 800 °C, (b) 900 °C (c) 1000 °C and (d) 1200 °C observed by FEG-SEM.

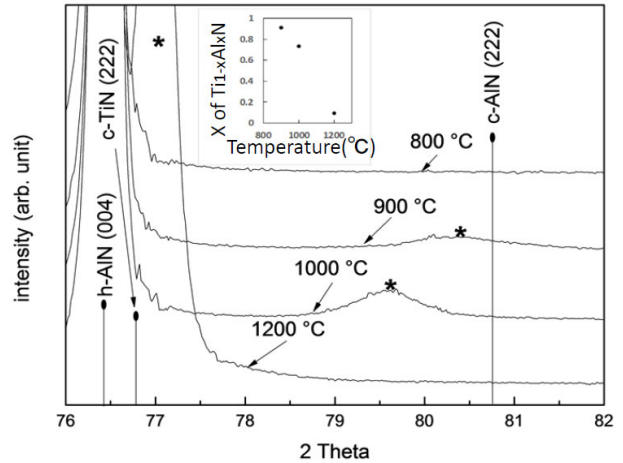


Fig. 2. X-ray diffraction patterns of the layers fabricated on monocrystalline AlN at (a) 800 °C, (b) 900 °C, (c) 1000 °C and (d) 1200 °C.

than 1000 °C, and some of them seem to grow in a columnar shape. It can be considered that this difference results from the reactivity between $TiCl_4$ and condensed AlN. Generally, as temperature is raised, reaction rate increases. If the reaction rate increases in this system, it can be expected that $TiCl_4$ and AlN react as soon as $TiCl_4$ reaches the AlN surface, leading to grow in a columnar shape. In other words, surface diffusion is limited. In contrast, at temperature lower than 1000 °C, it can be considered that reaction rate is not as high compared to the system at 1200 °C, therefore, sufficient time to diffuse on the surface exists, leading to an increase of surface flatness. Figure 2 shows X-ray diffraction patterns of the layers fabricated on monocrystalline AlN at (a) 800 °C, (b) 900 °C, (c) 1000 °C and (d) 1200 °C. The intensity is represented in logarithm scale. The marks of * indicate the position of the peak of $Ti_{1-x}Al_xN$ (222). The intensity is represented in logarithm scale. The inserted graph indicates the evolution of x in $Ti_{1-x}Al_xN$ against temperature. It can be seen from Fig. 2 that there is no peak of $Ti_{1-x}Al_xN$ (222) for the sample deposited at 800 °C. The position of the peaks for the other samples are shifted towards lower θ side by increasing the deposition temperature. That indicates that Al content in the fabricated layer decreases with increasing temperature.

References

- [1] H. Abe *et al.*, JAERI-Res. 96-047, 1 (1996).
- [2] R. Boichot *et al.*, Surf. Coat. Tech. **205**, 1294 (2010).
- [3] P. H. Mayrhofer *et al.*, J. Appl. Phys. **100**, 9490 (2006).

T. Taguchi ^{a)}, S. Yamamoto ^{b)} and H. Ohba ^{a)}

^{a)} Tokai Quantum Beam Science Center, TARRI, QST,

^{b)} Department of Advanced Functional Materials Research, TARRI, QST

Since the discovery of carbon nanotubes (CNTs) in 1991, many researchers have synthesized a lot of new one-dimensional nanostructured materials such as nanotubes, nanorods and nanowhiskers for potential applications. Some of them have reported that many nanomaterials such as TiC, NbC, BN, SiO₂ and GaN nanostructures are fabricated from CNTs as the template. SiC is well known as not only wide-band-gap semiconducting material for high temperature and high power use but also high temperature structural materials. Therefore, SiC offers exciting opportunities in electronic devices and in structural materials at high temperature. We have reported that polycrystalline single-phase SiC nanotubes were synthesized [1, 2]. Furthermore, the amorphous SiC nanotubes were also successfully synthesized by the ion irradiation of the polycrystalline SiC nanotubes at under 100 °C [3]. However, the effect of ion irradiation on crystal lattice plane spacing change in SiC nanotube has not been known yet. In the present study, we investigated the lattice plane spacing change of SiC nanotube during the ion irradiation by using in-situ transmission electron microscopy (TEM) observation technique.

Carbon nanotubes (GSI Creos Corporation, Tokyo, Japan) are used as the template. The C-SiC coaxial nanotubes are synthesized by heating CNTs with Si powder (The Nilaco Corporation, Tokyo, Japan) at 1200 °C for 100 h in a vacuum. And then single-phase SiC nanotubes were formed by the heat treatment of C-SiC coaxial nanotubes at 800 °C for 4 h in air. The molybdenum grid holder, which deposits the SiC nanotubes, are irradiated with 200 keV Si⁺ ions from 400 kV ion implanter at room temperature and 700 °C in TEM (Model JEM-4000FX, JEOL Ltd., Japan) operating at 400 kV. In-situ TEM observation of SiC nanotube under Si⁺ ions irradiation is carried out. The ion fluence is up to 9.2×10^{20} ions/m², and the corresponding irradiation damage is calculated by SRIM 2008 to be 24.1 dpa.

Figure 1 shows the effect of ion fluence on the crystal lattice plane spacing in SiC nanotube by ion irradiation at room temperature and 700 °C, evaluated from selected area electron diffraction patterns of in-situ TEM. From this result, the lattice plane spacing of crystals in the nanotube increases in increasing ion fluence at room temperature, while that at 700 °C decreases monotonically up to the irradiation damage of 24.1 dpa. Many defects induced by ion irradiation may remain in SiC, and their amount increases with increasing irradiation damage at room temperature, eventually converting the crystals to amorphous SiC. This could explain the increasing lattice

plane spacing in the SiC nanotube irradiated at room temperature. At irradiation damage higher than 1.1×10^{20} ions/m², we could not evaluate the lattice plane spacing due to complete amorphization of SiC crystals.

Some researchers have reported that the XRD peak of bulk SiC shifted to a lower angle after neutron irradiation at room temperature as well as above 700 °C, which denotes lattice expansion in bulk SiC. In this study, the lattice plane spacing irradiated at 700 °C, however, decreases slightly unlike previous findings for bulk SiC. We deduce that a larger number of inherent structural defects exist in the outer surface region of the nanotube in order to buffer the residual tensile stress generated in the SiC nanotube [3]. The lattice plane spacing slightly decreases from 0.254 to 0.252 nm, which is very consistent with the {111} lattice plane spacing of bulk 3C-SiC [4]. These results support that the lattice plane spacing in the as-synthesized SiC nanotube may be slightly larger due to these inherent defects [4]. Atomic rearrangement in the crystals of SiC nanotube may occur during ion irradiation at temperatures higher than 700 °C, because atomic defects and atoms can migrate and be released easily from the surface. It is, therefore, considered that the lattice plane spacing decreases with increasing irradiation damage at the irradiation temperature of 700 °C because the number of atomic defects actually decreases.

References

- [1] T. Taguchi *et al.*, J. Am. Ceram. Soc., **88**, 459 (2005).
- [2] T. Taguchi *et al.*, Physica E, **28**, 431 (2005).
- [3] T. Taguchi *et al.*, Appl. Surf. Sci., **403**, 308 (2017).
- [4] T. Taguchi *et al.*, Acta Materialia, **154**, 90 (2018).

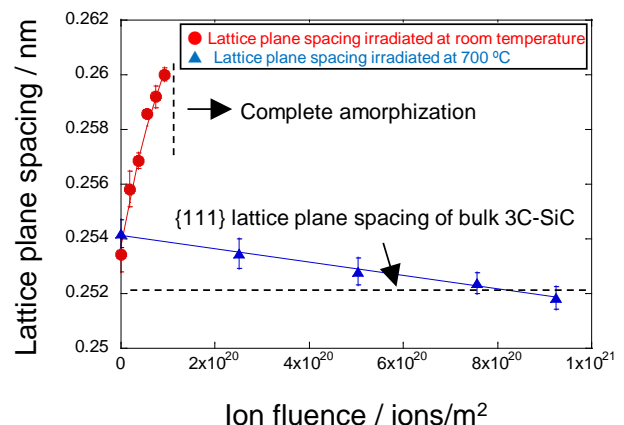


Fig. 1. Effect of ion fluence on the crystal lattice plane spacing in SiC nanotube by ion irradiation at room temperature and 700 °C.

H. Abe ^{a)} and Y. Yoneda ^{b)}

^{a)} Department of Advanced Functional Materials Research, TARRI, QST,
^{b)} Energy and Environment Materials Science Division, MSRC, JAEA

Nanoparticle oxide of Bi-Ti-O system course is formed by ion irradiation in TiO₂ host material. These materials are called smart materials [1]. Smart materials have the ability to perform both sensing and actuating functions and are capable of imitating this rudimentary aspect of life. Especially, we focused on the magnetostrictive materials, “Terfenol”, TbDyFe₂ system is a typical magnetostrictive actuator with strong coupling between magnetic field and mechanical motion [2].

When the host material of the ion irradiation is selected, it is necessary to consider the following two. One must be a host material in which the implanted ions diffuse easily. Another is the damage tolerance by the ion irradiation of the host material. The implanted ions cohere, and the oxide particles are made by depriving the host material of oxygens. Therefore, the host material should be a crystal with a large randomness. One can evaluate the randomness of the crystalline materials by combining high-energy X-ray diffraction and pair-distribution function (PDF) analysis. The raw data were corrected for background, absorption, multiple-scattering, and inelasticity effects and were normalized to the incident flux and the total sample scattering cross section to yield the total scattering structure function, $S(Q)$. This was Fourier transformed according to

$$G(r) = \frac{2}{\pi} \int Q[S(Q) - 1] \sin(Qr) dQ \quad (1)$$

Local structure information was extracted from the PDF by using trial structures to modeling in real space.

The irradiated Bi₂O₃ were changed to Bi₂Ti₂O₇ through heating process. The host TiO₂ was not damaged seriously by the bismuth (Bi⁺) irradiation owing to its diffuse crystal system. We performed the Bi⁺ irradiation at TIARA ion implanter and the grown nanoparticles were evaluated by synchrotron X-ray at BL14B1 in SPring-8. We selected Bi as an irradiating metal ion. Since Bi is heavy atom and the structure factor of X-ray diffraction is large. After the Bi atoms are implanted in the TiO₂ host material, the Bi can be detected easily owing to the large contrast of the structure factor between the irradiation Bi and the host TiO₂. The implanted Bi was hardly detected by laboratory X-ray measurements with Cu-K α radiation ($\lambda = 1.54051 \text{ \AA}$). We measured high energy X-ray diffraction with the energy of 60 keV ($\lambda = 0.20538 \text{ \AA}$) to detect the buried Bi. The Bi⁺ ions with 350 keV were implanted in the 0.1 mm depth from the TiO₂ surface, which was estimated using the SRIM code [3].

The irradiated TiO₂ pellet was annealed in air at 800 °C to oxide implanted Bi. The host TiO₂ was irradiated heavily, and the irradiated area was damaged. We performed PDF analysis to evaluate the damage of the host TiO₂. The local

structures of the as-irradiated and annealed TiO₂ were found to be almost the same. Since the deformation of the crystal structure by the ion irradiation was very little, the recovery of the crystalline by the annealing was hardly seen. The bond distribution of the nearest-neighbor distance of Ti-O has only changed slightly by the annealing, as provided in Fig 1. The PDF reveals that the host TiO₂ was not damaged both through the Bi₂O₃ implant process by the Bi⁺ ion irradiation and through the Bi₂Ti₂O₇ sintering process by the annealing. There is the SmFe₂ enough as a possibility like a structure TiO₂ host material.

We fabricated oxide nanoparticles in paraelectric host material. TiO₂ and MgO are the candidate for the host material. TiO₂ has diffuse crystal structure, but MgO has highly ordered crystal structure. The high damage tolerance is demanded for the host material owing to the heavy and high energy ion irradiation. The irradiating Bi ions existed as oxide Bi₂O₃ in the host TiO₂ and changed to Bi₂Ti₂O₇ through sintering process. The Bi₂Ti₂O₇ nanoparticles are grown by depriving host TiO₂ of Ti and O. This technique can be used to make the ferroelectric nanoparticle in the paraelectric host material and realize the structure of magnetostrictive material similar to SmFe₂.

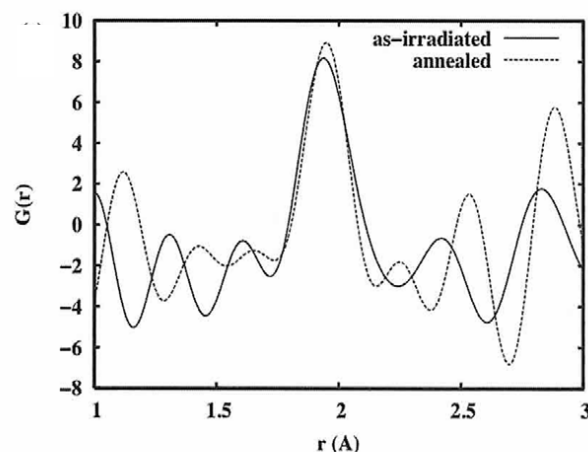


Fig. 1. Structure functions of PDFs $G(r)$ of as-irradiated and annealed TiO₂ as around the nearest-neighbor distance r (Å) of Ti-O.

References

- [1] R. E. Newnham: *Acta Cyst.* **A54**, 729-37 (1998).
- [2] S. Yang *et al.*, *Phys. Rev. Lett.* **104**, 197201 (2010).
- [3] J. F. Ziegler, *Handbook of Ion Implantation Technology*, 1 (Elsevier, Amsterdam 1992).

1 - 24 Development of Hydrogen Permselective Membranes by Radiation-induced Graft Polymerization into Ion-Beam Irradiated Poly Vinylidene Chloride Films

S. Hasegawa, A. Hiroki, S. Sawada and Y. Maekawa

Department of Advanced Functional Material Research, TARRI, QST

Separation and purification of gas molecules with similar physical and chemical properties are an important matter in industry. In the present system for the gas separation and purification, however, it is accompanied by a large energy loss [1]. The permselective membranes are required to reduce the energy loss.

Radiation-induced graft polymerization is a useful technique for introducing new functional polymers into polymer substrates. When polymer films are irradiated with heavy ion beam, radicals are produced in the latent track. Graft polymerization of vinyl monomers is carried out by using these radicals, resulted in a formation of a cylindrical and nano-scale graft-polymer region. In this work, we propose a development of hydrogen permselective membranes by the combination of ion-beam irradiation and graft polymerization (Fig. 1(a)).

Poly (vinylidene chloride) (PVDC, ASAHI-KASEI Corp. 25 μm thickness) film having high barrier properties against oxygen and water vapor were used for substrate film. To introduce graft-polymer regions for a gas permeation, p-trimethoxysilyl styrene (TMSS) was used for a silyl-containing vinyl monomer having a hydrogen permselective property. The PVDC films were irradiated by 310 MeV Kr ions ($^{84}\text{Kr}^{20+}$) with ion fluence of 1×10^{10} ions/cm². The irradiated PVDC films were immersed into TMSS solution (TMSS/toluene=50:50 vol%) at 60 °C. (Fig. 1(b)). For a comparison, the radiation-induced graft polymerization was also carried out with the PVDC film γ -irradiated with 160 kGy.

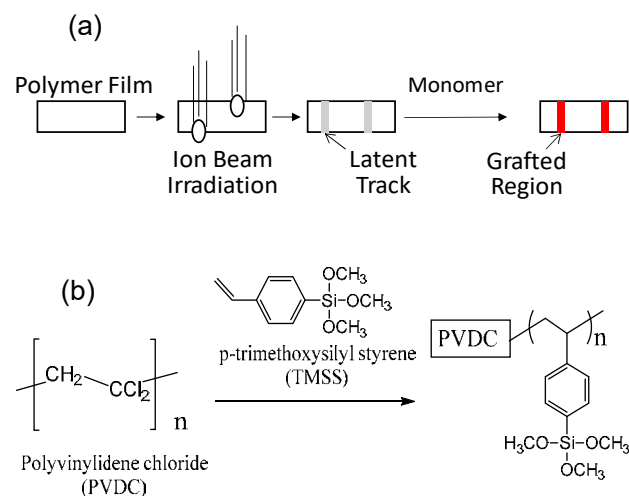


Fig. 1. Synthetic illustration (a) and chemical scheme (b) of gas permselective films prepared by the combination of ion beam irradiation and graft polymerization.

Grafting degrees (GDs) of TMSS-grafted PVDC prepared by γ - (a) and ion beam (b) irradiations are plotted as a function of grafting time in Fig. 2. The GDs of TMSS-grafted PVDC increased with the grafting time, and reached 37% and 12% at 24 hours, respectively.

Permeabilities of hydrogen, oxygen, and nitrogen were measured by a decompression method. The PVDC substrate showed a low gas permeation and permselectivity (Table 1). The gas permeability of PVDC irradiated with Kr ions (1×10^{10} ions/cm²) showed 4.5-5.0 $\times 10^4$ times higher than that of the substrate, but there was no H₂ permselectivity. The TMSS-grafted PVDC (GD=12%) prepared by ion beam irradiation showed the suppression of gas permeability by more than 10³ times. The highest permeation ratios are 5.8 (H₂/O₂) and 6.0 (H₂/N₂), respectively. On the other hand, the TMSS-grafted PVDC (GD=19%) prepared by γ -irradiation showed higher permeability than that of the sample prepared by ion beam irradiation, whereas it showed lower H₂ permselectivity to O₂ (2.5) and N₂ (0.5), respectively. Accordingly, the TMSS-grafted PVDC prepared by ion beam irradiation would exhibit hydrogen permselectivity because the graft polymers with an affinity for hydrogen molecules formed moderate nano-scale tracks for H₂.

Reference

[1] R. W. Baker, Ind. Eng. Chem. Res. **41**, 1393 (2002).

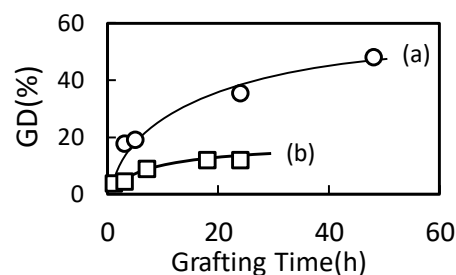


Fig. 2. Plots of GDs of TMSS-grafted PVDC films as a function of reaction time:(a) graft polymerization by γ -rays and (b) by ion beam irradiation.

Table 1

Permeability and permeation ratio with TMSS-grafted PVDC films.

Treatment*	GD (%)	Permeability $\times 10^{-8}$ (mol/sec.m ² .Pa)			H ₂ /O ₂	H ₂ /N ₂
		H ₂	O ₂	N ₂		
-	-	0.0002	0.0001	0.0001	1.1	1.2
1	-	7.7	5.6	5.9	1.3	1.4
1+3	12	0.0064	0.0011	0.0011	5.8	6.0
2+3	19	0.083	0.16	0.34	2.5	0.5

*1: Ion Beam irradiation, 2: γ -rays irradiation, 3: Graft Polymerization

Development of Radiation-grafted Cation and Anion Exchange Membranes for Reverse Electrodialysis Process

S. Sawada ^{a)}, M. Yasukawa ^{b)}, M. Higa ^{b)} and Y. Maekawa ^{a)}

^{a)} Department of Advanced Functional Materials Research, TARRI, QST,

^{b)} Graduate School of Science and Technology for Innovation, Yamaguchi University

Reverse electrodialysis (RED) is a promising eco-friendly technology to produce electricity from natural salinity gradients between sea and river water [1]. The RED cell is composed of many sets of cation- and anion-exchange membranes (CEM and AEM) that transport Na⁺ and Cl⁻, respectively, from the seawater to river water side. These ionic movements cause an electron current in the external circuit between the cathode and anode of the RED cell to generate power. To achieve high output power, CEMs and AEMs with low ionic resistivity, sufficient chemical stability, and mechanical strength are strongly required.

In this study, we prepared the CEMs and AEMs for a RED system by a radiation-induced grafting method. In these CEMs and AEMs, graft chains possessing cation and anion exchange groups are covalently bonded to polymer mainchains in the film used as a base material. The base polymer parts steadily maintain the mechanical strength of the prepared CEM and AEM, which makes two things possible: (i) thinning of membranes and (ii) increasing of an ion exchange capacity.

The 50 μm thick ethylene-co-tetrafluoroethylene (ETFE) film was irradiated with 10 kGy γ-rays. After the irradiation, a CEM was prepared by grafting of styrene monomer into the ETFE film and subsequent sulfonation. An AEM was prepared by grafting of chloromethyl styrene (CMS) into the ETFE film and subsequent quaternarization. The ion exchange capacity (IEC) of the CEM and AEM was measured by a neutralization titration method. The area resistivity of the CEM and AEM immersed in a 0.6 M NaCl aqueous solution was measured by a two-probe AC impedance technique.

Grafting degrees of styrene and CMS increased with grafting reaction time. Depending on the grafting degree, the IEC of the radiation-grafted CEMs and AEMs were controlled in the range of 0.9 - 2.4 mmol/g and 0.4 - 1.6 mmol/g, respectively. Figure 1 shows the relationship between the IEC and area resistivity for the CEMs and AEMs. Area resistivity drastically decreased with the ion exchange capacity. The minimum area resistivity is 0.28 Ω cm² at 2.4 mmol/g (83 μm thick) and 0.39 Ω cm² at 1.6 mmol/g (80 μm thick) for the CEM and AEM, respectively. These values are excellently lower than the resistivities of the commercial CEM (CMX, 168 μm thick, Astom Co. Japan) and AEM (AMX, 156 μm thick, Astom Co. Japan). This was due to both thinness of membranes and high ion exchange capacity, both of which can be achieved by the radiation grafting technique.

Based on the area resistivity of the radiation-grafted CEM and AEM, the output performance of RED system was predicted. The maximum output power density, W_{MAX} , is theoretically expressed as follows [2]:

$$W_{MAX} = \frac{\left\{ \frac{2NR}{F} \ln \left(\frac{C_{SW}}{C_{RW}} \right) \right\}^2}{N (R_{CEM} + R_{AEM} + R_{SW} + R_{RW})}, \quad (1)$$

N: Number of CEM/AEM pairs, R: Gas constant, F: Faraday constant, C_{SW} : Seawater concentration, C_{RW} : River water concentration, R_{CEM} : Resistivity of CEM, R_{AEM} : Resistivity of AEM, R_{SW} : Resistivity of seawater, R_{RW} : Resistivity of river water.

In this trial calculation, the parameter values were set as follows: N = 100, $C_{SW} = 0.6$ mol/L, and $C_{RW} = 0.06$ mol/L. The R_{CEM} and R_{AEM} (the minimum values in Fig. 1) were shown in Table 1, and substituted into equation (1). The predicted W_{MAX} was 315 W/m², being 1.4-times higher than that for the case of CMX/AMX. This result suggests that the high-power RED system is feasible by using the radiation-grafted CEMs and AEMs.

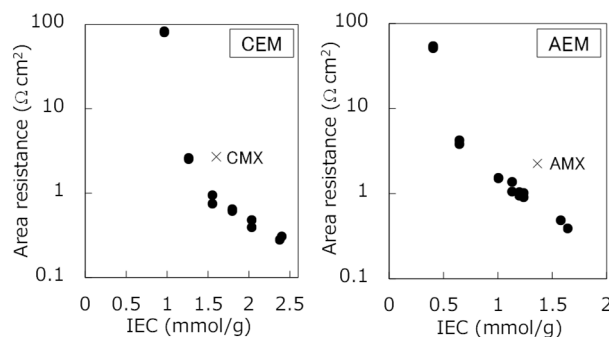


Fig. 1. Relationship between the IEC and area resistivity for radiation-grafted CEMs and AEMs.

Table 1

The predicted W_{MAX} of the RED system using different CEM/AEM combinations.

CEM		AEM		W_{MAX} (W/m ²)
Type	R_{CEM} (Ω cm ²)	Type	R_{AEM} (Ω cm ²)	
Grafted	0.28	Grafted	0.39	315
CMX	2.7	AMX	2.2	228

Acknowledgment

This work was supported by JSPS KAKENHI (Grant Number: 16K06839).

References

- [1] J. Veerman *et al.*, *J. Membr. Sci.* **343**, 7 (2009).
- [2] N. Y. Yip *et al.*, *Environ. Sci. Tech.* **48**, 4925 (2014).

The Relationship Between Membrane Properties and Hierarchical Structure of Radiation Grafted Anion Conducting Polymer Electrolyte Membranes

K. Yoshimura^{a)}, Y. Zhao^{a)}, A. Hiroki^{a)}, H. Shishitani^{b)},
S. Yamaguchi^{b)} and Y. Maekawa^{a)}

^{a)} Department of Advanced Functional Materials Research, TARRI, QST,

^{b)} Daihatsu Motor Co., Ltd.

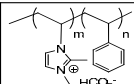
Anion-conducting polymer electrolyte membranes (AEMs) are one of the key materials for alkaline-type fuel cells (AEMFC), which have potential advantages against proton-conducting polymer electrolyte membrane fuel cells (PEMFC). In the AEMFC, electrochemical reactions are more facile than in acidic medium, and non-precious metals such as nickel, cobalt and iron can be utilized instead of platinum as a catalyst. Because of high temperature and highly basic fuel cell operating condition, it is desirable to develop high performance AEMs. Therefore, it is crucial to thoroughly understand relations of the current AEMs microstructures with ion conductivity, mechanical and alkaline stabilities. Recently, our group developed a new series of AEMs by radiation-induced grafting method, where 2-methyl-*N*-vinylimidazole (Im) and styrene (St) monomers were grafted into poly(ethylene-co-tetrafluoroethylene) (ETFE) base films with a dose of 80 kGy from a ⁶⁰Co γ -ray source at room temperature followed by alkylation and ion exchange reactions [1]. These AEMs exhibit well-balanced properties of high ion conductivity (> 100 mS/cm in OH⁻ form) and good alkaline stability. In this work, we investigate the morphological change with monomer compositions (Im : St ratio) in the graft-copolymers and elucidate the interplay between the morphology and properties by using a small-angle neutron scattering (SANS) method.

To understand the relationship between morphology and property and how the structure change with graft compositions, we have prepared three AEMs in HCO₃⁻ form with a similar ion exchange capacity (IEC) but different monomer compositions, denoted as ImSt64, ImSt46 and ImSt28. The properties of these AEMs are listed in Table 1. The SANS experiments were performed at KWS-2 at FRM II, Germany.

Since the IECs were settled to be ~ 1.0 mmol/g, the total number density of imidazolium groups is expected to be same for all AEMs, hence the ion conductivity is also

Table 1

Chemical structure and membrane properties of imidazolium-graft AEMs.

	Grafting Degree (%)	Composition (m/n)	IEC (mmol/g)	Water Uptake (%)	Conductivity of OH ⁻ form (mS/cm)
ImSt64	30	6/4	0.95	15	58
ImSt46	53	4/6	1.02	24	50
ImSt28	110	2/8	1.12	35	60

similar as shown in the Table 1. To examine the effects of the hydrophobicity of graft-copolymers on the AEMs, alkaline durability tests were performed in 1 M KOH at 80 °C. The degradation rate of anionic groups in AEMs followed the order of ImSt64 > ImSt46 > ImSt28. This indicates that the alkaline stability of the AEMs become poorer with the increase of hydrophobic St.

Figure 1 shows the SANS profiles of the AEMs equilibrated in D₂O. Pronounced peaks at about $q = 1.7 \text{ nm}^{-1}$ were observed in styrene rich samples (ImSt46 and ImSt28), resulting from nanoscale phase separation structure. This nanoscale phase separation in ion channels might be a key factor for lower alkaline stability. (*i.e.*, the alkaline hydrolysis is accelerated in water-rich region like puddles.) On the other hand, ImSt64 does not possess any specific structure at a length scale < 10 nm. Thus, imidazolium groups are efficiently isolated from alkaline solution and shows higher alkaline stability.

We have demonstrated the effects of the hydrophobicity of graft-copolymers on membrane electrochemical properties and alkaline durability. Interestingly, a reverse relationship that higher hydrophobicity results in lower alkaline durability was found. This phenomenon was interpreted by the hierarchical structures of AEMs.

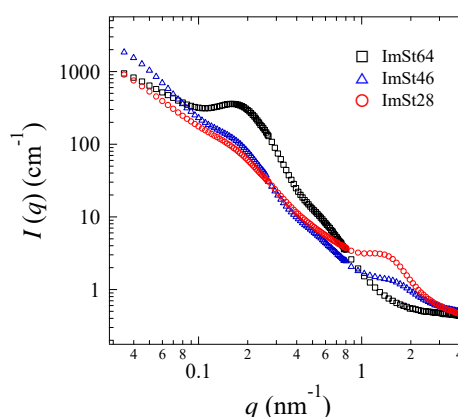


Fig. 1. SANS profiles of AEMs equilibrated in D₂O.

Acknowledgment

This work was supported by the ALCA program from the Japan Science and Technology Agency (JST).

Reference

[1] Y. Zhao *et al.*, *Soft Matter*, **12**, 1567 (2016).

1 - 27 Effect of γ -Ray Irradiation on Friction Property of Poly (vinyl alcohol) Cast-drying on Freeze-thawed Hybrid Gel

S. Sasaki^{a, b)}, S. Omata^{a, c)}, T. Murakami^{a, d)}, N. Nagasawa^{e)}, M. Taguchi^{e)} and A. Suzuki^{f)}

^{a)} Research Center for Advanced Biomechanics, Kyushu University,

^{b)} Institute for Material Chemistry and Engineering, Kyushu University,

^{c)} Department of Micro-Nano Mechanical Science and Engineering, Nagoya University,

^{d)} Faculty of Fukuoka Medical Technology, Teikyo University,

^{e)} Department of Advanced Functional Materials Research, TARRI, QST,

^{f)} Research Institute of Environment and Information Sciences, Yokohama National University

Introduction

Poly(vinyl alcohol) (PVA) is a high biocompatible synthetic polymer with low toxicity and excellent mechanical properties. Physically cross-linked PVA gels having hydrogen bonds are prepared without using a cross-linking agent via two methods. One is the repeated freeze-thawing (FT) of aqueous PVA solutions, while the other one is the cast-drying (CD) of them. Recently, a method for preparing the physically cross-linked PVA gel such as CD on FT hybrid gel was investigated. The CD on FT hybrid gel presents excellent friction properties in reciprocating friction tests in physiological saline, and is expected to be applied as a candidate material for an artificial cartilage. The present study aims to improve the hybrid gel by a radiation crosslinking technique.

Materials and Methods

PVA powder was dissolved in pure water at around 90 °C. As a first step, the solution was repeatedly frozen at -20 °C for 8 h and thawed at 4 °C for 9 h to obtain an FT hydrogel. Then as a second step, the aqueous PVA solution was decanted on the FT gel layer obtained by the first step and dried at 8 °C and 50% relative humidity for 7 days to obtain the CD on FT hybrid gel. The hybrid hydrogel was irradiated with γ -rays.

A ball-on-plate reciprocating friction test was conducted to evaluate the coefficient of friction, μ_k , by using a friction tester. The lubricant was pure water and set at body temperature (37 °C). Polycrystalline alumina ceramic ball of 26 mm diameter was used as an upper ball specimen. Sliding speed and total sliding distance were 20 mm/s and 300 m (stroke: 25 mm; total cycle: 6000), respectively.

Results and Discussion

μ_k of the hybrid gel was obtained by the reciprocating test and shown in Fig. 1 [1]. The hybrid gel at the dose of 10 kGy has a lower μ_k than that of the non-irradiated one. μ_k increased with an increase in the dose, in other word, the cross-linking density of PVA polymer chains.

Figure 2 shows photomicrographs of the hybrid gel surfaces after the reciprocating friction test. The distinct scratches were formed on the surface of the non-irradiated hybrid gel surface. In contrast, the irradiated surface features revealed that wear was suppressed by γ -ray irradiation. Scratches are likely to occur under higher dose rate conditions.

The hybrid gels become hard and also brittle by the

radiation cross-linked reaction. Therefore, reduction and increase of μ_k , and inhibition of scratch formation are considered to have been brought about by an increase in shear strength, a decrease in adhesive force and hardening of gel, as a result of the chemical cross-linking accompanied with scission of polymer chain. The water content of the hybrid gels is around 75% before γ -ray irradiation. It decreased but kept above 70%, which is close to that of the articular cartilage in human body (about 70-80%), after the irradiation at 10 kGy. The irradiation treatment by γ -rays at the dose rate of 5 kGy/h and the dose of 10 kGy and is expected to be an optimum production condition to actualize good friction and wear characteristics for an artificial cartilage gel.

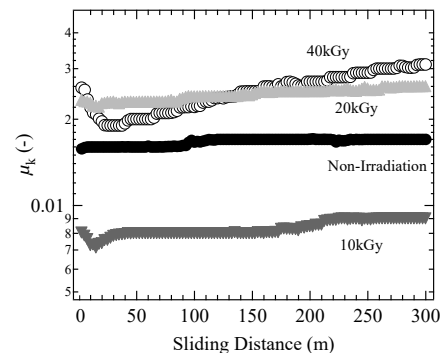


Fig. 1. Coefficient of friction of the hybrid gels irradiated with γ -rays at 5 kGy/h by reciprocating friction tests at 37 °C.

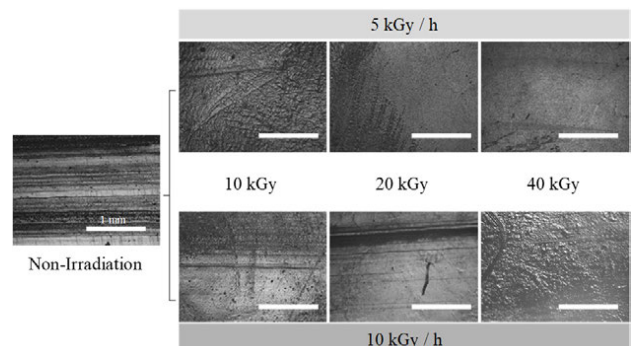


Fig. 2. Photomicrograph of the surface of the hybrid gels after the reciprocating friction test at 37 °C. Scale bar is 1 mm.

Reference

[1] S. Sasaki *et al.*, Gels 4, 30 (2018).

A. Idesaki and M. Taguchi

Department of Advanced Functional Materials Research, TARRI, QST

Polyethylene (PE), which has excellent electrical insulation, good flexibility, high chemical resistance, is applied for insulator of cables used in nuclear power plants. There are numerical reports on changes in properties of PE by irradiation of gamma-rays, electron beam, and so on, to evaluate radiation resistance of PE. Referring to several tens reports, we summarized experimental conditions in Table 1. We could find many reports in which experiments were conducted in atmospheres of air and oxygen because it is well-known that properties of PE degrade under presence of oxygen. However, we could find just a few reports in which experiments were conducted in atmosphere of water. In this work, mechanical properties of PE after irradiation of gamma-rays in water was evaluated in order to clarify the effect of water on changes in mechanical properties of PE.

Table 1

Experimental conditions in previously published literatures (44 literatures were referred. The number for atmosphere contains duplication).

Dose range (kGy)		~2000
Dose rate range (Gy/h)		5~1 × 10 ⁵
Temperature range (°C)		25~175
Atmosphere	Air	30
	Vacuum, Nitrogen	10
(Number of reports)	Oxygen	9
	Water	4

High density polyethylene (HDPE) and a crosslinking agent, 2,5-Bis(tert-butylperoxy)2,5-dimethylhexane, were mixed at 130 °C and then hot-pressed at 190 °C to prepare crosslinked HDPE sheet sample with thickness of 1 mm and 2 mm. The sheet samples were irradiated by gamma-rays in water or air at 60 °C. The dose rate of 0.5 kGy/h was applied in order to oxidize whole sheet sample with thickness of 1 mm in both atmospheres of water and air. Sufficient oxidation of the sample was confirmed by microscopic FT-IR spectra obtained along cross-sectional direction in the sample. After the irradiation, mechanical and chemical tests were conducted: tensile test (JIS K7161, K7162), stress-cracking test (JIS Z1703) and gel fraction measurement (solvent: boiling xylene, extraction time: 6 h). In the stress-cracking test, U-bent specimens with thickness of 2 mm were irradiated, and then number of cracks was counted after the irradiation.

The elongation at break decreased drastically to almost zero in the dose of 100 - 200 kGy in both atmospheres showing that HDPE becomes brittle as increasing in the dose (Fig. 1(a)). In the stress-cracking test, cracks were observed above 100 kGy in water and 300 kGy, in air (Fig. 1(b)). The gel fraction, which indicates the weight

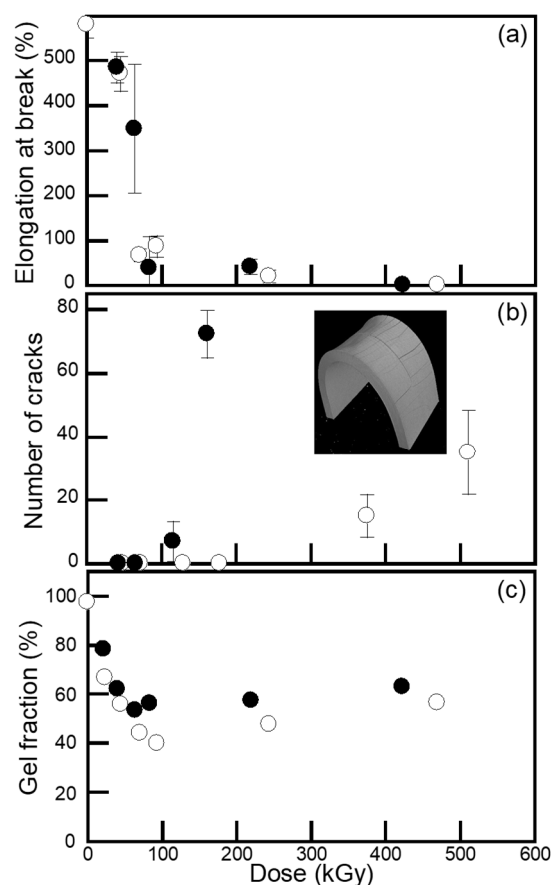


Fig. 1. Changes in properties of crosslinked HDPE after gamma-ray irradiation in water (●) and air (○): (a) tensile test (elongation at break), (b) stress-cracking test and (c) gel fraction measurement.

fraction of insoluble components, is an indicator for decomposition of molecules in HDPE; more decomposition of molecules leads smaller value of gel fraction. The gel fraction after the irradiation in water was slightly higher than that in air (Fig. 1(c)). This result suggests that decomposition of molecules was suppressed in the case of irradiation in water.

In the stress-cracking test, cracks are generated when the applied stress for the U-bent specimen becomes higher than fracture stress of HDPE. In the dose range of above 100 kGy, HDPE becomes brittle in both atmospheres that indicates the fracture stress of HDPE becomes low. When the molecules are decomposed, the applied stress in the U-bent specimen is relaxed. Such relaxation caused generation of cracks at high dose range in the case of irradiation in air. On the contrary, cracks started to generate in low dose range in the case of irradiation in water because relaxation of the applied stress was suppressed by less decomposition of molecules.

Y. Ueki and N. Seko

Department of Advanced Functional Materials Research, TARRI, QST

Radiation-induced grafting, one of the surface modification techniques of polymers, can impart desired functional groups into trunk polymers without deteriorating their physical and chemical properties. This technique was applied to the synthesis of a novel high-performance adsorbent. Especially, when a glycidyl methacrylate (GMA) is used as a grafting monomer, various functional groups could easily be introduced onto the trunk polymers through the epoxy ring opening reaction of GMA-grafted chains. Carboxyl, sulfonate and amine groups possess adsorptive affinities for metal ions, and grafted adsorbents containing these functional groups have been widely used in various fields such as recovery of rare metals, removal of toxic ions, water softening and deionization, and so on. However, these oxygen- and nitrogen-based functional groups are not necessarily optimum for the capturing of the heavy metal ions with relatively large atomic numbers such as Pb and Hg, because these oxygen- and nitrogen-based functional groups are classified into the "hard" and "medium" bases from the point of view of Hard and Soft Acids and Bases (HSAB) Theory. On the other hand, sulfur-based functional group is classified into the "soft" base, and its adsorptive affinity for Pb is higher than those of "hard" and "medium" bases. The objective of this study was to synthesize the fibrous metal adsorbent having sulfur-based functional group by the radiation-induced grafting and subsequent chemical modifications.

The synthesis scheme of the fibrous grafted adsorbent is shown in Fig. 1. Polyethylene nonwoven (PENW) fabric, of which the fiber diameter was 13 μm , was used as a trunk polymer. Firstly, the PENW fabric was irradiated with an electron beam (20 kGy) at the electron beam facility in TARRI. Then, the irradiated PENW fabric was reacted with a deaerated GMA emulsion (5 wt% GMA / 0.5 wt% Tween20/94.5 wt% H₂O) for 1 h at 40 °C. After grafting, the GMA-grafted fabric was aminated with 0.5 M piperazine (PIP) solution for 24 h at 80 °C, and then treated with CS₂ solution (20 wt% CS₂/35 wt% 10 M NaOH aq./45 wt% methanol) for 24 h at 40 °C, to introduce dithiocarbamate (-NCS₂⁻) groups onto the GMA-graft chains. The dithiocarbamate group containing two sulfur atoms acts as a bidentate chelating ligand through sulfur atoms.

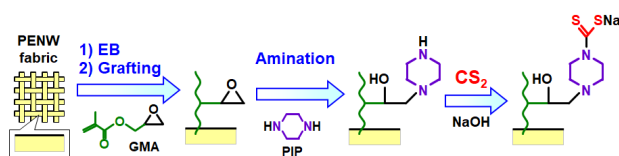


Fig. 1. Synthesis schemes of the fibrous grafted adsorbent.

Table 1 shows the effect of amination condition on the degree of amination (Da), PIP density, crosslinked PIP (C-PIP) ratio and dithiocarbamate group density, respectively. In the case of H₂O, the amination could hardly proceed, and its dithiocarbamate group density became almost zero (Density: 0.005 mmol-NCS₂⁻/g-ad.). On the other hand, in the case of organic solvents, the amination could effectively proceed, and consequently the Da reached over 50% regardless of the organic solvent types. However, the actual dithiocarbamate group densities of those adsorbents were considerably lower than the predicted values which were estimated by the PIP densities of each adsorbent. The dithiocarbamate group was introduced into only 12% or less of existing PIP in the adsorbent. The reason for this lower dithiocarbamate group density was thought to be that the PIP was self-crosslinked. In other words, two nitrogen atoms of PIP both reacted with two epoxy groups on the GMA-grafted chains and form the crosslinking structure as shown in Fig. 2. The self-crosslinking of the PIP could be improved somewhat by using the high concentration of PIP solution. In the case of 5 M PIP-ethanol solution, the self-crosslinking of the PIP was suppressed, and its dithiocarbamate group density became about 3.5 times higher than that of 0.5 M PIP-ethanol solution. The Pb adsorption capacity of fibrous grafted adsorbent treated with 5 M PIP-ethanol solution was 0.179 mmol-Pb/g-ad.

Table 1

Effect of amination conditions on Da, PIP density, C-PIP ratio and dithiocarbamate group density.

Amination condition (PIP conc. / Solvent)	Da [%]	PIP density [mmol/g-ad.]	C-PIP ratio [%]	NCS ₂ ⁻ density [mmol/g-ad.]
0.5 M PIP / H ₂ O	5.2	0.24	-	0.005
0.5 M PIP / Ethanol	51.6	1.98	94.6	0.106
0.5 M PIP / 1-Propanol	51.1	1.98	95.0	0.098
0.5 M PIP / 1-Butanol	51.1	1.96	93.3	0.131
0.5 M PIP / DMSO	57.5	2.18	88.9	0.242
0.5 M PIP / DMF	58.4	2.24	88.0	0.268
<hr/>				
0.5 M PIP / Ethanol	51.6	1.98	94.6	0.106
1.0 M PIP / Ethanol	54.9	2.12	92.1	0.167
2.0 M PIP / Ethanol	60.8	2.28	92.1	0.179
5.0 M PIP / Ethanol	72.5	2.63	86.4	0.358

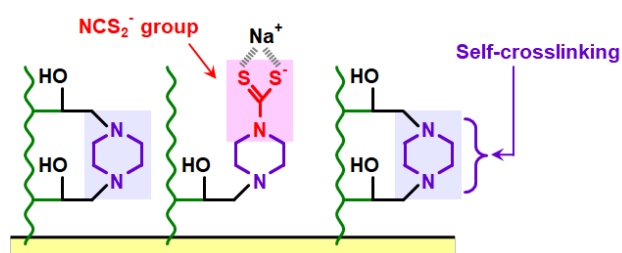


Fig. 2. Self-crosslinking of PIP in GMA-grafted chains.

1 - 30 Development of Boron Removal Technique Combined Grafted Powder Adsorbent with Spring Type Filter

H. Hoshina ^{a)}, N. Kasai ^{a)}, S. Mononobe ^{b)}, K. Kato ^{b)} and N. Seko ^{a)}

^{a)} Department of Advanced Functional Materials Research, TARRI, QST,
^{b)} Monobe Engineering

An effluent standard value of boron is established at below 10 mg/L by the Water Pollution Control Act in Japan. However, there is no way to effectively reduce the boron concentration to the effluent standard value for hot spring water including boron at a high concentration. Thus the provisional standard that relaxed the effluent standard value is applied to a particular business such as hot spring inns. Therefore, it is necessary to find out a new technique which can remove boron easily and efficiently [1].

In this study, a new boron removal technique combined grafted powder adsorbent with spring type filter capable of precision filtration was invented, and was evaluated its performance of boron removal.

The adsorbent for boron removal was synthesized by radiation induced graft polymerization using cellulose powder having high contact efficiency with water as a trunk material. The cellulose powder was irradiated with absorbed dose of 20 kGy by electron beam. After irradiation, it was contacted with deoxidized emulsion solution, which was a mix of glycidyl methacrylate (GMA), Tween 20, and purified water. The grafting of GMA was carried out at 40 °C for 1 hour. The GMA-grafted powder was chemically converted to *N*-methyl-D-glucamine (NMDG) [2]. The NMDG density of powder adsorbent was 1.9 mmol/g-adsorbent.

The evaluation of new boron removal technique was investigated by passing the 50 mg/L of boron solution through the spring type filter covered with the grafted powder adsorbent (Fig. 1). A total 4 L of boron solution was circulated at a flow rate of 1.6 L/min, and the effluent and the circulating water in a tank were collected at regular intervals. The concentration of boron in collected samples was measured by an induced coupled plasma atomic emission spectroscopy [ICP-AES, Perkin Elmer Inc., Optima 4300 DV].

The result of boron removal test was shown in Fig. 2. Boron was not detected in the effluent until the water passing time reached 5 minutes, which means that all of the boron was adsorbed when the boron solution passed through the spring type filter covered with grafted powder adsorbent. The boron concentration was less than 4 mg/L in any of effluent. In this system, the boron solution in the tank was diluted with the circulated effluent and the concentration of boron gradually decreased. The concentration of boron in the reserved tank became less than 10 mg/L, which is the effluent standard value at the water passing time of 13 minutes. By passing through for 30 minutes, it was possible to reduce the boron concentration to 1.6 mg/L corresponding to 1/30 of the

initial concentration. These results indicate that the new boron removal technique could efficiently remove boron at a high flow rate by specific pores of the powder adsorbent produced by the spring type filter.

References

- [1] H. Hoshina *et al.*, JAEA Takasaki Annu. Rep. 2006, JAEA-Review **2007-060**, 42 (2008).
- [2] H. Hoshina *et al.*, J. Ion Exchange, **21**, 153 (2010).

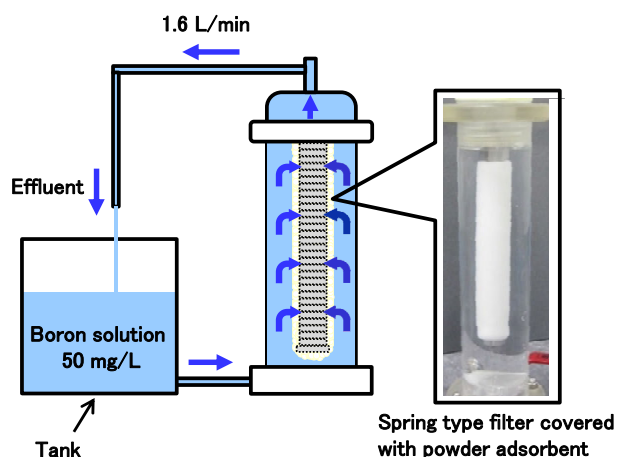


Fig. 1. The evaluation of boron removal technique combined grafted powder adsorbent with spring type filter using 50 mg/L of boron solution.

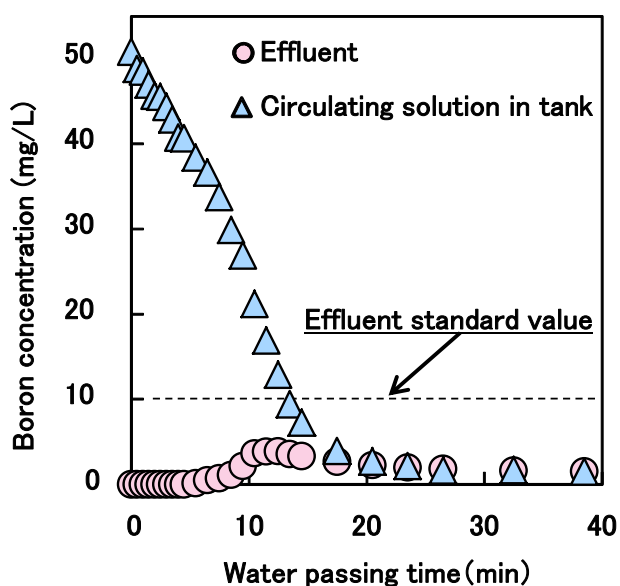


Fig. 2. The performance of the new boron removal technique.

1 - 31 Amidoxime and Ammonium Fabric Adsorbents Prepared by Radiation Grafting for Chromium Removal

J. Chen, N. Hayashi, Y. Ueki and N. Seko

Department of Advanced Functional Materials Research, TARRI, QST

Chromium are widely used in industrial processes, and the wastewater from these industries contains both Cr(III) and Cr(VI) ions. The Cr(VI) is much more toxic than Cr(III). The traditional adsorption technique that uses particles such as active carbon as the adsorbents requires additional separation process. In this work, we modified an existing nonwoven fabric by radiation grafting. Thus, the adsorbent/water separation process can be eliminated when the resulting fabric adsorbent is used for chromium removal.

For this purpose, the polyethylene coated polypropylene (PE/PP) nonwoven fabric was first electron-beam irradiated by electron accelerator. The irradiated fabric was then immersed in an oxygen-free monomer solution for grafting. An amidoxime adsorbent was synthesized by co-grafting of acrylonitrile (AN) and methacrylic acid (MAA) and subsequent amidoximation with hydroxylamine, while an ammonium fabric adsorbent was synthesized by grafting of chloromethylstyrene (CMS) and subsequent quaternization with trimethylamine. The ability of the resultant fabric adsorbents for the chromium removal was tested in the batch and column modes.

The graft polymerizations for AN/MAA and CMS were carried at 40 °C. After the grafting, the thickness and the surface area of the grafted fabric increased. The AN/MAA-grafted fabric was amidoximated in a hydroxylamine solution at 80 °C for more than 15 min, under which the cyanide groups (CN) of the graft chain reacted with the hydroxylamine, yielding the amidoxime groups, resulting in the amidoxime-chelating fabric adsorbent. On the other hand, the CMS-grafted fabric was quaternized in trimethylamine solution at 80 °C for more than 30 min, where the trimethylamine reacted with the chloromethyl groups on the graft chains, yielding the quaternary ammonium groups, resulting in the quaternary ammonium fabric adsorbent. In this work, the amidoxime adsorbent and the ammonium adsorbent with high density of functional group of 4.5 and 3.5 mmol/g, respectively, were used in the adsorption tests for the chromium removal study because they possibly have high absorption capacity and the adequate mechanical strength for actual application.

Figure 1 shows the results of chromium removal from Cr(III) and Cr(VI) solution by batch and column mode adsorption test at pH 5.0.

At pH 5.0, the Cr(VI) was in the forms of HCrO_4^- and CrO_4^{2-} , while the Cr(III) was in the forms of Cr^{3+} , $\text{Cr}(\text{OH})^{2+}$ and $\text{Cr}(\text{OH})_2^+$. As shown in Fig. 1 (a), both the Cr(III) and Cr(VI) could be removed by ammonium adsorbents, and

the Cr(III) could be also removed by the amidoxime adsorbents to a large extent.

Therefore, the ammonium adsorbent was used for the column test. However, although the Cr(III) concentration (0.1 ppm) in the inflow solution was very low, as shown in Fig. 1 (b), the Cr(III) was soon detected in the outflow solution. The Cr(III) adsorption capacity of the adsorbents was only about 0.12 mg/g. On the contrary, when the Cr(VI) solution was fed, the Cr(VI) ions could be removed up to a large outflow volume more than 600 mL, showing a high Cr(VI) adsorption capacity of about 130.65 mg/g. The high Cr(VI) adsorption capacity of the ammonium adsorbents was due to the well anion exchange between the Cr(VI) anions and the adsorbents. To remove the Cr(III) from water, similar test was performed using the amidoxime adsorbents. In this case, it was found that the amidoxime fabric adsorbent was well removed the Cr(III) up to a high amount volume of 120 mL, showing a reasonable Cr(III) adsorption capacity of 31.68 mg/g.

Furthermore, both the ammonium and amidoxime adsorbents could be easily regenerated by sodium hydroxide, where the adsorbed chromium was eluted into the solution, so that the metal ions could be recycled and the adsorbents could be reused.

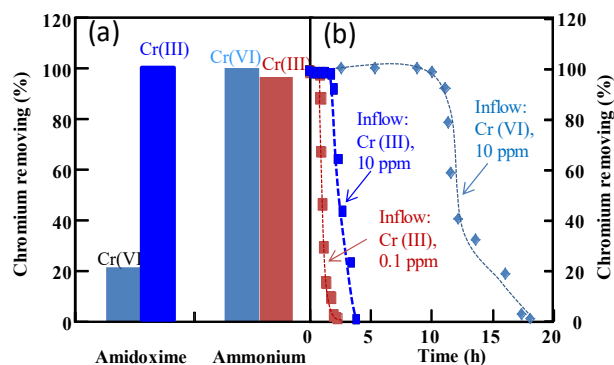


Fig. 1. Chromium removal by amidoxime and ammonium adsorbents at pH 5.0. (a) Batch mode; and (b) column mode, flow rate, 60 mL/h.

T. Makabe^{a)}, M. Oshida^{a)}, H. Sando^{a)}, N. Mizote^{a)}, Y. Ueki^{b)} and N. Seko^{b)}^{a)} Mitsuba R&D Center, Mitsuba Corporation,^{b)} Department of Advanced Functional Materials Research, TARRI, QST

The surface of silicone rubber substrate was crosslinked by electron beam irradiation using a low-energy electron beam accelerator. The surface hardness of the crosslinked silicone rubber increased with the increasing irradiation dose. As a result, the friction coefficients under dry and wet conditions were lower than those of un-crosslinked one.

我々はこれまでに放射線グラフト重合法を用いて、ゴムの表面改質に関する研究に取り組み、親水性モノマーをゴム基材表層に固定化することにより低摩擦係数を示す新規表面改質ゴムの開発に成功してきた[1]。

本研究では、ゴムの中でも耐熱性に優れているシリコンゴムの摩擦係数の低下を目的として、電子線架橋処理によるシリコンゴムの表面改質とその効果について調査した。

ゴム基材として、シリコンゴムシートを用いた。窒素雰囲気下において、シリコンゴムシートに対して低エネルギー電子加速器を用いて電子線架橋処理を行い、表面架橋型シリコンゴムを得た(加速電圧: 250 kV, 電流: 5 mA, 照射線量: 118, 235, 942 kGy)。得られた架橋型シリコンゴムの物性評価として、硬度測定、及び、摩擦係数測定(乾燥状態及び水介在状態)を行った。

Figure 1 に電子線照射線量とシリコンゴムシートの表面硬度の関係を示す。硬度測定には、デュロメーターA 硬度計を用い、ゴムシートの照射面を測定した。Figure 1 に示すようにシリコンゴムシートの表面硬度は、照射線量の増加に伴い増加した。この硬度増加は、シリコンゴムシート表層に架橋構造が新たに構築されたことを示唆し、シリコンゴムの表面改質に対しても電子線架橋処理が有効であることがわかった。

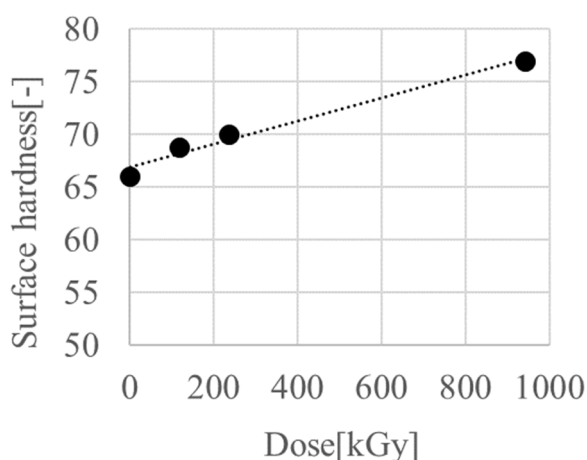


Fig. 1. Relationship between the irradiation dose and the surface hardness.

Figure 2 に電子線照射線量と表面架橋型シリコンゴムシートの摩擦係数の関係を示す。摩擦係数は、回転円盤型摩擦試験機にて、速度 1.27 m/s、荷重 20 gf で測定した。ゴムシートは、円盤ガラスに 45°で接触させ、接触面は乾燥状態、または、水介在状態とした。

乾燥状態における表面架橋型シリコンゴムシートの摩擦係数は、電子線照射により低下し、照射線量 118 kGy 以降においては一定の値となった。この摩擦係数の低下は、電子線架橋により表面が硬化し、真実接触面積が低下したことによるものと考えられる。また、水介在状態における摩擦係数も電子線照射により僅かに低下した。これは、電子線照射によりシリコンゴム表層に親水基が導入され、水に対する濡れ性が向上したためであると考えられる。以上の結果から、シリコンゴムシートへの摩擦低減手法としては、電子線架橋が有効であり、100 kGy 程度の電子線照射でもシリコンゴムシート表面の摩擦係数を低下できることがわかった。

今後は、表面架橋型シリコンゴムの水への濡れ性や摩耗特性などの表面特性を測定し、表面架橋型シリコンゴムの工業材料としての有効性を確認する。

Reference

[1] N. Mizote *et al.*, J. Appl. Polym. Sci., **123**, 2172-76 (2012).

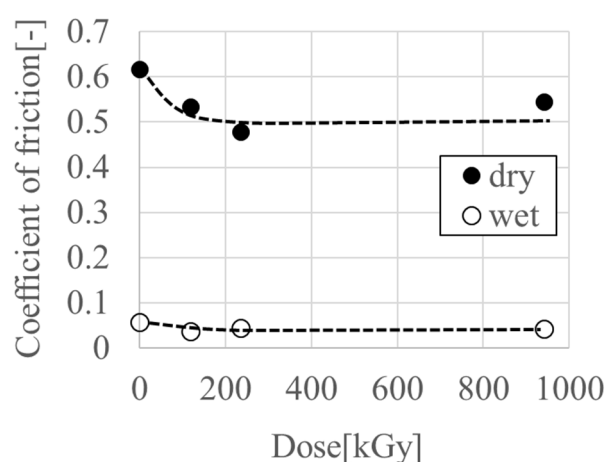


Fig. 2. Relationship between the irradiation dose and the coefficient of friction.

1 - 33 Study on Hydrogen Generation from Cement Solidified Products Loading Low-level Radioactive Liquid Wastes at Tokai Reprocessing Plant

F. Sato, R. Matsushima and Y. Ito

Waste Management Department, TRTDC, JAEA

Cement solidification of Low-level radioactive Liquid Wastes (LLWs) generated from Tokai reprocessing plant is planned in Low-level radioactive Waste Treatment Facility (LWTF). There are two kinds of LLWs, concentrated liquid waste and phosphate liquid waste. In LWTF. The concentrated liquid wastes are categorized into "sodium carbonate effluent" with low radioactivity and "slurry" with comparatively high radioactivity by radionuclide separation process and nitric acid ion decomposition process [1].

The sodium carbonate effluent is planned to solidify with BC cement, which is a mixture of 70 wt% Blast Furnace Slag and 30 wt% Ordinary Portland Cement. And the phosphate liquid waste is also planned to solidify with a commercial product of JGC Co., 'Super Cement'. It is an alkali activated slag cement with various minor additives.

It is known that $G(H_2)$ value of a cement solidified product containing radionuclides varies with cement and effluent composition. In this study, as in last year, we investigated hydrogen production from cement solidified samples containing these effluents [2].

Figure 1 shows an example of the irradiation samples. The samples were prepared by mixing simulated liquid waste and these cements using the composition planned in LWTF [3], then filled into a container ($\phi 13 \text{ mm} \times 50 \text{ mm H}$) at 20°C for 3 weeks or more. After curing, these samples were put into a vial container (50 mL) one by one and were sealed with rubber septum. These samples were irradiated by Co-60 gamma-rays at about 2.5 kGy/h for 20 hours (shown in Fig. 2). After the gamma irradiation, concentration of hydrogen gas generated in the vial was measured by gas chromatography.

As a result of the irradiation test, the followings were clarified:

When the sodium carbonate effluent is solidified with the BC cement, it became clear that the $G(H_2)$ value of the solidified product is about 0.02 to 0.15 n/100 eV. It is known that G value of sodium carbonate solution rises as carbonate concentration increases [4]. But in this study, it was found that the G value of the cement solidified product of the sodium carbonate effluent decreased as the salt packing ratio increases (10 - 30 wt%) regardless of the mixing ratio of water and cement (W/C: 0.45-0.85). It is considered that the carbonate salt in the product suppresses H_2 gas generation by gamma-rays.

Assuming the waste liquid with insufficient in the nitric acid ion decomposition, effluent of sodium carbonate (70-90%) with sodium nitrate (5-15%) and sodium nitrite (5-15%) was solidified with the BC cement and irradiated. $G(H_2)$ value of the solidified product containing nitrate and

nitrite is smaller than that of pure carbonate (0.02 to 0.06 n/100 eV). It is considered that nitrate and nitrite salt have a higher suppression effect of H_2 gas generation from solidified products than carbonate salt.

When the phosphate liquid waste is solidified with the Super Cement after insolubilizing of the phosphate salt using calcium hydroxide, it became clear that the $G(H_2)$ value of the solidified product is about 0.06 to 0.17 n/100 eV and increase as W/C ratio increase (0.95-2.15) regardless salt packing ratio. It is considered that main components of this waste such as calcium phosphate have no suppressing effect on H_2 gas generation, and as the water contained in the solidified product increases, the amount of water decomposed into H_2 gas also increased.

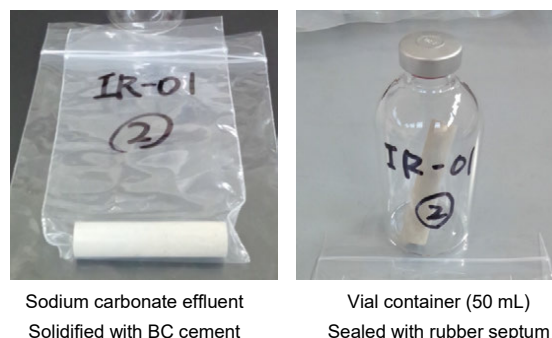


Fig. 1. Example of irradiation samples.

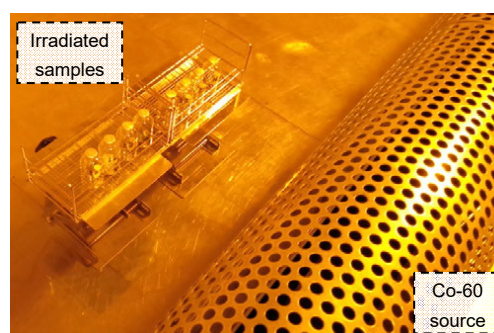


Fig. 2. Status of sample irradiation by Co-60.

References

- [1] A. Sugaya *et al.*, WM2011 Conf. 11078 (2011).
- [2] Y. Ito *et al.*, Proc. 2017 Fall Meet. AESJ, IH01 (2017).
- [3] R. Matsushima *et al.*, Proc. 2017 Fall Meet. AESJ, IH02 (2017).
- [4] R. Nagaiishi *et al.*, Proc. 2016 Spring Meet. AESJ, 2I21 (2016).

1 - 34 Effects of Displacement Damage, Helium and Hydrogen on Electrical Properties of Silicon Carbide

T. Nozawa ^{a)}, M. Ando ^{a)}, T. Taguchi ^{b)} and H. Tanigawa ^{a)}

^{a)} Department of Fusion Reactor Materials Research, RFI, QST,

^{b)} Tokai Quantum Beam Science Center, TARRI, QST

Silicon carbide (SiC) is a promising candidate material of liquid metal breeding blanket for a fusion DEMO reactor due to perceived merits such as superior therm-mechanical properties, chemical inertness, irradiation stability, etc. Of many properties of concern, electrical insulation as a key function to apply SiC to functional structure of flow channel inserts for the dual cool blanket system [1] has recently been more focused. One of the notable features of electrical properties of SiC by irradiation in-situ was radiation-induced electrical conductivity (RIC), which is generally induced by electric excitation, and radiation-induced electrical degradation (RIED)-like behavior [2-5]. It was found in gamma-ray and low fluence 14 MeV neutron irradiation experiments that RIC was dependent of irradiation fluence, however this should be masked by the dominant thermal effect at high temperatures. It was also noted that morphological change of the irradiated surface of SiC might affect the RIED-like behavior. However, knowledge about the synergetic effect of displacement damage at higher dose on RIC and RIED was missing. Furthermore transmutation effect needs to be identified for fusion application. This study therefore aims to evaluate the effects of displacement damage with He/H co-irradiation on electrical properties by single/dual/triple ion beam simulated irradiation experiments.

High-purity and high-crystallinity SiC strip fabricated by the chemical vapor deposition (CVD) was irradiated by single, dual and triple ion beams. Self-ion of 6.0 MeV Si²⁺ was applied to provide displacement damage inside SiC and the damage level was approximately 10 and 30 dpa. In cases of dual and triple ion beam irradiation, 1.0 MeV He⁺ and 340 keV H⁺ ions were simultaneously irradiated to evaluate the effect of transmutation He/H atoms induced by fusion neutron irradiation. For all tests, irradiation temperature was ranged in 600 - 1000 °C. Surface and volume electrical resistivity was measured before and after irradiation at room temperature by the AC impedance method. For that purpose, two probe guard ring method was applied to evaluate leak current at the specimen. Thin film Pt electrodes were deposited on a disk specimen with a diameter of 3 mm and a thickness of 50 μm. Details of the specimen configuration and the electric circuit for the measurement were described in [6].

Figure 1 summarizes the effect of irradiation dose and temperature on surface and volume resistivity of CVD SiC. Marked reduction of the surface resistivity was obvious by irradiation at comparably higher irradiation temperatures (> 900 °C), while no electrical degradation was identified at the operation temperature range, i.e., 600 - 700 °C. Importantly, limited data can suggest no significant dose

dependence to < 30 dpa. By considering data scatter for non-irradiated specimen case, it is speculated that the impact of He/H co-irradiation was minor. By contrast, no significant degradation of volume resistivity was expected. This is not surprising since the damage area induced by ion irradiation was limited to the very tiny surface and major part of SiC was physically unchanged by irradiation.

References

- [1] P. Norajitra *et al.*, Fusion Eng. Des., **69**, 669-73 (2003).
- [2] T. Tanaka *et al.*, J. Plasma Fusion Res., **9**, 282-87 (2010).
- [3] B. Tsuchiya *et al.*, Fusion Eng. Des., **86**, 2487-90 (2011).
- [4] B. Tsuchiya *et al.*, J. Nucl. Mater., **455**, 645-48 (2014).
- [5] B. Tsuchiya *et al.*, J. Plasma Fusion Res., **90**, 47-51 (2014).
- [6] N. Okubo *et al.*, Nucl. Instrum. Meth. Phys. Res. B, **314**, 208-10 (2013).

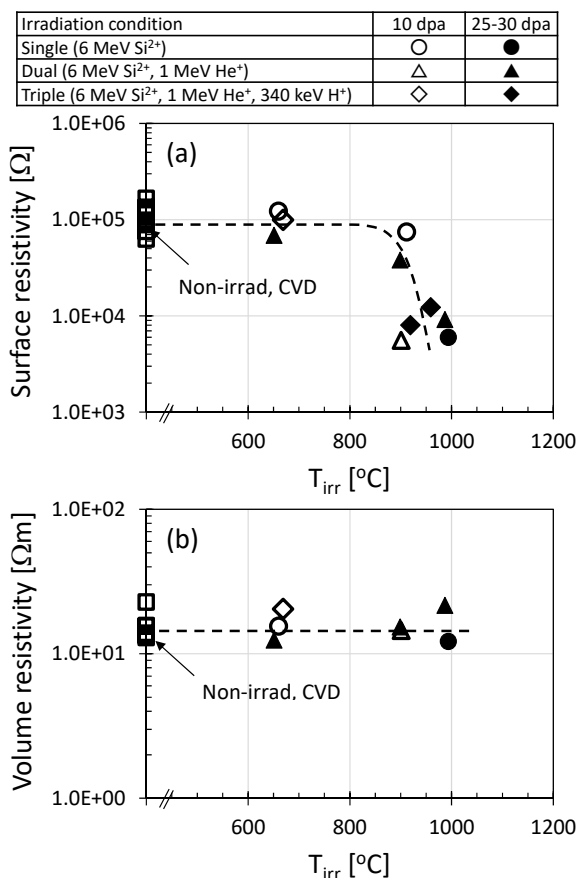


Fig. 1. Dose dependence of (a) surface and (b) volume resistivity of CVD SiC.

1 - 35 Effects of Self-Ion Irradiation on Rhenium Distribution and Microstructure in Tungsten-Rhenium Alloy

T. Miyazawa^{a)}, T. Hwang^{a)}, S. Nogami^{a)}, A. Hasegawa^{a)} and H. Tanigawa^{b)}

^{a)} Graduate School of Engineering, Tohoku University,

^{b)} Department of Fusion Reactor Materials Research, RFI, QST

Tungsten (W) is the primary candidate materials as a diverter or a plasma facing material (PFM) in fusion devices, primarily due to its high melting temperature, good thermal conductivity and low sputtering rate [1].

For diverter, recrystallization and radiation induced embrittlement, the effects of transmuted atoms of W itself are key issues. Rhenium (Re) is known elements that transmute from W by neutron capture reaction. Process optimization is in progress and more radiation-tolerant W alloys are being made. However, information of its irradiation effects is quite required, because recent neutron irradiation results suggest that behavior of W after irradiation is complicated and that radiation induced defects depends on neutron/ion irradiation sources [2]. At the first step, examining especially only the effect of displacement was desired.

W-3%Re alloy after removal of residual stress was used in this experiment. Ion irradiation was performed at TIARA facility of QST. Eighteen MeV W⁶⁺ ions were irradiated to induce displacement damages (single-ion irradiation). Irradiation condition is 1 dpa and 800 °C.

The specimens for atom probe tomography (APT) were prepared from the irradiated specimens. The needle-like specimens for APT were fabricated by using focused-ion beam (FIB) systems (Helios NanoLab 600i or Quanta 200 3D, FEI) at IMR, Tohoku University, Oarai. APT was conducted with 3D-LEAP 4000X HR, CAMECA, which has

a reflection lens that prolongs the time of flight. Since the flight time can be matched with the kinetic energy of each ion, the total detection efficiency is 42%. The temperature of the sample stage was 55 K and analysis was conducted with the laser assist mode. The laser pulse energy and repetition rate were 100 pJ and 100 kHz, respectively. To confirm the segregation of Re, isoconcentration and segregation analyses were performed. The concentration (in mass percent) of Re and Os were obtained from the number of atoms based on the AP data.

Figure 1 shows APT images of W-3%Re alloy before and after irradiation. Re atoms were distributed homogeneously in the specimen before and after irradiation. Figure 2 shows bright field TEM micrograph of W-3%Re. Dislocation loops and voids were observed but no precipitates were observed. While Re cluster was formed in neutron-irradiated pure W which had 0.5% of transmuted Re [4]. These different results are considered to be caused by the difference of irradiation rate (dpa/s) between self-ion irradiation and neutron irradiation. Further study is required in order to clarify the mechanism.

References

- [1] H. Bolt *et al.*, J. Nucl. Mater. **329-33**, 66 (2004).
- [2] M. Fukuda *et al.*, J. Nucl. Mater. **442**, S273 (2013).
- [3] T. Hwang *et al.*, J. Nucl. Mater. **207**, 78 (2018).
- [4] T. Hwang *et al.*, Nucl. Mater. Energy **9**, 430 (2016).

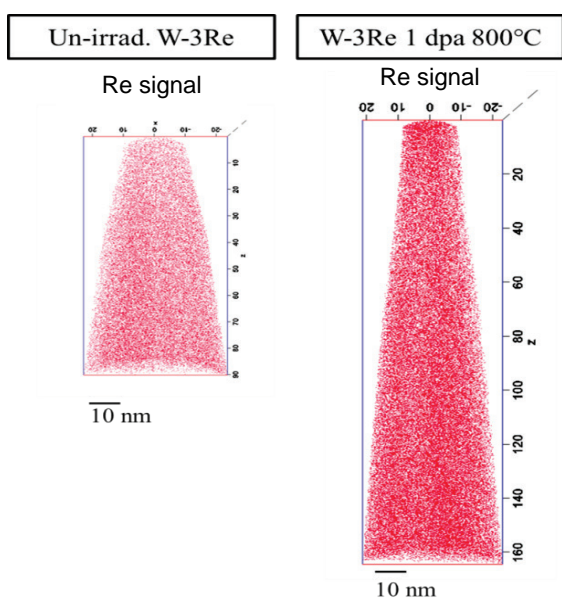


Fig. 1. APT images of W-3%Re before and after irradiation [3].

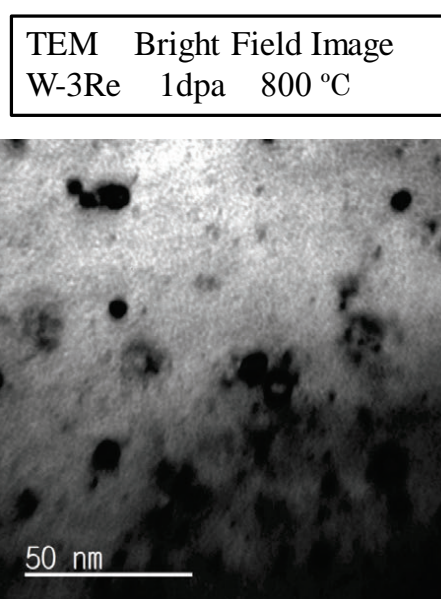


Fig. 2. TEM microstructure of W-3%Re irradiated to 1 dpa at 800 °C [4].

1 - 36 Hydrogen Gas Measurements of Phosphate Cement Irradiated During Heat Treatment

K. Irisawa ^{a)}, I. Kudo ^{b)}, T. Taniguchi ^{a)}, M. Namiki ^{c)}, T. Osugi ^{a)} and O. Nakazawa ^{a)}

^{a)} Radioactive Waste Processing and Disposal Research Department, NBTC, JAEA,

^{b)} ADVAN ENG. Co., Ltd.,

^{c)} Inspection Development Company Ltd.

From the viewpoint of waste management, prevention of radiolytic H₂ gas is favorable as much as possible, in order to reduce the risks of fire and explosion during long-term storage and disposal. An alternative cementation technique minimized water content by heat treatment, therefore, is being developed [1, 2]. In the cementation technique, phosphate cement hardening *via* acid-base reaction is used instead of conventional cement hardening *via* hydration, because removal of water doesn't prevent solidification of the phosphate cement. The feasibility of the cementation technique by heat treatment has been demonstrated in the laboratory-scale experiment [1, 2]. The optimal temperature was approximately 90 °C under non-irradiation condition. The actual wastes are radioactive, and it is still unclear whether the produced phosphate cement is beneficial for the prevention of radiolytic H₂ gas or not. Hence, in this study, radiolytic H₂ gas generated from the phosphate cement was directly measured. A temperature-control cell, in which internal temperature was at 90 °C, was developed [3] and improved in this study. Radiolytic H₂ gas and water vapor were recovered outside irradiation chamber in the food irradiation facility.

Figure 1 shows the improved temperature-control cell and gas circulation line. The synthesized phosphate cement [1] was placed in the improved cell. The phosphate cement was dehydrated at 90 °C and irradiated by 40 Gy/h of γ-ray for 7 days (total 6.7 kGy). The atmosphere gas was circulated, and water vapor in the cell was recovered. The H₂ gas generated from the phosphate cement was measured by gas chromatography (GC-2014, Shimadzu Ltd.). The G_γ(H₂) (molecules/100 eV) is calculated as follows

$$G_{\gamma}(H_2) = \frac{M_{H_2} \times N_A \times 1.6 \times 10^{-17}}{R \times w}$$

where M_{H2} is H₂ amount (mol), N_A is Avogadro constant (molecules/mol), R is absorbed dose (J/g) and w is the sample weight (g). Figure 2 shows the G_γ(H₂) of the phosphate cement and evaporated water (wt%) from the phosphate cement. The evaporated water (wt%) increased with time, and 50 wt% of water content remained in the phosphate cement. The water content agreed with that under non-irradiation condition [1]. The G_γ(H₂) of the phosphate cement decreased with time. The G_γ(H₂) became negligibly small on 7 days. The results indicated that the cementation technique by heat treatment could reduce radiolytic H₂ gas. It was found that the G_γ(H₂) of the phosphate cement by heat treatment was smaller than that of the conventional cement with 0.35 of water to cement ratio (0.06±0.01 molecules/100 eV [4]).

Consequently, in this study, the radiolytic H₂ gas measurement of phosphate cement during heat treatment was successful by using the improved cell. It was found that the cementation technique could reduce radiolytic H₂ gas, and led to reduce the risks of fire and explosion.

Acknowledgment

This work was funded by the Japan Science and Technology Agency, Japan (research grant No. 273604).

References

- [1] K. Irisawa *et al.*, Proc. ICAPP 2017, No. 17618, [Fukui & Kyoto, Japan] (2017/04).
- [2] I. Garcia-Lodeiro *et al.*, Cem. Concr. Res., **109**, 243-53 (2018).
- [3] K. Irisawa *et al.*, QST Takasaki Annu. Rep. 2016, **QST-M-8**, 63 (2018).
- [4] M. Takahashi and T. Fujita, CRIEPI Rep., L11020 (2013).

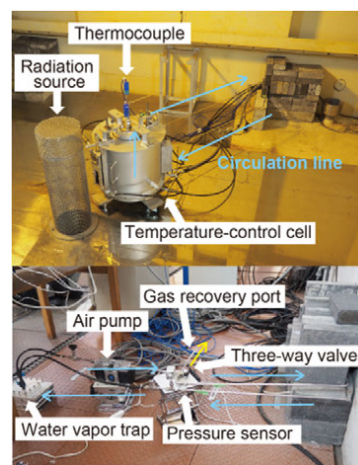


Fig. 1. The improved temperature-control cell and gas circulation line.

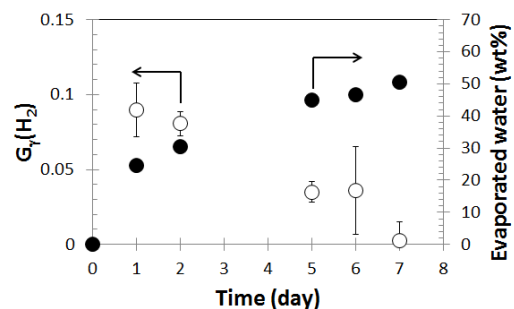


Fig. 2. The G_γ(H₂) value of the phosphate cement dehydrated at 90 °C under γ ray irradiation (40 Gy/h) in 7 days and evaporated water (wt%) from the phosphate cement.

1 - 37 Effect of Damage Depth Profile on Hydrogen Isotope Dynamics in W

Y. Oya^{a)}, K. Azuma^{a)}, A. Togari^{a)}, Q. Zhou^{b)}, T. Miyazawa^{c)} and T. Chikada^{a)}

^{a)} Graduate School of Science, Shizuoka University,

^{b)} Faculty of Science, Shizuoka University,

^{c)} Division of Technical Service, Shizuoka University

Introduction

Tungsten (W) is the candidates for the plasma facing materials in future D-T fusion reactors like ITER due to its lower sputtering yield and higher melting point. Under working condition, W will be exposed to 14 MeV neutron produced by D-T fusion reaction, and energetic particles including hydrogen isotope, helium ion and ion exchange particles. The damages introduced by charge-exchanged particles are concentrated near the surface region, while that induced by 14 MeV neutrons are extended throughout the bulk [1]. For the development of the effective fuel recycling and the safety operation, it is important to understand how the damage distribution in W contributes on hydrogen isotope retention enhancement. Therefore, this study focuses on the effect of damage distribution controlled by heavy ion irradiation with various energy on D retention behavior in W.

Experimental

A disk-type polycrystalline W (6 mm ϕ \times 0.5 mm t) purchased from A.L.M.T. Corp. Ltd were used. To remove impurities and damages introduced during the polishing processes, the samples were heat-treated at 1173 K under ultrahigh vacuum ($< 10^{-6}$ Pa). Combination of 0.8 MeV Fe⁺ ion and 6 MeV Fe²⁺ ion was irradiated into the samples at room temperature with the damage levels of 0.03-0.3 dpa (displacement per atom) by 3 MV tandem accelerator in Takasaki Ion Accelerators for Advanced Radiation Application (TIARA) at National Institutes for Quantum and Radiological Science and Technology (QST). Thereafter, 1.0 keV D₂⁺ was implanted with the ion fluence of 1.0×10^{22} D⁺ m⁻², and the D desorption behaviors were evaluated by thermal desorption spectroscopy (TDS) measurements. In addition, the Transmission Electron Microscope (TEM, JEM 2000EX, JASCO Inc.) observations at Kyushu University were conducted.

Result & Discussion

Figure 1 shows the TEM images of dislocation loop for Fe ion irradiation implanted W. It was clear that the density of dislocation loops (black dots in Fig.1) near the surface for 0.8 MeV Fe ion implanted W was higher than that for the 6 MeV Fe ion damaged-W, and which was similar to 0.8 MeV-6 MeV Fe ion irradiated W. From the results, it was found that defects by 0.8 MeV Fe ion irradiation are dominant on the outermost surface of the composite irradiation W sample.

Figure 2 shows the D₂ TDS spectra for Fe ion damaged-W samples with various damage distributions. The D₂ TDS spectra were assumed to consist of four major

D desorption stages located at 400 K, 550 K, 650 K and 850 K. Based on our previous studies, the D desorption stages at Peaks 1 to 4 were corresponded to the desorption of D adsorbed on the sample surface or trapped by dislocation loops, vacancies, vacancy clusters and voids, respectively. In the combination of 0.8 MeV and 6 MeV Fe ion irradiation sample, the total D retentions in the samples were decreased by the increasing the damage concentration introduced near the surface region by 0.8 MeV Fe ions. It is considered that the amount of D retained by the surface adsorption or dislocation loop is saturated since it is not changed by the irradiation damage amount. In addition, as the defect density by 0.8 MeV Fe ion irradiation increased, the amount of D retention in vacancy cluster and voids decreased. From this result, it was considered that the D retention in the sample was suppressed by the defect near the surface.

Acknowledgment

The Fe ion implantation was done in the facility sharing system of National Institutes for Quantum and Radiological Science and Technology.

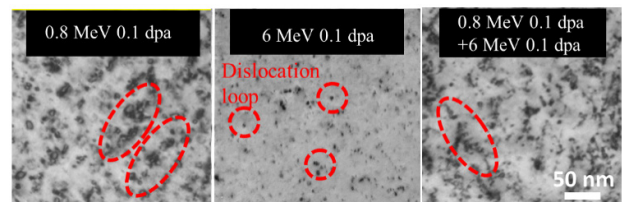


Fig. 1. TEM image (dislocation loops) for Fe ion irradiated W (observed at R.T).

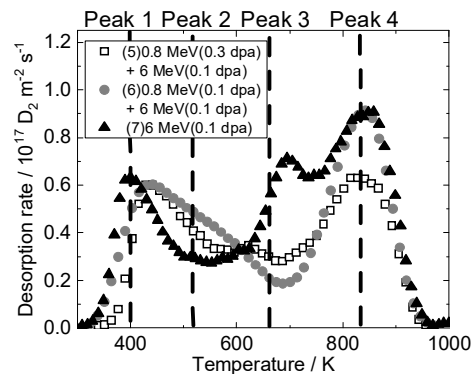


Fig. 2. D₂ TDS spectra for Fe ion irradiated W samples.

Reference

[1] H. Fujita *et al.*, Phys. Scripta, **T167**, 014068 (2016).

1 - 38 Experimental Results of Swelling Behavior of FMS Steels Under ADS Irradiation Conditions

N. Okubo and N. Ishikawa

Fuels and Materials Engineering Division, NSEC, JAEA

In ADS (Accerlater Driven System), the target beam window will be heavily irradiated under severe conditions, where displacement damage, high concentration of He and H atom accumulations will occur simultaneously by high energy spallation neutrons. Degradation of mechanical properties and size change of the components after irradiation should be suppressed within a range permissible for the system design. High fluence neutron irradiation experiments are practically difficult due to the long time to finalize PIEs (Post Irradiation Examinations). Especially, nuclear transmutation gas concentration in present experimental reactor irradiation is not sufficient for estimating He and H impacts over several 10 dpa. Simultaneous ion irradiation experiments are powerful techniques for simulating the irradiation fields of Fusion and ADS systems, especially, He and H effect. Experimental results are important for the modeling of material irradiation effects like a swelling. In this study, the swelling behaviors of ferritic/martensitic steels (FMS) in the case of simultaneous irradiation of self ions as displacement damage, helium and/or hydrogen at high temperature were addressed.

Simultaneous ion irradiation experiments have been conducted in TIARA (Takasaki Ion Accelerators for Advanced Radiation Application) facility of QST. Irradiations using 10 MeV-Fe³⁺, 1.05 MeV-He⁺ and 0.38 MeV-H⁺ ions were done for T91 specimens at 500 °C. The specimen size was 6 mm wide, 3 mm high and 0.75 mm thick. After cutting this size, the irradiation surface was mechanically polished to a mirror finish and then electro-polished. The irradiation area was 2 by 2 mm². Experimental conditions were determined by using the SRIM code [1]. The displacement damage value from the self-ion irradiation was also determined from a depth of 1 μm, though the projectile range (R_p) which was around 2 μm for 10 MeV-Fe³⁺ in the T91 composition. The helium and hydrogen generation rates were about 15 and 113 appm/dpa at 1 μm depth, respectively, which corresponded with the irradiation conditions of ADS. Depth distributions of He and H were individually broadened by 800 nm thick aluminum energy degraders, which rotated between +15° and -15° relative to the He and H beam directions. The labels of Single, Dual and Triple refer to only Fe, Fe + He and Fe + He + H co-irradiation, respectively. The swelling behavior was estimated from microstructures taken by using cross sectional TEM (Transmission Electron Microscopy) observations. The specimen for TEM observation was obtained from a 1 μm depth using an FIB (Focused Ion Beam). The sample surface damage layer induced by the 30 keV Ga FIB ions was removed using

flash polishing for 0.01 sec at 20 V in 20% H₂SO₄ and 80% Methanol below 4 °C.

The swelling behavior of ferritic martensitic steel, F82H was reported by Wakai, *et al.* [2] from the view point of fusion irradiation conditions. Here, swelling is reported for the case of ADS irradiation conditions. Figure 1 shows cross sectional TEM images of Single, Dual and Triple irradiated specimens at 500 °C between the irradiated surface and about 1.8 μm depth.

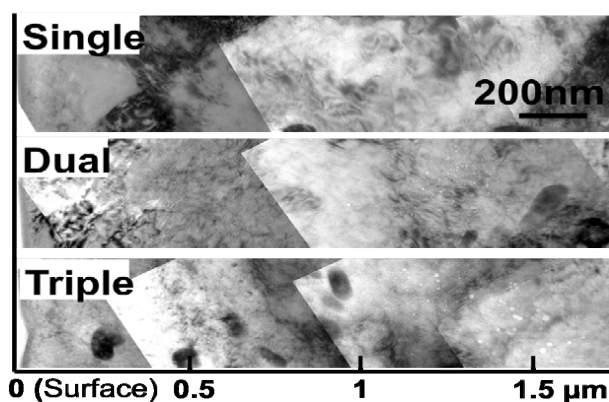


Fig. 1. Cross sectional TEM images of single, dual and triple irradiations, shown from irradiation surface to 1.75 μm depth, which is around damage peak depth of 10.5 MeV Fe³⁺ ions.

In the case of single ion irradiation, no cavities were observed at a displacement damage of 40 dpa (even at 100 dpa, which was at nuclear energy deposition peak, near R_p depth). In the cases of dual and triple irradiation, however, many cavities appeared and caused swelling around a depth from 900 nm to 1.6 μm. The mean cavity size for triple irradiation, however, obviously increases around 1.5 μm depth as compared with dual irradiation.

From analysis of TEM images, the swelling was 3% at 1.2 μm for dual irradiation. In the case of triple irradiation, the swelling was lower than that of dual irradiation at same depth. At a depth of 1.5 μm, however, the swelling was distinctly increased for triple irradiation to over 6% around 1.5 μm depth.

References

- [1] J. F. Ziegler "SRIM-2003". Nucl. Instrum. Meth. Phys. Res. B. **219-20**, 1027-36 (2004).
- [2] E. Wakai *et al.*, J. Nucl. Mater. **318**, 267-73 (2003).

M. Saito, Y. Noguchi, M. Kazawa, K. Nakata and N. Takeda

Department of ITER Project, NFI, QST

Introduction

The ITER blanket remote handling system (BRHS) will replace the blanket first walls (FWs) and shield blocks in the vacuum vessel (VV) after plasma shutdown [1]. This two-year maintenance campaign will replace all 440 FWs in an environment having a dose rate of 250 Gy/h. The ITER requirement is 1 MGy of radiation hardness for all BRHS parts, which corresponds to 180 days, however, a radiation hardness of 5 MGy, which corresponds to 2 years, was set as the target value to increase availability of the system. In this study, the material of the multicore cable sheath and the electroless Ni plating were investigated.

Results

Four compounds were prepared as shown in Table 1. Magnesium hydride and carbonized material layer are flame retardants, and the improved RH-2.5M is an improved compound from the RH-2.5M used in J-PARC. The sheets were irradiated with Co-60 gamma rays at 3000 Gy/h at room temperature and at atmospheric pressure. Figure 1 shows the elongation ratio after irradiation. The elongation of No. 2 and No. 3 decreased rapidly and was lower than 50% (the specification value) at 2 MGy. Degradation caused by radiation was reduced in No.4. Even after 5 MGy of irradiation, an elongation value of around 50% was obtained. Oxygen index was also measured by the flammability tests and increased when the flame-retardant treatment was added. Samples of No.2-No.4 met the oxygen index of 30 (the specification value) and no decrease in flame retardancy was observed with irradiation. Consequently, sample No. 4 was selected as the sheath material of the multicore cable.

The electroless Ni plating samples (surface roughness Ra is 1.6) were irradiated with Co-60 gamma rays at 1000 Gy/h in an environment using the saturated salt method (SSM) where relative humidity was kept at 20% using potassium acetate ($\text{CH}_3\text{CO}_2\text{K}$) as specified in JIS B 7920. The appearance of electroless Ni plating samples after irradiation testing is shown in Table 2. No surface degradation was observable with the naked eye on the samples irradiated up to 1 MGy under 20% humidity, but degradation was observed on the sample surfaces after 2 MGy of irradiation. In the quantitative results from SEM-EDX analysis as shown in Table 3, the percentage of oxygen was 2.55% for 0.7 MGy and 1.10% for 1 MGy, an increase of oxygen was not clearly observed in gamma ray irradiation at 20% humidity. However, the detected amount of oxygen increased markedly in the sample irradiated up to 2 MGy. The amount of N also increased, which was not observed in other samples.

Conclusion

The radiation hardness of ethylene propylene diene mischpolymer (EPDM) rubber after being treated with flame retardants was measured. Marked decreases in

elongation ratio were observed by the addition of flame retardants. Treating compounds with the stabilizer RH-2.5M limited the decrease in radiation hardness, which meets the specification of "total elongation of 50% after 5 MGy of irradiation". The electroless Ni plating did not degrade at 1 MGy under 20% humidity and can therefore be used to prevent corrosion of the BRHS in the VV if the total dose of the components is not greater than 1 MGy. However, surface degradation was observed on the samples irradiated up to 2 MGy under 20% humidity. The results of the surface analysis show that the amount of oxygen, hydroxide, and nitrate increase. The electroless Ni plating is not recommended for application in the components whose total dose is greater than 1 MGy where the in-VV humidity is 20% or higher.

Table 1. EPDM compounds.

	Base EPDM	Magnesium hydride	Carbonized material layer	Improved RH-2.5M
No.1	x			
No.2	x	x		
No.3	x	x	x	
No.4	x	x		x

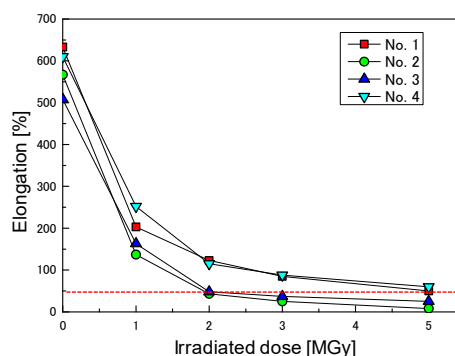


Fig. 1. Elongation ratio and oxygen indexes after irradiation.

Table 2. Surface of nickel plating samples after irradiation.

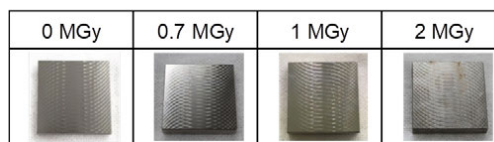


Table 3. Quantitative results from SEM-EDX analysis.

Dose (MGy)	C	N	O	P	Fe	Ni	Total
0.7	7.08	Not detected	2.55	10.78	0.70	78.89	100
1	4.50	Not detected	1.10	11.50	0.70	82.20	100
2	5.5	4.3	12.6	8.2	0.6	68.8	100

Reference

[1] A. Tesini *et al.*, Fusion Eng. Des. **83**, 810-16 (2008).

1 - 40 Development of Radiation Resistant Monitoring System in Light Water Reactor

T. Takeuchi^{a)}, N. Otsuka^{a)}, H. Nakano^{a)}, T. Iida^{b)}, O. Ozawa^{b)},
T. Shibagaki^{b)}, H. Komanome^{b)} and K. Tsuchiya^{a)}

^{a)} Department of JMTR, WMDC, JAEA,
^{b)} Ikegami Tsushinki Co., Ltd.

During the Fukushima Daiichi Nuclear disaster, almost all instruments for monitoring of the plant situation were broken down. In response to these provisions, development of a monitoring system available in Nuclear Power Plants during severe accidents have been addressed.

As problems of development of the system, radiation resistance of the image sensor used in the monitoring camera and that of power supply integrated circuits used in the visible light wireless transmission system were extracted [1, 2]. In this study, we conducted gamma irradiation tests on the parts of the developing system in order to investigate the irradiation degradation behavior of them and to improve their radiation resistance.

In order to investigate the influence of absorbed gamma dose on the image sensor, the dynamic ranges of acquired image brightness with respect to photo gate (PG) drive voltage at different absorbed dose were compared. On the other hand, the output voltage of the power supply IC commonly used in the camera and the visible light wireless transmission system with absorbed dose was measured. The gamma irradiation tests were carried out under the facility sharing system of the National Institutes for Quantum and Radiological Science and Technology.

Figure 1 shows a schematic diagram of the irradiation test systems in the γ -ray irradiation room. For the image sensor, a simple camera system connected to the PG drive voltage adjustment unit was installed in the irradiation room, and the output image was observed with a monitor. For the power supply IC, a constant voltage power supply for generating the input voltage was connected. The output voltage and IC surface temperature data were collected with a data logger in order to check the occurrence of short circuit due to dielectric breakdown.

Figure 2 shows the Image comparison with different absorbed dose and PG voltage. The dynamic range is the maximum at PG=-1.6 V before irradiation, PG=-0.2 V at cumulative dose 30.8 kGy, and PG=0 V at 151.1 kGy. It is found that the optimum PG driving voltage is affected by absorbed dose. The result indicates the possibility of a camera system with substantial radiation resistance improved by changing the PG drive voltage

Figure 3 shows the power IC output voltage and the surface temperature with absorbed dose. The output voltage sharply decreases around the absorbed dose of 10 to 15 kGy, returns to the immediate posture, turns to increase on the contrary near 20 kGy, thereafter, there is almost no influence by the cumulative dose. Also, there was no sharp rise in temperature by the occurrence of a

short circuit. The result shows the possibility of obtaining a stable output under the radiation environment by using pre-irradiated IC.

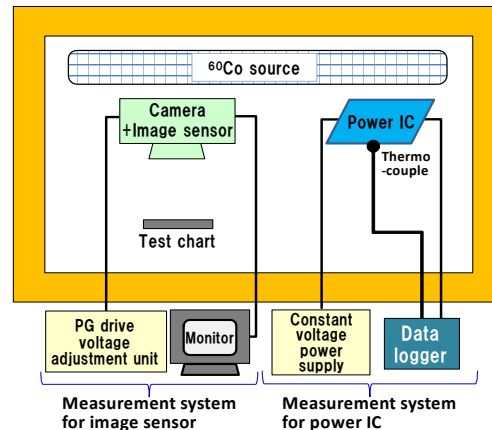


Fig. 1. Schematic diagram of the irradiation test systems in the γ -ray irradiation room.

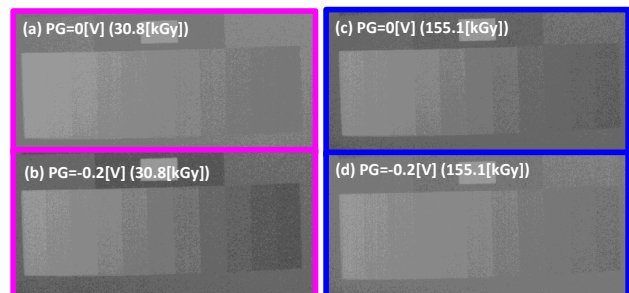


Fig. 2. Image comparison with absorbed dose at 30.8 kGy and PG voltage at (a) 0 V, (b) -0.2 V, and at 155.1 kGy and at (c) 0 V, (d) -0.2 V.

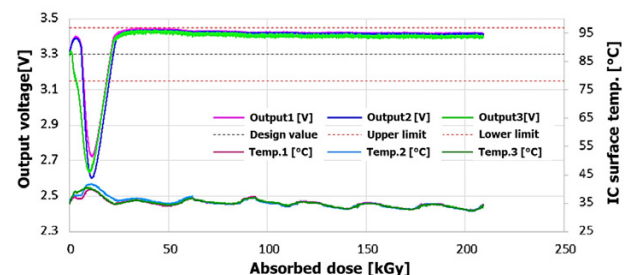


Fig. 3. Power IC output voltage and surface temperature with absorbed dose.

References

- [1] T. Takeuchi *et al.*, Proc. D&RS 2016, 263 (2016).
- [2] N. Otsuka *et al.*, Proc. D&RS 2016, 277 (2016).

Development of the Predicting Method for the Long Term Corrosion Under Irradiation

T. Sato, Y. Ishijima and F. Ueno

Fuels and Materials Engineering Division, NSEC, JAEA

In the Fukushima Daiichi Nuclear Power Station (1F), the seawater was injected into the reactor cores in the Unit 1, Unit 2 and Unit 3. The high dose of radiation has been continuing in the primary containment vessel (PCV) because of the molten fuel debris and the fission products. It is well known that H_2 , H_2O_2 , short life radicals, etc., are produced by water radiolysis [1]. The produced species are chemically active. In addition, it is considered that corrosion of the PCV is influenced by gamma-rays irradiation. To perform a suitable countermeasures against the corrosion of PCV, the corrosion environment and corrosion mechanism of carbon steel (CS), which was used as material of the PCV, under irradiation should be understood. In this study, in situ Oxidation-Reduction potential (ORP) measurements, which is one of major indexes to evaluate corrosion environments, were performed in diluted artificial seawater (ASW) under irradiation condition. Also, in situ measurements of the electrochemical impedance spectrometry (EIS) of CS were performed.

A schematic of the installed test cell is shown in Fig. 1 [2]. A plate-type Pt electrode was installed in the test cell as the working electrode (WE) to measure the ORP. And a flag-type CS specimen was installed as the WE to measure the EIS of CS, preventing the use of spot welding. The reference electrode was installed in the test cell to measure the ORP and EIS. An Hg/Hg₂Cl₂/0.1 M KCl with a double junction reference electrode was used.

The time variations of the measured ORPs of the diluted ASW is shown in Fig. 2. The increase in ORP after the irradiation was stopped and reached a constant value after about 4 hours as shown in the enlarged view of Fig. 2. The lifetimes of short-lived radicals are generally less than 1 s. The change in the ORP should be more rapid when the ORP is influenced by radicals. The slow variation of the ORP after stopping and restarting the irradiation indicated that the short-lived radicals did not have a large contribution to the ORP of the water and the corrosive conditions under direct irradiation. It was confirmed that the change in the ORP was determined by H₂ generated by the water radiolysis calculations.

The measured EIS is shown in Fig. 3. The higher frequency half-circles may be due to the oxide film resistance (R_f). R_f is determined by the composition and the thickness of the oxide formed at the surface of the CS. The difference in the R_f values obtained in the impedance measurements may be attribute to the difference in the thickness of the oxide films. This result indicated that oxide film growth may be enhanced by a higher dose rate of direct irradiation. The lower frequency half-circles may be due to the polarization resistance (R_p). The reciprocal of the R_p is generally proportional to the corrosion rate of CS. A smaller

R_p indicates a higher corrosion rate. The R_p of CS under 4000 Gy/h irradiation was smaller than that under 200 Gy/h irradiation. This result indicated that a higher dose rate of irradiation may enhance the corrosion of CS.

References

- [1] S. L. Caër, *Water*, 235-53 (2011).
- [2] T. Sato *et al.*, Proc. NPC2016, [Brighton, United Kingdom], (2016/10).

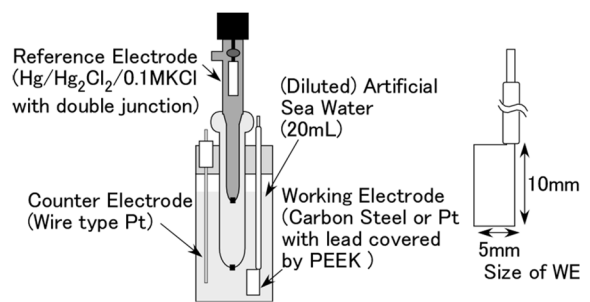


Fig. 1. Schematic of the electrochemical test cell.

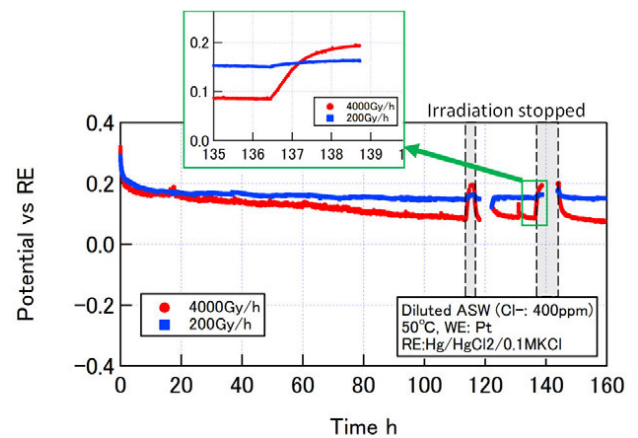


Fig. 2. Measured time dependent ORP in DASW.

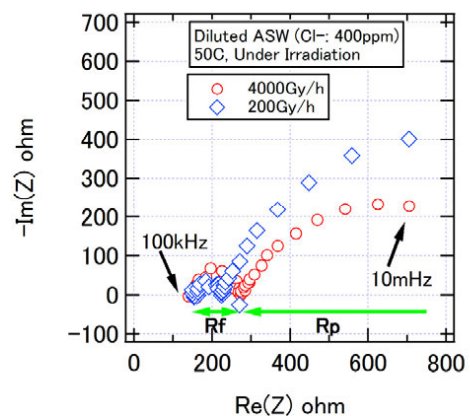


Fig. 3. Nyquist plots of measured EIS of CS.

1 - 42 Synergetic Effect of He, H and Displacement Damages on the Void Swelling Behavior of F82H

D. Hamaguchi, M. Ando and H. Tanigawa

Department of Fusion Reactor Materials Research, RFI, QST

Reduced activation ferritic/martensitic steels (RAFM) such as F82H and Eurofer97 are the candidates for the blanket structural materials in DEMO fusion reactor [1]. But one of the difficulties to estimate the effects of irradiation is a lack of irradiation facility that can produce an irradiation conditions close to fusion reactor environment. Therefore, we need to collect information on particular events that are expected to be specific under fusion neutron irradiations using existing irradiation facilities, such as fission reactors and ion-irradiation facilities. The unique feature of the microscopic events in steels by fusion neutron irradiation is an introduction of displacement damages with high He and H transmutation gas productions. One of the experimental methods to understand the effects of He and H gas on the development of irradiation damages is complex ion-beam irradiation experiments. Therefore, in this study, multiple ion irradiation experiments were carried out using TIARA complex irradiation facility to examine the synergetic effect of He and H on displacement damage development of F82H, especially on the swelling behavior.

The material used in this study was F82H IEA-heat, which is a standard version of F82H produced in Japanese fusion program. The basic chemical composition is Fe-8Cr-2W-0.2V-0.04Ta-0.1C. For the heat treatment, IEA-heat was normalized at 1040 °C for 0.63 h followed by a tempering at 750 °C for 1 h. The irradiations were carried out with 10.5 MeV Fe³⁺ ions plus 0.38 MeV H⁺ and/or 1.05 MeV He⁺ ions. To acquire irradiation dose and temperature dependence data on swelling behavior of F82H, irradiations were performed from 20 to 80 dpa with 20 dpa step at temperatures ranged from 400 to 500 °C. In following figures, triple-beam refers to He, H and Fe multiple ion-beam and dual-beam refers to He and Fe multiple ion-beam irradiation. In multiple ion-beam irradiation, He and H implantation rate were fixed to be 10 and 40 appm/dpa, respectively.

Figure 1 shows the cavity microstructure of F82H IEA irradiated up to 20 dpa at the temperatures from 400 to 500 °C. The cavities observed here could be distinguished into two types; rather large sized voids and tiny He bubbles. The high-density of cavity formation was already seen at the temperature of 400 °C for the case of multiple ion-beam irradiations, where no visible cavity forms for Fe ion single-beam irradiation case. At 400 °C, only tiny He bubbles with sizes around a few nm were observed, but, when irradiation temperature increased to 430 °C, size and density of the cavities rapidly increased and swelling peaked at around 470 °C. In addition, some effect of H co-implantation with He was seen; the density of the cavities for the case of triple-beam irradiations tend to become higher compared to dual-beam irradiated cases. The effect of H co-implantation

becomes clearer when irradiation dose increases. Figure 2 shows the cavity microstructures and cavity size distribution for the specimens irradiated up to 60 dpa at 470 °C. It is clearly seen here that average size of the cavity becomes larger and bi-modal size distribution becomes wider for the case of triple-beam irradiation compared to dual-beam irradiated case. The effect of the production of H with He under displacement damages was not positively discussed so far because it was believed to be less effective since the diffusion of H is rapid at higher temperatures in Fe-based system. But these results indicate the effect of H cannot be ignored in fusion neutron irradiation environment especially when irradiation dose becomes higher.

For swelling peak evaluation, the series of the irradiation study so far suggests the swelling of F82H peaks at around 470 °C and linearly increases with dose (see Fig. 3). But to confirm the swelling peak temperature, we need more irradiation data for precise evaluation.

Reference

[1] H. Tanigawa *et al.*, J. Nucl. Mater. **417**, 9-15 (2011).

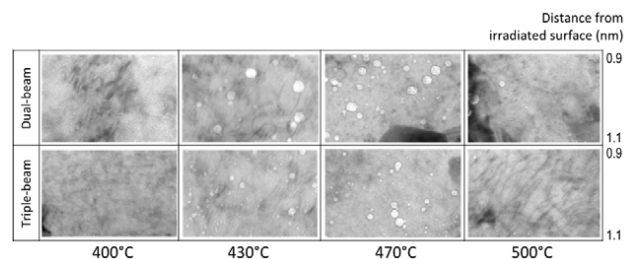


Fig. 1. Cavity microstructure of F82H-IEA irradiated up to 20 dpa with multiple ion-beam.

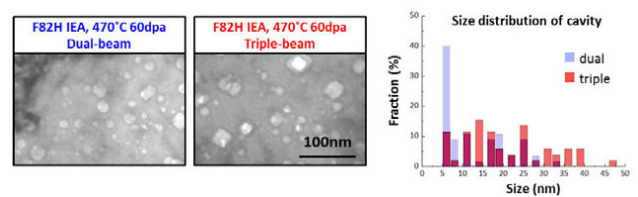


Fig. 2. Cavity microstructure and size distribution of F82H-IEA irradiated to 60 dpa at 470 °C with multiple ion-beam.

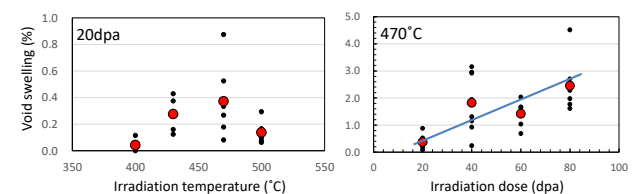


Fig. 3. Temperature and dose dependence of the void swelling for F82H-IEA.

Change in Hardness of FeCuMn Alloy by Energetic Ion Irradiation

A. Iwase^{a)}, T. Sumie^{a)}, F. Hori^{a)}, Y. Saitoh^{b)}, S. Semboshi^{c)} and Y. Okamoto^{d)}

^{a)} Department of Materials Science, Osaka Prefecture University,

^{b)} Department of Advanced Radiation Technology, TARRI, QST,

^{c)} Institute of Materials Research, Tohoku University,

^{d)} Energy and Environment Materials Science Division, MSRC, JAEA

Hardening and embrittlement by the irradiation become a serious problem for reactor pressure vessel steels which have been exposed to high flux energetic neutrons for a long period. In the previous study [1], we have used Fe-0.6wt.%Cu binary alloy samples as a model alloy for the reactor pressure vessel alloys, and have shown that the precipitation of Cu atoms induced by heavy ion irradiation causes the hardening of the samples. In the present report, we will show the result of the heavy ion irradiation on the hardness and atomic arrangements of Fe-Cu-Mn ternary alloy through the Vickers hardness and the EXAFS spectrum measurements.

We prepared samples of homogeneous Fe-0.6wt.%Cu-1.5wt.%Mn alloy by the thermal treatment at 800 °C. Such samples were irradiated with 16 MeV Au ions at 523 K. The Au ion fluences were $3 \times 10^{14}/\text{cm}^2$ and $3 \times 10^{15}/\text{cm}^2$. The change in hardness by the irradiation was measured by a Vickers hardness tester. To observe the local structures near Cu atoms and Mn atoms in Fe matrix, the EXAFS spectra were obtained around the Cu-K and Mn-K absorption edges by using the KEK photon factory.

Figure 1 shows the Au ion fluence dependence of the Vickers hardness. The hardness increases with increasing the ion fluence. Figures 2 and 3 show the EXAFS-FT spectrum around Cu-K edge and Mn-K edge, respectively, for the sample irradiated with the fluence of $3 \times 10^{15}/\text{cm}^2$. In each figure, the spectrum for the irradiated surface and that for the unirradiated surface are compared. The shapes of the EXAFS spectra for the unirradiated surface show the

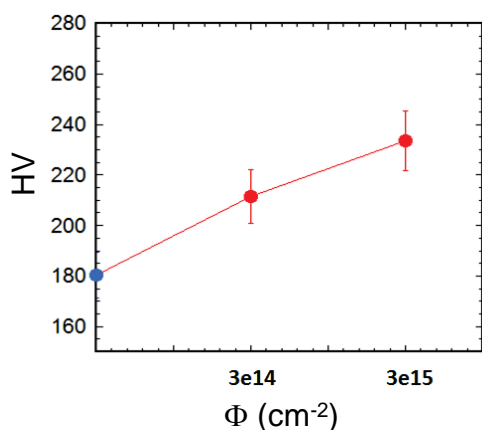


Fig. 1. Hardness as a function of 16 MeV Au ion fluence. Blue symbol: for unirradiated surface, Red symbols: for irradiated surfaces.

BCC structure. The result means that Mn and Cu atoms occupy the regular BCC site of Fe matrix. The decrease in the spectrum intensity by the irradiation is more remarkable for the Cu-K edge than for Mn-K edge.

The present result implies that Cu atoms, Mn atoms and/or the vacancies occupy the neighbor sites of the Cu atoms by the irradiation. Such change in atomic arrangements causes the increase in hardness of the samples.

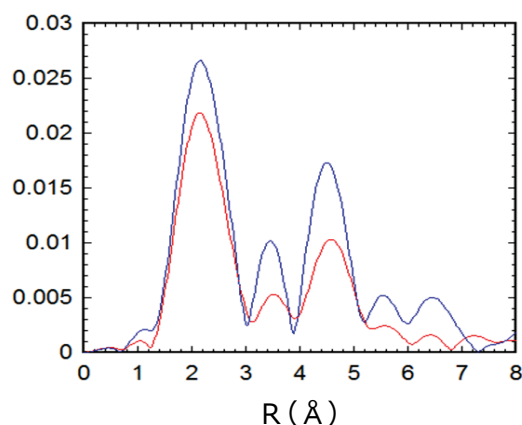


Fig. 2. EXAFS-FT spectra for Cu-K absorption edge. Blue line: for unirradiated surface. Red line: for irradiated surface.

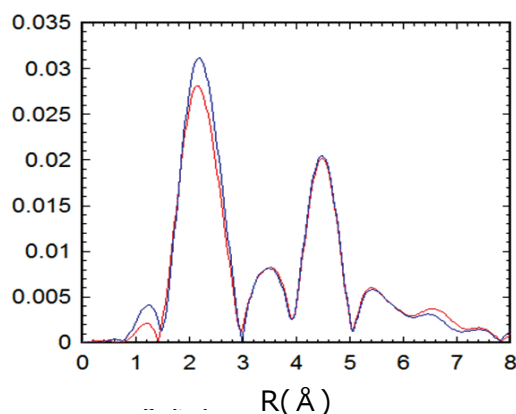


Fig. 3. EXAFS-FT spectra for Mn-K absorption edge. Blue line: for unirradiated surface. Red line: for irradiated surface.

Reference

[1] A. Iwase *et al.*, QST Takasaki Annu. Rep. 2016, **QST-M-8**, 55 (2018).

Study on Synthesis of Pd Catalyst from Eluent After Separation Process for High-level Liquid Waste Based on Radiation-induced Reaction

T. Ito ^{a)}, S.-Y. Kim ^{a)} and R. Nagaishi ^{b)}

^{a)} Department of Quantum Science and Energy Engineering, Tohoku University,

^{b)} Waste Management Division, CLADS, JAEA

Separation and recovery of platinum group metals (PGMs), namely Ru, Rh and Pd, contained in high-level liquid waste (HLLW) emitted from PUREX reprocessing are one of the important problems in nuclear chemistry. Large amounts of PGMs are produced in spent fuels and they are known to make vitrification of the waste difficult [1]. In addition, the recovered PGMs can be considered as a favorable semi-domestic resource [2]. For the purpose, we have studied an extraction chromatography method using solid state adsorbents, and then the developed adsorbents indicated excellent separation behaviors of Pd(II) from the simulated HLLW [3, 4]. However, the practical use of recovered Pd from the real HLLW is considered to be difficult because the radioactive ^{107}Pd (half-life = 6.5×10^6 years, $\beta_{\text{max}} = 34$ keV) is contained in the recovered Pd. Therefore, the use of weakly radioactive Pd as catalysts in a location isolated from civilians could be considered as one of the most appropriate ways.

To develop the synthesis method of an oxide-supported Pd catalyst using the recovered Pd, radiation-induced reactions were examined. From the literature [5], Pd(II) ions in HCl solution could be reduced by radiation irradiation, and the reaction was enhanced by addition of solid oxide.

In this study, we focused on the influence of HNO_3 as solvent and thiourea (TU) which was usually used for eluent of Pd(II). The 1 mM ($M = \text{mol/L}$) of Pd(II) contained HNO_3 solution and HNO_3 -TU mixed solution were packed in glass vials together with SiO_2 , Al_2O_3 and TiO_2 particles, respectively. These samples were statically irradiated at room temperature by γ -rays emitted from ^{60}Co in the ^{60}Co Irradiation Facilities, QST Takasaki. Dosimetry was conducted by a $\text{K}_2\text{Cr}_2\text{O}_7$ solution and cellulose triacetate film. The concentrations of Pd(II) ($C_{\text{Pd(II)}}$) in the liquid phase before and after the irradiation were analyzed by ICP-AES.

To first investigate the influence of HNO_3 , the solution containing 0.1 and 1 M HNO_3 were irradiated with the γ -rays. In the case of 1 M, the reduction of Pd(II) was not observed regardless of the presence or absence of the oxides. NO_3^- ion was considered to react as an electron scavenger. On the other hand, in the case of 0.1 M, black fine particles were observed after the irradiation and the oxides slightly turned black. The growth of black particles further continued after the irradiation. Figure 1 shows the $C_{\text{Pd(II)}}$ ratio (after / before) at equilibrium state. The $C_{\text{Pd(II)}}$ in the irradiated solutions after filtration with a $0.20 \mu\text{m}$ filter were decreased with increasing absorbed dose.

To investigate the influence of TU, the 0.1 M HNO_3 solution was irradiated with 1 mM Pd(II) and 0.1 M TU. Immediately after the irradiation, the black particle and the

color change of oxides were not observed visually. However, milky white and orange precipitates were gradually generated in the irradiated solutions after the filtration (Fig. 2), and the $C_{\text{Pd(II)}}$ in the liquid phase decreased. In addition, the decrease of $C_{\text{Pd(II)}}$ increased with increasing absorbed dose (Fig. 3), and these phenomena were not observed without the irradiation. Therefore, it is assumed that the radiolysis products of TU formed milky white precipitate and orange precipitate with Pd(II). The precipitates will be analyzed as a next study.

From the above results, it is found that additional plans are required to synthesize a Pd catalyst using a Pd(II) solution containing TU by γ -irradiation.

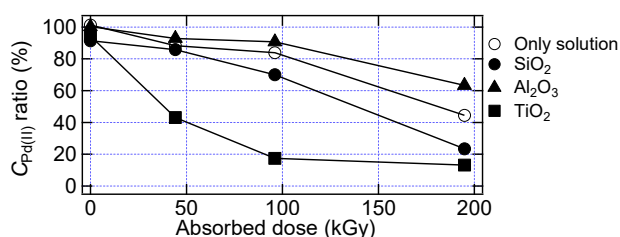


Fig. 1. Pd(II) concentration ratio after the γ -irradiation without TU (equilibrium, $[\text{Pd(II)}]_{\text{ini}}$: 1 mM, $[\text{HNO}_3]$: 0.1 M).



Fig. 2. Milky white and orange precipitate ($[\text{Pd(II)}]_{\text{ini}}$: 1 mM, $[\text{HNO}_3]$: 0.1 M, $[\text{TU}]$: 0.1 M, 195 kGy, temp.: r.t.).

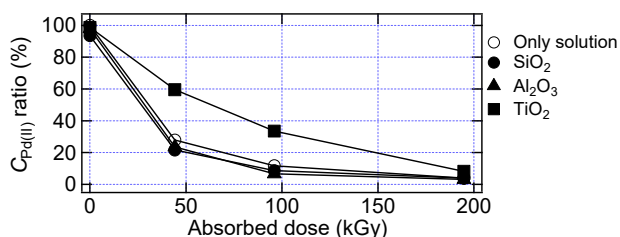


Fig. 3. Pd(II) concentration ratio after the γ -irradiation with TU (equilibrium, $[\text{Pd(II)}]_{\text{ini}}$: 1 mM, $[\text{HNO}_3]$: 0.1 M, $[\text{TU}]$: 0.1 M).

References

- [1] Ch. Krause, B. Luchscheiter, *J. Mater. Res.*, **6**, 2535 (1991).
- [2] Y. Kondo *et al.*, JAERI-M 91-147 (1991).
- [3] T. Ito *et al.*, *Sep. Sci. Technol.*, **48**, 2616 (2013).
- [4] Y. Xu *et al.*, *J. Radioanal. Nucl. Chem.*, **297**, 41 (2013).
- [5] R. Nagaishi, Japan Patent 5424297 B2 (2014.2.26).

1 - 45 Characterization of Adsorbent for U and Pu Recovery from Degraded PUREX Solvent

Y. Arai^{a)}, S. Ohno^{a)}, S. Watanabe^{a)}, A. Shibata^{a)}, K. Nomura^{a)}, M. Koka^{b)} and T. Satoh^{c)}

^{a)} Department of Reprocessing Technology Development, NBTC, JAEA,

^{b)} Beam Operation Co., Ltd.,

^{c)} Department of Advanced Radiation Technology, TARRI, QST

Extraction of U and Pu from dissolved solution of spent nuclear fuel is a main process of the reprocessing, and PUREX is an established solvent extraction procedure for that purpose. The process utilizes 30 wt% tributyl phosphate (TBP) diluted in n-dodecane (nDD) as the solvent, and U and Pu recover through extraction of them from acidic solution and back extraction into less acidic solution. During the process, degradation of TBP by radiolysis and hydrolysis give mainly dibutyl phosphate (DBP). The DBP forms strong complexes with Pu^{4+} , UO_2^{2+} and other metal ions at low acidic environment, therefore stripping of U and Pu into the low acidic solution cannot be expected. Long term storage of radioactive elements in the organic solvent should be avoided due to safety reasons, and an appropriate procedure for stripping U and Pu from the degraded solvent is required to be developed.

We have been trying to recover U and Pu from the degraded solvent by adsorption reaction, and adsorption performance of several types of resins were systematically evaluated using Zr as a simulant of Pu. Zr in simulated degraded PUREX solvent containing x wt% DBP+(30-x) wt% TBP in nDD ($0.9 < x < 9$) was successfully adsorbed onto chelating resin with iminodiacetic acid group. However, adsorption capacity is still not enough, and the iminodiacetic acid group seems not to efficiently work for the adsorption. In order to clarify the distribution state of adsorbed element, the cross section of the adsorbent is measured using micro-PIXE. The chemical state retained in the adsorbent is estimated by investigating the structure of the around Zr using EXAFS.

In this study, micro-PIXE analysis on cross section of the adsorbent and Zr-K Extended X-ray Absorption Fine Structure analysis on the adsorbent were carried out after loading Zr on them from the simulated degraded solvent to reveal the adsorption mechanism of cations from the organic phase, where analyses on adsorbent adsorbing Zr from nitric acid solution were also carried out for comparison.

Micro-PIXE analysis was carried out at light-ion microbeam line connected to a 3-MV single-ended accelerator in TIARA of QST, and Zr-K EXAFS measurements were carried out at BL27B beamline of PF, KEK, Japan.

Figure 1 shows mappings of X-ray intensities at specific energies obtained for cross sections of adsorbents loading Zr from the nitric acid solution and the simulated degraded solvent, where energy ranges of (a) and (b) correspond to 2000-2100 and 15600-15800 eV, respectively. Those

ranges were selected to involve $K\alpha$ of P ($E=2013$ eV) and Zr ($E=15700$ eV) and $L\alpha$ of Zr ($E=2040$ eV). The resin adsorbed Zr from the nitric acid solution should not contain P, therefore both mappings of (a) and (b) show Zr distributions on the cross section. However, P in the simulated degraded solvent apparently accompanied with Zr, and Zr complexes with TBP or DBP are possible to be adsorbed directly onto the resin. Zr-K edge EXAFS also suggests different adsorption mechanisms between these two systems as shown in Fig. 2. Quantitative analysis of EXAFS is currently performed to reveal adsorption reaction from the simulated degraded solvent.

Acknowledgment

The EXAFS measurements were carried out under the proposal of 2016G557 of the PF, KEK.

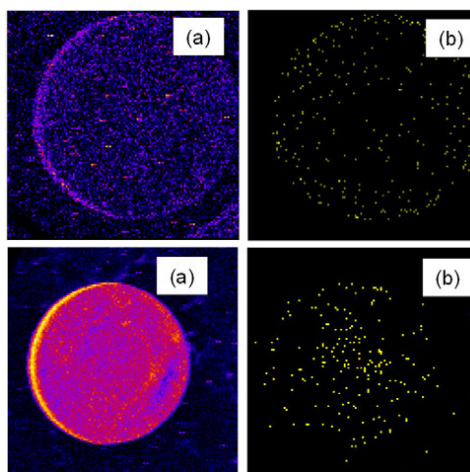


Fig. 1. Mappings of X-ray intensities at specific energies obtained for adsorbents loading Zr from the nitric acid solution (up) and the simulated degraded PUREX solvent (bottom). (a) 2000-2100 eV, (b) 15600-15800 eV.

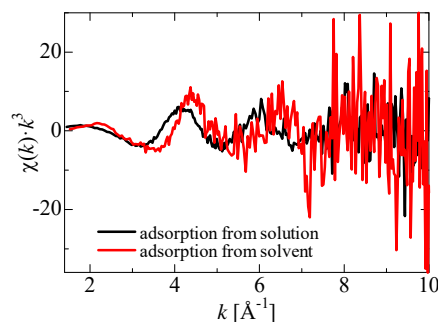


Fig. 2. EXAFS oscillation obtained for chelating resin adsorbing Zr from nitric acid solution and simulated degraded PUREX solvent.

Gamma-ray Irradiation Durability of CMPO Adsorbent for MA(III) Recovery

Y. Miyazaki ^{a)}, S. Watanabe ^{a)}, H. Kofuji ^{a)}, M. Koka ^{b)} and T. Satoh ^{c)}

^{a)} Fuel Cycle Design Department, Sector of Fast Reactor and Advanced Reactor
Research and Development, JAEA,

^{b)} Beam Operation Co., Ltd.,

^{c)} Department of Advanced Radiation Technology, TARRI, QST

Japan Atomic Energy Agency (JAEA) has been conducting the extraction chromatography technology, which is one of the promising methods for partitioning of trivalent minor actinides (MA(III): Am and Cm) from spent nuclear fuel [1]. In order to progress the implementation, not only the column performance but also its safety operation has to be guaranteed because 50wt% of the adsorbent is organic component. In fact, an extractant impregnated in the styrene-divinylbenzene copolymer that coats a porous silica particle (referred as SiO₂-P) forms complexes with radioactive elements during the column separation, which leads to degradation of the adsorbent by irradiation.

Alpha-ray irradiation degradation of CMPO (Fig. 1) impregnated adsorbent was quantitatively evaluated through He²⁺ ion beam irradiation and following systematic analyses [2]. However, influence of gamma-ray was shown to be more significant for degradation in the respect of adsorption performance [3]. In this study, amount of CMPO extractant remaining on the adsorbent after gamma ray irradiation was quantitatively evaluated and chemical form of degradation products caused by radiolysis were investigated.

Gamma-ray irradiation experiments were carried out at the irradiation room No. 1 of Co-60 Gamma-ray Irradiation Facility. Three g of CMPO/SiO₂-P adsorbent immersed in 30 mL of 3 M HNO₃ solution was sealed in a glass vial, and gamma ray was irradiated with 6 kGy/h up to 2 MGy. The irradiated adsorbents were separated from the solution and washed with 3 M HNO₃ solution to remove water-soluble degradation products. Organic compounds remaining on the adsorbents were extracted into dichloromethane by ultrasonic irrigation. Amount of CMPO in the organic compounds and chemical forms of the degradation products were determined by GC and GC/MS analyses, respectively.

About 42% of impregnated CMPO was remained on the adsorbent after irradiation. Distribution coefficient of Nd onto 2 MGy gamma ray irradiated CMPO/SiO₂-P adsorbent

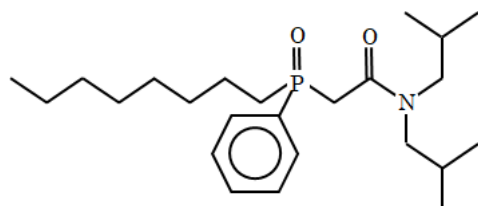


Fig. 1. CMPO.

was about a half of the initial value. About 10% of Nd might be extracted by degradation product of CMPO.

Degradation products evaluated by GC/MS analysis are shown in Table 1. A trivalent cation is extracted by 2-3 CMPO molecules through coordination of two O atoms in the molecules around the cation. Therefore, the product of ID=A is possible to extract trivalent cations with similar manner with CMPO. As well as adsorption, elution behavior of radioactive elements from the degradation product is necessary to investigate to avoid accumulation of them inside the packed column. He²⁺ ion beam irradiation on CMPO/SiO₂-P resulted in poor elution performance of Am³⁺, and the products of ID=A and B were also found after the He²⁺ ion beam irradiation. Therefore, investigation in behavior of those products must be one of tasks to predict durability and safety of the column during repeated operation.

Table 1

Structures of the degradation products of CMPO.

ID	Structure
A	
B	
C	

References

- [1] E. P. Horwitz *et al.*, *Anal. Chim. Acta*, **310**, 63 (1995).
- [2] S. Watanabe *et al.*, *QST Takasaki Annu. Rep. 2015 QST-M-2*, 85 (2017).
- [3] S. Watanabe *et al.*, *Proc. 12th IEMPT* (2012/09).

1 - 47 Synthetic Reference Sample by Electron Irradiation for IR Measurement of Carbon Concentration in Silicon Crystal

N. Inoue ^{a, b)}, S. Okuda ^{b)} and S. Kawamata ^{b)}

^{a)} Graduate School of Engineering, Tokyo University of Agriculture and Technology,
^{b)} Radiation Research Center, Osaka Prefecture University

Silicon power devices, including those for hybrid cars, are the most important use of silicon crystal now. For the silicon power devices carbon concentration ($[C]$) is the most important requirement to the Si wafers [1]. We established the measurement of 10^{14} atoms/cm³ difference between the sample and reference in 2005 [2]. However, there was always some carbon in the reference samples, and the total concentration could not be obtained. We solved this "reference problem" by "the defect engineering" [3]: Substitutional carbon C_s , natural abundance and its infrared absorption at 605 cm^{-1} is used for $[C]$ determination, is changed by the electron irradiation to the interstitial carbon C_i . About 8/10 or more of C_s can be converted to C_i which does not contribute to the above absorption. We have already shown the CZ silicon case in 2007 [3]. Recently FZ silicon has been applied to the power devices. Here, we show the FZ reference fabrication.

Silicon crystal suppliers provided the samples and worked with us to fabricate the synthetic reference. Several chips side by side were finished to 2 mm thick double side mirror polished samples. Electron irradiation was done at Takasaki Advanced Radiation Research Institute. The acceleration energy was 2 MeV, enough for penetration of 2 mm thick samples and the current was 5 mA. The electron dose was from 3×10^{14} to 5×10^{17} /cm². The samples in the chamber were filled with Ar gas flow and mounted on the water cooled stage to keep the temperature well below 200 °C. Infrared absorption measurement was done before and after irradiation at room temperature with 2 cm^{-1} wavenumber resolution. The measurement and noise reduction (spectrum processing) procedures were fully described in Ref. [4] and were informed to most leading Si crystal vendors in the world.

It is important to clarify the electron dose dependence of the removal of $[C_s]$, but there have been no such analyses. Figure 1 shows an example of the tentative result of the electron dose (F) dependence of loss of absorbance A (initial 0.002, $[C_s] = 2 \times 10^{15}$ atoms/cm³). The loss was observed clearly for a dose above 3×10^{15} /cm² and increased with the dose semi-logarithmically. The removal ratio approached 0.8. Thus, we may prepare about 1/5 $[C_s]$ sample from samples with any $[C_s]$. This dose dependence was confirmed for initial $[C_s]$ down to slightly lower than 1×10^{14} /cm³ [5]. The lowest $[C_s]$ realized was about 1×10^{13} /cm³.

Some crystal vendors perform the IR measurement of $[C_s]$ down to 1×10^{14} /cm³ using the synthetic reference already, much lower than the detection limit of SEMI standard 5×10^{14} /cm³ [6], (2×10^{15} /cm³ is claimed [7]).

IR measurement is the indirect method so that the conversion coefficient (calibration constant) from the absorption coefficient to $[C_s]$ is necessary, as we determined previously [7]. It, however, depends on the machine, "calibration problem and machine problem [4]." A block gauge with various $[C_s]$ [5] is also fabricated and used as the standard samples. We have constructed the measurement network instead of the conventional measurement standard system.

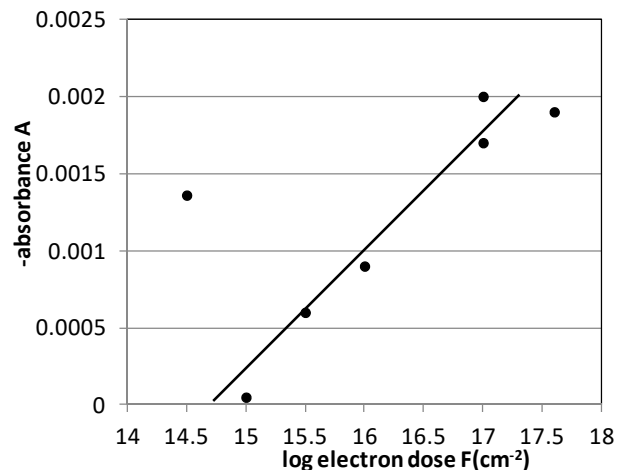


Fig. 1. An example of dependence of loss of absorbance A on the electron dose F .

References

- [1] T. Sugiyama *et al.*, Proc. 17th Symp. Power Semicond. Devices & ICs, 243 (2004).
- [2] N. Inoue *et al.*, Solid State Phenomena, **108-09**, 621 (2005).
- [3] N. Inoue *et al.*, Proc. Forum Sci. & Tech. Si Mater., JSPS, 217, [Niigata, Japan] (2007).
- [4] N. Inoue, Phys. Status Solidi C, 1-6 (2016). DOI 10.1002/pssc.201600068.
- [5] N. Inoue *et al.*, to be published in Proc. High Purity Semicond. (Electrochem. Soc. 2018).
- [6] ASTM F1391-1104, "The Annual Book of ASTM Standards", Vol. 10.05 (Amer. Soc. Testing & Mater., 2003), SEMI MF1391-1104.
- [7] H. Kiuchi *et al.*, DRIPXVII Abstr. 4A-02 (2017).
- [8] N. Inoue *et al.*, Emerging Semicond. Tech., STP 960, 365 (ASTM, 1987).

Part II

2. Life Science

2-01	Validation of Ion Species and Beam Size Availability in Collimating Ion Microbeam System of TIARA	78
	T. Funayama and M. Suzuki	
2-02	Reduction of Clonogenicity and Inhibition of 5-bromo-2'-deoxyuridine Incorporation in Glioblastoma Cells After Gamma-ray and Carbon-ion Irradiation	79
	Y. Yokota, Y. Morishita and T. Funayama	
2-03	Bystander Cellular Effects Induced in Normal Human Fibroblasts by 190 MeV $^{12}\text{C}^{6+}$ and 220 MeV $^{20}\text{Ne}^{8+}$ Ions	80
	M. Suzuki, T. Funayama, M. Suzuki and Y. Kobayashi	
2-04	LET and Ion Species Dependence of Oxidative Damage in DNA Sheet Generated Along Ion Beam Track	81
	A. Ito, A. Furuhashi, F. Ouchi, S. Yoshida, R. Hirayama, Y. Furusawa, Y. Yokota and T. Funayama	
2-05	Cell Cycle Arrest and Reentry in <i>Bombyx</i> Embryo at Cleavage Stage After Heavy Ion Irradiation	82
	R. Isoyama, Y. Umeda, Y. Souma, T. Funayama, Y. Yokota, M. Suzuki, T. Sakashita, Y. Kobayashi and K. Shirai	
2-06	Carbon-ion Microbeam Revealed Abscopal Activation of Microglia After Lesions by Irradiation in Medaka Embryonic Brain	83
	K. Nagata, K. Ohashi, T. Yasuda, M. Kamahori, T. Kajihara, B. Dutta, M. Suzuki, T. Funayama, T. Watanabe-Asaka, H. Mitani and S. Oda	
2-07	Development of Wettable Ultra-thin Microfluidic Chip for Immobilization of <i>C. elegans</i> During Microbeam Irradiation	84
	M. Suzuki, T. Sakashita, Y. Hattori, Y. Yokota, Y. Kobayashi and T. Funayama	
2-08	Effects of Carbon Ion Irradiation on Swimming in the Nematode <i>C. elegans</i>	85
	T. Sakashita, A. Yamasaki, M. Suzuki, S. Onoda, T. Sato, S. Yanase and Q.-M. Zhang-Akiyama	
2-09	Apparent Distance Between Lesions in DNA Irradiated with $^4\text{He}^{2+}$ Beam in a Cell-Mimetic Aqueous Solution	86
	K. Akamatsu and N. Shikazono	
2-10	Genome Wide Analysis of Rice Mutants Isolated from Ion-Beam-Mutagenized Population	87
	Y. Oono, H. Ichida, S. Nozawa, R. Morita, H. Kato, T. Abe and Y. Hase	
2-11	Mutation Frequency in Flavonoid Genes Under Different Flavonoid Phenotypic Conditions	88
	S. Hirata, S. Kitamura, K. Satoh, I. Narumi and Y. Oono	
2-12	Mutagenesis of the Oil-producing Algae by Ion Beam Irradiation	89
	H. Araie, Y. Hase, Y. Iwata, Y. Oono, I. Suzuki and Y. Shiraiwa	
2-13	Screening of Root Nodule Bacteria for Salinity Tolerance Using Ion Beams Irradiation	90
	M. Kubota, Y. Maruyama, K. Satoh, Y. Oono, N. Tomooka, N. Ohkama-Ohtsu and T. Yokoyama	

2-14	Ion Beam Breeding of Rice for the Mutation Breeding Project of the Forum for Nuclear Cooperation in Asia (FNCA)	91
	Y. Hase, A. Tanaka, S. Nozawa, Y. Oono, A. Koike and A. Takano	
2-15	The Moss <i>Physcomitrella patens</i> Is Hyperresistant to DNA Double-strand Breaks Induced by Ionizing Radiation	92
	Y. Yokota, N. Murakami, Y. Oono and A. N. Sakamoto	
2-16	Evaluation of Particle Fluence of Cluster and Monomer Ion Beams Using a Solid-state Track Detector	93
	Y. Hase, K. Satoh, A. Chiba and Y. Hirano	
2-17	Induction of Chromosomal Aberrations in <i>Albuca virens</i> (2n=6, Hyacinthaceae) via Ion Beam Irradiation	94
	S. Nishitani, K. Honda and S. Nozawa	
2-18	Improvement of Cut Flower Weight of Autumn-flowering Spray Chrysanthemum 'Kyura Syusa'	95
	M. Tamari, T. Minami, F. Tojima and Y. Hase	
2-19	Development of New Strains with Sporeless Mutation in Mushrooms Using Ion Beam Irradiation	96
	M. Ishikawa, M. Kasai, Y. Hase, S. Nozawa and K. Ouchi	
2-20	Breeding of Non-Urea Producing Gunma KAZE Yeasts Which Are Suitable for Export	97
	T. Watanabe, K. Satoh, Y. Oono, H. Hayashi and T. Masubuchi	
2-21	Effect of Ion-Beam Irradiation on the Sensitivity of Oleaginous Yeast <i>Lipomyces starkeyi</i> Against Fatty Acid Synthesis-Inhibitor Cerulenin	98
	P. Kahar, A.B. Juanssilfero, K. Satoh, Y. Oono, A. Kondo and C. Ogino	
2-22	Mutation Breeding of <i>Tweedia caerulea</i> 'Pure Blue' by Ion Beam Irradiation	99
	S. Tanioka, Y. Hase and S. Nozawa	
2-23	Genome Analysis of the Radioresistant Bacterium <i>Deinococcus aerius</i> TR0125	100
	K. Satoh, H. Arai, T. Sanzen, H. Hayashi, I. Narumi and Y. Oono	
2-24	Effect of Ion Beams and Gamma Rays Irradiation on Mutation Induction in <i>Bacillus subtilis</i> Spores	101
	N. H. P. Uyen, M. Furuta, K. Satoh and Y. Oono	
2-25	Study of the Lethal Effect Caused by the Various LET Particle Ion Beam in Budding Yeast <i>S. cerevisiae</i>	102
	Y. Matuo, A.N. Sakamoto, Y. Hase and K. Shimizu	
2-26	Microflora Analysis of Black Pepper Using MALDI-TOF Mass Spectrometry and Decontamination by Gamma-ray Irradiation	103
	H. Kameya, K. Kimura, H. Seito, T. Kojima and S. Todoriki	
2-27	Breeding of New Potted Flower Varieties Using Ion Beam	104
	M. Tsukagoshi, S. Nozawa and Y. Hase	
2-28	Creation of Mutant Cultivars by Ion Beam Irradiation to Diploid and Tetraploid <i>Tweedia caerulea</i>	105
	K. Yoshinaga, Y. Hase and S. Nozawa	
2-29	Analysis of Response Deficient Mutants of <i>Streptomyces coelicolor</i> to Contact-dependent Stimuli	106
	S. Asamizu, M. Yanagisawa, T. Ishizuka, K. Satoh, Y. Ohno and H. Onaka	

2-30	Knockout and Plasmid Complementation of the <i>pprA</i> Gene in the Radioresistant Bacterium <i>Deinococcus radiodurans</i>	107
	S. Tanabe, T. Sanzen, K. Satoh, Y. Oono and I. Narumi	
2-31	Effects of Growth Stages on Cadmium Accumulation in Shoot of Oilseed Rape Plants ...	108
	S. Nakamura, N. Suzui, Y.-G. Yin, S. Ishii, S. Fujimaki and N. Kawachi	
2-32	A Simulation Study on Imaging of Carbon-Ion Beams Using a Pinhole Camera Measuring Secondary Electron Bremsstrahlung	109
	M. Yamaguchi, Y. Nagao and N. Kawachi	
2-33	Development of a Cost-Effective Compton Camera for Targeted Alpha-Particle Radiotherapy	110
	Y. Nagao, M. Yamaguchi, S. Watanabe, N. S. Ishioka, N. Kawachi and H. Watabe	
2-34	Comparison of Iron Localization in <i>Lotus japonicus</i> Root Using Micro-PIXE	111
	J. Furukawa, M. Ouchi, Y. Noda, N. Yamada, T. Satoh and S. Satoh	
2-35	Analysis of Trace Elements in Acute Myelogenous Leukemia Cell Line Using In-Air Micro-PIXE	112
	T. Kasamatsu, Y. Kanai and H. Murakami	
2-36	Elemental Analysis of the Lungs in Patients with Idiopathic Pulmonary Fibrosis	113
	Y. Koga, T. Satoh, K. Kaira, M. Koka, T. Hisada and K. Dobashi	
2-37	Long-term Fluorine Penetration from Fluoride-containing Luting Materials to Dentin	114
	K. Okuyama, Y. Matsuda, H. Yamamoto, Y. Tamaki, T. Saito, M. Hayashi, H. Sano, Y. Yoshida, N. Yamada, M. Koka and T. Satoh	
2-38	Boron Analysis and Imaging of U251 Cells by Using Micro-Particle Induced X/Gamma-ray Emission	115
	K. Nakai, K. Endo, F. Yoshida, A. Matsumura, N. Yamada and T. Satoh	
2-39	Search Trace Elements in Brain Microvascular Endothelial Cells (BMECs) and Effects of Nicotine on Trace Element in BMECs	116
	E. Sakurai, E. Sakurai, K. Yanai, S. Matsuyama, Y. Ueki, Y. Kitayama, K. Ishii, M. Koka, T. Satoh and T. Kamiya	
2-40	Kinetics of Encapsulated Hyaluronic Acid-Protamine Particle After Intravenous Injection	117
	S. Harada, T. Segawa, S. Ehara and T. Satoh	
2-41	Astatinated Antibody Fragment for Reducing Renal Radioactivity Levels	118
	H. Suzuki, Y. Ohshima, S. Watanabe, T. Uehara, N.S. Ishioka and Y. Arano	

2 - 01 Validation of Ion Species and Beam Size Availability in Collimating Ion Microbeam System of TIARA

T. Funayama and M. Suzuki

Department of Radiation-Applied Biology Research, TARRI, QST

The collimating ion microbeam system of TIARA has been used for analyzing heavy-ion hit effect by targeting irradiation of cells or local region of individuals with micrometer sized ion beam [1]. The beam spot diameter is determined by a pinhole size of a microaperture that extracts beam to the atmosphere. By replacing microapertures, appropriate beam size can be selected with experimental purpose. In this report, we verified availability of ions that can be accelerated by AVF cyclotron in each microaperture using ELOSS code [2].

Microapertures are made of tantalum or gold disk with pinhole formed by laser processing. There are 6 microapertures with different size of pinhole and disk thickness, which determines availability of beam size for each ion species (Table 1). A hole opened by laser processing has a conjugated shape of constant diameter region and tapered region. Microapertures other than Ta60 use disks from which tapered region was removed, however, a disk of Ta60 does not. Therefore, the thickness of constant diameter region is unclear. To examine availability of Ta60 microaperture, an experiment to collimate 320 MeV carbon beam, which has stopping distance of 350 μm in tantalum, was carried out. As shown in Fig. 1, the ions passed only through the opening of 60 μm in diameter and did not through the disk in the other areas. This result indicated that the thickness of the disc excluding the taper region is 350 μm or more.

To verify ion availability for each microaperture, stopping distance of each ion in tantalum or gold was calculated by ELOSS code and compared with the metal disk thickness of microapertures. The results are shown in Table 2. By this verification, the minimum diameters of beam spots of $^4\text{He}^{2+}$ 63 MeV, $^{12}\text{C}^{6+}$ 190 MeV, and $^{20}\text{Ne}^{8+}$ 200 MeV, which became available for use in FY 2017, are determined as 180, 20 and 5 μm , respectively. In addition, availabilities of 10 and 15 MeV proton were also verified,

and revealed that minimum diameter of them are 60 and 180 μm , respectively. With these ions except He ion, experiment for verifying calculation were carried out by irradiating CR-39, and the obtained result agrees with the calculation result.

In this study, availability of ions in collimating ion microbeam system had expanded. We believe this result opens up the possibility of research using collimating ion microbeam system of TIARA.

Table 1. Microaperture available in collimating ion microbeam.

	Pinhole diameter (μm)	Aperture disk	
		Material	Thickness (μm)
Ta250	250	tantalum	500
Ta180	180	tantalum	500
Ta60	60	tantalum	500 (>350 w/o taper)
Ta20	20	tantalum	200
Au20	20	gold	200
Ta5	5	tantalum	100

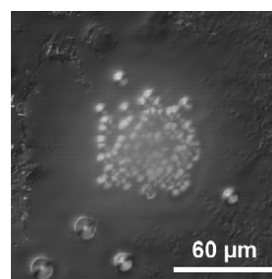


Fig. 1. Distribution of ion track collimated with Ta60 microaperture. CR39 film was irradiated with carbon ion ($^{12}\text{C}^{6+}$ 320 MeV), thereafter track was visualized with alkaline etching.

References

- [1] T. Funayama *et al.*, J. Radiat. Res. **49**, 71 (2008).
 [2] S. Tanaka *et al.*, J. Nucl. Sci. Tech. **37**, 840 (2000).

Table 2. Ion species and beam size availability in collimating ion microbeam system.

Ion	Particle Species	H ⁺	H ⁺	$^4\text{He}^{2+}$	$^4\text{He}^{2+}$	$^{12}\text{C}^{6+}$	$^{12}\text{C}^{5+}$	$^{12}\text{C}^{6+}$	$^{20}\text{Ne}^{8+}$	$^{20}\text{Ne}^{7+}$	$^{20}\text{Ne}^{8+}$	$^{40}\text{Ar}^{13+}$	$^{40}\text{Ar}^{14+}$
	Energy (MeV)	10	15	50	63	190	220	320	200	260	350	460	520
	LET (keV/ μm)	4.83	3.44	15.8	13.0	117.5	103.5	74.9	480.4	384.3	298.4	1283	1167
Stopping	Tantalum	210	390	300	430	160	200	350	60	80	120	60	70
Distance (μm)	Gold	190	350	270	390	150	180	320	60	80	110	60	60
	Water	1180	2440	1770	2680	930	1210	2370	270	420	700	250	310
Microaperture	Ta250	√	√	√	√	√	√	√	√	√	√	√	√
	Ta180	√	√	√	√	√	√	√	√	√	√	√	√
	Ta60	√	N/A	√	N/A	√	√	√*	√	√	√	√	√
	Ta20					√	√		√	√	√	√	√
	Au20					√	√		√	√	√	√	√
	Ta5								√	√		√	√

Reduction of Clonogenicity and Inhibition of 5-bromo-2'-deoxyuridine Incorporation in Glioblastoma Cells After Gamma-ray and Carbon-ion Irradiation

Y. Yokota^{a)}, Y. Morishita^{a, b)} and T. Funayama^{a)}

^{a)} Department of Radiation-Applied Biology Research, TARRI, QST,

^{b)} Tokyo College of Biotechnology

Glioblastoma is one type of the malignant brain tumors and refractory to various types of therapies. Survivors of radiotherapy for malignant brain tumors sometimes suffer from long-term side effects such as mental retardation and reduced learning ability. This is because radiosensitive neural stem cells (NSCs) are severely damaged and neurogenesis is inhibited after radiotherapy. Radiosensitization of brain tumors and/or radioprotection of NSCs are thus needed to keep the quality of life in patients. We have reported that human NSCs were more sensitive to carbon-ion irradiation than glioblastoma cells, interphase death was related to growth inhibition after irradiation in NSCs but not in glioblastoma cells [1], and apoptosis was markedly induced after irradiation in NSCs but not in glioblastoma cells [2]. This year, we report reduction of clonogenicity and inhibition of 5-bromo-2'-deoxyuridine (BrdU: an analogous molecule of thymidine) incorporation in glioblastoma cells after gamma-ray and carbon-ion irradiation.

A-172 cells derived from human glioblastoma were irradiated with gamma-rays at the Cobalt 60 Irradiation Facilities or carbon-ion beam ($^{12}\text{C}^{6+}$, 15.8 MeV/n, LET = 123 keV/ μm) at the HY1 port of TIARA. For clonogenicity assay, cells were harvested immediately after irradiation and repopulated to culture for 2 weeks. Formed colonies were fixed in formalin, stained with crystal violet, and counted to get survival rates. The doses that give 10% survival rate (D_{10}) were obtained from survival curves based on the single-hit multi-target model. For BrdU incorporation assay, cells were pulse-labeled with BrdU 24 h after irradiation and fixed in paraformaldehyde. BrdU was then detected using anti-BrdU antibody and secondary antibody conjugated with fluorescent dye.

Survival rates of glioblastoma cells were reduced in dose and radiation-type dependent manners (Fig. 1). The D_{10} values of gamma-rays and carbon ions were 3.97 Gy and 0.65 Gy, respectively. The RBE value based on the D_{10} was 6.11. To investigate the mechanism of reproductive death, BrdU incorporation was detected as an index of DNA synthesis. Twenty-four hours after carbon-ion irradiation at 8 Gy, BrdU incorporation was markedly inhibited (Fig. 2A). The rates of BrdU-positive cells were less after carbon-ion irradiation than after gamma-ray irradiation at the same doses (Fig. 2B). Taking together, inhibition of DNA synthesis may be a main pathway of radiation-induced reproductive death in apoptosis-resistant glioblastoma A-172 cells.

References

- [1] Y. Yokota *et al.*, QST Takasaki Annu. Rep. 2015 **QST-M-2**, 110 (2017).
 [2] Y. Yokota *et al.*, QST Takasaki Annu. Rep. 2016 **QST-M-8**, 85 (2018).

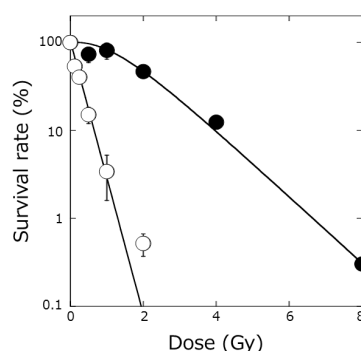


Fig. 1. Survival curves of glioblastoma cells irradiated with gamma-rays (closed circular) or carbon ions (open circular). Data represent mean \pm SE derived from 3 independent experiments.

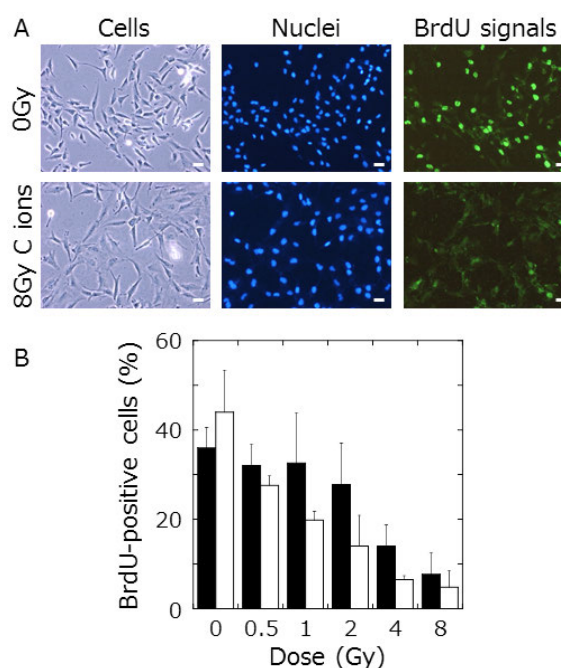


Fig. 2. Inhibition of BrdU incorporation into glioblastoma cells after irradiation. A. Typical images of cells, nuclei, and detected BrdU signals with and without carbon-ion irradiation. B. The rates of BrdU-positive cells after gamma-ray (closed column) or carbon-ion irradiation (open column). Data represent mean \pm SE derived from 3 independent experiments.

2 - 03

Bystander Cellular Effects Induced in Normal Human Fibroblasts by 190 MeV $^{12}\text{C}^{6+}$ and 200 MeV $^{20}\text{Ne}^{8+}$ Ions

M. Suzuki ^{a)}, T. Funayama ^{b)}, M. Suzuki ^{b)} and Y. Kobayashi ^{b)}

^{a)} Department of Basic Medical Sciences for Radiation Damages, NIRS, QST,

^{b)} Department of Radiation-Applied Biology Research, TARRI, QST

We have been studying the cellular bystander effects, such as cell killing and gene mutation, in normal human fibroblasts using the C-, Ne- and Ar-ion microbeams. Our data showed that the bystander cellular effects via gap-junction mediated cell-cell communication within 3 h after irradiation were induced in the cells irradiated with the C-ion microbeams, but not the Ne- and the Ar-ion microbeams. On the other hand, the bystander effects via the secreted factor, which was scavenged by ascorbic acid, to culture medium from the irradiated cells were induced with the C-, the Ne- and the Ar-ion microbeams after 24 h [1 - 3]. This year we examined whether the same bystander cellular effects were induced or not using C- and Ne-ion microbeams with different energies.

Normal human skin fibroblasts (NB1RGB) were obtained from Riken Bio Resource (Cell No. RCB0222). Half of the sample dishes were treated with a specific inhibitor of gap-junction mediated cell-cell communication (40 μM of γ -isomer of hexachloro-cyclohexane) from 3 h before irradiation. Irradiations were carried out by the 256-cross-stripe method [4] using C ions ($^{12}\text{C}^{6+}$, 190 MeV) and Ne ions ($^{20}\text{Ne}^{8+}$, 200 MeV) at the HZ1 port. The beam size of each ion microbeam was 20 μm in diameter and the irradiations in each point were performed to deliver 7 ions for carbon and 2 ions for neon. After the irradiations, sample dishes were incubated for each defined time of 3 h and 24 h in a CO_2 incubator at 37 $^\circ\text{C}$, and assayed cell-killing effect, which was measured by a colony-forming assay and mutation at the *HPRT* (Hypoxanthine-guanine phosphoribosyltransferase) locus, which was detected by the incidence of 6-thioguanine resistant clones.

The result of the cell-killing effect suggested that the bystander lethal effect was induced in the cells irradiated with C-ion microbeams via gap-junction mediated cell-cell communication within 3 h after the irradiation, but not Ne-ion microbeams (Fig. 1). It is consistent with the data using 220 MeV $^{12}\text{C}^{5+}$ ions and 260 MeV $^{20}\text{Ne}^{7+}$ ions previously reported [1]. The mutation frequency at 3 h was induced in the C-ion-irradiated cells beyond the expectation, which was irradiated all cells with C-ion broadbeams and it suggested the bystander effect via gap-junction mediated cell-cell communication within 3 h after the irradiation. However, no mutation was observed in the cells irradiated with Ne-ion microbeams. On the other hand, the bystander mutagenic effect was observed in the cells irradiated with both C and Ne ions at 24 h, having no relation to the gap-junction inhibitor (Fig. 2). The data is consistent with using 220 MeV $^{12}\text{C}^{5+}$ ions and 260 MeV $^{20}\text{Ne}^{7+}$ ions previously reported [3], suggesting the secreted-factor mediated

bystander effect, not gap-junction mediated cell-cell communication.

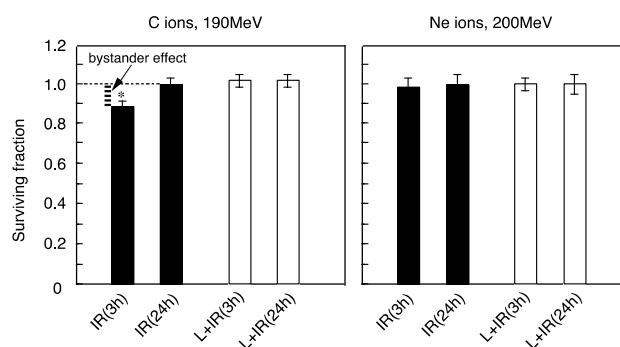


Fig. 1. Cell-killing effect induced in NB1RGB cells irradiated with the C- and Ne-ion microbeams at 3 and 24 h after the irradiation. The data showed the average and the standard deviation of 3 independent experiments for C ions and 2 for Ne ions. IR : microbeam-irradiated samples, L+IR : microbeam-irradiated samples treated with the gap-junction inhibitor ($p < 0.05$).

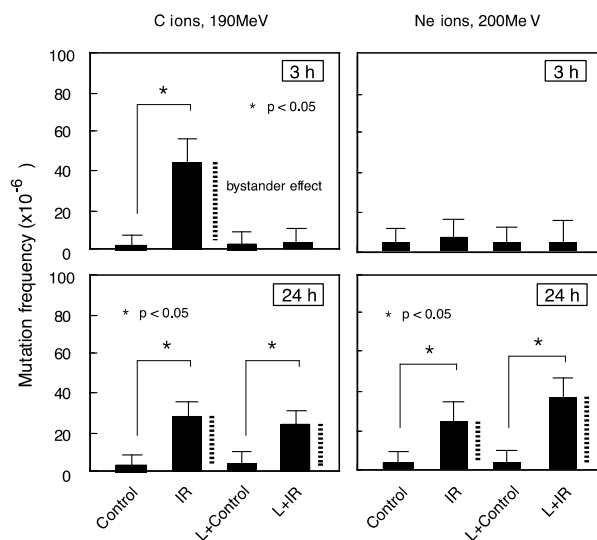


Fig. 2. Gene mutation induced in NB1RGB cells irradiated with the C- and Ne-ion microbeams at 3 and 24 h after the irradiation. The data showed the average and the standard deviation of 3 independent experiments for C ions and 2 for Ne ions.

References

- [1] M. Suzuki *et al.*, JAEA Takasaki Ann. Rep. 2014, JAEA-Review **2015-022**, 70 (2016).
- [2] M. Suzuki *et al.*, QST Takasaki Ann. Rep. 2015, **QST-M-2**, 118 (2017).
- [3] M. Suzuki *et al.*, QST Takasaki Ann. Rep. 2016, **QST-M-8**, 88 (2018).
- [4] M. Suzuki *et al.*, JAEA Takasaki Ann. Rep. 2006, JAEA-Review **2007-060**, 107 (2008).

2 - 04 LET and Ion Species Dependence of Oxidative Damage in DNA Sheet Generated Along Ion Beam Track

A. Ito ^{a)}, A. Furuhashi ^{a)}, F. Ouchi ^{a)}, S. Yoshida ^{a)}, R. Hirayama ^{b)}, Y. Furusawa ^{c)},
Y. Yokota ^{d)} and T. Funayama ^{d)}

^{a)} School of Engineering, Tokai University,

^{b)} Department of Charged Particle Therapy Research, NIRS, QST,

^{c)} Department of Basic Medical Sciences for Radiation Damages, NIRS, QST,

^{d)} Department of Radiation-Applied Biology Research, TARRI, QST

The track structure of heavy ions is generally recognized to consist of a core region with high ionization density and a penumbra region where secondary electrons mainly contribute to energy deposition, with relatively low LET nature. The biological effects of heavy ions should be characterized by such a track structure of energy deposition. We have been focusing on the detection of the low LET penumbra area in high-LET ion beam irradiation by using OH radical-induced DNA damage 8-hydroxydeoxyguanosine (8-OHdG). Our recent study detected significant production of 8-OHdG upon heavy ion irradiation to DNA sheet in water environment [1]. Particularly by irradiating DNA sheet set in parallel to incident proton beam we observed 8-OHdG generation along beam track. In the present study we reproduced 8-OHdG generation along a proton track, and measured the size of the generation area of 8-OHdG perpendicular to the beam direction. The result was also compared with the results obtained with ion beams supplied by HIMAC at the National Institute of Radiological Science (NIRS).

Ion beam irradiation was carried out as follows: 20 MeV proton beam at TIARA with an LET of 2.77 keV/ μm was irradiated to DNA sheet made on a coverglass in parallel with ion beam. The DNA sheet on which water is dropped was covered with mylar film to maintain water environment during irradiation. The similar irradiation setup was applied to HIMAC beams of 200 MeV Fe with an LET of 440 keV/ μm and 290 MeV C with an LET of 13 keV/ μm , although beam direction was horizontal instead of vertical direction at TIARA. The irradiated DNA sheet pretreated with Bouin fixative was processed according to a fluorescence immunostaining protocol using a fluorescence antibody against 8-OHdG. The obtained fluorescence images were analyzed with Image J, an image processing software.

Figure 1 shows the result for the proton beam. Upon irradiation of a dose as high as 200 Gy, we can detect a line-like image of 8-OHdG that was probably generated along a beam track (panel a). To measure the width of the 8-OHdG generation area, the picture was enlarged and at about 20 locations the width was measured (panel b). The similar measurement was repeated for several different tracks, and the averaged value was calculated with standard error (Table 1). For comparison, the widths of 8-OHdG areas induced by iron and carbon beams at HIMAC were listed in the same table.

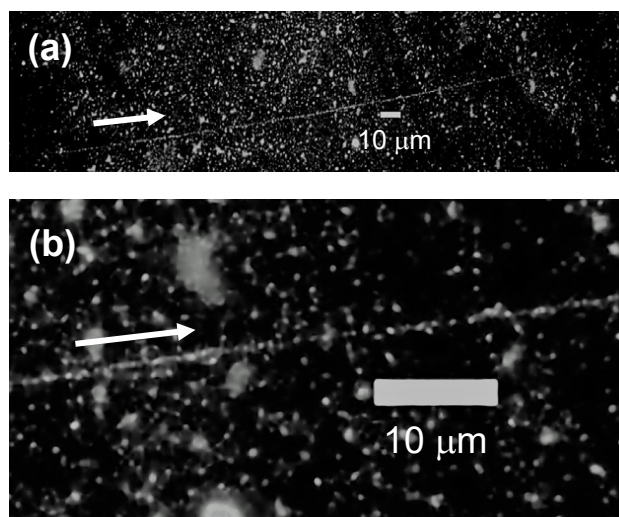


Fig. 1. 8-OHdG generation along 20 MeV proton beam track in DNA sheet. Panel (b) is an enlarged picture of panel (a). Arrows show the beam direction.

Table 1
Width of 8-OHdG area perpendicular to ion beam.

Ion species	Proton	Carbon	Iron
Width (μm)	0.63 ± 0.03	1.02 ± 0.06	7.55 ± 0.46

From the results of Table 1, the width of 8-OHdG area that corresponded to penumbra area was found to increase with increasing LET or mass of ions. The results are consistent with the theoretical study by Chatterjee and Schaefer [2]. To address the question which is a major determinant for the width of 8-OHdG area, LET or ion mass, the comparison between different ion species with similar LET would be interesting.

Acknowledgment

We thank Drs. M. Mitarai and K. Iohara, Central Research Institute of Maruha Nichiro Cooperation, for their courteous supply of DNA sample.

References

- [1] A. Ito *et al.*, QST Takasaki Annu. Rep. 2016, **QST-M-8**, 90 (2018).
- [2] A. Chatterjee and H. J. Schaefer, *Radiat. Environ. Biophys.*, **13**, 215-27 (1976).

2 - 05

Cell Cycle Arrest and Reentry in *Bombyx* Embryo at Cleavage Stage After Heavy Ion Irradiation

R. Isoyama^{a)}, Y. Umeda^{a)}, Y. Souma^{a)}, T. Funayama^{b)}, Y. Yokota^{b)}, M. Suzuki^{b)}, T. Sakashita^{b)}, Y. Kobayashi^{b)} and K. Shirai^{a)}

^{a)} Faculty of Textile Science and Technology, Shinshu University,

^{b)} Department of Radiation-Applied Biology Research, TARRI, QST

Checkpoints and DNA repair mechanisms are important for all living organisms, especially embryos. However, animals are considered to lack or have incomplete checkpoints or DNA repair mechanisms during early development.

When the silkworm (*Bombyx mori*) egg at cleavage stage is irradiated with heavy ions, the development of egg delays depending the dose of irradiation. Thereafter the eggs restart their developments without restoring the damaged DNA completely. These results indicate that check point, but not DNA repair mechanisms, function in silkworm egg at cleavage stage. The processes that the egg escapes the checkpoint resemble to checkpoint adaptation. However, until now, the detailed mechanisms of the cell cycle arrest in *Bombyx* eggs at cleavage stage have been unknown.

The purposes of this studies are to clear the timing of cell cycle arrest after heavy ion irradiation, and to examine whether cell cycle restarts in the egg that was irradiated with carbon ions ($^{12}\text{C}^{6+}$, 190 MeV) at Takasaki Ion Accelerator for Advanced Radiation Application (TIARA).

First of all, we investigate the fluctuation of Cyclin B in the egg during cleavage stage. Cyclin B activate M-CDK, so is an important factor to enter M phase. In *Drosophila* embryogenesis, Cyclin B levels in egg during cleavage stage were separated into two stages [1]. While, during 2nd–7th nuclear cleavage (cell cycle 2-7), Cyclin B shows little fluctuation in abundance, oscillations of Cyclin B were observed during 8th–13th nuclear cleavage (cell cycle 8-13). This change reflects the switchover of the cell cycle controls. The fluctuation of Cyclin B in *Bombyx* egg during cleavage stage was similar in pattern to that in *Drosophila* egg. During the early cleavage stage, Cyclin B was abundant and constant in amount (Fig. 1A). After middle of the cleavage stage, Cyclin B oscillated with 45-55 min cycle (Fig. 1B).

Next, the timing of cell cycle arrest was examined. The eggs at 6.5 h after oviposition were irradiated with 20 Gy of carbon ions, then the eggs were fixed and the position and number of nuclei were observed. At 2 h after irradiation (8.5 h after oviposition), 32 or 64 of nuclei was detected in the control (non-irradiated) eggs, while irradiate eggs have 8-16 nuclei (Fig. 2). These results indicate the cell cycle stopped immediately after irradiation.

Lots of eggs restarted their development until 18 h after oviposition at this dose (data was not shown). However, no eggs hatched. It is undoubtedly that eggs having the damage in genome restarted the cell cycle. We examined

whether cell cycle restarts in the egg that was irradiated with extremely high dose. The eggs irradiated with 500 Gy of carbon ion stopped their development at 12 h after oviposition. At 24 h after oviposition, the development of eggs had been observed (Data was not shown).

In the studies, we revealed that the silkworm eggs change their cell cycle control at middle of the cleavage stage. We also elucidated the cell cycle arrest in the eggs arise immediately after irradiation, but this arrest cannot continue during long time, even if the egg suffered damages severely.

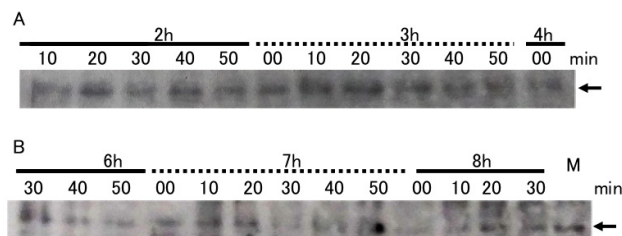


Fig. 1. Changes in Cyclin B in *Bombyx* eggs during early development. A) From 2 h 10 min to 4 h. B) From 6 h 30 min to 8 h 30 min. M: marker. Arrows indicate the position of Cyclin B.

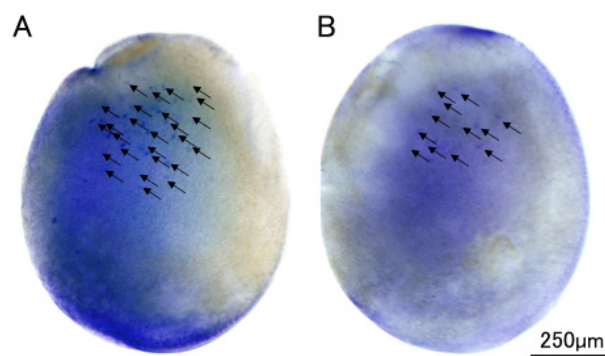


Fig. 2. Cell cycle arrest in the heavy-ion (20 Gy of carbon ion) irradiated egg (8.5 h after irradiation). A) non-irradiated egg, B) irradiated egg. Arrows indicate nuclei.

Reference

[1] B. A. Edgar *et al.*, *Genes & Develop.*, **8**, 440 (1994).

2 - 06 Carbon-ion Microbeam Revealed Abscopal Activation of Microglia After Lesions by Irradiation in Medaka Embryonic Brain

K. Nagata^{a)}, K. Ohashi^{a)}, T. Yasuda^{a)}, M. Kamahori^{a)}, T. Kajihara^{a)}, B. Dutta^{a)}, M. Suzuki^{b)}, T. Funayama^{b)}, T. Watanabe-Asaka^{a)}, H. Mitani^{a)} and S. Oda^{a)}

^{a)} Department of Integrated Biosciences, The University of Tokyo,

^{b)} Department of Radiation-Applied Biology Research, TARRI, QST

Microglia is the resident immune cells in vertebrate brain and evidences are accumulating that microglia are the pivotal cellular mediators of neuroinflammation in brain [1]. When central nervous system (CNS) is damaged in injury, infection, or trauma, microglia are activated to remove damaged cells via phagocytosis, which is essential for brain tissue repair. In embryonic brain of medaka, *Oryzias latipes*, irradiation induces apoptotic cell death of neurons which are engulfed and removed by microglia [2]. Activated microglia express L-plastin at first and then they express Apolipoprotein E (ApoE) in the late phase of phagocytosis, indicating that phagocytosis by microglia includes two steps and L-plastin and ApoE can be the indicators of each steps of microglial activation [3].

In this study, using TIARA we conducted targeted irradiation of only the right lobe of optic tectum using collimated microbeam (diameter = 250 μm) of carbon-ion ($^{12}\text{C}^{6+}$, 26.7 MeV/u) in developing brain of medaka embryo (3 days post-fertilization). After the targeted irradiation, apoptotic cell death was induced only in the irradiated region of optic tectum and only the microglia in the irradiated region were activated to express L-plastin. Against our expectations, we found that activated microglia expressing ApoE were then distributed over the whole optic tectum out of the irradiated region (Fig. 1). Furthermore, the microglial activation did not cease even after the clearance of apoptotic cell debris and continued for over 3 days after irradiation [3].

Cranial radiation therapy (CRT) is a widely-accepted treatment for intracranial tumors, however, CRT can induce radiation-induced brain injury (RIBI) in the healthy tissues surrounding the tumor. Irradiation induces necrosis in brain which can occur after several months following irradiation and is the most serious late adverse event in radiation therapy [4]. Clinical studies demonstrated that acute neural detrimental effects such as cognitive impairment can be induced in patients after CRT.

The findings in this study lead us to the idea that the persisted and excessive activation of microglia by irradiation could be a cause of the abscopal and/or adverse effects following irradiation in CRT in patients and that medaka embryonic brain is a promising model system with which we can investigate the dynamics of microglial activities. We are now confirming that the situation is the same in mouse brain as medaka embryonic brain, and also establishing transgenic medaka fish with GFP-labeled

microglia to make clear the dynamics of microglial activation after RIBI.

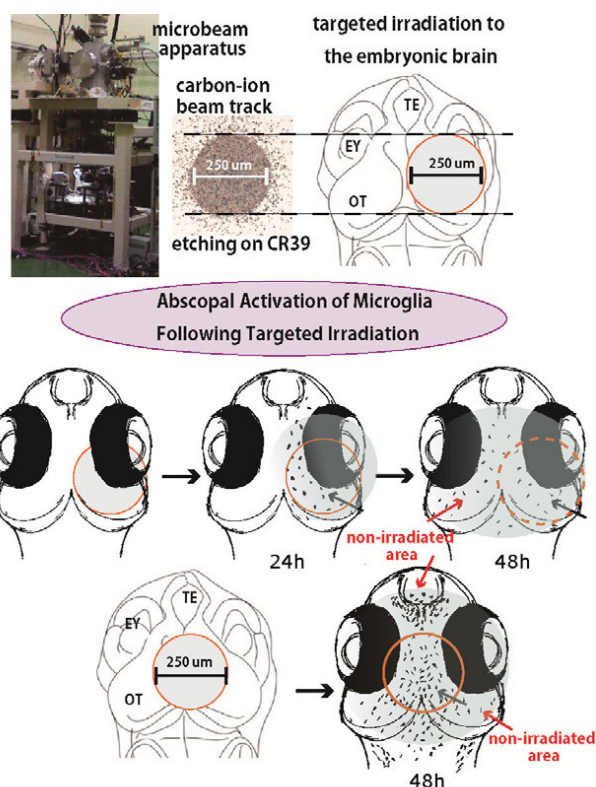


Fig. 1. Targeted irradiation with collimated carbon-ion microbeam in TIARA revealed the abscopal activation of microglia in developing brain of medaka embryo. With microbeam of which diameter was confirmed to be 250 μm on CR39, whole of the right lobe of optic tectum (OT) in medaka embryonic brain was irradiated, while telencephalon (TE) and left eye (EY) were not. When only the right OT or the middle part of mesencephalon was irradiated, only microglia in the irradiated area were activated (black arrows) for the first 24 hours after irradiation and then activated microglia appeared out of the irradiated area (red arrows) within 48 hours after irradiation.

References

- [1] W. J. Streit *et al.*, J. Neuroinflammation, **1**, 14 (2004).
- [2] T. Yasuda *et al.*, PLOS ONE, **10**, e0127325 (2015).
- [3] T. Yasuda *et al.*, Int. J. Mol. Sci., **18**, 1428 (2017).
- [4] N. Kondo *et al.*, Appl. Radiat. Isot., **106**, 242 (2015).

2 - 07 Development of Wettable Ultra-thin Microfluidic Chip for Immobilization of *C. elegans* During Microbeam Irradiation

M. Suzuki, T. Sakashita, Y. Hattori, Y. Yokota, Y. Kobayashi and T. Funayama

Department of Radiation-Applied Biology Research, TARRI, QST

Radiation such as X-rays, gamma rays, and heavy-ion beam is widely used for biological applications such as cancer diagnosis and treatment, and ion beam breeding. Furthermore, a lot of studies and technical developments to investigate the radiation effects are also proceeding. Microbeam irradiation is a powerful means to identify a site with radiation sensitivity in the living organisms. We have been developing a technology to irradiate individual cells under microscopic observation by heavy-ion microbeam. With the heavy-ion microbeam, we also have been establishing a method for targeted irradiation of several model organisms such as nematodes and medaka [1-2].

The nematode *Caenorhabditis elegans* is a widely used model animal for investigating the fundamental mechanisms responsible for numerous biological processes. Targeted radiation exposure allows the effective knockdown of specific regions or tissues such as the central nervous system (CNS), thus helping to identify their roles in processes such as locomotion. However, radiation targeting requires the animal to be immobilized, while anesthesia prevents the radiation-induced effects on functions such as locomotion to be observed immediately. We previously developed a polydimethylsiloxane (PDMS) microfluidic chip method for immobilizing individual *C. elegans* during irradiation without the need for anesthesia [1]. However, this was limited by the thickness of the chip (~2.5 mm), which prevented the actual irradiation dose passing through the animal to be measured, and by dehydration of the animals after prolonged immobilization in the microfluidic chip.

In the present study, we addressed these limitations and developed an improved chip, as well as identifying the suitable conditions to prevent dehydration. We developed a new ultra-thin, ion-penetrable PDMS microfluidic chips (Fig. 1), with wettability (hydrophilicity). Using a collimating microbeam system at TIARA, we demonstrated that carbon ions (with a range of approximately 1 mm) were able to pass through the microfluidic chip and be counted by an ion-counting system, thus allowing accurate measurement of the applied irradiation dose. We also examined the motility of individual *C. elegans* in relation to dehydration following immobilization (Fig. 2) for 1 h on the conventional PDMS microfluidic chip without wettability (Chip L) and the improved wettable chip (Chip B) in various types of buffer solution. Motility following on-chip immobilization reduced in pure water or high salt buffer (S buffer) or high phosphate buffer (M9 buffer) on Chip L, as a result of dehydration due to evaporation, but not on Chip B (Table 1). However, motility was unaffected on either chip in the presence of a gelatin-based buffer (W buffer), suggesting that dehydration may be prevented as a result of

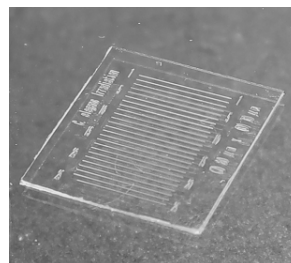


Fig. 1. Developed PDMS microfluidic chip (Chip B) for *C. elegans*. The thickness of this wettable PDMS microfluidic chip for *C. elegans* is 300 μm , and 25 straight microfluidic channels are formed on the surface (depth, 70 μm ; width, 60 μm).

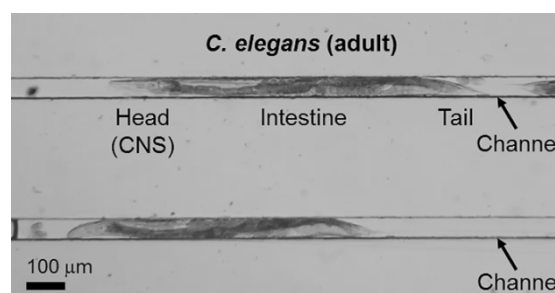


Fig. 2. *C. elegans* individuals enclosed in microfluidic channels on a wettable ultra-thin PDMS chip (overhead view).

Table 1

Effects of on-chip immobilization on motility of *C. elegans*.

	Pure water	S buffer	M9 buffer	W buffer
Chip L	reduced	reduced	reduced	n.a.
Chip B	n.a.	n.a.	n.a.	n.a.

n.a.: Not affected.

coating the body surface with gelatin. The improved chip and identification of the suitable buffer conditions will increase the applications of this system for immobilizing active *C. elegans* to study the effects of targeted irradiation, as well as having potential uses in optical imaging assays.

Acknowledgments

We thank the *Caenorhabditis* Genetic Center for providing strains of *C. elegans*, and the crew of the cyclotron of TIARA for their kind assistance with the experiments. The present study was supported in part by KAKENHI (JP24620013 and JP15K11921) from JSPS and a Scientific Grant of Innovative Research from JAEA.

References

- [1] M. Suzuki *et al.*, *J. Radiat. Res.* **58**, 881 (2017).
- [2] T. Yasuda *et al.*, *Int. J. Mol. Sci.* **18**, 1428 (2017).

Effects of Carbon Ion Irradiation on Swimming in the Nematode *C. elegans*

T. Sakashita^{a)}, A. Yamasaki^{a, b)}, M. Suzuki^{a)}, S. Onoda^{c)}, T. Sato^{d)},
S. Yanase^{e)} and Q.-M. Zhang-Akiyama^{b)}

^{a)} Department of Radiation-Applied Biology, TARRI, QST,

^{b)} Graduate School of Science, Kyoto University,

^{c)} Department of Advanced Functional Materials Research, TARRI, QST,

^{d)} Environment and Radiation Sciences Division, NSEC, JAEA,

^{e)} School of Sports & Health Science, Daito Bunka University

The nematode *C. elegans* has been used as a model organism for space life science experiments [1]. Significant changes of gene expression profiles in *C. elegans* were reported in the low Earth orbit mission with very low dose exposure (several mGy) [2]. It has been reported that the effective dose ranges of heavy ion beam on locomotion [3] and chemotaxis [4] were over several hundred Gy. However, there is no report on phenotype in *C. elegans* after low dose exposure of heavy ions. Recent development of imaging analysis allows us to measure various endpoints on swimming in *C. elegans*, and it is possible to measure using a loading unit installed at the Japanese experiment module, Kibo, in the international space station [1]. Thus, we explored a swimming parameter to detect an effect of carbon ion irradiation at a low dose.

Well-fed adults of *C. elegans* wild type grown at 20 °C on the plate spread with *E. coli* OP50 were used in all experiments. Animals on the agar plate were irradiated with high-energy carbon ions (¹²C, 18.3 MeV/u) at the doses of 0, 0.1, 1, 10, 100 Gy. Animals were washed and collected, and the 50-100 µL drop including *C. elegans* was injected into the chamber of the µ-Slide VI 4.0 (ibidi USA Inc., Madison, Wisconsin USA). Swimming movement of *C. elegans* in the chamber was video-recorded and analyzed using the software WormLab (MBF Bioscience, Williston USA) for imaging, tracking and analyzing. We selected the following parameters: 1) Speed: velocity along the central axis from one frame to the next, 2) Wavelength: period of the sine wave the best fits the worm's posture and 3) Bend angle: bending angle at the midpoint.

The frequency distribution of speed in *C. elegans* after high-energy carbon ion irradiation was not affected at all doses, as shown in Fig. 1. Also, the frequency distribution of wavelength of them made a slight change (data not shown). Only, we could detect the dramatic change in the pattern of the frequency distribution in angle of *C. elegans* irradiated with more than 1 Gy of carbon ions (Fig. 2). The wider angle-frequency distributes, the more winding *C. elegans* postures. It suggests the dose-dependent abnormality of muscular system in *C. elegans*. Taken together, we found the de novo endpoint, angle-frequency, of *C. elegans* phenotype, which was detectable at the 1 or 2 order of magnitude lower dose than those of conventional studies.

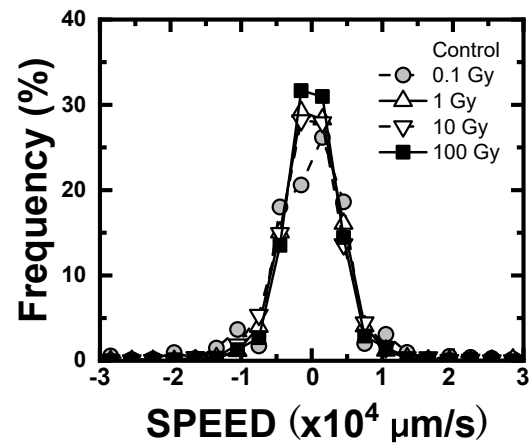


Fig. 1. Speed parameter of *C. elegans* irradiated with high-energy carbon ions at the doses of 0, 0.1, 1, 10, 100 Gy.

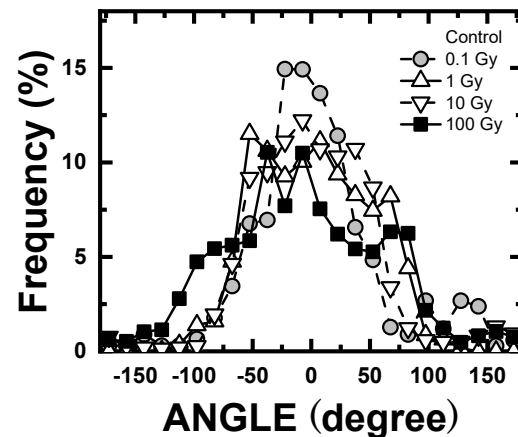


Fig. 2. Bend angle of *C. elegans* irradiated with high-energy carbon ions at the doses of 0, 0.1, 1, 10, 100 Gy.

References

- [1] A. Higashibata *et al.*, *Microgravity* **2**, 15022 (2016).
- [2] Y. Gao *et al.*, *J. Radiat Res.* **56**, 872 (2015).
- [3] M. Suzuki *et al.*, *J. Radiat Res.* **58**, 881 (2017).
- [4] T. Sakashita *et al.*, *Biol. Sci. Space.* **26**, 21 (2012).

K. Akamatsu and N. Shikazono

Department of Quantum Beam Life Science, KPSI, QST

Introduction

Ionizing radiation-induced DNA damage can cause mutation and carcinogenesis. In particular, “clustered damage”, that is a DNA region with two or more lesions within a few helical turns, is believed to be hardly repaired. This damage is considered to be induced around high-LET ionizing radiation tracks. However, detail of the damage is unknown. We have already developed a method for estimating localization of apurinic/aprimidinic sites (APs) on DNA using fluorescence resonance energy transfer (FRET) occurring between different fluorescent dyes (Alexa350 and Alexa488) (*hetero*-FRET). The FRET efficiency (E) was calculated from Alexa350 fluorescence intensities before/after enzymatic digestion of the labeled DNA with APs [1]. We succeeded in estimating qualities of clustered APs produced in $^4\text{He}^{2+}$ -, $^{12}\text{C}^{5+}$ -, and ^{60}Co γ -irradiated dry DNA film to study “direct” radiation effects using the method [2]. We also applied the method to aqueous DNA solution to study “indirect” radiation effects. However, there are some problems of the complex protocol and of the sensitivity due to the low extinction coefficient of Alexa350. We have, therefore, developed “*homo*-FRET” occurred between two or more Alexa488 molecules. We will obtain magnitude of FRET also from “fluorescence anisotropy” of *homo*-FRET between Alexa488 molecules [3]. The new protocol using *homo*-FRET enables us to estimate DNA damage localization without any enzymes and improves sensitivity to detect a clustered damage.

Experiments

•Sample preparation and irradiation

PUC19 digested by Sma I was used (linear formed) for DNA samples to be irradiated. The DNA was dissolved in 0.2 M Tris-HCl buffer (pH 7.5), which is a cell-mimetic condition, to be ~10 g/L. The DNA solution was transferred to a chamber (thickness: 1 mm), and was irradiated with $^4\text{He}^{2+}$ (12.5 MeV/u, LET: 19 keV/ μm , HY). Moreover, ^{60}Co γ -rays were also used as a standard radiation source at Kyoto University Research Reactor Institute.

•Preparation of fluorophore-labeled irradiated DNA and FRET observation [3]

The irradiated DNA (10 μL in water) and 10 μL of 100 mM Tris-HCl (pH 7.5) were mixed in a microtube. Two microliters of Alexa488/DMSO was added to the DNA solution and was incubated for 24 h at 35 $^\circ\text{C}$. The fluorophore-labeled DNA was purified by ethanol-precipitation followed by ultrafiltration. The fluorescence anisotropy was measured at 525 nm (ex. 470 nm).

The anisotropy, $\langle r \rangle$, is defined as follows:

$$\langle r \rangle = (I_{VV} - G \cdot I_{VH}) / (I_{VV} + 2 \cdot G \cdot I_{VH})$$

where I_{VV} is the fluorescence intensity when the excitation

and emission polarizers are both vertically oriented. I_{VH} is one when the excitation/emission polarizers are vertically/horizontally oriented. G is the grating factor defined as I_{HV}/I_{HH} .

The apparent averaged distance between APs, $\langle R \rangle$, can be calculated from $\langle r \rangle$ values obtained in this study.

Results and Discussion

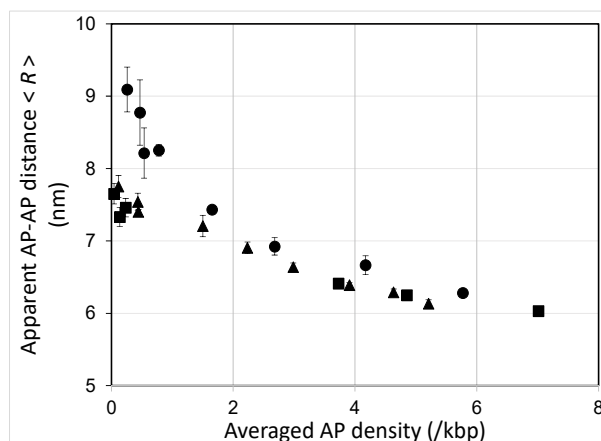


Fig. 1. Apparent AP-AP distance of DNA irradiated with ^{60}Co γ -rays (LET:0.2~0.3 keV/ μm (●), $^4\text{He}^{2+}$ (LET:19 keV/ μm) (■), and $^{12}\text{C}^{6+}$ (LET:87 keV/ μm , data from 151037) (▲) as a function of AP averaged density.

Figure 1 shows relationships between AP average density and apparent AP-AP distance, $\langle R \rangle$, for the He, C ion beams, and ^{60}Co γ -rays. This indicates that $\langle R \rangle$ for He ions are almost the same as those for C, whereas $\langle R \rangle$ for these ion beams are smaller than that for the γ -rays. An ion beam with LET: ~1000 keV/ μm would be needed for observing significant difference compared to the present experiments.

Acknowledgment

We would like to gratefully thank Dr. Takeshi Saito of Kyoto University Research Reactor Institute for supporting ^{60}Co γ -ray irradiation.

References

- [1] K. Akamatsu, N. Shikazono, *Anal. Biochem.* **433**, 171-80 (2013).
- [2] K. Akamatsu *et al.*, *Radiat. Res.* **183**, 105-13 (2015).
- [3] K. Akamatsu, N. Shikazono, T. Saito, *Anal. Biochem.* **536**, 78-89 (2017).

2 - 10 Genome Wide Analysis of Rice Mutants Isolated from Ion-Beam-Mutagenized Population

Y. Oono ^{a)}, H. Ichida ^{b)}, S. Nozawa ^{a)}, R. Morita ^{b)}, H. Kato ^{c)}, T. Abe ^{b)} and Y. Hase ^{a)}

^{a)} Department of Radiation-Applied Biology Research, TARRI, QST,

^{b)} Beam Mutagenesis Group, RIKEN Nishina Center, RIKEN,

^{c)} Radiation Breeding Division, Institute of Crop Science, NARO

Ion beams are recognized as useful mutagens for plant and microbe breeding because they are thought to cause mutations by distinct mechanism from chemical mutagens or gamma rays. The characteristics of the ion-beam-induced mutations were analyzed using a few marker genes; however, little is known about how much extent of mutations are induced by ion beams in a whole genome level. To understand the property of induced mutations at a genomic level, here, we conducted exome analysis of genomic DNA of rice mutants isolated from a carbon ion-beam-mutagenized population.

Rice cultivar Nipponbare (M1 plants) were grown from seeds irradiated with 40 Gy of 320-MeV ¹²C⁶⁺ ions (LET on surface = 76 keV/μm). Subsequently, M2 seeds were harvested from independent M1 plants and sown again on soil to screen morphological mutants in a green house and the paddy field of Radiation Breeding Division of the National Agriculture and Food Research Organization (NARO) [1, 2]. Five independent mutants (2 dwarfs (line A and B) and 3 early heading date mutants (line C-E)) of which phenotype was confirmed in the M3 generation were chosen for the exome analysis. Genomic DNA was extracted from leaves of a single M2 (line A) or M3 (line B-E) plant. The extracted genomic DNA was fragmented, ligated to barcode adapters for Next Generation Sequencing (NGS), and hybridized with custom biotin-labelled oligonucleotide library covering rice exon targets. The hybridized double strand DNA fragments were captured with streptavidin magnetic beads, washed, and amplified by PCR with post capture primers, followed by NGS using Illumina HiSeq. Analysis of NGS data was conducted with the high-performance bioinformatics pipeline for rice exome sequencing [3]. The resulting reads were mapped to the Os-Nipponbare-Reference-IPGSP-1.0 reference sequence. To avoid calling polymorphisms between sequences of the Nipponbare reference in the database and the original Nipponbare line used for the ion-beam mutagenesis in this experiment, all the data of 5 mutant lines were unified, followed by line-specific polymorphisms were extracted.

A total of 56 mutations including 24 single nucleotide variations (SNVs), 28 insertions and deletions (InDels), and 4 others (3 replacements and 1 inversion) were detected in the 5 lines (Table 1). The average number of mutations per line was 11.2±3.3, which was smaller than the number between 70 to 508 obtained by exome analysis of the EMS-mutagenized rice DNA samples [4]. Thirty-eight percent of the total SNVs were G-to-A and

C-to-T (GC > AT) transitions. Another major SNVs were AT > GC transitions, which account for 33% of the total SNVs. Regarding to size of InDels, half of them are 1 bp and most of them except 3 deletions, 46 bp-, 128 bp-, and 33.6K bp-deletions, were less than 10 bp. A large inversion (535K bp) was also detected.

We found 19 mutations that caused deletion of genes or changes in amino acid sequence of proteins. Ten of them were homozygous. Because the average number of such homozygous mutations per line was 2, it could be easy to extrapolate a causal gene responsible for the mutant phenotype. Indeed, we have found strong candidate genes very likely causing the mutant phenotype in the 4 out of the 5 mutants.

Table 1

Number of mutations detected in exome analysis of rice mutants isolated from the ion-beam- mutagenized population.

Line	Number of mutations			
	Total	SNVs	InDels	Others
A	10	3	7	0
B	16	7	9	0
C	9	4	3	2
D	13	7	5	1
E	8	3	4	1
Total	56	24	28	4

Acknowledgments

This work was supported by Cabinet Office, Government of Japan, Cross-ministerial Strategic Innovation Promotion Program (SIP), “Technologies for creating next-generation agriculture, forestry and fisheries” (funding agency: Bio-oriented Technology Research Advancement Institution, NARO). The NGS data analysis was conducted using RIKEN supercomputer system “HOKUSAI GreatWave” under project number Q17208.

References

- [1] Y. Oono *et al.*, QST Takasaki Annu. Rep. 2015, **QST-M-2**, 127 (2017).
- [2] Y. Oono *et al.*, QST Takasaki Annu. Rep. 2016, **QST-M-8**, 93 (2018).
- [3] H. Ichida *et al.*, RIKEN Accel. Prog. Rep., **49**, 254 (2016).
- [4] I. M. Henry *et al.*, Plant Cell, **26**, 1382 (2014).

2 - 11 Mutation Frequency in Flavonoid Genes Under Different Flavonoid Phenotypic Conditions

S. Hirata ^{a, b)}, S. Kitamura ^{b)}, K. Satoh ^{b)}, I. Narumi ^{a)} and Y. Oono ^{b)}

^{a)} Graduate School of Life Sciences, Toyo University,

^{b)} Department of Radiation-Applied Biology Research, TARRI, QST

Ion beams are useful tools to induce mutations in plants and microorganisms and make it possible to produce their valuable varieties. Analyses of ion beams-induced mutants/mutations associating with their producing protocols are necessary to obtain knowledge on relationships between mutagenesis procedures and the resultant mutants/mutations. Previously, we reported an experimental system that can easily detect mutated tissues by visual inspection using two genes required to produce flavonoid pigments. Preliminary experiment using this system indicated that mutation frequencies were remarkably different between the two flavonoid genes [1]. Here, additional experiments were conducted with this system to know the relationships between those mutation frequencies and irradiated conditions.

Our experimental system is based on the loss of heterozygosity (LOH). Flavonoid pigments such as anthocyanins are synthesized *via* single enzymatic pathway in Arabidopsis, and knockout-homozygosity of a gene involved in the pathway results in a flavonoid-less phenotype in seed coat. Immature seeds of *ban* mutant are red, whereas those of *tt4 ban* and *tt8 ban* mutants are transparent. Mature seeds of *tt4 ban* and *tt8 ban* are white yellow and pale-brown to yellow color, respectively, and distinguishable from each other. Therefore, when a F1 hybrid of *tt4 ban* and *tt8 ban* (the genotype is *TT4/tt4 TT8/tt8 ban/ban*) was mutagenized, immature seeds derived from mutated cells of *tt4* or *tt8* could be detected by inspecting the loss of red pigments, and their mature seeds could tell us which gene is mutated. The F1 seeds obtained by crossing were sown on nutrient media, and 1-day-old seedlings were irradiated with 190 MeV carbon ion beams accelerated by an AVF cyclotron at TIARA, TARRI, QST. In this procedure, two sucrose concentration media (0.1 and 2.5%) were used to change flavonoid accumulation patterns (Fig. 1), due to strong activation of *TT4* expression by sucrose [2]. Irradiated seedlings were grown to flowering and immature seed color was observed. If immature seeds without red pigments were found, they were kept growing and the color of the mature seeds was checked.

Result with irradiated and non-irradiated F1 plants is shown in Table 1. In 2,060 plants derived from 0.1% of sucrose media, 15 LOH events were found in immature seeds. Observation of these mature seeds indicated that the seed color of one plant was similar to that of *tt4*, and the seed color of the remaining 14 plants was similar to that of *tt8*. In 2,060 plants from 2.5% sucrose media, *tt8* type phenotype was also more frequently observed than *tt4* type phenotype (Table 1). In control experiments

without irradiation, mutation frequencies of *TT4* and *TT8* were similar to each other among 3283 plants (Table 1).

The results of higher mutation frequency in *TT8* than *TT4* are consistent with those of previous experiment using 220 MeV carbon ion beams [1]. One of the possible reasons of this difference in mutation frequency could be the differences in gene size: *TT4* and *TT8* are 1,789 and 4,643 bp in length, respectively. However, this gene size difference seems to be not enough to explain large difference in mutation frequency observed here. The higher mutation frequency in *TT8* was observed irrespectively of sucrose concentration (Table 1), suggesting that differences in mutation frequency might not be related to gene expression levels. It is known that *tt4* mutation leads a complete flavonoid-less phenotype in all developmental phase including vegetative stage, whereas *tt8* mutation shows no effects in vegetative stage [3]. Therefore, we should consider the possibility that *tt4*-mutated cells might be difficult to survive during vegetative stage by overcoming the competition with surrounding non-mutated cells, resulting in less contribution to seed coat formation. Further analysis in vegetative tissues such as leave would give us hints for biased mutation frequencies observed in this system.

References

- [1] S. Hirata *et al.*, QST Takasaki Annu. Rep. 2016, **QST-M-8**, 94 (2018).
- [2] C. Solfanelli *et al.*, *Plant Physiol.*, **140**, 637 (2006).
- [3] N. Nesi *et al.*, *Plant Cell*, **12**, 1863 (2000).

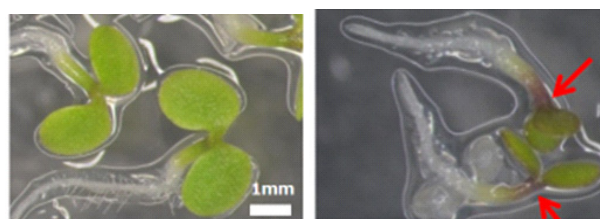


Fig. 1. Seedlings grown on 0.1% (left) and 2.5% (right) sucrose media. Anthocyanins (red arrows) are remarkable in right panel.

Table 1
Screening of *tt* mutations on F1 plant.

Irradiation Dose (Gy)	Sucrose Concentration (%)	Number of F1 plants surveyed	Number of plants with color less seeds		
			Total	<i>tt4</i> type	<i>tt8</i> type
0	0.1	2,051	4	2	2
0	2.5	1,232	2	1	1
20	0.1	2,060	15	1	14
20	2.5	2,152	17	2	15

2 - 12

Mutagenesis of the Oil-producing Algae by Ion Beam Irradiation

H. Araie^{a)}, Y. Hase^{b)}, Y. Iwata^{c)}, Y. Oono^{b)}, I. Suzuki^{d)} and Y. Shiraiwa^{d)}

^{a)} Department of Biosciences, Kanto Gakuin University College of Science and Engineering,

^{b)} Department of Radiation-Applied Biology Research, TARRI, QST,

^{c)} Electronics and Photonics Research Institute, AIST,

^{d)} Faculty of Life and Environmental Sciences, University of Tsukuba

For biofuel production using microalgae, it is necessary to mutate the algae to improve the productivity of biomass or oil contents. In this study, we focused on very-long-alkyl ketones so-called alkenone (Fig. 1) that are thought to be good candidates for biofuels [1]. We selected one of the alkenone-producing haptophytes, *Tisochrysis lutea*, to mutate by heavy ion beam irradiation that is known as a good method to introduce the large-scale rearrangement of the chromosome to obtain useful mutants [2, 3]. In addition, this method is useful since obtained mutants can be applicable in open culture system as a non-GMO.

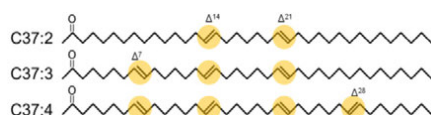


Fig. 1. Alkenone structures. Carbon number of these alkenones are 37 and they have two to four *trans*-type double bonds and keto group at a C2 position.

Previously, we reported dose-dependency of the colony formation after 0–320 Gy of carbon ion irradiations (26.7 MeV/u) (Fig. 2). We screened mutants that showed high alkenone productivity from the irradiated cells. To investigate the effects of the second-round mutagenesis on the mutant, we irradiated carbon ion beams to the high alkenone-producing mutants.

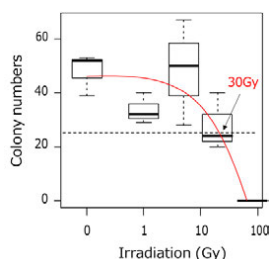


Fig. 2. A boxplot of dose-dependency for colony formation. 150 cells dropped on the plate were irradiated with 0, 1, 5, 20 and 80 Gy. Number of colonies were counted at 7 days after irradiation. Red line: Binomial approximation formula of median, Dotted line: Half line of colony number, Arrow: Dose for half of colony formation.

For screening, we stained neutral lipids, mainly alkenones, with Nile Red (final conc. 1 $\mu\text{g}/\text{mL}$) in the cells cultured for 14 d in a 96-well plate and detected fluorescence of the neutral lipids by a microplate reader (SYNERGY HTX, BioTek). The excitation and emission wavelengths were 485 and 575 nm for detecting neutral

lipids, and 440 and 575 nm to determine the chlorophyll content, respectively. In this experiment, we irradiated 0, 5, 10, 20 and 40 Gy to wild-type cells and 5, 10, 20 and 30 Gy to two of the high alkenone-producing mutants.

As the results of irradiation to the wild-type cells, it was suggested that 30 Gy dose around LD_{50} is suitable to enhance the oil productivity (Fig. 3). The change in the median was small while the variance became large. There was a correlation between lipid content and chlorophyll content. It is suggested that high biomass strains could be obtained by heavy ion beam irradiation. And in the case of irradiation to the high alkenone-producing strains, one strain showed small median and variance (Fig. 4A), but another showed a slight increase of median and variance (Fig. 4B). Figure 4B suggested that it is possible to further improve the productivity of high alkenone-producing strain by the second-round mutagenesis. It looks better to use a lower dose for the second-round irradiation, since the variance was declined at 30 Gy.

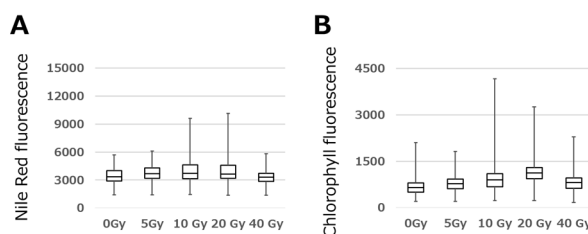


Fig. 3. A boxplot of dose-dependency for Nile Red fluorescence (A) and Chlorophyll fluorescence (B).

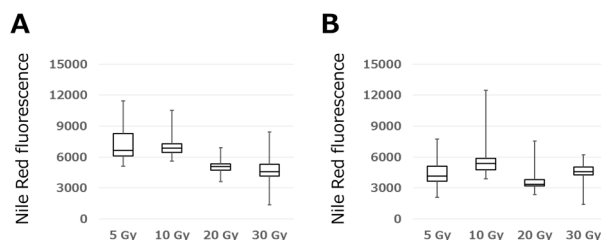


Fig. 4. A boxplot of dose-dependency for Nile Red fluorescence in high alkenone-producing strain C8_38 (A) and C8_45 (B).

References

- [1] G. W. O'Neil *et al.*, Energy Fuels **29**, 922-30 (2015).
- [2] S. Ota *et al.*, Biotechnology for Biofuels **9**, 13 (2016).
- [3] K. Yamada *et al.*, Sci. Rep. **6**, 26327 (2016).

2 - 13 Screening of Root Nodule Bacteria for Salinity Tolerance Using Ion Beams Irradiation

M. Kubota ^{a)}, Y. Maruyama ^{a)}, K. Satoh ^{b)}, Y. Oono ^{b)}, N. Tomooka ^{c)},
N. Ohkama-Ohtsu ^{d)} and T. Yokoyama ^{d)}

^{a)} Graduate school of Agriculture, Tokyo University of Agriculture and Technology,

^{b)} Department of Radiation-Applied Biology Research, TARRI, QST,

^{c)} Genetic Resources Center, National Agriculture and Food Research Organization,

^{d)} Institute of Agriculture, Tokyo University of Agriculture and Technology

Vigna marina is one of wild legumes, which called as Hamaazuki, are distributed at the vicinity of the coast from tropical to sub-tropical regions and *Vigna marina* can grow at 400 mM NaCl condition. Furthermore, we found that the root nodules on *Vigna marina* have a symbiotic relationship with rhizobia that related to the genus *Sinorhizobium* having high stress tolerance (500 mM NaCl, 45 °C, pH 10.5) [1]. Above both symbiotic partners showed extremely high salt tolerance, however, nodulation of *Vigna marina* with *Sinorhizobium* is inhibited by over 80 mM NaCl stress. In this study, to improve symbiotic performance of *Vigna marina* with *Sinorhizobium* under high salt conditions, we attempted to obtain isolates enhancing higher symbiotic performance to *V. marina* under high salt conditions using ion beam mutation breeding based on the previous our study [2].

Sinorhizobium bacterial cells were irradiated with carbon ion-beams (¹²C⁶⁺, 190 MeV, 148.7 keV/μm) accelerated by an AVF cyclotron at TIARA, TARRI, QST. The optimum irradiation dose of the carbon ion beam to obtain survival ratio at 0.01% in *Sinorhizobium* cells was the 100 Gy. The cell suspensions (10 μL) were transferred to YMB (Yeast Mannitol Broth: 0.05% yeast extract, 0.5% mannitol, 0.05% K₂PO₄, 0.02% MgSO₄, 0.01% NaCl; pH 6.8) and incubated for 4 days. Germinated seeds of *V. marina* were inoculated by the bacterial culture and growth under 80 mM NaCl condition. The cultivation was for 30 days. After cultivation, fresh weight, dry weight, nodule number and acetylene reduction activity (ARA) were measured.

The results showed a difference in growth of shoot and in nodulation activity between wild-type (WT) and mutant strain at 20 days which was irradiated with ion beams (Fig. 1). After *V. marina* was inoculated with irradiated-mutant strain, several root nodules were observed and confirmed under 80 mM NaCl. At 30 days, ARA was recorded as the nitrogen fixation activity. The WT and ion beam-irradiated mutant strain showed different levels of nitrogen fixation activities under the high salt conditions (Fig. 2). The significant result was shown by ion beam irradiation mutant strain. This strain showed increases of nitrogen fixing activities compared with WT.

According to the results, the mutation breeding method of *Sinorhizobium* by irradiation ion beams was successfully to create salt-tolerant mutants enhancing activities of root nodulation and nitrogen fixation under salinity stress.

Regarding to know the mode of the actions of the phenomenon, we need further tests.

References

- [1] N. Tomooka *et al.*, Proc. 14th NIAS Int. Workshop Genetic Resources, 11 (2011).
[2] K. Takeda *et al.*, JAEA Takasaki Annu. Rep. 2012, JAEA-Review 2013-059, 114 (2014).

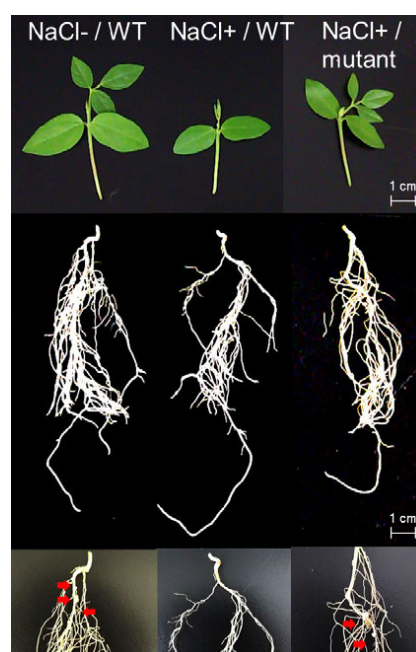


Fig. 1. Nodulation activity at 20 days. Arrows indicate root nodules.

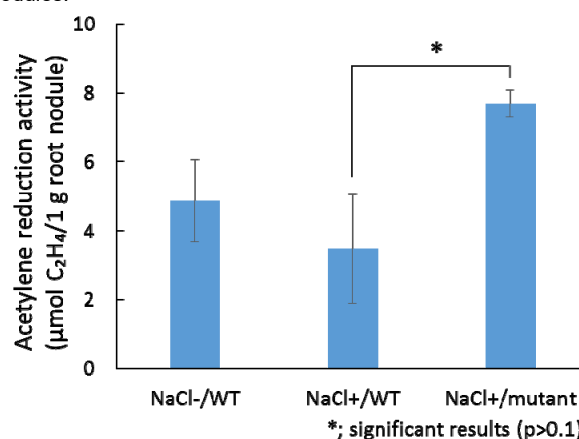


Fig. 2. Nitrogen fixation activity at 30 days.

2 - 14 Ion Beam Breeding of Rice for the Mutation Breeding Project of the Forum for Nuclear Cooperation in Asia (FNCA)

Y. Hase ^{a)}, A. Tanaka ^{b)}, S. Nozawa ^{c)}, Y. Oono ^{a)}, A. Koike ^{d)} and A. Takano ^{d)}

^{a)} Department of Radiation-Applied Biology Research, TARRI, QST,

^{b)} Takasaki Advanced Radiation Research Institute (TARRI), QST,

^{c)} Research Planning and Promotion Office, QuBS, QST,

^{d)} Nuclear Safety Research Association

The Forum for Nuclear Cooperation in Asia (FNCA) is a framework for the peaceful use of atomic energy led by the Cabinet Office/ MEXT of the government of Japan. At present, ten countries are engaged in the project 'Mutation Breeding of Rice for Sustainable Agriculture (2013-2017)' under the Mutation Breeding Project of the FNCA. Ion beams from TIARA AVF cyclotron have been utilized in several countries to mutagenize rice seeds that meet the demands of the participating countries [1].

As this is the final year of the ongoing project, progress and achievement in each country were summarized at the workshop held in Korea in October 2017. The representative achievement related to the use of ion beams are three new rice varieties released in Bangladesh (BINAdhan-14, -18 and -19). The BINAdhan-14 is an early maturing and high yielding variety, which was already described in the previous report [1]. The BINAdhan-18 is a high-yielding variety suitable for irrigated cultivation in Boro season (from winter to spring). This variety matures around 2 weeks earlier than parental variety BRRIdhan-29 (Fig. 1). The BINAdhan-19 is derived from NERICA (New Rice for Africa) variety NERICA-10. The NERICA is an interspecific hybrid between Asian rice (*Oryza sativa*) and African rice (*O. glaberrima*). Therefore, BINAdhan-19 is highly drought tolerant, as is the NERICA-10. In addition, BINAdhan-19 has shorter plant height, matures earlier and gives higher yield compared to the parental variety. The BINAdhan-19 can be grown under rain-fed condition following direct seeding in Aus and Aman season (from spring to summer, and summer to winter, respectively). In recent years, arsenic contamination of underground water is becoming a severe problem in Bangladesh. Although the yield is not very high compared to the modern high-yielding varieties, the BINAdhan-19 can be grown even in the drought prone or hilly area, and therefore it is expected to contribute to the sustainable agriculture. These results also demonstrate that early maturity and short plant height are reasonable targets that can be achieved by ion beam breeding, and these improvements often result in the increase of the yield.

The all participating countries confirmed that low-input sustainable agriculture is the most important theme in the future under dramatic climate changes such as droughts, floods and significant increase in temperature. They also agreed to start another five-year project entitled 'Mutation

Breeding of Major Crops for Low-input Sustainable Agriculture under Climate Change (2018-2022)'. The current project focus on rice breeding, while in the next five-year project, major crops in each country such as soybean and wheat will also be covered. In order to prepare the mutant population for the next project, soybean seeds from Vietnam, wheat seeds from Mongolia, rice seeds of local sticky variety from Korea, and rice seeds of salt-tolerant local landrace from Bangladesh were irradiated with 190 MeV carbon ions (LET: 149 keV/ μ m) or 63 MeV helium ions (29 keV/ μ m) in the appropriate dose range. Those seeds will be cultivated to prepare mutant population from spring 2018 for further screening of promising mutant lines to cope with global climate change and environmental destruction.

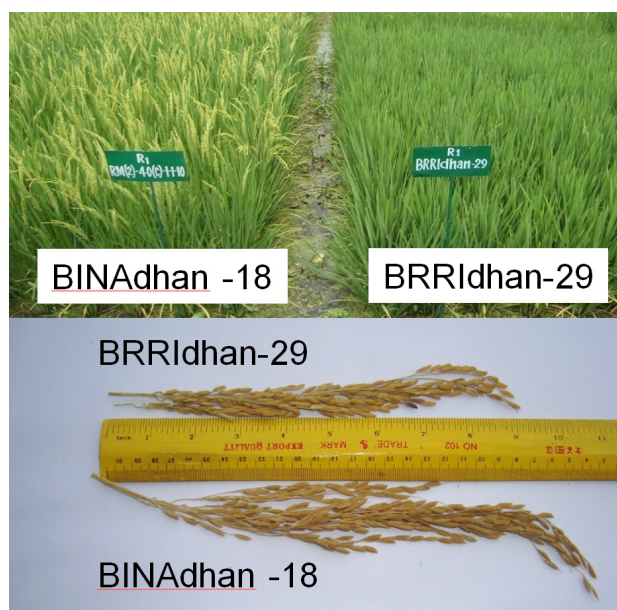


Fig. 1. The new variety Binadhan-18 and the parental variety BRRIdhan-29. The BINadhan-18 matures earlier and has longer panicles than the parental variety.

Reference

- [1] A. Tanaka *et al.*, QST Takasaki Annu. Rep. 2016, **QST-M-8**, 99 (2018).

2 - 15 The Moss *Physcomitrella patens* Is Hyperresistant to DNA Double-strand Breaks Induced by Ionizing Radiation

Y. Yokota, N. Murakami, Y. Oono and A. N. Sakamoto

Department of Radiation-Applied Biology Research, TARRI, QST

Organisms show diverse radiosensitivity in a broad range. Terrestrial plants are often hyperresistant to ionizing radiation and thus are expected to have distinctive genome maintenance strategies [1]. Ionizing radiation induces various types of DNA damage. Among them, double-strand breaks (DSBs) are the most serious biologically. We previously compared DSB induction rates immediately after gamma-ray irradiation between *Nicotiana tabacum* cells and Chinese hamster cells, and reported that the induction rate per DNA per Gy in the former was only one-third of the latter [2]. The moss *Physcomitrella patens* is an ideal model plant because of available genome information, easy protoplast culture, and feasible genome editing. In this study, we analyze the relationship between radiosensitivity and DSB induction rate of *P. patens*.

Protonemata of the moss *P. patens* were disrupted with a homogenizer and subcultured weekly. Protoplasts were isolated from the protonemata in enzyme solution including Macerozyme R-200 and Cellulase Onozuka RS, and were irradiated with gamma-rays at the Cobalt 60 Irradiation Facilities. Irradiated protoplasts were cultured for 2-3 weeks to be formed visible colonies. The numbers of colonies were counted to obtain the survival rates after irradiation. In addition, pulsed-field gel electrophoresis (PFGE) assay was performed to evaluate the DSB induction rate as previously described [2].

Survival rates of the moss protoplasts were reduced in dose-dependent manners (Fig. 1). The 50% lethal dose (LD₅₀) of gamma-rays was 277 Gy, which indicated that the moss cells were prominently more radioresistant than mammalian cells. To investigate the mechanism of hyper-radioresistance found in the moss, the DSB induction rate was measured by the PFGE assay immediately after irradiation. Fractions of genomic DNA smaller than 1.6 Mb, defined as threshold size to detect radiation-induced DNA fragmentation, increased in dose-dependent manner (Fig. 2A). Radiation-induced DSBs per Gb DNA linearly increased with increasing dose (Fig. 2B). The slope of the regression line indicated that the DSB induction rate was 2.2 per Gb DNA per Gy. The rate in *P. patens* was half to one-third of those reported in mammals and yeasts (Table 1), indicating that DSBs are avoided to produce in the moss. Moss protonemata possess 511 Mb DNA in each cell. DSB induction rate per cell per LD₅₀ dose in *P. patens* was thus calculated to be 311, which is three- to six-times higher than those in mammals and yeasts. The moss is predicted to possess unidentified mechanism to inhibit DSB induction and provide resistance to high number of DSBs.

References

- [1] Y. Yokota *et al.*, Int. J. Radiat. Biol. **79**, 681 (2003).
- [2] Y. Yokota *et al.*, Radiat. Res. **163**, 520 (2005).
- [3] Y. Yokota *et al.*, Genes **9**, 76 (2018).
- [4] K. M. Prise *et al.*, Int. J. Radiat. Biol. **74**, 173 (1998).

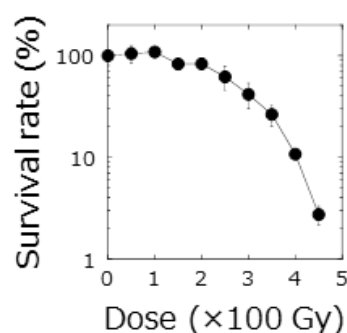


Fig. 1. Survival curve of the moss protoplasts irradiated with gamma-rays. The data represent mean \pm SE of 3 independent experiments.

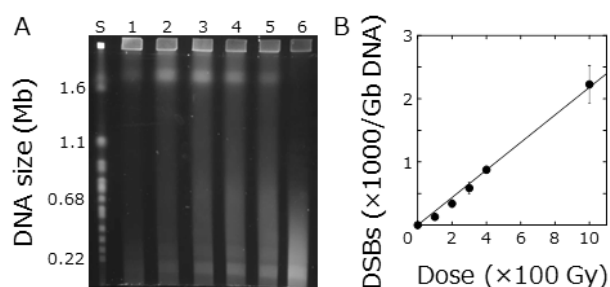


Fig. 2. DSB induction in gamma-ray-irradiated *P. patens* cells. **A.** A typical image of PFGE. Lane S is size standards. Lanes 1-6 are genome DNA extracted from *P. patens* cells irradiated at 0, 100, 200, 300, 400 and 1000 Gy, respectively. **B.** Relationship between the DSB induction rate and dose. The data represent mean \pm SE of 3 independent experiments.

Table 1

DSB induction rates in the moss *P. patens*, Chinese hamster and yeast.

Organism	DSB induction rate	
	/Gb DNA/Gy	/cell/LD ₅₀
Moss	2.2	311
Chinese hamster	6.6 [2]	99 [3]
Yeast	5.4 [4]	52 [3]

Numbers in square brackets indicate references.

2 - 16 Evaluation of Particle Fluence of Cluster and Monomer Ion Beams Using a Solid-state Track Detector

Y. Hase^{a)}, K. Satoh^{a)}, A. Chiba^{b)} and Y. Hirano^{b)}

^{a)}Department of Radiation-Applied Biology Research, TARRI, QST,

^{b)}Department of Advanced Radiation Technology, TARRI, QST

The cluster ion-specific irradiation effects have been observed in the analysis of ion-material interaction due to their unique feature such as very high-density energy deposition [1]. The cluster ion beams may also cause a unique irradiation effects in biological samples, however, hardly applied so far. This study is aimed to establish an irradiation method of cluster ions for bacteria and investigate the cluster ion-specific effects by comparing the irradiation effects of cluster and monomer ion beams.

The results of preliminary experiments suggested that the cluster ion beams were slightly less effective per particle on the survival reduction than monomer ion beams [2]. However, this is quite unlikely, because twice or more number of atoms per particle are bombarded in case of cluster ion beams compared to monomer ion beams. One possible reason is an inaccurate measurement of the beam current using a Faraday cup due to high emission of secondary charged particles by cluster ion beams [3]. In order to evaluate the accuracy of the measurement of beam current using a Faraday cup, we measured the particle fluence using a solid-state track detector.

The ion beams used here are 2 MeV C, 4 MeV C₂ and 6 MeV C₃. The beam size was 5 mm ϕ and the beam current was adjusted to 1.0 pA by the Faraday cup equipped in the irradiation chamber at the Tandem C (TC) beam line. The 1/100 attenuator was used to attenuate the beam current. A solid-state track detector (Baryotrack, Nagase Landauer, Ltd.) was irradiated with the fluence of 1.5×10^6 particles/cm² using a specially designed operating software. The irradiation time was around 3 seconds. The track detector was etched with 6 M KOH solution at 60 °C for 50 minutes. The etch-pit image was captured by a CCD camera under a microscope and the number of etch-pit per a captured area (0.169 \times 0.225 mm) was counted using the Image J software package. Ten areas were measured for each irradiated spot.

Table 1 shows the particle fluence observed in three independent experiments. The 4 MeV C₂ and 6 MeV C₃ showed 20~33% less fluence compared to 2 MeV C in the first and second experiment. However, the equivalent fluences were observed in the third experiment in both cluster and monomer ion beams. This result suggests that the attenuation by 1/100 attenuator is not reproducible between different ion species and experimental days.

In order to attain the accurate attenuation for the measurement of particle fluence, a rotating disk device with a 250- μ m laser-processed micro slit was fabricated. The rotating disk was installed into the beam line and rotated at 50 Hz to attenuate the beam current. The calculated attenuation rate is 1/1,000. We performed the same

measurement except that the irradiation time was around 30 seconds for the irradiation using the rotating disk device. Again, the attenuation with 1/100 attenuator was not stable between the ion species (Table 2). In contrast, even though conducted on the same day, equivalent particle fluences were observed when the rotating disk device was used. These results suggest that the measurement of beam current with the Faraday cup equipped in the TC line is accurate with the possible errors of 3~4% in both cluster and monomer ion beams. Since the 1/100 attenuator was not used for the irradiation of bacterial samples, the reason for the difference of cell killing effect between cluster and monomer ion beams is still unclear. Further experiments are necessary to confirm the reproducibility of the results.

Table 1
Particle fluence of monomer and cluster ion beams measured by a solid-state track detector in three independent experiments.

	2 MeV C	4 MeV C ₂	6 MeV C ₃
Exp. 1	1.88 \pm 0.17	1.47 \pm 0.07 (-22%)	1.50 \pm 0.07 (-20%)
Exp. 2	2.04 \pm 0.35	1.42 \pm 0.06 (-30%)	1.37 \pm 0.09 (-33%)
Exp. 3	1.34 \pm 0.32	1.34 \pm 0.06 (\pm 0%)	1.40 \pm 0.06 (+4%)

Values are mean \pm SD ($\times 10^6$ particles/cm², n = 60)
Values in parenthesis indicate the increase or decrease rate compared to the value of 2 MeV C in each experiment.
1/100 attenuator was used to attenuate the beam current.

Table 2
Particle fluence measured by a solid-state track detector using different beam attenuation method.

	2 MeV C	4 MeV C ₂	6 MeV C ₃
1/100 Attenuator	1.65 \pm 0.46	1.29 \pm 0.07 (-22%)	1.45 \pm 0.05 (-12%)
Rotating disk device	1.56 \pm 0.21	1.61 \pm 0.08 (+3%)	1.62 \pm 0.07 (+4%)

Values are mean \pm SD ($\times 10^6$ particles/cm², n \geq 10)
Values in parenthesis indicate the increase or decrease rate compared to the value of 2 MeV C in each measurement.

References

- [1] A. Chiba *et al.*, Nucl. Instrum. Meth. Phys. Res. B, **315**, 81-84 (2013).
- [2] Y. Hase *et al.*, QST Takasaki Annu. Rep. 2016, **QST-M-8**, 103 (2018).
- [3] K. Hirata *et al.*, Appl. Phys. Lett. **86**, 044105 (2005).

2 - 17 Induction of Chromosomal Aberrations in *Albuca virens* ($2n=6$, Hyacinthaceae) via Ion Beam Irradiation

S. Nishitani ^{a)}, K. Honda ^{b)} and S. Nozawa ^{c)}

^{a)} Osaka Prefectural Minoo-Higashi High School,

^{b)} Faculty of Agriculture & Life Science, Hirosaki University,

^{c)} Research Planning and Promotion Office, QuBS, QST

The low chromosome number of *Albuca virens* (syn. *Ornithogalum virens*) makes this species an ideal model for cytological assessments among students. However, the associated limitation is that three pairs of homologous chromosomes are very similar to each other (Fig. 1). We intended to generate new karyotype strains of *A. virens* suitable for middle- or higher-level education as a teaching material for cytological laboratory exercises.

The small bulbs ($\phi 10\text{mm}$) of clone "2009A" derived from one seedling were used for ion beam irradiation experiments. Ten bulbs each were exposed to total doses of 0, 0.5, 1, 2, 5, and 10 Gy of 100 MeV $^4\text{He}^{2+}$ beams from the AVF cyclotron in TIARA at QST. The irradiated bulbs were transplanted to adequate culture soil and sprouting new adventitious roots were collected for cytological analysis. Chromosome preparations from root tips were conducted by squashing or enzymatic maceration/air-drying (EMA) method, followed by Giemsa staining.

While all irradiated bulbs were survived, the plant height decreased significantly upon irradiation exceeding 2 Gy after one month (data not shown). Chromosomal aberrations were detected upon irradiation of only 1 and 5 Gy.

The Robertsonian fusion between Chromosome No.1 and No. 2 accompanied with partial loss of Chromosome No.2, was observed upon irradiation at 5 Gy (20% (2/10), Fig. 2a, b). One root tip consisted of aberrant cells with one small fragment chromosome. The percentage of cells with one small fragment chromosome varied in root tips observed (93% (28/30) and 50% (10/20), respectively).

The simple translocation between Chromosome No.2 and No.3 was observed in 1 Gy exposed section (10% (1/10 plants), Fig. 3a, b). Normal and translocated chromosomes were observed as chimera in the same root tip. Approximately one-third of the observed cells (32.7% (32/98)) contained translocated chromosomes.

The aforementioned chromosomal aberrations were chimeric within the bulb and were finally excluded owing to the dominant growth of normal cells. This study shows that ion beam irradiation to bulbs of *A. virens* effectively induces chromosomal aberrations; hence, it is necessary to strategize the protocol to obtain fixed new karyological strains.

References

- [1] P. P. Jauhar *et al.*, *J. Hered.* **73**, 243 (1982).
 [2] P. Goldblatt *et al.*, *South African J. Bot.* **77**, 581 (2011).

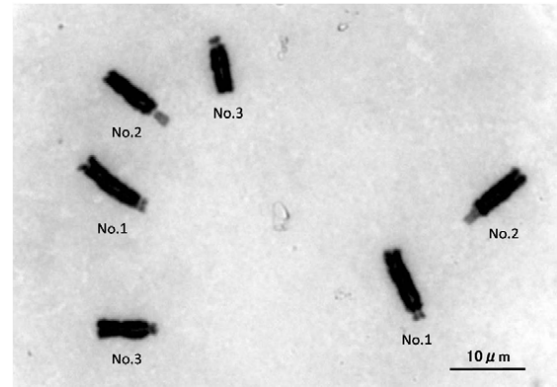


Fig. 1. Metaphase chromosomes of *A. virens* ($2n=6$). Three pairs of homologous chromosomes resemble each other. They are named No.1, No.2 and No.3 in order of length. Chromosome No.2 is SAT (Sine Acido Thymonucleinic) chromosome.

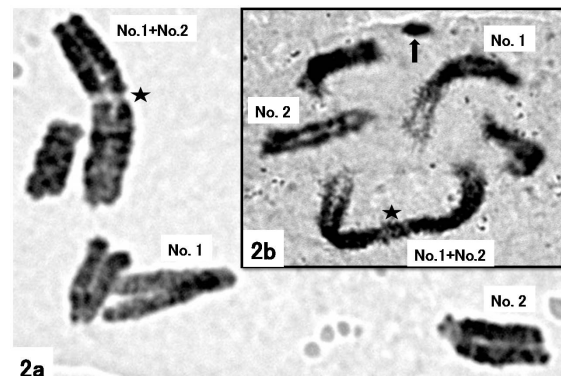


Fig. 2. A robertsonian fusion chromosome between chromosome No.1 and No.2 in 5 Gy exposed section without (2a) or with (2b) a fragment of chromosome No.2 (arrow). The asterisks indicate the fusion position of the chromosomes.

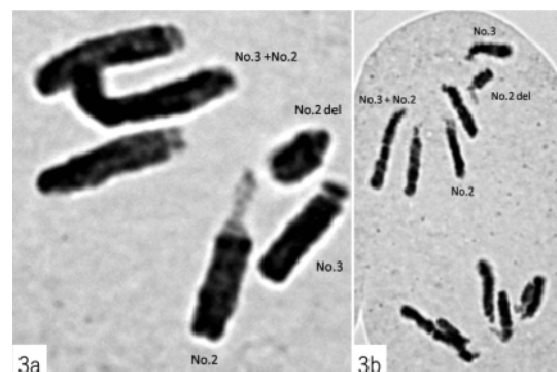


Fig. 3. The simple translocation between Chromosome No.2 and No.3 detected upon irradiation of 1 Gy. Metaphase (3a) and anaphase (3b). "Del's" indicate the partial deletions of chromosome No.2.

2 - 18 Improvement of Cut Flower Weight of Autumn-flowering Spray Chrysanthemum 'Kyura Syusa'

M. Tamari^{a)}, T. Minami^{a)}, F. Tojima^{a)} and Y. Hase^{b)}

^{a)} Kagoshima Prefectural Institute for Agricultural Development,
^{b)} Department of Radiation-Applied Biology Research, TARRI, QST

In order to improve the cut flower weight of autumn-flowering spray chrysanthemum variety 'Kyura Syusa', 6,240 regenerated plants derived from carbon-ion irradiated leaf cultures were screened. We selected 30 plants that showed good growth and early flowering trait. All of the selected plants had higher cut flower weight than that of control plants. The selected plants will be further examined in winter 2018 to confirm the cut flower weight and other agricultural traits.

2016年に品種登録された「きゅらシューサー」は、交配によって作出された純白色の鹿児島県育成スプレーギクである。商品性が高く草丈伸長性に優れ、夏場の南西諸島でも採穂が良好であることから沖永良部地区を中心に急速に栽培が増加している。しかし低温期の栽培では開花が遅れるなどの改善点があり 2015年から低温開花性を付与した変異体育成に取り組んできた[1]。一方、我々は秋輪ギク「神馬」へのイオンビーム照射により、無側枝性が強くなるとともに茎葉のボリュームが向上した「新神」を選抜した事例がある[2]。この事例を元に、2017年からイオンビーム照射による変異誘発により、開花が早く切り花重が重い個体の選抜を開始した。

葉片(2 mm × 4 mm)からの不定芽再生系を用い[1]、置床1週間後の「きゅらシューサー」の葉片に320 MeV炭素イオンを照射し、再生個体を得た。順化・発根させた個体をビニールハウスで40日間母株養成した。定植苗の開花反応を揃えるため、採穂した穂は5℃の冷蔵庫で2週間冷蔵後に挿し芽し、発根した苗を再び5℃の冷蔵庫で2週間冷蔵した。2017年9月29日に農業開発総合センター花き部(指宿市)のガラス温室2棟に、12月開花作型で6,240個体を定植した。定植から10月18日まで暗期中断5時間の電照(栄養成長期間19日間)を行った。葉片培養を経ない通常苗を対照区とした。

今回の作型において対照区(通常苗)の平均到花日数は62日であった。定植した6,240個体から到花日数が61日より早く、生育良好な30個体を選抜した(Table 1)。選抜個体の85 cm切り花重は、いずれも対照区の平均的な切り花重を上回っていた。また、同一ハウス内で栽培した5,700個体について到花日数別個体割合を調査した。61日より早く開花した個体割合は、0 Gyで14.4%、1 Gyで16.1%、2 Gyで17.1%、3 Gyで18.0%であった(Table 2)。また70日までに開花しなかった個体は照射区で増加しており、到花日数の長短に有意差は認められないものの、開花期の分散が見られた。

1次選抜した30個体は、2018年12月系統選抜試験で他の低温開花性選抜系統と併せて切り花重および早期開花性を確認し選抜を図る。早期開花性と切り花重の向上により、全国で広く栽培できる白系秋スプレーギク品種の選抜を目指す。

References

[1] Tamari *et al.*, QST Takasaki Annu. Rep. 2016, QST-M-8, 98 (2018).

[2] Ueno *et al.*, JAEA Takasaki Annu. Rep., 2003, 53-55 (2004).

Table 1. Characteristics of selected plants.

Selected plant	Dose (Gy)	Days to flowering	Plant height (cm)	Number of primary flowers	85-cm cut flower weight (g)
B29SY-1	0	58	109	15	72
B29SY-2	1	54	92	14	62
B29SY-3	1	54	93	15	95
B29SY-4	1	56	104	13	70
B29SY-5	1	57	105	15	84
B29SY-6	1	57	110	13	70
B29SY-7	1	57	112	16	79
B29SY-8	1	58	106	14	70
B29SY-9	1	59	100	12	61
B29SY-10	1	59	104	16	71
B29SY-11	1	59	105	12	63
B29SY-12	1	59	106	12	65
B29SY-13	1	59	108	13	57
B29SY-14	1	60	103	11	59
B29SY-15	2	53	105	18	92
B29SY-16	2	55	106	15	70
B29SY-17	2	56	115	17	81
B29SY-18	2	58	91	16	88
B29SY-19	2	58	102	13	76
B29SY-20	2	58	103	14	76
B29SY-21	2	58	103	17	76
B29SY-22	2	58	106	11	61
B29SY-23	2	58	109	17	72
B29SY-24	2	58	109	14	76
B29SY-25	2	58	117	13	73
B29SY-26	3	53	106	16	78
B29SY-27	3	54	102	19	82
B29SY-28	3	55	102	18	82
B29SY-29	3	57	115	15	68
B29SY-30	3	60	112	18	73
Control (n=2)	-	62	116	12	51

Table 2. Distribution of the days to flowering.

Dose (Gy)	No. of plants examined	53-56 days	56-57 days	58-61 days	62-66 days	67-70 days	> 71 days*
0	180	0 (0%)	4 (2.2%)	22 (12.2%)	52 (28.9%)	81 (45.0%)	21 (11.7%)
1	2,460	1 (0%)	34 (1.4%)	359 (14.6%)	543 (22.1%)	961 (39.1%)	562 (22.8%)
2	1,740	8 (0.5%)	33 (1.9%)	257 (14.8%)	283 (16.3%)	705 (40.5%)	454 (26.1%)
3	1,320	11 (0.8%)	21 (1.6%)	205 (15.5%)	240 (18.2%)	531 (40.2%)	312 (23.6%)
Total	5,700						

Numbers in parenthesis represent the percentage of total.

* Plants that did not flowered are included.

2 - 19 Development of New Strains with Sporeless Mutation in Mushrooms Using Ion Beam Irradiation

M. Ishikawa ^{a)}, M. Kasai ^{a)}, Y. Hase ^{b)}, S. Nozawa ^{c)} and K. Ouchi ^{a)}

^{a)} Mushroom Research Laboratory, Hokuto Corporation,

^{b)} Department of Radiation-Applied Biology Research, TARRI, QST,

^{c)} Research Planning and Promotion Office, QuBS, QST

To develop novel strains of sporeless mutants, protoplasts derived from a commercial strain of *Pleurotus* sp. were irradiated with 320 MeV of carbon ion beam. As a result, three sporeless mutants were obtained with the dose of 40 Gy, 80 Gy and 160 Gy. In addition, nine other mutants with different traits such as pileus color from the original strain were obtained. Morphological and cultivation characteristics of these mutants suggested that 20 Gy or 40 Gy were thought to be adequate for developing sporeless mutants with sufficient quality for commercial use.

きのこの孢子飛散が引き起こす様々な問題を解決するため、イオンビーム照射により無孢子性品種を開発し実用化することを目的とした。孢子飛散量の多いヒラタケ属品種「HOX 1 号」[1]を供試体とし、無孢子性変異のスクリーニングおよび照射線量の検討を行った。

「HOX 1 号」子実体からプロトプラストを取得し、 1.0×10^4 個/mL に調製した。寒天培地に塗布し、カプトンフィルムで密封した。その後高崎量子応用研究所の AVF サイクロトロンにより発生させたイオンビーム ($^{12}\text{C}^{6+}$, 320 MeV) を 5 Gy-160 Gy の範囲で計 3 回の照射実験を行った。培地ごとに再生したコロニーを計数し、イオンビーム無照射培地における再生コロニー数に対する照射培地のコロニー数から生存率を算出した。再生コロニーを分離して子実体を発生させ、傘を黒紙上に置いて 20 °C で一晚静置した後、孢子落下の有無を目視で確認した。孢子落下がみられない、あるいは「HOX 1 号」よりも孢子落下量が少ない菌株については栽培試験を反復し、孢子落下量の再現性が確認できたものを無孢子性変異体とした。また、無孢子性変異以外にも、栽培試験の過程において「HOX 1 号」と比べて明らかに形質に変化があった菌株や、菌糸生長不良や栽培工程で不都合な形質がみられた菌株も、変異体とみなし、変異率を算出した。

5 Gy から 160 Gy の線量で照射したところ、線量の増加に伴い生存率の低下が見られた (Fig. 1A, Table 1)。一方で、線量の増加に伴い変異率は増加し、菌糸生長不良や子実体生育不良を伴う菌株が多く見られた (Fig. 1B, Table 1)。計 3 回の照射実験から取得した 1179 株を栽培したところ、目的とする無孢子性変異体は 40 Gy、80 Gy、160 Gy 照射区でそれぞれ 1 株ずつ得られた (Fig. 2)。しかし、いずれの変異体も子実体の形態が「HOX 1 号」とは異なり、さらに子実体の生育も遅かった。実用品種を得るには、孢子形成に關与する遺伝子の変異が生じるような線量で照射する必要があるが、これらの 3 株では子実体の形態および栽培性に関する遺伝子にも変異が生じた可能性がある。本研究では、無孢子性以外にも傘色等に関する変異体が 9 株得られたが、このうち 80 Gy、160 Gy 照射区で得られた 3 株は全て菌糸生長不良や子実体生育不良といった不良形質を伴っていた。一方で、20 Gy、40 Gy 照射区で得た 6 株のうち 4 株は不良形質を伴うことなく、傘色または傘模様の変異が見られた。これらの 4 株では傘色または傘模様に関する遺伝子の変異が生じた可能性が高いため、この線量で照射実験を重ねることで不良形質を伴わない無孢子性変異体の取

得も可能であると考えられた。

以上の結果より、20 Gy、40 Gy が実用的な変異体獲得に適していることが明らかになった。

Reference

[1] 石川ら, 日本きのこ学会誌, **24**(1), 7-15 (2016).

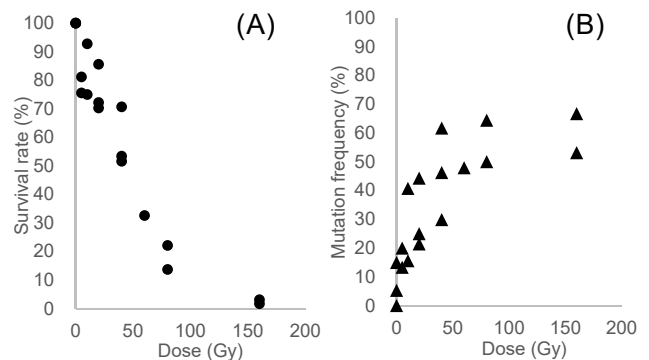


Fig. 1. Effects of ion beam irradiation on (A) survival rate of HOX 1 protoplasts and (B) induction of mutation.

Table 1

Effects of ion beam irradiation on protoplasts survival and induction of mutation.

Dose (Gy)	Experiment No.1		Experiment No.2		Experiment No.3	
	Survival rate (%)	Mutation frequency (%)	Survival rate (%)	Mutation frequency (%)	Survival rate (%)	Mutation frequency (%)
0	100.0	15.0	100.0	5.3	100.0	0.0
5	75.6	20.0	81.2	13.3		
10	75.0	40.7	92.8	15.6		
20	72.2	44.3	85.6	25.0	70.3	21.4
40	51.6	61.7	70.7	29.9	53.4	46.2
60			32.6	47.9		
80	13.7	64.4	22.1	50.0		
160	3.1	53.1	1.7	66.7		



Fig. 2. Fruit bodies and spore prints of HOX 1 and sporeless mutants obtained by ion beam irradiation with the dose of 40 Gy, 80 Gy and 160 Gy.

2 - 20 Breeding of Non-Urea Producing Gunma KAZE Yeasts Which Are Suitable for Export

T. Watanabe ^{a)}, K. Satoh ^{b)}, Y. Oono ^{b)}, H. Hayashi ^{c)} and T. Masubuchi ^{a)}

^{a)} Gunma Industrial Technology Center,

^{b)} Department of Radiation-Applied Biology Research, TARRI, QST,

^{c)} Faculty of Engineering, Maebashi Institute of Technology

Urea is a main precursor in Japanese sake of ethyl carbamate which is classified the group 2A “probably the cause of cancer” by International Agency for Research on Cancer. Therefore, it is considered that the countries regulating volume of ethyl carbamate in Japanese sake would be increased. The purpose of this study was to reduce the volume of ethyl carbamate in Japanese sake, we attempted to breed Gunma KAZE yeasts that do not produce urea. In this year, we obtained some candidates of non-urea producing mutants from KAZE2 by natural mutation and ion-beam irradiation mutagenesis. We also demonstrated laboratory scale sake brewing experiment using 200 g of total rice.

In the yeast cells, arginine (Arg) is hydrolyzed to ornithine (Orn) and urea by arginase. Thus, researchers had used canavanine, analog of Arg, to obtain Arg transporter or arginase inactivate mutants. Kitamoto *et al.* reports that non-urea producing yeasts can be isolated from CAO medium containing canavanine, Arg, and Orn [1]. The arginase-inactivated mutants, as non-urea producing mutants, grow on Orn medium, but not on Arg medium [1]. The merit of this method is candidates can be obtained without mutagenesis treatment. However, in the previous report, the growth of KAZE2 in CAO medium could not be suppressed [2].

Thus, we first tried to suppress growth of false-positive colonies of KAZE2. After several modifications with methods of pre-incubation and concentrations of CAO medium, we obtained 4 candidates from 400 plates without mutagenesis treatment (Table 1). This natural mutation efficiency was about 1/430 times lower than that of Kyokai no. 9, a parent strain of KAZE2 [1]. Then, we demonstrated ion-beam irradiation as described previously [2]. After freeze-dried treatment, cells were irradiated with carbon ion beams (¹²C⁵⁺, 220 MeV, 75-200 Gy) accelerated by the AVF cyclotron at TIARA, TARRI, QST. The efficiencies were increased over 7 times compared with the natural mutation (Table 1).

From these 89 candidates, 50 arginase-inactivated mutants were selected as non-urea producing mutants. Fermentation experiments in liquid medium revealed that only 8 candidates produced ethanol as rapid as KAZE2 did. Thus, laboratory scale sake brewing experiment was performed using 200 g of total rice. Natural mutants (NM-1 and NM-3) brewed slower than KAZE2 did (Fig. 1). On the other hand, most of ion-beam irradiation mutants brew as rapid as KAZE2 did. KAZE2 produced 4.9 mg/L of urea in sake brewing (Table 2). Without 75Gy-6, no urea was detected in sake brewing using each candidate (Table 2).

The fermentation profiles of 100Gy-5 and 100Gy-7 were virtually the same as that of parent strain KAZE2 (Table 2).

In this study, we isolated non-urea producing yeasts from Gunma KAZE yeast, KAZE2 in order to reduce ethyl carbamate in Japanese sake. Ion-beam irradiation so much contributed to isolate canavanine resistant mutants from KAZE2.

Table 1

Efficiency of obtained candidates with each absorbed dose.

Absorbed dose (Gy)	Plate no.	Candidates	Efficiency
-	400	4	0.01
75	280	50	0.18
100	140	19	0.14
125	40	3	0.08
150	40	5	0.13
200	40	8	0.20

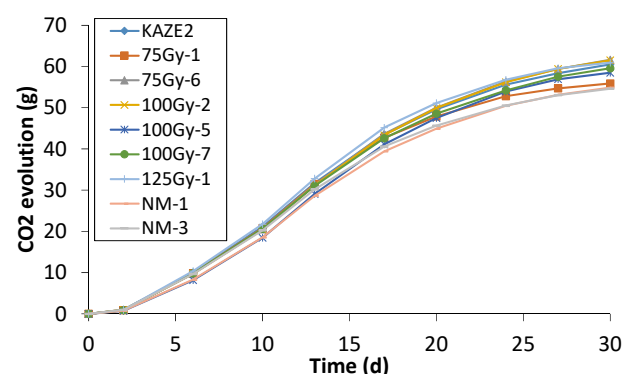


Fig. 1. Time course of CO₂ evolution.

Table 2

Summary of laboratory sake brewing experiments.

	Urea (mg/L)	Ethyl Caproate (mg/L)	Acidity	Alcohol (%)	Sensory Score
KAZE2	4.9	6.8	2.7	18.2	2.9
75Gy-1	ND	7.1	2.8	16.9	3.0
75Gy-6	2.8	2.7	2.6	18.7	4.1
100Gy-2	ND	2.6	2.8	18.3	3.2
100Gy-5	ND	7.2	2.7	17.6	2.8
100Gy-7	ND	8.1	2.9	18.1	2.8
125Gy-1	ND	6.9	2.7	18.4	3.3
NM-1	ND	13.3	3.0	16.6	3.2
NM-3	ND	14.7	2.9	16.6	3.6

ND: not detected

References

- [1] K. Kitamoto *et al.*, J. Brewing Soc. Jpn., **87**, 598 (1992).
- [2] T. Masubuchi *et al.*, QST Takasaki Annu. Rep. 2016, **QST-M-8**, 107 (2018).

Effect of Ion-Beam Irradiation on the Sensitivity of Oleaginous Yeast *Lipomyces starkeyi* Against Fatty Acid Synthesis-Inhibitor Cerulenin

P. Kahar^{a)}, A. B. Juanssilfero^{b)}, K. Satoh^{c)}, Y. Oono^{c)}, A. Kondo^{a, b)} and C. Ogino^{b)}

^{a)} Graduate School of Science, Technology and Innovation (STIN), Kobe University,

^{b)} Graduate School of Engineering, Kobe University,

^{c)} Department of Radiation-Applied Biology Research, TARRI, QST

Single cell oils (SCO) or microbial systems that produce and store oil, have attracted significant research attention recently, primarily in response to the rising price of petroleum. Oleaginous microbes can convert substrates such as carbon dioxide, sugars, and organic acids to SCO. Among them, *Lipomyces starkeyi* is a particularly well-suited host given its impressive native abilities, including the capability to utilize a wide variety of carbon sources. We had demonstrated the profiles of intracellular lipid accumulation and fatty acid changes in *L. starkeyi* Ls-D35 strain. This strain could consume glucose and xylose for cell growth and lipid production simultaneously even the inhibitory chemical compounds (ICCs) contained in the medium [1,2]. The ICCs used in the evaluation was almost similar those were released in real biomass hydrolysate upon the hot water treatment. Therefore, we suggest that Ls-D35 could be used as a yeast platform for conversion of lipids from real biomass.

Unfortunately, Ls-D35 strain produces starch rather than fatty acids/lipid when the concentration of nitrogen source becomes higher than the carbon sources [3]. In this case, a large portion of starch was produced as extracellular carbon storage, then degraded by α -amylase produced by this strain after the nitrogen source was depleted. Production of starch by Ls-D35 strain could be observed as the starchy colonies formation on the plate containing rich nitrogen source. Production of starch could reduce the accumulation of fatty acids during lipid production. Therefore, the reduction of starch formation is a breakthrough for high lipid production in Ls-D35 strain.

In this study, we attempted to obtain strains reducing of starch formation by irradiation of carbon ion beams ($^{12}\text{C}^{5+}$, 220 MeV), accelerated by the AVF cyclotron at TIARA, TARRI, QST. The irradiation dose was varied at 0, 500, 1000, 1500, 2000, 2500, 3000 Gy, and the mutated strains were plated on the nitrogen-rich yeast-extract/peptone medium containing glucose and xylose (20 g/L) with cerulenin (20 μM), and cultivated at 30 °C.

Figure 1 showed the vary diluting colony formation of the mutated strain (500 to 3000 Gy), compared with the LS-D35 (wild-type) strain (0 Gy, without irradiation) by triplicated experiment. As shown in the figure, the increase of irradiation dose could reduce the colony formation due to the damage of genome and cellular function. The colony formation was preserved even by 500 Gy (yellow frame), but we suggest that lower than 500 Gy was preferable to obtain *Lipomyces* mutant colonies. Unlike the wild-type strain, we observed that the mutant strains formed

non-starchy colonies. In case of Ls-D35 strain, the irradiation dose lower than 500 Gy could give a variety of mutation, probably due to the production of small alteration on the genome enables the cells to keep its growth on the selection medium. However, we cannot understand why the 1500 and 3000 Gy-irradiated did not affect the strain (Fig. 1, red frame). We assumed some samples might be not irradiated uniformly under the treatment, needs to be avoided in the next evaluation. As controls, *Yarrowia lipolytica* strains I118, J32 and CLIB122 were plated without ion-beam irradiation (green frame). As observed, only Ls-D35 produces starch and no starch production observed after irradiation even at 500 Gy. It means that low irradiation is sufficient to achieve the goal of study.

Cerulenin has inhibitory effects on the activity of the enzyme fatty acid synthase. The 500 Gy-irradiated mutant strains showed the reduction of starch production by increasing the resistance of the strain against the cerulenin. The further study is required to demonstrate the lipid production of 500 Gy-mutated Ls-D35 strain and to confirm the reduction of starch formation.

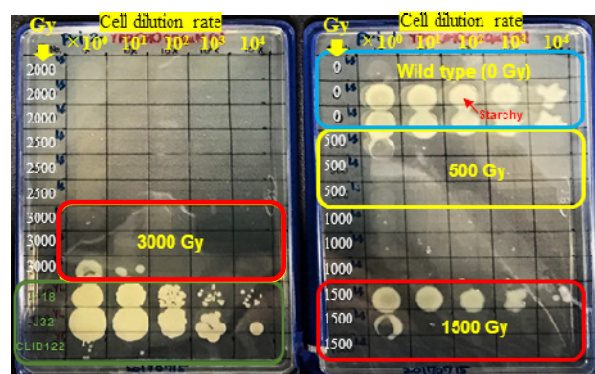


Fig. 1. Effect of carbon ion beams irradiation on the colony formation of *L. starkeyi* D35. The cells were diluted at 10^0 , 10^1 , 10^2 , 10^3 , 10^4 -folds. The growth profiles with irradiation dose from 0 (no treat), 500, 1000 and 1500 Gy were shown in right plate. The others from 2000, 2500 and 3000 Gy were shown in left plate, together with the control strains (*Y. lipolytica* I118, J32 and CLIB122).

References

- [1] A. B. Juanssilfero *et al.*, J. Biosci. Bioeng. **125**, 695 (2018).
- [2] A. B. Juanssilfero *et al.*, Biochem. Eng. J. **137**, 182 (2018).
- [3] D. W. Koenig and D. F. Day, Eur. J. Biochem. **183**, 161 (1989).

2 - 22

Mutation Breeding of *Tweedia caerulea* 'Pure Blue' by Ion Beam Irradiation

S. Tanioka ^{a)}, Y. Hase ^{b)} and S. Nozawa ^{c)}

^{a)} Development Production Union of Blue Star,

^{b)} Department of Radiation-Applied Biology Research, TARRI, QST,

^{c)} Research Planning and Promotion Office, QuBS, QST

We examined the effect of irradiation dose on germination and growth of *Tweedia caerulea* 'Pure Blue' and clarified the irradiation dose suitable for breeding. Doses suitable for mutation were 150 Gy for 'Pure Blue'.

Tweedia caerulea は南米原産の草花で、国内では「ブルースター」や「オキシペタラム」という名前で流通している。*Tweedia caerulea* の育種は、国内の生産者によって進められてきた。著者はハチを用いた虫媒によって交配および選抜に取り組み、丸みを帯びた花弁で花色の青色が鮮明な'ピュアブルー'を作出した。現在では、'ピュアブルー'が国内の *Tweedia caerulea* の切り花流通の大半を占める品種になっている。しかし、現在所有している育種源では営利栽培に向く新たな形質を有する個体の作出が難しく、新品種の作出が停滞している。花屋は使用場面や用途に応じて花材を選定することから、'ピュアブルー'とは異なる花色や花型へのニーズが強まっており、*Tweedia caerulea* に対する今後の消費者の需要動向が危惧される。そのため、新たな花色や花型の交配親として利用できる優良系統の育成が必要であり、イオンビーム照射による突然変異体の作出が期待されている。しかし、*Tweedia caerulea* のイオンビーム照射による育種の知見がなく、育種に適した照射線量は不明である。そこで、照射線量の違いが *Tweedia caerulea*'ピュアブルー'の発芽および生育に及ぼす影響について検討し、育種に適した照射線量を明らかにする。

供試品種は、青色系品種'ピュアブルー'を用いた。突然変異誘発に適した照射条件を探索することを目的に、平成 29 年 6 月 20 日に高崎量子応用研究所のサイクロトロンを使用して 50 MeV ヘリウムイオンを 25, 50, 100, 150, 200, 250, 300, 400 および 500 Gy で照射した。種子を 6 cm シャーレ内に配置して上面をカプトン膜で覆った試料を、HY1 ポートの深度制御種子照射装置を用いて連続的に照射した。

処理した'ピュアブルー'の種子を平成 29 年 7 月 3 日に、無処理区は 33 粒、25 Gy 処理区は 30 粒、50 Gy 処理区は 28 粒、100 Gy 処理区は 30 粒、150 Gy 処理区は 35 粒、200 Gy 処理区は 27 粒、250 Gy 処理区は 32 粒、300 Gy 処理区は 33 粒、400 Gy 処理区は 31 粒、500 Gy 処理区は 32 粒を育苗用培土には種し、反復なしで発芽試験を実施した。平成 29 年 7 月 31 日に発芽率および正常個体率を調査した。なお、正常個体は、植物体の萎縮や黄化、生育の遅延・停止が認められない個体とした。

'ピュアブルー'の発芽率は、50 および 200 Gy で最も高く、500 Gy で最も低かった。正常個体率は、線量が強くなるほど減少し、150 Gy で 59%、200 Gy で 8%にまで減少し、最も減少幅が大きく、250 Gy 以上で 0%、500 Gy ですべての苗が枯死した (Table 1)。

本結果より、'ピュアブルー'のイオンビーム育種に適した線量は 150 Gy であると考えられた。

本研究結果を基に照射処理した種子をは種して得られた実生苗を用いて、圃場での自家受粉によって変異形質を有する個体を作成することができれば、*Tweedia caerulea* におけるイオンビーム照射による育種方法を確立できると考えられる。

Table 1

The effect of dose difference on germination rate and normal individual.

Absorbed dose (Gy)	Number of sowing	Germination rate (%)	Normal individual (%)
0	33	97	97
25	30	93	79
50	28	96	74
100	30	83	68
150	35	83	59
200	27	96	8
250	32	72	0
300	33	73	0
400	31	29	0
500	32	0	0

Genome Analysis of the Radioresistant Bacterium *Deinococcus aerius* TR0125

K. Satoh^{a)}, H. Arai^{b)}, T. Sanzen^{a, c)}, H. Hayashi^{b)}, I. Narumi^{c)} and Y. Oono^{a)}

^{a)} Department of Radiation-Applied Biology Research, TARRI, QST,

^{b)} Faculty of Engineering, Maebashi Institute of Technology,

^{c)} Faculty of Life Science, Toyo University

Introduction

Although the radioresistance of organisms varies greatly among species, there is a group of bacteria that shows extraordinary resistance to radiation. Members of the genus *Deinococcus* are the best known as radioresistant bacteria, and about 70 *Deinococcus* species have been isolated from various environments over 60 years since first isolation of *D. radiodurans* [1]. The resistance of *Deinococcus* species is attributed to highly proficient DNA repair capacity [2]. Recently, the whole genome sequences of some *Deinococcus* bacteria have been determined. These provide important information to elucidate the unique features of *Deinococcus* bacteria.

While *Deinococcus aerius* strain TR0125 was initially isolated as an orange-pigmented, non-motile, desiccation tolerant, UV- and gamma-resistant, and coccoid bacterium from the upper troposphere in Japan [3]. In this study, we determined and analyzed the draft genome sequence of *D. aerius* strain TR0125.

Experimental procedures

The genome sequence of *D. aerius* strain TR0125 was determined by a whole-genome shotgun strategy. The pyrosequencing data were accumulated using the Roche GS FLX+ and GS Junior+ Systems. The obtained sequence data were assembled using the GS *De Novo* Assembler ver. 3.0. Automatic annotation was performed using the Microbial Genome Annotation Pipeline [4]. The tRNA and rRNA operon (5S/16S/23S) detections were performed using the tRNA scan software ver. 1.23 [5] and RNAmmer software ver. 1.2 [6], respectively. Moreover, the radiation/desiccation response motif (RDRM) of strain TR0125 was then searched by a Virtual Footprint program [7] and a GENETYX-MAC software package.

Results and discussion

The draft genome sequence of *D. aerius* strain TR0125 was 4,524,446 bp in total length, with a 50-fold average coverage, G+C average content of 68.0% and comprised 43 large contigs (>500 bp) (Table 1). High G+C average content of strain TR0125 was also consistent with *Deinococcus* species. We predicted a total of 4,446 protein-coding sequences, total of 52 tRNAs and 1 rRNA operon from the draft genome sequence of strain TR0125, respectively (Table 1) [8]. Although many *Deinococcus* bacteria possess multiple rRNA operons, TR0125 genome possesses only one rRNA operon playing important components for protein synthesis. This might be related that strain TR0125 exhibited much slower growth than *D. radiodurans*.

Analysis of the draft genome sequence indicated that strain TR0125 possesses a DNA damage response regulator (encoded by *pprI* homolog) and 33 radiation/desiccation response regulons (*pprA*, *recA*, *ddrA*, *ddrO* homologs etc.), which are involved in the unique radiation/desiccation response system in *Deinococcus* species. RDRM of strain TR0125 consists of 17-base partially palindromic sequence, TTNNG(N₇)CNNA.

In future, the draft genome sequence of *D. aerius* will be useful for elucidating the common principles of the radioresistance based on the extremely efficient DNA repair mechanisms in *Deinococcus* species by the comparative analysis of genomic sequences.

Table 1

General features of draft genome sequence of *D. aerius* strain TR0125.

Size (bp)	4,524,446
G+C content (%)	68.0
Depth	50
No. of all contigs	135
No. of large contigs (>500 bp)	43
CDSs	4,446
tRNA	52
rRNA (5S/16S/23S)	1/1/1

References

- [1] A. W. Anderson *et al.*, Food Technol. **10**, 575 (1956).
- [2] Y. Ishino & I. Narumi, Curr. Opin. Microbiol. **25**, 103 (2015).
- [3] Y. Yang *et al.*, Int. J. Syst. Evol. Microbiol. **59**, 1862 (2009).
- [4] H. Sugawara *et al.*, Abstr. 20th Int. Conf. Genome Informatics, **S-001**, 1 (2009).
- [5] P. Schattner *et al.*, Nucleic Acids Res. **33**, W686 (2005).
- [6] K. Lagesen *et al.*, Nucleic Acids Res. **35**, 3100 (2007).
- [7] R. Münch *et al.*, Bioinformatics **21**, 4187 (2005).
- [8] K. Satoh *et al.*, Genome Announc. **6**, e00080-18 (2018).

2 - 24 Effect of Ion Beams and Gamma Rays Irradiation on Mutation Induction in *Bacillus subtilis* Spores

N. H. P. Uyen ^{a)}, M. Furuta ^{a)}, K. Satoh ^{b)} and Y. Oono ^{b)}

^{a)} Quantum Radiation Engineering, Graduate School of Osaka Prefecture University,

^{b)} Department of Radiation-Applied Biology Research, TARRI, QST

Introduction

Bacillus subtilis is known as Gram-positive, rod-shaped, aerobic, spore-forming bacterium that is naturally found in soil. The spore is resistant to environmental factors such as heat, desiccation, chemical, and radiation [1]. Besides, ionizing radiation induces DNA damages including single-strand breaks and double-strand break and generates reactive oxygen species which also induces DNA strand breaks. Ion beams have a high linear energy transfer (LET, keV/μm) and give DNA damage containing double-strand break locally (clustered damage) than gamma rays do [2]. Recently, ion beams have been used for mutation breeding in biological objects including rice, flowers and bacteria [3]. Mutations in the RNA polymerase β subunit of the *B. subtilis*, encoded by *rpoB* gene, related to rifampicin resistance and can be generated by irradiation method.

In this work, we utilized ion beams to check mutation induction for rifampicin to characterize the mutation by high LET ion beam irradiation to *B. subtilis* spores.

Experimental procedures

The spores of *B. subtilis* 168 (*trpC2*) were prepared by inoculating the vegetative cells onto the Schaeffer's sporulation medium [4] at 37 °C for 4 days, harvested and treated sequentially with 1 mg/mL lysozyme and 1% SDS. Aliquots (1 mL) of the spore suspensions at 10⁹ CFU/mL were dropped onto the sterilized cellulose membrane and dried then irradiated four kinds of ion beams (⁴He²⁺ [50 MeV; 19.4 keV/μm], ¹²C⁵⁺ [220 MeV; 121.8 keV/μm], ¹²C⁶⁺ [190 MeV; 148.7 keV/μm]; ²⁰Ne⁸⁺ [350 MeV; 440.8 keV/μm] and ⁴⁰Ar¹³⁺ [460 MeV; 1649.6 keV/μm]) accelerated by an AVF cyclotron at TIARA, TARRI, QST or with ⁶⁰Co gamma rays (0.2 keV/μm) at Osaka Prefecture University. The irradiation doses ranged from 0.6 to 6 kGy.

Irradiated spores were recovered from membranes, spread onto either LB agar supplemented with rifampicin (Rif, 50 μg/mL) or the Spizizen agar [5] supplemented with 5-Fluorouracil (5-FU, 1 μM), and incubated at 37 °C for 3 days to screen mutants. The numbers of Rif- or 5-FU-resistant (Rif^R or FU^R) colonies were counted. All the obtained Rif^R colonies were picked up by toothpicks, spotted onto the new Rif-LB agar, and incubated for 3 days to confirm the Rif resistance.

Results and discussion

The previous results showed that the spores exhibited sensitivities to gamma rays and four kinds of ion beams depending on radiation dose. The ¹²C⁵⁺ ion-irradiated spores showed the most sensitivity among the ion beams used for irradiations. The lethal effect of spore was estimated to be in the order ¹²C⁵⁺ > ¹²C⁶⁺ > ²⁰Ne⁸⁺ > ⁴He²⁺ >

⁶⁰Co > ⁴⁰Ar¹³⁺. The relative biological effectiveness value of ¹²C⁵⁺ ion beams was 3.03, suggesting that ¹²C⁵⁺ ion beams had the most lethal effects for *B. subtilis* spores [6].

By the screening of Rif^R mutants, a certain number of mutants was obtained for each ion beams irradiation without ¹²C⁶⁺ as shown in Table 1. In ⁴He²⁺, ⁶⁰Co, ⁴⁰Ar¹³⁺ irradiation, shown the lower lethal effect to *B. subtilis* spores, more Rif^R mutant colonies were obtained compared to irradiation of the higher lethal effected ion beams (¹²C⁵⁺ and ²⁰Ne⁸⁺). The trend of the mutagenic effect with the appearance of Rif^R mutants did not show the similar trend as the lethal effect. On the other hand, FU^R mutants were not obtained by this screening because appeared colonies were too small and unclear to pick up to confirm the resistance.

References

- [1] F. Kunst *et al.*, Nature, **390**, 249 (1997).
- [2] C. F. Dunne, Br. J. Hosp. Med., **74**, 166 (1999).
- [3] S. Mahadthanapuk, Nucl. Instrum. Meth. Phys. Res. B, **326**, 209 (2014).
- [4] P. Schaeffer *et al.*, Proc. Natl. Acad. Sci. USA, **54**, 704 (1965).
- [5] J. Spizizen, Proc. Natl. Acad. Sci. USA, **44**, 1072 (1958).
- [6] N. H. P. Uyen *et al.*, QST Takasaki Annu. Rep. 2016, **QST-M-8**, 104 (2018).

Table 1

The number of Rif^R mutant colony in the selected media.

Radiations	Dose (kGy)	No. of Rif ^R
¹² C ⁵⁺	0.6	6
	0.8	0
	1.0	0
	2.0	0
	1.0	0
¹² C ⁶⁺	2.0	0
	4.0	0
	6.0	0
	2.0	0
²⁰ Ne ⁸⁺	4.0	1
	6.0	0
	0.8	6
⁴ He ²⁺	1.0	15
	2.0	11
	4.0	6
	6.0	2
	2.0	21
⁶⁰ Co	4.0	48
	6.0	5
	2.0	0
⁴⁰ Ar ¹³⁺	4.0	14
	6.0	4
	2.0	0

Study of the Lethal Effect Caused by the Various LET Particle Ion Beam in Budding Yeast *S. cerevisiae*

Y. Matuo ^{a)}, A. N. Sakamoto ^{b)}, Y. Hase ^{b)} and K. Shimizu ^{c)}

^{a)} Department of Nuclear Power and Energy Safety Engineering, University of Fukui,

^{b)} Department of Radiation-Applied Biology Research, TARRI, QST,

^{c)} Radioisotope Research Center, Osaka University

Our research group has been studying ion beam-induced mutations in budding yeast S288c (*RAD*⁺), which is a model of eukaryotic cells. We demonstrated that high-linear energy transfer (high-LET; 107 keV/μm) carbon ion beams are more mutagenic than low-LET gamma rays. A remarkable feature of yeast mutations induced by carbon ions was their distribution at a hotspot near the linker regions of nucleosomes in the *URA3* gene, whereas mutations induced by gamma rays were uniformly distributed through the *URA3* gene [1]. To elucidate the mechanism of the mutation, we investigated the effects of high-LET carbon ion beams (190 MeV, LET: 149 keV/μm) on lethality and then compared the results with those of carbon ion beams (LET: 13, 25, 50, 75, and 107 keV/μm) and neon ion beams (400 MeV, LET: 317 keV/μm) obtained in our previous study. *Saccharomyces cerevisiae* S288c haploid cells were grown in YPD medium and transferred to membrane filters, and irradiated with carbon ion beams (LET: 149 keV/μm) with a dose of 1-200 Gy at TIARA. After irradiation, the membrane filters were incubated on YPD plates at 30 °C for two days. Cell survival was

assessed by colony forming efficiency.

In previous studies, yeast cells were irradiated with carbon (LET: 107 keV/μm) and neon ions (LET: 317 keV/μm) at TIARA or with carbon ions (LET: 13 - 75 keV/μm) at HIMAC-NIRS, QST.

The survival of yeast cells irradiated with ion beams of various LETs are summarized in Fig. 1. Cell survival decreased with an increase in the dose in each ion. At the same dose, the higher LET beam caused greater lethality. However, high-LET neon ions (LET: 317 keV/μm) were not significantly more lethal than high-LET carbon ions (LET: 107 keV/μm). The lethality of LET on cells seems to reach a limit above a certain level. This tendency may be related to an overkill effect. In future, we will examine a mutagenesis effect by the various LET particle ion beams.

Reference

[1] Y. Matuo *et al.*, *Mutat. Res.* **602**, 7-13 (2006).

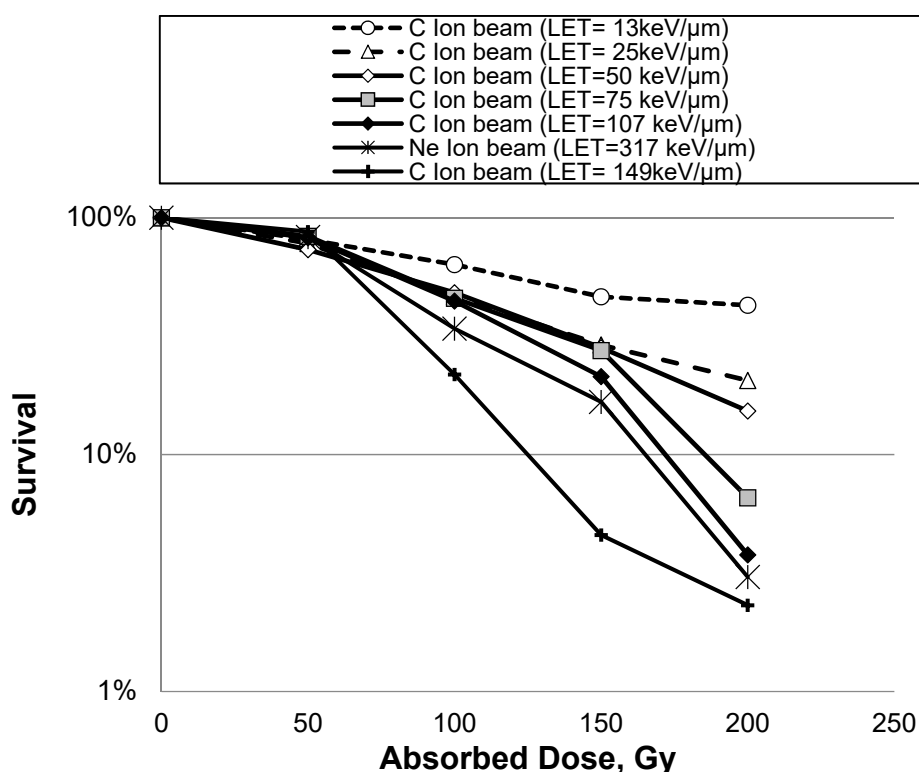


Fig. 1. Survival rates for yeast strain S288c after irradiation with carbon and neon ion.

2 - 26 Microflora Analysis of Black Pepper Using MALDI-TOF Mass Spectrometry and Decontamination by Gamma-ray Irradiation

H. Kameya^{a)}, K. Kimura^{a)}, H. Seito^{b)} T. Kojima^{b)} and S. Todoriki^{a)}

^{a)} Food Research Institute, National Agriculture and Food Research Organization (NARO),

^{b)} Department of Advanced Radiation Technology, TARRI, QST

Food poisoning outbreaks of pathogens derived from contaminated spices have been reported [1]. Gamma-ray irradiation is effective for microbial decontamination of dried spices with the least deterioration of organoleptic quality [2]. Recently, the application of electron beam (EB) generated by an accelerator has drawn attention from food processing industries. Indeed, International Atomic Energy Agency (IAEA) is implementing a research project to develop a novel food irradiation technique with new concepts on the basis of introducing low energy electron accelerators. Under the IAEA research project "D61024 DEXAFI" and collaboration with INCT, Poland, we have investigated the efficacy of low energy EB (< 300 keV) irradiation for spice decontamination in comparison with gamma-ray irradiation. In the present study, we analyzed the microflora of black pepper samples and examined the effects of gamma-ray irradiation on viability of bacteria.

Black pepper was obtained from INCT, Poland. The black pepper samples packaged in plastic bags, each of which was 20 g, were irradiated with gamma-ray from Co-60 in No 6 cell at Takasaki institute in QST. Aliquots of pepper corns (4 g) irradiated and those unirradiated were homogenized in PBS buffer (20 mL) by milling. The homogenized solution was serially diluted and a portion of them (0.1 mL) was spread on Tryptic soy agar (TSA) plate. TSA plates were incubated at 30 °C for 24 hours to count the viable cells. For species identification, single colonies were picked up and subjected to a microbial identification system based on MALDI-TOF mass spectrometry (MALDI Biotyper, Bruker).

Table 1 shows the microflora of the unirradiated black pepper, which was analyzed by MALDI Biotyper. Twelve species of bacteria were found, and most of them belong to the *Bacillus* spp. Characteristically, occurrence of *Cronobacter Sakazaki* was confirmed in the sample. The radiation tolerance of this bacterium has been reported to be increased during drying in powdered formula [3] and *C. sakazakii* was reported to occur in dried spices [4].

Table 2 shows the total aerobic plate counts of the black pepper samples before and after gamma-ray irradiation. Unirradiated black pepper was highly contaminated with spore forming bacteria (10^6 cfu/g, cfu: colony forming unit), because the viable counts of this sample remained the almost same after heating for 20 min at 80 °C. The flourish of spore forming bacteria was in an agreement with the result of Biotyper analysis. The bacterial number was reduced to 10^3 cfu/g by gamma-ray irradiation at 5 kGy.

Noteworthy, the survived bacteria were predominantly non-spore forming bacteria. *C. sakazakii* that was a radio-tolerant non-spore-forming bacterium might have survived the irradiation of 5-kGy gamma-ray. Gamma-ray irradiation at 10 kGy reduced the bacterial count lower than the detection limit. The efficacies of low energy EB for microbial decontamination of spices will be compared with those of gamma-rays and high energy EB in future.

Table 1

Microbial spices exist in black pepper samples explored by MALDI Biotyper.

Species	%
<i>Bacillus subtilis</i>	36.7
<i>Bacillus pumilus</i>	23.3
<i>Bacillus altitudinis</i>	21.7
<i>Bacillus vallismortis</i>	5
<i>Aeromonas veronii</i>	1.7
<i>Bacillus amyloliquefaciens</i>	1.7
<i>Bacillus cereus</i>	1.7
<i>Bacillus megaterium</i>	1.7
<i>Bacillus mojavensis</i>	1.7
<i>Cronobacter sakazakii</i>	1.7
<i>Enterobacter cloacae</i>	1.7
<i>Enterococcus casseliflavus</i>	1.7

* Sixty colonies were randomly analyzed with Biotyper.

Table 2

Aerobic plate counts for black peppers (Unit: cfu/g).

	untreated	5 kGy	10 kGy
before heating	8.4×10^6	6.6×10^3	$< 0.5 \times 10^{2**}$
after heating*	7.7×10^6	9.7×10^2	$< 0.5 \times 10^{2**}$

* 80 °C, 20min ** less than detection limit

Acknowledgment

The present work is in a collaboration with Institute of Nuclear Chemistry and Technology (INCT), Poland.

References

- [1] J. M. Van Doren *et al.*, Food Microbiology, **36**, 456 (2013).
- [2] J. Farkas, In: R. A. Molins (Ed.): Food Irradiation: Principles and Applications., John Wiley & Sons, Inc., Oxford. 291-312 (2001).
- [3] T. M. OSAILI *et al.*, J. Food Protect., **71**, 934 (2008).
- [4] M. Garbowska *et al.*, Food Microbiology, **49**, 1 (2015).

2 - 27 Breeding of New Potted Flower Varieties Using Ion Beam

M. Tsukagoshi^{a)}, S. Nozawa^{b)} and Y. Hase^{c)}

^{a)} Study Group for Farmer Advanced Technology Informatization Research of Takasaki,

^{b)} Research Planning and Promotion Office, QuBS, QST,

^{c)} Department of Radiation-Applied Biology Research, TARRI, QST

To establish ion-beam breeding technology for potted flowers, lavender, blue daisies, and rhodansemums, cuttings of these plants were irradiated by He (63 MeV) ions and effects of the irradiation were examined. The result showed number of surviving plants in lavenders and blue daisies was reduced by the irradiation with over 40 Gy. Detecting mutations in flower color is a challenge for the future.

高崎市は鉢花類の生産が盛んであり、オリジナル品種の育成は、有利販売や地域の活性化に非常に有用である。鉢花類の育種は、一般に系統間の交雑または枝変わり等の選抜が利用されるが、従来の育種は、長い年月を必要とすること、望まれる形質や性質を得ることが困難な場合も多いこと、種子を獲得することが難しい品目では育種が進まないことなど課題も多い。本研究では、花き類で利用されているイオンビーム育種を中心とした突然変異育種技術を活用するため、高崎量子応用研究所において照射を行った。

今回の研究には、鉢花生産に用いられるラベンダー (*Lavandula L.*)、ブルーデイジー (*Felicia Cass.*)、ローダンセマム (*Rhodanthemum (Vogt) B. H. Wilcox et al.*) を材料とし、高崎量子応用研究所イオン照射研究施設の AVF サイクロトロンを利用して、イオンビーム照射を行った。照射するイオン種は He-63 MeV を用い、0~100 Gy の範囲で吸収線量を変化させ、変異誘発に適した吸収線量の検討を行った。

具体的な実施方法は、脇芽の分裂組織にイオンビームが到達するよう、茎および葉を調整した挿穂をシャーレ内に配置後、カプトン膜で覆い、深度制御種子照射装置の運転台を用いてヘリウムイオンを連続的に照射した。照射量は 0, 10, 20, 30, 40, 60, 80, 100 Gy の 8 段階で行った (Table 1)。照射後は、重イオン準備室内の培養器内で保管した。



Fig. 1. Plants after irradiation (Left : Rhodanthemum, Right : Felicia Cass).

(照射方法)

1 回あたりの総所要時間 = 1 時間

(照射日 : 平成 29 年 6 月 6 日、11 月 8 日)

(サンプル搬入) → (照射 ~ 1 分 × 40 回 + 搬送時間) →

(片付け、照射装置内で冷却)

その後、生産者のほ場で開花まで管理し、生育及び変異の状況について調査を行った (Fig. 1)。

1 回目の照射 (6 月 6 日) では、ラベンダー、ブルーデイジーで 40 Gy 以上の照射で生存株数が少なくなった。60 Gy 以上の強い線量でも生育したが、伸長している枝は頂部ではなく、照射の影響が少ない下部のわき芽から発生しているものであり、60 Gy 以上の照射では植物の生育に著しい影響を与えられたと考えられた。一方、ローダンセマムでは、照射後の活着率が悪く生育しなかった。ローダンセマムは、育苗・生育時の温度管理が難しい品目であり、育苗時の高温も影響したと思われる。

生存した株はそのまま開花まで管理し、無処理株と比較を行ったが、花色への変異は確認できなかった。

Table 1. Number of surviving plants.

Gy	Lavender	Blue Daisy	Rhodanthemum
0	4/6	7/7	0/7
10	4/6	12/14	0/14
20	9/9	10/14	0/14
30	9/9	12/14	0/14
40	3/9	9/14	0/14
60	0/9	8/14	0/14
80	0/9	5/7	0/14
100	3/9	5/7	0/14

Note. Denominator: Irradiation number, Numerator: Survival number.

2 回目の照射 (11 月 8 日) は、低温時期となり生産者ほ場での育苗は難しいことから、照射後の穂をインキュベーター (12 時間日長、20 °C) で密閉挿しにより発根処理を行った。しかし、ほとんどが生育不良となり、開花調査はできなかった。

今後は、1 回目の照射結果から、ラベンダーとブルーデイジーについては、30 Gy 付近を中心とした線量による照射を行い、変異株の発生状況について検討を行う。ローダンセマムについては、今回の試験では生育不良となったため、再度適性照射量について検討を行う。また、育苗方法については照射後の生育に課題が残っているので、照射個体を発根苗にするなど管理体系の見直しも必要である。

2 - 28 Creation of Mutant Cultivars by Ion Beam Irradiation to Diploid and Tetraploid *Tweedia caerulea*

K. Yoshinaga ^{a)}, Y. Hase ^{b)} and S. Nozawa ^{c)}

^{a)}Development Committee of Blue Star,

^{b)}Department of Radiation-Applied Biology Research, TARRI, QST,

^{c)}Research Planning and Promotion Office, QuBS, QST

We examined the effect of different irradiation doses on germination and growth of *Tweedia caerulea* and determined the irradiation dose suitable for breeding. The doses suitable for mutation were 150 Gy in 'Pegasus Blue' and 'Pegasus White', 100 Gy in 'Hoppi Blue', 200 Gy in 'Hoppi White', 50 Gy for 'Inca Red' and 'Bukai Pink'.

Tweedia caerulea は南米原産の草花で、国内では「ブルースター」や「オキシペタラム」という名前で流通している。*Tweedia caerulea* の育種は、国内の生産者によって進められ、「ピュアブルー」を筆頭に、白色系品種、花が大型化する4倍体品種等を作成してきた。しかし、近年では新たな品種の作出が停滞しており、今後の消費者の需要動向が危惧されることから、新たな花色や花型の交配親として利用できる優良系統の育成が必要である。しかし、*Tweedia caerulea* でのイオンビーム照射による育種の知見がなく、育種に適した照射線量は不明である。そこで、*Tweedia caerulea* において照射線量の違いが発芽および生育に及ぼす影響について検討し、育種に適した照射線量を明らかにする。

供試品種は、4倍体の青色系品種「ペガサスブルー」、4倍体の白色系品種「ペガサスホワイト」、2倍体の青色系品種「ホッピブルー」、2倍体の白色系品種「ホッピホワイト」、2倍体の赤色系品種「インカレッド」および2倍体のピンク系品種「部会ピンク」を用いた。各品種について、突然変異誘発に適した照射条件を探索することを目的に、平成29年6月20日に高崎量子応用研究所のサイクロトロンを使用して50 MeVヘリウムイオンを25, 50, 100, 150, 200, 250, 300, 400および500 Gyで照射した。平成29年7月4日に、各処理区あたり10粒を育苗用培土には種し、3反復発芽試験を実施した。平成29年7月31日に発芽率、8月24日に、正常個体率を調査した。なお、正常個体は、植物体の萎縮や黄化、生育の遅延・停止が認められない個体とした。照射方法は、種子を6 cmシャーレ内に配置後、カプトン膜で覆い、HY1ポートの深度制御種子照射装置を用いて連続的に照射した。

「ペガサスブルー」では、発芽率は200 Gyで最も高く、100, 300 および 500 Gy で最も低く、正常個体率は、100 Gy以下で100%であったが、150 Gy以上で減少し、300 Gy以上で0%であった。「ペガサスホワイト」では、発芽率は25 Gyで最も高く、500 Gyで最も低く、正常個体率は25 Gy以下で100%であったが、50 Gy以上で減少し、300 Gy以上で0%であった。「ホッピブルー」では、発芽率は50 Gyで最も高く、300 および 400 Gy で最も低く、正常個体率は25 Gyで100%であったが、50 Gy以上で減少し、250 Gy以上で0%であった。「ホッピホワイト」では、発芽率は25, 50 および 100 Gy で最も高く、250 および 400 Gy で最も低く、正常個体率は25, 50 および 150 Gy で100%であったが、100 および 200 Gy で減少し、250 Gy以上で0%、400 Gy以上ですべての苗が枯死した。「インカレッド」では、発芽率は50 Gyで最も高く、150, 300 および 500 Gy で最も低く、正常個体率は50 Gyで最も高く、100 Gyで減少し、150 Gy以上で0%、500 Gyですべての苗が枯死した。

「部会ピンク」では、発芽率は50 および 100 Gy で最も高く、400 および 500 Gy で0%、正常個体率は25 および 200 Gy で100%、50 および 100 Gy で減少し、150, 250 および 300 Gy で0%であった(Table 1)。本結果より各品種のイオンビーム育種に適した線量は、「ペガサスブルー」および「ペガサスホワイト」が150 Gy、「ホッピブルー」が100 Gy、「ホッピホワイト」が200 Gy、「インカレッド」および「部会ピンク」が50 Gyであると考えられた。

本研究結果を基に照射処理した種子をばらして得られた実生苗を用いて、本ぼでの自家受粉によって変異形質を有する個体を作成することができれば、*Tweedia caerulea* におけるイオンビーム照射による育種方法を確立することができると思われる。

Table 1. The effect of different doses on germination rate and structural intactness (%).

Breed name : Pegasus Blue			Breed name : Pegasus White		
dose (Gy)	Germination rate (%)	Normal individual (%)	dose (Gy)	Germination rate (%)	Normal individual (%)
0	30	100	0	87	100
25	30	100	25	80	100
50	33	100	50	77	96
100	17	100	100	77	91
150	27	88	150	70	36
200	40	30	200	63	25
250	37	22	250	57	6
300	17	0	300	73	0
400	37	0	400	57	0
500	17	0	500	43	0

Breed name : Hoppi Blue			Breed name : Hoppi White		
dose (Gy)	Germination rate (%)	Normal individual (%)	dose (Gy)	Germination rate (%)	Normal individual (%)
0	73	100	0	27	100
25	33	100	25	40	100
50	60	94	50	40	100
100	50	53	100	40	91
150	33	11	150	13	100
200	47	13	200	27	50
250	37	0	250	7	0
300	23	0	300	13	0
400	23	0	400	7	-
500	37	0	500	10	-

Breed name : Inca Red			Breed name : Bukai Pink		
dose (Gy)	Germination rate (%)	Normal individual (%)	dose (Gy)	Germination rate (%)	Normal individual (%)
0	10	67	0	27	88
25	10	67	25	3	100
50	20	83	50	10	67
100	17	25	100	10	75
150	7	0	150	3	0
200	10	0	200	3	100
250	10	0	250	7	0
300	7	0	300	3	0
400	13	0	400	0	-
500	7	-	500	0	-

2 - 29 Analysis of Response Deficient Mutants of *Streptomyces coelicolor* to Contact-dependent Stimuli

S. Asamizu ^{a)}, M. Yanagisawa ^{a)}, T. Ishizuka ^{a)}, K. Satoh ^{b)}, Y. Ohno ^{b)} and H. Onaka ^{a)}

^{a)} Graduate School of Agricultural and Life Sciences, The University of Tokyo,

^{b)} Department of Radiation-Applied Biology Research, TARRI, QST

Actinomycetes, filamentous Gram-positive bacteria, have been known as a major source of bioactive natural products which can be drug candidates. Recent genome analyses of actinomycetes revealed the previously unrecognized “cryptic” gene clusters, indicating the huge potential of actinomycetes to produce more diverse secondary metabolites. We have studied about the bacterial interaction induced production of secondary metabolites by actinomycetes. *Tsukamurella pulmonis* TP-B0596 (here after Tp) had been shown to possess ability to induce production of secondary metabolites by *Streptomyces* species, which are not produced in single culture [1]. Until now, 10 classes, total 27 new compounds had been isolated from the co-culture with various *Streptomyces* sp. and Tp (the method named combined-culture) [2]. Object of this study is to elucidate the gene(s) which are involved in the response for activation of secondary metabolism within actinomycetes. Elucidation of the mechanism can be expected to lead for creation of genetic tools to generate novel bioactive natural products.

Streptomyces species respond to mycolic acid-containing bacteria by production of secondary metabolism in a contact dependent manner [2, 3]. Here we investigated the gene(s) responsible for the activation of secondary metabolism induced by Tp to explore the molecular basis of the response mechanism of *Streptomyces* species. Using *Streptomyces coelicolor* JCM4020 as a model strain, we employed carbon ion beams (¹²C⁵⁺, 220 MeV), accelerated by the AVF cyclotron at TIARA, induced mutagenesis to generate spore mutant library of *S. coelicolor*. Then we screened the undecylprodigiosin (RED) production deficient mutants of *S. coelicolor* by mixing them with Tp on agar plates using red / white phenotype of the colonies as indication. Through this process, we obtained 118 mutants from around 152,000 tested spores. We further tested the phenotype of the 118 mutants by growth on minimum medium and formation of aerial mycelia, and finally obtained 59 mutants which were deficient in induced RED production but were not deficient in growth and development. Until now, we have re-sequenced the genome of 16 mutants and identified the 44 mutations (Table 1). As a result, mutants obtained from 100 Gy irradiation contained average 2.0 mutations (14 mutations in 7 mutants). Mutants obtained from 200 Gy irradiation contained average 3.3 mutations (30 mutations in 9 mutants). The variation of nucleotide mutations included 31 substitutions, 5 insertions, and 8 deletions. These total

44 nucleotide mutations led to the amino acid mutations; 13 missense mutations, 2 nonsense mutations, 9 frameshift mutations, 1 amino acid insertion, 2 amino acid deletions, and 17 silent mutations. We confirmed some of the mutated genes by gene complementation and found that glutamate synthase (*gltB*) and elongation factor G (*fusA*) were responsible for the RED deficient phenotypes in respective mutants. We are now investigating the involvement of the other 10 hypothetical proteins which may responsible for the phenotype of 3 mutants found in this study. Also, further re-sequencing of the genome for the 35 remaining mutants will lead to the identification for the additional mutation points responsible of the response of *Streptomyces* species.

Table 1

Type of mutations found in RED response deficient mutants.

Mutation type	DNA sequence change	Number
Substitution	G/C>A/T	21
	A/T>G/C	5
	G/C>G/C	4
	A/T>A/T	0
	CC>TT	1
Total (substitution)		31
Deletion	delG/C	5
	delA/T	0
	delCG	1
	delGCG	1
	delTCG	1
	Total (deletion)	8
Insertion	insCC/GG	3
	insGAT	1
	insAGCTT	1
Total (insertion)		5

References

- [1] H. Onaka *et al.*, Appl. Environ. Microbiol., **77**, 400 (2011).
- [2] H. Onaka, J. Antibiot., **70**, 865 (2017).
- [3] S. Asamizu *et al.*, PLOS One, **10**, e0142372 (2015).

2 - 30 Knockout and Plasmid Complementation of the *pprA* Gene in the Radioresistant Bacterium *Deinococcus radiodurans*

S. Tanabe^{a)}, T. Sanzen^{a, b)}, K. Satoh^{b)}, Y. Oono^{b)} and I. Narumi^{a)}

^{a)} Faculty of Life Sciences, Toyo University,

^{b)} Department of Radiation-Applied Biology Research, TARRI, QST

Although the radioresistance of organisms varies greatly among species, there is a group of bacteria that shows extraordinary resistance to ionizing radiation. Members of the genus *Deinococcus* are the best known as radioresistant bacteria. Radioresistance of *Deinococcus* species is attributed to their highly proficient DNA repair capacity, in which a set of proteins involved in DNA repair is induced following exposure to ionizing radiation [1, 2]. PprA (named after pleiotropic protein promoting DNA repair) has been known for its role in radioresistance in *D. radiodurans* [3]. Earlier, PprA was shown to contribute in double-strand break repair by stimulating DNA ends joining activities of T4 DNA ligase, *E. coli* DNA ligase and a deinococcal DNA ligase [3, 4]. Recently, the interaction of DNA gyrase A subunit and DNA topoisomerase IB with PprA have been demonstrated [5, 6]. In this study, to delineate the detailed function of PprA in DNA repair, a *pprA* knockout strain and its plasmid-complemented strain of *D. radiodurans* was generated and survivals of the strains following exposure to gamma-rays was measured. Moreover, a library of mutant PprA that probably lost DNA binding activity was made by random mutagenesis and expressed in XPA2.

A *pprA* knockout stain XPA2 was generated by the double crossover-mediated mutagenesis technique using the spectinomycin adenyltransferase gene as a marker. The wild-type *pprA* gene with its upstream promoter region was cloned in an *Escherichia coli*-*D. radiodurans* shuttle vector pRADN1 [7] to yield pHOB12pprAwt. XPA2 was transformed with pRADN1 and pHOB12pprAwt to generate a negative control stain (XPA2 carrying RADN1) and a plasmid-complemented strain (XPA2 carrying pHOB12pprAwt), respectively. The *pprA* gene was mutagenized by error-prone PCR or hydroxylamine treatment using an *E. coli* expression system [8]. The wild-type *pprA* in pHOB12pprAwt was then replaced by the mutant *pprA* to generate pHOB12pprAmut series.

Figure 1 shows the gamma-ray sensitivity of wild-type, negative control, and plasmid-complemented strains carrying wild-type *pprA*. The negative control strain exhibited significant sensitivity to gamma-rays compared to wild-type. On the other hand, the plasmid-complemented strain showed resistance to gamma-rays at the same level as wild-type, suggesting that complete complementation was achieved in this experimental system. Table 1 shows the list of mutant PprA library that expressed in XPA2 carrying pHOB12pprAmut series. The library could be categorized according to the sensitivity to mitomycin-C.

Acknowledgment

The present work was supported by grants from the Ministry of Education, Culture, Sports, Science and Technology of Japan [grant number 17K07730 to I. Narumi].

References

- [1] I. Narumi, Trends Microbiol. **11**, 422 (2003).
- [2] Y. Ishino *et al.*, Curr. Opin. Microbiol. **25**, 103 (2015).
- [3] I. Narumi *et al.*, Mol. Microbiol. **54**, 278 (2004).
- [4] S. Kota *et al.*, Biochem. Cell. Biol. **88**, 783 (2010).
- [5] S. Kota *et al.*, J. Genet. **93**, 349 (2014).
- [6] S. Kota *et al.*, PLoS One, **9**, e285288 (2014).
- [7] H. Ohba *et al.*, Gene, **363**, 133 (2005).
- [8] S. Kota *et al.*, Extremophiles, **20**, 195 (2016).

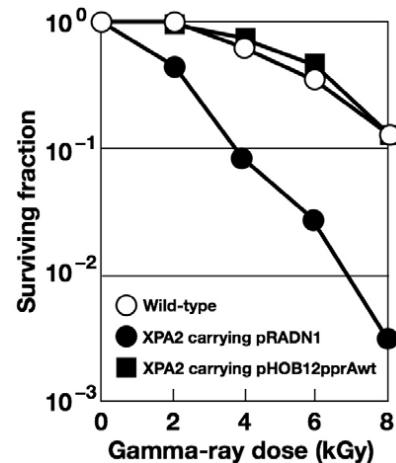


Fig. 1. Sensitivity of *D. radiodurans* strains WT (open circles), XPA2 containing plasmid pRADN1 (closed circles), and XPA2 containing pHOB12pprAwt (closed squares) to gamma-rays.

Table 1

The list of mutant PprA library that expressed in XPA2 carrying pHOB12pprAmut series.

Amino acid substitution in mutant PprA	Complementation (Mitomycin-C)
L60P, A69V, L164P, W183R	Complete
A139P, W146L, G149E, S173F, R192C, R196C, R196H	Partial
G61R, K133E, W146R, R150C, R150H, A181D, R201P, G206E, G206R, R252C, R252H	None

2 - 31 Effects of Growth Stages on Cadmium Accumulation in Shoot of Oilseed Rape Plants

S. Nakamura^{a)}, N. Suzui^{b)}, Y.-G. Yin^{b)}, S. Ishii^{b)}, S. Fujimaki^{b)} and N. Kawachi^{b)}

^{a)} Faculty of Life sciences, Tokyo University of Agriculture,

^{b)} Department of Radiation-Applied Biology Research, TARRI, QST

Cadmium (Cd) is one of toxic elements. Cd that enters the food chain threatens our health seriously. Therefore, it is necessary to reduce Cd accumulation in farm products. Mutation of gene, which encodes *OsNramp5*, decrease Cd content in shoots of rice plants (*Oryza sativa* L.) [1]. However, Cd behavior in leafy vegetables is not fully understood. Leafy vegetables are edible at various growth stages. It is important to elucidate how Cd accumulates at various growth stages of leafy vegetables. We used oilseed rape plants (*Brassica napus* L.) in our study. We tried to elucidate effects of growth stages on Cd accumulation in oilseed rape plants by analyzing the experimental data which is obtained from Positron Emitting Tracer Imaging System (PETIS) experiments.

¹⁰⁷Cd (half-life 6.5 h) was used as a positron emitter in our PETIS experiments. ¹⁰⁷Cd was produced and purified as previously described [2, 3]. Fourteen-day-old, 18-day-old and 26-day-old seedlings, grown hydroponically in a growth chamber which can control plant growth condition completely were used in our PETIS experiments. After setting test plants in an experimental apparatus, PETIS experiments were started by adding a total of 10 μ M Cd including purified ¹⁰⁷Cd to each culture solution. Images of the ¹⁰⁷Cd distribution in plants were obtained every 4 minutes for 12 h. Time-activity curves, temporal changes of ¹⁰⁷Cd signals in specific regions of interest (leaves, node and so on), were generated from these PETIS data, following the methods of Nakamura *et al.*, 2013 [4].

We could obtain fine serial images of Cd behavior in 14-day-old, 18-day-old and 26-day-old plants. Figure 1 showed serial images of Cd behavior in 14-day-old plants. Strong signals of ¹⁰⁷Cd were found in the node of shoot base in each plant (Fig. 2). However, the site with the strongest ¹⁰⁷Cd signal was different in each plant (Fig. 2). Leaves were sites with the strongest ¹⁰⁷Cd signals in 14-day-old plants (Fig. 2A). The node where the petiole occurred was the site with the strongest ¹⁰⁷Cd signal in 18-day-old plants (Fig. 2B). The node of shoot base was the site with the strongest ¹⁰⁷Cd signal in 26-day-old plants

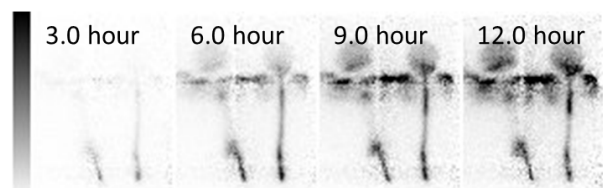


Fig. 1. Time series of PETIS images showing the ¹⁰⁷Cd signal (0-12 h) after decay correction. Fourteen-day-old plants are exposed to ¹⁰⁷Cd in the root medium.

(Fig. 2B). These results demonstrated that the site with the strongest ¹⁰⁷Cd signal changes according to the growth stage of oilseed rape plants.

The node is an important site for mineral distribution in plants [5]. There were different patterns in ¹⁰⁷Cd accumulation in the node of shoot base in 14-day-old plant and 26-day-old plant (Fig. 3). These results suggested Cd capacity in the node of shoot base has effects on Cd translocation from roots to shoots.

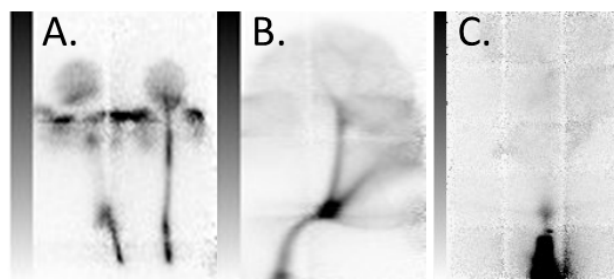


Fig. 2. Accumulation of ¹⁰⁷Cd signals in oilseed rape plants. This image is integration of obtained images, corresponding to 12 h (From 0 h to 12 h after the start of experiments). (A) 14-day-old plant, (B) 18-day-old plant, (C) 26-day-old plant.

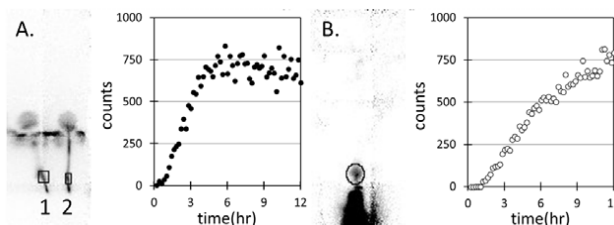


Fig. 3. Time-course analyses of ¹⁰⁷Cd signals accumulation in node of shoot base (A) 14-day-old plant (No.2) and (B) 26-day-old plant. This graph indicates the intensity of ¹⁰⁷Cd signals after decay correction.

References

- [1] S. Ishikawa *et al.*, Proc. Natl. Acad. Sci. USA **109**, 19166 (2012).
- [2] N. S. Ishioka *et al.*, JAEA Takasaki Ann. Rep. 2005 162 (2006).
- [3] S. Fujimaki *et al.*, Plant Physiol., **152**, 1796-806 (2010).
- [4] S. Nakamura *et al.*, J. Exp. Bot., **64**, 1073-81 (2013).
- [5] N. Yamaji and J. F. Ma, Trends Plant Sci. **19**, 556 (2014).

A Simulation Study on Imaging of Carbon-Ion Beams Using a Pinhole Camera Measuring Secondary Electron Bremsstrahlung

M. Yamaguchi, Y. Nagao and N. Kawachi

Department of Radiation-Applied Biology Research, TARRI, QST

Imaging methods for therapeutic carbon-ion beams are important to realize precise dose control. Recently, our group showed by simulation and experimental studies that secondary electron bremsstrahlung (SEB) emitted from the beam trajectories is useful to image therapeutic proton beams using a pinhole camera [1, 2]. In this work, we evaluated applicability of the method for carbon-ion beams by a simulation study.

Monte Carlo simulations were performed on a supercomputer system at JAEA. The Particle and Heavy Ion Transport code System (PHITS) [3] version 2.96 was utilized. Figure 1 represents a three-dimensional view of the geometry of the simulations. A right-hand coordinate system was defined in the simulation space so that its origin was located at the mass center of the water in a water phantom. The axis of the carbon-ion beams was set to the x-axis of the coordinate system and the direction of the movement of the incident carbon ions was set to the positive direction of the x-axis. The y-axis was set upwards.

The water phantom consisted of a ceiling-opened acrylic (polymethyl methacrylate) container and the water. The thickness of the wall and base of the container was 0.5 cm. The outer length, height and width of the container were 20, 20 and 10 cm, respectively. The phantom has a two-fold rotational symmetry around the y-axis. The heights of the origin and the surface of the water from the outside of the base of the container were 8.5 and 17 cm, respectively.

A pinhole camera was placed approximately 100 cm apart from the water phantom. It consists of a tungsten shield having a 0.15-cm-diameter pinhole with an opening angle of $\pm 15^\circ$ and a $2 \times 2 \times 0.1$ cm³ board of cerium-doped gadolinium aluminium gallium garnet (GAGG). The camera has a four-fold symmetry along the z-axis. The center of the pinhole was placed at $z = 98$ cm. A sensitive volume ($1.57 \times 1.57 \times 0.1$ cm³) was set in the center of the GAGG board. It was partitioned into 32×32 matrix. In each simulation, an image of the beam trajectory was acquired by recording each count of energy depositions by SEB in each pixel in the matrix during the beam injection. The lower and upper thresholds of the energy deposition were set to 30 and 60 keV, respectively. The field of view of the pinhole camera at the water phantom corresponded to a 29.3×29.3 cm² square. It was divided into 32×32 pixels by the partitioning of the sensitive volume.

These simulations were performed with varying the beam energy in three values, 278, 249 and 218 MeV/u. The positions of the Bragg peaks for the respective

energies were $x = 4.87, 2.35$ and -0.16 cm in order.

Figure 2 represents the acquired images by the simulations. The beam trajectories were clearly imaged. Each length of the region having high counts along the x-axis just coincides with that of the beam trajectory.

In conclusion, we performed feasibility study of imaging method using a pinhole camera measuring SEB for carbon-ion beams by the Monte Carlo method. The result showed that the beam trajectories were clearly imaged by SEB observation using a pinhole camera.

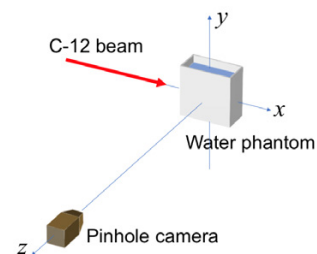


Fig. 1. A three-dimensional view of the simulation geometry.

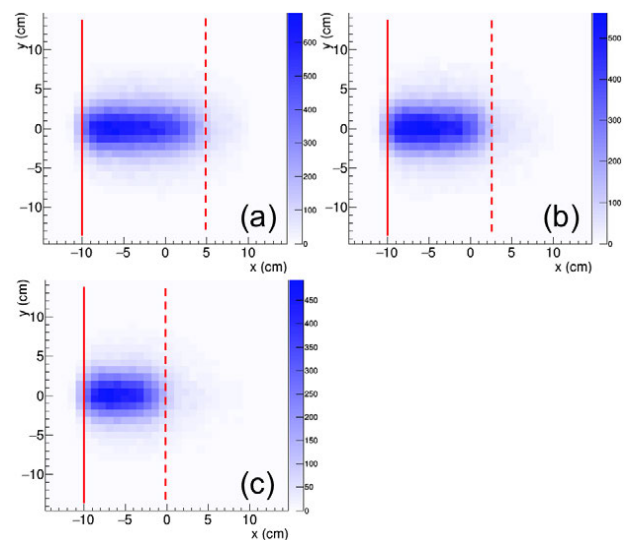


Fig. 2. The resultant images for the beam energy of (a) 278, (b) 249 and (c) 218 MeV/u. Solid and dashed lines represent the injection surfaces of the water phantom and the Bragg-peak positions.

References

- [1] M. Yamaguchi *et al.*, Nucl. Instrum. Meth. Phys. Res. A **833**, 199 (2016).
- [2] K. Ando *et al.*, Phys. Med. Biol. **62**, 5006 (2017).
- [3] T. Sato *et al.*, J. Nucl. Sci. Tech. **55**, 684 (2018).

Development of a Cost-Effective Compton Camera for Targeted Alpha-Particle Radiotherapy

Y. Nagao ^{a)}, M. Yamaguchi ^{a)}, S. Watanabe ^{a)}, N. S. Ishioka ^{a)},
N. Kawachi ^{a)} and H. Watabe ^{b)}

^{a)} Department of Radiation-Applied Biology Research, TARRI, QST,

^{b)} Cyclotron and Radioisotope Center, Tohoku University

Astatine-211 is a promising radionuclide for targeted α -particle radiotherapy of cancers [1]. It is required to image the distribution of targeted radiotherapeutic agents in a patient's body before or during treatment for optimization of treatment strategies and determination of the suitability of a given agent for a particular patient. Because the biodistribution of ^{211}At is different from that of ^{131}I , which is a common radiohalogen in conventional planar or single-photon emission computed tomography imaging, it is important to image ^{211}At directly.

Astatine-211 and its daughter radionuclide (^{211}Po) emit gamma rays (570, 687, and 898 keV) at the total intensity of 0.9%. These gamma rays are not substantially attenuated in the body, and hence, Compton cameras are suitable for visualizing ^{211}At distribution noninvasively.

We developed a Compton camera to demonstrate its capability of imaging ^{211}At with the gamma rays [2]. It has two detectors: a scatterer and an absorber. The scintillator material of both the detectors is cerium-doped gadolinium aluminum gallium garnet (GAGG). The scatterer is a 21-mm \times 21-mm \times 5-mm GAGG array block coupled to a silicon photomultiplier. The absorber is a 42-mm \times 42-mm \times 10-mm GAGG array block coupled to a flat panel type multianode photomultiplier tube. The distance between the front ends of the two GAGG array blocks is approximately 15 mm. A commercially available data acquisition (DAQ) system for a positron emission tomography camera was diverted to reduce cost. Figure 1 shows a photograph of the Compton camera head and the circuit board and the rack in the DAQ system.

Astatine-211 was produced via the $^{209}\text{Bi}(\alpha, 2n)^{211}\text{At}$ reaction using the cyclotron at TIARA. Ion beams ($^4\text{He}^{2+}$, 50 MeV) were degraded by a 0.4-mm aluminum plate, and a bismuth metal target (10 mm \times 10 mm \times 0.25 mm thickness) was bombarded with incident energy of 28.1 MeV and beam current of 3 μA for 3 h [3]. The irradiated target was dissolved in 0.5 mL of concentrated nitric acid. A portion of the nitric acid (0.125 mL) containing 20 MBq of ^{211}At in a 0.5-mL conical vial was used as a point-like source.

We performed imaging experiments of the point-like ^{211}At source using the developed Compton camera [4]. First, the 17.9-MBq source was placed at approximately 3 cm in front of the center (along x axis) of the camera and measured for 10 min. Second, the 16.6-MBq source was shifted toward the minus direction of x axis by approximately 2 cm and measured for 10 min.

The measured data were screened using the energy

window of 570 ± 53 keV ($\pm 9\%$). The selected data were imaged by list-mode maximum-likelihood expectation maximization algorithm with 10 iterations.

Figure 2 shows the reconstructed images. The source was clearly imaged and the 2-cm shift was consistently reproduced.

In conclusion, we developed a cost-effective Compton camera for targeted α -particle radiotherapy. We performed imaging experiments of the point-like ^{211}At source using the developed Compton camera, and the source was successfully imaged. This technique can be useful for targeted α -particle radiotherapy.

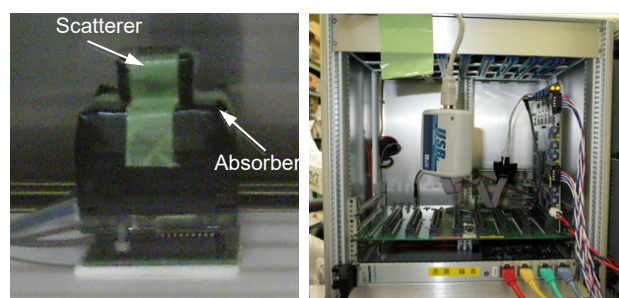


Fig. 1. A photograph of the Compton camera head (left) and the circuit board and the rack in the DAQ system (right).

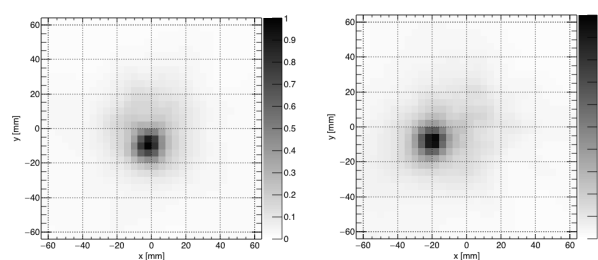


Fig. 2. Reconstructed images of a point-like source of ^{211}At at $x = 0$ mm (left) and at $x = -20$ mm (right) [4].

Acknowledgment

The present work was partly supported by JSPS KAKENHI Grant Number JP16K15351.

References

- [1] Y. Ohshima *et al.*, *Eur. J. Nucl. Med. Mol. Imaging*, **45**, 999 (2018).
- [2] Y. Nagao *et al.*, *Nucl. Instrum. Meth. Phys. Res. A*, **912**, 20 (2018).
- [3] K. Ogawa *et al.*, *Nucl. Med. Biol.*, **42**, 875 (2015).
- [4] Y. Nagao *et al.*, *Appl. Radiat. Isot.*, **139**, 238 (2018).

2 - 34 Comparison of Iron Localization in *Lotus japonicus* Root Using Micro-PIXE

J. Furukawa^{a)}, M. Ouchi^{a)}, Y. Noda^{a)}, N. Yamada^{b)}, T. Satoh^{b)} and S. Satoh^{a)}

^{a)}Life and Environmental Sciences, University of Tsukuba,

^{b)}Department of Advanced Radiation Technology, TARRI, QST

Plants need various elements for its growth. Not only major elements, such as nitrogen, phosphorous and potassium, but many essential trace elements are needed for plant development. The analysis of trace element content and localization in the focused organ or tissue is important to identify its functions. Especially, under some stress conditions, information about the localization of trace elements in the tissue level is highly valuable for investigating where the deficiency or toxicity of elements is detected and how to control the mechanisms for keeping homeostasis of plant body. Micro-PIXE (Particle Induced X-ray Emission) method can detect multi-element distributions in the same sample and visualize those localizations with high-resolution images [1, 2]. In this study, iron (Fe) localization in the roots of *Lotus japonicus* was focused. *L. japonicus* is a model legume and its two experimental lines, MG-20 and B-129, have a diversity in some metal concentrations including Fe in seed [3]. For understanding the mechanisms related to this Fe accumulation variety, the concentration and localization of Fe involved in the translocation step from root to shoot was investigated.

After the 4-week-cultivation of MG-20 and B-129 with hydroponics using 1/10 Hoagland's solution, above ground shoot part and root were harvested. After the ICP-AES measurement, Fe concentration in shoot was higher in MG-20, but its concentration in root was obviously higher in B-129. These Fe allocation pattern suggests the Fe translocation activity from root to shoot is low in B-129. As for the Fe translocation from soil to shoot, some transmembrane and/or intracellular steps are needed, such as uptake into the root cell, transfer from root surface cell to stele, the center of root, and xylem loading around the vascular bundles.

To identify what kind of steps are involved in the suppression of Fe translocation from root to shoot in B-129, the comparison of Fe localization between two cultivars using Micro-PIXE was carried out. As for the preparation of PIXE imaging, the samples were embedded in the compound for a freeze sectioning and sliced to 20 μm sections by freezing microtome and then pasted on the polycarbonate film for 3 MeV H^+ beam exposure. In the root tips, the spectrum of Fe was not observed in MG-20, however, B-129 sample showed Fe signals (Fig. 1). At the middle part of root, Fe accumulation around the root center was observed in both cultivars. For understanding the root structure more in detail, potassium (K) image was obtained with the same sample. Comparing the Fe and K localization,

it was revealed that the Fe was accumulating at the stele. In B-129, Fe concentration in stele was higher than MG-20 and Fe was accumulated at the center part of stele.

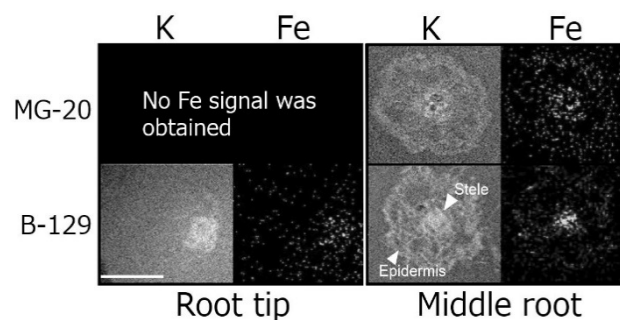


Fig. 1. Iron (Fe) and potassium (K) localization images with Micro-PIXE in the root of MG-20 and B-129 cultivars. Left panel shows the root tip and the right shows the middle part of root. Arrowheads show stele and epidermis of root.

Based on the Fe localization patterns in the root tissue, the hypothesis explaining the Fe deficiency in B-129 shoot was obtained. The Fe ion absorbed at the root surface was transferred in the root tissue to the stele. Around the xylem vessels, Fe ion was loaded into the xylem vessels in MG-20 but not in B-129. In *Arabidopsis*, it is known that the mutation in one gene involved in long distance Fe translocation induces shoot Fe deficiency and root Fe accumulation [4, 5]. To identify the responsible genes in *L. japonicus*, the expression levels of candidate genes were investigated in root. In B-129 lines, the expression of some IREG genes, which encode putative Fe xylem loading transporter, were suppressed compared to MG-20. The experiment using IREG knock-out line in MG-20 will reveal the Fe translocation mechanisms from root to shoot in *L. japonicus*.

References

- [1] T. Yamamoto *et al.*, JAEA Takasaki Annu. Rep. 2014, 88 (2016).
- [2] Y. Noda *et al.*, QST Takasaki Annu. Rep. 2015, **QST-M-2**, 151 (2017).
- [3] M. A. Klein and M. A. Grusak, *Genome*, **52**, 677-91 (2009).
- [4] E. Delhaize, *Plant Physiol.*, **111**, 849-55 (1996).
- [5] T. P. Durrett *et al.*, *Plant Physiol.*, **144**, 197-205 (2007).

Analysis of Trace Elements in Acute Myelogenous Leukemia Cell Line Using In-Air Micro-PIXE

T. Kasamatsu, Y. Kanai and H. Murakami

Graduate School of Health Sciences, Gunma University

Acute Myelogenous leukemia (AML) is a cancer of the myeloid line of blood cells, characterized by the rapid growth of abnormal cells that build up in the bone marrow and blood, and interfere with normal blood cells. Symptoms include feeling tired, easy bleeding, and increased risk of infection. As an acute leukemia, AML progresses rapidly and is typically fatal within weeks or months if left untreated. To elucidate the pathophysiology of AML, we analyzed the trace elemental changes in AML cell using in-air micro-PIXE method.

One AML cell line, HL-60, was used in this study. For comparison, a multiple myeloma cell line KMS-11 was also used. Both HL-60 and KMS-11 were grown in RPMI with 10% heat-inactivated fetal bovine serum, and antibiotics. HL-60 cells were treated with 0 nM and 850 nM doxorubicine (DXR), an anthracycline antibiotic with antineoplastic activity, for 24 h. Cells were centrifuged by cytocentrifuge for 500 rpm, 15 minutes on a 0.5 μm polycarbonate film after washing and resuspension in TRIS-HNO₃ (pH 7.4). The film was sunk into isopentane chilled with liquid nitrogen down to its melting point (-160 °C), then lyophilized by vacuum evaporation at 1.3 Pa. The samples thus prepared were analyzed by in-air micro-PIXE with 3.0-MeV proton beams having 1- μm diameter, from the single-ended accelerator in TIARA.

In X-ray spectrum derived from HL-60, potassium yield was higher than KMS-11 (Fig. 1). Other elemental yields were almost similar among these cell lines. Subsequently, we compared the spectrum between 0 nM and 850 nM DXR

treatment HL-60 cells. Potassium yield of 850 nM DXR treatment cells was lower than 0 nM DXR treatment cells (Fig. 1). There were no differences in other elemental yields.

Almost all cells possess an Na⁺-K⁺-ATPase, which pumps Na⁺ out of the cell and K⁺ into the cell and leads to a K⁺ gradient across the cell membrane (K⁺_{in}>K⁺_{out}). Cell proliferation and apoptosis are two counterparts that share the responsibility for maintaining normal tissue homeostasis. Evidence has been accumulating from fundamental studies indicating that tumour cells possess various types of potassium channels, and that these potassium channels play important roles in regulating tumour cell proliferation and apoptosis, *i.e.* facilitating unlimited growth and promoting apoptotic death of tumour cells [1]. Doxorubicin intercalates between base pairs in the DNA helix, thereby preventing DNA replication and ultimately inhibiting protein synthesis. Additionally, doxorubicin inhibits topoisomerase II which results in an increased and stabilized cleavable enzyme-DNA linked complex during DNA replication and subsequently prevents the ligation of the nucleotide strand after double-strand breakage. In this study, DXR treatment caused the decrease of intracellular potassium levels in HL-60. Our result suggested that DXR may affect the cell death via potassium homeostasis directly or indirectly.

Reference

- [1] Z. Wang *et al.*, Pflugers Arch. **448**, 274-86, (2004).

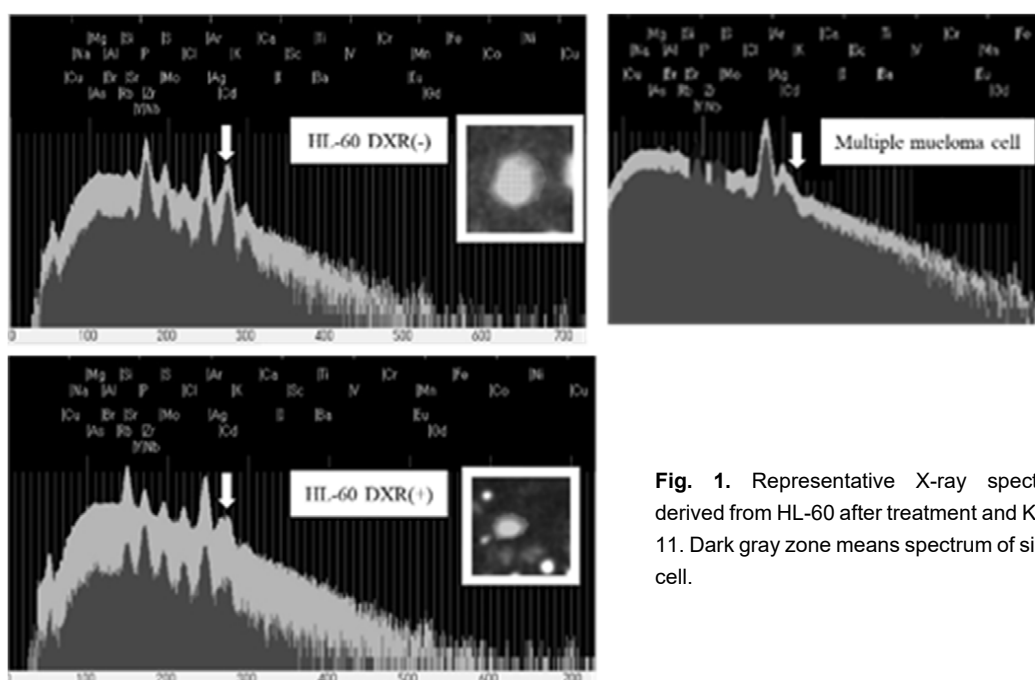


Fig. 1. Representative X-ray spectrum derived from HL-60 after treatment and KMS-11. Dark gray zone means spectrum of single cell.

Elemental Analysis of the Lungs in Patients with Idiopathic Pulmonary Fibrosis

Y. Koga ^{a)}, T. Satoh ^{b)}, K. Kaira ^{c)}, M. Koka ^{d)}, T. Hisada ^{a)} and K. Dobashi ^{e)}

^{a)} Department of Allergy and Respiratory Medicine, Gunma University Graduate School of Medicine,

^{b)} Department of Advanced Radiation Technology, TARRI, QST,

^{c)} Department of Oncology Clinical Development, Gunma University Graduate School of Medicine,

^{d)} Beam Operation Co., Ltd.,

^{e)} Jobu Respiratory Hospital

It has been well known that inhalation of asbestos can be a risk factor of interstitial pneumonia. The relationship between inhalation of elements and interstitial pneumonias still remains unknown. Any biomarkers indicating prognosis of interstitial pneumonia has not been established yet. In this study, we focused on idiopathic pulmonary fibrosis (IPF) showing usual interstitial pneumonia in the histology and examined the inhaled elements in the lung by in-air micro particle-induced X-ray emission analysis (in-air micro PIXE). The relationship between elements in the lung contents and the progression of IPF were analyzed. In-air micro PIXE detected various elements in the lung. Among them, inhaled silica/silicates were correlated with annual declined forced vital capacity and diffusing capacity for carbon monoxide. Other elements detected by in-air micro PIXE did not show any association of the progression of IPF. These results indicate that accumulated silica/silicates in the lung are associated with the progression of IPF. This study showed that in-air micro PIXE can detect small amount of inhaled elements in the lung and is useful for the analysis of progression in IPF patients.

はじめに

微量な肺組織内の元素分布の測定が可能な高感度大気マイクロ PIXE (Particle Induced X-ray Emission) の手法を用いて我々は肺と縦隔リンパ節における元素濃度の検討を行ってきた[1]。本研究では、特発性肺線維症を対象とした肺組織中の微量元素解析を行い、肺組織中の元素濃度と特発性肺線維症の進行度との関連性を検討した。

方法

肺組織パラフィン切片にイオンマイクロビームを照射し組織切片内の元素分布を測定した。組織内元素濃度は、組織分布を示す sulphur を分母とした比率で算出した。対象は特発性間質性肺炎のうち、胸腔鏡下肺生検で病理学的に Usual interstitial pneumonia pattern を呈している特発性肺線維症とした。

結果

大気マイクロ PIXE 分析により、肺組織中の Al, Mg, Si, S, P, Ca, Fe, Zn を検出した。肺組織中のシリカと特発性肺線維症努力性肺活量(FVC)、一酸化炭素肺拡散能(D_{Lco})の変化との間に有意な相関関係を認めた(Fig. 1)。シリカ以外の肺組織中元素と肺機能の推移に相関関係は認められなかった。

考察

大気マイクロ PIXE によって検出された肺組織中の微量のシリカ含有量の増加が、特発性肺線維症の進行度と相関関係にあることが示された。

Reference

[1] Y. Koga *et al.*, Environ. Health Prev. Med. **21**(6), 492-500 (2016).

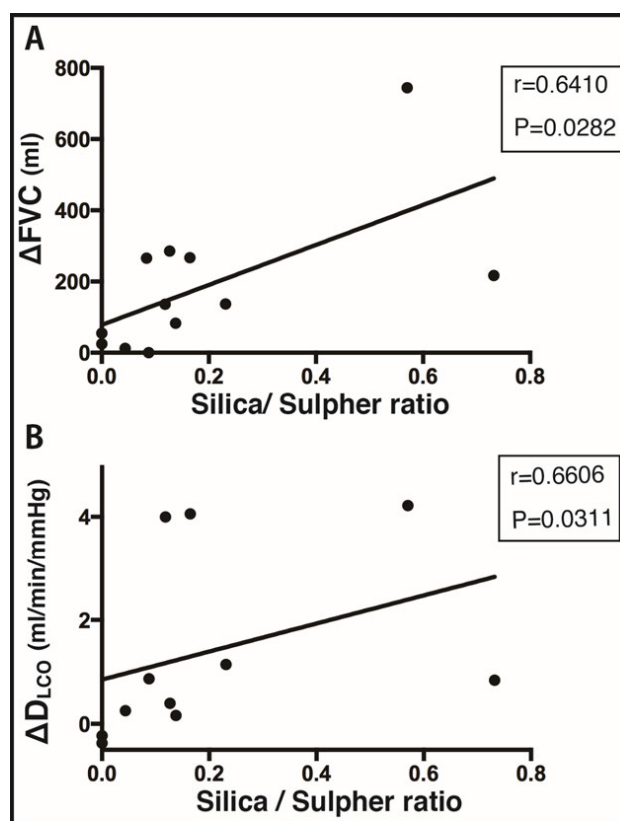


Fig. 1. Relationship between annual declined pulmonary functions and accumulated silica/silicates in the lung. Accumulation of silica/silicates in the lung significantly correlated with both annual declined forced vital capacity (FVC) (A) and diffusing capacity for carbon monoxide (D_{Lco}) (B).

2 - 37 Long-term Fluorine Penetration from Fluoride-containing Luting Materials to Dentin

K. Okuyama^{a)}, Y. Matsuda^{b)}, H. Yamamoto^{c)}, Y. Tamaki^{a)}, T. Saito^{b)}, M. Hayashi^{c)}, H. Sano^{d)}, Y. Yoshida^{d)}, N. Yamada^{e)}, M. Koka^{f)} and T. Satoh^{e)}

^{a)} School of Dentistry, Asahi University,

^{b)} School of Dentistry, Health Sciences University of Hokkaido,

^{c)} Graduate School of Dentistry, Osaka University,

^{d)} Faculty of Dental Medicine, Hokkaido University,

^{e)} Department of Advanced Radiation Technology, TARRI, QST,

^{f)} Beam Operation Co., Ltd.

Introduction

There are some kinds of dental luting materials (cements) in the market, and some of them have a function of fluoride releasing from material for secondary caries prevention after cementing with prosthetic appliances (crown or bridge). Previously, penetration of fluorine from fluoride-containing luting materials to adjacent dentin was evaluated after 4-weeks pH cycling [1]. In this study, distribution of fluorine after 8-weeks pH cycling was evaluated by in-air micro PIXE/PIGE system at TIARA.

Materials and Methods

Extracted human teeth were used in this study. Each tooth crown was cut and grinded to expose a flat dentin surface. An acrylic resin plate (2 mm thickness) was cemented with four kinds of fluoride-containing luting materials (Fuji Luting EX: FL, Fuji I: FO, SA Luting plus: SA, BeautiCem SA: BC) on the dentin surface. The specimen was embedded by epoxy resin and then the outer dentin surface including dentin-luting material-resin plate interface was exposed. The embedded specimen was sliced (about 500 μm thickness) and coated with wax except for exposed dentin surface. Each sliced sample was carried out on pH cycling (pH: 4.5 and 7.0; simulate daily acid attacking) for 8-weeks for preparing artificial carious dentin using an automatic pH-cycling system [2]. After pH cycling, calcium and fluorine distribution were analyzed by an in-air micro-PIXE/PIGE system with a 1.7-MeV $^1\text{H}^+$ microbeam at TIARA [3]. The outermost surface of the dentin was defined at the position containing 5% of the calcium concentration in intact dentin. For the comparison of fluorine uptake and calcium contents, fluorine and calcium concentration in each specimen was calculated at area of 100 μm from the defined surface. The obtained data of fluorine or calcium was analysis by Mann-Whitney U test, or Games-Howell test, respectively ($\alpha=0.05$).

Results

Figure 1 shows concentration of penetrated fluorine into dentin around each material at 100 μm depth area from superficial surface. FL indicated highest concentration of fluorine among all materials.

For the amount of calcium contents on an area 100 μm from the defined surface after pH cycling, FL showed higher amounts of calcium than that of SA ($p<0.05$) [FL: 17.3 ± 4.8 , FO: 11.7 ± 5.4 , SA: 5.7 ± 5.9 , BC: 8.9 ± 8.1 ($\times 10^6$) (ppm $\times\mu\text{m}$)].

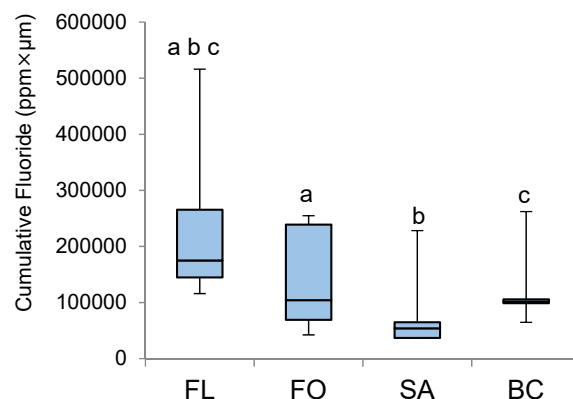


Fig. 1. Concentration of penetrated fluorine into dentin around each material at 100 μm depth area from superficial surface (ppm $\times\mu\text{m}$). Same letters indicate significant differences ($p<0.05$).

Discussion

High concentration of fluorine was exhibited on FL, because this material released largest amounts of fluoride to water compared among all materials [4]. Moreover FL shows highest calcium concentration. These results indicate that high fluorine concentration in tooth structure might be caused less demineralization, and fluorine and calcium concentration might be related. This relation is agreed with previous report [5].

Conclusion

The amount of fluorine penetration on dentin might be depend on amount of fluoride release from each material and related with remained amount of calcium.

References

- [1] K. Okuyama *et al.*, QST Takasaki Annu. Rep. 2016, **QST-M-8**, 113 (2018).
- [2] Y. Matsuda *et al.*, Dent. Mater. J. **24**, 280-85 (2006).
- [3] H. Yamamoto *et al.*, Nucl. Instrum. Meth. Phys. Res. B, **210**, 388-94 (2003).
- [4] K. Okuyama *et al.*, J. Jpn. Dent. Mater. **36**, 398 (2016).
- [5] K. Yagi *et al.*, Sci. Rep., **7**, 13450 (2017).

K. Nakai ^{a)}, K. Endo ^{b)}, F. Yoshida ^{b)}, A. Matsumura ^{b)}, N. Yamada ^{c)} and T. Satoh ^{c)}

^{a)} Department of Neuro-rehabilitation, Ibaraki Prefectural University Hospital,

^{b)} Department of Neurosurgery, Faculty of Medicine, University of Tsukuba,

^{c)} Department of Advanced Radiation Technology, TARRI, QST

Boron Neutron Capture Therapy is one of the particle radiotherapies, which has developed for treatment of malignancies. For this therapy, boron existence and penetration of thermal neutron into the target tissue are required. In this study, we used micro ion beam particle induced gamma-ray emission (PIGE) to confirm the boron distribution of 2 hours after boron exposure *in vitro*.

U251 human glioma cell line was used. p-boronophenylalanine (BPA) was dissolved to make a concentration of 160 or 800 $\mu\text{g}^{10}\text{B}/\text{mL}$ in culture medium. Micro particle-induced X-ray emission (PIXE) and micro particle-induced gamma-ray emission (PIGE) analysis were performed at Takasaki Ion Accelerators for Advanced Radiation Application (TIARA, Takasaki, Japan). The freeze-dried cellular samples were mounted and element (Potassium, Phosphate and Boron) distribution images and whole spectrum was detected. These elements showed existence of the cells [1].

Figure 1 shows 2-dimensional image of U251 cells. Figure 1(C) reveals a cell containing boron. Figure 2 shows that washing with PBS decrease boron. Boron distribution in boron exposure group matched with those of other cellular element (P, K), but the distribution of boron in boron exposure followed with washing group was undetectable. The boron concentration measured by ICP-AES (Fig. 3) was $22.12 \pm 1.78 \mu\text{g}/10^7$ cells in boron exposure group, and $3.90 \pm 0.43 \mu\text{g}/10^7$ cells in exposure and wash group.

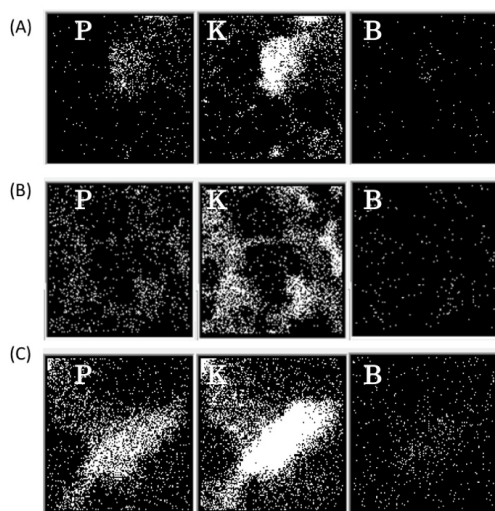


Fig. 1. Micro-PIXE and PIGE Image of U251 Cells with Boron (A) control (normal medium only). (B) 160 μg B/mL BPA-containing medium, 2 h exposure. (C) 800 μg B/mL BPA-containing medium, 2 h exposure. P and K images were from PIXE, B were from PIGE. Images are 50 μm in length and width.

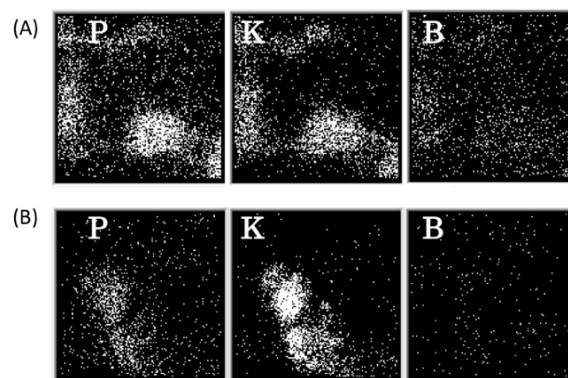


Fig. 2. Micro-PIXE and PIGE Image of U251 Cells with/without Medium Wash (A) Medium were only aspirated after 800 μg B/mL BPA containing medium, 2 h exposure. (B) Wash with PBS after boron exposure. 800 μg B/mL BPA containing medium, 2 h exposure. P and K images were from PIXE, B images were from PIGE. Images are 50 μm in length and width.

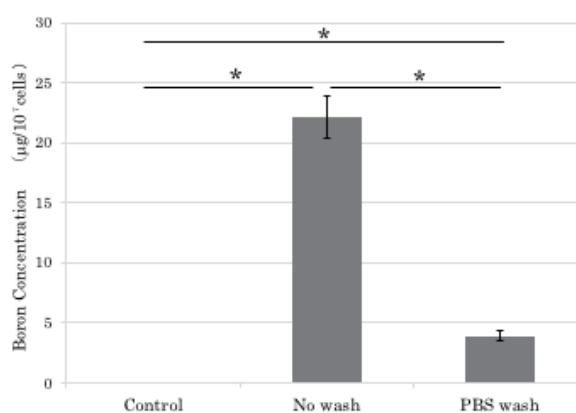


Fig. 3. ICP-AES measurement of Boron amount with/without Medium Wash. No wash meant medium were only aspirated after 800 μg B/mL BPA containing medium, 2 h exposure. PBS Wash with PBS after boron exposure. 800 μg B/mL BPA containing medium, 2 h exposure.

These results require further investigation as to whether boron compounds have been incorporated into the cells.

References

- [1] K. Endo *et al.*, *Oncol. Res.* **16**(2), 57-65 (2006).
- [2] K. Nakai *et al.*, *Appl. Radiat. Isot.* **106**, 166-70 (2015).

2 - 39 Search Trace Elements in Brain Microvascular Endothelial Cells (BMECs) and Effects of Nicotine on Trace Element in BMECs

E. Sakurai^{a, b)}, E. Sakurai^{c)}, K. Yanai^{b)}, S. Matsuyama^{d)}, Y. Ueki^{d)}, Y. Kitayama^{d)}, K. Ishii^{d)}, M. Koka^{e)}, T. Satoh^{f)} and T. Kamiya^{g)}

^{a)} Faculty of Pharmacy, Iwaki Meisei University,

^{b)} Department of Pharmacology, School of Medicine, Tohoku University,

^{c)} Faculty of Pharmaceutical Sciences, Tokushima Bunri University,

^{d)} Department of Quantum Science and Energy Engineering, Tohoku University,

^{e)} Beam Operation Co., Ltd.,

^{f)} Department of Advanced Radiation Technology, TARRI, QST,

^{g)} Faculty of Science and Technology, Gunma University

Microvascular cells act as a barrier to protect our body from dangerous matter. Blood vessels of brain have a defense system called "blood brain barrier". Brain microvascular endothelial cells (BMEC) are major structural and functional component of the brain blood barrier (BBB). BBB has important roles that maintain the homeostasis of the central nervous system.

Lung microvascular endothelial cells (LMECs) also play in preventing an injury by air pollutants through respiratory organs. Our previous reports show trace metals such as zinc, manganese, magnesium copper and nickel act to protect from oxidative stress by nicotine in LMECs.

On the other side, it is well known that nicotine is an abuse drug to get addicted. Nicotine can easily pass to brain microvascular endothelial cells (BMECs). However, there no report on the change in function of BMECs treated with nicotine. So, we investigated the effects of nicotine and on BMECs by focusing on changes in intracellular element levels using in-air micro-PIXE analysis. In-air micro-PIXE was developed at the Takasaki Ion Accelerators for Advanced Radiation Application (TIARA), QST. Micro-PIXE allows analyzing the spatial distribution of the elements quantitatively.

Three weeks old male C57BL/6J mice purchased from Japan SLC. Mice BMECs were isolated using a modification of the technique described by Magee et al [1]. The procedures of cell culture on collagen-coated polycarbonate film (2.54 cm²) for microanalysis were described in previous reports. The cells were washed two times with 1 mL of Krebs buffer, and pre-incubated with 0.9 mL of Krebs buffer at 37 °C for 5 min. Then, Krebs buffer containing 0-200 μM nicotine was added to the each film, and cells were incubated for 5 min. The cells on the 5 μm polycarbonate films were washed 7 times with THAM buffer. The specimens were promptly dipped into 2-methylbutane and chilled with liquid nitrogen and then freeze-dried overnight in the vacuum stage [1].

Figure 1 showed the images (50 × 50 μm) of sodium, potassium, phosphorus, sulfur, chloride and calcium in BMECs after treatment with 0, 0.2, 20, and 200 μM nicotine for 5 min. Distribution image in Fig. 1 shows potassium and chloride density were increased when BMECs were treated

with 0.2 μM nicotine (indicated by an asterisk). It is well known, potassium is high concentration in intracellular fluid and chloride concentration is high in extracellular fluid. So, chlorine level in BNECs may increase after stimulation by 0.2 μM nicotine.

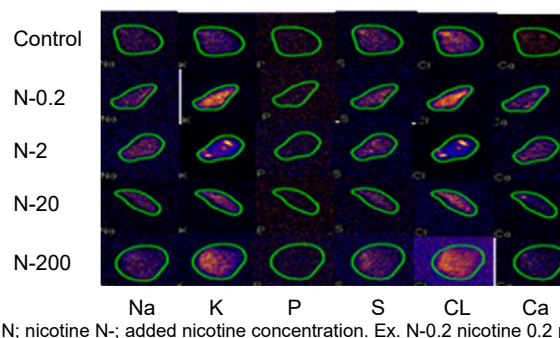


Fig. 1. Distributions images (50 μm × 50 μm) of sodium, potassium, phosphorus, sulfur, chloride, calcium after addition of 0-200 μM nicotine on rats BMECs for 5 min.

Figure 2 showed the images of magnesium, aluminum, iron, manganese, zinc, copper and nickel in the same BMECs in Fig. 1.

The results showed that BMECs have magnesium, aluminum and iron. Trace elements in superoxide dismutase (SOD) such as manganese, zinc copper and nickel were detected in treated-nicotine BMECs.

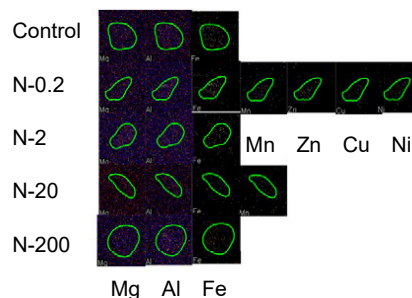


Fig. 2. Magnesium, aluminum and iron detected after addition of 0-200 μM nicotine on rats BMECs for 5 min.

Reference

[1] E. Sakurai *et al.*, QST Takasaki Annu. Rep. 2016, **QST-M-8**, 117 (2018).

2 - 40 Kinetics of Encapsulated Hyaluronic Acid-Protamine Particle After Intravenous Injection

S. Harada ^{a)}, T. Segawa ^{a)}, S. Ehara ^{a)} and T. Satoh ^{b)}

^{a)} Department of Radiology, School of Medicine, Iwate Medical University,

^{b)} Department of Advanced Radiation Technology, TARRI, QST

Introduction

We have been developing a method of targeted delivery of anti-cancer drugs using radiosensitive microparticles that release anti-cancer drugs in response to radiation, aiming to increase anticancer effects and reduce adverse effects [1]. First, the radiosensitive microparticles are delivered to the tumor. Second, the tumor is irradiated, and the anticancer drug is released from radiosensitive microparticles. Third, the released anticancer drug arrives at the tumor, and antitumor effects are enhanced synergistically with radiation. Fourth, adverse effects are reduced by localization of the anticancer drug to the tumor. Recently, our reports have shown that protamine and hyaluronic acid electrostatically bind to each other and absorb anticancer drugs in their solution to form hyaluronic acid-protamine nanoparticles that contain anticancer drugs. Lipid nanotubules (Coatsome-EL-010) then encapsulate those particles. When those encapsulated particles are irradiated, hyaluronic acid in the particle decomposes to N-acetyl-glucosamine, which results in the release of the anticancer drug from the particle [2].

Previously, we delivered radiosensitive particles to tumors that were inoculated in the left hind legs of mice [1]. As the tumor was located at the surface of the left leg, we could deliver particles to the tumor through direct injection near the tumor. However, this direct injection method did not allow for the delivery of particles to the tumor and in organs at deep sites, for example, the lungs, liver, and kidneys. One of the considerable answers to this problem is that the particles are delivered to tumors in organs at deep sites through the bloodstream by intravenous injection. In this study, the kinetics of radiosensitive nanoparticles in the body when injected into the tail vein *in vivo* in C3He/N mice.

Methods and Materials

Generation of particles: One mL of protamine solution (4 mg/mL) and 1 mL of hyaluronic acid solution were added to 2 mL of carboplatin solution (platinum (Pt)-containing anticancer drug, 1 mg/mL), and the resulting solution was stored at room temperature for 40 min. Finally, 2 mL of this solution was injected into one vial of Coatsome-EL-010 and stored for 30 min at room temperature, before being used for experiments.

Treatments and harvest of samples: A total of 1×10^{10} particles were injected into the tail vein of each mouse (C3He/N, 6 weeks) that harbored an MM48 tumor (mouse breast cancer) in the left hind leg. One, 3, 6, 9, 12, and 24 h after injection, the tumors, lungs, brain, liver, and spleen were excised. The excised organs were then routinely processed to target for micro-PIXE camera imaging.

Micro-PIXE camera: The particles were imaged using the micro-PIXE camera, based on the distribution of Pt in

carboplatin. All micro-PIXE analyses were carried out at the Takasaki Advanced Radiation Research Institute in National Institutes for Quantum and Radiological Science and Technology. The number of trapped particles was expressed as the average number of particles in 10 views of micro-PIXE camera images ($12 \times 12 \mu\text{m}$).

Results

Generated particles: The generated particles observed using the micro-PIXE camera based on Pt distribution are shown in Fig. 1. The mean diameter of the particles was 743.2 ± 21.4 nm. The hot spot of Pt was observed in the center of the particles.

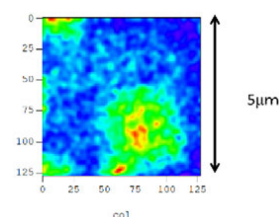


Fig. 1. Generated Particles. Observed by micro PIXE camera.

The number of trapped particles: The number of trapped particles in the tumor, lungs, brain, liver, and spleen is shown in Fig. 2. The greatest numbers of trapped particles were observed 6 hours after injection, which were 4.6 ± 0.32 in the tumor and 1.1 ± 0.1 in the lungs. In the other organs, there were slight increases in trapped organs, which were less than one capsule.

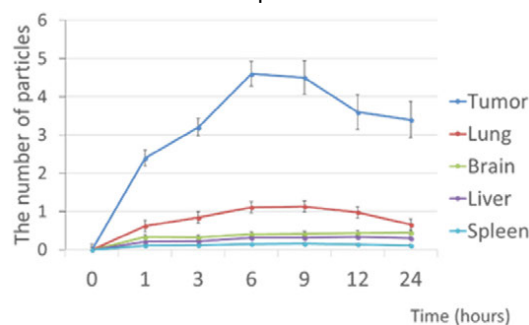


Fig. 2. The number of trapped particles in tumors, lung, brain, liver, and spleen is plotted versus time (hours).

Discussion

It is well known that tumor vessels have a coarse structure. Their openings between endothelial cells are wider than those of any other normal vessels, which results in greater permeability of particles in tumor vessels [1]. In this study, the greatest delivery of particles was observed in the tumor. The phenomenon that is considered is that greater permeability of particles resulted in greater delivery of particles in the tumor.

References

- [1] S. Harada *et al.*, Biomed. Pharmacother. **70**, 196 (2015).
- [2] S. Harada *et al.*, Int. J. PIXE **24**, 137 (2014).
- [3] Xiaoyang Xu *et al.*, Trends Mol. Med. **21**, 223 (2015).

Astatinated Antibody Fragment for Reducing Renal Radioactivity Levels

H. Suzuki^{a)}, Y. Ohshima^{b)}, S. Watanabe^{b)}, T. Uehara^{a)},
N. S. Ishioka^{b)} and Y. Arano^{a)}

^{a)} Graduate School of Pharmaceutical Sciences, Chiba University,

^{b)} Department of Radiation-Applied Biology, TARRI, QST

Due to their high linear energy transfer and short path lengths, α -emitters have paid attention to targeted α therapy. Radium-223 has been approved in Japan to treat bone metastases of prostate cancer in 2016. Actinium-225 labeled prostate-specific membrane antigen inhibitor showed robust therapeutic efficacy to advanced-stage of prostate cancer patients [1].

²¹¹At is one of the most promising α -emitters for the targeted α therapy. ²¹¹At can be obtained by a cyclotron. Although polypeptides such as IgG and F(ab)₂ have been evaluated as vehicles to deliver ²¹¹At to cancer cells, the relatively short half-life of ²¹¹At (7.2 h) is suitable to low molecular weight polypeptides (LMWPs) such as Fab.

However, high and persistent localization of radioactivity is observed after injection of LMWPs [2], due to slow elimination rates of radiometabolites after lysosomal proteolysis in the renal cells, following glomerular filtration and subsequent reabsorption into renal cells. To solve this problem, we developed 3'-iodohippuryl-*N*^ε-maleoyl-L-lysine (HML) that liberates 3-iodohippuric acid by the action of renal brush border membrane enzymes before incorporating into renal cells. Since astatine is a homologous element with iodine, the chemical design of HML also applied to ²¹¹At-labeled LMWPs. We prepared [²¹¹At]HML-labeled Fab, and evaluated its biodistribution.

²¹¹At was produced via the ²⁰⁹Bi(α , 2n)²¹¹At reaction, and isolated from an irradiated target by the dry distillation method. Figure 1 shows the synthetic scheme for ²¹¹At-labeled Fab. Briefly, the stannyl precursor of HML and *N*-chlorosuccinimide (NCS) was added to a solution of ²¹¹At in methanol, and reacted for 15 min at room temperature. After stopping the reaction by adding an aqueous solution of Na₂S₂O₅, the crude product of [²¹¹At]HML was reacted with thiol groups of Fab introduced by 2-iminothiolane for 1.5 h. The reaction product was purified by spin column to provide [²¹¹At]HML-labeled Fab in 41.6% radiochemical yield. For the comparison, [¹²⁵I]HML-labeled Fab and [¹²⁵I]SIB labeled Fab were also prepared and used for biodistribution study.

The biodistribution of [²¹¹At]HML-labeled Fab in normal mice is shown in Fig. 2. The blood clearance of [²¹¹At]HML-labeled Fab was similar to those of [¹²⁵I]HML-labeled and [¹²⁵I]SIB-labeled Fabs. Renal radioactivity levels of [²¹¹At]HML-labeled Fab were lower than those of [¹²⁵I]SIB-labeled Fab, and comparable to

those of [¹²⁵I]HML-labeled Fab. However, [²¹¹At]HML-labeled Fab showed higher radioactivity levels in stomach and spleen when compared with [¹²⁵I]-labeled Fab, indicating deastatination of [²¹¹At]HML-labeled Fab *in vivo*. The similar radioactivity levels of [²¹¹At]HML- and [¹²⁵I]HML-labeled Fabs in the blood and the kidney indicate that the chemical design of HML is applicable to ²¹¹At-labeled LMWPs. Efforts are being focused on developing ²¹¹At-labeled benzoic acid derivatives that are resistant against *in vivo* deastatination.

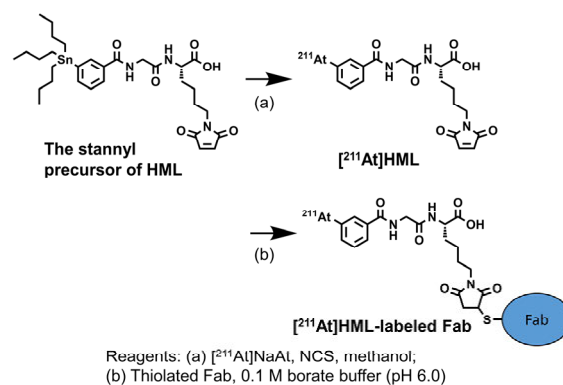


Fig. 1. Synthetic scheme of [²¹¹At]HML-labeled Fab.

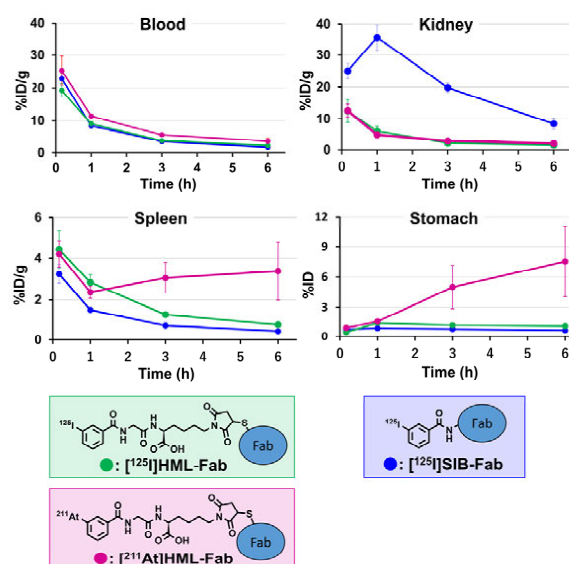


Fig. 2. Biodistribution of radiolabeled Fab fragments.

References

- [1] C. Kratochwil *et al.*, J. Nucl. Med. **57**, 1941 (2016).
- [2] C. W. Choi *et al.*, Cancer Res., **55**, 5323 (1995).
- [3] Y. Arano *et al.*, Cancer Res., **59**, 128 (1999).

Prat II

3. Advanced Quantum-Beam Technology

3-01	Fabrication of Mach-Zehnder Waveguide Embedded in Biocompatible Thin Film by Proton Beam Writing	121
	W. Kada, S. Miura, R. Takahashi, K. Kasuya, Y. Wang, K. Miura, M. Koka, T. Satoh, N. Yamada, Y. Ishii, T. Kamiya and O. Hanaizumi	
3-02	Refractive Index Change and Thermo-Optic Effect in Polydimethylsiloxane Nanocomposites with Oxide Nanoparticles Induced by Proton Beam Writing	122
	Y. Kaneko, H. Hayashi, Y. Ishii and H. Nishikawa	
3-03	Quantification of Damage to a Biomolecular Sample in Transmission SIMS Using MeV C ₆₀ Primary Ions	123
	H. Ishii, J. Sawada, K. Nakajima, A. Chiba, K. Yamada, Y. Hirano, K. Narumi, Y. Saitoh and K. Kimura	
3-04	Lithium Distribution Analysis in All-solid-state Lithium Battery Using Maxicrobeam PIXE and PIGE Techniques	124
	K. Mima, K. Yoshino, K. Suzuki, Y. Yamada, T. Satoh, M. Finsterbusch, K. Fujita, T. Kamiya, A. Yamazaki and Y. Kato	
3-05	Vacancy-induced Magnetism in GaN Film Probed by Spin-polarized Positron Beam	125
	M. Maekawa, S. Sakai, K. Wada, A. Miyashita and A. Kawasuso	
3-06	Dopant Dependence on Vacancy Defects in Ion-Beam Synthesized β -FeSi ₂ Films	126
	A. Yabuuchi, A. Kinomura, M. Maekawa and A. Kawasuso	
3-07	Properties of Scintillation Emission Signal from Nd:YAG/Cr:YAG Composite by Gamma Ray Irradiation	127
	H. Ohba, K. Tamura, M. Saeki, T. Taguchi, H. Lim, T. Taira and I. Wakaida	
3-08	Status Report on Technical Developments of the TIARA AVF Cyclotron	128
	H. Kashiwagi, N. Miyawaki and S. Kurashima	
3-09	Dynamic Behavior of Elements with Low Atomic Numbers in Lithium Oxide Ceramics Under Irradiation	129
	B. Tsuchiya, S. Yamamoto, K. Takahiro and S. Nagata	
3-10	Analysis of Linear Energy Transfer Effects on the Scintillation Properties of Ce:Gd ₃ Al ₂ Ga ₃ O ₁₂ (GAGG)	130
	M. Koshimizu, S. Kurashima, A. Kimura, M. Taguchi, T. Yanagida, H. Yagi, T. Yanagitani, Y. Fujimoto and K. Asai	
3-11	Measurements of Relative Angular Distribution of the n-p Elastic Scattering Reaction for 45-MeV Neutrons	131
	T. Matsumoto, A. Masuda, H. Harano and S. Kurashima	
3-12	Photo-stimulated Luminescence of G2000 and Recovery by Annealing	132
	A. Yokoyama, W. Kada, K. Miura and O. Hanaizumi	
3-13	Technical Development of Continuous Uniform Ion Irradiation for Production of Track-etched Membranes	133
	Y. Yuri, T. Yuyama, K. Yoshida, T. Ishizaka, I. Ishibori, H. Yamamoto, M. Aizuka, T. Nara and W. Yokota	

3-14	Flux Enhancement of Carbon Ion Beams Guided by Cylindrical Glass Channel	134
	K. Motohashi, N. Miyawaki, K. Narumi and Y. Saitoh	
3-15	The Number Distribution of Emitted Negative Secondary Ions for Sub MeV C ₆₀ Impacts ..	135
	K. Hirata, K. Yamada, A. Chiba, Y. Hirano, K. Narumi and Y. Saitoh	
3-16	Shape Elongation of Embedded Metal Nanoparticles Induced by C ₆₀ Cluster Ion Irradiation	136
	H. Amekura, K. Narumi, A. Chiba, Y. Hirano, K. Yamada, S. Yamamoto and Y. Saitoh	
3-17	Observation of Magnetic Depth Profiles for C Cluster Ion Irradiated FeRh Thin Films with Depth-resolved X-ray Magnetic Circular Dichroism	137
	T. Matsui, R. Soma, A. Iwase, M. Sakamaki, K. Amemiya and Y. Saitoh	
3-18	Porous Structure on Ge Surface Formed by C ₆₀ Ion Beam Irradiation	138
	N. Nitta, H. Tsuchida, T. Oishi, S. Tomita, K. Sasa, K. Hirata, H. Shibata, Y. Hirano, K. Yamada, A. Chiba, Y. Saitoh, K. Narumi and Y. Hoshino	
3-19	Ion Energy Dependence of Optical Absorption Spectra for Silica Glass Implanted with Ag Ions	139
	K. Fukuda, F. Hori, Y. Saitoh, S. Semboshi, H. Amekura and A. Iwase	
3-20	Micro-PIXE Analysis Study of Ferrite Products Synthesized from Simulated Radioactive Liquid Waste Containing Chemical Hazardous Elements	140
	T. Abe, T. Shimazaki, T. Osugi, O. Nakazawa, N. Yamada, Y. Yuri and T. Satoh	
3-21	Ion Beam Induced Luminescence of Eu ³⁺ Extracted by HDEHP	141
	S. Watanabe, W. Kada, H. Matsuura, M. Koka and T. Satoh	
3-22	Dating of the Yamada Fault Distributed on Tango Peninsula Using Radiation Defect Radical Centers	142
	T. Fukuchi	
3-23	Preliminary Test of a Penning Ionization Gauge Ion Source with Electromagnets for a Compact Ion Microbeam System	143
	Y. Ishii, T. Ohkubo and Y. Miyake	
3-24	Reduction of Beam Diameter by Optimization of an Extraction Condition in a Compact Ion Microbeam System	144
	T. Ohkubo and Y. Ishii	
3-25	Status Report on Technical Developments of Electrostatic Accelerators	145
	Y. Hirano, A. Chiba, K. Yamada, A. Yokoyama, Y. Ishii and T. Nara	

3 - 01 Fabrication of Mach-Zehnder Waveguide Embedded in Biocompatible Thin Film by Proton Beam Writing

W. Kada^{a)}, S. Miura^{a)}, R. Takahashi^{a)}, K. Kasuya^{a)}, Y. Wang^{a)}, K. Miura^{a)}, M. Koka^{b)}, T. Satoh^{c)}, N. Yamada^{c)}, Y. Ishii^{c)}, T. Kamiya^{a)} and O. Hanaizumi^{a)}

^{a)} Faculty of Science and Technology, Gunma University,

^{b)} Beam Operation Co., Ltd.,

^{c)} Department of Advanced Radiation Technology, TARRI, QST

Proton Beam Writing (PBW) is an advantageous tool for micrometer-scaled material modification for forming embedded structure inside of the various target with beneath of high intensity energy deposition around the Bragg peak of MeV protons. So far, we have fabricated a prototype of a Mach-Zehnder (MZ) waveguide for optical communication integrated in a polydimethylsiloxane (PDMS) thin film using PBW technology [1, 2]. These waveguides are designed to form optical switches by making thermal heaters on one of the two divided waveguides. By enabling such technology to be applied to various materials, it is possible to expand its application fields toward various research areas. As an example of these approach, we have demonstrated fabrication of MZ waveguide by PBW for biocompatible photopolymer thin film.

PBW was performed at a microbeam line of 3 MV single-ended accelerator at TARRI/QST. Biocompatible photopolymer of MED-610 [3] was formed as flexible thin film (Fig. 1) by three dimensional printer system (Stratasys Objet30Prime). System allows us to form desired structure with the material installed at the device. Thin film of MED-

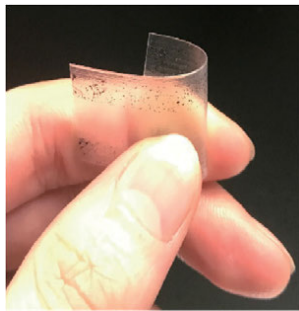


Fig.1. Example of flexible film of MED-610.

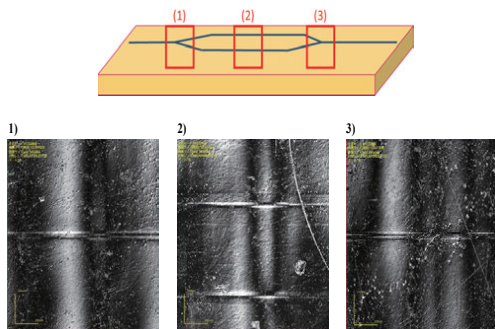


Fig. 2. Schematic illustration and partially expanded optical microscope image of MZ waveguide embedded in biocompatible polymerfilm of MED-610.

610 with thickness less than 40 μm was formed and fixed on an aluminum plate for irradiation of proton microbeam with energy from 0.75 - 1.75 MeV. Entire MZ waveguide structure with dimension of 40 mm \times 20 mm was formed by combined movement of beam scanning and sample stage. Figure 2 shows a schematic illustration and partially expanded optical microscope images of the MZ waveguide drawn in the film. Although film had unduration, it was possible to observe the structure of MZ waveguide in biocompatible flexible film of MED-610.

To examine optical throughput of the device fabricated in the biocompatible flexible film of MED-610, a fiber laser (SANTEC, ECL-210) with center wavelength of 1.55 μm was employed and the infrared light transportation through the sample was observed as near-field pattern (NFP) by an IR vidicon camera (Hamamatsu Photonics Ltd., C2741-03). Figure 3 indicates that two different excitation condition was controlled by input fibre laser. However this was not affective to the optical output of the MZ waveguide formed in MED-610. From the result it was suggested that single-mode light propagation was formed at beam fluence from 400 to 600 nC/mm^2 .

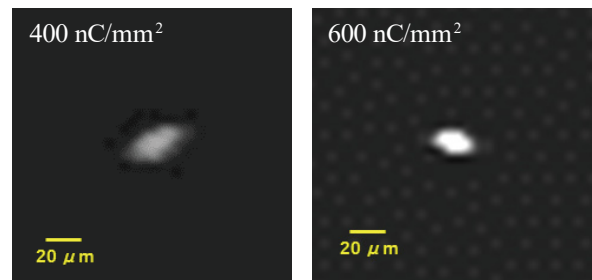


Fig. 3. NFPs from MZ waveguide embedded in biocompatible polymer film of MED-610 drawn by PBW process with fluence 400 and 600 nC/mm^2 .

Acknowledgment

The present work was partially supported by JSPS KAKENHI JP15K04731.

References

- [1] W. Kada *et al.*, Nucl. Instrum. Meth. Phys. Res. B, **348**, 218 (2015).
- [2] R. K. Parajuli *et al.*, Jpn. J. Appl. Phys., **55**, 6S1, 06GD01 (2016).
- [3] MED-610 biocompatible photopolymer, Additive Manufacturing LLC (<https://additivemanufacturingllc.com/wp-content/uploads/2015/04/MED-610.pdf>, access date 2018/06/01).

3 - 02

Refractive Index Change and Thermo-Optic Effect in Polydimethylsiloxane Nanocomposites with Oxide Nanoparticles Induced by Proton Beam Writing

Y. Kaneko ^{a)}, H. Hayashi ^{b)}, Y. Ishii ^{c)} and H. Nishikawa ^{a, b)}

^{a)} Department of Electrical Engineering, Shibaura Institute of Technology (SIT),

^{b)} SIT Research Laboratories, SIT,

^{c)} Department of Advanced Radiation Technology, TARRI, QST

Proton beam writing (PBW) is a direct writing technique of waveguides in various polymeric materials such as polymethylmethacrylate (PMMA) and polydimethylsiloxane (PDMS). Optical switching was demonstrated by a Mach-Zehnder interferometer embedded in these polymer optical waveguides using thermo-optic (TO) effects [1].

In this study, nanoparticles of titania, silica, and alumina in diameter of 10 to 21 nm (SIGMA-ALDRICH) were mixed with PDMS (Dow Corning, Sylgard 184) to obtain nanocomposites to modify the optical properties of PDMS. Ultrasonic homogenizer (Hirschner, UP-50H) was applied to the mixture of the nanoparticles and curing agent of the Sylgard 184. Then, the curing agent was mixed with the PDMS prepolymer by a planetary centrifugal mixer (THINKY, ARE-250) to obtain the nanoparticles/PDMS composites. These mixtures were spin coated on Si substrates at 8000 rpm for 240 s to form 5 μm thick films. These films were cured at 125 $^{\circ}\text{C}$ for 20 min in air.

The refractive index of the PDMS composites increased by 0.001 to 0.008 after mixing of these nanoparticles with concentration of 1.0 wt%. Proton beam irradiation was carried out using either a proton beam writer at SIT, or a microbeam line with a single-ended accelerator at QST Takasaki.

Figure 1 shows the refractive index changes induced by 1.0-MeV proton beam irradiation. We observed refractive index increase of 0.007 for the titania/PDMS composite with a fluence of 100 nC/mm^2 , which is high enough to write optical waveguides embedded in the nanocomposites using proton beam writing.

The thermo-optic coefficient (dn/dT) of these nanocomposites were evaluated by spectroscopic ellipsometry in the temperature range of 25 - 65 $^{\circ}\text{C}$. Figure 2 shows the refractive index changes of the PDMS and nanoparticles/PDMS composites as a function of the temperature. The TO effect of the titania/PDMS composite is more significant than those of PDMS and composites with silica and alumina nanoparticles. The titania/PDMS nanocomposite is suitable for optical switching devices utilizing the TO effect with low power consumption.

Reference

[1] W. Kada *et al.*, Nucl. Instrum. Meth. Phys. Res. B, **348**, 218-22 (2015).

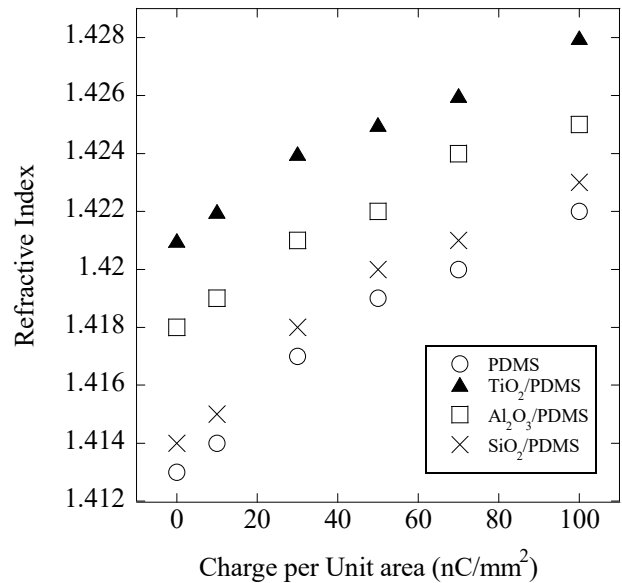


Fig. 1. Refractive index at wavelength of 632 nm as a function of 1.0-MeV proton beam fluence on PDMS and PDMS composites with 1.0 wt% nanoparticles of titania, alumina, and silica.

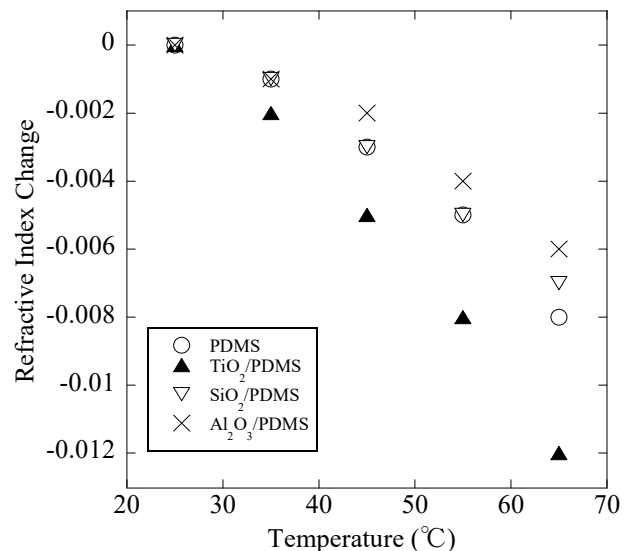


Fig. 2. Refractive index changes as a function of temperature obtained for PDMS and nanoparticle/PDMS composites with 1.0 wt% nanoparticles of titania, alumina, and silica at wavelength of 632 nm.

3 - 03 Quantification of Damage to a Biomolecular Sample in Transmission SIMS Using MeV C₆₀ Primary Ions

H. Ishii^{a)}, J. Sawada^{a)}, K. Nakajima^{a)}, A. Chiba^{b)}, K. Yamada^{b)}, Y. Hirano^{b)}, K. Narumi^{b)}, Y. Saitoh^{b)} and K. Kimura^{a)}

^{a)} Department of Micro Engineering, Kyoto University,

^{b)} Department of Advanced Radiation Technology, TARRI, QST

Secondary ion mass spectrometry (SIMS) in transmission geometry, where a thin film sample is bombarded with swift ions from the backside surface and secondary ions emitted in the forward direction are mass analyzed, is referred to as transmission SIMS. Our recent study [1] has suggested that transmission SIMS using MeV C₆₀ primary ions is a promising technique with higher sensitivity to biomolecules. Sensitivity to an analyte in SIMS is generally defined as the useful ion yield obtained from a given (sputtered) amount of the analyte. However, the sensitivity to a biomolecule can decline with irradiation fluence even for a homogeneous sample, because an accumulation of ion-induced damage on the sample surface will decrease surface concentration of the intact molecules and hence the useful ion yield. The present study is intended to quantify ion-induced damage to a biomolecular sample in transmission SIMS using MeV C₆₀ ions and to compare the sensitivity of transmission SIMS with that of conventional SIMS in reflection geometry.

Thin film samples of phenylalanine (thickness ~70 nm) were prepared by vacuum evaporation on 30-nm thick self-supporting silicon nitride (SiN) membranes. These samples were irradiated from the SiN side at the incident angle of 45° by 6 MeV C₆₀⁺ ions extracted from the 3 MV tandem accelerator of TARRI, QST. Mass spectra of positive secondary ions emitted in the forward direction were measured as a function of the irradiation fluence to determine the disappearance cross section [2] of intact molecules, which is a measure of ion-induced damage accumulating at the sample surface. Similar samples of phenylalanine with a gold δ-layer embedded between the phenylalanine film and the SiN membrane were also irradiated from the SiN side by 6 MeV C₆₀⁺ ions at the incident angle of 45°. These samples were ex-situ analyzed by Rutherford backscattering spectroscopy (RBS) to determine the sputtering yield of phenylalanine.

Figure 1 shows mass spectra of positive secondary ions in transmission SIMS using 6 MeV C₆₀⁺ primary ions at various values of irradiation fluence. The yield of intact molecular ions (protonated phenylalanine, *m/z* 166) decreases as the fluence increases. This indicates that fragmentation of phenylalanine molecules is induced by the irradiation and a part of the fragments remains on the surface. The disappearance cross section of intact molecules was determined from the decay of the yield of intact molecular ions. The cross section in transmission geometry is $(3.1 \pm 0.4) \times 10^{-12}$ cm², which is ~1.8 times larger than that in reflection geometry.

The sputtering yield of phenylalanine was determined by the difference in thicknesses of the phenylalanine films before and after the irradiation. The sputtering yield in transmission geometry was about 3.0×10^4 molecules/C₆₀ ion. This is ~3 times lower than that in reflection geometry.

These results reveal that higher yield of intact molecular ions in transmission SIMS using MeV C₆₀ primary ions compared to that in conventional SIMS is not due to higher sputtering yield, but to higher efficiency in desorption of intact molecular ions. The larger disappearance cross section in transmission SIMS can be explained as resulting from the lower sputtering yield, which allows larger part of the fragments to remain on the sample surface.

In conclusion, transmission SIMS provided ~6 times higher sensitivity to phenylalanine than conventional SIMS as long as in the static SIMS regime (Fig. 2), which demonstrates that transmission SIMS using MeV C₆₀ primary ions has potential as an analysis technique with ultrahigh sensitivity to biomolecules.

References

- [1] K. Nakajima *et al.*, Appl. Phys. Lett. **104**, 114103 (2014).
- [2] F. Kollmer, Appl. Surf. Sci. **231-32**, 153 (2004).

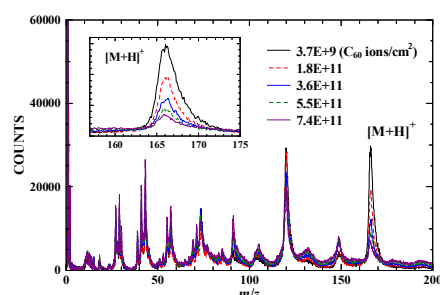


Fig. 1. Transmission SIMS spectra after various values of irradiation fluence of 6 MeV C₆₀⁺ ions.

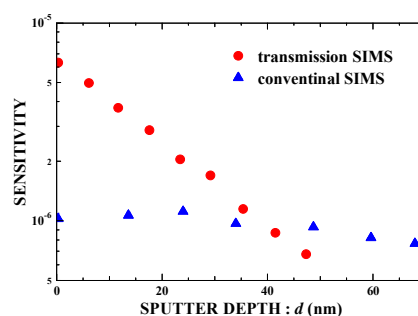


Fig. 2. Sensitivity to phenylalanine in transmission SIMS and conventional SIMS as a function of the sputter depth.

3 - 04 Lithium Distribution Analysis in All-solid-state Lithium Battery Using Maxicrobeam PIXE and PIGE Techniques

K. Mima ^{a)}, K. Yoshino ^{b)}, K. Suzuki ^{b)}, Y. Yamada ^{b)}, T. Satoh ^{c)}, M. Finsterbusch ^{d)}, K. Fujita ^{a)}, T. Kamiya ^{e)}, A. Yamazaki ^{f)} and Y. Kato ^{d)}

^{a)} The Graduate School for the Creation of New Photonics Industries,

^{b)} Department of Chemical Science and Engineering, School of Materials and Chemical Technology, Tokyo Institute of Technology,

^{c)} Department of Advanced Radiation Technology, TARRI, QST,

^{d)} Forschungszentrum Jülich GmbH, represented by its Board of Directors, for: Institute of Energy and Climate Research (IEK-1),

^{e)} Graduate School of Science and Technology, Gunma University,

^{f)} Faculty of Pure and Applied Sciences, University of Tsukuba

For confirming the feasibility of micrometer scale lithium distribution in the all-solid-state lithium battery, the cross section of pellet type battery was analyzed by PIXE and PIGE measurements. A three-layered pellet-type batteries (cathode: LiNbO₃-coated LiCoO₂+Li₁₀GeP₂S₁₂/solid electrolyte: Li₁₀GeP₂S₁₂/anode: TiS₂+Li₁₀GeP₂S₁₂) and a two layered battery (Cathode: LLZ:Ta/solid electrolyte: LLZ) were prepared for the measurements. Via lithium density mapping of the cross section of the prepared battery, the regions of the composite electrodes and the solid electrolyte layer were identified. The results indicate that the PIXE/PIGE analysis of lithium distribution with a micrometer-scale spatial resolution for the all-solid state batteries of the sulfide based solid electrolyte and the LLZ solid electrolyte is feasible. Further analysis for the cathode/anode composite electrodes with the time dependent states of charge could provide important information to design a composite for high-performance all-solid-state lithium batteries.

全固体リチウムイオン電池は蓄積されるエネルギー密度が高く、かつ高い安全性や耐久性を持つため実用化に向けた研究開発が精力的に進められている [1, 2]。このバッテリーは、すべて固体微粒子で構成されており、均一な微粒子の分布や十分な接触領域を実現する事がよい電子やイオン伝導のため必要である。これまで、複合電極のμ構造と電気化学動作の関係は、SEM, XRD, X-ray spectroscopy, Raman imaging 等で調べられてきた。しかしながら、これらの計測ではリチウム分布の変化を直接計測することは出来なかった。本研究の目標は、全固体電池におけるリチウムの分布の変化をイオンビーム分析で直接的に可視化することである。

30:70)の3層からなっている。電極を切断した端面を、図1の写真のようにカプトンで真空封じした、照射窓に固定し、3 MeVの陽子マイクロビームを端面の3層の境界近傍に照射して。境界面近くのリチウム濃度分布を計測した。

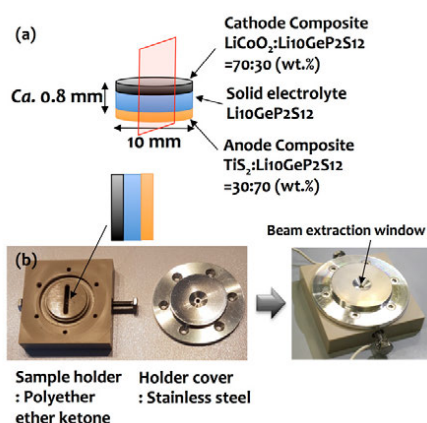


Fig. 1. Schematic drawing of the three-layer pellet cell and photographs of the sample holder.

サルファ固体電池サンプルは、図1に示す様にカソード合材(6-4 mg: LiNbO₃-coated LiCoO₂と固体電解質 Li₁₀GeP₂S₁₂の重量比 70:30)、固体電解質(80.4 mg)とアノード合材(10.2 mg: TiS₂と固体電解質の重量比

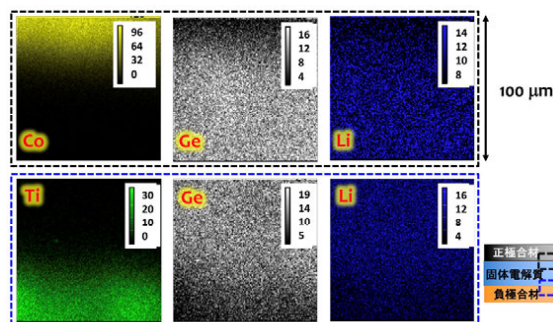


Fig. 2. Elemental distributions by μ-PIXE and μ-PIGE. The full scale is 100 μm. Upper and lower panels are for the cathode and anode electrode surface areas respectively.

図2に各種元素の濃度分布計測の結果を示す。図は固体電解質のGeと活物質のCo(Cathode), Ti(Anode)の分布に合わせて、リチウムの分布を示したものであり、白く見える領域が濃度の高いところである。この結果により、CathodeとAnode中のリチウム濃度が電解質層に比べて低いのを確認し、リチウム濃度の充放電による変化を観測可能であると結論づけた。次回の実験では、In-situでリチウム濃度の時間・空間変化を観測する予定である。

References

- [1] Y. Kato *et al.*, Nature Energy **1**, 16030 (2016).
- [2] T. Hakari *et al.*, Advanced Sustainable Systems **1**, 1700017 (2017).

M. Maekawa, S. Sakai, K. Wada, A. Miyashita and A. Kawasuso

Department of Advanced Functional Materials Research, TARRI, QST

Gallium nitride (GaN) is a material which is expected to exhibit ferromagnetism due to the introduction of cation vacancies [1]. However, it is difficult to relate directly the origin of the ferromagnetism to vacancies, because conventional measurement techniques have sensitivity only to either magnetism or defects. The spin-polarized positron annihilation spectroscopy (SP-PAS) is the promising method, because this method is sensitive to both vacancies and electron spins. Actually, the existence of excess electron spins at cation vacancies in ZnO introduced by oxygen ion implantation was confirmed by the SP-PAS method [2]. In this study, we explored the vacancy-induced magnetism in p-type gallium nitride films by the SP-PAS method.

Samples used in this study were Mg-doped p-type GaN films with the thickness of 2 μm grown on sapphire substrates. The nominal carrier density was $3 \times 10^{17} \text{ cm}^{-3}$. These samples were implanted with nitrogen ions at 100 keV to doses of $1 \times 10^{15} \sim 1 \times 10^{17} \text{ cm}^{-2}$ at room temperature using a 400 kV ion implanter. The Doppler-broadening annihilation radiation (DBAR) spectra were obtained in the magnetic fields of $\pm 0.91 \text{ T}$ at 300 K. Magnetization (M-H) curves were also obtained by a superconducting quantum interference device (SQUID) apparatus.

The Doppler shift of 511 keV annihilation gamma ray corresponds to the momentum of electrons which annihilate with positrons. The central area intensity of 511 keV peak is characterized as 'S parameter', which increases with the size and the density of vacancy-type defects. Figure 1 shows the ion dose dependence of S parameter obtained from the DBAR measurements. After nitrogen implantation, S parameter increases to around 1.05 and shows no significant dose dependence. This means that positrons are fully trapped at one type of vacancies. The obtained S parameter agrees with that for the Ga vacancies in GaN ($S=1.048$) [3]. From this result, it is confirmed that Ga vacancies are the major positron trapping centers.

Figure 2(a) shows the differential DBAR spectra in positive and negative magnetic fields. We call such differential DBAR spectra 'magnetic Doppler-broadening (MDB)' spectra. Gray fine lines are raw experimental data and bold lines are 10-points smoothed data. MDB intensity increases for doses of $1 \times 10^{16} \text{ cm}^{-2}$ and $1 \times 10^{17} \text{ cm}^{-2}$. This indicates that excess electron spins exist at Ga vacancies.

To confirm whether the vacancies induce magnetism or not, M-H measurements were carried out. Figure 2(b) shows the M-H curves for the same samples. In contrast to the MDB intensities shown in Fig. 2(a), practically no

magnetizations are observed in any conditions. One possible reason for this contradiction is different sensitivities of MDB and SQUID. Nitrogen implantation for a shallow region could not introduce the sufficient number of spins for the SQUID measurement, while the MDB measurement can selectively detect excess electron spins only at vacancies in the ion implanted region. For more detailed discussions, the further experimental studies are under progress.

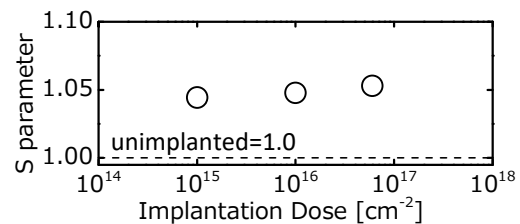


Fig. 1. Dose dependence of S parameters before and after nitrogen implantation.

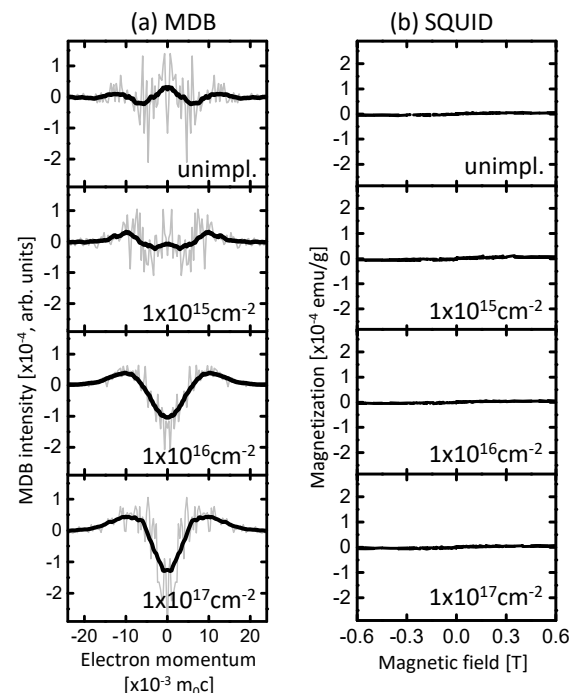


Fig. 2. Dose dependence for GaN samples of (a) MDB and (b) M-H measurements.

References

- [1] O. Volnianska and P. Boguslawski, *J. Phys. Condens. Matter*, **22**, 073202 (2010).
- [2] M. Maekawa *et al.*, *Appl. Phys. Lett.* **110**, 172402 (2017).
- [3] S. Hautakangas *et al.*, *Phys. Rev.* **B73**, 193301 (2006).

Dopant Dependence on Vacancy Defects in Ion-Beam Synthesized β -FeSi₂ Films

A. Yabuuchi^{a)}, A. Kinomura^{a)}, M. Maekawa^{b)} and A. Kawasuso^{b)}

^{a)}Institute for Integrated Radiation and Nuclear Science, Kyoto University,

^{b)}Department of Advanced Functional Materials Research, TARRI, QST

β -FeSi₂, having a band gap corresponding to the infrared region of the 1.5 μ m band, is expected as infrared-light receiving/emitting devices since it does not contain rare metals or harmful elements and has an excellent optical absorption coefficient [1]. The ion-beam synthesis (IBS) technique, which is forming β -FeSi₂ in the surface layer of the Si substrate by annealing after implanting Fe ions into Si, is well compatible with the Si-LSI process. Thus, it attracts attention as a technique for realizing the LSI internal optical wiring, however, further enhancement of the emission intensity is demanded. The emission intensity of IBS β -FeSi₂ is reported to be enhanced with Al-doping in contrast with Mn-doping [2]. The enhancement of the emission intensity by Al-doping is considered to be caused by filling Si vacancies which acts as nonradiative recombination centers with Al atoms, however, the direct evidence of reducing Si vacancies by Al-doping is still not shown. We have observed IBS β -FeSi₂ films by using a slow positron beam and obtained a result suggesting that Al-doping induces more vacancy defects. In this study, dopant dependence on vacancy defects in the films was investigated.

High-resistivity FZ-Si(100) substrates were implanted with a maximum energy of 100 keV Fe⁺ ions to a total dose of 1×10^{17} ions/cm² at room temperature. Mn⁺, Al⁺, Co⁺, P⁺ ions were additionally implanted as doped samples to a total dose of 5×10^{15} ions/cm² with a maximum energy of 100 keV, 50 keV, 100 keV, 60 keV, respectively. After the ion implantation, the substrates were annealed at 800 °C for 2 hours in vacuum to synthesize the β -FeSi₂. According to the previous studies [1, 3], the β -FeSi₂ layer is reported to be formed with a thickness of 50 nm at the surface of the Si substrate under these implantation and annealing conditions. The Doppler broadening of annihilation radiation (DBAR) spectra were acquired for each sample at room temperature with varying incident positron energies. All the samples were treated with dilute hydrofluoric acid to remove the native oxide film before the positron annihilation measurements.

Figures 1 and 2 show the peak intensity of DBAR spectra (S parameters) for the undoped, Mn-, Al-, Co-, and P-doped IBS β -FeSi₂ samples as a function of incident positron energy. The solid lines are fitted using the VEPFIT code [4]. The incident-energy region of 1-4 keV in these samples corresponds to the IBS β -FeSi₂ layer. The Al-doped β -FeSi₂ sample, which is reported to be enhanced the emission intensity, shows the large S values compared to the undoped sample. The S parameter also increases when doping P atoms which occupy Si sites as same as Al

atoms. In contrast, no significant increase in S parameter is observed when doping Mn or Co atoms which occupy Fe sites. In β -FeSi₂, Mn and Al atoms act as acceptors, and Co and P atoms act as donors, however, the result shows that the difference in conduction type does not significantly affect the S parameter change. Our result suggests that the doping of the atoms which occupy Si sites introduces more vacancies in IBS β -FeSi₂ films.

References

- [1] M. Sugiyama *et al.*, Thin Solid Films, **381**, 225 (2001).
- [2] Y. Terai and Y. Maeda, Appl. Phys. Lett., **84**, 903 (2004).
- [3] Y. Maeda *et al.*, Phys. Procedia, **11**, 83 (2011).
- [4] A. van Veen *et al.*, AIP Conf. Proc., **218**, 171 (1991).

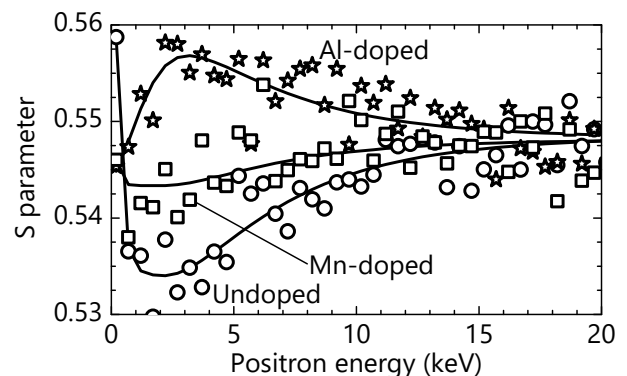


Fig. 1. S parameters for the undoped (open circles), Mn-doped (open squares), and Al-doped (open stars) β -FeSi₂ samples as a function of incident positron energy. Mn and Al atoms occupy Fe and Si sites, respectively. The incident-energy region of 1-4 keV is corresponds to the IBS β -FeSi₂ layer.

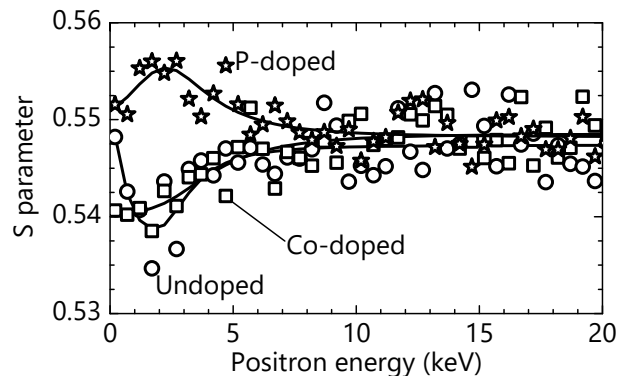


Fig. 2. S parameters for the undoped (open circles), Co-doped (open squares), and P-doped (open stars) β -FeSi₂ samples as a function of incident positron energy. Co and P atoms occupy Fe and Si sites, respectively. The incident-energy region of 1-4 keV is corresponds to the IBS β -FeSi₂ layer.

Properties of Scintillation Emission Signal from Nd:YAG/Cr:YAG Composite by Gamma Ray Irradiation

H. Ohba^{a)}, K. Tamura^{a)}, M. Saeki^{a)}, T. Taguchi^{a)}, H. Lim^{b)}, T. Taira^{b)} and I. Wakaida^{c)}

^{a)} Tokai Quantum Beam Science Center, TARRI, QST,

^{b)} Institute for Molecular Science, National Institutes of Natural Sciences (NINS),

^{c)} Remote Technology Division, CLADS, JAEA

Decommissioning of TEPCO Fukushima Daiichi nuclear power plant (F1-NPP) needs information on post-accident environment inside nuclear reactor core. In the F1-NPP, molten fuel debris (mixture of melted fuel core, fuel cladding and construction materials) might be submerged in water inside the reactor core. There is not enough space for inspecting the reactor core, because many pipes for water and electric supply occupy the inside space. Moreover, a high radiation field hinders people's access. Thus, a remote sensing technique that is available in a narrow space is crucial for the inspection of the F1-NPP.

To remotely inspect the site and the properties of the fuel debris for their recovery at the post-accident nuclear reactor of the F1-NPP, a fiber-optic probe laser-induced breakdown spectroscopy (LIBS) is considered one of the promising methods [1]. Giant-pulse microchip laser (MCL) is compact with high peak power of MW level [2]. Since the feature is suitable for LIBS application, it was applied to remote LIBS system, where MCL is set close to the target and bright plasma is generated by direct laser irradiation with the reduced risk of the fiber damage. Based on this innovative system, effective remote inspection system is expected. However, radiation effects to optical properties and laser operation needs to be investigated considering their influences in the radiation environment. For the application of the MCL in radiation environments, influences of the laser medium by the radiation need to be studied. Since scintillation emission is one of the radiation effects observed during the irradiation, the behaviors need to be studied. In this study, as an influence to the properties by high dose irradiation environment, scintillation emission from the YAG composite used in MCL was measured.

Scintillation emission was measured for a monolithic Nd:YAG/Cr:YAG composite ceramics (Konoshima Chemical Inc.), where Nd:YAG is a gain medium (Nd dopant 1.1%) and Cr:YAG is a saturable absorber (initial transmittance 30%) with a dimension of $3.0 \times 3.0 \times 10.0$ (L) mm (Nd:YAG 8.2 mm, Cr:YAG 1.8 mm). The YAG composite was set in a holder in an irradiation area at the No.1 ⁶⁰Co gamma irradiation facility at QST Takasaki. The composite was irradiated with gamma ray (1.173 MeV, 1.333 MeV) using ⁶⁰Co source in atmosphere at room temperature. In this experiment, dose rate was increased step by step from 0 to 10^4 Gy/h by approaching the composite to the radiation source and changing the distance.

Emission from the composite was collected and delivered with an optical fiber (Mitsubishi, STU600, high-

OH, 0.6 mm core, L = 10 m). One end of the optical fiber was set close to the composite side surface. Emission from the composite was transmitted through the fiber, and was measured with a spectrometer set outside of the irradiation area. Another fiber with the same characteristic, where one end close to the composite was capped, was also set along with the fiber as a reference signal. Net signal intensity was estimated as a difference of the two fiber signals.

Figure 1 shows the emission spectra from the YAG composite during the gamma-ray irradiation for the dose rate from 0.19 to 10 kGy/h. In these scintillation spectra, specific peaks corresponding to fluorescence from excited neodymium ions were observed. The intensity of the spectra increased with the increase of the dose rate. The scintillation signal intensity for the YAG composite was proportional to the radiation dose rate, and stable with elapsed time. The features make the YAG composite suitable to radiation dose monitor applicable to severe radiation environments.

References

- [1] M. Saeki *et al.*, J. Nucl. Sci. Tech., **51**, 930-38 (2014).
- [2] H. Sakai *et al.*, Opt. Express **16**, 19891-99 (2008).

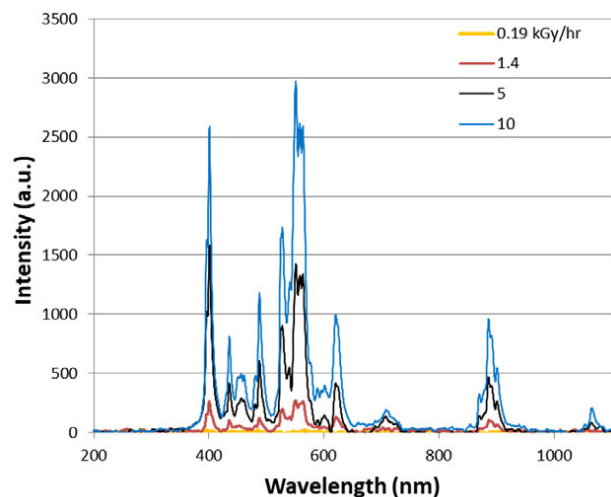


Fig. 1. Emission spectra from Nd:YAG/Cr:YAG microchip composite induced by gamma-ray irradiation for the dose rate from 0.19 to 10 kGy/h.

H. Kashiwagi, N. Miyawaki and S. Kurashima

Department of Advanced Radiation Technology, TARRI, QST

Emittance shape control in low energy beam line

In the TIARA AVF cyclotron, various light/heavy ion beams are frequently switched. In order to switch beams efficiently, we are developing an injection tuning method based on the measurements of the emittance of the beam and the acceptance of the cyclotron [1]. The emittance and the acceptance are measured at IS2 in the low energy beam transport line. It is necessary to change the excitation current of the electromagnets upstream of IS2 in order to change the emittance shape to match the acceptance at IS2. We have developed a method for determining the excitation current of electromagnets to obtain the specified emittance shape using the upstream emittance obtained by transporting the beam in the reverse direction. The upstream emittance is obtained by particle tracking calculation using the measured emittance (particle distribution) and inverse matrixes of each beam line element (drift, solenoid, and dipole magnet). Using the emittance from the calculation, the parameter fitting is performed by the beam transport program TRANSPORT to determine the electromagnet parameters so that the specified emittance shape at IS2 is obtained.

Preliminary tests of this method were carried out with a 50.22 keV O^{6+} beam using part of beam transport line from IS1 to IS2. The beam line consists of two solenoid magnets and three drifts. In the experiment, y - y' emittance was measured, and was used for calculations. Results are shown in Fig. 1. Emittance at IS1 (b) was obtained from measured emittance at IS2 (a). Two examples of the results of beam shape control for several specified Twiss parameters are shown (c1) (c2). In each case, the emittance measurement result (color) and the calculation result (white) are in good agreement. It was confirmed that the emittance shape control by this method is effective.

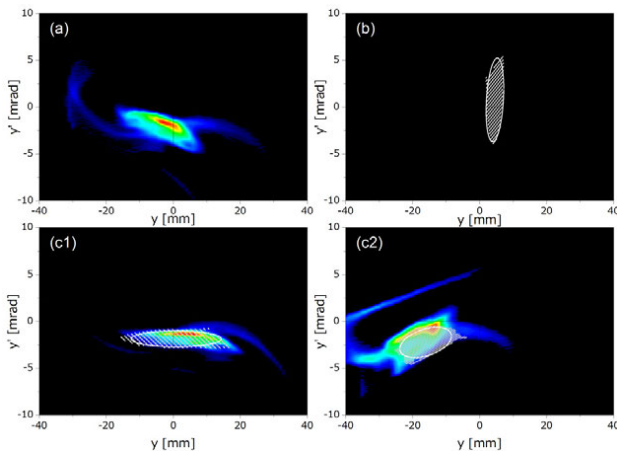


Fig. 1. Measured and calculated emittance. (a) Initial Emittance at IS2, (b) Calculated emittance at IS1, (c1, 2) Measured and calculated emittance at IS2.

Evaluation of the phase bunching effect on extraction

The enhancement of the beam extraction efficiency from a cyclotron results in an increase in the beam intensity. Reducing the radial emittance just before extraction is required to enhance the beam extraction efficiency. Phase bunching has the potential to reduce the radial emittance because of the improvement of the beam energy spread with decreased the beam phase width. Therefore, the radial emittance in the cyclotron was investigated to evaluate the phase bunching effect at extraction.

The radial emittance was calculated with the geometric orbit analysis model [2] using the measurement result of the correlation between the beam phase and the orbit position at the first turn. The radial emittances in the center region were estimated to be less than $2 \text{ mm} \times 40 \text{ mrad}$ for no phase bunching condition of 107 MeV $^4\text{He}^{2+}$ and for the phase bunching condition of 260 MeV $^{20}\text{Ne}^{7+}$. The calculations of the particle distribution at extraction were performed for 27 particles with initial conditions that were combinations of $-1, 0, \text{ and } +1 \text{ mm}$ and $-20, 0, \text{ and } +20 \text{ mrad}$ determined from the radial emittance in the center region and with the relative initial phases that were combinations of $-5, 0 \text{ and } 5 \text{ RF degrees}$. The radial emittance of 260 MeV $^{20}\text{Ne}^{7+}$ was smaller than that of 107 MeV $^4\text{He}^{2+}$, as shown in Fig. 2. Phase bunching was effective in reducing the radial emittance at extraction. Furthermore, the extraction efficiency of 260 MeV $^{20}\text{Ne}^{7+}$ was more than twice that of 107 MeV $^4\text{He}^{2+}$. Therefore, phase bunching in the center region increased the extraction efficiency and the extracted beam intensity.

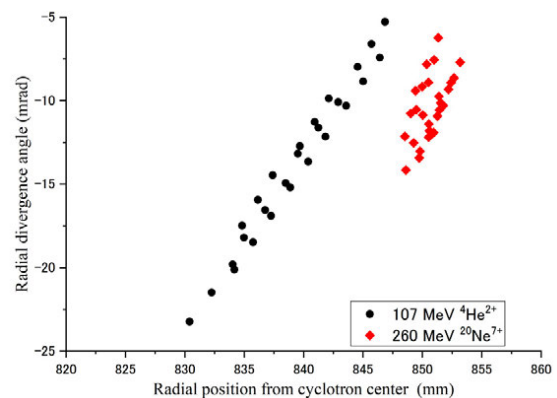


Fig. 2. Calculated particle distributions in the radial phase space before extraction.

References

- [1] H. Kashiwagi *et al.*, Rev. Sci. Instrum. **85** 02A735 (2014).
- [2] N. Miyawaki *et al.*, Nucl. Instrum. Meth. Phys. Res. **A**, **715**, 126 (2013).

3 - 09 Dynamic Behavior of Elements with Low Atomic Numbers in Lithium Oxide Ceramics Under Irradiation

B. Tsuchiya ^{a)}, S. Yamamoto ^{b)}, K. Takahiro ^{c)} and S. Nagata ^{d)}

^{a)} Department of General Education, Faculty of Science and Technology, Meijo University,

^{b)} Department of Advanced Functional Materials Research, TARRI, QST,

^{c)} Materials Science and Engineering, Kyoto Institute of Technology,

^{d)} Institute for Materials Research, Tohoku University

Lithium oxides (Li_2TiO_3 , Li_2ZrO_3 , Li_4SiO_4 , LiAlO_2 , LiCoO_2 , and so on) are potential candidates as tritium breeding materials in fusion devices [1]. It is of significant importance to investigate the relationship of radiation damage processes and dynamic behaviors of hydrogen as well as lithium atoms in lithium oxides under charging and heating by combining in situ radiation measurements with post-irradiation examinations.

Figures 1 and 2 show typical Rutherford backscattering spectrometry (RBS) spectra of backscattered O^{2+} ions and typical elastic recoil detection (ERD) spectra of recoiled H^+ and Li^+ ions, respectively, from the deposition of 24 nm Au and 65 nm LiCoO_2 on LAMP ($\text{Au}/\text{LiCoO}_2/\text{LAMP}$) without and with applying voltages at 1.0 and 1.5 V, as measured using 9.0-MeV O^{2+} ion-probe beams from a tandem accelerator. The horizontal axes (Channel Number) for the RBS and ERD spectra correspond to energies of the backscattered O^{2+} ions and recoiled H^+ and Li^+ ions, respectively, and represent the depth from the surface. On the vertical axes, the counts/energy in the RBS and ERD spectra correspond to the concentrations of doped and constituent elements such as ^1H , ^3Li , ^{27}Co , ^{32}Ge , and ^{79}Au in $\text{Au}/\text{LiCoO}_2/\text{LAMP}$.

The thickness of each Au and LiCoO_2 thin film was determined from approximately 512 - 557 and 265 - 297 channels of Fig. 1, taking into account the Rutherford backscattering cross-sections of O^+ ions in the case of constituent elements in $\text{Au}/\text{LiCoO}_2/\text{LAMP}$, the stopping cross-sections for O^+ ions, and the solid angle of detection.

On the other hand, the sharp and broad peaks at approximately 280-349 and 350-549 channels in ERD of Fig. 2 correspond to the H and Li concentrations in LiCoO_2 thin films. The Li peak becomes broader than the H peak, because the range straggling due to the stopping power of Li is larger than that of H in the Au, LiCoO_2 film and the Al absorber. It is assumed by the basis of our previous experimental results that the H peak ranging from approximately 280-349 channels in ERD spectrum for the uncharged-sample may probably correspond to H atoms absorbed by the LiCoO_2 film, as the H concentration in the Au film was quite low. The each peak at around 300 and 342 channels in ERD spectrum for the charged-sample up may probably indicate H or water (H_2O) retained in the LiCoO_2 films and H_2O adsorbed only onto the surface of the Au thin film, respectively. Also, it is assumed in this present study that each area at approximately 350 and 500 channels indicates Li concentration at the interfaces

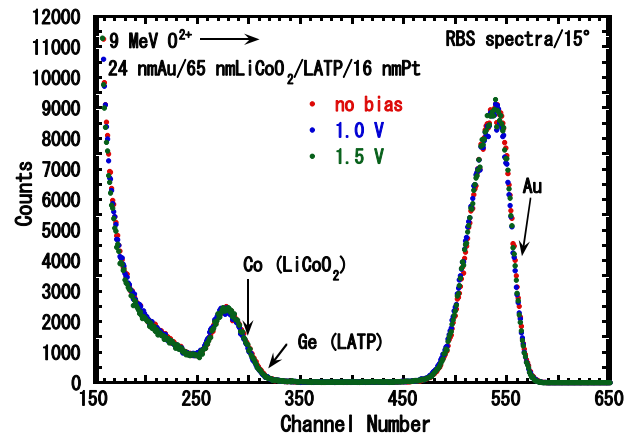


Fig. 1. Typical RBS spectra of back-scattered O^{2+} ions from 24 nm Au/65 nm $\text{LiCoO}_2/\text{LAMP}/16$ nm Pt without and with applying voltages at 1.0 and 1.5 V at room temperature, obtained by using 9.0-MeV O^{2+} ion-probe beams.

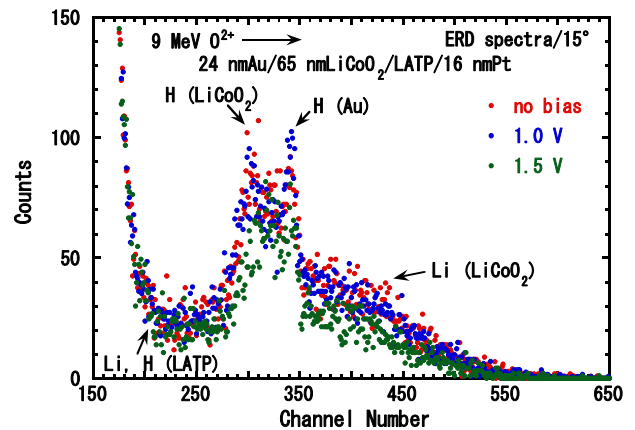


Fig. 2. Typical ERD spectra of recoiled H^+ and Li^+ ions from 24 nm Au/65 nm $\text{LiCoO}_2/\text{LAMP}/16$ nm Pt without and with applying voltages at 1.0 and 1.5 V at room temperature, obtained by using 9.0-MeV O^{2+} ion-probe beams.

between LiCoO_2 and LAMP, LiCoO_2 and Au, respectively. It appears from Fig. 2 that the Li concentrations at the interfaces as well as LiCoO_2 thin film decrease after applying up to 1.5 V. The gradual degradation of Li distribution in the LiCoO_2 thin film uniformly occurs to the depth.

Reference

- [1] C. E. Johnson, K. Noda, N. Roux, J. Nucl. Mater. **258-63**, 140-48 (1998).

Analysis of Linear Energy Transfer Effects on the Scintillation Properties of Ce:Gd₃Al₂Ga₃O₁₂ (GAGG)

M. Koshimizu^{a)}, S. Kurashima^{b)}, A. Kimura^{c)}, M. Taguchi^{c)}, T. Yanagida^{d)},
H. Yagi^{e)}, T. Yanagitani^{e)}, Y. Fujimoto^{a)} and K. Asai^{a)}

^{a)} Graduate School of Engineering, Tohoku University,

^{b)} Department of Advanced Radiation Technology, TARRI, QST,

^{c)} Department of Advanced Functional Materials Research, TARRI, QST,

^{d)} Division of Materials Science, Nara Institute of Science and Technology,

^{e)} Konoshima Chemical Co. Ltd.

The effects of linear energy transfer (LET), or excitation density, on scintillation properties should be elucidated in pulse shape discrimination for the neutron detection of events based on the (n, α) reactions of ${}^6\text{Li}$ or ${}^{10}\text{B}$ and in the detection of heavy charged particles. Conventionally, the scintillation properties dependent on LET has been discussed as the LET dependence of the light yield within a framework of Birks model, which treats quenching owing to excited states interaction in a quasi-static model. However, to elucidate the scintillation properties dependent on LET, one has to know the dynamical aspects of excited states including their interaction. From this viewpoint, measurements of temporal profiles of scintillation are a powerful tool to elucidate the LET dependence and underlying basic processes. In recent years, our group has been studying temporal profiles of scintillation using pulsed ion beams to reveal the physics responsible for the linear energy transfer effects on scintillation. Among those effects, we have observed a competition between the energy transfer from the host to the luminescence centers and the quenching due to the excited state interactions in the host, in Ce-doped Gd₂SiO₅ (GSO) [1]. To obtain more general insight, we have analyzed herein the LET effects on the scintillation properties of Ce:Gd₃Al₂Ga₃O₁₂ (GAGG) single crystals and ceramics.

The temporal profiles of scintillation under pulsed ion beam irradiation were obtained using an AVF cyclotron at TIARA, QST, Japan. Details of the measurement system are shown in Ref. [2]. The time resolution of the system was about 2 ns at half-width at half maximum. The samples were irradiated in air with 20-MeV H⁺, 50-MeV He²⁺, and 220-MeV C⁵⁺. The LET was changed over more than two orders of magnitude. The scintillation was detected with a photomultiplier tube, and the detection signals were delivered to a digital oscilloscope. The temporal profiles of scintillation have been obtained as the averaged signals over 1000 pulses.

Figures 1 and 2 show the temporal profiles of scintillation for different ions irradiations in the rise and decay regimes, respectively. In this study, the LET was higher for the heavier ion irradiation. The rise was significantly slower at high LET, whereas the LET effect was not pronounced in the decay regime. The LET effect in the rise regime is similar to that previously reported for

GSO [1] and for the lithium glass scintillator GS20 [3] and is attributed to a competition between the energy transfer from the host to the luminescence centers and the quenching due to the excited state interactions in the host. The observations in this study strongly suggest that this competition is an important process in the effects of LET on scintillation. The LET effects were quite similar for the single crystal and transparent ceramics.

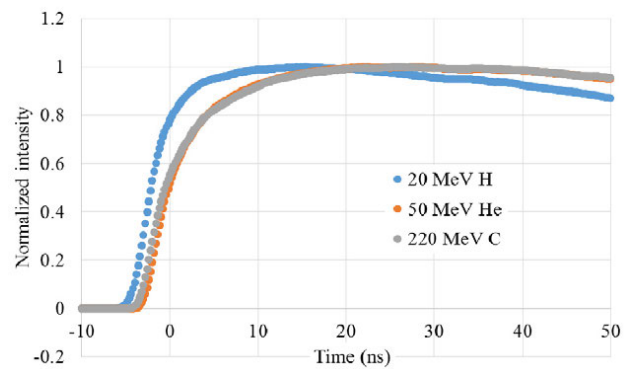


Fig. 1. Scintillation temporal profiles of Ce-doped GAGG for a short time scale.

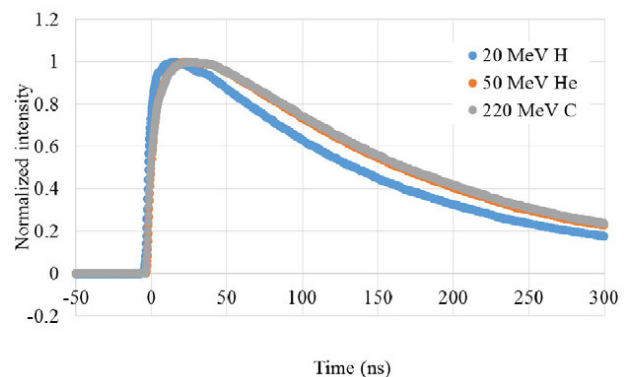


Fig. 2. Scintillation temporal profiles of Ce-doped GAGG for a long time scale.

References

- [1] T. Yanagida *et al.*, Nucl. Instrum. Meth. Phys. Res. B, **409**, 27 (2017).
- [2] M. Koshimizu *et al.*, Rev. Sci. Instrum., **86**, 013101 (2015).
- [3] M. Koshimizu *et al.*, J. Lumin., **169**, 678 (2016).

3 - 11 Measurements of Relative Angular Distribution of the n-p Elastic Scattering Reaction for 45-MeV Neutrons

T. Matsumoto ^{a)}, A. Masuda ^{a)}, H. Harano ^{a)} and S. Kurashima ^{b)}

^{a)}National Metrology Institute of Technology, National Institute of Advanced Industrial Science and Technology, ^{b)}Department of Advanced Radiation Technology, TARRI, QST

In many cases, recoil protons produced by the n-p elastic scattering reaction are used in neutron detectors and neutron dosimeters [1]. Especially, information on the angular distribution of n-p elastic scattering reaction is important for proton recoil telescopes (PRTs) that are used to determine the neutron fluence in neutron energy region above several MeV [2]. Energy dependent detection efficiency of a PRT is usually obtained using simulation codes with an evaluated data file such as LA150 and JENDL-HE files. However, the angular distribution of the n-p elastic scattering reaction has discrepancy between LA150 and JENDL-HE2007 in high energy region above 20 MeV. In our previous study, a PRT composed of a Si surface barrier detector and a liquid scintillation detector was developed to measure high energy neutrons above 20 MeV. The recoil angle of 10 degrees was used in the PRT. In this case, the detection efficiency for 45-MeV neutrons had 5% discrepancy between LA150 and JENDL-HE2007 [2].

We have experimentally verified the relative angular distribution of the n-p elastic scattering reaction for 45-MeV and 60-MeV neutrons that are used to calibrate neutron dosimeters and neutron detectors at TIARA. In the present experiments, the relative angular distribution for 45-MeV neutrons is verified by changing the recoil angle from 10 to 30 degrees using the proton recoil telescope composed of a 6.0-cm diameter and 0.5-mm thick Si detector (ΔE) and a 7.62-cm diameter and 7.62-cm thick liquid scintillation detector (E) as shown in Fig. 1. The neutrons were produced by the ${}^7\text{Li}(p,n)$ reaction in the LC0 beam line at TIARA. A high-density polyethylene plate was used as an n-p converter in the PRT. A carbon plate was also used to subtract background due to carbon included in polyethylene. Proton pulse height spectra of the liquid scintillation detector were successfully observed for ΔE -E coincidence measurements of the PRT as shown in Fig. 2. The neutron fluences were derived for the setup of recoil angles of 10 and 30 degrees, respectively, using detection efficiencies calculated with the MCNPX code as shown in Fig. 3. The difference of detection efficiency between the LA150 and JENDL-HE files was extracted from the MCNPX calculations. Error bar in Fig. 3 shows only statistical uncertainty. The final results will be obtained after various corrections. Moreover, we will also measure the n-p elastic scattering reaction at 45-MeV for 15, 20 and 25 degrees in laboratory system in 2018.

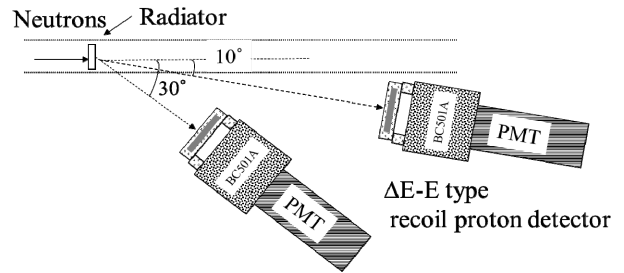


Fig. 1. Experimental setup in the present experiments.

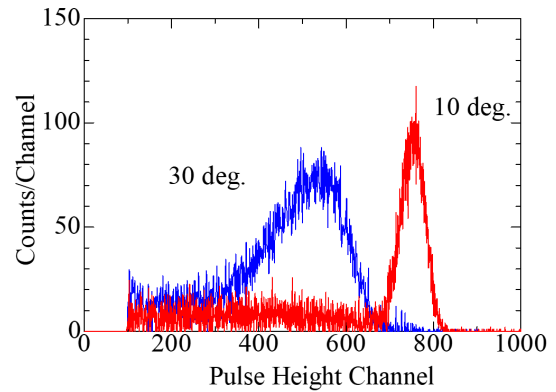


Fig. 2. Proton pulse height spectra of the liquid scintillation detector obtained from ΔE -E coincidence measurements.

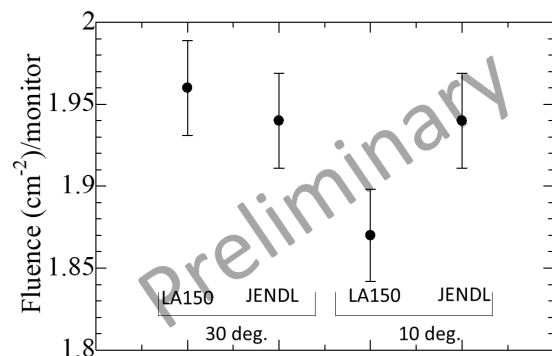


Fig. 3. Preliminary results of the present experiments. Neutron fluences were derived for the setup of recoil angles of 10 and 30 degrees.

References

- [1] T. Shimoyama *et al.*, Radiat. Protect. Dosim. **126**, 130 (2007).
- [2] T. Matsumoto *et al.*, J. Nucl. Sci. Tech. **54(5)**, 529 (2017).

A. Yokoyama^{a, b)}, W. Kada^{b)}, K. Miura^{b)} and O. Hanaizumi^{b)}

^{a)} Department of Advanced Radiation Technology, TARRI, QST,
^{b)} Graduate School of Science and Technology, Gunma University

Carbon beams having energy of the order of hundreds of MeV/n, which are used in heavy ion therapy, can damage DNA in malignant tumor cells. Since the radiation sensitivity of tumor tissue is higher than that of normal tissue, cells are annihilated using beam irradiation. An energy-controlled carbon beam is irradiated to a tumor to impart large energy transfer in the ion-beam range (Bragg peak). To avoid the irradiation on the normal tissue outside the tumor, collimators and various filters are set to adjust the Bragg peak and the irradiation area. Currently, Markus type ionization chambers are used to measure the dose distribution in a tumor at 10 points along and orthogonal to the beam direction in treatment planning. For safe treatment, it is necessary to obtain more measurement points, but it is inefficient to measure by using the ionization chamber. Therefore, efficient measurement methods are required such as three-dimensional dose-distribution images within a few minutes.

Scintillators are tested to obtain dose-distribution images in real time. However, detailed images could not be obtained owing to scintillation saturation [1]. Photo-stimulated luminescence (PSL) materials are distinguished by visible light exposure after the radiation. If a PSL glass material having a dynamic dose ranging from mGy to Gy is made by adjusting the amount of activator and the kind of elements, the granted total dose can be known by the readout PSL intensity. In addition, unlike imaging plates, PSL glass materials prepared in Sumita Optical Inc. are transparent, which enable us to observe three-dimensional beam trajectories. The observation, however, is not in real time.

The following two activities were conducted in fiscal 2017: (1) A glass material with potential applications in PSL (G2000) was characterized by PSL and photoluminescence excitation measurement (PLE). (2) Annealing temperature was investigated to recover the glass material irradiated ⁶⁰Co γ -rays because the samples were damaged by γ -rays generated in the therapy.

PSL and PLE spectra of G2000 were measured using F-4500 Hitachi fluorescence spectrophotometer at room temperature. In PSL measurements, 632 nm light was used as an excitation light. A filter was placed in front of a photomultiplier in the spectrometer to cut off the excitation light. The obtained PSL peaks that emerged at 497, 550, 592, and 628 nm are attributed to the interlevel transitions in electronic energy levels of Tb³⁺. As shown in Fig. 1, PLE of G2000 was measured at 542 nm emission and four peaks at 636, 676, 700, and 753 nm were obtained between 600 and 800 nm. Wavelength of 753 nm, where the maximum intensity of PLE was obtained, was used in

the following PSL measurements.

To investigate the annealing temperature to recover from damage by radiation irradiation, ⁶⁰Co γ -rays were irradiated on each G2000 sample at a rate of 100 Gy/h for 1 h. PSL spectra were measured. The G2000 irradiated by γ -rays between 100 °C and 800 °C were annealed at an interval of 100 °C. As a result, PSL intensity of the G2000 annealed at 600 °C was as the same as that of the G2000 without irradiation of γ -rays. For annealing temperature under 500 °C, a negligible change was found in comparison with the sample before annealing. On the contrary, the intensity of the sample annealed over 700 °C was about two times greater than the sample before annealing. It was thought that G2000 damaged with γ -rays was recovered by annealing at 600 °C for 1 h. On the contrary, the damage did not recover under 500 °C and the composition changed by clouding over 700 °C.

There are several limitations to this study. First limitation is that the same-lot samples were used in the measurements, but the uniformity of the doped Tb were not all the same. Additionally, heating and cooling rate of the electric furnace was not controlled during the annealing treatment. In future, γ -rays at a dose of more than 100 Gy and dependence of γ -ray fluence rate will be investigated. Annealing conditions for recovery of G2000 irradiated carbon beam used in the therapy will also be investigated in the future.

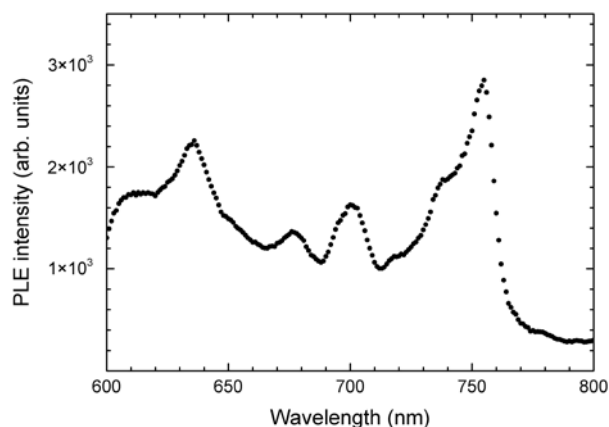


Fig. 1. PLE Spectrum of G2000.

Acknowledgment

This work was supported by KAKENHI, Grant-in-Aid for Young Scientists (B) JP15K18321.

Reference

[1] L. Torrisi *et al.*, Nucl. Instrum. Meth. Phys. Res. B, **170** 523 (2000).

3 - 13 Technical Development of Continuous Uniform Ion Irradiation for Production of Track-etched Membranes

Y. Yuri ^{a)}, T. Yuyama ^{a)}, K. Yoshida ^{a)}, T. Ishizaka ^{a)}, I. Ishibori ^{a)}, H. Yamamoto ^{b)}, M. Aizuka ^{b)}, T. Nara ^{a)} and W. Yokota ^{a)}

^{a)} Department of Advanced Radiation Technology, TARRI, QST,

^{b)} Functional Products Division, Nitto Denko Corporation

Track-etched porous membranes, produced by heavy-ion irradiation and chemical etching of polymer films, are promising as a functional material since the membranes has cylindrical pores with a fixed diameter at a uniform area density owing to the controlled ion irradiation and subsequent chemical treatment. We have conducted a joint research on the technical development of continuous uniform ion irradiation for the production of track-etched polymer membranes at the TIARA cyclotron facility.

An effort has been still made on the increase of beam current and its monitoring during long-time irradiation of samples mainly for 350-MeV ¹²⁹Xe ion beams [1]. Usually, the beam from the cyclotron was multiply-scattered with a thin foil to form sufficiently a uniform (<10%) beam using multipole magnets, which resulted in the loss of heavy-ion beams due to the charge exchange. Here, to increase the beam current available on the target, a uniform beam was formed without relying on multiple scattering. The nonuniformity of the profile was corrected to some degree with outer harmonic and trim coils of the cyclotron. Finally, the on-target beam current was increased by a few times although the uniformity of the beam profile was deteriorated (>10%, within the tolerance).

In the real-time monitoring of beam current, the relative beam intensity was measured at two different locations, namely, at a beam slit where the tail of the beam profile was scraped for on-target beam shaping and at a thin wire stretched near the target. It was almost impossible to monitor the stability of beam current with the wire because the wire current was affected probably by the electrostatic discharge in the roll-to-roll film transfer. On the other hand, such an effect was not observed in the slit current and its fluctuation was estimated at about 1% for a stable beam.

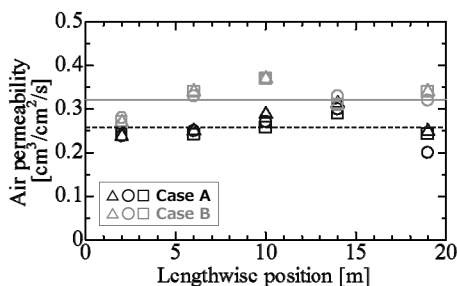


Fig. 1. Air permeability of track-etched PET films measured at different lengthwise positions. Two cases are shown where the pore density ($\sim 10^6 \text{ cm}^{-2}$) and diameter ($\sim 2 \text{ }\mu\text{m}$) are different. Three symbols indicate the three measurement positions in the width direction of the films. Solid and dashed lines correspond to the average in each case.

Roll-to-roll heavy-ion irradiation of long polyethylene terephthalate (PET) films was performed under various conditions. After the chemical etching process to form track pores in the film, the air permeability was measured at different positions of the long film to evaluate the characteristics as a porous membrane, as shown in Fig. 1. The present result indicates that the rms variation of the air permeability is about 10%, smaller than that of other commercial porous membranes.

Moreover, we have succeeded in forming a compound pore structure by double ion irradiation, as demonstrated in Fig. 2. The ion irradiation and etching process was repeated twice to generate non-penetrating large pores and penetrating small pores in a PET film. With this technique, two incompatible characteristics of porous membranes, namely, the permeability and physical strength, have been achieved at a preferable level.

In summary, we have developed the beam technique to form a horizontally-elongated uniform intensity distribution using multipole magnets and the roll-to-roll irradiation system that continuously transfers long polymer films. The beam formation, the measurement of the beam profile and relative beam current, and the continuous irradiation of long polymer films were achieved under various conditions such as ion species, kinetic energy, fluence, and vacuum pressure. We have demonstrated that track-etched porous polymer membranes of higher performance, compared to existing other porous membranes, can be produced at the TIARA cyclotron.

Reference

- [1] H. Yamamoto *et al.*, QST Takasaki Annu. Rep. 2016, **QST-M-8**, 137 (2018).

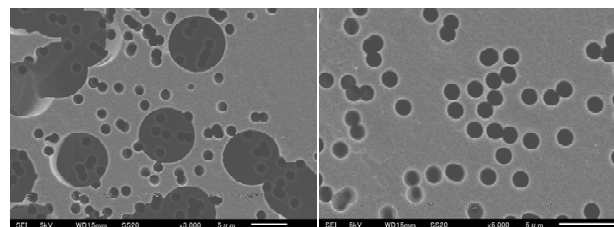


Fig. 2. SEM images of a track-etched PET film that has larger ($\phi 7.6 \text{ }\mu\text{m}$) non-penetrating pores only in one side. This film was irradiated with Xe ion beams twice. The beam energy was degraded with a mask in the first irradiation so that the beam stopped in the middle of the film. After the first etching, the film was again exposed to Xe ion beams without energy degradation to form smaller ($\phi 1.3 \text{ }\mu\text{m}$) penetrating pores.

K. Motohashi^{a)}, N. Miyawaki^{b)}, K. Narumi^{b)} and Y. Saitoh^{b)}

^{a)} Department of Biomedical Engineering, Toyo University,

^{b)} Department of Advanced Radiation Technology, TARRI, QST

Ion beam guiding by insulator surfaces [1] has attracted attention due to its potential application for the development of novel microbeam technology. Electric charging caused by the interaction between slow, highly charged ions and the inner wall surfaces of glass capillary allows an ion beam to deflect as well as to converge without changing its energy and charge states.

The convergence mechanism of fast proton or helium ion beams has not been clarified yet [2], although this mechanism has been applied to particle-induced X-ray spectrometry (PIXE) in the atmosphere [3]. We attribute this to the difficulty in controlling the inner wall surfaces of glass capillary, including the inner curvature, smoothness, and vacuum, particularly in very thin capillary.

To mitigate this problem, we have been developing the cylindrical glass channel (CGC) [4], which comprises a cylindrically concave glass lens and a cylindrically convex glass lens facing each other with a gap of ~ 1 mm. The transmission probability and the kinetic energy of outgoing ions from the CGC suggested that 4-MeV carbon ions guided by the channel were converged [5]. In the present study, to confirm this ion beam convergence experimentally, we attempted to measure the flux of the outgoing ion beam.

Figure 1 shows the experimental setup of this study. The CGC can be tilted around the entrance hole. 3.24-MeV C^{3+} ion beam partially mixed with 4-MeV C^{4+} ion beam entered the entrance hole. The outgoing particles were detected using a Si-surface barrier detector (SBD) placed along the direction of the observation angle. Four CR39 sheets were pasted on a plate mounting a slit and the SBD to measure the flux of the outgoing particles. The SBD and the CR39s on the mounting plate could be moved linearly as one body. Another two CR39 sheets were pasted on the front panel of the CGC to measure the flux of the incoming ion beam (not shown in the figure).

Figure 2 shows the energy spectra of the primary ion beam (a) and the outgoing particles at the tilt angle $\theta = +1^\circ$ (b), which were measured using the SBD. The horizontal

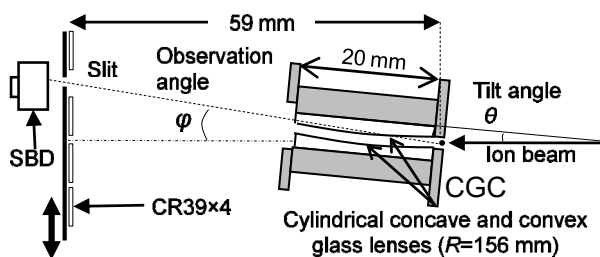


Fig. 1. The experimental setup of the present study.

axis is the relative pulse height of the signals. The outgoing particles clearly retained the energy of the primary ions.

Figure 3 shows the CR39 irradiation marks of the primary ion beam (a) and the outgoing particles (b) at the tilt angle $\theta = +1^\circ$. These figures were obtained via computational analysis of the optical microscope images. The left side of the Fig. 3(b) disappeared like a half moon because the ion beam was blocked at exit edge of the cylindrical concave glass lens. Note that background marks due to scattered ions are uniformly observed in Fig. 3(b). The areal number density of them was evaluated to be $7.84 \times 10^8 \text{ m}^{-2}$ at the outside area of the half moon. The flux of the outgoing particles was calculated by subtracting its value from the areal number density ($= 3.50 \times 10^9 \text{ m}^{-2}$) of all marks in the area of the half moon. As a result, the flux ($= 1.70 \times 10^8 \text{ m}^{-2} \text{ s}^{-1}$) of the outgoing particles is larger than that ($= 1.19 \times 10^8 \text{ m}^{-2} \text{ s}^{-1}$) of the primary ion beam by a factor of 1.4. Thus, convergence of fast heavy ions using the CGC was confirmed.

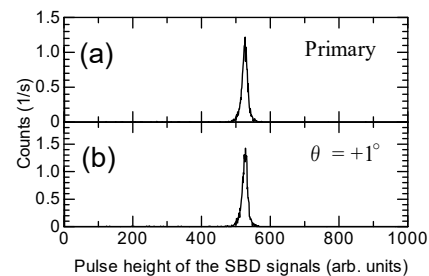


Fig. 2. The energy spectra of primary ion beam (a) and outgoing particles at $\theta = +1^\circ$ and $\varphi = 0^\circ$ (b).

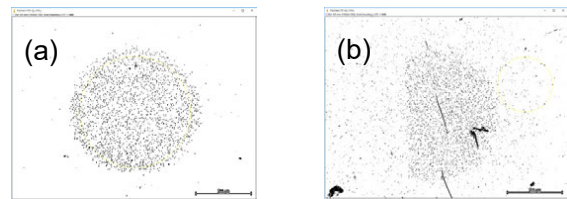


Fig. 3. CR39 irradiation marks (16 s duration) of primary ion beam (a) and outgoing particles (b) at the tilt angle $\theta = +1^\circ$.

References

- [1] N. Stolterfoht *et al.*, Phys. Rev. Lett. **88**, 133201 (2002).
- [2] T. Nebiki *et al.*, J. Vac. Sci. Tech. A, **21**, 1671 (2003).
- [3] N. Fujita *et al.*, Nucl. Instrum. Meth. Phys. Res. B, **269**, 1023 (2011).
- [4] K. Motohashi *et al.*, Jpn. J. Appl. Phys. **52**, 07630 (2013).
- [5] K. Motohashi *et al.*, Jpn. J. Appl. Phys. **56**, 046301 (2017).

3 - 15 The Number Distribution of Emitted Negative Secondary Ions for Sub MeV C₆₀ Impacts

K. Hirata ^{a)}, K. Yamada ^{b)}, A. Chiba ^{b)}, Y. Hirano ^{b)}, K. Narumi ^{b)} and Y. Saitoh ^{b)}

^{a)} Research Institute for Material and Chemical Measurement, AIST,
^{b)} Department of Advanced Radiation Technology, TARRI, QST

Secondary ions (SIs), produced upon a primary ion impact on a target, are emitted from the target surface with various emission parameters. Although the distribution of the number of SIs emitted for one primary ion should include information on how the SIs are emitted from the target, their detailed measurements and analysis have not been performed. One of the reasons is that the mean SI number per impact for monoatomic primary ions is too small to accurately obtain the distributions. Cluster ion impacts give different energy transfer from monoatomic ion impacts, which considerably enhances the mean numbers of emitted SIs in comparison with the impact of the corresponding monoatomic ion with the same velocity [1]. The higher mean number of emitted SIs allows to measure their number distributions [2]. In this paper, we report statistical analysis of the number distribution of negative SIs (N-SIs) for 0.27-MeV C₆₀ ion impacts on a poly methyl methacrylate (PMMA) target.

The experiments were performed using a 0.27-MeV C₆₀²⁺ ion beam at QST/Takasaki [3]. A direct C₆₀ ion beam with a current of several tens of fA was pulsed by electrostatic deflection plates triggered by a pulse generator and a series of collimators to obtain single impact per pulse condition. The pulsed C₆₀ ion beam was incident on a PMMA film target at an angle of 45° to the target surface. The number of N-SIs for each ion pulse were counted by a time-of-flight (TOF) SI mass spectrometer, based on event-by-event measurements. The counted N-SI number *p* were analyzed using an analytical model that can derive the number distributions of emitted SIs *n* from experimental counting data obtained by a TOF SI ion mass spectrometer combined with pulsed primary ion beams [2].

Figure 1 shows the probability distribution of *p* for 0.27-MeV C₆₀²⁺ together with the distribution calculated using the analytical model, which assumes that the emitted N-SI number *n* has a probability distribution with a mean number *μ*, *P_n(μ)*. In the figure, only the event data for *p* ≥ 1 are used because it is impossible for *p*=0 to distinguish between events where no SI is emitted by the primary ion impact and where no primary ion exists for the start signal. Therefore, the calculated *p* distribution *P_{cal}(p)* can be expressed by

$$P_{cal}(p) = \sum_{n=1}^{n_{max}} \frac{P_n(\mu)}{1 - P_0(\mu)} \frac{{}_n C_p (1-\gamma)^{n-p} \gamma^p}{1 - (1-\gamma)^n}$$

where *γ* is the SI detection efficiency and *P₀(μ)* is the probability that an SI is not emitted even when the primary ion is incident on the target [2]. As sub MeV C₆₀ impacts provide high SI emission yields and the mean number per

impact for organic targets are the order of 10 or greater, *P₀(μ)* can be assumed to be ≈ 0.

The dashed line in the figure shows the results of the least-squares fits of the model to the experimental *p* distribution under the condition that the number distribution of *n* follows two Polya distributions:

$$P_n(\mu) = a_1 P_n(\mu, b) + (1 - a_1) P_n(2\mu, b)$$

$$P_n(\mu, b) = \left(\frac{\mu^n}{n!}\right) (1 + b\mu)^{-n-1/b} \prod_{i=1}^n [1 + (i-1)b]$$

where *b* is a parameter and *a₁* is the probability of a single-impact event. When *b* = 0, *P_n(μ, b)* becomes the Poisson distribution. The fitted line, calculated by taking into consideration both of single- and double-impact events for one ion pulse, can accurately reproduce the experimental data. The fitting parameters obtained in the fit were *a₁* ≈ 1 and *b* ≈ 0, showing that the experiment was performed under the single impact condition and that the number distribution of the emitted SIs for one impact can be well approximated by the Poisson distribution [2].

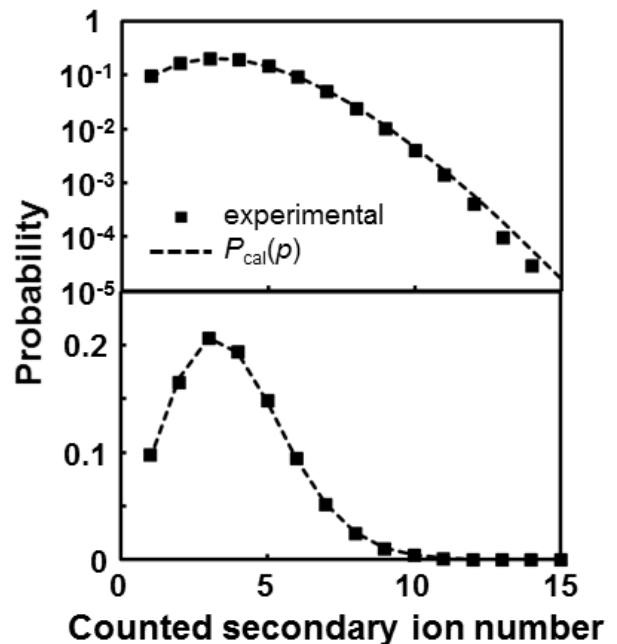


Fig. 1. Probability distribution of the counted N-SI number for 0.27 MeV C₆₀²⁺ impact.

References

- [1] K. Hirata *et al.*, Appl. Phys. Lett. **81**, 3669 (2002).
- [2] K. Hirata *et al.*, J. Chem. Phys. **145**, 234311 (2016).
- [3] K. Hirata *et al.*, Nucl. Instrum. Meth. Phys. Res. B, **266**, 2450 (2008).

3 - 16 Shape Elongation of Embedded Metal Nanoparticles Induced by C₆₀ Cluster Ion Irradiation

H. Amekura ^{a)}, K. Narumi ^{b)}, A. Chiba ^{b)}, Y. Hirano ^{b)}, K. Yamada ^{b)},
S. Yamamoto ^{b)} and Y. Saitoh ^{b)}

^{a)} Research Center for Advanced Measurement and Characterization,
National Institute for Materials Science (NIMS),

^{b)} Department of Advanced Radiation Technology, TARRI, QST

Shape elongation of embedded nanoparticles (NPs) induced under swift heavy ion (SHI) irradiation has been extensively studied for this decade [1]. While the mechanism is still under debate, the majority agree with an assumption that large electronic energy deposition induced by SHIs plays an important role.

SHI is primarily defined by its high velocity, *i.e.*, large kinetic energy per nucleon, which is higher than ~ 0.1 MeV/u. An arising question is whether the shape elongation of NPs is induced under irradiation with slow ions but high electronic stopping power S_e . We have irradiated Zn NPs with 6 MeV C₆₀⁺ ions, which have a slow velocity of 0.008 MeV/u. The S_e value of the C₆₀ ions was estimated as the sum of independent 60 pieces of 0.1 MeV (=6 MeV/60) carbon monomer ions. The estimated value was 15.5 keV/nm in silica, which was comparable to S_e of 200 MeV Xe SHIs.

However, contrary to SHIs, the cluster ions interact with NPs in shallow depth only. A C₆₀ ion injected into a solid can be no longer stable as in a vacuum. Each of carbon atom consisting a C₆₀ molecule is subjected to atomic collisions with constituent atoms in the solid. The interatomic distances increase with the depth and finally the C₆₀ ion is no longer a cluster ion but 60 pieces of C monomer ions. While the ion range of 100 keV C-monomer ion is 315 nm in silica, the cluster effect can be active only much shallower than the ion range. We formed Zn NPs in the surface layer of silica (SiO₂) shallower than 70 nm [2] using 60 keV Zn⁺ ion implantation to a fluence of 1×10^{17} ions/cm².

The irradiation of C₆₀⁺ ions was carried out at TARRI, QST, using a newly developed high-flux C₆₀ negative ion source. While the samples were irradiated with four different energies, *i.e.*, 1, 2, 4, and 6 MeV of C₆₀ beams, the beam current was utilized always higher than ~ 50 pA through an aperture of 3 mm in diameter. To detect the shape elongation of NPs by the optical linear dichroism (OLD) spectroscopy [3], the samples were irradiated with an incident angle of 45°.

Figure 1 shows the fluence dependence of shape elongation of Zn NPs irradiated with 6 MeV C₆₀⁺ cluster ions, which was detected by OLD method [3]. For comparison, the dependence under 200 MeV Xe¹⁴⁺ ion irradiation is also plotted [4]. The elongation induced by 6 MeV C₆₀ ions is comparable to that of 200 MeV Xe ions in the low fluence region between 10¹¹ and 10¹² ions/cm². In this fluence region, the elongation increases linearly with

the fluence. However, 6 MeV C₆₀ ions show the deviation from the linearity at the fluences higher than 10¹² ions/cm², while 200 MeV Xe ions maintain the linearity up to 10¹³ ions/cm². With exceeding 10¹³ ions/cm², the elongation induced with 6 MeV C₆₀ ions turns to decrease. The deviation from the linearity above 10¹² ions/cm² and the decrease exceeding 10¹³ ions/cm² are both ascribed to the enhanced sputtering of cluster ions. A decrease of Zn content was confirmed by RBS at high fluences. At the highest fluences, loss of the color of Zn NPs was also confirmed by the naked eye.

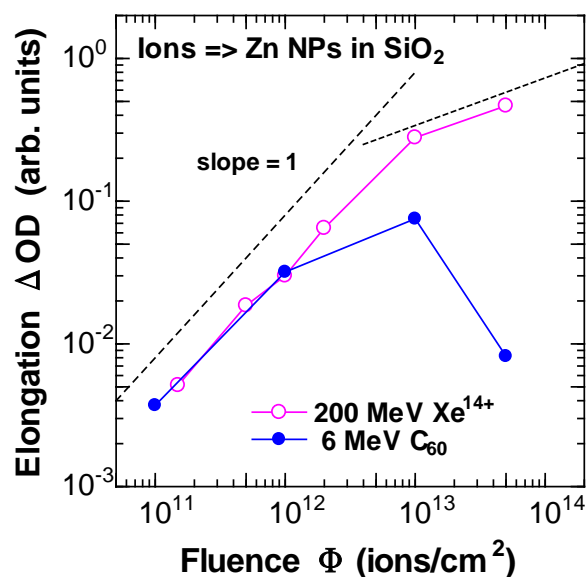


Fig. 1. Fluence dependence of shape elongation of Zn nanoparticles in SiO₂, irradiated with 6 MeV C₆₀⁺ cluster ions. For reference, the dependence of 200 MeV Xe¹⁴⁺ ions is also plotted. The elongation was determined by optical linear dichroism spectroscopy [3].

References

- [1] G. Rizza and M. C. Ridgway, in "Ion Beam Modification of Solids", ed. W. Wesch and E. Wendler, Chap. 11 (Springer, New York, 2016).
- [2] H. Amekura and N. Kishimoto, in "Lecture Notes in Nanoscale Science and Technology" Vol. 5, ed. Z. Wang, p. 1–75 (Springer, New York) (2009).
- [3] H. Amekura *et al.*, Phys. Rev. **B**, **83**, 205401 (2011).
- [4] H. Amekura *et al.*, Nanotechnology **25**, 435301 (2014).

3 - 17 Observation of Magnetic Depth Profiles for C Cluster Ion Irradiated FeRh Thin Films with Depth-resolved X-ray Magnetic Circular Dichroism

T. Matsui^{a)}, R. Soma^{b)}, A. Iwase^{b)}, M. Sakamaki^{c)}, K. Amemiya^{c)} and Y. Saitoh^{d)}

^{a)} Faculty of Liberal Arts and Sciences, Osaka Prefecture University,

^{b)} Department of Materials Science, Osaka Prefecture University,

^{c)} Institute of Materials Structure Science, High Energy Accelerator Research Organization,

^{d)} Department of Advanced Radiation Technology, TARRI, QST

Equi-atomic FeRh is known to exhibit a first order phase transition from anti-ferromagnetic to ferromagnetic around room temperature. It was revealed that ion beam irradiation induced the ferromagnetic state below room temperature, which was mainly determined by elastic deposition energy by ion irradiation [1 - 3]. According to our previous studies on Au cluster ion beam irradiation of FeRh thin films, however, we revealed that the magnetic moment of the sample irradiated with the Au₃ cluster ion was larger than that of the sample irradiated with the Au single ion especially in the surface region of the samples, even when the same number of Au ions were irradiated [4]. Considering these results, the cluster ion irradiation is possibly considered to be a method to effectively deposit the ion irradiation energy at the surface region, which may accelerate the magnetic phase transition from AFM to FM. In the present studies, we examined the effect of carbon cluster ion beam irradiation on the depth profile of magnetization in the surface of FeRh thin films by depth-resolved technique in the X-ray magnetic circular dichroism (XMCD).

Iron-Rhodium thin films about 50 nm thick were fabricated by using ion beam sputtering of Fe₅₀Rh₅₀ target on MgO(100) substrates. Then the samples were irradiated with 2 MeV C₄ and 1 MeV C₂ cluster ion as well as with 0.5 MeV C₁ ion beam at room temperature at TARRI, QST. The ion fluence has been determined to be 1.5×10^{14} C/cm² and 4.5×10^{14} C/cm². Then magnetic properties were characterized by a SQUID magnetometer as well as X-ray magnetic circular dichroism (XMCD) measurements in total electron yield mode (TEY). Furthermore, a depth-resolved XMCD measurement was also performed to evaluate the depth profile of ion beam irradiation induced ferromagnetism for the samples. Both TEY and depth-resolved XMCD measurements were carried out at Beam Line #16A at KEK-PF.

Figure 1 shows the probing depth dependence of the magnetic moment for unirradiated and irradiated samples with C₁ ion and C₂, C₄ cluster ions. The plotted values of the magnetic moment at each depth can be attributable to the average magnetic moment from surface to each depth. As clearly seen in the figure, the different profiles of the magnetic moments can be observed for each irradiated sample. It should be noted that depth profile of each sample significantly depends on the cluster ion number as well as the ion fluence. In the case of the sample irradiated with C₁

ions, the magnetic moment increases with increasing the depth. Hereby the magnetic moment of the C₂ irradiated sample shows a steep increase with increasing the depth, then gradually saturates from 15 nm region in the depth. In contrast to this, the magnetic moment decreases as the probing depth increases for the C₂ cluster ion irradiated sample with larger ion fluence (4.5×10^{14} C/cm²). These results indicate that that the cluster ion irradiation effectively causes the ion irradiation induced ferromagnetism.

By using this technique suitably, the surface magnetic ordering state can be designedly modified. Although it is still unknown that the cluster ion irradiation can deposit the relatively larger elastic collision energy at the surface region rather than single ion beam or not, it can conclude that the cluster ion beam is possible to deposit apparent elastic collision energy effectively. The detailed mechanism of such behavior as well as the experimental results on the irradiation effect for C cluster ion with increased cluster number, will be considered and communicated in near future.

References

- [1] M. Fukuzumi *et al.*, Nucl. Instrum. Meth. Phys. Res. B, **230**, 269 (2005).
- [2] M. Fukuzumi *et al.*, Nucl. Instrum. Meth. Phys. Res. B, **245**, 161 (2006).
- [3] N. Fujita *et al.*, J. Appl. Phys. **107**, 09E302 (2010).
- [4] T. Koide *et al.*, J. Appl. Phys. **115**, 17B722 (2014).

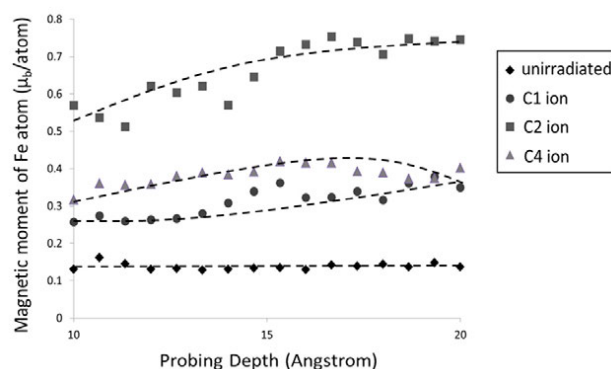


Fig. 1. Probing depth dependence of magnetic moment of Fe atom for unirradiated and irradiated samples under the fluence of 1.5×10^{14} C/cm².

Porous Structure on Ge Surface Formed by C₆₀ Ion Beam Irradiation

N. Nitta^{a)}, H. Tsuchida^{b)}, T. Oishi^{a)}, S. Tomita^{c)}, K. Sasa^{d)}, K. Hirata^{e)}, H. Shibata^{f)},
Y. Hirano^{g)}, K. Yamada^{g)}, A. Chiba^{g)}, Y. Saitoh^{g)}, K. Narumi^{g)} and Y. Hoshino^{h)}

^{a)} School of Environmental Science and Engineering, Kochi University of Technology,

^{b)} Quantum Science and Engineering Center, Kyoto University,

^{c)} Institute of Applied Physics, University of Tsukuba,

^{d)} Tandem Accelerator Complex, University of Tsukuba,

^{e)} Research Institute for Material and Chemical Measurement, AIST,

^{f)} The Institute of Scientific and Industrial Research, Osaka University,

^{g)} Department of Advanced Radiation Technology, TARRI, QST,

^{h)} Department of Mathematics and Physics, Kanagawa University

Porous structure formation on surfaces of Ge, GaSb, and InSb by ion-beam irradiation has been reported in order to clarify the formation mechanism [1]. The formation mechanism of porous structures under ion-beam irradiation involves self-organizing point defects (vacancies and interstitial atoms) in the cascade [2]. A semiconductor with a porous structure has a potential for application at electric and photonic materials such as TFT (thin film transistors), photonic crystals, and quantum dots. It is necessary to control the size of a porous structure for applications. In the previous study, GaSb surfaces were irradiated with cluster-ion beams of Cu_n⁺ (n = 1-3) [3]. The large porous structure was obtained by Cu₃⁺-ion irradiation. Cluster-ion irradiation enhanced the defect creation for the overlap between cascades. It is effective for the growth of a porous structure. In this paper, we report Ge surfaces were irradiated with C₆₀ cluster beams with two different energies of 540 keV and 6 MeV.

The experiments were performed using two types of ion accelerators (the ion implanter and the tandem Pelletron accelerator) at TIARA, QST. A well-collimated C₆₀ beam with an incident energy of 540 keV or 6 MeV was incident parallel to the surface normal of a sample. A sample was a mirror polished Ge single crystal wafer with (001) orientation. A fluence of C₆₀ beam was set to 3×10^{11} – 3×10^{14} cm⁻². The fluence was determined from the measurement of carbon implanted into a sample with ¹²C(p,p)¹²C resonance elastic scattering reaction using an ion accelerator at Kanagawa University. The irradiation temperature was room temperature. The as-irradiated surface was evaluated with scanning electron microscopy (SEM) at Kochi University of Technology.

Figure 1 shows surface SEM images of Ge irradiated with 540-keV C₆₀²⁺ beams. The porous structure like a ridge was observed on the surfaces. The average size of the ridge was approximately 50 nm at fluence of 3×10^{14} cm⁻². The size of the ridge increased with increasing fluence.

Figure 2 shows surface SEM images of Ge irradiated with 6-MeV C₆₀⁺ beams. The porous structure like a rock with facets was observed. The average size of the rock was approximately 60 nm at fluence of 2×10^{14} cm⁻². The

observed porous structures were significantly large compared with the result for atomic beam irradiation. This indicates that the cluster-ion irradiation generates a large number of point defects, and forms a large size porous structure.

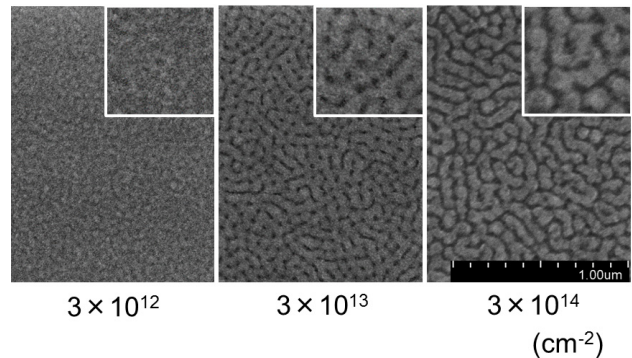


Fig. 1. Surface SEM images of Ge irradiated with 540-keV C₆₀²⁺ beams. The inset is an enlarged view of the SEM image.

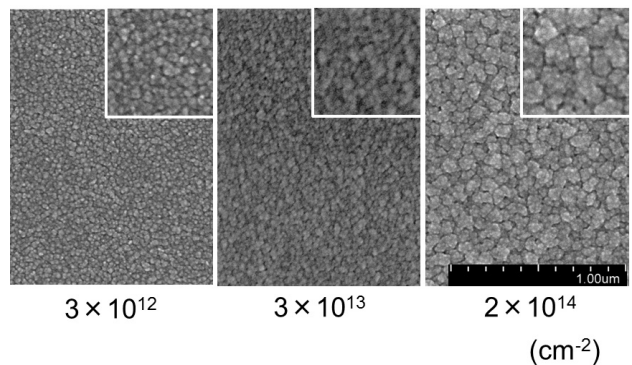


Fig. 2. Surface SEM images of Ge irradiated with 6-MeV C₆₀⁺ beams. The inset is an enlarged view of the SEM image.

References

- [1] Y. Yanagida, T. Oishi, T. Miyaji, C. Watanabe and N. Nitta, *Nanomaterials*, **7**, 180 (2017).
- [2] N. Nitta *et al.*, *J. Appl. Phys.* **92**, 1799-802 (2002).
- [3] H. Tsuchida, N. Nitta, *et al.*, *J. Appl. Phys.* **123**, 161548 (2018).

3 - 19 Ion Energy Dependence of Optical Absorption Spectra for Silica Glass Implanted with Ag Ions

K. Fukuda ^{a)}, F. Hori ^{a)}, Y. Saitoh ^{b)}, S. Semboshi ^{c)}, H. Amekura ^{d)} and A. Iwase ^{a)}

^{a)}Department of Materials Science, Osaka Prefecture University,

^{b)}Department of Advanced Radiation Technology, TARRI, QST,

^{c)}Institute of Materials Research, Tohoku University,

^{d)}Research Center for Advanced Measurement and Characterization, National Institute for Materials Science (NIMS)

To investigate the implantation energy dependence of the optical absorption spectrum, silica glass (SiO_2) samples with the dimension of $5 \times 5 \times 1 \text{ mm}^3$ were implanted with 50 - 380 keV Ag ions by using an ion-implanter. The implantation dose was $7 \times 10^{16} / \text{cm}^2$. After the ion implantation, the effects of the implantation energy on optical absorption spectra were studied by means of UV-vis spectrometer. To observe the microstructure of Ag-implanted samples, the transmission electron microscope (TEM) was used.

Figure 1 shows the optical absorption spectra for the range of wavelength between 200 nm and 800 nm. As can be seen in the figure, an absorption band around 400 nm is observed irrespective of the implantation energy. This absorption peak is well known as due to the surface plasmon resonance. For the samples implanted with 200 and 380 keV Ag ions, in addition to the 400 nm absorption peak, another peak can be observed around 600 nm.

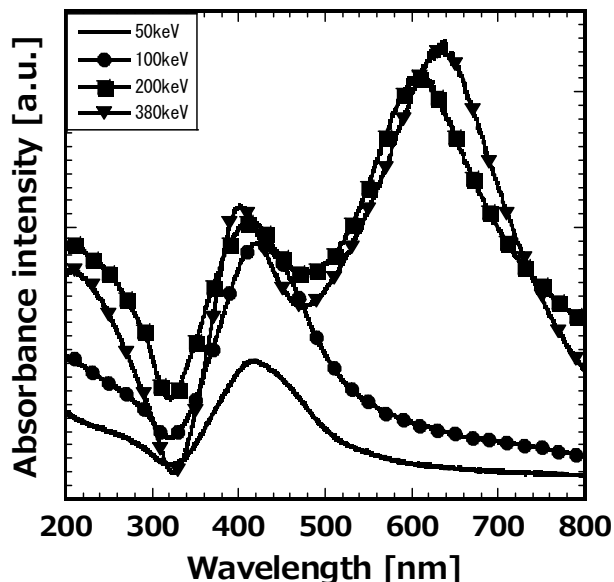


Fig. 1. Optical absorption spectra for the Ag-implanted silica glass samples with the fluence of $7 \times 10^{16} \text{ cm}^{-2}$ at various energies (50-380 keV).

Figures 2 and 3 show the TEM images of Ag clusters in silica glass samples. The ion beam direction is shown in each figure. The distribution of Ag spherical nanoparticles with the diameter of 5 - 20 nm was confirmed. For the samples implanted with higher energy (200 keV) Ag ions, Ag spherical nanoparticles with the large space density

were observed. On the other hand, for the samples implanted with lower energy (100 keV) Ag ions, the space density of Ag clusters is smaller than that for the case of 200 keV Ag ion irradiation. A similar trend can be found for 50 keV Ag ion implantation and 380 keV Ag ion implantation. The absorption peaks around 600 nm is, therefore, due to the interaction among Ag nanoparticles.

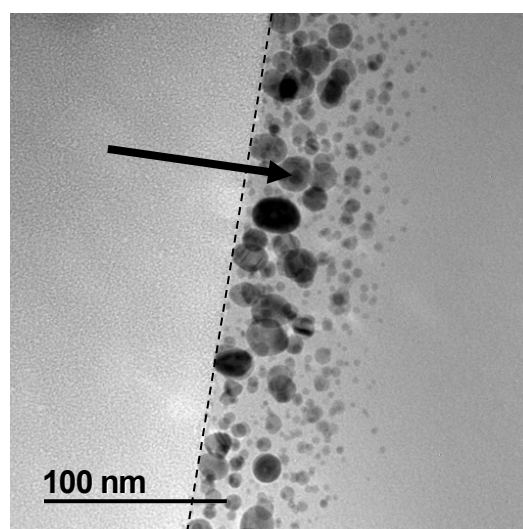


Fig. 2. TEM image of Ag implanted silica glass sample with the fluence of $7 \times 10^{16} \text{ cm}^{-2}$ for the implantation energy of 100 keV. Dashed line indicates the sample surface.

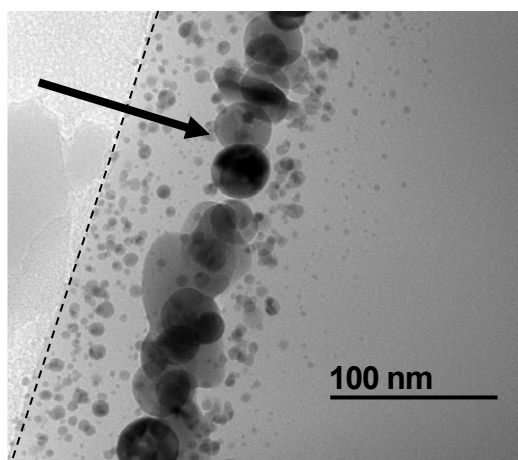


Fig. 3. TEM image of Ag implanted silica glass samples with the fluence of $7 \times 10^{16} \text{ cm}^{-2}$ for the implantation energy of 200 keV. Dashed line indicates the sample surface.

3 - 20 Micro-PIXE Analysis Study of Ferrite Products Synthesized from Simulated Radioactive Liquid Waste Containing Chemical Hazardous Elements

T. Abe ^{a)}, T. Shimazaki ^{a)}, T. Osugi ^{a)}, O. Nakazawa ^{a)}, N. Yamada ^{b)}, Y. Yuri ^{b)} and T. Satoh ^{b)}

^{a)} Radioactive Waste Processing and Disposal Research Department, NBTC, JAEA,

^{b)} Department of Advanced Radiation Technology, TARRI, QST

Radioactive liquid waste generated from nuclear facilities includes not only radionuclides but also chemical hazardous elements. Chemical hazardous elements are toxic to human and have a risk of environmental pollution after disposal as well as radionuclides. Therefore, radioactive wastes have to be solidified with adequate materials to prevent elution of hazardous and radioactive elements for the disposal. Our previous experiments have shown that the amount of elution exceeded environmental standard when we treated a Pb (above 1.24%) solution with Ordinary Portland Cement. It is necessary to add further treatment to prevent elution of hazardous elements before cementation.

A ferrite process is one of the methods to treat heavy metals in liquid wastes. Heavy metal ions in the solution are incorporated and captured by substitution in the lattice of formed magnetite structure, in which the chemical formula is $MeFe_2O_4$ (Me: heavy metal). Many studies on synthetic conditions of ferrite have been reported. The ferrite is synthesized by heating ferric hydroxide precipitate ($FeO(OH)-H_2O$) in the solution.

Many former studies have focused on the crystal structure and magnetism of synthesized ferrite products. Few studies on coexisting anions remaining in ferrite products have been reported. The coexisting anion has a possibility to affect solidification. It is necessary to study coexisting anions for solidifying treated ferrite by cement. Anions in the synthesized ferrite are included in the added reagent as an iron source. They are supposed as impurities of ferrite because the chemical formula of ferrite is $MeFe_2O_3$. Micro-PIXE is the most suitable method as it is possible to

analyze these impurities with high sensitivity and micrometer-scale two-dimensional analysis.

In this study, some ferrite products synthesized by the simulated liquid waste with various metal ions are treated with ferrite synthesized by various iron sources. The difference of elemental composition of the ferrites is investigated by use of Micro-PIXE system of TIARA.

Table 1 shows conditions of the ferrite processing. The synthesized ferrites washed twice by distilled water and dried were analyzed. Table 2 shows dominant crystal structure of synthesized ferrites analyzed by X-ray diffractometer (XRD, Rigaku Ultima IV, $Cu(K\alpha)$ -50 kV, 40 mA). Two types of crystal phase as Magnetite (M) and Goethite (G) have been identified. The structure of ferrite depends on both metal ion and iron source.

We investigated the correlation between metal ion and anions of the synthetic ferrite by measuring the element composition of the ferrite in the micron range. Figure 1 shows the correlation diagrams of PIXE signal strength between metal ion and anion. The Micro-PIXE analysis was carried out with 3 MeV H^+ beam of the TIARA single-ended accelerator. The correlations of Ag have narrow distributions. The correlations of Pb have wide distributions along x-axis. On the other hand, those of Cr have wide distributions along y-axis. Each distribution does not depend on anion species. The different correlations with metal ions except for anion species have been found. It suggests the possibility that ionic valence of chemical hazardous elements affect the state of coexistent anions. To observe this reason is further investigation.

Table 1

Conditions of the ferrite processing.

Target Metal ions (Me)	Ag, Pb, Cr
Fe source reagent	$FeSO_4$, $FeCl_2$, $FeBr_2$
Concentration of Me in the simulated liquid wastes (ppm)	1,000
pH in the simulated liquid wastes	11
Temperature ($^{\circ}C$)	70
Oxidizing air (L/min)	1.7
Reaction time (h)	2

Table 2

Main structures of synthesized ferrites.

	$FeSO_4$	$FeCl_2$	$FeBr_2$	$FeO(OH)$
Ag	M	M	M	G
Pb	M	G	G	G
Cr	M	M	M	G

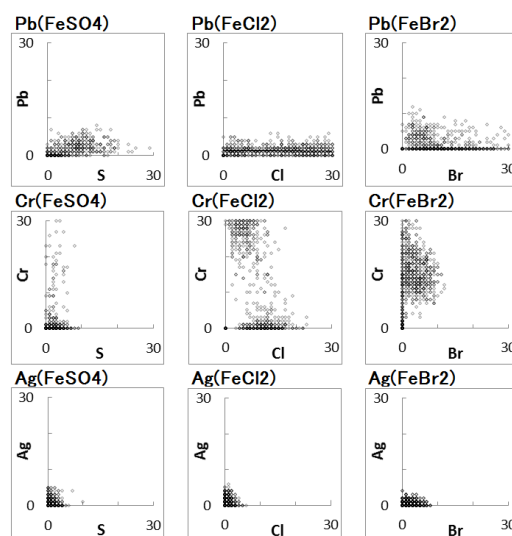


Fig. 1. Correlation diagram of signal strength between Me and anion.

Ion Beam Induced Luminescence of Eu^{3+} Extracted by HDEHP

S. Watanabe ^{a)}, W. Kada ^{b)}, H. Matsuura ^{c)}, M. Koka ^{d)} and T. Satoh ^{e)}

^{a)} Department of Reprocessing Technology Development, NBTC, JAEA,

^{b)} Division of Electronics and Informatics, Faculty of Science and Technology, Gunma University,

^{c)} Atomic Energy Research Laboratory, Tokyo City University,

^{d)} Beam Operation Co., Ltd.,

^{e)} Department of Advanced Radiation Technology, TARRI, QST

Partitioning and transmutation of minor actinides (MA(III); Am(III) and Cm(III)) in spent nuclear fuel is an important strategy for reduction in volume and radiotoxicity of the radioactive waste. Japan Atomic Energy Agency has been developing the extraction chromatography technology for separation of MA(III) from other fission products. In this technology, adsorbent is prepared by impregnating an extractant into styrene divinyl benzene copolymer coating around porous silica particle (referred as $\text{SiO}_2\text{-P}$), and MA(III) are recovered through adsorption and elution reactions inside the packed column. The adsorption reaction has been believed to progress with solvent extraction reaction observed in liquid-liquid extraction system even in the solid-liquid system. However, our previous research showed that local structure around adsorbed cations in the adsorbent sometimes show slightly different coordination from that observed in the solvent extraction system [1]. The difference might be caused by different degree of freedom of the extractant between in the polymer and in diluent of the solvent. In order to achieve efficient MA(III) recovery by the extraction chromatography, adsorption mechanism is required to be precisely revealed.

Recently, we have been focusing on ion-beam induced luminescence (IBIL) analysis as promising to evaluate chemical state of the adsorbed cation due to its sensitivity for chemical environment of target materials. Our previous study has shown that IBIL spectrum of Eu^{3+} loaded in the adsorbent strongly depend on ligands coordinating around the cation [2]. In this study, IBIL and Extended X-ray Absorption Fine Structure (EXAFS) analyses on the solvent and adsorbent systems were carried out for HDEHP extractant which is promising for separation of MA(III) from trivalent lanthanides. Structural difference between these systems were discussed.

HDEHP/ $\text{SiO}_2\text{-P}$ was prepared as the usual procedure, and $\text{Eu}(\text{III})$ was loaded into them by batch-wise operation. IBIL measurements were carried out at light-ion microbeam line connected to a 3-MV single-ended accelerator in TIARA of QST. Detail analytical conditions are described in Ref. [3]. Eu-L_{III} EXAFS measurements were carried out at BL27B beamline of PF, KEK, Japan.

IBIL spectra of HDEHP extractant, HDEHP diluted by n-dodecane (nDD) and the porous silica with the polymer ($\text{SiO}_2\text{-P}$) did not show any line or band spectra. As seen in Fig. 1, the adsorbent and the solvent loading Eu^{3+} showed characteristic spectra, therefore those could be attributed to luminescence from Eu^{3+} extracted by HDEHP.

The characteristic peaks in the spectra at 580 - 600,

610-630, 650-660 and 700-710 nm could be attributed to $^5\text{D}_0 \rightarrow ^7\text{F}_1$, $^5\text{D}_0 \rightarrow ^7\text{F}_2$, $^5\text{D}_0 \rightarrow ^7\text{F}_3$ and $^5\text{D}_0 \rightarrow ^7\text{F}_4$ transitions of Eu^{3+} , respectively [4]. Distinct difference between 2 spectra was found in the $^5\text{D}_0 \rightarrow ^7\text{F}_2$ transition which is called hypersensitive transition of lanthanide ion and is sensitive to complexed lanthanides. Therefore, complexing forms of Eu^{3+} with HDEHP in those system are considered to be different. EXAFS analysis showed that the numbers of the nearest neighboring O atoms around Eu^{3+} and the nearest $\text{Eu}^{3+}\text{-O}$ distances are almost the same for the adsorbent and the solvent. The results imply that extractions of Eu^{3+} by HDEHP in both system progress according to the following equation,



The difference in the IBIL spectra between the 2 systems must be caused by different symmetry of HDEHP coordinating around Eu^{3+} . In the solvent system, 3 dimers of HDEHP are considered to coordinate around a Eu^{3+} symmetrically. Further analysis on the IBIL spectra is currently underway.

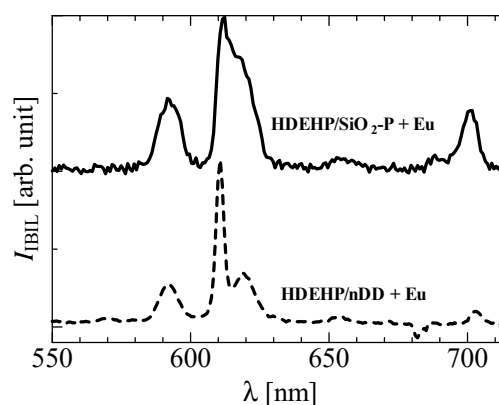


Fig. 1. IBIL spectra of Eu^{3+} loaded in the adsorbent and in the solvent.

Acknowledgment

The EXAFS measurements were carried out under the proposal of 2016G557 of the PF, KEK.

References

- [1] Y. Sano *et al.*, J. Nucl. Sci. Tech. **54**, 10, 1058-64 (2017).
- [2] S. Watanabe *et al.*, QST Takasaki Annual Rep. 2016 **QST-M-8**, 60 (2018).
- [3] W. Kada *et al.*, Nucl. Instrum. Meth. Phys. Res. B, **372**, 151-55 (2016).
- [4] K. Binnemans, Coordin. Chem. Rev. **295**, 1-45 (2015).

T. Fukuchi

Graduate Faculty of Interdisciplinary Research, University of Yamanashi

It is an urgent issue to assess the activity of unrecognized active faults in the region with unclear tectonic landform or without Quaternary overlying sediments since such active faults actually caused earthquake disaster such as the 2018 Osaka earthquake (M 6.1). At the present stage, we have no way of the assessment but to determine the age of fault rocks produced at the time of fault movement with absolute dating techniques. The ESR (electron spin resonance) dating technique is available in estimating the age of fault rocks using radiation defect radical centers derived from fault-rock-forming minerals.

When we apply the ESR dating technique to fault rocks, we assume that ESR signals in fault rocks have been once reset by frictional heating [1]. Then, the ESR age (T) is calculated by dividing the total radiation dose (TD) to which the fault rocks have been subjected since the resetting of the ESR signals by the annual radiation dose (D); $T = TD/D$. The TD is obtained by extrapolating the growth curve calculated from the ESR intensities before and after artificial γ -irradiation.

However, the ESR signals are not always reset completely near the Earth's surface because frictional heat hardly rises. When the ESR signals are incompletely reset, the TD s obtained are overestimated, and then the ESR ages obtained are older than the actual age (T_a) of the latest fault movement. Therefore, the ESR ages (T_{esr}) theoretically give the upper limit of the actual age ($T_a \leq T_{esr}$).

Here, I apply the ESR technique to fault rocks collected from the Yamada fault located in Toyooka city on Tango Peninsula. Although the Yamada fault may have moved in the 1927 Kita Tango earthquake, its actual activity is still unclear. The artificial γ -irradiation for determining the TD s was carried out with a ^{60}Co source at No.2 irradiation room in the food irradiation facility, Takasaki Advanced Radiation Research Institute, QST. The irradiation dose rate is 390 Gy/h.

As a result of ESR measurements, the surface E' center, Al and Ti centers in quartz [1] were detected from the Yamada fault gouge just on the fault plane, which was formed by the latest fault movement. Moreover, the γ -irradiation shows that they regularly increase with increasing radiation dose, implying that these radical centers probably give more precise TD values (Fig. 1).

The ESR age of $0.19\text{-}0.26 \pm 0.08$ Ma is obtained from the fault gouge using the surface E' center created in quartz by shearing. This result shows that the age (T_a) of the latest fault movement along the Yamada fault is estimated as $T_a \leq 0.19\text{-}0.26 \pm 0.08$ Ma on the basis of the principle of ESR dating of fault movement, and then this supports that the

Yamada fault is indeed an active fault that has moved in the Middle-Late Pleistocene. Thus, I conclude that the ESR dating technique is available for the assessment of fault activity of unrecognized active faults that have moved in the Middle Pleistocene.

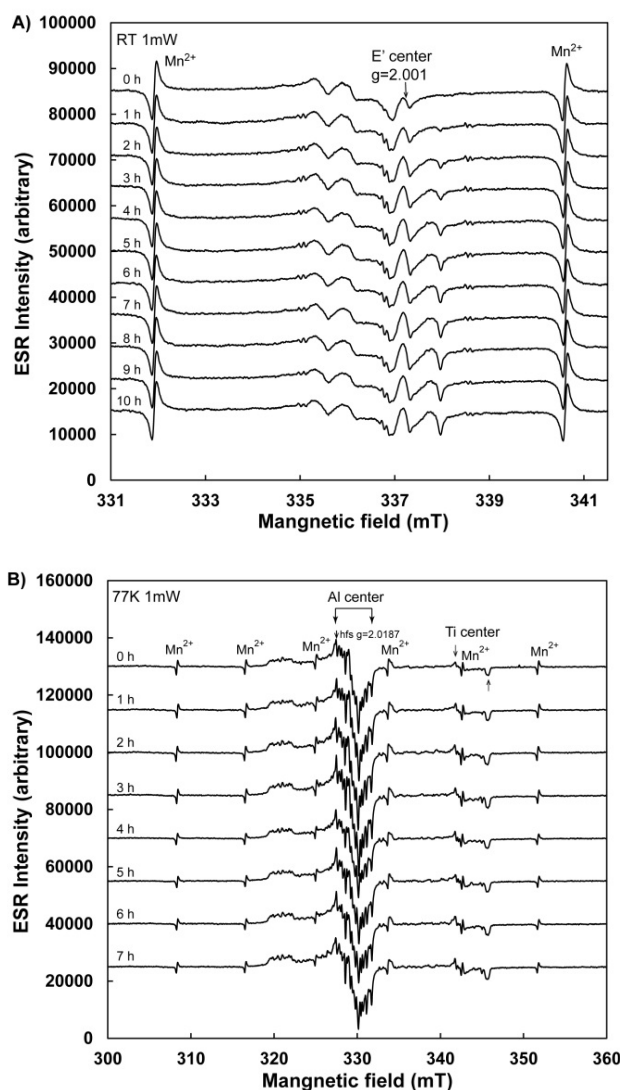


Fig. 1. A) γ -irradiation effect on the surface E' center in quartz in the Yamada fault gouge just on the fault plane. B) γ -irradiation effect on the Al and Ti centers in quartz in the Yamada fault gouge just on the fault plane. The irradiation dose rate is 390 Gy/h and the irradiation time is 0-10 hours.

Reference

- [1] T. Fukuchi, ESR dating of fault movement-Its principle and practice. Fukadaken Library 63, 45pp (2004).

3 - 23 Preliminary Test of a Penning Ionization Gauge Ion Source with Electromagnets for a Compact Ion Microbeam System

Y. Ishii^{a)}, T. Ohkubo^{a)} and Y. Miyake^{b)}

^{a)} Department of Advanced Radiation Technology, TARRI, QST,
^{b)} Beam Seiko Inc. Ltd.

A compact ion microbeam system within a size of $2 \times 2 \times 2 \text{ m}^3$ that produces an ion beam of $1 \text{ }\mu\text{m}$ diameter at energy of 1 MeV , hereinafter referred to as “MeV μ -beam system”, is under development for the installation in a typical laboratory with space of $6 \times 8 \times 3 \text{ m}^3$. As a first step of the development, a prototype of the compact ion microbeam system that produced an ion microbeam up to 120 keV ($120 \text{ keV } \mu$ -beam system) was designed and constructed to confirm the effectiveness of the usage of a three-stage compact electrostatic focusing lens with a high demagnification factor (three-stage acceleration lens) [1]. This system has a dedicated duoplasmatron-type ion source [2]. A $2.6\text{-}\mu\text{m}$ -diameter hydrogen ion beam was produced step by step by reducing the divergence angle of incident beam into the lens and by decreasing residual gas pressure [3]. The energy upgrade of $120 \text{ keV } \mu$ -beam system up to 1 MeV is now attempted by enhancing the voltage of the three-stage acceleration lens to 1 MV (MeV μ -beam system). On the other hand, the duoplasmatron-type ion source can generate a hydrogen ion beam with the energy of less than 1 keV and the brightness of $5 \text{ A}/(\text{m}^2 \text{ sr V})$. These specifications are suitable for the three-stage acceleration lens, but the installation of the ion source in the MeV μ -beam system is difficult due to its large power consumption, over 1 kW , and its use of a thoriated-tungsten filament, which requires frequent replacement, as well as its large cylindrical shape with a 15 cm ϕ base and 25 cm height with a cooling device.

A typical Penning ionization gage (PIG) ion source with cold cathodes is suitable for the MeV μ -beam system from the point of view of possible low power consumption. However, the ion beam has the features of low brightness and energy on the order of 10 keV . The MeV μ -beam system requires the aforementioned ion beam brightness for a beam current of over 10 pA at a focusing point on a sample. The system also requires beam energy below 2 keV to permit a large demagnification factor at the three-stage acceleration lens. Although the ion beam energy spread of over 20 eV , which is generated by the PIG ion source and causes the chromatic aberration, has an effect on the formation of the ion microbeam, the aberration can be controlled to some extent by reducing the divergence angle of the incident ion beam. Therefore, the development of an ion source that produces ion beam with high brightness ion beams is more important than that of the ion source that produces ion beam with narrow energy spread. Concerning typical PIG ion sources, the main reason of the low beam brightness was attributed to generating a large

beam current from low-density plasma in a large volume using a cathode with a through-holes with diameters as much as several mm from the consideration of configurations of their ion sources. Therefore, a PIG ion source with high-density plasma in a small volume and a cathode with a small through-hole was considered to be effective to generating a high brightness ion beam.

In this study, a hydrogen ion beam was generated using the prototype PIG ion source that was developed in fiscal 2016 as described in Ref. [4]. Then the brightness of a hydrogen ion beam was measured within the beam energy of 2 keV as a preliminary test.

The PIG ion source was connected to a test bench as shown in Fig. 1. A collimator with $0.2 \text{ mm}\phi$ and a Faraday cup connected to a pico-ammeter were set downstream at positions of 60 mm and 500 mm from the ion source, respectively.

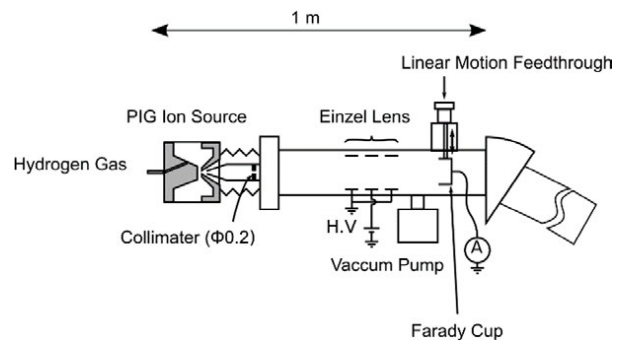


Fig. 1. Experimental setup for the measurement of ion beam brightness. The PIG ion source was connected to a test bench for an ion source.

A hydrogen ion beam was generated from the ion source. Beam current through the collimator was measured to be 12.5 nA at extraction voltage of 1.1 kV . The solid angle was estimated to be $8.73 \times 10^{-6} \text{ sr}$, then the brightness to be $52 \text{ A}/(\text{m}^2 \text{ sr V})^{-1}$. This brightness was sufficient for the MeV μ -beam system.

References

- [1] Y. Ishii *et al.*, Nucl. Instrum. Meth. Phys. Res. B, **332**, 156-59 (2014).
- [2] Y. Ishii *et al.*, Nucl. Instrum. Meth. Phys. Res. B, **113**, 75-77 (1996).
- [3] Y. Ishii *et al.*, Nucl. Instrum. Meth. Phys. Res. B, **404**, 65-68 (2017).
- [4] Y. Ishii *et al.*, QST Takasaki Annu. Rep. 2016, **QST-M-8**, 136 (2018).

T. Ohkubo and Y. Ishii

Department of Advanced Radiation Technology, TARRI, QST

Proton microbeams formed by a MeV class large accelerator system are useful for proton beam writing (PBW), particle induced X-ray emission (PIXE) analysis and several other micro-analyses with 1 μm spatial resolution. Currently, the size of the MeV class large system restricts the development of PBW and PIXE, in particular, in small laboratories. A more compact system to generate proton microbeam is necessary.

A several hundred keV class compact proton microbeam system has been developed at TARRI, QST, instead of the MeV class large system. This compact system is expected to be installed in average-sized laboratories in universities and industrial facilities so that PBW and PIXE may be used more widely. The compact microbeam system comprises a duoplasmatron-type ion source and an electrostatic lens system, whose total length is approximately 900 mm. The ion source uses hydrogen gas to generate a proton beam and the lens system is composed of an extraction stage and three acceleration stages. The several hundred keV lens system is a prototype for a 1 MeV lens system and can be upgraded by a proportional expansion. Each of the acceleration stages has a series of disk-shaped electrodes with a small center hole (known as acceleration lens), in which an ion beam is accelerated and focused simultaneously. By using the acceleration lens for focusing ion beams, much higher demagnification can be obtained by a much shorter lens system as compared to that in the conventional long and large lens system. In a previous experiment, the beam diameter was limited to 5.8 μm at 120 keV [1], while the beam diameter should be reduced to approximately 1 μm for applications of the compact microbeam system.

In this study, the distance D between the anode electrode and the extraction electrode in the extraction stage was made shorter to optimize extraction stage conditions and to approach a proton beam diameter of 1 μm . According to ion optics simulations performed when the distance D was changed from 15 mm to 10 mm, the demagnification became 2.2 times larger, about 200 overall. In addition, reduction of D results in a shorter beam path length in the extraction stage and corresponds to a decrease of interactions between an extracted beam and the residual gas that is hindrance to microbeam formation [2]. Given these changes in D , the beam diameter was expected to be reduced to less than 2.6 μm (5.8 divided by 2.2) and to approach 1 μm .

An experiment to reduce the beam diameter was performed under the condition shown in Fig. 1, with distance D shortened to 10 mm. A proton beam was extracted from the duoplasmatron-type ion source with an anode hole of 200 μm in diameter, which corresponded to

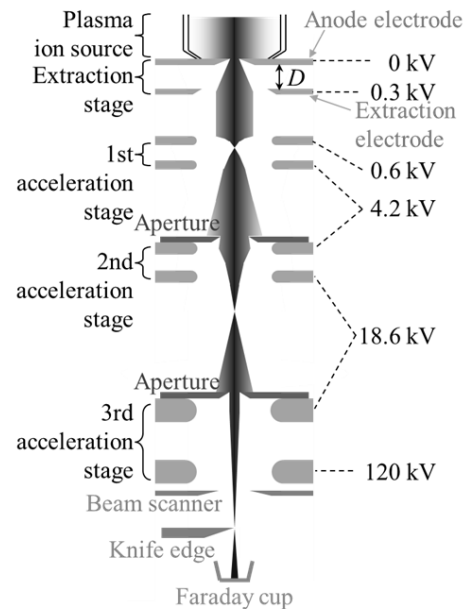


Fig. 1. Schematic of the several hundred keV compact proton microbeam system.

the object beam diameter of the lens system. An extraction voltage of 0.3 kV was applied to the extraction electrode in the extraction stage. After the extracted proton beam was slightly accelerated and focused with another 0.3 kV, the beam was injected to the three acceleration stages. Acceleration voltages of 4.2, 18.6, and 120 kV were applied to each acceleration lens, respectively. The final focal point was formed outside the third acceleration lens at a working distance of 160 mm. The beam diameter was evaluated by moving a microbeam over a diamond knife edge with a sharp tip using an electrostatic scanner system, in which the beam current was measured by a Faraday cup. The beam diameter in full width at half maximum (FWHM) was 1.8 μm and the beam current was approximately 30 pA with the stability of 2% at the final beam energy of 120 keV. These beam parameters are comparable to those of the MeV class large system used in present PIXE and PBW experiments, except for dissimilar kinetic energy.

This compact system will become a great tool to advance lab-on-chip productions and biological cell analyses.

References

- [1] T. Ohkubo and Y. Ishii, *Rev. Sci. Instrum.*, **86**, 036102 (2015).
- [2] Y. Ishii, T. Ohkubo, *et al.*, *Nucl. Instrum. Meth. Phys. Res. B*, **348**, 79-82 (2015).

Y. Hirano, A. Chiba, K. Yamada, A. Yokoyama, Y. Ishii and T. Nara

Department of Advanced Radiation Technology, TARRI, QST

Stabilization of C₆₀ ion beam intensity using CsI

A new oven-rod was developed to increase the intensity of MeV-energy C₆₀ ion beams in fiscal 2017 [1]. To increase the beam intensity for the experiments with the higher fluence irradiations, current applied to a filament (0.8 mmφ × 50 mm) emitting thermal electrons for production of negative C₆₀ ions had to be increased up to the limit of a permissible range of the filament (more than 30 A). However, excess overheating of the filament made the beam intensity decrease and unstable because the carbide adhered on the filament surface and increased the work function of it. In order to obtain the electron emission sufficiently from the filament under the condition of reducing the temperature of the filament as low as possible, we attempted to use the chemical characteristics of Cs that decreased the work function of a metal surface. As a method for sending Cs to the surface of the filament, a CsI powder was mixed in C₆₀ sample because CsI had the two favorable characteristics that were the similar sublimation temperature of C₆₀ and moderate stability in air. The thermally dissociated Cs from CsI on the hot filament decreased the work function of the filament surface. As a result of this method, the enough beam intensity for the higher fluence irradiations was stable at lower current of about 20 A.

Measurement of ion beam energy shift using resonance nuclear reaction and commercial AC voltage fluctuation

The parallel shifts of trace-element positions in 2D distribution image by the in-air-micro-PIXE analysis were occasionally observed within 2 μm in several hours without movement of the sample. A cause of the shifts was considered to be the instability of ion beam energy. It was attributed to the voltage fluctuation of power supplies of the Single-ended accelerator and the micro beam line due to ac voltage fluctuation of commercial supply. In fiscal 2017, the two types of time fluctuation of the beam energy from the Single-ended accelerator and the ac-voltage of commercial supply were measured to obtain the relationship between them. In the beam energy measurement, the resonance nuclear reaction of $^{27}\text{Al}(p, \gamma)^{28}\text{Si}$, with the resonance energy width of 100 eV and the wide of cross section at 1772 keV γ -ray was used because it determined the beam energy accurately. Before the measurement, the accelerator voltage and the beam intensity were set to the acceleration voltage according to the beam energy of several keV above the reaction energy and 600 nA at a target, respectively. The γ -ray yields were measured every hour from 10 AM to 21 PM using an NaI scintillation detector. In the estimation of the beam energy of each hour, the yield of γ -ray in the

resonance nuclear reaction was plotted as a function of the beam energy between 0 and 5 kV. On the other hand, the commercial AC voltage was measured using a power quality analyzer (CW500, Yokogawa, Japan) at an interval of 1 minute during the beam energy measurement. The measured mean beam energy and the beam stability were 1002.2 keV and 5.8×10^{-4} , respectively. The fluctuation of the commercial ac voltage was range from 201 V to 208 V. In this measurement, the relationship between the beam energy from the Single-ended accelerator and the ac-voltage of commercial supply was not observed.

Development of time-of-flight secondary ion mass spectrometry measurement system

Time-of-flight (TOF) secondary ion mass spectrometry using sub-MeV-energy cluster ion beam has various advantages including enhancement of secondary ions required for chemical structure characterization and prevention of charging effects in secondary ion mass spectra for organic targets [2]. A secondary ion mass spectrometry measurement system is developed using C₆₀ ion beam from the 400 kV Ion Implanter. In the measurement system, only the difference in TOF of secondary ions was measured using a time analyzer (Ortec, 9308). Measuring accurately the emitted secondary ion number was difficult because secondary ions had the same mass-to-charge ratio (same flight time) and could not be discriminated. Therefore, in order to measure the wave height of a detector signal that changed depending on the number of incident secondary ions in addition to the flight time, the time analyzer was replaced with a high-speed oscilloscope (National Instruments, PXIe-5164). The PXIe-5164 features a user programmable FPGA, the sampling rate is up to 1 GS/s and the data transfer rate is 3.5 GB/s. In fiscal 2017, a LabVIEW program for the measurement of the flight time of secondary ions was developed using PXIe-5164 for device-test, and the measured secondary ion mass spectrum was confirmed to be comparable to the spectrum measured by the time analyzer. In the future, we will develop the program to analyze the wave height of the detector signal and measure accurate emitted secondary ion number.

References

- [1] Y. Hirano *et al.*, QST Takasaki Annu. Rep. 2016, **QST-M-8**, 134 (2017).
- [2] K. Hirata *et al.*, Nucl. Instrum. Meth. Phys. Res. B, **314**, 39-42 (2013).

Prat II

4. Status of Quantum-Beam Facilities

4-01	Utilization Status at TIARA Facility	148
	A. Hanaya, I. Ishibori, H. Takizawa, S. Watanabe, H. Kaneko, S. Kaneya, M. Kawabata, K. Saga and Y. Nakamura	
4-02	Operation of the AVF Cyclotron	149
	S. Kurashima, K. Yoshida, T. Yuyama, T. Ishizaka, I. Ishibori, N. Miyawaki, H. Kashiwagi, Y. Yuri, T. Nara, To. Yoshida, Tu. Yoshida, S. Ishiro, S. Kanou, K. Takano, H. Saitoh, T. Atobe and K. Akaiwa	
4-03	Operation of Electrostatics Accelerators in TIARA	150
	A. Chiba, K. Yamada, A. Yokoyama, Y. Hirano, T. Nara, T. Takayama, S. Kanai, Y. Aoki, M. Hashizume, Y. Takahashi and M. Hasegawa	
4-04	Operation of the Electron Accelerator and the Gamma-ray Irradiation Facilities	151
	T. Agematsu, S. Uno, R. Yamagata, H. Seito, Y. Nagao, S. Yamasaki, N. Yagi, M. Takagi, K. Nagai and T. Asai	
4-05	Utilization Status of the Electron Accelerator and the Gamma-ray Irradiation Facilities ...	152
	T. Agematsu, S. Uno, R. Yamagata, H. Seito, Y. Nagao, S. Yamasaki, N. Yagi, M. Takagi, K. Nagai and T. Asai	
4-06	Radiation Monitoring in TIARA	153
	Safety Management Section	
4-07	Radioactive Waste Management in TIARA	154
	N. Higuchi	
4-08	Facility Use Program in Takasaki Advanced Radiation Research Institute (TARRI)	155
	S. Nozawa, H. Hanaya and M. Seki	

4 - 01

Utilization Status at TIARA Facility

H. Hanaya ^{a)}, I. Ishibori ^{a)}, H. Takizawa ^{a)}, S. Watanabe ^{a)},
H. Kaneko ^{b)}, S. Kaneya ^{b)}, M. Kawabata ^{b)}, K. Saga ^{b)} and Y. Nakamura ^{b)}

^{a)} Department of Advanced Radiation Technology, TARRI, QST,

^{b)} Takasaki Establishment, Radiation Application Development Association

Research & industrial use

Four kinds of accelerators, cyclotron and three electrostatic accelerators (tandem accelerator, single-ended accelerator and an ion implanter), are used at the TIARA facility to meet various researchers' needs. Research fields that the cyclotron was used for the past 5 years are shown in Fig. 1. Total utilization time was in the range of 2200 to 2300 hours per year until FY 2015. However, in FY 2016 and FY 2017, total utilization time was reduced due to the remodeling of a cooling system of the cyclotron facility and repair of the main coil of the cyclotron. Therefore, the trend of the research fields was changed from FY 2016. The utilization time of "Basic Techniques of Quantum Beam" extremely decreased, as compared with the other three research fields.

On the other hand, for the three electrostatic accelerators, as shown in Fig. 2, the utilization time including "Material Science" and "Basic Techniques of Quantum Beam" accounted for more than about 80% of the total time. The utilization time of "Facility use program" had increased since FY 2016, because the treatment of JAEA users was changed from "Internal use" to "Facility use program".

The trend of the number of users for the past 5 years is shown in Fig. 3. The total number of users increased until

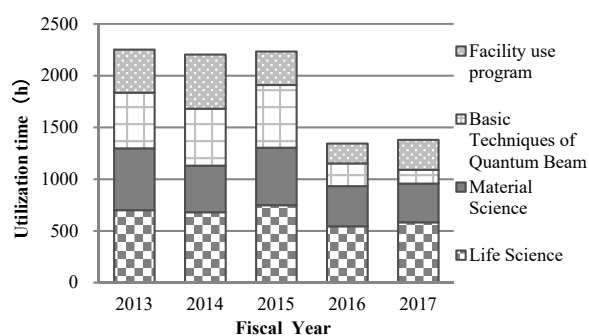


Fig. 1. Trend of research activities for cyclotron for the past 5 years.

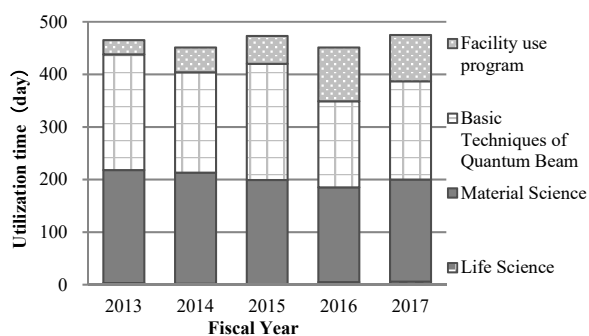


Fig. 2. Trend of research activities for the three electrostatic accelerators for the past 5 years.

FY2014, but it had decreased since FY 2015. The trend of the number of project category for the past 5 years is shown in Fig. 4. The number of projects was in the range of 120 to 140 per year until FY 2015. However, the number had decreased since FY 2016, because projects of "Cooperation priority research", "Joint research" and "Internal use" were unified.

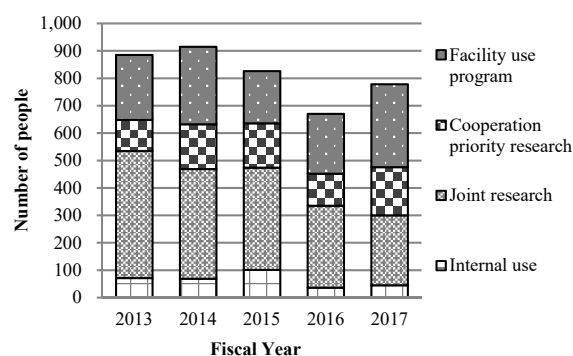


Fig. 3. Trend of the number of users for the past 5 years.

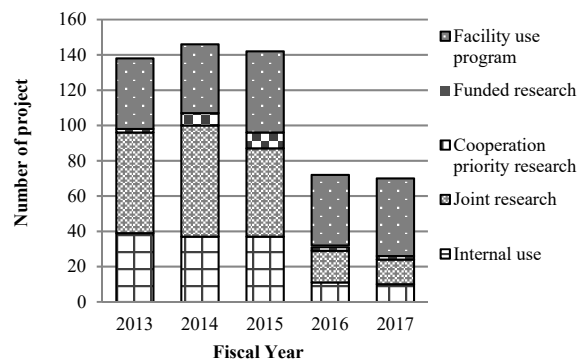


Fig. 4. Trend of the number of projects for the past 5 years.

The others

QST Takasaki science festa 2017 was held successfully in December 12 and 13, 2017 at Takasaki city gallery. The numbers of oral presentations and the poster sessions were 23 and 78, respectively. The participants of the festa was 539 people, and 224 people increased as compared with the last meeting.

The QST Takasaki annual report 2016 including 17 research projects and 130 individual research papers was published. About 660 books were mainly distributed to domestic related departments. In addition, 43 English letters, which wrote the URL about an electric version of the annual report, were also sent to overseas related departments.

4 - 02

Operation of the AVF Cyclotron

S. Kurashima^{a)}, K. Yoshida^{a)}, T. Yuyama^{a)}, T. Ishizaka^{a)}, I. Ishibori^{a)}, N. Miyawaki^{a)},
H. Kashiwagi^{a)}, Y. Yuri^{a)}, T. Nara^{a)}, To. Yoshida^{b)}, Tu. Yoshida^{b)}, S. Ishiro^{b)},
S. Kanou^{b)}, K. Takano^{b)}, H. Saitoh^{b)}, T. Atobe^{b)} and K. Akaiwa^{b)}

^{a)} Department of Advanced Radiation Technology, TARRI, QST,

^{b)} Beam Operation Co., Ltd.

Operation

An electrical short between two pancakes of the upper main coil of the cyclotron was found in December, 2016 [1]. The temporary repair to bypass 4 of 10 pancakes of the main coil was carried out in April and May. The maximum energy of the cyclotron (K-value) was reduced to about 60%, as a result. To supply various ion beams under such conditions, beam developments were carried out intensively and 14 beams such as 350 MeV $^{129}\text{Xe}^{26+}$ and 2.67 MeV/u cocktail ions were successfully accelerated. The lost beam time due to the repair and the beam developments was recovered by 8 times extended operations till Saturday early-evening. Figure 1 shows monthly operation times.

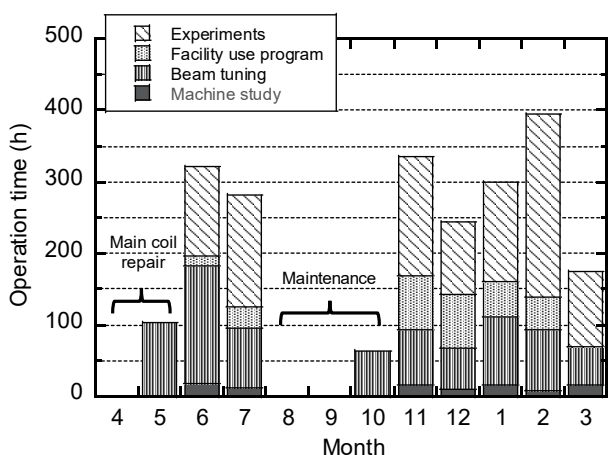


Fig. 1. Monthly operation times in fiscal 2017.

Table 1 shows the statistics of the cyclotron operation of fiscal 2017, with the data of fiscal 2016 for comparison. The total operation time amounted to 2219 h. The percentages of operation time of the year used for regular experiments, facility use program and promotion of shared use program,

Table 1

Statistics for cyclotron operation.

Fiscal year	2016	2017
Beam service time (h)	1407	1340
Beam tuning (h)	535	783
Machine study (h)	11	96
Total operation time (h)	1953	2219
Change of particle and/or energy	156 times	181 times
Change of beam course	199 times	214 times
Change of harmonic number	75 times	68 times
The number of experiments	339	252
Cancellation due to machine trouble	11	0

beam tuning, and beam development are 47.2%, 13.1%, 35.3%, and 4.4%, respectively. There was no cancellation of the experiments due to machine troubles. The accumulative operation time was 82236 h and the total number of experiments was 11945 from the first beam extraction in 1991 to March, 2018.

Maintenance

A vacuum leak occurred in the 1st RF cavity of the cyclotron. Due to operation under the locally bad vacuum condition for 3 months, the contact fingers were melted and adhered to the outer cavity wall as shown in Fig. 2. The vacuum leak was occurred at the joint part of the piping for the compressed air. All O-rings used at the piping of the RF cavities and the melted contact fingers were replaced during the regular yearly maintenance.

The axle bearings of the shield door of the No.3 heavy ion room were replaced to prevent sudden failure such as happened to the No.5 heavy ion room in fiscal 2016. An electric locking system of the basement door of the room was broken and was also replaced.

We are going to replace the upper and lower main coils in fiscal 2018. However, the shield door of the cyclotron room is rather small to carry the main coils with outer diameter of about 3 m through it. Therefore, the shield wall of 4 m in thickness of the cyclotron room will be temporarily bored to carry the main coils in.

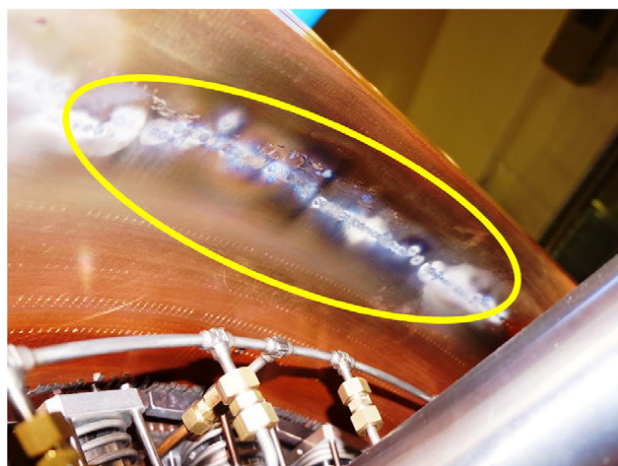


Fig. 2. A picture of the damaged 1st RF cavity. The contact fingers were melted and adhered to the cavity wall.

Reference

[1] I. Ishibori *et al.*, QST Takasaki Annu. Rep. 2016, **QST-M-8**, 165 (2018).

4 - 03

Operation of Electrostatic Accelerators in TIARA

A. Chiba ^{a)}, K. Yamada ^{a)}, A. Yokoyama ^{a)}, Y. Hirano ^{a)}, T. Nara ^{a)},
T. Takayama ^{b)}, S. Kanai ^{b)}, Y. Aoki ^{b)}, M. Hashizume ^{b)},
Y. Takahashi ^{b)} and M. Hasegawa ^{b)}

^{a)} Department of Advanced Radiation Technology, TARRI, QST,

^{b)} Beam Operation Co., Ltd.

Operation and Status

Three electrostatic accelerators in TIARA have almost operated in accordance with the original operating plan in fiscal year (FY) 2017. The operating rate of 100% has been achieved in the tandem accelerator and the single-ended accelerator. On the other hand, two days for the experiments using the ion beam accelerated by the ion implanter had to be canceled due to a serious failure of its ion source device. The relatively minor trouble cases, such as communication error in the control systems, extreme deterioration of the acceleration voltage stability, and destabilization of the ion sources, occurred frequently in each accelerator; nevertheless, the annual operating times including the conditioning operations of three accelerators kept the same level as usual, as the results of the preventive maintenance and the rapidly coping with the troubles.

The utilization rate of ion species used in the tandem accelerator in FY 2017 is shown in Fig. 1. The utilization of C₆₀ ion beam has increased year by year with increasing the beam current along with the development of ionization techniques and has extended to approximately 1/4 of all ion species.

New ion beam

A Nd⁺ ion beam became utilizable in the ion implanter. The vaporized NdCl₃ is ionized by Ar plasma in an arc chamber of a Freeman type ion source. The Nd⁺ ion beam was required for the experiments on a formation of the single-photon sources in a semi-conductor. Figure 2 shows the mass spectrum of the ion beam extracted from the ion source. The Nd⁺ ion beam of 150 nA was accelerated with a total voltage of 215 kV.

Maintenance

The number of trouble cases and maintenance concerning the electrostatic accelerators in FY 2016 and FY 2017 is shown in Table 1. In FY 2017, the number of serious troubles, which need repairing or replacement of the electronic device or the equipment of beam transfer, decreased to almost half of them in FY 2016. While there was no serious trouble regarding the tandem accelerator, the minor troubles successively happened, many of which were communication error between network PCs in the control system, hang-up of the deteriorated PC, and fault of the sequencer modules. To keep the compatibility with the interface and the sequencer modules, it is necessary to install a PC equipped with the same motherboard type as that of the existing PC. However, it was difficult to get the same type of the motherboard produced more than 10 years ago. The control system of not only the tandem

accelerator but also the other accelerators urgently needs to be renewed.

In the ion implanter, the power supply of an electron emitting filament in the ion source broke down during an irradiation experiment. It is impossible to replace this power supply with the general one, because this power supply is equipped with a characteristic mechanism by which its output current is controlled automatically according to the plural parameters of the ion source. This serious trouble was coped by rapid ordering the same type of the power supply. It would be hard to cope with future similar troubles because the production of many devices had already finished.

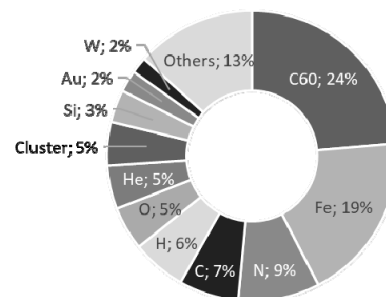


Fig. 1. Utilization rate of ions in tandem accelerator.

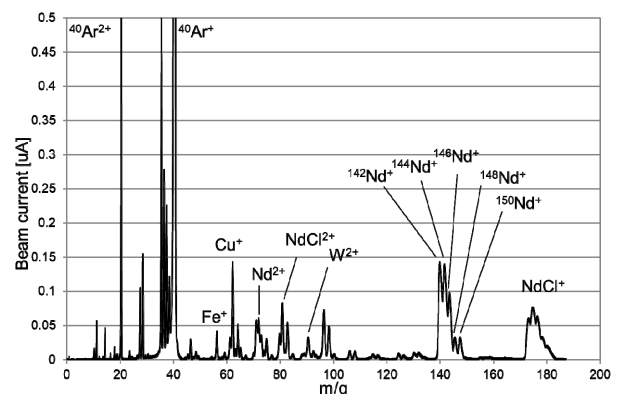


Fig. 2. Mass spectrum of ion beam produced in the ion implanter using a sample of NdCl₃.

Table 1

Number of trouble cases and maintenance in FY 2016 and FY 2017.

	Tandem		Single-ended		Ion implanter	
	2016	2017	2016	2017	2016	2017
Minor trouble	18	33	14	6	17	18
Serious trouble	6	0	4	6	5	2
Maintenance	11	16	11	13	8	10

4 - 04

Operation of the Electron Accelerator and the Gamma-ray Irradiation Facilities

T. Agematsu ^{a)}, S. Uno ^{a)}, R. Yamagata ^{a)}, H. Seito ^{a)}, Y. Nagao ^{a)}, S. Yamasaki ^{a)}, N. Yagi ^{b)}, M. Takagi ^{b)}, K. Nagai ^{b)} and T. Asai ^{b)}

^{a)} Department of Advanced Radiation Technology, TARRI, QST,

^{b)} Takasaki Establishment, Radiation Application Development Association

Operation

The electron accelerator and the ⁶⁰Co gamma-ray irradiation facilities were operated approximately smoothly in Fiscal Year (FY) 2017.

The annual operation time of the electron accelerator in this FY was 845 h, including 132 h of conditioning operation. The operation time in recent years is shown in Fig. 1. The annual operation time decreased in FY 2014 because the operation time was changed from 8:30-23:00 to 9:00-17:30 for effective operation. Furthermore, there were a lot of trouble in FY 2014 and FY 2015, and the operation time decreased. The annual irradiation time in FY 2016 increased due to smooth operation. Although there was trouble in the high frequency power supply unit of the accelerator for one month, the irradiation time in FY 2017 increased because long time irradiation increased.

The ⁶⁰Co gamma-ray irradiation facilities consisting of three buildings with eight irradiation rooms cover a wide dose-rate range from 10⁻¹ to 10⁴ Gy/h as of January 2018. The annual operation times of the first and the second cobalt irradiation facilities and the food irradiation facility were 20739 h, 14101 h and 14536 h, respectively, as shown in Fig. 2.

Maintenance

• Electron accelerator

The high frequency power supply unit of the accelerator broke down at the end of October 2017. It required one month for repair. After the repair, scheduled maintenance of this power supply unit was carried out at the end of December 2017. The SF₆ gas leaked slowly from connection of the drain valve of the storage tank when the accelerator tank was opened for scheduled maintenance in October 2017. The SF₆ gas was returned soon to the accelerator tank from the storage tank, and the leak was stopped. After that, operation of the accelerator was continued, and the repair of gas leak was carried out in March 2018. The trouble of the horizontal beam line, which might be due to trouble at the electron-gun, occurred at the beginning of December 2017. This repair is scheduled in FY 2018.

• Gamma-ray irradiation facilities

The periodical maintenance check mainly on mechanical systems for radiation source transportation is performed every year on one of the three gamma-ray irradiation facilities in turn. The maintenance check of the second irradiation facility was done in September 2017 with suspension of operation for nineteen days. The purifier system for the water pools of the three gamma-ray

irradiation facilities was damaged by long-time use. At this system, the troubles such as corrosion of piping for electric cables and a miss of the liquid-flow route were repaired in March 2018.

Old sixty-four pencil sources of ⁶⁰Co were delivered to Japan Radioisotope Association (JRIA) for disposal. Total amount of ⁶⁰Co sources of all the facilities at the Takasaki Institute have decreased by isotope decay and disposal of old ⁶⁰Co sources. New ⁶⁰Co sources were not installed in FY 2017. Therefore, the maximum dose rate has decreased more largely than usual years.

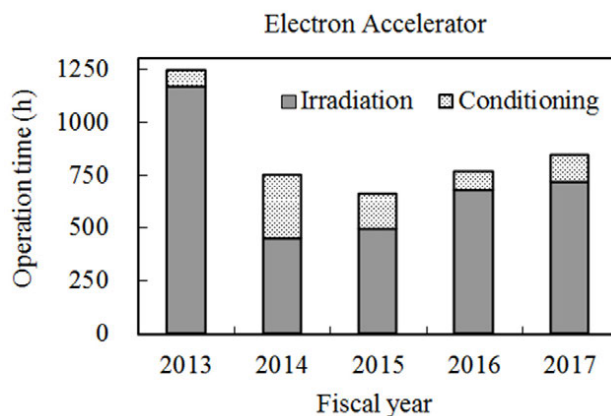


Fig. 1. Annual operation time of the electron accelerator.

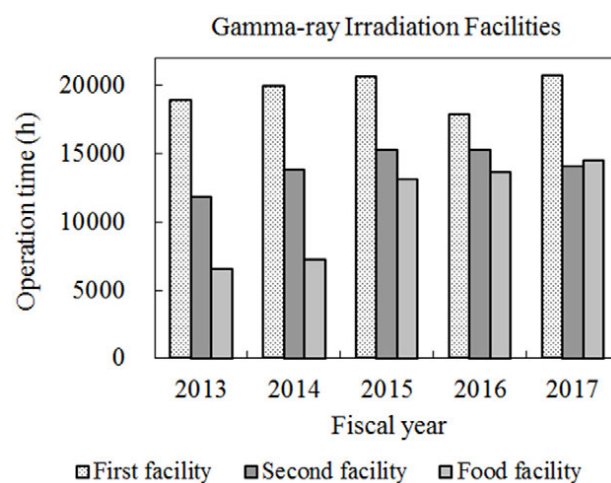


Fig. 2. Annual operation times of the ⁶⁰Co gamma-ray irradiation facilities.

4 - 05

Utilization Status of the Electron Accelerator and the Gamma-ray Irradiation Facilities

T. Agematsu^{a)}, S. Uno^{a)}, R. Yamagata^{a)}, H. Seito^{a)}, Y. Nagao^{a)}, S. Yamasaki^{a)},
N. Yagi^{b)}, M. Takagi^{b)}, K. Nagai^{b)} and T. Asai^{b)}

^{a)}Department of Advanced Radiation Technology, TARRI, QST,

^{b)}Takasaki Establishment, Radiation Application Development Association

The electron accelerator and the three gamma-ray irradiation facilities were operated for various research subjects according to the operation plans in fiscal year (FY) 2017. Figure 1 shows the number of irradiation experiments in each research field in FY 2013-2017. The number of irradiation experiments at the accelerator decreased from FY 2014 by following two causes. The first cause was the change of the operation time from 8:30-23:00 to 9:00-17:30 for efficient operation in FY 2014. The second cause was that many troubles happened in FY 2014 - 2015. The accelerator mainly served for graft-polymerization in new material development, radiation effect studies on semiconductors and various experiments by visiting users. The first cobalt irradiation facility mainly served for long-term radiation resistance testing of cables used in nuclear power plants and nuclear reactor facilities. The second cobalt irradiation facility, including the irradiation room No.6 operated on hourly schedule, mainly served for development of new functional materials and other research subjects of visiting users. The food irradiation facility having a lower-dose-rate field served for radiation resistance testing at wide dose-rate range.

QST was established in April 2016, and the several research fields at JAEA were reclassified in QST. 'Materials for space', 'Nuclear facilities', 'Material processing', 'Heat-resistant materials' and 'Environment' were combined into 'Materials science'. 'Resources & Biotechnology' and 'Basic technology' were relabelled to 'Life science' and 'Quantum beam science', respectively. Figure 2 shows the irradiation time of experiments in each research field in FY 2013-2017. The classification of the users who remained in JAEA was changed from 'internal users' to 'external users' from FY 2016. Therefore, at the gamma-ray facilities, the irradiation time of internal users decreased, and that of 'Facility use program' increased. Furthermore, because of the influence of procedure

for transfer from JAEA to QST, the irradiation time decreased in FY 2016 and 2017 compared to FY 2015. On the other hand, at the accelerator, the irradiation time increased due to smooth operation in FY 2017 compared to FY 2014-2015, which had a lot of trouble, and FY 2016, which had small trouble. Irradiation experiments for recovery from the accident at the Fukushima Daiichi Nuclear Power Station of Tokyo Electric Power Company were carried out as mainly 'Facility use program' by external users.

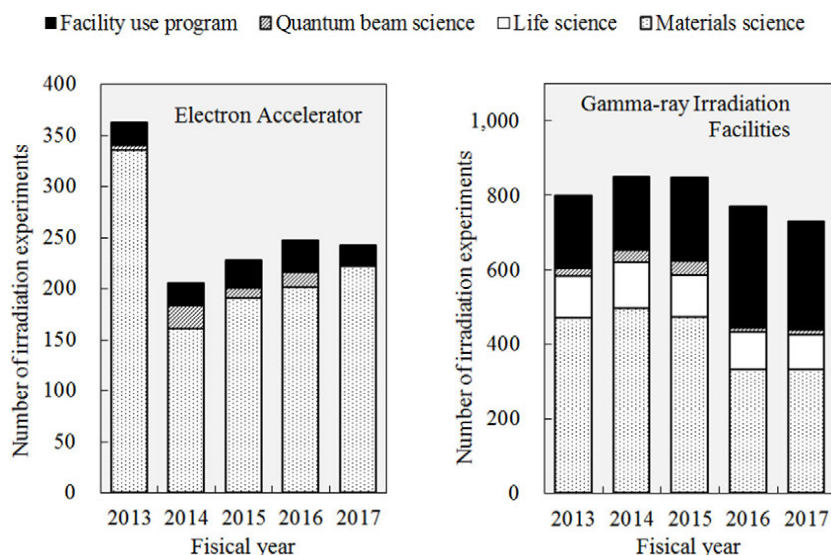


Fig. 1. The number of irradiation experiments (FY 2013-2017).

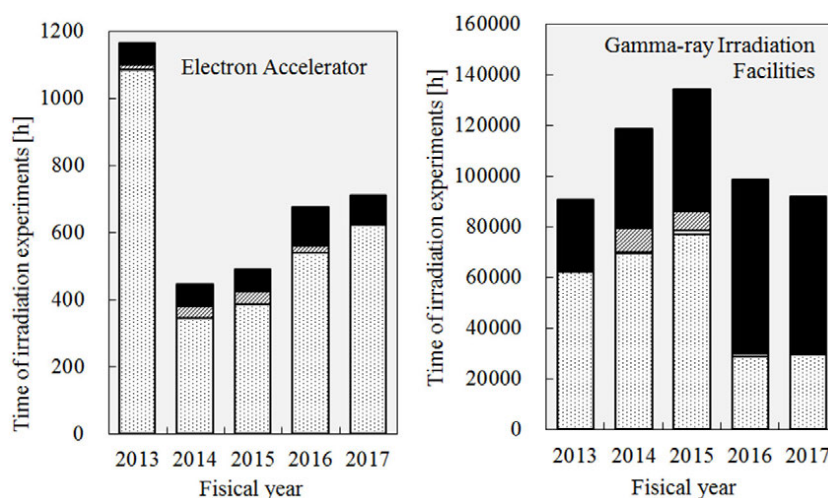


Fig. 2. The time of irradiation experiments (FY 2013-2017).

4 - 06

Radiation Monitoring in TIARA

Safety Management Section

Department of Administrative Services, TARRI, QST

Individual monitoring

(1) Individual monitoring for the radiation workers

Table 1 shows a distribution of effective dose of the radiation workers in FY 2017. The effective dose values of almost all radiation workers were below the detection limit of 0.1 mSv.

The maximum dose of the radiation workers was 0.3 mSv/y by desorption work of positron source.

Table 1

Distributions of the effective dose of the radiation workers in FY 2017.

Items		Number of persons in each period				
		1st quarter	2nd quarter	3rd quarter	4th quarter	Annual
Distribution range of effective dose	HE < 0.1	381	411	489	503	595
	$0.1 \leq HE \leq 1.0$	3	2	1	4	9
	$1.0 < HE \leq 5.0$	0	0	0	0	0
HE: Effective dose (mSv)	$5.0 < HE \leq 15.0$	0	0	0	0	0
	$15.0 < HE$	0	0	0	0	0
Total number of persons (A)		384	413	490	507	604
Exposure above 1 mSv	Number of persons (B)	0	0	0	0	0
	$(B)/(A) \times 100(\%)$	0	0	0	0	0
Mass effective dose (Person·mSv)		0.3	0.3	0.1	0.6	1.3
Mean dose (mSv)		0.00	0.00	0.00	0.00	0.00
Maximum dose (mSv)		0.1	0.2	0.1	0.3	0.3

*1 The dose by the internal exposure was not detected.

(2) Individual monitoring for the visitors and others

Table 2 shows the number of people who temporarily entered the radiation controlled areas. The effective doses of all people were less than 0.1 mSv.

Table 2

The number of people who temporarily entered the radiation controlled areas in FY 2017.

Periods	1st quarter	2nd quarter	3rd quarter	4th quarter	Total
Number of persons	849	958	1,116	977	3,900

Monitoring of radioactive gases and dusts

Table 3 shows the maximum radioactive concentrations and total activities for radioactive gases released from the stack of TIARA, during each quarter of FY 2017.

Small amounts of ^{41}Ar , ^{11}C and ^{13}N were detected occasionally during the operation of the cyclotron or experiments, but the particulate substances (^{65}Zn , etc.) were not detected.

Table 3

Monitoring results of released radioactive gases and dust in FY 2017.

Nuclide	Periods Items	1st quarter	2nd quarter	3rd quarter	4th quarter	Total
		^{41}Ar	Maximum concentration	$<1.4 \times 10^{-4}$	$<1.4 \times 10^{-4}$	
	Activity	0	0	0	5.3×10^7	5.3×10^7
^{11}C	Maximum concentration	$<1.4 \times 10^{-4}$	$<1.4 \times 10^{-4}$	$<1.4 \times 10^{-4}$	$<1.4 \times 10^{-4}$	
	Activity	1.0×10^7	1.6×10^7	4.1×10^7	3.0×10^8	3.7×10^8
^{13}N	Maximum concentration	—	$<1.4 \times 10^{-4}$	$<1.4 \times 10^{-4}$	1.4×10^{-4}	
	Activity	—	1.4×10^7	3.3×10^8	3.4×10^8	6.8×10^8
^{65}Zn	Maximum concentration	$<4.7 \times 10^{-10}$	$<7.0 \times 10^{-10}$	$<4.3 \times 10^{-10}$	$<4.8 \times 10^{-10}$	
	Activity	0	0	0	0	0

Unit : Bq/cm³ for Maximum concentration, Bq for Activity.

Monitoring for external radiation and surface contamination

The monitoring for external radiation and surface contamination was routinely performed in/around the radiation controlled areas. Neither anomalous value of dose equivalent rate nor surface contamination was detected.

Figure 1 shows a typical example of distribution of the dose equivalent rate in the radiation controlled area of the cyclotron building.

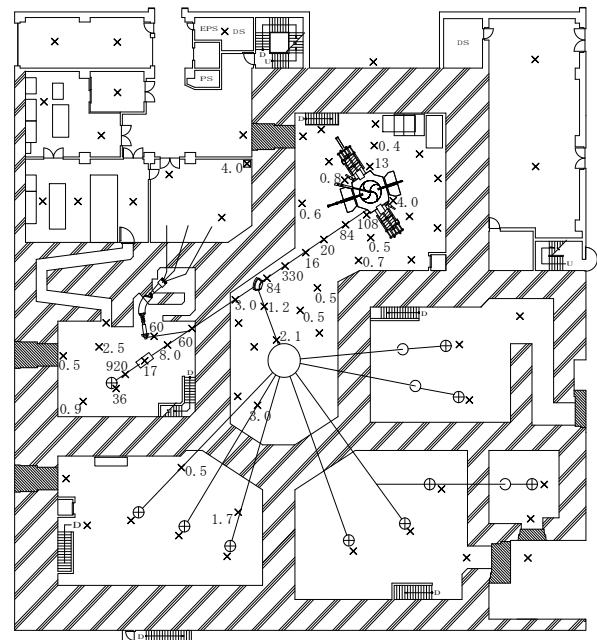


Fig. 1. Dose equivalent rate distribution in the radiation controlled area of the cyclotron building. Measurement date: 16th, 26th and 29th March 2017, Measuring position: Indicated with × (1 m on the floor), Unit: µSv/h. (The values are not indicated if less than 0.2 µSv/h.)

N. Higuchi

Department of Administrative Services, TARRI, QST

Radioactive waste management

The radioactive waste generated in TIARA is managed by Utilities and Maintenance Section. The main radioactive waste is the solid waste generated from research experiments and the maintenance of the cyclotron. Other radioactive waste is the liquid waste such as inorganic waste fluids generated from research experiments and the air-conditioning machines in controlled area. These wastes are managed according to their properties. Radioactive waste is stored in a storage facility and handed over to the RI Association for disposal.

Solid radioactive waste

Table 1 shows the amounts of various types of solid wastes generated in each quarter of FY 2017. Combustible waste is papers and clothes, etc. Flame-retardant waste is rubber gloves, plastic articles, and polyethylene articles.

Incombustible waste is metallic pieces, the glasses, and contaminated parts. Solid waste emitting α , β , and γ is classified according to the properties.

Liquid radioactive waste

Table 2 shows the amounts of liquid waste generated in each quarter of FY 2017. Most of liquid waste was inorganic waste water generated from chemical experiments and condensed water from the operation of air conditioning units placed in each room of the radiation controlled area. The largest quantity of waste water in summer season (2nd quarter) is mainly due to the condensed water. After the treatment of evaporation of water, inorganic water is reused in the radiation controlled area. Only small amounts of concentrated liquid are generated by the treatment.

Table 1
Radioactive solid waste generated in FY 2017.

Items	Amounts	Amounts of generation in each period (m ³)				Total	Number of package /drum
		1st quarter	2nd quarter	3rd quarter	4th quarter		
Category β, γ^*		0.04	0.36	0.24	0.56	1.20	29
	Combustible	0.02	0	0.04	0.14	0.20	5
	Flame-retardant	0.02	0.36	0.20	0.30	0.88	22
	Incombustible(Compressible)	0	0	0	0.08	0.08	2
	„ (Incompressible)	0	0	0	0.04	0.04	0
	Laboratory animal	0	0	0	0	0	0
	Filters	0	0	0	0	0	0
Category α^*		0	0.20	0	0.24	0.44	10
	Combustible	0	0.02	0	0.04	0.06	2
	Flame-retardant	0	0.12	0	0.16	0.28	6
	Incombustible(Compressible)	0	0.04	0	0	0.04	1
	„ (Incompressible)	0	0	0	0	0	0
	Laboratory animal	0	0.02	0	0.04	0.06	1
	Filters	0	0	0	0	0	0

* defined by amount in Bq (β, γ): < 2 GBq, (α): (A) < 37 MBq (B) \leq 37 MBq,

** 50-liter drum.

Table 2
Radioactive liquid waste generated in FY 2017.

Items	Amounts	Amounts of generation in each period (m ³)				Total	Number of package /drum
		1st quarter	2nd quarter	3rd quarter	4th quarter		
Category β, γ^*		13.10	16.38	4.26	3.90	37.63	-
1) Inorganic		13.10	16.38	4.26	3.90	37.63	-
	Inorganic	12.72	16.38	4.26	3.87	37.23	treatment
	Sludge, Evaporation residue	0.375	0	0	0.025	0.40	16**
2) Organic		0	0	0	0	0	0
	Organic	0	0	0	0	0	0
	Oil	0	0	0	0	0	0
Category α^*		0	0	0	0	0	0

* defined by concentrations in Bq/mL (β, γ Inorganic): < 200 kBq, (Organic): < 2 kBq, (α): \leq 1.85 kBq,

** 50-liter container.

4 - 08

Facility Use Program in Takasaki Advanced Radiation Research Institute (TARRI)

S. Nozawa, H. Hanaya and M. Seki

Research Planning and Promotion Office, QuBS, QST

Introduction

The usage of the facilities in QST is widely allowed for many users in universities, public institutes, R&D divisions of private companies, and so on (hereafter 'outside users'). FACILITY USE PROGRAM is a service on the basis of fee-charging in the usage for outside users. These outside users can access to the Co-60 gamma-rays, electron beams, and various ion beams that have been provided from the facilities of Co-60 gamma-ray, an electron accelerator, and TIARA's four ion accelerators, and some of off-line analysis instruments, respectively. In this program, the research proposals from the outside users are reviewed every half a year, from the viewpoints of the availability and the validity of the experimental plans by the expert committee member. The confirmed research proposals had been carried out under the facility use program.

Classification of Facility Use Program in FY2017

Charging system for the Facility Use Program is classified by the purpose of irradiation and intending to publication of results, as shown in Table 1. The amount of charging fee had been calculated from handling, irradiation, and expendable fees, in addition to additional consumables and additional labor charges. For research and development (R&D) users who will intend to disclose the results of experiment by publication, partially exempted charges were applied for irradiation. For Except R&D using, such as commercial irradiation, the depreciation cost for irradiation facilities were charged additionally.

Table 1

Charging system for Facility Use Program in FY2017.

	R&D		Commercial
	Intended for Publication	Not Intended for Public disclosure	
Purpose	Research and Development		Except R&D
Belonging of Results	Non-proprietary	Proprietary	
Duty for publishing	Yes	No need to public disclosure	
Charging fees*	A	B	C

*A = handling fees + expendables fee (other charges are exempted),

B = Charging fee "A" + irradiation fee + radioactive waste disposal expenses,

C = Charging fee "B" + depreciation cost for irradiation facilities.

Number of irradiation experiments in FY2017

The number of irradiation experiments for each facility in FY2017 is shown in Table 2.

Table 2

Frequency of irradiation experiments at each facility in this program in FY2017.

Facility	Users' affiliate	University	Institute	Company	Total
TIARA	AVF cyclotron	18	11	26	55
	3 MV tandem accelerator	19	11	3	33
	3 MV single-ended accelerator	4	9	0	13
	400 kV ion implanter	13	6	0	19
Co-60 gamma-ray irradiation facilities		30	53	218	301
Electron accelerator		10	2	9	21
Total		94	92	256	442

In Table 2, about three hundred irradiation experiments were carried out at the Co-60 gamma-ray irradiation facilities. In this number, more than two hundred irradiation experiments that had been carried out by outside users in private companies were included. The largest part of irradiation experiments at the AVF cyclotron had also been carried out by outside users in private companies.

The irradiation experiments that were performed by private company's users are increasing year by year. Many of them were not experts for irradiation experiments, and they needed the more information about the irradiation facilities and the related techniques. For example, the practical information about how to use the facilities; application of proposals, time table of experiments, performance of equipment, arrangement of samples, charging system, and so on, were required. Therefore, we provide the basic information for the outside users, *i.e.* access to facilities, method for payment, duties, and etc.

The other detailed information about this program is available on QST website as follows:

<http://www.qubs.qst.go.jp/kyoyo/index.html>.

Appendices

Appendix 1	Publication List	158
Appendix 2	Type of Research Collaboration and Facilities Used for Research	179
Appendix 3	Examples of Typical Abbreviation Name for Organizations in National Institutes for Quantum and Radiological Science and Technology, and Japan Atomic Energy Agency	181

Appendix 1 Publication list

Items in gray show the works in collaboration with other projects of QST.

Bold letters and numbers at the last of each item mean as follows.

Letter : Accelerators or irradiation facilities used for the work.

C : Cyclotron, **T** : Tandem accelerator, **S** : Single-ended accelerator, **I** : Ion implanter,

E : Electron accelerator, **G** : Gamma-ray irradiation facilities, **N** : Not used.

Number that contains hyphen: Serial number of the related paper in Part II.

P1-1 Functional Polymer Research Project

Papers

- 1) T. Hamada, S. Hasegawa and Y. Maekawa, "Control of Radiation/Living Graft Polymerization in the Solid State", *Macromol. Chem. Phys.*, **218**, 1700346 (2017). **G**
 - 2) K. Yoshimura, Y. Zhao, S. Hasegawa, A. Hiroki, Y. Kishiyama, H. Shishitani, S. Yamaguchi, H. Tanaka, S. Koizumi, M. Appavou, A. Radulescu, D. Richter and Y. Maekawa, "Imidazolium-Based Anion Exchange Membranes for Alkaline Anion Fuel Cells: (2) Elucidation of the Ionic Structure and its Impact on Conducting Properties", *Soft Matter*, **13**, 8463-73 (2017). **G, 1-26**
 - 3) 吉村 公男, 前川 康成, "アルカリ型燃料電池用アニオン伝導電解質膜の開発", *Isotope News*, **754**, 32-35 (2017). **G, 1-26**
 - 4) 深谷 敦子, 太田 優子, 飯村 伸明, 立野 晃, 高橋 克巳, 前川 康成, "PEEK をベースとしたグラフト型電解質膜の電気化学装置への適用", *化学工業*, **69**, 52-57 (2018). **G**
 - 5) 廣木 章博, "重粒子線治療用ポリマーゲル線量計の開発", *Isotope News*, **752**, 16-19 (2017). **G, E**
 - 6) 廣木 章博, 田口 光正, "シート状ポリマーゲル線量計材料による3次元線量分布評価", *医学物理*, **37**, 181-85 (2017). **G, E**
- #### Proceedings
- 1) Y. Maekawa, K. Yoshimura, K. Takeuchi, A. Hiroki, S. Watanabe, T. Hagiwara, H. Shishitani, S. Yamaguchi and H. Tanaka, "Alkaline Durable Anion-Conducting Electrolyte Membranes Prepared by Radiation Induced Grafting of 2-Methyl-4-vinylimidazole for Non-Platinum Direct Hydrazine Hydrate Fuel Cells", *ECS Transactions*, **80**, [National harbor, USA] (2017/10). **G**
 - 2) H. C. Yu, K. Yoshimura, Y. Zhao, A. Hiroki, H. Shishitani, S. Yamaguchi, H. Tanaka and Y. Maekawa, "Synthesis, Characterization, and Alkaline Stabilities of p-(2-imidazoliumyl) Styrene-Grafted Anion-Conducting Electrolyte Membranes Prepared By Radiation-Induced Grafting for Fuel Cells", *Abstr. 232nd ECS Meet.*, I01E-1623, [National Harbor, USA] (2017/10). **G**
 - 3) S. Hasegawa, S. Sawada, Y. Maekawa, S. Azami, T. Hagiwara, "Development of hydrogen permselective membrane by using radiation-induced graft polymerization", *Abstr. ICOM 2017*, P1.150, [San Francisco, USA] (2017/07). **G, 1-24**
 - 4) Y. Zhao, K. Yoshimura, Y. Maekawa, "Using small angle scattering method to reveal the required structure for anion exchange fuel cell membranes with high performance", *Abstr. Int. Conf. Neutron Scattering 2017*, TuP 124, [Daejeon, Korea] (2017/07). **G**
 - 5) S. Sawada, Y. Maekawa, "Preparation of novel bipolar membranes by radiation-induced asymmetric grafting technique for fuel cell application", *IUMRS-ICAM 2017*, Abstr. A7-O28-011, [Kyoto, Japan] (2017/08). **G, 1-25**
 - 6) H. C. Yu, K. Yoshimura, H. Shishitani, S. Yamaguchi, H. Tanaka, Y. Maekawa, "p-(2-imidazoliumyl) Styrene-Grafted Anion Conducting Electrolyte Membranes Prepared by Radiation-Induced Grafting for Fuel Cell", *IUMRS-ICAM 2017*, Abstr. A7-O28-014, [Kyoto, Japan] (2017/08). **G**
 - 7) T. Hamada, K. Yoshimura, A. Hiroki, Y. Maekawa, "Synthesis and Characterization of Aniline-Containing Anion-Conducting Polymer Electrolyte Membranes by Radiation-Induced Graft Polymerization", *IUMRS-ICAM 2017*, Abstr. A7-O28-15, [Kyoto, Japan] (2017/08). **G**
 - 8) K. Takeuchi, K. Yoshimura, A. Hiroki, Y. Maekawa, "Alkaline-durable Anion-conducting Electrolyte Membranes Containing Poly(4-vinyl-2-methyl-imidazole) Prepared by Radiation-induced Grafting", *IUMRS-ICAM 2017*, Abstr. A7-P30-019, [Kyoto, Japan] (2017/08). **G**
 - 9) S. Sawada, M. Yasukawa, M. Higa, Y. Maekawa, "Preparation of cation and anion exchange membranes for reverse electro dialysis by radiation-induced grafting method", *Abstr. 5th Int. Conf. Nanotech. Mater. Sci.*, P 56, [Dubai, UAE] (2017/10). **G, 1-25**
 - 10) 吉村 公男, H. C. Yu, ザオ ユエ, 廣木 章博, 猪谷 秀幸, 岸山 佳央, 山口 進, 田中 裕久, 前川 康成, "放射線グラフト型アニオン伝導電解質膜の燃料電池特性と階層構造の関係", 第 60 回放射線化学討論会, 要旨集 3-O-10, [産総研・筑波] (2017/09). **G, 1-26**
 - 11) 澤田 真一, 安川 政宏, 比嘉 充, 前川 康成, "逆電気透析発電用放射線グラフト陽イオン交換膜の水・イオン輸送特性", 2017 年 電気化学秋季大会, 要旨集 2K04, [長崎大・長崎] (2017/09). **G, 1-25**
 - 12) 澤田 真一, 後藤 光暁, 越川 博, 喜多村 茜, 比嘉 充, 八巻 徹也, "重イオンビームグラフト法で作製したカチオン・アニオン交換膜の輸送特性評価と海水電気透析への応用", 日本原子力学会 2018 年春の年会, 要旨集 2107, [大阪大・吹田] (2018/03). **G, 1-25**
- #### Patents
- 1) 猪谷 秀幸, 岸山 佳央, 阿部 寛樹, 山口 進, 吉村 公男, 趙 躍, 廣木 章博, 前川 康成, "陰イオン交換樹脂およびアルカリ型燃料電池用電解質膜" 出願 2017-173786 (2017/09/11).
 - 2) 田口 光正, 廣木 章博, 木村 敦, 大山 智子, 中島 健吾, 青木 伊知男, 村山 周平, "MRI 造影剤、及び MRI 造影剤の製造方法" 出願 2017-116241 (2017/06/13).

P1-2 Advanced Catalyst Research Project

Papers

- 1) S. Yamamoto, M. Sugimoto, H. Koshikawa, T. Hakoda and T. Yamaki, "Orientational control of CeO₂ films on sapphire substrates grown by magnetron sputtering", *J. Cryst. Growth*, **486**, 262-67 (2017). **S, 1-10**
- 2) 野村 幹弘, 今林 慎一郎, 澤田 真一, 八巻 徹也, 田中 伸幸, 久保 真治, "高効率な水素製造を可能にするイオン交換膜型ベンゼン反応器の開発", *クリーンエネルギー*, **8**, 44-47 (2017).

- E, G**
- 3) 八巻 徹也, 喜多村 茜, 澤田 真一, 越川 博, “高エネルギーイオンビームによるナノ構造制御機能膜の研究 – フッ素系高分子多孔膜とイオン交換膜を中心に –”, 日本海水学会誌, **72**, 62-74 (2018). **C, I, 1-08**
- 4) M. Nomura, T. Kodaira, A. Ikeda, Y. Naka, H. Nishijima, S. Imabayashi, S. Sawada, T. Yamaki, N. Tanaka, S. Kubo, “Development of ion exchange membranes for the membrane Bunsen reaction of the thermochemical hydrogen production by Iodine-Sulfur process”, *J. Chem. Eng. Jpn.*, **51** (9), 726-31 (2018). **G, E**
- 5) K. Kakitani, T. Kimata, T. Yamaki, S. Yamamoto, T. Taguchi, T. Kobayashi, W. Mao and T. Terai, “The interface between platinum nanoparticle catalysts and an Ar⁺-irradiated carbon support”, *Surf. Coat. Tech.* **355**, 259-63 (2018). **I**
- 6) A. Horio, T. Sakurai, K. Kayama, G. B. V. S. Lakshmi, D. K. Avasthi, M. Sugimoto, T. Yamaki, A. Chiba, Y. Saitoh and S. Seki, “Remarkable effect of halogenation of aromatic compounds on efficiency of nanowire formation through polymerization/crosslinking by high-energy single particle irradiation”, *Radiat. Phys. Chem.*, **142**, 100-06 (2018). **C**
- Proceedings**
- 1) 小川 達彦, 八巻 徹也, 佐藤 達彦, “凝縮相における低エネルギー電子の微視的放射線作用の研究～ NE102 シンチレータの発光・消光の再現 ～”, 第 64 回応用物理学会春季学術講演会, 予稿集 14p-E204-8, [パシフィコ横浜・横浜] (2017/03). **T, I, 1-15**
- 2) 八巻 徹也, 越川 博, 佐藤 裕真, 山本 春也, 杉本 雅樹, 澤田 真一, “イオンビーム照射による高分子多孔膜への導電層形成と電気メッキ用テンプレートとしての活用”, 日本膜学会 39 年会, 要旨集 1A-4, [早稲田大・東京] (2017/05). **C, I, 1-08**
- 3) A. Idesaki, S. Yamamoto, M. Sugimoto and T. Yamaki, “Effect of ion implantation on precursor polymers for synthesis of carbon material with catalytic performance”, *Abstr. 12th Pacific Rim Conference on Ceramic and Glass Technology (PACRIM12), PACRIM-S4-029-2017, [Waikoloa, USA] (2017/05).* **I, 1-12**
- 4) 八巻 徹也, 澤田 真一, 越川 博, 喜多村 茜, 後藤 光暁, 比嘉 充, “海水濃縮応用を目指したイオンビームによるナノ構造制御イオン交換膜の合成”, 2017 年度日本海水学会 68 年会, 講演要旨集 O-05 & P-05, [京都市国際交流会館・京都] (2017/06). **C, I, 1-08**
- 5) 大森 理之, 八巻 徹也, 越川 博, 澤田 真一, 安川 政宏, 比嘉 充, “イオン照射グラフト重合により作製したモザイク荷電膜を用いた圧透析による脱塩特性評価”, 2017 年度日本海水学会 68 年会, 講演要旨集 P-30S, [京都市国際交流会館・京都] (2017/06). **C**
- 6) 木村 壮宏, 池田 歩, 西嶋 陽之, 野村 幹弘, 今林 慎一郎, 澤田 真一, 八巻 徹也, 田中 伸幸, 久保 真治, “熱化学水素製造 IS プロセス用イオン交換膜の耐久性”, 日本膜学会 39 年会, 要旨集 P-32S, [早稲田大・東京] (2017/05). **E, G, I, 1-19**
- 7) T. Yamaki, “Fluoropolymer-based nanostructured membranes created by swift-heavy-ion irradiation and their energy and environmental applications” **[Invited talk]**, *Proc. 19th Int. Conf. Radiat. Eff. Insulators (REI-19), [Versailles, France] 165 (2017/07).* **C, I, 1-08**
- 8) 八巻 徹也, “荷電粒子ビームを利用した燃料電池電極触媒の開発 – 高活性・高耐久化に向けた X 線吸収分光への期待 –” **[招待講演]**, 平成 29 年度文部科学省ナノテクノロジープラットフォーム事業微細構造解析プラットフォーム放射光設備利用講習会, [量研高崎・高崎] (2017/08). **C, I, S, 1-08**
- 9) T. Yamaki, “Metal nanocatalysts prepared by ion beam irradiation for hydrogen energy devices” **[Invited talk]**, *Proc. Int. Conf. Accel. Mater. & Med. Sci. (ICAMMS '17), IT-08, [Dubai, UAE] (2017/08).* **C, I, S, 1-08**
- 10) T. Mori, A. Rednyk, A. Suzuki, S. Ito, S. Yamamoto, N. Isaka, Y. Yamamoto, T. Ishida, T. Tanji and F. Ye, “Interface structure design of cermet anode of SOFC using trace amount of sputtered PtOx” **[Invited talk]**, *Abstr. 15th Int. Conf. Adv. Mater. (IUMRS-ICAM 2017), A7-I29-001, [Kyoto, Japan] (2017/08).* **S**
- 11) T. Yamaki, K. Kakitani, T. Kimata, S. Yamamoto, W. Mao, T. Terai, I. Shimoyama, D. Matsumura, T. Taguchi, A. Iwase and T. Kobayashi, “Activity Enhancement of platinum nanoparticle catalysts by ion-beam induced defects”, *Abstr. 15th Int. Conf. Adv. Mater. (IUMRS-ICAM 2017), D1-O29-007, [Kyoto, Japan] (2017/08).* **I, 1-08**
- 12) H. Ohba, M. Saeki, K. Tamura, T. Taguchi, S. Yamamoto, A. Matsumoto, K. Akaoka and I. Wakaida, “Fiber-optic remote LIBS of materials in environment of high-dose radiation”, *Abstr. 2nd Asian Symposium on Laser Induced Breakdown Spectroscopy (ASLIBS2017), O-31, [Tokushima, Japan] (2017/08).* **G, 3-07**
- 13) 八巻 徹也, 佐藤 裕真, 越川 博, 山本 春也, 杉本 雅樹, 澤田 真一, “イオン穿孔膜における多彩な孔形状: エネルギー付与量の制御による試み”, 膜シンポジウム 2017, 講演要旨集 215, [富山大・富山] (2017/11). **C, 1-08**
- 14) 八巻 徹也, 山本 春也, 田口 富嗣, 小林 知洋, “電離放射線による液相還元を利用した金属ナノ微粒子の形成” **[招待講演]**, 日本化学会新領域研究グループ「液相高エネルギー化学の新展開」研究会(電気学会 電子材料研究会と共催)– 物質生成・材料合成を目指した高エネルギープロセス –, *EFM-17-014, [甲南大・東京] (2017/09).* **E, S, 1-08**
- 15) 木全 哲也, 垣谷 健太, 山本 春也, 田口 富嗣, 松村 大樹, 下山 巖, 岩瀬 彰宏, 小林 知洋, 八巻 徹也, 寺井 隆幸, “炭素担体へのイオン照射による Pt ナノ微粒子触媒の活性向上 – 界面構造に XAFS 測定で迫る –” **[招待講演]**, 2017 年第 78 回応用物理学会秋季学術講演会, 予稿集 6p-S41-1, [福岡国際会議場・福岡] (2017/09). **S, I, 1-14**
- 16) 山本 春也, 垣谷 健太, 杉本 雅樹, 越川 博, 田口 富嗣, 八巻 徹也, “親水化処理したセリア膜への電子線還元法による Pt 微粒子形成”, 2017 年電気化学秋季大会, 講演要旨集 1H22, [長崎大・長崎] (2017/09). **S, E, 1-10**
- 17) 森 利之, アンドリー レドニク, 鈴木 彰, 山本 春也, 伊坂 紀子, 伊藤 滋啓, “極微量白金族金属酸化物を用いた酸化物形燃料電池アノード層内機能性界面の設計”, 2017 年電気化学秋季大会, 講演要旨集 2I25, [長崎大・長崎] (2017/09). **S**
- 18) T. Mori, A. Rednyk, A. Suzuki, S. Ito, S. Yamamoto, N. Isaka, Y. Yamamoto, T. Ishida and T. Tanji, “Design of high functional interface in anode of IT-SOFC”, *European Congress and Exhibition on Advanced Materials and Processes (EUROMAT 2017), E1-O-TUE-AM2, [Thessaloniki, Greece] (2017/09).* **S**
- 19) 出崎 亮, 山本 春也, 杉本 雅樹, 八巻 徹也, “イオン注入法を利用した高分子材料からの窒素添加炭素系触媒の合成”, 2017 年電気化学秋季大会, 講演要旨集 1H21, [長崎大・長崎] (2017/09). **I, 1-12**
- 20) 土屋 文, 高廣 克己, 山本 春也, “加熱された全固体リチウムイオン二次電池中のリチウムイオン伝導挙動”, 日本金属学会

- 2017 年秋期講演大会, 講演プログラム 57, [北海道大・札幌] (2017/09). **T, I, 3-09**
- 21) 山本 春也, 杉本 雅樹, 越川 博, 田口 富嗣, 八巻 徹也, “ α -Al₂O₃ 基板上に形成する CeO₂ 膜の結晶配向性に及ぼす蒸着速度の影響”, 第 27 回日本 MRS 年次大会, アブストラクト集 C-O6-011, [横浜市海港記念会館・横浜] (2017/12). **S, 1-10**
- 22) 森 利之, シブラ チャウハン, 山本 春也, 小林 知洋, 伊坂 紀子, 伊藤 滋啓, “Pt/C 上の酸素還元反応 (ORR) 活性に与える CeOx ナノワイヤー表面の反応活性促進効果”, 第 27 回日本 MRS 年次大会, アブストラクト集 S-O6-006, [横浜市海港記念会館・横浜] (2017/12). **S**
- 23) 出崎 亮, 山本 春也, 杉本 雅樹, 八巻 徹也, “前駆体高分子へのイオン注入を利用した窒素添加炭素系触媒の合成”, 第 44 回炭素材料学会年会, 講演要旨集 1C05, [桐生市市民文化会館・桐生] (2017/12). **I, 1-12**
- 24) K. Kakitani, T. Kimata, T. Yamaki, S. Yamamoto, T. Taguchi, I. Shimoyama, D. Matsumura, A. Iwase, T. Kobayashi, T. Terai and W. Mao, “The interface between platinum nanoparticle catalysts and an Ar⁺-irradiated carbon support”, Int. Conf. Surface Modification of Materials by Ion Beams (SMMIB-2017), O02, [Lisbon, Portugal] (2017/07). **S, I**
- 25) 垣谷 健太, 木全 哲也, 八巻 徹也, 山本 春也, 田口 富嗣, 下山 巖, 松村 大樹, 岩瀬 彰宏, 小林 知洋, 毛 偉, 寺井 隆幸, “イオンビームによる炭素担体の格子欠陥を利用した Pt ナノ微粒子触媒の作製: 耐久性評価”, 2017 年電気化学秋季大会, 講演要旨集 1H23, [長崎大・長崎] (2017/09). **S, I**
- 26) 垣谷 健太, 木全 哲也, 八巻 徹也, 山本 春也, 小林 知洋, 毛 偉, 寺井 隆幸, “炭素担体のイオンビーム照射欠陥による白金ナノ粒子触媒の高性能化”, 日本学術振興会産業協力研究会第 117 委員会「炭素材料」第 324 回研究会, 117-324-B-1, [東京大・東京] (2017/12). **S, I**
- 27) 佐藤 裕真, 越川 博, 山本 春也, 杉本 雅樹, 澤田 真一, 八巻 徹也, “イオン穿孔膜における微細孔の形状制御: ろう斗型穿孔の形成”, 2017 年電気化学秋季大会, 講演要旨集 1E17, [長崎大・長崎] (2017/09). **C, 1-13**
- 28) 木村 壮宏, 池田 歩, 野村 幹弘, 西嶋 陽之, 今林 慎一郎, 澤田 真一, 八巻 徹也, 田中 伸幸, 久保 真治, “熱化学水素製造用放射線グラフト膜の耐久性”, 化学工学会関東支部東京大会, 要旨集 A105, [早稲田大・東京] (2017/08). **E, G, 1-19**
- 29) T. Yamaki, T. Kodaira, S. Sawada, N. Tanaka, S. Kubo and M. Nomura, “Cation exchange membranes prepared by radiation-induced graft polymerization for the electrochemical Bunsen reaction”, Abstr. 7th World Hydrogen Tech. Conv. (WHTC2017), ESN-HP-P045, [Prague, Czech Republic] (2017/07). **E, G, 1-08**
- 30) S. Yamamoto, T. Taguchi, K. Kakitani, H. Koshikawa and T. Yamaki, “Electron beam induced formation of Pt particles on ceria films”, Abstr. 15th Int. Conf. Adv. Mater. (IUMRS-ICAM 2017), A7-P30-009, [Kyoto, Japan] (2017/08). **S, E, 1-10**
- 31) A. Rednyk, T. Mori, A. Suzuki, S. Ito and S. Yamamoto, “Improving of anode in solid oxide fuel cell by deposition of negligible amount of platinum group metal oxides (PtOx, PdOx, RhOx and RuOx)”, Abstr. 15th Int. Conf. Adv. Mater. (IUMRS-ICAM 2017), A7-P30-010, [Kyoto, Japan] (2017/08). **S**
- 32) T. Taguchi, S. Yamamoto and H. Oba, “Synthesis of new-structured carbon nanomaterials inside silicon carbide nanotubes by ion irradiation-induced changes”, Abstr. 15th Int. Conf. Adv. Mater. (IUMRS-ICAM 2017), D1-P28-004, [Kyoto, Japan] (2017/08). **T, I, 1-22**
- 33) H. Koshikawa, Y. Sato, S. Yamamoto, M. Sugimoto, S. Sawada, T. Yamaki and K. Kakitani, “Preparation of conductive layer on polyimide ion-track membrane by Ar ion implantation”, Abstr. Int. Conf. Surface Modification of Materials by Ion Beams (SMMIB-2017), SA-P15, [Lisbon, Portugal] (2017/07). **C, S, I, 1-09**
- 34) K. Kakitani, T. Kimata, T. Yamaki, S. Yamamoto, W. Mao, T. Terai, I. Shimoyama, D. Matsumura, T. Taguchi, A. Iwase and T. Kobayashi, “Activity enhancement of platinum nanoparticle catalysts by ion-beam-induced defects”, Abstr. 68th Annu. Meet. Int. Soc. Electrochem., S06-008, [Providence, USA] (2017/08). **S, I**
- 35) K. Kakitani, T. Kimata, T. Yamaki, S. Yamamoto, T. Taguchi, D. Matsumura, I. Shimoyama, A. Iwase, T. Kobayashi and T. Terai, “X-ray absorption study of platinum nanoparticle catalysts on ion-beam-irradiated carbon support”, Abstr. Int. Symp. Novel Energy Nanomaterials, Catalysts and Surfaces for Future Earth, 2P-25, [Tokyo, Japan] (2017/08). **S, I**
- 36) 大森 理之, 八巻 徹也, 澤田 真一, 越川 博, 垣花 百合子, 安川 政宏, 比嘉 充, “イオン飛跡グラフト重合法により作製したモザイク荷電膜の電解質選択透過性”, 膜シンポジウム 2017, 講演要旨集 P-28S, [富山大・富山] (2017/11). **C**
- 37) 大森 理之, 八巻 徹也, 澤田 真一, 越川 博, 垣花 百合子, 安川 政宏, 比嘉 充, “イオン飛跡グラフト重合法により作製したモザイク荷電膜の圧透析特性評価”, 第 32 回中国四国地区高分子若手研究会, PA05, [ホテルかめ福・山口] (2017/11). **C**
- 38) 佐藤 裕真, 越川 博, 山本 春也, 杉本 雅樹, 澤田 真一, 八巻 徹也, “エネルギー付与量の深さ分布を利用したイオン穿孔の形状制御”, 日本化学会関東支部群馬地区研究交流発表会, 要旨集 P-29, [群馬大・桐生] (2017/12). **C, 1-13**
- 39) 鹿沼 裕貴, 杉本 雅樹, 出崎 亮, 山本 春也, 越川 博, 八巻 徹也, “高温電子線照射による窒素添加炭素系触媒の作製”, 第 44 回炭素材料学会年会, 講演要旨集 PI34, [桐生市市民文化会館・桐生] (2017/12). **E, 1-17**
- 40) 木村 壮宏, 野村 幹弘, 西嶋 陽之, 今林 慎一郎, 澤田 真一, 八巻 徹也, 田中 伸幸, 久保 真治, “放射線グラフト膜の長期耐酸性検討”, 化学工学会第 49 回秋季大会, 講演発表要旨集 PA111, [名古屋大・名古屋] (2017/09). **E, G, 1-19**
- 41) 木村 壮宏, 野村 幹弘, 西嶋 陽之, 今林 慎一郎, 澤田 真一, 八巻 徹也, 田中 伸幸, 久保 真治, “カチオン交換膜の高濃度耐酸性検討”, 第 7 回 CSJ 化学フェスタ 2017, 予稿集 P7-106, [タワーホール船堀・東京] (2017/10). **G, E, 1-19**
- 42) 木村 壮宏, 野村 幹弘, 西嶋 陽之, 今林 慎一郎, 澤田 真一, 八巻 徹也, 田中 伸幸, 久保 真治, “膜ブレンゼン反应用カチオン交換膜の開発”, 膜シンポジウム 2017, 講演要旨集 P-7S, [富山大・富山] (2017/11). **E, G, 1-19**
- 43) 木村 壮宏, 野村 幹弘, 西嶋 陽之, 今林 慎一郎, 澤田 真一, 八巻 徹也, 田中 伸幸, 久保 真治, “熱化学水素製造 IS プロセス用イオン交換膜の耐久性”, 第 37 回水素エネルギー協会大会, P05, [タワーホール船堀・千葉] (2017/12). **E, G, 1-19**
- 44) 八巻 徹也, “荷電粒子ビームを利用した燃料電池電極触媒の開発 - 高活性・高耐久化に向けた X 線吸収分光への期待 -” 【招待講演】, JAEA-QST 放射光科学シンポジウム 2018, [量研関西・佐用] (2018/03). **C, S, I, 1-08**

- 45) 八巻 徹也, 垣谷 健太, 木全 哲也, 山本 春也, 松村 大樹, 下山 巖, 寺井 隆幸, “イオンビームによる炭素担体の格子欠陥を利用した Pt ナノ微粒子触媒の作製: X 線吸収微細構造測定”, 電気化学会第 85 回大会, 講演要旨集 2A05, [東京理科大・東京] (2018/03). **C, S, I, 1-08**
- 46) 八巻 徹也, 垣谷 健太, 木全 哲也, 山本 春也, 小林 知洋, 寺井 隆幸, 岩瀬 彰宏, “イオンビーム照射した炭素担体上の白金ナノ粒子(1)触媒活性と耐久性の向上”, 日本原子力学会 2018 年春の年会, 予稿集 2I08, [大阪大・吹田] (2018/03). **C, S, I, 1-08**
- 47) 山本 春也, 垣谷 健太, 宮下 敦巳, 田口 富嗣, 越川 博, 八巻 徹也, “放射線還元法によりセリア膜上に形成した Pt ナノ粒子”, 電気化学会第 85 回大会, 講演要旨集 2A04, [東京理科大・東京] (2018/03). **S, E, 1-10**
- 48) 越川 博, 佐藤 裕真, 山本 春也, 杉本 雅樹, 澤田 真一, 八巻 徹也, “イオン穿孔膜をテンプレートとした酸化チタンナノコーンの光触媒性能”, 電気化学会第 85 回大会, 講演要旨集 2L05, [東京理科大・東京] (2018/03). **C**
- 49) 垣谷 健太, 木全 哲也, 八巻 徹也, 山本 春也, 田口 富嗣, 下山 巖, 松村 大樹, 岩瀬 彰宏, 小林 知洋, 毛 偉, 寺井 隆幸, “イオンビーム照射した炭素担体上の白金ナノ粒子(2)X 線吸収微細構造測定による局所構造分析”, 日本原子力学会 2018 年春の年会, 予稿集 2I09, [大阪大・吹田] (2018/03). **S, I**
- 50) 佐藤 裕真, 越川 博, 山本 春也, 杉本 雅樹, 澤田 真一, 八巻 徹也, “イオン穿孔膜の孔形状制御とテンプレート応用”, 電気化学会第 85 回大会, 講演要旨集 2L06, [東京理科大・東京] (2018/03). **C, 1-13**
- 51) 佐藤 裕真, 越川 博, 山本 春也, 杉本 雅樹, 澤田 真一, 八巻 徹也, “イオン穿孔膜をテンプレートとした白金ナノコーンの作製: 形状制御”, 日本化学会第 98 年春季年会, 予稿集 1I2-12, [日本大・船橋] (2018/03). **C, 1-13**
- 52) 鹿沼 裕貴, 杉本 雅樹, 出崎 亮, 山本 春也, 越川 博, 八巻 徹也, “高温電子線照射による窒素添加炭素系触媒の作製: 照射温度の影響”, 日本化学会第 98 回春季年会, 予稿集 1C3-34, [日本大・船橋] (2018/03). **E, 1-17**
- 53) 野村 幹弘, 木村 壮宏, 西嶋 陽之, 今林 慎一郎, 澤田 真一, 八巻 徹也, 田中 伸幸, 久保 真治, “熱化学水素製造のための放射線グラフト膜の耐久性検討”, 化学工学会第 83 年会, 講演発表要旨集 J316, [関西大・吹田] (2018/03). **E, G, 1-19**
- 54) 竹内 健太郎, 大森 理之, 垣花 百合子, 安川 政宏, 比嘉 充, “界面重合を用いた PAN 系 FO 膜の作製と水輸送特性評価”, 第 32 回中国四国地区高分子若手研究会, PB06, [ホテルかめ福・山口] (2017/11). **N**
- 55) 木全 哲也, 垣谷 健太, 山本 春也, 八巻 徹也, 寺井 隆幸, 中村 一隆, “ラマン分光による Pt ナノ微粒子を堆積したイオン照射グラファイトの構造解析”, 第 65 回応用物理学会春季学術講演会, 予稿集 18a-P3-6, [早稲田大・東京] (2018/03). **S, I, 1-14**
- 56) 澤田 真一, 後藤 光暁, 越川 博, 喜多村 茜, 比嘉 充, 八巻 徹也, “重イオンビームグラフト法で作製したカチオン・アニオン交換膜の輸送特性評価と海水電気透析への応用”, 日本原子力学会 2018 年春の年会, 予稿集 2I07 [大阪大・吹田] (2018/03). **C, 1-25**
- 57) T. Kimura, M. Nomura, H. Nishijima, S. Imabayashi, S. Sawada, T. Yamaki, N. Tanaka, S. Kubo, “Acid stability of radiation grafting membranes”, Proc. 5th joint Workshop between Chungnam National University and Shibaura Institute of Technology on Green Energy Chemistry (5th CNU-SIT workshop), P-7, [Tokyo, Japan] (2017/07). **E, G, 1-19**
- 58) 石飛 宏和, 山本 春也, 大場 晃介, 中川 紳好, 越川 博, 八巻 徹也, “電子線照射・空気酸化によるレドックスフロー電池に用いる電極材の活性化”, 電気化学会第 85 回大会, 講演要旨集 1H07, [東京理科大・東京] (2018/03). **E, 1-18**

P1-3 Positron Nano-Science Research Project

Papers

- 1) K. Wada, T. Shirasawa, I. Mochizuki, M. Fujinami, T. Takahashi, M. Maekawa, A. Kawasuso, M. Kimura and T. Hyodo, “Observation of low-energy positron diffraction patterns with a linac-based slow-positron beam”, e-J. Surf. Sci. Nanotech., **16**, 313-19 (2018). **N**
- 2) A. Kawasuso, M. Maekawa, A. Miyashita, K. Wada, T. Kaiwa and Y. Nagashima, “Positronium formation at Si surfaces”, Phys. Rev. B, **97**, 245303-1~8 (2018). **N**
- 3) K. Wada, A. Miyashita, M. Maekawa, S. Sakai, A. Kawasuso, “Spin-Polarized Positron Beams with ^{22}Na and ^{68}Ge and Their Applications to Materials Research”, AIP Conf. Proc. 1970, 040001-1~8 (2018). **N**
- 4) A. Miyashita, M. Maekawa, K. Wada, A. Kawasuso, S. Entani, T. Watanabe, S. Sakai, “Spin polarization of graphene and h-BN on Co(0001) and Ni(111) observed by spin-polarized surface positronium spectroscopy”, Phys. Rev. B, **97** 195405-1~5 (2018). **N**
- 5) M. Maekawa, H. Abe, A. Miyashita, S. Sakai, S. Yamamoto, and A. Kawasuso, “Vacancy-induced ferromagnetism in ZnO probed by spin-polarized positron annihilation spectroscopy”, Appl. Phys. Lett., **110**, 172402-1~5 (2017). **C, 3-05**
- 6) D. D. Wang, B. Zhao, N. Qi, Z. Q. Chen and A. Kawasuso, “Vacancy-mediated ferromagnetism in Co-implanted ZnO studied using a slow positron beam”, J. Mater. Sci., **52**, 7067-76 (2017). **N**
- 7) H. Li, M. Maekawa, A. Miyashita, A. Kawasuso, “Spin-Polarized Positron Annihilation Study on Some Ferromagnets”, Defect and Diffusion Forum, **373**, 65-70 (2017). **N**
- 8) M. Maekawa, K. Wada, A. Miyashita and A. Kawasuso, “Construction of a surface positronium lifetime spectroscopy apparatus with a spin-polarized low energy positron beam”, J. Phys. Conf. Ser. **791**, 021009 (2017). **C, 3-05**
- 9) M. Maekawa, S. Sakai, A. Miyashita, A. Kawasuso, “Spin-polarized positron annihilation measurement on Ga vacancies in p-type GaN”, e-J. Surf. Sci. Nanotech. **16**, 347-350 (2018) **C, 3-05**

Proceedings

- 1) T. Hyodo, I. Mochizuki, A. Ichimiya, M. Kimura, N. Toge, T. Shidara, Y. Fukaya, S. Shamoto, K. Wada, M. Maekawa, A. Kawasuso, M. Fujinami, T. Shirasawa, T. Takahashi, H. Ariga, K. Asakura, S. Iida, Y. Nagashima, “Positron surface studies at KEK: Positron diffraction and positronium TOF”, 8th Int. Symp. Surf. Sci., (ISSS-8), [Tsukuba, Japan] (2017/10). **N**
- 2) M. Maekawa, S. Sakai, K. Wada, A. Miyashita, A. Kawasuso, “Vacancy-induced magnetism in metal oxides or nitrides probed by spin-polarized positron beam”, 8th Int. Symp. Surf. Sci., (ISSS-8), [Tsukuba, Japan] (2017/10). **C, 3-05**
- 3) K. Wada, T. Shirasawa, I. Mochizuki, M. Fujinami, M. Maekawa, A. Kawasuso, and T. Hyodo, “A Low-Energy Positron Diffraction Experiment System with a Linac-Based Slow-Positron Beam”, 8th

- Int. Symp. Surf. Sci., (ISSS-8), [Tsukuba, Japan] (2017/10). N
- 4) A. Kawasuso, A. Miyashita, M. Maekawa, K. Wada, S. Entani and S. Sakai, “Spin polarizations of graphene or h-BN-covered ferromagnetic surfaces observed by spin-polarized positron beam spectroscopy”, 8th Int. Symp. Surf. Sci., (ISSS-8), [Tsukuba, Japan] (2017/10). N
- 5) A. Yabuuchi, A. Kinomura, M. Maekawa, and A. Kawasuso, “Study of Ion-Beam-Synthesized β -FeSi₂ Films Probed by a Slow Positron Beam”, Positron Studies of Defects (PSD-17), Oral Presentation, Abstr. O-24, 62 [Dresden, Germany] (2017/09). C, 3-06
- 6) A. Kawasuso, “Application of spin-polarized positron annihilation spectroscopy to spintronics materials” **【Invited talk】**, Int. Workshop Phys. Positrons at Jefferson Lab, JPos2017, [Newport News, USA] (2017/09). N
- 7) K. Wada, A. Miyashita, M. Maekawa, S. Sakai and A. Kawasuso, “Spin-Polarized Positron Beams with ²²Na and ⁶⁸Ge and Their Applications to Materials Research”, AIP Conf. Proc. **1970**, 040001 (2018). Int. Workshop Phys. with positrons at Jefferson lab. (JPos17) [Newport News, USA] (2017/09). N
- 8) T. Hyodo, I. Mochizuki, A. Ichimiya, M. Kimura, N. Toge, T. Shidara, Y. Fukaya, S. Shamoto, K. Wada, M. Maekawa, A. Kawasuso, M. Fujinami, T. Shirasawa, T. Takahashi, H. Ariga, K. Asakura, S. Iida, Y. Nagashima, “Surface studies at SPF, KEK: Positron diffraction and positronium TOF”, 12th Int. Workshop Positron and Positronium Chemistry, [Lublin, Poland] (2017/08-09). N
- 9) K. Wada, “Development of low-energy positron diffraction systems in Japan” **【Invited talk】**, School of Phys. & Tech., Wuhan University, [Wuhan, China] (2017/06). N
- 10) K. Wada, “Positron diffraction experiments in Japan” **【Invited talk】**, 3rd China-Japan Joint Workshop on Positron Science (JWPS2017), 6-8, [Hefei, China] (2017/06). N
- 11) A. Kawasuso, “Applications of spin-polarized positron spectroscopy to some ferromagnets” **【Invited talk】**, Int. Workshop Comput. Sci. 2017, [Kanazawa, Japan] (2017/02). N
- 12) 和田 健, 白澤 徹朗, 望月 出海, 藤浪 真紀, 前川 雅樹, 河裾 厚男, 高橋 敏男, 兵頭 俊夫, “低速陽電子回折 (LEPD)による表面ホログラフィ実験の進捗状況”, 第 2 回陽電子回折研究会, [KEK・つくば] (2018/03). N
- 13) 前川 雅樹, 境 誠司, 宮下 敦巳, 和田 健, 河裾 厚男, “スピン偏極陽電子ビームによる窒化ガリウム薄膜の空孔誘起磁性評価”, 日本物理学会第 73 回年次大会, プログラム 24pK507-7, [東京理科大・野田] (2018/03). C, 3-05
- 14) 河裾 厚男, 前川 雅樹, 和田 健, 宮下 敦巳, 渡邊 貴弘, 圓谷 志郎, 境 誠司, “スピン偏極陽電子ビームによるグラフェン・窒化ホウ素/強磁性薄膜のスピン偏極の検出”, 日本物理学会第 73 回年次大会, プログラム 24pB403-2, [東京理科大・野田] (2018/03). N
- 15) 藪内 敦, 木野村 淳, 前川 雅樹, 河裾 厚男, “イオンビーム合成法で作製した β -FeSi₂ 膜の低速陽電子ビームによる評価”, 第 65 回応用物理学会 春季学術講演会, プログラム 19a-F202-6, [早稲田大・東京] (2018/03). C, 3-06
- 16) 兵頭 俊夫, 和田 健, 白澤 徹郎, 望月 出海, 藤浪 真紀, 前川 雅樹, 河裾 厚男, 高橋 敏男, “低速陽電子回折法による表面構造解析”, 平成 29 年度 KEK 量子ビームサイエンスフェスタ, [茨城県立県民文化センター・水戸] (2018/03). N
- 17) 河裾 厚男, “陽電子を利用した表面・スピントロニクス材料の研究”, 第 6 回先進的放射光メスバウアー分光研究会, (2018/03). N
- 18) 前川 雅樹, 和田 健, 宮下 敦巳, 河裾 厚男, “ポジトロニウム飛行時間測定装置の開発”, 平成 29 年度京都大学原子炉実験所専門研究会「陽電子科学とその理工学への応用」, [京都大・熊取町] (2017/12). C, 3-05
- 19) 和田 健, 白澤 徹朗, 望月 出海, 藤浪 真紀, 前川 雅樹, 河裾 厚男, 高橋 敏男, 兵頭 俊夫, “低速陽電子回折実験装置の開発”, 平成 29 年度京都大学原子炉実験所専門研究会「陽電子科学とその理工学への応用」, [京都大・熊取町] (2017/12). N
- 20) 河裾 厚男, 前川 雅樹, 和田 健, 宮下 敦巳, “シリコン表面におけるポジトロニウム生成”, 平成 29 年度京都大学原子炉実験所専門研究会「陽電子科学とその理工学への応用」, [京都大・熊取町] (2017/12). N
- 21) 河裾 厚男, 前川 雅樹, 和田 健, 宮下 敦巳, 圓谷 志郎, 境 誠司, “スピン偏極陽電子ビームによるグラフェン・窒化ボロン/コバルト系のスピン偏極状態の観測”, 日本物理学会 2017 年秋季大会, プログラム 23aB32-10, [岩手大・盛岡] (2017/09). N
- 22) 南川 英輝, 中西 俊輔, 前川 雅樹, 河裾 厚男, 間嶋 拓也, 今井 誠, 斉藤 学, 土田 秀次, “単結晶 Si のイオン照射欠陥蓄積におけるフラックス効果”, 日本物理学会 2017 年秋季大会, プログラム 22pA18-12, [岩手大・盛岡] (2017/09). N
- 23) 前川 雅樹, 境 誠司, 圓谷 史郎, 河裾 厚男, “スピン偏極陽電子ビームによるイオン照射窒化ガリウム薄膜の空孔局在電子スピンの検出”, 日本物理学会 2017 年秋季大会, プログラム 21pA45-4, [岩手大・盛岡] (2017/09). C, 3-05
- 24) 和田 健, 白澤 徹郎, 望月 出海, 藤浪 真紀, 前川 雅樹, 河裾 厚男, 兵頭 俊夫, “加速器ベース低速陽電子ビームを用いた低速陽電子回折実験装置の開発”, 日本物理学会 2017 年秋季大会, プログラム 21pA45-3, [岩手大・盛岡] (2017/09). N
- 25) 前川 雅樹, 和田 健, 宮下 敦巳, 河裾 厚男, “スピン偏極ポジトロニウム分光装置の開発”, 第 54 回放射線アイントープ研究発表会, [東京大・東京] (2017/07). C, 3-05
- 26) 河裾 厚男, 前川 雅樹, 和田 健, 宮下 敦巳, “シリコン表面におけるポジトロニウム生成の温度依存性”, 第 54 回放射線アイントープ研究発表会, [東京大・東京] (2017/07). N

P1-4 Two-dimensional Material Spintronics Research Project

Papers

- 1) A. V. Kuklin, A. A. Kuzubov, E. A. Kovaleva, H. Lee, P. B. Sorokin, S. Sakai, S. Entani, H. Naramoto, P. Avramov, “The direct exchange mechanism of induced spin polarization of low-dimensional π -conjugated carbon- and h-BN fragments at LSMO(001) MnO-terminated interfaces”, J. Mag. Mag. Mater. **440**, 23-29 (2017). N
- 2) M. Maekawa, H. Abe, A. Miyashita, S. Sakai, S. Yamamoto, and A. Kawasuso, “Vacancy-induced ferromagnetism in ZnO probed by spin-polarized positron annihilation spectroscopy”, Appl. Phys. Lett., **110**, 172402-1~5 (2017). C, 3-05
- 3) Y. Yamada, A. V. Kuklin, S. Sato, F. Esaka, N. Sumi, C. Zhang, M. Sasaki, E. Kwon, Y. Kasama, P. V. Avramov, S. Sakai, “Electronic structure of Li⁺@C60: Photoelectron spectroscopies of the Li⁺@C₆₀[PF₆] salt and STM of the single Li⁺@C₆₀ molecules on Cu(111)”, Carbon **133**, 23-30 (2018). N
- 4) S. Entani, M. Honda, I. Shimoyama, S. Li, H. Naramoto, T. Yaita, S. Sakai, “Effective adsorption and collection of cesium from

- aqueous solution using graphene oxide grown on porous alumina”, *Jpn. J. Appl. Phys.* **57**, 04FP04 (2018). **N**
- 5) T. Watanabe, Y. Yamada, A. Koide, S. Entani, S. Li, Z. I. Popov, P. B. Sorokin, H. Naramoto, M. Sasaki, K. Amemiya, S. Sakai, “Interface-induced perpendicular magnetic anisotropy of Co nanoparticles on single-layer h-BN/Pt(111)”, *Appl. Phys. Lett.* **112**, 022407 (2018). **N**
- 6) S. Li, T. Nakatani, K. Matsuda, Y. Sakuraba, X. Xu, T. Sasaki, H. Tajiri, Y. Miura, T. Furubayashi, K. Hono, “Enhancement of current-perpendicular-to-plane giant magneto-resistance outputs by improved B2-order in polycrystalline $\text{Co}_2(\text{Mn}_{0.6}\text{Fe}_{0.4})\text{Ge}$ Heusler alloy films by the insertion of amorphous CoFeBTa underlayer”, *Acta Mater.* **142**, 49-57 (2018). **N**
- 7) T. Nakatani, S. Li, Y. Sakuraba, T. Furubayashi, K. Hono, “Advanced CPP-GMR spin-valve sensors for narrow reader applications”, *IEEE Trans. Magn.* **54**, 1-11 (2018). **N**
- 8) M. Maekawa, S. Sakai, A. Miyashita, A. Kawasuso, “Spin-polarized positron annihilation measurement on Ga vacancies in p-type GaN”, *e-J. Surf. Sci. Nanotech.* **16**, 347-350 (2018). **C, 3-05**
- 9) K. Takaoka, K. Mitsuhashi, M. Takizawa, S. Entani, S. Sakai, “Chemical and electronic state analysis of oxidizing graphene”, *e-J. Surf. Sci. Nanotech.* **16**, 320-23 (2018). **N**

Proceedings

- 1) K. Wada, A. Miyashita, M. Maekawa, S. Sakai and A. Kawasuso, “Spin-Polarized Positron Beams with ^{22}Na and ^{68}Ge and Their Applications to Materials Research”, *AIP Conf. Proc.* **1970**, 040001 (2018). *Int. Workshop Phys. with positrons at Jefferson lab. (JPos17) [Newport News, USA] (2017/09)*. **N**

Book

- 1) S. Majumdar, P. Avramov, S. Sakai, “Manipulating Spins at Molecular Level; An Insight into the Ferromagnet-Organic Interface”, *Spin in Organics (Vol. 4): A World Scientific Reference*, CHAPTER 1 World Scientific Publishing Company (WSPC) /Imperial College Press (IPC), 1-61 (2018). **N**

Patent

- 1) K. Hasegawa, T. Ukai, E. Yamakawa, S. Entani, S. Sakai, “Perpendicular magnetic recording medium and magnetic storage apparatus”, Patent No. US9,640,213 B2 (2017/05/02). **N**

Press-TV

- 1) “リチウム内包フラーレンの電子の振る舞いを初めて解明～次世代有機半導体材料としての応用に道を拓く～”, プレス発表: 日本経済新聞等に掲載 (2018/03/16).

P1-5 Semiconductor Radiation Effect Research Project

Papers

- 1) T. Astner, J. Gugler, A. Angerer, S. Wald, S. Putz, N. Mauser, M. Trupke, H. Sumiya, S. Onoda, J. Isoya, J. Schmiedmayer, P. Mohn, J. Majer, “Solid-state electron spin lifetime limited by phononic vacuum modes”, *Nature Materials*, **17**, 313-17 (2018). **E**
- 2) M. Pfender, N. Aslam, H. Sumiya, S. Onoda, P. Neumann, J. Isoya, C. Meriles, J. Wrachtrup, “Nonvolatile nuclear spin memory enables sensor unlimited nanoscale spectroscopy of small spin clusters”, *Nature Communications*, **8** (834), 1-12 (2017). **E**
- 3) T. Kageura, K. Kato, H. Yamano, E. Suaebah, M. Kajiya, S. Kawai, M. Inava, T. Tanii, M. Haruyama, K. Yamada, S. Onoda, W. Kada, O. Hanaizumi, T. Teraji, J. Isoya, S. Kono, H. Kawarada, “Effect of a radical exposure nitridation surface on the charge stability of shallow nitrogen-vacancy centers in diamond”, *Appl. Phys. Exp.*, **10** (5), 055503-(1-4), 2017. **I**
- 4) T. Ohshima, T. Satoh, H. Kraus, G. V. Astakhov, V. Dyakonov, P. G. Baranov, “Creation of Silicon Vacancy in Silicon Carbide by Proton Beam Writing toward Quantum Sensing Applications”, *J. Phys. D: Appl. Phys.* **51**, 333002-1~14 (2018). [Topical Review] **S, I, E**
- 5) H. N. My Duong, M. A. P. Nguyen, M. Kianinia, T. Ohshima, H. Abe, K. Watanabe, T. Taniguchi, J. H. Edgar, I. Aharonovich, Milos Toth, “Effects of High-Energy Electron Irradiation on Quantum Emitters in Hexagonal Boron Nitride”, *ACS Applied Materials and Interfaces* **10**, 24886-91 (2018). **E**
- 6) M. Widmann, M. Niethammer, T. Makino, T. Rendler, S. Lasse, T. Ohshima, J. Ul Hassan, N. T. Son, S.-Y. Lee, J. Wrachtrup, “Bright single photon sources in lateral silicon carbide light emitting diodes”, *Appl. Phys. Lett.* **112**, 203102-1~4 (2018). **E**
- 7) J. R. Ball, Y. Yamashiro, H. Sumiya, S. Onoda, T. Ohshima, J. Isoya, D. Konstantinov, and Y. Kubo, “Loop-gap microwave resonator for hybrid quantum systems”, *Appl. Phys. Lett.*, **112**, 204102-1~5 (2018). **E**
- 8) M. Fischer, A. Sperllich, H. Kraus, T. Ohshima, G. V. Astakhov, V. Dyakonov, “Highly Efficient Optical Pumping of Spin Defects in Silicon Carbide for Stimulated Microwave Emission”, *Phys. Rev. Appl.* **9**, 054006-1~8 (2018). **E**
- 9) Y. Miyazawa, M. Ikegami, H.-W. Chen, T. Ohshima, M. Imaizumi, Kazuyuki Hirose and T. Miyasaka, “Tolerance of perovskite solar cell to high-energy particle irradiations in space environment”, *iScience*, **2**, 148-55 (2018). **I, E**
- 10) R. G. Ryan, A. Stacey, K. M. O'Donnell, T. Ohshima, B. C. Johnson, L. C. L. Hollenberg, P. Mulvaney and D. A. Simpson, “Impact of surface functionalization on the quantum coherence of nitrogen-vacancy centers in nanodiamonds”, *ACS Appl. Mater. Inter.*, **10**, 13143-49 (2018). **E**
- 11) R. Nagy, M. Widmann, M. Niethammer, D. B. R. Dasari, I. Gerhardt, Ö. O. Soykal, M. Radulaski, T. Ohshima, J. Vučković, N. T. Son, I. G. Ivanov, S. E. Economou, C. Bonato, S.-Y. Lee and Jörg Wrachtrup, “Quantum properties of dichroic silicon vacancies in silicon carbide”, *Phys. Rev. Appl.*, **9**, 034022 (2018). **E**
- 12) Y. Ruan, D. A. Simpson, J. Jeske, H. Eberdorff-Heidepriem, D. W. M. Lau, H. Ji, B. C. Johnson, T. Ohshima, S. Afshar, V. L. Hollenberg, A. D. Greentree, T. M. Monro and B. C. Gibson, “Magnetically sensitive nanodiamond-doped tellurite glass fibers”, *Sci. Rep.*, **8**, 1268 (2018). **E**
- 13) M. H. Wong, A. Takeyama, T. Makino, T. Ohshima, K. Sasaki, A. Kuramata and S. Yamakoshi, “Radiation hardness of b-Ga₂O₃ metal-oxide-semiconductor field-effect transistors against gamma-ray irradiation”, *Appl. Phys. Lett.*, **112**, 023503-1~5 (2018). **G**
- 14) K. K. Lee, D. Wang, S. Onoda and T. Ohshima, “Reliability of gamma-irradiated n-channel ZnO thin-film transistors: electronic and interface properties”, *Radiat. Eff. Defects S.*, **173**, 250-60 (2018). **G**
- 15) Y. Abe, T. Umeda, M. Okamoto, R. Kosugi, S. Harada, M. Haruyama, W. Kada, O. Hanaizumi, S. Onoda and T. Ohshima, “Single photon sources in 4H-SiC metal-oxide-semiconductor field-effect transistors”, *Appl. Phys. Lett.*, **112**,

- 031105-1~5 (2018). **N**
- 16) H. Sasaki, T. Hisaka, K. Kadoiwa, T. Oku, S. Onoda, T. Ohshima, Eiji Taguchi and H. Yasuda, "Ultra-high voltage electron microscopy investigation of irradiation induced displacement defects on AlGaIn/GaN HEMTs", *Microelectron. Reliab.*, **81**, 312-19 (2018). **T**
- 17) I. Capan, T. Brodar, Z. Pastuovic, R. Siegele, T. Ohshima, S.-I. Sato, T. Makino, L. Snoj, V. Radulović, J. Coutinho, V. J. B. Torres and K. Demmouche, "Double negatively charged carbon vacancy at the h- and k- sites in 4H-SiC: Combined Laplace-DLTS and DFT study", *J. Appl. Phys.*, **123**, 161597-1~6 (2018). **T, I**
- 18) Z. Pastuovic, R. Siegele, I. Capan, T. Brodar, S.-I. Sato and T. Ohshima, "Deep level defects in 4H-SiC introduced by ion implantation: the role of single ion regime", *J. Phys. Condens. Mat.*, **29**, 1-8 (2017). **T, I**
- 19) C. F. de las Casas, D. J. Christle, J. Ul Hassan, T. Ohshima, N. T. Son and D. D. Awschalom, "Stark tuning and electrical charge state control of single divacancies in silicon carbide", *Appl. Phys. Lett.*, **111**, 262403-1~5 (2017). **E**
- 20) D. J. Christle, P. V. Klimov, C. F. de las Casas, K. Szasz, V. Ivady, V. Jokubavicius, J. Ul Hassan, M. Syjarvi, W. F. Koehl, T. Ohshima, N. T. Son, E. Janzen, A. Gali and D. D. Awschalom, "Isolated spin qubits in SiC with a high-fidelity infrared spin-to-photon interface", *Phys. Rev. X*, **7**, 021046-1~12 (2017). **E**
- 21) D. Kobayashi, K. Hirose, T. Makino, S. Onoda, T. Ohshima, S. Ikeda, H. Sato, E. C. I. Enobio, T. Endoh and H. Ohno, "Soft errors in 10-nm-scale magnetic tunnel junctions exposed to high-energy heavy-ion radiation", *Jpn. J. Appl. Phys.*, **56**, 0802B4-1~10 (2017). **C**

Proceedings

- 1) S. Sato, T. Sugaya, T. Nakamura, and T. Ohshima, "Defect Characterization of III-V Quantum Structure Solar Cells Using Photo-Induced Current Transient Spectroscopy", *Proc. IEEE 44th Photovoltaic Specialists Conf.* 167, [Washington DC, USA] (2017/06). **E, 1-02**
- 2) M. Sugai, M. Imaizumi, T. Nakamura, and T. Ohshima, "Effect of luminescence coupling between InGaP and GaAs subcells to external quantum efficiency in triple-junction solar cells", *Proc. IEEE 44th Photovoltaic Specialists Conf.* 168, [Washington DC, USA] (2017/06). **C, T, I, E, 1-02**

Book

- 1) T. Ohshima, M. Imaizumi, "Space Irradiation Effects on Solar Cells", Chapter 15 of "Applications of Laser-Driven Particle Acceleration" Edited by P. R. Bolton, K. Parodi, J. Schreiber, CRC Press, Taylor & Francis Group, ISBN9781498766418, 236-49 (2018). **C, T, I, E**

P1-6 Biocompatible Materials Research Project

Papers

- 1) T. Yanagida, M. Koshimizu, Y. Fujimoto, S. Kurashima, K. Iwamatsu, A. Kimura, M. Taguchi, G. Okada, N. Kawaguchi, "Analysis of excitation density effects on the scintillation properties of Ce:Gd₂SiO₅ (GSO) crystals", *Nucl. Instrum. Meth. Phys. Res. B*, **409**, 27-30 (2017). **C, 3-10**
- 2) M. Koshimizu, S. Kurashima, A. Kimura, M. Taguchi, T. Yanagida, Y. Fujimoto, K. Asai, "Analysis of linear energy transfer effects on the scintillation properties of a Bi₄Ge₃O₁₂ crystal", *Nucl. Instrum. Meth. Phys. Res. B*, **409**, 19-22 (2017). **C, 3-10**
- 3) Y. Kumagai, A. Kimura, M. Taguchi, M. Watanabe, "Hydrogen Production by Gamma-Ray Irradiation from Different Types of Zeolites in Aqueous Solution", *J. Phys. Chem., Part C* **121**, 407-11 (2017). **G**
- 4) Y. Kumagai, A. Kimura, M. Taguchi, M. Watanabe, "Radiation-induced degradation of aqueous 2-chlorophenol assisted by zeolites", *J. Radioanal. Nucl. Chem.* **316**, 341-08 (2018). **G**
- 5) S. Sasaki, S. Omata, T. Murakami, N. Nagasawa, M. Taguchi, A. Suzuki, "Effect of Gamma Ray Irradiation on Friction Property of PVA CD on FT Hybrid gel" *Gels* **4** (2), 30, (2018); doi:10.3390-gels4020030. **G, 1-27**
- 6) 廣木 章博, 田口 光正, "シート状ポリマーゲル線量計材料による3次元線量分布評価", *医学物理*, **37**巻, 186-89 (2017). **G, E**
- 7) 廣木 章博, "重粒子線治療用ポリマーゲル線量計の開発", *Isotope News*, **752**, 16-19 (2017). **G, E**
- 8) 大山 智子, "放射線架橋ゼラチンハイドロゲルの開発と機能性足場材料への応用", *放射線化学* **103**号, 39-40 (2017). **G, E**
- 9) 大山 智子, "量子ビーム技術を駆使した機能性バイオデバイスの開発", *放射線と産業*, **142**号, 22-23 (2017). **G**

- 10) 大山 智子, "先端医療実現に向けた機能材料創製", *化学工業日報* 8月22日 (2017). **G**
- 11) 長澤 尚胤, "量子ビームを用いた生体適合性材料の微細加工", *化学工業* (2018年1月). **S**

Proceedings

- 1) 長澤 尚胤, 木村 敦, 出崎 亮, 山田 尚人, 江夏 昌志, 佐藤 隆博, 石井 保行, 田口 光正, "プロトンビームライティング法による生体適合性ヒドロゲルの微細加工", 平成 29 年度繊維学会年次大会, [タワーホール船堀, 東京] (2017/06). **S**
- 2) N. Nagasawa, A. Kimura, A. Idesaki, N. Yamada, M. Koka, T. Satoh, Y. Ishii, M. Taguchi, "Microfabrication of Biocompatible Hydrogel by Proton Beam Writing", *Abstr. 15th Int. Conf. Adv. Mater. (IUMRS-ICAM 2017)*, [Kyoto, Japan] (2017/08). **S**

Patents

- 1) 田口 光正, 廣木 章博, 山下 真一, "ポリマーゲル線量計, 当該線量計を用いた放射線測定方法, 情報管理手段および方法, システム", 特許第 6212695 号, 特許登録日:2017/09/29. **G, E**
- 2) 大山 智子, 田口 光正, Barba Bin Jeremiah Duenas (バーバビン ジェレマイア デュナス), 木下 忍, 井出 崇, "試験用基材, 及び試験用基材の製造方法", 出願番号:特願 2017-113092, 出願日:2017/06/08, 共同出願人:(株)アイエレクトロニクス.
- 3) 田口 光正, 廣木 章博, 木村 敦, 大山 智子, 中島 健吾, 青木 伊知男, 村山 周平, "MRI 造影剤, 及び MRI 造影剤の製造方法", 出願番号:特願 2017-116241, 貴ケース番号: Q20037JP, 弊所ケース番号: A00019JP01CH, 出願日: 2017/06/13.

P1-7 Environmental Polymer Research Project

Papers

- 1) J. F. Madrid, Y. Ueki, L. V. Abad, T. Yamanobe, N. Seko, "RAFT-mediated graft polymerization of glycidyl methacrylate in emulsion from polyethylene/polypropylene initiated with gamma-radiation", *J. Appl. Polym. Sci.* **134**, 45270 (2017). **G**
- 2) J. Chen and N. Seko, "Effects of RAFT agent on the chloromethylstyrene polymerizations in a simultaneous radiation grafting system", *Polymers*, **9**, 307 (2017). **G, 1-31**
- 3) N. Seko, H. Hoshina, N. Kasai, T. Shibata, S. Saiki and Y. Ueki, "Development of a water purifier for radioactive cesium removal from contaminated natural water by radiation-induced graft polymerization", *Radiat. Phys. Chem.*, **143**, 33-37 (2018). **E**
- 4) Y. Ueki, S. Saiki, H. Hoshina, and N. Seko, "Biodiesel fuel production from waste cooking oil using radiation-grafted fibrous catalyst", *Radiat. Phys. Chem.*, **143**, 41-46 (2018). **E, 1-29**
- 5) 佐伯 誠一, 瀬古 典明, "高分子への放射線照射効果", *RADIOISOTOPES*, **66**, 469-77 (2017). **E, G**

Proceedings

- 1) J. F. Madrid, L. V. Abad, Y. Ueki, T. Yamanobe and N. Seko, "Functionalization of PE/PP with oxirane groups via RAFT-mediated gamma-radiation induced graft polymerization of emulsified glycidyl methacrylate", 32nd Philippine Chemistry Congress, OC-04, [Palawan, Philippines] (2017/05). **G**
- 2) 瀬古 典明, "放射線(量子ビーム)加工技術を用いた機能性材料の開発"【招待講演】, 第106回複合材料懇話会, [群馬大・桐生] (2017/06). **E, G**
- 3) 林 菜月, 陳 進華, 濱田 崇, 大道 正明, 瀬古 典明, "ポリスチレン薄膜上の放射線グラフトブラシのナノ構造観察", 第66回高分子討論会, 要旨集 1Pb024, [愛媛大・松山] (2017/09). **E**
- 4) J. F. Madrid, L. V. Abad, Y. Ueki, T. Yamanobe and N. Seko, "RAFT-mediated polymerization in emulsion phase: gamma- and electron-beam initiated grafting", 第66回高分子討論会, 要旨集 1Pf008, [愛媛大・松山] (2017/09). **G**
- 5) 陳 進華, 瀬古 典明, 林 菜月, "クロロメチルスチレンのETFEフィルムへの同時グラフト重合に及ぼすRAFT剤の影響", 第66回高分子討論会, 要旨集 2Pf028, [愛媛大・松山] (2017/09). **G, 1-31**
- 6) 鈴木 伸郎, 柴田 卓弥, 尹 永根, 保科 宏行, 藤巻 秀,

瀬古 典明, 河地 有木, "植物体内のセシウム動態を可視化するポジトロン放出トレーサの開発", 日本土壤肥料学会2017年度仙台大会, 要旨集 P4-3-1, [東北大・仙台] (2017/09). **C**

- 7) J. Chen, N. Hayashi and N. Seko, "RAFT polymerization in simultaneous radiation grafting of chloromethylstyrene onto ETFE films", *Proc. 15th Pacific Polymer Conf. (PPC-15)*, PS4-06, [Xiamen, China] (2017/12). **G, 1-31**
- 8) N. Seko, V. T. Quang, N. Hayashi, Y. Ueki and J. Chen, "Effect of alcohol on radiation emulsion grafting of GMA onto PE nonwoven fabrics", *Proc. 15th Pacific Polymer Conf. (PPC-15)*, PS4-12, [Xiamen, China] (2017/12). **E**
- 9) N. Hayashi, J. Chen, Y. Ueki and N. Seko, "Novel separation of trivalent and hexavalent chromium by fibrous graft adsorbent", *Proc. 15th Pacific Polymer Conf. (PPC-15)*, PS8-04, [Xiamen, China] (2017/12). **E**
- 10) 大場 弘則, 佐伯 盛久, 瀬古 典明, "Cs吸着材のレーザー誘起ブレイクダウン分光分析", 第14回茨城地区分析技術交流会, [いばらき量子ビーム研究センター・東海村] (2017/12). **E, 3-07**

- 11) 濱田 崇, 保科 宏行, 瀬古 典明, "水中のホウ素を除去可能な水不溶性グルカミン誘導体の開発", 第52回日本水環境学会年会, 要旨集 P-E04, [北海道大・札幌] (2018/03). **G**
- 12) 保科 宏行, 笠井 昇, 瀬古 典明, 物部長順, 加藤 耕一, "電子線グラフト吸着材とばね式フィルターを融合させたホウ素除去技術の開発", 第52回日本水環境学会年会, 要旨集 P-E07, [北海道大・札幌] (2018/03). **E, 1-30**

Patents

- 1) 瀬古 典明, 天田 春代, 保科 宏行, "吸着材の製造方法", 登録 6165431 (2017/06/30). **E, G**
- 2) 瀬古 典明, 玉田 正男, 佐伯 誠一, "金属捕集材", 登録 6300340 (2018/03/09). **E, G**
- 3) 濱田 崇, 保科 宏行, 瀬古 典明, "グルカミン誘導体, グルカミン誘導体からなる金属吸着剤, グルカミン誘導体からなる金属吸着剤を備える金属抽出装置, 金属抽出キット", 出願 2018-040662 (2018/03/07). **G**
- 4) 瀬古 典明, 保科 宏行, 笠井 昇, "グラフトセルローズパウダー及びこれを用いたろ過方法", 出願 2018-042450 (2018/03/08). **E, G**

P1-8 Element Separation and Analysis Research Project

Papers

- 1) T. Taguchi, S. Yamamoto and H. Ohba, "Ion irradiation-induced novel microstructural change in silicon carbide nanotubes", *Acta Materialia*, **154**, 90-99 (2018). **I, 1-22**
- 2) A. Matsumoto, H. Ohba, M. Toshimitsu, K. Akaoka, A. Ruas, T. Sakka, "Fiber-optic laser-induced breakdown spectroscopy of zirconium metal in the air: The special feature of the plasma produced by the long-pulse laser", *Spectrochimica Acta Part B: Atomic Spectroscopy*, **142**, 37-49 (2018). **N**
- 3) 佐伯 盛久, 浅井 志保, 大場 弘則, "レーザー微粒子化反応を利用した放射性廃液からの白金族元素分離法の開発", *ぶんせき*, (4), 138-43 (2018). **N**
- 4) 蓬田 匠, 浅井 志保, 佐伯 盛久, 半澤 有希子, 堀田 拓摩, 江坂 文孝, 大場 弘則, 北辻 章浩, "107PdのICP-MS測定のためのレーザー誘起光還元法による非接触・選択的パラジウム分離 - 分離条件とPd回収率の関係 -", *分析化学*, **66**, 647-52 (2017). **N**

- 5) Y. Kurosaki, K. Yokoyama, "Quantum optimal control of the isotope-selective rovibrational excitation of diatomic molecules", *Chem. Phys.*, **493**, 183-93 (2017). **N**
- 6) A. Ruas, A. Matsumoto, H. Ohba, K. Akaoka, I. Wakaida, "Application of laser-induced breakdown spectroscopy to zirconium in aqueous solution", *Spectrochim. Acta B*, **131**, 99-106 (2017). **N**
- 7) T. Taguchi, S. Yamamoto, H. Ohba, R. Tsubakiyama, K. Miyajima, "Effect of surface treatment on photoluminescence of silicon carbide nanotubes", *Appl. Surf. Sci.*, **403**, 308-13 (2017). **I, 1-22**
- 8) K. Tamura, S. Toyama, "Laser cutting performances for thick steel specimens studied by molten metal removal conditions", *J. Nucl. Sci. Tech.* **54**, 1011-17 (2017). **N**
- 9) K. Tamura, R. Yamagishi, "Observation of the molten metal behaviors during the laser cutting of thick steel specimens using attenuated process images", *J. Nucl. Sci. Tech.*, **54**, 655-61

- (2017). **N**
- 10) K. Kakitani, T. Kimata, T. Yamaki, S. Yamamoto, T. Taguchi, T. Kobayashi, W. Mao and T. Terai, "The interface between platinum nanoparticle catalysts and an Ar⁺-irradiated carbon support", *Surf. Coat. Tech.* **355**, 259-63 (2018). **I**
- Proceedings**
- 1) 佐伯 盛久, 田口 富嗣, 大場 弘則, 松村 大樹, 辻 卓也, 蓬田 匠, "時間分解 X 線吸収分光による水溶液中パラジウムイオンのレーザー微粒子化反応研究", 電気学会研究会資料, EFM-17-015 (2017). **N**
- 2) 大場 弘則, 佐伯 盛久, 瀬古 典明, "Cs 吸着材のレーザー誘起ブレイクダウン分光分析", 第 14 回茨城地区分析技術交流会, [いばらき量子ビーム研究センター・東海村] (2017/12). **E, 3-07**
- 3) H. Ohba, M. Saeki, K. Tamura, T. Taguchi, S. Yamamoto, A. Matsumoto, K. Akaoka and I. Wakaida, "Fiber-optic remote LIBS of materials in environment of high-dose radiation", 2nd Asian Symposium on Laser Induced Breakdown Spectroscopy (ASLIBS2017), O-31, [Tokushima, Japan] (2017/08). **G, 3-07**
- 4) T. Taguchi, S. Yamamoto and H. Oba, "Synthesis of new-structured carbon nanomaterials inside silicon carbide nanotubes by ion irradiation-induced changes", Abstr. 15th Int. Conf. Adv. Mater. (IUMRS-ICAM 2017), D1-P28-004, [Kyoto, Japan] (2017/08). **T, I, 1-22**
- Press-TV**
- 1) "放射線環境中のセラミックスがもつ自己修復能力の発見〜セラミックスの表面を観察する新しい手法による成果〜", プレス発表: 電気新聞, 日刊工業新聞, 日経産業新聞に掲載 (2017/10/30).

P1-9 Advanced Functional Polymer Materials Research Group

Papers

- 1) T. Hamada, S. Hasegawa and Y. Maekawa, "Control of Radiation/Living Graft Polymerization in the Solid State", *Macromol. Chem. Phys.*, **218**, 1700346 (2017). **G**
- 2) K. Yoshimura, Y. Zhao, S. Hasegawa, A. Hiroki, Y. Kishiyama, H. Shishitani, S. Yamaguchi, H. Tanaka, S. Koizumi, M. Appavou, A. Radulescu, D. Richter and Y. Maekawa, "Imidazolium-Based Anion Exchange Membranes for Alkaline Anion Fuel Cells: (2) Elucidation of the Ionic Structure and its Impact on Conducting Properties", *Soft Matter*, **13**, 8463-73 (2017). **G, 1-26**
- 3) 吉村 公男, 前川 康成, "アルカリ型燃料電池用アニオン伝導電解質膜の開発", *Isotope News*, **754**, 32-35 (2017). **G, 1-26**
- 4) 深谷 敦子, 太田 優子, 飯村 伸明, 立野 晃, 高橋 克巳, 前川 康成, "PEEK をベースとしたグラフト型電解質膜の電気化学装置への適用", *化学工業*, **69**, 52-57 (2018). **G**
- 5) 廣木 章博, "重粒子線治療用ポリマーゲル線量計の開発", *Isotope News*, **752**, 16-19 (2017). **G, E**
- 6) 廣木 章博, 田口 光正, "シート状ポリマーゲル線量計材料による 3 次元線量分布評価", *医学物理*, **37**, 181-85 (2017). **G, E**
- 7) J. F. Madrid, Y. Ueki, L. V. Abad, T. Yamanobe, N. Seko, "RAFT-mediated graft polymerization of glycidyl methacrylate in emulsion from polyethylene/polypropylene initiated with gamma-radiation", *J. Appl. Polym. Sci.* **134**, 45270 (2017). **G**
- 8) J. Chen and N. Seko, "Effects of RAFT agent on the chloromethylstyrene polymerizations in a simultaneous radiation grafting system", *Polymers*, **9**, 307 (2017). **G, 1-31**
- 9) N. Seko, H. Hoshina, N. Kasai, T. Shibata, S. Saiki and Y. Ueki, "Development of a water purifier for radioactive cesium removal from contaminated natural water by radiation-induced graft polymerization", *Radiat. Phys. Chem.*, **143**, 33-37 (2018). **E**
- 10) Y. Ueki, S. Saiki, H. Hoshina, and N. Seko, "Biodiesel fuel production from waste cooking oil using radiation-grafted fibrous catalyst", *Radiat. Phys. Chem.*, **143**, 41-46 (2018). **E, 1-29**
- 11) 佐伯 誠一, 瀬古 典明, "高分子への放射線照射効果", *RADIOISOTOPES*, **66**, 469-77 (2017). **E, G**
- Proceedings**
- 1) Y. Maekawa, K. Yoshimura, K. Takeuchi, A. Hiroki, S. Watanabe, T. Hagiwara, H. Shishitani, S. Yamaguchi and H. Tanaka, "Alkaline Durable Anion-Conducting Electrolyte Membranes Prepared by Radiation Induced Grafting of 2-Methyl-4-vinylimidazole for Non-Platinum Direct Hydrazine Hydrate Fuel Cells", *ECS Transactions*, **80**, [National harbor, USA] (2017/10). **G**
- 2) H. C. Yu, K. Yoshimura, Y. Zhao, A. Hiroki, H. Shishitani, S. Yamaguchi, H. Tanaka and Y. Maekawa, "Synthesis, Characterization, and Alkaline Stabilities of p-(2-imidazoliumyl) Styrene-Grafted Anion-Conducting Electrolyte Membranes Prepared by Radiation-Induced Grafting for Fuel Cells", Abstr. 232nd ECS Meet., I01E-1623, [National Harbor, USA] (2017/10). **G**
- 3) S. Hasegawa, S. Sawada, Y. Maekawa, S. Azami, T. Hagiwara, "Development of hydrogen permselective membrane by using radiation-induced graft polymerization", Abstr. ICOM 2017, P1.150, [San Francisco, USA] (2017/07). **G, 1-24**
- 4) Y. Zhao, K. Yoshimura, Y. Maekawa, "Using small angle scattering method to reveal the required structure for anion exchange fuel cell membranes with high performance", Abstr. Int. Conf. Neutron Scattering 2017, TuP 124, [Daejeon, Korea] (2017/07). **G**
- 5) S. Sawada, Y. Maekawa, "Preparation of novel bipolar membranes by radiation-induced asymmetric grafting technique for fuel cell application", IUMRS-ICAM 2017, Abstr. A7-O28-011, [Kyoto, Japan] (2017/08). **G, 1-25**
- 6) H. C. Yu, K. Yoshimura, H. Shishitani, S. Yamaguchi, H. Tanaka, Y. Maekawa, "p-(2-imidazoliumyl) Styrene-Grafted Anion-Conducting Electrolyte Membranes Prepared by Radiation-Induced Grafting for Fuel Cell", IUMRS-ICAM 2017, Abstr. A7-O28-014, [Kyoto, Japan] (2017/08). **G**
- 7) T. Hamada, K. Yoshimura, A. Hiroki, Y. Maekawa, "Synthesis and Characterization of Aniline-Containing Anion-Conducting Polymer Electrolyte Membranes by Radiation-Induced Graft Polymerization", IUMRS-ICAM 2017, Abstr. A7-O28-15, [Kyoto, Japan] (2017/08). **G**
- 8) K. Takeuchi, K. Yoshimura, A. Hiroki, Y. Maekawa, "Alkaline-durable Anion-conducting Electrolyte Membranes Containing Poly(4-vinyl-2-methyl-imidazole) Prepared by Radiation-induced Grafting", IUMRS-ICAM 2017, Abstr. A7-P30-019, [Kyoto, Japan] (2017/08). **G**
- 9) S. Sawada, M. Yasukawa, M. Higa, Y. Maekawa, "Preparation of cation and anion exchange membranes for reverse electro dialysis by radiation-induced grafting method", Abstr. 5th Int. Conf. Nanotech. Mater. Sci., P 56, [Dubai, UAE] (2017/10). **G, 1-25**
- 10) 吉村 公男, H. C. Yu, ザオ ユエ, 廣木 章博, 猪谷 秀幸, 岸山 佳央, 山口 進, 田中 裕久, 前川 康成, "放射線グラフト型アニオン伝導電解質膜の燃料電池特性と階層構造の関係", 第 60 回放射線化学討論会, 要旨集 3-O-10, [産総研・筑波] (2017/09). **G, 1-26**

- 11) 澤田 真一, 安川 政宏, 比嘉 充, 前川 康成, “逆電気透析発電用放射線グラフト陽イオン交換膜の水・イオン輸送特性”, 2017 年 電気化学秋季大会, 要旨集 2K04, [長崎大・長崎] (2017/09). **G, 1-25**
- 12) 澤田 真一, 後藤 光暁, 越川 博, 喜多村 茜, 比嘉 充, 八巻 徹也, “重イオンビームグラフト法で作製したカチオン・アニオン交換膜の輸送特性評価と海水電気透析への応用”, 日本原子力学会 2018 年春の年会, 要旨集 2107, [大阪大・吹田] (2018/03). **G, 1-25**
- 13) J. F. Madrid, L. V. Abad, Y. Ueki, T. Yamanobe and N. Seko, “Functionalization of PE/PP with oxirane groups via RAFT-mediated gamma-radiation induced graft polymerization of emulsified glycidyl methacrylate”, 32nd Philippine Chemistry Congress, OC-04, [Palawan, Philippines] (2017/05). **G**
- 14) 瀬古 典明, “放射線(量子ビーム)加工技術を用いた機能性材料の開発”【招待講演】, 第 106 回複合材料懇話会, [群馬大・桐生] (2017/06). **E, G**
- 15) 林 菜月, 陳 進華, 濱田 崇, 大道 正明, 瀬古 典明, “ポリスチレン薄膜上の放射線グラフトブランのナノ構造観察”, 第 66 回高分子討論会, 要旨集 1Pb024, [愛媛大・松山] (2017/09). **E**
- 16) J. F. Madrid, L. V. Abad, Y. Ueki, T. Yamanobe and N. Seko, “RAFT-mediated polymerization in emulsion phase: gamma- and electron-beam initiated grafting”, 第 66 回高分子討論会, 要旨集 1Pf008, [愛媛大・松山] (2017/09). **G**
- 17) 陳 進華, 瀬古 典明, 林 菜月, “クロロメチルスチレンの ETFE フィルムへの同時グラフト重合に及ぼす RAFT 剤の影響”, 第 66 回高分子討論会, 要旨集 2Pf028, [愛媛大・松山] (2017/09). **G, 1-31**
- 18) 鈴井 伸郎, 柴田 卓弥, 尹 永根, 保科 宏行, 藤巻 秀, 瀬古 典明, 河地 有木, “植物体内のセシウム動態を可視化するポジロン放出トレーサの開発”, 日本土壌肥科学会 2017 年度仙台大会, 要旨集 P4-3-1, [東北大・仙台] (2017/09). **C**
- 19) J. Chen, N. Hayashi and N. Seko, “RAFT polymerization in simultaneous radiation grafting of chloromethylstyrene onto ETFE films”, Proc. 15th Pacific Polymer Conf. (PPC-15), PS4-06, [Xiamen, China] (2017/12). **G, 1-31**
- 20) N. Seko, V. T. Quang, N. Hayashi, Y. Ueki and J. Chen, “Effect of alcohol on radiation emulsion grafting of GMA onto PE nonwoven fabrics”, Proc. 15th Pacific Polymer Conf. (PPC-15), PS4-12, [Xiamen, China] (2017/12). **E**
- 21) N. Hayashi, J. Chen, Y. Ueki and N. Seko, “Novel separation of trivalent and hexavalent chromium by fibrous graft adsorbent”, Proc. 15th Pacific Polymer Conf. (PPC-15), PS8-04, [Xiamen, China] (2017/12). **E**
- 22) 大場 弘則, 佐伯 盛久, 瀬古 典明, “Cs 吸着材のレーザー誘起ブレイクダウン分光分析”, 第 14 回茨城地区分析技術交流会, [いばらき量子ビーム研究センター・東海村] (2017/12). **E, 3-07**
- 23) 濱田 崇, 保科 宏行, 瀬古 典明, “水中のホウ素を除去可能な水不溶性グルカミン誘導体の開発”, 第 52 回日本水環境学会年会, 要旨集 P-E04, [北海道大・札幌] (2018/03). **G**
- 24) 保科 宏行, 笠井 昇, 瀬古 典明, 物部 長順, 加藤 耕一, “電子線グラフト吸着材とばね式フィルターを融合させたホウ素除去技術の開発”, 第 52 回日本水環境学会年会, 要旨集 P-E07, [北海道大・札幌] (2018/03). **E, 1-30**

Patents

- 1) 猪谷 秀幸, 岸山 佳央, 阿部 寛樹, 山口 進, 吉村 公男, 趙 躍, 廣木 章博, 前川 康成, “陰イオン交換樹脂およびアルカリ型燃料電池用電解質膜” 出願 2017-173786 (2017/09/11).
- 2) 田口 光正, 廣木 章博, 木村 敦, 大山 智子, 中島 健吾, 青木 伊知男, 村山 周平, “MRI 造影剤、及び MRI 造影剤の製造方法” 出願 2017-116241 (2017/06/13).
- 3) 瀬古 典明, 天田 春代, 保科 宏行, “吸着材の製造方法”, 登録 6165431 (2017/06/30). **E, G**
- 4) 瀬古 典明, 玉田 正男, 佐伯 誠一, “金属捕集材”, 登録 6300340 (2018/03/09). **E, G**
- 5) 濱田 崇, 保科 宏行, 瀬古 典明, “グルカミン誘導体, グルカミン誘導体からなる金属吸着剤, グルカミン誘導体からなる金属吸着剤を備える金属抽出装置, 金属抽出キット”, 出願 2018-040662 (2018/03/07). **G**
- 6) 瀬古 典明, 保科 宏行, 笠井 昇, “グラフトセルロースパウダー及びこれを用いたろ過方法”, 出願 2018-042450 (2018/03/08). **E, G**

P2-1 Ion Beam Mutagenesis Research Project

Papers

- 1) K. Satoh, H. Arai, T. Sanzen, Y. Kawaguchi, H. Hayashi, S. Yokobori, A. Yamagishi, Y. Oono and I. Narumi, “Draft genome sequence of the radioresistant bacterium *Deinococcus aerius* TR0125, isolated from the high atmosphere above Japan”, Genome Announc., **6** (9), e00080-18 (2018). **C, 2-23**
- 2) Y. Yokota and A. N. Sakamoto, “The moss *Physcomitrella patens* is hyperresistant to DNA double-strand breaks induced by γ -irradiation”, Genes (Basel), **9**, 76 (2018). **G, 2-02**
- 3) A. Miyagi, S. Kitano, Y. Oono, Y. Hase, I. Narumi, M. Yamaguchi, H. Uchimiya and M. Kawai-Yamada, “Evaluation of metabolic changes in oxalate-rich plant *Rumex obtusifolius* L. caused by ion beam irradiation”, Plant Physiol. Biochem., **122**, 40-5 (2018). **C**
- 4) Y. Hase, K. Satoh, S. Kitamura and Y. Oono, “Physiological status of plant tissue affects the frequency and types of mutations induced by carbon-ion irradiation in *Arabidopsis*”, Sci. Rep., **8**, 1394 (2018). **C, 2-16**
- 5) Y. Akita, S. Kitamura, R. Mikami and H. Ishizaka, “Identification of functional flavonol synthase genes from fragrant wild cyclamen (*Cyclamen purpurascens*)”, J. Plant Biochem. Biotechnol., **27**, 147-55 (2018). **N**
- 6) S. Mikuriya, M. Kasai, K. Nakashima, Natasia, Y. Hase, T. Yamada, J. Abe and A. Kanazawa, “Frequent generation of mutants with coincidental changes in multiple traits via ion-beam irradiation in soybean”, Genes Genet. Syst., **92**, 153-61 (2017). **C**
- 7) A. N. Sakamoto, V. T. T. Lan, S. Fujimoto, S. Matsunaga and A. Tanaka, “An ion beam-induced *Arabidopsis* mutant with marked chromosomal rearrangement”, J. Radiat. Res., **58**, 772-81 (2017). **C**
- 8) 横田 裕一郎, “植物細胞と動物細胞における DNA 損傷の定量と放射線応答の比較”, 放射線と産業, **143** 号, 11-14 (2017). **G, 2-02, 2-15**

Proceedings

- 1) 佐藤 勝也, “産業微生物のインビーム育種”, 理研シンポジウム「イオンビーム品種改良プラットフォームの形成」, 要旨集 5, [理化学研究所・和光] (2018/01). **C, 2-23**
- 2) 長谷 純宏, 佐藤 勝也, 北村 智, 大野 豊, “炭素イオン照射したシロイヌナズナの乾燥種子と幼苗に生じた突然変異の比較”, 理研シンポジウム「イオンビーム品種改良プラットフォーム

- ムの形成」, 要旨集 4, [理化学研究所・和光] (2018/01).
C, 2-14
- 3) 大野 豊, “加速器施設・生物照射装置とイオンビーム変異誘発研究”, 理研シンポジウム「イオンビーム品種改良プラットフォームの形成」, 要旨集 3, [理化学研究所・和光] (2018/01).
C, 2-10
- 4) 新家 弘也, 長谷 純宏, 大野 豊, 鈴木 石根, “重イオンビーム照射によるアルケノン高生産藻の育種”, 関東学院大学 理工/建築・環境学会研究発表講演会, 発表講演論文集 10-11, [関東学院大・横浜] (2017/11).
C, 2-12
- 5) Natasia, S. Mikuriya, M. Kasai, K. Nakashima, Y. Hase, T. Yamada, J. Abe and A. Kanazawa, “Ion-beam irradiation frequently induces simultaneous alterations of multiple traits in soybean”, 日本育種学会第132回講演会, プログラム 317 [岩手大・盛岡] (2017/10).
C
- 6) 青山 直子, 納富 麻子, 松尾 洋一, 岡部 春奈, 古藤田 信博, 長谷 純宏, 田中 義樹, “放射線育種を利用した機能性成分含有カンキツの育成 (第 3 報) 照射育成実生集団における葉中ノビレチン含有量”, 九州農業研究発表会, 果樹部会要旨集 1, [佐賀大・佐賀] (2017/09).
C
- 7) 長谷 純宏, 佐藤 勝也, “生物試料に対するクラスターイオン照射効果の検討”, かけはし:TIA 連携プログラム探索推進事業シンポジウム「準相対論的巨大大イオンビームが招く世界」, 4-1, [つくば国際会議場・つくば] (2017/09).
T, 2-16
- 8) 宮城 敦子, 西丸 拓也, 針谷 のぞみ, 大野 豊, 長谷 純宏, 長野 稔, 石川 寿樹, 山口 雅利, 川合 真紀, “イオンビーム育種による低シュウ酸イネの作出”, 第 35 回日本植物細胞分子生物学会大会, 1B-02, [大宮ソニックシティー・さいたま] (2017/08).
C
- 9) H. Araie, Y. Hase, Y. Oono, I. Suzuki and Y. Shiraiwa, “Breeding of alkenones producing haptophyte using heavy ion-beam irradiation”, Abstr. 11th ASIA-PACIFIC MARINE BIOTECHNOLOGY CONFERENCE (APMBC) 2017, 7, [Honolulu, USA] (2017/05).
C, 2-12
- 10) 平田 翔也, 鳴海 一成, 北村 智, 佐藤 勝也, 大野 豊, “植物色素合成遺伝子 *Ban*, *TT4*, *TT8* を利用した突然変異頻度を簡便に推定する実験系の構築”, 第 59 回 日本植物生理学会年会, プログラム P402, [札幌コンベンションセンター・札幌] (2018/03).
C, 2-11
- 11) 大野 豊, 市田 裕之, 野澤 樹, 森田 竜平, 加藤 浩, 阿部 知子, 長谷 純宏, “イネ炭素イオンビーム誘発変異体のエキソーム解析”, 第 59 回 日本植物生理学会年会, プログラム P398, [札幌コンベンションセンター・札幌] (2018/03).
C, 2-10
- 12) 平田 翔也, 北村 智, 佐藤 勝也, 鳴海 一成, 大野 豊, “植物色素合成遺伝子に着目した遺伝子発現と変異誘発頻度の関係を調べるための検出系の開発”, 第 40 回日本分子生物学会年会, プログラム 2P-1216, [神戸ポートアイランド・神戸] (2017/12).
C, 2-11
- 13) 横田 裕一郎, 坂本 綾子, “モデル植物ヒメツリガネゴケは 100 Gy のガンマ線照射後も増殖能が全く低下しない”, 第 60 回日本放射線影響学会大会, 要旨集 P164, [京葉銀行文化プラザ・千葉] (2017/10).
C, 2-15
- 14) 長谷 純宏, 佐藤 勝也, 北村 智, 大野 豊, “炭素イオンビームを照射したシロイヌナズナ乾燥種子と幼苗に生じた突然変異の比較”, 第 60 回日本放射線影響学会大会, 要旨集 P136, [京葉銀行文化プラザ・千葉] (2017/10).
C, 2-14
- 15) K. Satoh, “Dreamy future by ion beam breeding of sake yeast and industrial microorganisms”, IUMRS-ICAM 2017 (15th Int. Conf. Adv. Mater.), D1-I29-006, [Kyoto, Japan] (2017/08).
C, 2-23
- ### Patents
- 1) 長谷川 徹, 伊藤 健二, 新井 和俊, 渡邊 孝政, 遠山 宏和, 平松 裕邦, 鈴木 良地, 二村 幹雄, 奥村 義秀, 辻 孝子, 近藤 満治, 石川 高史, 青木 献, 竹内 良彦, 野村 浩二, 小久保 恭明, 山本 雅春, 西尾 譲一, 加藤 博美, 浅見 逸夫, 長谷 純宏, 野澤 樹, “きく品種「舞夢白」”, 出願 32605 (2017/11/24).
- 2) 長谷川 徹, 伊藤 健二, 新井 和俊, 渡邊 孝政, 遠山 宏和, 平松 裕邦, 鈴木 良地, 二村 幹雄, 奥村 義秀, 辻 孝子, 近藤 満治, 石川 高史, 青木 献, 竹内 良彦, 野村 浩二, 小久保 恭明, 山本 雅春, 西尾 譲一, 加藤 博美, 浅見 逸夫, 長谷 純宏, 野澤 樹, “きく品種「舞夢紫」”, 出願 32606 (2017/11/24).
- 3) 長谷川 徹, 伊藤 健二, 新井 和俊, 渡邊 孝政, 遠山 宏和, 平松 裕邦, 二村 幹雄, 奥村 義秀, 辻 孝子, 近藤 満治, 石川 高史, 青木 献, 竹内 良彦, 野村 浩二, 小久保 恭明, 山本 雅春, 西尾 譲一, 加藤 博美, 鬼頭 温文, 浅見 逸夫, 長谷 純宏, 野澤 樹, “きく品種「舞夢黄」”, 出願 32607 (2017/11/24).
- 4) 木戸 君枝, 永吉 実孝, 吉永 竜次, 今給黎 征朗, 仁田尾 学, 田之頭 優樹, 白尾 史, 長谷 純宏, 野澤 樹, 大野 豊, “きく品種「立神」”, 登録 26327 (2017/11/16).
- 5) 木戸 君枝, 永吉 実孝, 吉永 竜次, 今給黎 征朗, 仁田尾 学, 田之頭 優樹, 白尾 史, 長谷 純宏, 野澤 樹, 大野 豊, “きく品種「冬馬」”, 登録 26326 (2017/11/16).
- 6) 石坂 宏, 近藤 恵美子, 亀有 直子, 田中 淳, 長谷 純宏, “シクラメン「みやびの舞」”, 登録 26250 (2017/09/28).
- ### Press・TV
- 1) “華麗な花びら「かがり弁」の輪ぎく3品種を開発しました～ブライダルなど輪ぎくの新たな需要を開拓します～”, プレス発表: 朝日新聞, 中日新聞, 上毛新聞, 東愛知新聞, 化学工業日報, 農業新聞に掲載 (2017/11/24).
C
- 2) “イオンビームが植物の染色体構造をがらりと変えることを発見 - 植物ゲノムはしなやかに進化を目指す -”, プレス発表: 化学工業日報, 科学新聞, 時事ドットコムに掲載 (2017/06/13).
C

P2-2 Microbeam Radiation Biology Research Project

Papers

- 1) M. Suzuki, Y. Hattori, T. Sakashita, Y. Yokota, Y. Kobayashi, T. Funayama, “Region-specific irradiation system with heavy-ion microbeam for active individuals of *Caenorhabditis elegans*”, *J. Radiat. Res.* **58**(6), 881-86 (2017).
C, 2-07
- 2) T. Yasuda, M. Kamahori, K. Nagata, T. Watanabe-Asaka, M. Suzuki, T. Funayama, H. Mitani and S. Oda. “Abscopal activation of microglia in embryonic fish brain following targeted irradiation with heavy-ion microbeam”, *Int. J. Mol. Sci.* **18**, 1428 (2017); doi:10.3390/ijms18071428.
C, 2-06
- 3) 保田 隆子, 舟山 知夫, 三谷 啓志, 尾田 正二, “メダカ胚で明らかになった放射線により活性化された脳内免疫細胞ミクログリアの動態”, 放射線生物研究, *Radiat. Biol. Res. Commun.* **53**, 31 (2018).
C, 2-06
- 4) K. Saito, T. Funayama, Y. Yokota, T. Murakami, and Y. Kobayashi, “Histone deacetylase inhibitors sensitize murine B16F10 melanoma cells to carbon ion irradiation by inducing G1

- phase arrest”, *Biol. Pharm. Bull.* **40**, 844-51 (2017). C
- 5) Z. Soh, M. Suzuki, and T. Tsuji, “An estimation method for environmental friction based on body dynamic model of *Caenorhabditis elegans*”, *J. Robot. Network Artificial Life*, **4**, 32-40 (2017). N
- 6) N. Autsavapromporn, T. Konishi, C. Liu, I. Plante, T. Funayama, N. Usami, N. E. I. Azzam, and M. Suzuki, “A correlation of long term effects and radiation quality in the progeny of bystander cells after microbeam radiations: The experimental study of radiotherapy for cancer risk mitigation”, *J. Phys. Conf. Series*, **860** 012026 (2017). C

Proceedings

- 1) T. Yasuda, T. Funayama, H. Mitani and S. Oda, “Abscopal Activated Immune Cell of Microglia Following Targeted Irradiation with Heavy-Ion Microbeam in Embryonic Fish Brain” **[Invited talk]**, 63rd Annu. Int. Meet. Radiat. Res. Soc., Symp. Radiat. Neurology, [Cancun, Mexico] (2017/10). C, 2-06

P2-3 Medical Radioisotope Application Research Project

Papers

- 1) Y. Ohshima, H. Sudo, S. Watanabe, K. Nagatsu, A. Tsuji, T. Sakashita, Y. M. Ito, K. Yoshinaga, T. Higashi, N. S. Ishioka, “Antitumor effects of radionuclide treatment using α -emitting *meta*-²¹¹At-astato-benzylguanidine in a PC12 pheochromocytoma model”, *Eur. J. Nucl. Med. Mol. Imaging*, **45**, 999-1010 (2018). C

- 2) A. Shinohara, H. Hanaoka, T. Sakashita, T. Sato, A. Yamaguchi, N. S. Ishioka, Y. Tsushima, “Rational evaluation of the therapeutic effect and dosimetry of auger electrons for radionuclide therapy in a cell culture model”, *Annal. Nucl. Med.*, **32** (2), 114-22 (2018). C

Proceedings

- 1) 須郷 由美, 大島 康宏, 山口 藍子, 花岡 宏史, 塚田 和明, 橋本 和幸, 川端 方子, 佐伯 秀也, 永井 泰樹, 石岡 典子, “⁶⁴Cu イオンのがん診断/治療用薬剤としての有用性の検討”, 第 17 回放射線医薬品・画像診断薬研究会/第 1 回日本核医学会分科会放射性薬品科学研究会, 要旨集 B-2, [京都市勧業館「みやこめっせ」・京都] (2017/09). C
- 2) 橋本 和幸, 川端 方子, 佐伯 秀也, 佐藤 俊一, 塚田 和明,

須郷 由美, 永井 泰樹, 初川 雄一, 石岡 典子, “重陽子照射で発生する加速器中性子によって製造するがん治療用 ⁶⁷Cu の比放射能評価”, 2017 放射化学学会年会・第 61 回放射化学討論会, 要旨集 P27, [筑波大・つくば] (2017/09). C

- 3) Y. Nagao, M. Yamaguchi, S. Watanabe, N. S. Ishioka, N. Kawachi, H. Watabe, “Astatine-211 imaging by a Compton camera for targeted α -particle radiotherapy”, 2017 IEEE NSS/MIC, [Atlanta, USA] (2017/10). C, 2-32

Patents

- 1) 石岡 典子, 近藤 浩夫, 渡辺 茂樹, “放射性同位体の製造方法, 放射性同位体製造装置”, 特願 2017-210442 (2017/10/31). C
- 2) 花岡 宏史, 山口 藍子, 中島 崇仁, 樋口 徹也, 対馬 義人, 荒野 泰, 鈴木 博元, 石岡 典子, 大島 康宏, “放射性フッ素標識化合物”, 特願 2017- 212377 (2017/11/02). C, 2-41
- 3) 荒野 泰, 上原 知也, 鈴木 博元, 田中 浩士, 石岡 典子, 渡辺 茂樹, “放射性医薬”, 特願 2018-15904 (2018/01/31). C, 2-41

P2-4 Generation of Radioisotopes with Accelerator Neutrons Research Project

Papers

- 1) F. Minato, K. Tsukada, N. Sato, S. Watanabe, H. Saeki, M. Kawabata, S. Hashimoto, Y. Nagai, “Measurement and Estimation of the ⁹⁹Mo Production Yield by ¹⁰⁰Mo(*n*, 2*n*)⁹⁹Mo”, *J. Phys. Soc. Jpn.* **86**, 114803-1~6 (2017). C
- 2) Y. Nagai, Y. Nakahara, M. Kawabata, Y. Hatsukawa, K. Hashimoto, H. Saeki, S. Motoishi, A. Ohta, T. Shiina, Y. Kawauchi, “Quality of ^{99m}TcO₄⁻ from ⁹⁹Mo Produced by ¹⁰⁰Mo(*n*, 2*n*)⁹⁹Mo”, *J. Phys. Soc. Jpn.* **86**, 053202-1~4 (2017). C
- 3) M. Kawabata, S. Motoishi, H. Saeki, K. Hashimoto, Y. Nagai, “Recovery Efficiency of ¹⁰⁰MoO₃ Irradiated by Accelerator Neutrons”, *J. Phys. Soc. Jpn.* **86**, 053201-1~3 (2017). C
- 4) I. Nishinaka, A. Yokoyama, K. Washiyama, H. Makii, K. Hahsimoto, “Production of iodine radionuclides using ⁷Li ion beams”, *J. Radioanal. Nucl. Chem.*, **314**, 1947-65 (2017). N
- 5) 永井 泰樹, 塚田 和明, “がん診断と治療の両方に適した ⁶⁷Cu の新製造法と利用”, *Isotope News*, **753**, 28-32 (2017). C
- 6) 川端 方子, 永井 泰樹, “がん診断と治療用放射性銅-67 医薬品の国産化に向けて”, 市民のためのがん治療の会, シリーズ「がん治療の今」, No.322 20170502, http://www.com-info.org/medical.php?ima_20170502_kawabata_nagai. C
- 7) K. Hirose, K. Nishio, H. Makii, I. Nishinaka, S. Ohta, T. Nagayama, N. Tamura, S. Goto, A. N. Andreyev, M. J. Vermeulen, S. Gillespie, C. Barton, A. Kimura, H. Harada, S. Meigo, S. Chiba, T. Ohtsuki, “Simultaneous measurement of neutron-induced fission and capture cross sections for ²⁴¹Am at

neutron energies below fission threshold”, *Nucl. Instrum. Meth. Phys. Res. A*, **856**, 133-38 (2017). N

- 8) S. Q. Yan, Z. H. Li, Y. B. Wang, K. Nishio, M. Lugaro, A. I. Karakas, H. Makii, P. Mohr, J. Su, Y. J. Li, I. Nishinaka, K. Hirose, Y. L. Han, R. Orlandi, Y. P. Shen, B. Guo, S. Zeng, G. Lian, Y. S. Chen, and W. P. Liu, “The ⁹⁵Zr(*n*, γ)⁹⁶Zr cross section from the surrogate ratio method and its effect on s-process nucleosynthesis”, *Astrophys. J.* **848**, 98-1~8 (2017). N
- 9) K. Hirose, K. Nishio, S. Tanaka, R. Leguillon, H. Makii, I. Nishinaka, R. Orlandi, K. Tsukada, J. Smallcombe, M. J. Vermeulen, S. Chiba, Y. Aritomo, T. Ohtsuki, K. Nakano, S. Araki, Y. Watanabe, R. Tatsuzawa, N. Takaki, N. Tamura, S. Goto, I. Tsekhanovich, A. N. Andreyev, “Role of multichance fission in the description of fission-fragment mass distributions at high energies”, *Phys. Rev. Lett.* **119**, 222501-1~6 (1997). N

Proceedings

- 1) I. Nishinaka, K. Hashimoto, H. Makii, “Development of a ²¹¹Rn/²¹¹At generator based on dry-chemistry”, Abstr. 10th Int. Symp. Targeted Alpha Therapy, P93, [Kanazawa, Japan] (2017/05-06). N
- 2) I. Nishinaka, K. Hashimoto, H. Makii, “²¹¹Rn/²¹¹At generator based on dry- chemistry”, Abstr. 9th Int. Conf. Isot. & Expo, 9ICI, P12 [Doha, Qatar] (2017/11). N
- 3) Y. Shin, S. Ooe, K. Murakami, T. Taniguchi, E. Maeda, N. Yamada, K. Washiyama, A. Yokoyama, I. Nishinaka, “Wet chemistry of radon and astatine for the development of a

- ²¹¹Rn/²¹¹At generator”, Abstr. 10th Int. Symp. Targeted Alpha Therapy, P94, [Kanazawa, Japan] (2017/05-06). **N**
- 4) 橋本 和幸, 川端 方子, 佐伯 秀也, 佐藤 俊一, 塚田 和明, 須郷 由美, 永井 泰樹, 初川 雄一, 石岡 典子, “重陽子照射で発生する加速器中性子によって製造するがん治療用⁶⁷Cuの比放射能評価”, 2017 放射化学学会年会・第 61 回放射化学討論会, 要旨集 P27, [筑波大・つくば] (2017/09). **C**
- 5) 川端 方子, 中原 勇人, 初川 雄一, 本石 章司, 佐伯 秀也, 太田 朗生, 椎名 孝行, 河内 幸正, 橋本 和幸, 永井 泰樹, “加速器中性子により製造された^{99m}Moから分離した^{99m}Tc溶液の品質評価”, 2017 放射化学学会年会・第 61 回放射化学討論会, 要旨集 P19, [筑波大・つくば] (2017/09). **C**
- 6) 初川 雄一, 塚田 和明, 橋本 和幸, 佐藤 哲也, 浅井 雅人, 豊嶋 厚史, 永井 泰樹, 谷森 達, 園田 伸也, 株木 重人, 木村 寛之, 高田 敦史, 水本 哲也, 早川 岳人, 高木 誠也, “コンプトン (ETCC) 撮像用テクネチウム同位体製造研究”, 2017 放射化学学会年会・第 61 回放射化学討論会, 要旨集 1B05, [筑波大・つくば] (2017/09). **N**
- 7) 西中 一郎, 橋本 和幸, 牧井 宏之, “乾式化学に基づく²¹¹Rn/²¹¹At ジェネレータ開発”, 2017 放射化学学会年会・第 61 回放射化学討論会, 要旨集 1B08, [筑波大・つくば] (2017/09). **N**
- 8) 瀬川 麻里子, 西中 一郎, 藤 暢輔, 井上 徹, “核医学用²¹¹At生成の効率化に向けたカメラ型アルファ線イメージング”, 2017 放射化学学会年会・第 61 回放射化学討論会, 要旨集 1B11, [筑波大・つくば] (2017/09). **N**
- 9) 新 裕喜, 川崎 康平, 山田 記大, 横山 明彦, 鷲山 幸信, 西中 一郎, “²¹¹Rn - ²¹¹At ジェネレーター開発のためのアスタチン溶媒抽出の研究”, 2017 放射化学学会年会・第 61 回放射化学討論会, 要旨集 P13, [筑波大・つくば] (2017/09). **N**
- 10) 須郷 由美, 大島 康宏, 山口 藍子, 花岡 宏史, 塚田 和明, 橋本 和幸, 川端 方子, 佐伯 秀也, 永井 泰樹, 石岡 典子, “^{64/67}Cu イオンのがん診断/治療用薬剤としての有用性の検討”, 第 17 回放射線医薬品・画像診断薬研究会/第 1 回日本核医学会分科会放射性薬品科学研究会, 要旨集 B-2, [京都市勧業館「みやこめっせ」・京都] (2017/09). **C**

P2-5 Radiotracer Imaging Research Project

Papers

- 1) Y. Miyoshi, K. Hidaka, T. Okayasu, D. Yasutake, M. Kitano, “Effects of local CO₂ Enrichment on strawberry cultivation during the winter season”, *Environ. Control Biol.*, **55**, 165-70 (2017). **N**
- 2) 平野 裕之, 高木 賢二, 福井 久智, 太田 祐士, 田中 真弓, 秦野 歳久, 栗田 圭輔, 山口 充孝, 河地 有木, 大間知 聡一郎, 斎藤 英之, 平塚 一, “排水全量の放射能モニタリング装置の実用化”, 鹿島技術研究所年報, **65**, 153-58 (2017). **N**
- 3) T. Yabe, M. Komori, T. Toshito, M. Yamaguchi, N. Kawachi and S. Yamamoto, “Estimation and correction of produced light from prompt gamma photons on luminescence imaging of water for proton therapy dosimetry”, *Phys. Med. Biol.*, **63**, 04NT02, [8 pages] (2018). **N, 2-32**
- 4) M. Yamaguchi, Y. Nagao, K. Ando, S. Yamamoto, M. Sakai, R. K. Parajuli, K. Arakawa and N. Kawachi, “Imaging of monochromatic beams by measuring secondary electron bremsstrahlung for carbon-ion therapy using a pinhole x-ray camera”, *Phys. Med. Biol.*, **63**, 045016, [12 pages] (2018). **N, 2-32**
- 5) K. Ando, M. Yamaguchi, S. Yamamoto, T. Toshito and N. Kawachi, “Development of a low-energy x-ray camera for the imaging of secondary electron bremsstrahlung x-ray emitted during proton irradiation for range estimation”, *Phys. Med. Biol.*, **62**, 5006-20 (2017). **N, 2-32**
- 6) K. Ando, S. Yamamoto, K. Kurita, N. Suzui, Y.-G. Yin, S. Ishii, N. Kawachi, “Development of a low-energy high resolution X-ray camera for high-energy gamma photon background environments”, *J. Nucl. Sci. Tech.*, **54**, 933-39 (2017). **N**
- 7) K. Kurita, N. Suzui, Y.-G. Yin, S. Ishii, H. Watabe, S. Yamamoto, N. Kawachi, “Development of a Cherenkov light imaging system for studying the dynamics of radiocesium in plants”, *J. Nucl. Sci. Tech.*, **54**, 662-67 (2017). **N**
- 8) N. Suzui, Y.-G. Yin, S. Ishii, H. Sekimoto, N. Kawachi, “Visualization of zinc dynamics in intact plants using positron imaging of commercially available ⁶⁵Zn”, *Plant Meth.*, **13**, 40 (2017). **N**
- 9) A. Kishimoto, J. Kataoka, T. Taya, L. Tagawa, S. Mochizuki, S. Ohsuka, Y. Nagao, K. Kurita, M. Yamaguchi, N. Kawachi, K. Matsunaga, H. Ikeda, E. Shimosegawa and J. Hatazawa, “First demonstration of multi-color 3-D *in vivo* imaging using ultracompact Compton camera”, *Sci. Rep.*, **7**, 2110-1-7 (2017). **N, 2-33**
- 10) T. Taya, J. Kataoka, A. Kishimoto, L. Tagawa, S. Mochizuki, T. Toshito, M. Kimura, Y. Nagao, K. Kurita, M. Yamaguchi and N. Kawachi, “Optimization and verification of image reconstruction for a Compton camera towards application as an on-line monitor for particle therapy”, *J. Instrum.*, **12**, P07015-0~15 (2017). **N, 2-33**
- 11) J. Kataoka, A. Kishimoto, T. Taya, S. Mochizuki, L. Tagawa, A. Koide, K. Sueoka, H. Morita, T. Maruhashi, K. Fujieda, T. Kurihara, M. Arimoto, H. Okochi, N. Katsumi, S. Kinno, K. Matsunaga, H. Ikeda, E. Shimosegawa, J. Hatazawa, S. Ohsuka, T. Toshito, M. Kimura, Y. Nagao, M. Yamaguchi, K. Kurita and N. Kawachi, “Ultracompact Compton camera for innovative gamma-ray imaging”, *Nucl. Instrum. Meth. Phys. Res. A*, **912**, 1-5 (2018). **N, 2-33**
- 12) Y. Nagao, M. Yamaguchi, N. Kawachi and H. Watabe, “Development of a cost-effective Compton camera using a positron emission tomography data acquisition system”, *Nucl. Instrum. Meth. Phys. Res. A*, **912**, 20-23 (2018). **N, 2-33**
- ### Proceedings
- 1) Y. Nagao, M. Yamaguchi, S. Watanabe, N. S. Ishioka, N. Kawachi, H. Watabe, “Astatine-211 imaging by a Compton camera for targeted α -particle radiotherapy”, 2017 IEEE NSS/MIC, [Atlanta, USA] (2017/10). **C, 2-33**
- 2) 鈴木 伸郎, 柴田 卓弥, 尹 永根, 保科 宏行, 藤巻 秀, 瀬古 典明, 河地 有木, “植物体内のセシウム動態を可視化するポジトロン放出トレーサの開発”, 日本土壌肥科学会 2017 年度仙台大会, 要旨集 P4-3-1, [東北大・仙台] (2017/09). **C**
- ### Patent
- 1) 酒井 真理, 中野 隆史, 荒川 和夫, 菊地 美貴子, 山口 充孝, 長尾 悠人, 河地 有木, “粒子線モニタリング装置, 粒子線モニタリング方法, 粒子線モニタリングプログラム”, 出願番号 2017-215079 (2017/11/07). **N**
- ### Press・TV
- 1) 量研・群馬大学・名古屋大学, “粒子線治療に役立つ新たなビーム可視化法を開発～目に見えない陽子線や重粒子線の到

達位置をオンタイムで画像化～”, プレス発表:科学新聞に掲載(2018/02/15). N

- 2) 早稲田大学・大阪大学・量研・浜松ホトニクス, “世界最軽量「手のひらサイズ 580g」医療用ガンマ線可視化カメラを開発 世界初・生体マウスのマルチアングル撮影, 多色高精度 3D 画像を

短時間で撮影可能に”, プレス発表:日本経済新聞朝刊, 科学新聞, 上毛新聞に掲載(2017/05/18).

- 3) NHK スペシャル, “被曝の森 2018”, 2018 年 3 月放映.

P2-6 Radiation and Biomolecular Science Research Project

Papers

- 1) H. Fukunaga, K. Kaminaga, T. Sato, N. Usami, R. Watanabe, K. Butterworth, T. Ogawa, A. Yokoya, and K. M. Prise, “Application of an ex vivo tissue model to investigate radiobiological effects on spermatogenesis”, *Radiat. Res.* **189**, 661-67 (2018). N
- 2) T. Kai, A. Yokoya, M. Ukai, K. Fujii, T. Toigawa, and R. Watanabe, “Significant role of non-thermal equilibrated electrons in the formation of deleterious complex DNA damage”, *Phys. Chem. Chem. Phys.* **20**, 2838-44 (2018). N
- 3) K. Fujii, Y. Izumi, A. Narita, K. Ghose, P. Lopez-Tarifa, A. Touati, R. Spezia, R. Vuilleumier, M. -P. Gaigeot, M. -F. Politis, M. -A. Herve du Penhoat, and A. Yokoya, “Roles of Hydration for Oxidizing Decomposition of 2-deoxy-D-ribose by Ionization of Oxygen K-Shell Electrons”, *Radiat. Res.* **189**, 264-72 (2018). N
- 4) Y. Izumi, K. Matsuo, K. Fujii, A. Yokoya, M. Taniguchi, and H. Namatame, “Circular dichroism spectroscopic study on structural alterations of histones induced by post-translational modifications in DNA damage responses: Lysine-9 methylation of H3”, *J. Radiat. Res.* **59**, 108-15 (2018). N
- 5) 渡辺 立子, 甲斐 健師, 服部 佑哉, “計算機シミュレーションによる放射線生物作用の初期過程の研究”, *RADIOISOTOPES*, **66**, 525-30 (2017). N
- 6) Y. Yonetani, “Solvent-coordinate free-energy landscape view of water-mediated ion-pair dissociation”, *Mol. Phys.*, **115**, 2987-98 (2017). N
- 7) H. Fukunaga, K. T. Butterworth, A. Yokoya, T. Ogawa and K. M. Prise, “Low-dose radiation-induced risk in spermatogenesis”, *Int. J. Radiat. Biol.* **93**, 1291-98 (2017). N
- 8) H. Fukunaga, A. Yokoya, Y. Taki, K. M. Prise, “Radiobiological Implications of Fukushima Nuclear Accident for Personalized Medical Approach”, *Tohoku J. Exp.* **242**, 77-81 (2017). doi: 10.1620/tjem.242.77. N
- 9) 渡辺 立子, “シミュレーションによって推定される放射線誘発 DNA 損傷の特徴”, *放射線と産業*, **143**, 26-30 (2017). N
- 10) A. Yokoya and T. Ito, “Photon-induced Auger Effect in Biological Systems: A Review”, *Int. J. Radiat. Biol.* **93**, 734-56 (2017). N
- 11) Y. Izumi, K. Fujii, S. Yamamoto, K. Matsuo, H. Namatame, M. Taniguchi, and A. Yokoya, “DNA damage response induces structural alterations of histone H3-H4”, *J. Radiat. Res.* **58**, 59-65 (2017). N
- 12) 西久保 開, 泉 雄大, 藤井 健太郎, 松尾 光一, 松本 義久, 横谷 明德, “VUV-CD スペクトル測定による DNA 修復タンパク質 XRCC4 の二次構造解析”, 第 31 回日本放射光学会年会・放射光科学合同シンポジウム, 要旨集 P329, [つくば国際会議場・つくば] (2018/01). N
- 13) 神長 輝一, 浜田 涼, 宇佐美 徳子, 鈴木 啓司, 横谷 明德, “細胞内局所 X 線照射法を用いたミトコンドリアの放射線応答研究”, 第 40 回日本分子生物学会年会, 要旨集 1P-0577, [神戸国際会議場・神戸] (2017/12). N
- 14) Y. Hattori, H. Komiya, A. Yokoya, R. Watanabe, D. Kurabayashi, “A mathematical model of enhanced DNA repair effect on cell survival in radiation-induced adaptive responses”, *Abstr. 17th Int. Symp. Microdosimetry (MICROS2017)*, Oral Presentation, [Venice, Italy] (2017/11). N
- 15) T. Kojima, H. Aihara, Y. Kodashima, H. Makishima, S. Nakiri, S. Takada, H. Shimada, C. Ozga, X. Holzapfel, Ph. Schmidt, C. Küstner-Wetekamm, H. Otto, A. Knie, A. Ehresmann,

- S. Takada, H. Shimada, C. Ozga, X. Holzapfel, Ph. Schmidt, C. Küstner-Wetekamm, H. Otto, A. Knie, A. Ehresmann, A. Yokoya, K. Fujii, Y. Fukuda, M. Ukai, "Novel analytical study for reaction intermediates in the primary radiation interaction of DNA using a synchrotron radiation induced luminescence spectroscopy", Abstr. 17th Int. Symp. Microdosimetry (MICROS2017), Oral Presentation, [Venice, Italy] (2017/11). N
- 16) K. Nishikubo, Y. Izumi, K. Fujii, Y. Matsumoto, A. Yokoya, "Structural Analysis of DNA Repair Protein (XRCC4) Applying Circular Dichroism in an Aqueous Solution", Abstr. 17th Int. Symp. Microdosimetry (MICROS2017), Poster Presentation, [Venice, Italy] (2017/11). N
- 17) A. Yokoya, H. Nakae, Y. Obata, K. Kaminaga, "Visualization of DNA Repair Process in Mammalian Cells Transformed by Plasmid DNA Exposed to X-rays in vitro", Abstr. 17th Int. Symp. Microdosimetry (MICROS2017), Poster Presentation, [Venice, Italy] (2017/11). N
- 18) R. Hamada, R. Ono, K. Kaminaga, Y. Kimura, K. Suzuki, A. Yokoya, "Mitochondrial membrane potential, morphology, and ATP production in mammalian cells exposed to X-rays", Abstr. 17th Int. Symp. Microdosimetry (MICROS2017), Poster Presentation, [Venice, Italy] (2017/11). N
- 19) Y. Hattori, H. Komiya, A. Yokoya, R. Watanabe, D. Kurabayashi, "Computational analysis of bystander signaling in cellular population irradiated with microbeam", 第 55 回日本生物物理学会年会, 予稿集 p166, [熊本大・熊本] (2017/09). N
- 20) 福永 久典, 神長 輝一, 佐藤 卓也, Karl Butterworth, 横谷 明德, 小川 毅彦, Kevin Prise, "精巣組織器官培養法を用いた放射線照射影響の検討と治療への応用", 第 40 回日本分子生物学会年会, 要旨集 4AT18-06, [神戸ポートアイランド・神戸] (2017/12). N
- 21) 横谷 明德, 藤井 健太郎, 島田 紘行, 鶴飼 正敏, 神長 輝一, 大和田 謙二, 町田 晃彦, 西村 由希子, 今岡 達彦, "シンクロトロン放射をツールとする放射線による DNA 損傷と細胞学的応答の研究", 第 40 回日本分子生物学会年会, 要旨集 2AW05-5, [神戸ポートアイランド・神戸] (2017/12). N
- 22) 服部 佑哉, 渡辺 立子, 倉林 大輔, 横谷 明德, "放射線適応応答に関する細胞内シグナリングの数理モデル化", 第 27 回日本数理生物学会年会, 予稿集 S187, [北海道大・札幌] (2017/10). N
- 23) 服部 佑哉, 小宮山 裕人, 倉林 大輔, 横谷 明德, 渡辺 立子, "セルオートマトンをベースとした放射線適応応答解析モデルの構築", 第 30 回自律分散システムシンポジウム, 予稿集 p183, [名城大・名古屋] (2017/01). N
- 24) 鬼澤 美智, 芳賀 芳範, 田中 成典, 鯉淵 誠也, 横谷 明德, "ハロゲン化ピリミジンを含む DNA の放射線増感の電子物性の研究"【招待講演】, 第 60 回日本放射線影響学会大会, 要旨集 P81, [京葉銀行文化プラザ・千葉] (2017/10). N
- 25) 横谷 明德, 神長 輝一, 浜田 涼, 宇佐美 徳子, 鈴木 啓司, "マイクロビームX線照射後のミトコンドリア活性の変化"【招待講演】, 第 60 回日本放射線影響学会大会, 要旨集 P90, [京葉銀行文化プラザ・千葉] (2017/10). N
- 26) 浜田 涼, 小野 莉菜, 神長 輝一, 木村 由佳, 鈴木 啓司, 横谷 明德, "ヒト正常細胞への X 線照射によるミトコンドリア量及び ATP 産生量の変化", 第 60 回日本放射線影響学会大会, 要旨集 P126, [京葉銀行文化プラザ・千葉] (2017/10). N
- 27) 西久保 開, 泉 雄大, 藤井 健太郎, 松本 義久, 横谷 明德, "シンクロトロン放射を用いた CD スペクトル測定による DNA 修復タンパク質 XRCC4 の溶液中での構造解析", 第 60 回日本放射線影響学会大会, 要旨集 P130, [京葉銀行文化プラザ・千葉] (2017/10). N
- 28) 中上 裕貴, 小畑 結衣, 神長 輝一, 横谷 明德, "非照射細胞への放射線誘発 DNA 損傷の導入とライブセル観察による修復動態の観察", 第 60 回日本放射線影響学会大会, 要旨集 P156, [京葉銀行文化プラザ・千葉] (2017/10). N
- 29) 西村 由希子, 横谷 明德, 神長 輝一, 工藤 健一, 宇佐美 徳子, 柿沼 志津子, 今岡 達彦, "放射線による細胞競合を解析するための蛍光タンパク質発現ラット乳腺細胞培養技術", 第 60 回日本放射線影響学会大会, 要旨集 P161, [京葉銀行文化プラザ・千葉] (2017/10). N
- 30) 服部 佑哉, 今岡 達彦, 横谷 明德, 渡辺 立子, "乳腺の末梢芽状突起の低線量放射線応答モデルの構築", 第 60 回日本放射線影響学会大会, 要旨集 P166, [京葉銀行文化プラザ・千葉] (2017/10). N
- 31) 杉本 理峻, 小林 涼香, 服部 佑哉, 渡辺 立子, 立花 章, 横谷 明德, "Ca²⁺を含む細胞内シグナル分子濃度をパラメータとした放射線適応応答誘導の反応経路ネットワークシステムのモデル化の試み", 第 60 回日本放射線影響学会大会, 要旨集 P168, [京葉銀行文化プラザ・千葉] (2017/10). N
- 32) 神長 輝一, 浜田 涼, 宇佐美 徳子, 鈴木 啓司, 横谷 明德, "X 線マイクロビームを用いた細胞小器官への放射線影響", 第 60 回日本放射線影響学会大会, 要旨集 P170, [京葉銀行文化プラザ・千葉] (2017/10). N
- 33) 大内 則幸, "ゲノム突然変異による表現型変化の発がんへの影響", 第 60 回日本放射線影響学会大会, 要旨集 P174, [京葉銀行文化プラザ・千葉] (2017/10). N
- 34) 米谷 佳晃, "水中におけるイオンペア解離カイネティクスの多様性とその起源", 第 31 回分子シミュレーション討論会, 要旨集 105S, [金沢商工会議所・金沢] (2017/11-12). N
- 35) Y. Yonetani, "Critical solvent structure for the rate constant of ion-pair dissociation", 第 33 回化学反応討論会, 要旨集 1P22, [名古屋大・名古屋] (2017/06). N
- 36) 中上 裕貴, "非照射細胞への放射線誘発 DNA 損傷の導入とライブセル観察による修復動態の観察", 平成 29 年度若手放射線生物学研究会専門研究会, 要旨集 P14, [東京大・東京] (2017/09). N
- 37) 浜田 涼, 小野 莉菜, 神長 輝一, 木村 由佳, 横谷 明德, 鈴木 啓司, "X 線照射によるヒト線維芽細胞におけるミトコンドリア量及び活性の変化", 平成 29 年度若手放射線生物学研究会専門研究会, 要旨集 P16, [東京大・東京] (2017/09). N
- 38) 杉本 理峻, 小林 涼香, 服部 佑哉, 渡辺 立子, 立花 章, 横谷 明德, "細胞内シグナル分子濃度をパラメータとした放射線適応応答誘導の反応経路ネットワークシステムのモデル化に向けた取り組み", 平成 29 年度若手放射線生物学研究会専門研究会, 要旨集 P17, [東京大・東京] (2017/09). N
- 39) 西久保 開, 泉 雄大, 藤井 健太郎, 松本 義久, 横谷 明德, "シンクロトロン放射を用いた CD スペクトル測定による DNA 修復タンパク質 XRCC4 の構造解析", 若手放射線生物学研究会平成 29 年度専門研究会, 要旨集 P18, [東京大・東京] (2017/09). N
- 40) 鬼澤 美智, 芳賀 芳範, 田中 成典, 鯉淵 誠也, 横谷 明德, "5-ブロモウラシルを含む DNA の放射線増感の電子物性の研究", 若手放射線生物学研究会平成 29 年度専門研究会, 要旨集 P20, [東京大・東京] (2017/09). N
- 41) 小林 涼香, 横谷 明德, "X 線照射された細胞における Ca²⁺濃度の変化", 若手放射線生物学研究会平成 29 年度専門研究会, 要旨集 P31, [東京大・東京] (2017/09). N
- 42) 鯉淵 誠也, 藤井 健太郎, 横谷 明德, "DNA 構成元素の内殻励起によって誘発される DNA 損傷の定量実験", 若手放射線生物学研究会平成 29 年度専門研究会, 要旨集 P32, [東

- 京大・東京] (2017/09). N
- 43) 小野 莉菜, 横谷 明德, “X 線照射された細胞内部の温度分布測定”, 若手放射線生物学研究会平成 29 年度専門研究会, 要旨集 P33, [東京大・東京] (2017/09). N
- 44) 木村 由佳, 横谷 明德, “放射線照射によるミトコンドリア動態変化の観察”, 平成 29 年度若手放射線生物学研究会専門研究会, 要旨集 P34, [東京大・東京] (2017/09). N
- 45) 小畑 結衣, 中上 裕貴, 横谷 明德, “X 線照射された DNA に対する非照射細胞内の修復応答の研究”, 平成 29 年度若手放射線生物学研究会専門研究会, 要旨集 P35, [東京大・東京] (2017/09). N
- 46) M. A. Herve du Penhoat, A. Souchaud, R. Vuilleumier, M. P. Gaigeot, K. Fujii, A. Yokoya, M. F. Politis, “Fragmentation of Doubly-Ionized Deoxyribose” **[Invited talk]**, Abstr. 1st QST Int. Symp. “Quantum Life Science”, P15, [Chiba, Japan] (2017/07). N
- 47) A. Yokoya, “High Brilliance Synchrotron Radiation as a Tool for Studies of Radiation Damage to DNA and Resulting Cellular Responses” **[Invited talk]**, Abstr. 1st QST Int. Symp. “Quantum Life Science”, P15, [Chiba, Japan] (2017/07). N
- 48) K. Fujii, M. F. Politis, M. A. Herve du Penhoat, A. Yokoya, “Ultrafast Proton Transfer between DNA-Sugar Molecule and Hydrated Water induced by K-Ionization of Oxygen”, Abstr. 1st QST Int. Symp. “Quantum Life Science”, P25, [Chiba, Japan] (2017/07). N
- 49) A. Yokoya, T. Imaoka, T. Ohshima, S. Onoda, K. Owada, K. Fujii, K. Yamakawa, M. Adachi, H. Oba, M. Yamada, H. Kono, H. Murakami, N. Ouchi, Y. Yonetani, R. Igarashi, Y. Izumi, S. Tanaka, M. Hatano, S. Takeuchi, “Quantum Life Sciences in QST”, Abstr. 1st QST Int. Symp. “Quantum Life Science”, P28, [Chiba, Japan] (2017/07). N
- 50) K. Ohwada, T. Imaoka, K. Fujii, A. Machida, T. Watanuki, Y. Nishimura, A. Yokoya, “X-ray Small Angle Scattering Measurement for Sectioned Rat Tumor Specimen as the First Step of Speckle Measurement Applying Coherent X-rays”, Abstr. 1st QST Int. Symp. “Quantum Life Science”, P24, [Chiba, Japan] (2017/07). N
- 51) K. Nishikubo, Y. Izumi, K. Fujii, Y. Matsumoto, A. Yokoya, “Structural Analysis of DNA Repair Protein (XRCC4) by Applying Circular Dichroism at Synchrotron VUV Beamline”, Abstr. 1st QST Int. Symp. “Quantum Life Science”, P27, [Chiba, Japan] (2017/07). N
- 52) N. B. Ouchi, “Study of the effect of physical properties of cell on Tumorigenesis using spatially extended model”, Abstr. 33rd Int. Sym. Radiat. Biol. Center, Theme: Cutting Edge of Radiation and Cancer Biology, P42, [Kyoto, Japan] (2017/12). N
- 53) K. Nishikubo, Y. Izumi, K. Fujii, K. Matsuo, Y. Yamamoto, A. Yokoya, “Secondary Structural Analysis of XRCC4 Protein using HiSOR-VUVCD”, Abstr. 22nd Hiroshima Int. Symp. Synchrotron Radiat., P86-87, [Higashi-Hiroshima, Japan] (2018/03). N

P2-7 Biomolecular Function Research Project

Papers

- 1) T. Hiromoto, F. Meilleur, R. Shimizu, C. Shibazaki, M. Adachi, T. Tamada, R. Kuroki, “Neutron structure of the T26H mutant of T4 phage lysozyme provides insight into the catalytic activity of the mutant enzyme and how it differs from that of wild type.” *Protein Sci.* **26**, 1953-63 (2017). N
- 2) K. Maekawa, M. Adachi, Y. Matsuzawa, Q. Zhang, R. Kuroki, Y. Saito, M. B. Shah, “Structural Basis of Single-Nucleotide Polymorphisms in Cytochrome P450 2C9”, *Biochemistry* **56**, 5476-80 (2017). N
- 3) M. Adachi, Y. Kagotani, R. Shimizu, H. Ohba, Y. Kurosaki, M. Saeiki, Y. Yonetani, A. Yokoya “Start of study for understanding and application of quantum coherence in proteins” 1st QST Int. Symp. “Quantum Life Science”, [Chiba, Japan] (2017/07). N
- 4) 柴崎 千枝, 清水 瑠美, 新井 栄揮, 安達 基泰, “ヒトカゼインキナーゼ II の触媒活性に係わる新たな水素結合ネットワークの発見”, 2017 年度量子ビームサイエンスフェスタ (第 9 回 MLF シンポジウム, 第 35 回 PF シンポジウム), P1-096L, [茨城県立県民文化センター・水戸] (2018/03). N

Book

- 1) K. Akutsu, M. Adachi, Y. Kawakita, “J-PARC Workshop 「Deuterated Materials Enhancing Neutron Science for Structural Function Applications」” JAEA-Review 2018-002, 36 Pages, (2018). N

Press・TV

- 1) “薬物代謝の個人差を究明～薬物代謝酵素の特性を明らかにして副作用を抑えた薬剤開発に道筋～”, プレス発表: 科学新聞, 日刊工業新聞(オンライン版)に掲載 (2017/10/30). N

P2-8 Biomolecular Structure and Dynamics Research Project

Papers

- 1) S. Fujiwara, “Dynamic aspects of amyloid fibrils of a-synuclein related to the pathogenesis of Parkinson's disease”, *J. Alzheimers Dis. Parkinsonism*, **7**, 310 (2017). N
- 2) H. Ohno, K. Takeda, S. Niwa, T. Tsujinaka, Y. Hanazono, Y. Hirano and K. Miki, “Crystallographic characterization of the high-potential iron-sulfur protein in the oxidized state at 0.8 Å resolution”, *PLoS ONE*, **12**, e0178183 (2017). N
- 3) T. Hiromoto, F. Meilleur, R. Shimizu, C. Shibazaki, M. Adachi, T. Tamada, R. Kuroki, “Neutron structure of the T26H mutant of T4 phage lysozyme provides insight into the catalytic activity of the mutant enzyme and how it differs from that of wild type.” *Protein Sci.* **26**, 1953-63 (2017). N
- 4) K. Yonezawa, N. Shimizu, K. Kurihara, Y. Yamazaki, H. Kamikubo and M. Kataoka, “Neutron crystallography of photoactive yellow protein reveals unusual protonation state of

- Arg52 in the crystal”, *Sci. Rep.*, **7**, 9361 (2017). N
- 5) S. Fujiwara, T. Chatake, T. Matsuo, F. Kono, D. Tominaga, K. Shibata, A. Sato-Tomita and N. Shibayama, “Ligation-Dependent Picosecond Dynamics in Human Hemoglobin as Revealed by Quasielastic Neutron Scattering”, *J. Phys. Chem. B*, **121**, 8069-77 (2017). N
- 6) T. Matsuo, D. Tominaga, F. Kono, K. Shibata and S. Fujiwara, “Modulation of the picosecond dynamics of troponin by the cardiomyopathy-causing mutation K247R of troponin T observed by quasielastic neutron scatter”, *Biochem. Biophys. Acta*, **1865**, 1781-89 (2017). N
- Proceedings**
- 1) 藤原 悟, “蛋白質の構造とダイナミクスの相関”, ISSP WORKSHOP 「小角・反射率・高分解能研究会～JRR3 の再稼働を見据えて～」, [東京大・柏] (2017/04). N
- 2) 平野 優, 福原 宏章, 有木 真吾, 中 裕規, 上田 光宏, 玉田 太郎, “シマミズ由来低温活性を保持する糖質分解酵素の結晶構造”, 第 17 回日本蛋白質科学会年会, 要旨集 3P-008, [仙台国際センター・仙台] (2017/06). N
- 3) 玉田 太郎, 長谷 成記, 平野 優, 小坂 恵, 上村 一雄, 金尾 忠芳, “無機硫黄化合物加水分解酵素の結晶構造”, 第 17 回日本蛋白質科学会年会, 要旨集 3P-020, [仙台国際センター・仙台] (2017/06). N
- 4) 玉田 太郎, “電子伝達タンパク質の中性子結晶構造解析”, 第 17 回 iBIX 研究会, [いばらき量子ビーム研究センター・東海村] (2017/06). N
- 5) T. Tomoyori, “The design of a versatile TOF neutron diffractometer providing a complementary use of neutron and X-ray scattering from biomacromolecular single-crystal with large unit cells”, *Int. Conf. Neutron Optics (NOP 2017)*, [Nara, Japan] (2017/07). N
- 6) S. Fujiwara, “Detection of multiscale protein dynamics by quasielastic neutron scattering”, Mini-Symposium "Frontier of Protein Dynamics Research", [Tokai, Japan] (2017). N
- 7) T. Tamada, “Neutron Protein Crystallography at J-PARC/MLF”, Mini-Symposium "Frontier of Protein Dynamics Research", [Tokai, Japan] (2017). N
- 8) T. Tamada, “High-resolution neutron crystal structural studies of electron transfer proteins”, 第 55 回日本生物物理学会年会, 要旨集 2SMA-4, [熊本大・熊本] (2017/09). N
- 9) S. Fujiwara, T. Matsuo, F. Kono, S. Takata, Y. Sugimoto, T. Kikuchi, K. Nakajima and T. Chatake, “Coordinated analysis of protein hydration water by small-angle scattering, quasielastic neutron scattering, and neutron crystallography”, 第 55 回日本生物物理学会年会, 要旨集 1pos074, [熊本大・熊本] (2017/09). N
- 10) F. Kono, T. Matsuo, S. Takata, Y. Sugimoto and S. Fujiwara, “Structural characterization of amyloid fibrils of human α -synuclein by small-angle scattering”, 第 55 回日本生物物理学会年会, 要旨集 3pos018, [熊本大・熊本] (2017/09). N
- 11) T. Matsuo, F. Kono and S. Fujiwara, “Effects of E244D mutation of cardiac troponin T on the structure of thin filaments by small-angle X-ray scattering”, 第 55 回日本生物物理学会年会, 要旨集 3pos079, [熊本大・熊本] (2017/09). N
- 12) 松尾 龍人, 荒田 敏昭, 小田 俊郎, 中島 健次, 河村 聖子, 菊地 龍弥, 藤原 悟, “中性子準弾性散乱による蛋白質と水と水のダイナミクス解析”, MLF チョッパーユーザーミーティング “DIRECTION 2017”, [いばらき量子ビーム研究センター・東海村] (2017/10). N
- 13) S. Fujiwara, “Protein deuteration using algal peptone for neutron scattering”, J-PARC Workshop “Deuterated materials enhancing neutron science for structure function applications”, [Tokai, Japan] (2017/10). N
- 14) 平野 優, 栗原 和男, 日下 勝弘, 木村 成伸, 三木 邦夫, 玉田 太郎, “酸化型 NADH シトクロム *b5* 還元酵素の中性子構造解析”, 平成 29 年度日本結晶学会年会, 要旨集 24-P-51, [JMS アステールプラザ・広島] (2017/11). N
- 15) 平野 優, 中 裕規, 有木 真吾, 上田 光宏, 玉田 太郎, “シマミズ由来 α アミラーゼの低温活性発現機構”, 平成 29 年度日本結晶学会年会, 要旨集 24-P-55, [JMS アステールプラザ・広島] (2017/11). N
- 16) 玉田 太郎, “立体構造から迫る酵素の低温活性発現機構”, 第 2 回次世代生物研究会, [大阪府立大・大阪] (2017/11). N
- 17) 平野 優, 栗原 和男, 日下 勝弘, 木村 成伸, 三木 邦夫, 玉田 太郎, “NADH シトクロム *b5* 還元酵素の中性子構造解析”, 日本中性子科学会第 17 回年会, 要旨集 C2-03, [福岡大・福岡] (2017/12). N
- 18) 栗原 和男, 平野 優, 玉田 太郎, “高分子量タンパク質結晶を測定可能な J-PARC 単結晶中性子回折装置”, 日本中性子科学会第 17 回年会, 要旨集 P1-45, [福岡大・福岡] (2017/12). N
- 19) 玉田 太郎, “モノクローナル完全ヒトアゴニスト抗体 KMTR2 により惹起される TRAIL-R2 の超重合状態”, 2017 年度生命科学系学会合同年次大会, 要旨集 2PW07-6, [神戸ポートアイランド・神戸] (2017/12). N
- 20) 平野 優, 有木 真吾, 中 裕規, 上田 光宏, 玉田 太郎, “シマミズ由来生デンブレン分解酵素の低温活性保持機構”, 2017 年度生命科学系学会合同年次大会, 要旨集 3P-0108, [神戸ポートアイランド・神戸] (2017/12). N
- 21) 玉田 太郎, “中性子と X 線を相補的に用いたタンパク質の構造解析”, 2017 年度第 2 回水とナノ構造研究会, [東北大・仙台] (2018/03). N
- 22) 平野 優, “X 線と中性子を利用した酸化還元タンパク質の高分解能立体構造解析”, 日本生物物理学会北海道支部会, [北海道大・札幌] (2018/03). N
- Patent**
- 1) 玉田 太郎, 平野 優, “低温活性が改善された酵素及びその製造方法”, 出願 2017-219234 (2017/11/14). N

P3-1 Laser Compton Scattering Gamma-ray Research Project

Papers

- 1) H. Ohgaki, I. Daito, H. Zen, T. Kii, K. Masuda, T. Misawa, R. Hajima, T. Hayakawa, T. Shizuma, M. Kando, and S. Fujimoto, “Nondestructive Inspection System for Special Nuclear Material Using Inertial Electrostatic Confinement Fusion Neutrons and Laser Compton Scattering Gamma-rays”, *IEEE Trans. Nucl. Sci.* **64**, 1635-40 (2017). N
- 2) T. Hayakawa, T. Nakamura, H. Kotaki, M. Kando, T. Kajino, “Explosive Nucleosynthesis Study Using Laser Driven γ -ray Pulses”, *Quantum Beam Sci.* **1** (1), 3 (2017). N
- 3) M. Fujiwara, K. Nakai, N. Takahashi, T. Hayakawa, T. Shizuma, S. Miyamoto, G. T. Fan, A. Takemoto, M. Yamaguchi, M. Nishimura, “Production of medical ^{99m}Tc isotope via photonuclear reaction”, *Phys. Part. Nuclei* **48**, 124-33 (2017). N
- 4) J. W. Shin, M. K. Cheoun, T. Kajino, T. Hayakawa, “Short-baseline electron antineutrino disappearance study by using neutrino

- sources from $^{13}\text{C} + ^9\text{Be}$ reaction”, *J. Cosmol. Astropart. Phys.*, JCAP 04, 004 (2017). N
- 5) J. K. Koga and T. Hayakawa, “Possible precise measurement of Delbrück scattering using polarized photon beams”, *Phys. Rev. Lett.* **118**, 204801 (2017). N
 - 6) M. Omer and R. Hajima, “Including Delbrück Scattering in GEANT4”, *Nucl. Instrum. Meth. Phys. Res. B*, **405**, 43-49 (2017). N
 - 7) Y. Taira, T. Hayakawa and M. Katoh, “Gamma-ray vortices from nonlinear inverse Thomson scattering of circularly polarized light”, *Sci. Rep.* **7**, Article number: 5018 (2017). N
 - 8) F. Wang, B. H. Sun, Z. Liu, R. D. Page, C. Qi, C. Scholey, S. F. Ashley, L. Bianco, I. J. Cullen, I. G. Darby, S. Eeckhaudt, A. B. Garnsworthy, W. Gelletly, M. B. Gomez-Hornillos, T. Grahn, P. T. Greenlees, D. G. Jenkins, G. A. Jones, P. Jones, D. T. Joss, R. Julin, S. Juutinen, S. Ketelhut, S. Khan, A. Kishada, M. Leino, M. Niikura, M. Nyman, J. Pakarinen, S. Pietri, Z. Podolyak, P. Rahkila, S. Rigby, J. Saren, T. Shizuma, J. Sorri, S. Steer, J. Thomson, N. J. Thompson, J. Uusitalo, P. M. Walker, S. Williams, H. F. Zhang, W. Q. Zhang, L. H. Zhu, “Spectroscopic factor and proton formation probability for the $d_{3/2}$ proton emitter $^{151\text{m}}\text{Lu}$ ”, *Phys. Lett. B*, **770**, 83-87 (2017). N
 - 9) T. Kawasaki, S. Naito, Y. Sano, T. Hayakawa, T. Shizuma, R. Hajima, and S. Miyamoto, “Measurement of deflection on germanium and gold prisms using 1.7 MeV laser Compton scattering γ -rays”, *Phys. Lett. A*, **381** (36), 3129-33 (2017). N
 - 10) N. Nakamura, R. Kato, T. Miyajima, M. Shimada, T. Hotei and R. Hajima, “S2E simulation of an ERL-based high-power EUV-FEL source for lithography”, *IOP Conf. Series: J. Phys.: Conf. Series* **874**, 012013 (2017). N
 - 11) T. Shizuma, T. Hayakawa, I. Daito, H. Ohgaki, S. Miyamoto, and F. Minato, “Low-lying dipole strength in ^{52}Cr ”, *Phys. Rev. C* **96**, 044316 (2017). N
 - 12) R. Hajima and R. Nagai, “Generating carrier-envelope-phase stabilized few-cycle pulses from a free-electron laser oscillator”, *Phys. Rev. Lett.* **119**, 204802 (2017). N
- Proceedings**
- 1) T. Miyajima, K. Harada, Y. Honda, E. Kako, R. Kato, T. Miura, N. Nakamura, T. Obina, M. Shimada, R. Takai, K. Umemori, M. Yamamoto, R. Hajima, R. Nagai, T. Hotei, N. Nishimori, “60 pC Bunch Charge Operation of the Compact ERL at KEK.”, *Proc. 8th Int. Part. Accel. Conf. (IPAC-2017)*, 890-93, [Copenhagen, Denmark] (2017/05). N
 - 2) N. Nakamura, R. Kato, T. Miyajima, M. Shimada, R. Hajima, T. Hotei, “S2E Simulation of an ERL-Based High-Power EUV-FEL Source for Lithography”, *Proc. 8th Int. Part. Accel. Conf. (IPAC-2017)*, 894-97, [Copenhagen, Denmark] (2017/05). N
 - 3) M. Sawamura, R. Hajima, H. Hokonohara, Y. Iwashita, H. Tongu, T. Kubo, T. Saeki, “Press Forming Tests of Superconducting Spoke Cavity for Laser Compton Scattered Photon Sources”, *Proc. 8th Int. Part. Accel. Conf. (IPAC-2017)*, 1031-33, [Copenhagen, Denmark] (2017/05). N
 - 4) M. Koizumi, T. Shizuma, M. Omer and R. Hajima, “Effects of γ -ray Polarization in NRF-based Nondestructive Assay of Nuclear Materials”, *Proc. 58th Annu. Meet. Inst. Nucl. Mater. Manag. (INMM)*, 510-16, [Indian Wells, USA] (2017/07). N
 - 5) 西森 信行, 永井 良治, 沢村 勝, 羽島 良一, “アルカリアンチモン光陰極高電圧電子銃から mA ビーム生成”, 第 14 回日本加速器学会年会, プロシーディングス 41-44, [北海道大・札幌] (2017/08). N
 - 6) 中村 典雄, 加藤 龍好, 宮島 司, 島田 美帆, 布袋 貴大, 羽島 良一, “半導体リソグラフィのための ERL を用いた EUV FEL 光源の S2E シミュレーション”, 第 14 回日本加速器学会年会, プロシーディングス 334-37, [北海道大・札幌] (2017/08). N
 - 7) 羽島 良一, 永井 良治, “数サイクル光パルス発生のための FEL シミュレーション”, 第 14 回日本加速器学会年会, プロシーディングス 843-46, [北海道大・札幌] (2017/08). N
 - 8) 沢村 勝, 羽島 良一, 佐伯 学行, 久保 毅幸, 江並 和宏, 岩下 芳久, 頓宮 拓, 銚之原 久雄, “超伝導スポーク空洞開発の現状”, 第 14 回日本加速器学会年会, プロシーディングス 949-52, [北海道大・札幌] (2017/08). N
 - 9) 阪井 寛志, 梅森 健成, 加古 永治, 許斐 太郎, 沢村 勝, 篠江 憲治, 野上 隆史, 古屋 貴章, 本田 融, “Field emission 抑制のための超伝導空洞組立のクリーン作業改善に向けて”, 第 14 回日本加速器学会年会, プロシーディングス 444-48, [北海道大・札幌] (2017/08). N
 - 10) 沢村 勝, 阪井 寛志, 梅森 健成, 許斐 太郎, 古屋 貴章, “C 形導波管を用いた HOM カップラーの高周波特性”, 第 14 回日本加速器学会年会, プロシーディングス 953-56, [北海道大・札幌] (2017/08). N
- Press・TV**
- 1) “ガンマ線の光渦を発生させる手法を発見 – 新しい同位体分析や非破壊検査技術への応用が期待される –”, プレス発表: 日刊工業新聞 他 1 件に掲載 (2017/07/10).
 - 2) “光子と光子の相互作用の検証方法を提案 – 量子電磁力学が 20 世紀に予測した現象の理解が期待される –”, プレス発表: Excite ニュース 他 14 件に掲載 (2017/05/15).

P3-2 Beam Engineering Section

Papers

- 1) Y. Ishii, T. Kojima, “Reduction of the divergence angle of an incident beam to enhance the demagnification factor of a two-stage acceleration lens in a gas ion nanobeam system of several tens of keV”, *Nucl. Instrum. Meth. Phys. Res. B*, **420**, 12-17 (2018). N, 3-23
- 2) R. Sano, S. Hayakawa, H. Hayashi, Y. Ishii, H. Nishikawa, “Micro-structuring of epoxy resists containing nanoparticles by proton beam writing”, *Nucl. Instrum. Meth. Phys. Res. B*, **404**, 228-32 (2017). S
- 3) Y. Ishii, T. Ohkubo, Tomihiro Kamiya, “Reduction of a beam diameter by decreasing the divergence angle of an incident beam in a compact ion microbeam system producing several-hundred-keV beam”, *Nucl. Instrum. Meth. Phys. Res. B*, **404**, 65-68 (2017). N, 3-23
- 4) T. Ohkubo, Y. Ishii, “Beam diameter reduction by optimization of an extraction condition in a compact ion microbeam system”, *Physics Procedia*, **90**, 79-84, (2017). N, 3-24
- 5) T. Yanagida, M. Koshimizu, Y. Fujimoto, S. Kurashima, K. Iwamatsu, A. Kimura, M. Taguchi, G. Okada, N. Kawaguchi, “Analysis of excitation density effects on the scintillation properties of Ce:Gd₂SiO₅ (GSO) crystals”, *Nucl. Instrum. Meth. Phys. Res. B*, **409**, 27-30 (2017). C, 3-10
- 6) M. Koshimizu, S. Kurashima, A. Kimura, M. Taguchi, T. Yanagida, Y. Fujimoto, K. Asai, “Analysis of linear energy

transfer effects on the scintillation properties of a Bi₄Ge₃O₁₂ crystal”, Nucl. Instrum. Meth. Phys. Res. B, **409**, 19-22 (2017).

C, 3-10

7) 百合 庸介, 倉島 俊, “放射線利用研究のための高エネルギーイオンビーム照射技術の開発”, 応用物理, 第 **86** 巻, 第 10 号, 881-86 (2017/10).

C, 3-13

8) H. Hayashi, S. Matsuzaki, K. Nakajima, K. Narumi, Y. Saitoh, M. Tsujimoto, M. Toulemonde, and K. Kimura, “Local heating induced by single MeV C₆₀ ion impacts”, Nucl. Instrum. Meth. Phys. Res. B, **406**, 591-95 (2017).

T, 3-03

9) R. Soma, Y. Saitoh, M. Sakamaki, K. Amemiya, A. Iwase, and T. Matusi, “Irradiation effect on magnetic properties of FeRh thin films with energetic C₆₀ cluster ion beam”, AIP Advances online available Vol. 8 Issue 5, 056433 (2018).

T, 3-17

10) K. Yoshino, K. Suzuki, Y. Yamada, T. Satoh, M. Finsterbusch, K. Fujita, T. Kamiya, A. Yamazaki, K. Mima, M. Hirayama, and R. Kanno, “Lithium distribution analysis in all-solid-state lithium battery using microbeam particle-induced X-ray emission and particle-induced gamma-ray emission techniques”, Int. J. PIXE, **27**, 01n02, 11-20 (2017).

S, 3-04

11) T. Segawa, S. Harada, S. Ehara, K. Ishii, T. Satoh, T. Kamiya, K. Sera, S. Goto, “Encapsulated Protamine-Hyaluronic Acid Particles for Targeting Carboplatin Directed by Radiation”, Int. J. PIXE, **27**, 01n02, 37-42 (2017).

S, 2-40

12) H. Kojima, Y. Kaneno, M. Ochi, S. Semboshi, F. Hori, Y. Saitoh, N. Ishikawa, Y. Okamoto, A. Iwase, “Ion species/energy dependence of irradiation -induced lattice structure transformation and surface hardness of Ni₃Nb and Ni₃Ta intermetallic compounds”, Mater. Trans. **58**, 739748 (2017).

T, 1-43

13) H. Kojima, M. Ochi, Y. Kaneno, S. Semboshi, F. Hori, Y. Saitoh, A. Iwase, “Thermal stability of energetic ion irradiation induced amorphization for Ni₃Nb and Ni₃Ta intermetallic compounds”, Trans. Mater. Res. Soc. Jpn., **42**, 41-45 (2017).

T, 1-43

14) R. Mayumi, S. Semboshi, Y. Okamoto, Y. Saitoh, T. Yoshiie, A. Iwase, “Radiation enhanced precipitation of solute atoms in AlCu binary alloys -energetic ion irradiation experiment and computer simulation-”, Trans. Mater. Res. Soc. Jpn., **42**, 9-14 (2017).

T, 1-43

15) M. Ochi, H. Kojima, K. Fukuda, Y. Kaneno, S. Semboshi, F. Hori, Y. Saitoh, A. Iwase “Thermal stability of irradiation-induced metastable lattice structures in NiTi intermetallic compound”, Trans. Mater. Res. Soc. Jpn., **43**, 53-56 (2018).

T, 1-43

16) M. Ochi, H. Kojima, F. Hori, Y. Kaneno, S. Semboshi, Y. Saitoh, Y. Okamoto, N. Ishikawa, A. Iwase, “Effect of elastic collisions and electronic excitation on lattice structure of NiTi bulk intermetallic compound irradiated with energetic ions”, Nucl. Instrum. Meth. Phys. Res. B, **427**, 14-19 (2018).

T, 1-43

17) 小嶋 拓治, “放射線化学を利用した線量計測と国際規格”, RADIOISOTOPES, **66**, 513-18 (2017).

E, G

18) 小嶋 拓治, “放射線加工処理等における大線量計測の現状について”, 放計協ニュース, **59**, 2-7 (2017).

E, G

19) 平野 貴美, 千葉 敦也, 山田 圭介, 薄井 絢, “MeV 級 C₆₀ ビームの生成”, 放射線と産業, **142** 号, 24 (2017).

T, 3-25

Proceedings

1) T. Satoh, W. Kada, T. Ohkubo, N. Yamada, A. Yokoyama, T. Kamiya, Y. Ishii, “Development and Application of an Elemental Mapping System using an Ion Microbeam Development and Application of an Elemental Mapping System using an Ion Microbeam”, 15th Int. Conf. Adv. Mater. (IUMRS-ICAM 2017), [Kyoto, Japan] (2017/08).

S

2) Y. Ishii, T. Ohkubo, H. Kashiwagi, Y. Miyake, “Development of Prototype PIG Ion Source with Electric Magnet for Compact Ion Microbeam System”, Abstr. 17th Int. Conf. Ion Source, [Geneva, Switzerland] (2017/10).

N, 3-23

3) 長澤 尚胤, 木村 敦, 出崎 亮, 山田 尚人, 江夏 昌志, 佐藤 隆博, 石井 保行, 田口 光正, “プロトンビームライティング法による生体適合性ヒドロゲルの微細加工”, 平成 29 年度繊維学会年次大会, [タワーホール船堀, 東京] (2017/06).

S

4) N. Nagasawa, A. Kimura, A. Idesaki, N. Yamada, M. Koka, T. Satoh, Y. Ishii, M. Taguchi, “Microfabrication of Biocompatible Hydrogel by Proton Beam Writing”, 15th Int. Conf. Adv. Mater. (IUMRS-ICAM 2017), [Kyoto, Japan] (2017/08).

S

5) N. Miyawaki, S. Kurashima, A. Chiba, K. Yoshida, T. Yuyama, T. Ishizaka, K. Yamada, A. Yokoyama, Y. Hirano, T. Satoh, H. Kashiwagi, Y. Yuri, T. Ohkubo, I. Ishibori, S. Okumura, T. Nara, “PRESENT STATUS OF TIARA AT QST”, Proc. 14th Annu. Meet. Part. Accel. Soc. Jpn., 1409-11 [Sapporo, Japan] (2017/08).

C, 3-08

6) 百合 庸介, 湯山 貴裕, 吉田 健一, 石坂 知久, 石堀 郁夫, 山本 元, “TIARA サイクロトロンにおける重イオンビームの連続均一照射技術の開発”, Proc. 14th Annu. Meet. Part. Accel. Soc. Jpn., 720-23, [Sapporo, Japan] (2017/08).

C, 3-13

7) N. Miyawaki, M. Fukuda, S. Kurashima, H. Kashiwagi, “Effect of phase bunching of the central region on extracted beam from the TIARA AVF cyclotron”, Proc. 14th Annu. Meet. Part. Accel. Soc. Jpn. 384-85, [Sapporo, Japan] (2017/08).

C, 3-08

8) H. Kashiwagi, N. Miyawaki, S. Kurashima, “Test of beam transport based on beam emittance measurement in the injection line of the TIARA AVF cyclotron”, Proc. 14th Annu. Meet. Part. Accel. Soc. Jpn. 1123-25, [Sapporo, Japan] (2017/08).

C, 3-08

9) 金子 優斗, 林 秀臣, 石井 保行, 西川 宏之, “光導波路応用へ向けた PDMS 系コンポジットの陽子線照射効果の検討”, 2017 年放電学会年次大会, 講演論文集 No.3-6, [琉球大・西原町] (2017/11).

S, 3-02

10) 澁谷 泰一, 林 秀臣, 石井 保行, 中河原 僚介, 丸山 大貴, 内田 諭, 西川 宏之, “誘電泳動法を用いた PMMA ピットへの金ナノ粒子捕集における電極材料依存性”, 2017 年放電学会年次大会, 講演論文集 No.3-7, [琉球大・西原町] (2017/11).

S, 3-02

Patents

1) S. Furuyama, Y. Nagai, J. Moriyama, Y. Yuri, T. Yuyama, T. Ishizaka, I. Ishibori, K. Yoshida, Y. Maekawa, H. Koshikawa, T. Yamaki, M. Asano, “Method for producing porous polymer film and porous polymer film”, US9708453 (2017/07/18 認定).

C, 3-13

2) 山本 元, 相塚 万理恵, 百合 庸介, 湯山 貴裕, 吉田 健一, 石坂 知久, “防水通気フィルタ及び防水通気部材”, 特願 2018-058021 (2018/03/26 出願).

C, 3-13

External Research Groups Except for Takasaki Advanced Radiation Research Institute

Papers

- 1) C. Ohmori, M. Paoluzzi, “RF Amplifier using VRF151G and BLF 574 Power RF Mosfets”, CHARM Radiation Test Report. **G, 1-06**
- 2) T. Hwang, M. Fukuda, S. Nogami, A. Hasegawa, H. Usami, K. Yabuuchi, K. Ozawa, H. Tanigawa, “Effect of self-ion irradiation on hardening and microstructure of tungsten”, Nucl. Mater. Energy, **9**, 430-35 (2016). **C, T, S, 1-35**
- 3) H. Fujita, Y. Uemura, S. Sakurada, K. Azuma, Q. Zhou, T. Toyama, N. Yoshida, Y. Hatano, T. Chikada, Y. Oya, “The damage depth profile effect on hydrogen isotope retention behavior in heavy ion irradiated tungsten”, Fusion Eng. Des., **125**, 468-72 (2017). **T, 1-37**
- 4) K. Azuma, Y. Uemura, S. Sakurada, H. Fujita C. Hu, Y. Hatano, N. Yoshida M. Shimada, D. Buchenauer, T. Chikada, Y. Oya, “Effect of sequential Fe²⁺- C⁺implantation on deuterium retention in W”, Fusion Eng. Des., **124**, 231-34 (2017). **T, 1-37**
- 5) S. Sakurada, Y. Uemura, H. Fujita, K. Azuma, T. Toyama, N. Yoshida, T. Hinoki, S. Kondo, Y. Hatano, M. Shimada, D. Buchenauer, T. Chikada, Y. Oya, “Impact of Annealing on Deuterium Retention Behavior in Damaged W”, Fusion Sci. Tech., **72**, 785-88 (2017). **T, 1-37**
- 6) Y. Oya, K. Azuma, A. Togari, Q. Zhou, Y. Hatano, M. Shimada, R. Kolasinski, D. Buchenauer, “Interaction of hydrogen isotopes with radiation damaged tungsten”, Advances in Intelligent Systems and Computing, **660**, 41-49 (2017). **T, 1-37**
- 7) Y. Uemura, S. Sakurada, H. Fujita, K. Azuma, Q. Zhou, Y. Hatano, N. Yoshida, H. Watanabe, M. Oyaizu, K. Isobe, M. Shimada, D. Buchenauer, R. Kolasinski, T. Chikada, Y. Oya, “Effect of helium irradiation on deuterium permeation behavior in tungsten”, J. Nucl. Mater., **490**, 242-46 (2017). **T, 1-37**
- 8) 岩瀬 彰宏, “Ni基金属間化合物のイオンビーム照射誘起構造相変態と表面硬さに及ぼす効果”, 金属学会報「まてりあ」, **57** 巻, 51-59 (2018). **T, 1-43**
- 9) N. Inoue and Y. Kawamura, “Infrared defect dynamics—Nitrogen-vacancy complexes in float zone grown silicon introduced by electron irradiation”, J. Appl. Phys., **123**, 185701 (2018). **E, 1-47**
- 10) K. Akamatsu, N. Shikazono, T. Saito, “New method for estimating clustering of DNA lesions induced by physical/chemical mutagens using fluorescence anisotropy”, Anal. Biochem. **536**, 78-89 (2017). **T, 2-09**
- 11) 赤松 憲, “細胞の運命を左右する「クラスターDNA損傷」の探求 - FRETを利用して -”, 放射線と産業 **143**, 21-25 (2017). **T, 2-09**
- 12) 松田 康裕, 奥山 克史, 山本 洋子, 大木 彩子, K. M. Mosammat, 佐野 英彦, 斎藤 隆史, “フッ化物含有知覚過敏抑制材による象牙質表面の脱灰抑制効果”, 日本歯科保存学雑誌, **60**, 273-81 (2017). **S, 2-37**
- 13) K. Yagi, H. Yamamoto, R. Uemura, Y. Matsuda, K. Okuyama, T. Ishimoto, T. Nakano, M. Hayashi, “Use of PIXE/PIGE for sequential Ca and F measurements in root carious model”, Sci. Rep. **7**, 13450 (2017). **S, 2-37**
- 14) 中井 啓, “ホウ素中性子捕捉療法に用いる新規ホウ素化合物の開発の現状”, 茨城県立医療大学紀要 (1342-0038), **22**, 1-9 (2017). **S, 2-38**
- 15) 金子 優斗, 林 秀臣, 西川 宏之, “TiO₂/ポリジメチルシロキサンコンポジット材料の陽子線による改質”, 電気学会論文誌 A, **137** (11), 652-53 (2017). **S, 3-02**
- 16) 中河原 僚介, 内田 諭, 澁谷 泰一, 西川 宏之, “誘電泳動アセンブリにおける金ナノ粒子ダイナミクスの数値シミュレーション”, 電気学会論文誌 E **137** (4), 107-14 (2017). **S, 3-02**
- 17) B. Tsuchiya, S. Nagata, T. Sugiyama and K. Tokunaga, “Effects of Ion Irradiation on H₂O and CO₂ Absorption and Desorption Characteristics of Li₂ZrO₃ and Pt-coated Li₂ZrO₃”, Int. J. Hydrogen Energ., **42**, 23746-50 (2017). **G, 3-09**
- 18) 土屋 文, “反跳粒子検出法による全固体リチウムイオン二次電池内の軽元素の動的解析”, 日本表面科学, J. Surf. Sci. Soc. Jpn., **38** (4), 182-87 (2017). **G, 3-09**

Proceedings

- 1) 大森 千広, Paoluzzi Mauro, 田村 文彦, 長谷川 豪志, 杉山 泰之, “LIU (LHC入射器アップグレード)-RFの現状とCERNメイラン地区加速器の広帯域化”, 第14回日本加速器学会年会, プロシーディングス 12-16, [北海道大・札幌] (2017/08). **G, 1-06**
- 2) 川端 康夫, 松田 浩朗, 松元 和伸, 田頭 茂明, 石井 恒次, 大森 千広, 芝田 達伸, 吉岡 正和, “放射線環境下 (J-PARC) における測位センサネットワークシステムの耐久性と防災用アプリの適用計画”, 第14回日本加速器学会年会, プロシーディングス 1282-86, [北海道大・札幌] (2017/08). **G, 1-06**
- 3) 橋本 義徳 他, “小型 OSL 線量計の大線量応答”, 平成 29 年放射線安全取扱部会年次大会, ポスター発表, [淡路夢舞台国際会議場・淡路] (2017/10). **G, 1-06**
- 4) K. Irisawa, T. Taniguchi, M. Namiki I. G. Loderio, T. Osugi, T. Sakakibara, O. Nakazawa, Y. Meguro, H. Kinoshita, “Heat treatment of phosphate-modified cementitious matrices for safe storage of secondary radioactive aqueous wastes in Fukushima Daiichi Nuclear Power Plant”, Proc. ICAPP 2017, 17618, [Kyoto & Fukui, Japan] (2017/04) **N, 1-36**
- 5) 渡辺 恭志, 武内 伴照, 小沢 治, 駒野目 裕久, 赤堀 知行, 土谷 邦彦, “A New Radiation Hardened CMOS Image Sensor for Nuclear Plant”, Proc. pf 2017 Int. Image Sensor Workshop (IISW2017), (<http://www.imagesensors.org/Past%20Workshops/2017%20Workshop/2017%20Papers/P41.pdf>), 206-09, [Hiroshima, Japan] (2017/05-06). **G, 1-40**
- 6) D. Hamaguchi, M. Ando, H. Kurotaki, H. Tanigawa, “Study on the synergetic effect of H and He with displacement damage of F82H by means of ion-irradiations”, Proc. 18th Int. Conf. Fusion Reactor Mater. (ICFRM-18), [Aomori, Japan] (2017/06). **T, S, 1-42**
- 7) N. Inoue and Y. Kawamura, “Synthetic reference sample by electron irradiation for IR measurement of 10¹⁴ cm⁻³ carbon concentration in silicon crystal”, Abstr. 29th Int. Conf. Defects Semicond., TuP-14, [Matsue, Japan] (2017/08). **E, 1-47**
- 8) 井上 直久, 河村 裕一, “シリコン結晶中の低濃度炭素の測定 (XI) 電子線照射による 1×10¹³ cm⁻³ までの赤外参照試料とブロックゲージの作製”, “Measurement of carbon concentration in silicon crystal (XI) Fabrication of reference sample and block gauge down to 10¹³ cm⁻³”, 第 78 回応用物理学会, 予稿集 No. 6p-A-503-8, [福岡国際会議場・福岡] (2017/08). **E, 1-47**
- 9) 井上 直久, 河村 裕一, “シリコン結晶中の低濃度炭素の測定 (XII) 10¹³ cm⁻³ 迄の検出と 10¹⁴ cm⁻³ までの高精度測定”, “Measurement of carbon concentration in silicon crystal (XII) Detection of 10¹³ cm⁻³”, 第 78 回応用物理学会, 予稿集 No. 6p-A-503-9, [福岡国際会議場・福岡] (2017/08). **E, 1-47**
- 10) 井上 直久, 河村 裕一, “シリコン結晶中の低濃度炭素の測定 (XIII) 参照試料とブロックゲージとスペクトルと測定プロセスの共有による高感度高精度測定ネットワークの形成と実用化”,

- “Measurement of carbon concentration in silicon crystal (XIII) Procedure down to 10^{14} cm^{-3} ”, 第 78 回応用物理学会, 予稿集 No. 6p-A-503-10, [福岡国際会議場・福岡] (2017/08). **E, 1-47**
- 11) N. Inoue and Y. Kawamura, “Accurate measurement of carbon concentration in silicon crystal down to 10^{14} cm^{-3} by the second generation infrared absorption spectroscopy,” Abstr. 17th Int. Conf. DRIP (Defects-Recognition, Imaging and Physics in Semiconductors), 1C-06, [Valladolid, Spain] (2017/10). **E, 1-47**
- 12) N. Inoue and Y. Kawamura, “Nitrogen - point defect complexes in as-grown, irradiated and annealed FZ silicon studied by infrared absorption” Abstr. 17th Int. Conf. DRIP (Defects-Recognition, Imaging and Physics in Semiconductors), 1C-06, [Valladolid, Spain] (2017/10). **E, 1-47**
- 13) 井上 直久, 河村 裕一, “シリコン結晶の高感度赤外吸収と赤外欠陥動力学(12)窒素ドーパ FZ 結晶の熱処理によるライフタイム減少について”, “High sensitivity infrared absorption spectroscopy and infrared defect dynamics of silicon crystal (12) On the lifetime degradation of nitrogen doped FZ silicon by annealing”, 第 65 回応用物理学会春季学術講演会, 予稿集 No. 18p-D103-21, [早稲田大・東京] (2018/03). **E, 1-47**
- 14) 井上 直久, 河村 裕一, “シリコン結晶中の低濃度炭素の測定 (XIV) $1 \times 10^{13} \text{ cm}^{-3}$ までの赤外用人工ブロックゲージの作製と共有”, “Measurement of carbon concentration in silicon crystal (XIV) Fabrication of reference sample and block gauge down to 10^{13} cm^{-3} for IR measurement”, 第 65 回応用物理学会春季学術講演会, 予稿集 No. 18p-D103-22, [早稲田大・東京] (2018/03). **E, 1-47**
- 15) 井上 直久, 河村 裕一, “シリコン結晶中の低濃度炭素の測定 (XV) $1 \times 10^{13} \text{ cm}^{-3}$ までの第二世代赤外吸収測定の国際ネットワーク”, “Measurement of carbon concentration in silicon crystal (XV) “2nd generation IR measurement down to 10^{13} cm^{-3} in the international network”, 第 65 回応用物理学会春季学術講演会, 予稿集 No. 18p-D103-23, [早稲田大・東京] (2018/03). **E, 1-47**
- 16) N. Inoue and Y. Kawamura, “Measurement of Low Carbon Concentration in Polycrystalline Silicon by Second Generation Infrared Absorption Spectroscopy”, Abstr. 15th High Purity and High Mobility Semicond., H02-1184, (Electrochem. Soc.), [Cancun, Mexico] (2018/02). **E, 1-47**
- 17) N. Inoue and Y. Kawamura, “Measurement of low concentration nitrogen in CZ silicon by infrared absorption spectroscopy”, Abstr. 15th High Purity and High Mobility Semicond., H02-1182, (Electrochem. Soc.), [Cancun, Mexico] (2018/02). **E, 1-47**
- 18) A. Ito, “Observation of DNA oxidative damage induced by high LET radiation”, 第 55 回日本生物物理学会, [熊本大・熊本] (2017/09). シンポジウム, “量子ビーム技術を活用した放射線生物物理学の最前線”, シンポジスト. **C, 2-04**
- 19) 税所 康正, 伊藤 敦, “OH ラジカルの収量(G 値)の LET 依存性に関する数理モデル”, 日本放射線影響学会第 60 回大会, [京葉銀行文化プラザ・千葉] (2017/10). **C, 2-04**
- 20) 松尾 陽一郎, 泉 佳伸, 古澤 佳也, 下川 卓志, 清水 喜久雄, “重粒子線による突然変異誘発の分子機構の解析”, 日本放射線影響学会第 60 回大会, 要旨集 P-138, [京葉銀行文化プラザ・千葉] (2017/10). **C, 2-25**
- 21) Y. Kaneko, H. Hayashi, H. Nishikawa, “Effects of Proton Beam Irradiation on Optical Properties of TiO_2 /polydimethylsiloxane Composite Material”, Proc. 23rd Int. Conf. Ion Beam Anal. (IBA 2017), P1-33, 122-23, [Sydney, Australia] (2017/10). **S, 3-02**
- 22) Y. Kaneko, H. Hayashi, H. Nishikawa, “Effects of Proton Beam Irradiation on Polydimethylsiloxane Containing TiO_2 Nanoparticles, D1-O30-006, Symposium D-1, Innovative material technologies utilizing ion beams”, IUMRS-ICAM2017, [Kyoto, Japan] (2017/08-09). **S, 3-02**
- 23) 西川 宏之, “プロトンビームライティングによる多種多様な材料の微細加工・改質と応用”, 一般社団法人大阪ニュークリアサイエンス協会 (ONSA), 第 72 回 ONSA 先端科学研究会, [住友クラブ・大阪] (2017/07). **S, 3-02**
- Book**
- 1) K. Mima, K. Fujita, Y. Kato, S. Inoue, S. Sakabe, “Nuclear Reaction Analysis of Li-Ion Battery Electrodes by Laser-Accelerated Proton Beams”, Chapter 17, “Applications of Laser-driven Particle Acceleration”, ALPA Book, Taylor & Francis Group, to be published, 16p (2018). **S, 3-04**
- Patent**
- 1) 渡辺 恭志, 小沢 治, 武内 伴照, 土谷 邦彦, “光検出素子, 固体撮像装置及びその駆動方法”, 特願 2017-078851 (2017/04). **G, 1-40**

Appendix 2 Type of Research Collaboration and Facilities Used for Research

Paper No.	Type of Research Collaboration*1					Irradiation Facilities*2						Paper No.	Type of Research Collaboration*1					Irradiation Facilities*2					
	Joint Res.	Entr. Res.	Coop. Res.	Inter. Use	Ext. Use	C	T	S	I	E	G		Joint Res.	Entr. Res.	Coop. Res.	Inter. Use	Ext. Use	C	T	S	I	E	G
1-01	●								◎			1-46	●										◎
1-02	●					◎	◎		◎	◎		1-47				●					◎		
1-03					●				◎														
1-04				●							◎	2-01				●		◎					
1-05	●										◎	2-02				●		◎					◎
1-06					●						◎	2-03	●					◎					
1-07					●	◎						2-04	●					◎					
1-08				●		◎						2-05	●					◎					
1-09				●		◎						2-06	●					◎					
1-10				●				◎				2-07				●		◎					
1-11				●		◎						2-08				●				◎			
1-12				●					◎			2-09				●		◎					
1-13				●		◎						2-10	●					◎					
1-14				●					◎			2-11	●					◎					
1-15				●N								2-12	●					◎					
1-16				●		◎						2-13	●					◎					
1-17				●						◎		2-14	●					◎					
1-18				●						◎		2-15	●										◎
1-19				●						◎	◎	2-16				●			◎				
1-20				●							◎	2-17				●		◎					
1-21					●				◎			2-18	●					◎					
1-22				●			◎		◎			2-19				●		◎					
1-23	●								◎			2-20	●					◎					
1-24				●		◎					◎	2-21	●					◎					
1-25	●										◎	2-22				●		◎					
1-26	●										◎	2-23	●										◎
1-27	●										◎	2-24	●					◎					
1-28	●									◎	◎	2-25	●					◎					
1-29				●						◎		2-26	●										◎
1-30				●						◎		2-27				●		◎					
1-31				●						◎		2-28				●		◎					
1-32	●									◎		2-29	●					◎					
1-33					●						◎	2-30	●										◎
1-34				●			◎	◎	◎			2-31	●					◎					
1-35	●						◎					2-32				●N							
1-36					●					◎	◎	2-33	●					◎					
1-37					●		◎					2-34			●				◎				
1-38					●		◎	◎	◎			2-35			●				◎				
1-39				●							◎	2-36			●				◎				
1-40					●						◎	2-37			●				◎				
1-41					●						◎	2-38			●				◎				
1-42				●			◎	◎	◎			2-39			●				◎				
1-43					●		◎					2-40			●				◎				
1-44					●						◎	2-41	●							◎			
1-45	●										◎												

Paper No.	Type of Research Collaboration*1					Irradiation Facilities*2						Paper No.	Type of Research Collaboration*1					Irradiation Facilities*2					
	Joint Res.	Entr. Res.	Coop. Res.	Inter. Use	Ext. Use	C	T	S	I	E	G		Joint Res.	Entr. Res.	Coop. Res.	Inter. Use	Ext. Use	C	T	S	I	E	G
3-01	●							◎															
3-02	●							◎															
3-03			●						◎														
3-04	●							◎															
3-05				●					◎														
3-06	●								◎														
3-07				●																	◎		
3-08				●			◎																
3-09					●																	◎	
3-10					●		◎																
3-11	●						◎																
3-12				●																		◎	
3-13	●						◎																
3-14	●							◎															
3-15			●					◎		◎													
3-16	●							◎															
3-17			●					◎															
3-18			●							◎													
3-19	●									◎													
3-20	●								◎														
3-21	●								◎														
3-22					●																	◎	
3-23				●N																			
3-24				●N																			
3-25				●				◎	◎	◎													
4-01							◎	◎	◎	◎													
4-02							◎																
4-03								◎	◎	◎													
4-04											◎	◎											
4-05											◎	◎											
4-06							◎	◎	◎	◎													
4-07							◎	◎	◎	◎													
4-08							◎	◎	◎	◎	◎	◎											
Total	45	0	11	36	21	43	19	22	25	14	30												
*1 Type of Research Collaboration Joint Res. : Joint research with external users Entr. Res. : Research entrusted to QST Coop. Res. : Cooperative research with plural universities through The University of Tokyo Inter. Use : Internal use Ext. Use : Common use based on two programs of "QST-facility-use" and "Creation of Research Platforms and Sharing of Advanced Research Infrastructure" supported from MEXT												*2 Utilization of Irradiation Facilities C : AVF Cyclotron T : 3 MV Tandem Electrostatic Accelerator S : 3 MV Single-ended Electrostatic Accelerator I : 400 kV Ion Implanter E : 2 MV Electron Accelerator G : Co-60 Gamma-ray Irradiation Facilities N : Non-use of irradiation facilities at TARRI											

Appendix 3 Examples of Typical Abbreviation Name for Organizations in National Institutes for Quantum and Radiological Science and Technology, and Japan Atomic Energy Agency

◆Directorate, Institute, Center, Laboratory etc.

【QST (量子ビーム科学技術研究開発機構): National Institutes for Quantum and Radiological Science and Technology】

QuBS	量子ビーム科学研究部門	:	<u>Q</u> uantum <u>B</u> eam <u>S</u> cience Research Directorate
TARRI	高崎量子応用研究所	:	<u>T</u> akasaki <u>A</u> dvanced <u>R</u> adiation <u>R</u> esearch <u>I</u> nstitute
NFI	那珂核融合研究所	:	<u>N</u> aka <u>F</u> usion <u>I</u> nstitute
RFI	六ヶ所核融合研究所	:	<u>R</u> okkasho <u>F</u> usion <u>I</u> nstitute
KPSI	関西光科学研究所	:	<u>K</u> ansai <u>P</u> hoton <u>S</u> cience <u>I</u> nstitute
NIRS	放射線医学総合研究所	:	<u>N</u> ational <u>I</u> nstitute of <u>R</u> adiological <u>S</u> ciences

【JAEA (日本原子力研究開発機構): Japan AtomErgy Agency】

NSRI	原子力科学研究所	:	<u>N</u> uclear <u>S</u> cience <u>R</u> esearch <u>I</u> nstitute
NSEC	原子力基礎工学研究センター	:	<u>N</u> uclear <u>S</u> ciences and <u>E</u> ngineering <u>C</u> enter
MSRC	物質科学研究センター	:	<u>M</u> aterials <u>S</u> ciences <u>R</u> esearch <u>C</u> enter
FRCC	高速炉サイクル研究開発センター	:	<u>F</u> ast <u>R</u> eactor <u>C</u> ycle System Research and Development <u>C</u> enter
ORDI	大洗研究所	:	<u>O</u> arai <u>R</u> esearch and <u>D</u> evelopment <u>I</u> nstitute
HTGRC	高温ガス炉研究開発センター	:	<u>H</u> TGR Research and Development <u>C</u> enter
WMDC	環境技術開発センター(大洗研)	:	<u>W</u> aste <u>M</u> anagement and <u>D</u> ecommissioning Technology Development <u>C</u> enter
NFCEL	核燃料サイクル工学研究所	:	<u>N</u> uclear <u>F</u> uel <u>C</u> ycle <u>E</u> ngineering <u>L</u> aboratories
NBTC	環境技術開発センター(サイクル研)	:	<u>N</u> uclear <u>B</u> ackend <u>T</u> echnology <u>C</u> enter
TRTDC	再処理技術開発センター	:	<u>T</u> okai <u>R</u> eprocessing <u>T</u> echnology <u>D</u> evelopment <u>C</u> enter
CLADS	廃炉国際共同研究センター	:	<u>C</u> ollaborative <u>L</u> aboratories for <u>A</u> dvanced <u>D</u> ecommissioning <u>S</u> cience
J-PARC	J-PARCセンター	:	<u>J</u> - <u>P</u> ARC Center

◆Department, Division, Center etc.

【QST】

- ・量子ビーム科学研究部門、研究企画室
Research Planning and Promotion Office, QuBS, QST
- ・量子ビーム科学研究部門、高崎量子応用研究所、先端機能材料研究部
Department of Advanced Functional Materials Research, TARRI, QST
- ・量子ビーム科学研究部門、高崎量子応用研究所、放射線生物応用研究部
Department of Radiation-Applied Biology Research, TARRI, QST
- ・量子ビーム科学研究部門、高崎量子応用研究所、放射線高度利用施設部
Department of Advanced Radiation Technology, TARRI, QST
- ・量子ビーム科学研究部門、高崎量子応用研究所、東海量子ビーム応用研究センター
Tokai Quantum Beam Science Center, TARRI, QST

- ・量子ビーム科学研究部門、高崎量子応用研究所、管理部
Department of Administrative Services, TARRI, QST
- ・量子ビーム科学研究部門、関西光科学研究所、光量子科学研究部
Department of Advanced Photon Research, KPSI, QST
- ・量子ビーム科学研究部門、関西光科学研究所、量子生命科学研究所
Department of Quantum Beam Life Science, KPSI, QST
- ・核融合エネルギー研究開発部門、那珂核融合研究所、ITERプロジェクト部
Department of ITER Project, NFI, QST
- ・核融合エネルギー研究開発部門、六ヶ所核融合研究所、核融合炉材料研究開発部
Department of Fusion Reactor Materials Research, RFI, QST
- ・放射線医学総合研究所、放射線障害治療研究部
Department of Basic Medical Sciences for Radiation Damages, NIRS, QST
- ・放射線医学総合研究所、加速器工学部
Department of Accelerator and Medical Physics, NIRS, QST

【JAEA】

- ・原子力基礎工学研究センター、環境・放射線科学ディビジョン
Environment and Radiation Sciences Division, NSEC, JAEA
- ・原子力基礎工学研究センター、燃料・材料工学ディビジョン
Fuels and Materials Engineering Division, NSEC, JAEA
- ・物質科学研究センター、放射光エネルギー材料研究ディビジョン
Energy and Environment Materials Science Division, MSRC, JAEA
- ・先端基礎研究センター
Advanced Science Research Center, JAEA
- ・環境技術開発センター(大洗研)、材料試験炉部
Department of JMTR, WMDC, JAEA
- ・高温ガス炉研究開発センター、水素熱利用研究開発部
Department of Hydrogen and Heat Application Research and Development, HTGRC, JAEA
- ・J-PARCセンター、加速器ディビジョン
Accelerator Division, J-PARC, JAEA
- ・再処理技術開発センター、環境保全部
Waste Management Department, TRTDC, JAEA
- ・環境技術開発センター、基盤技術研究開発部
Radioactive Waste Processing and Disposal Research Department, NBTC, JAEA
- ・環境技術開発センター(核燃料サイクル工学研)、再処理技術開発試験部開発部
Department of Reprocessing Technology Development, NBTC, JAEA
- ・高速炉・新型炉研究開発部門、燃料サイクル設計部
Fuel Cycle Design Department, Sector of Fast Reactor and Advanced Reactor Research and Development, JAEA
- ・廃炉国際共同研究センター、廃棄物処理処分ディビジョン
Waste Management Division, CLADS, JAEA

QST Takasaki Annual Report 2017

(Ed) Hiroyuki YAMAMOTO

Date of Publishing : March 2019

Editorial committee : Hiroyuki YAMAMOTO, Yasuhiko KOBAYASHI, Yasunari MAEKAWA,
Yuichi SAITOH, Takahiro SATOH, Noboru SUZUKI, Kazumasa NARUMI,
Koichi HIROTA and Satoshi WATANABE

Publication : Takasaki Advanced Radiation Research Institute
National Institutes for Quantum and Radiological Science and Technology
1233 Watanuki, Takasaki, Gunma Japan 370-1292

Tel : +81-27-346-9610

E-mail : taka-tiaraplan@qst.go.jp

Homepage : <http://www.taka.qst.go.jp>

©2018 National Institutes for Quantum and Radiological Science and Technology
All Rights Reserved

Printed in Japan

QST-M-16

<http://www.qst.go.jp>